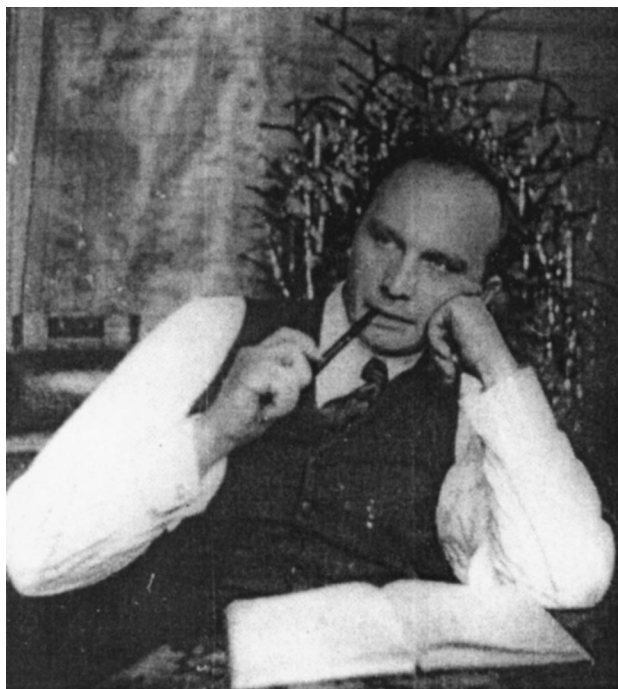


Lev Vasilievich Shubnikov (1901–1937): On the centennial of his birth

[DOI: 10.1063/1.1414585]



September 29, 2001 marks the 100th anniversary of the birth of Lev Vasilievich Shubnikov, one of the most outstanding experimental physicists of the twentieth century. Shubnikov was the founder and director of the first cryogenics laboratory in the USSR, and his pioneering work laid the foundation for many extremely important fields in modern condensed-matter physics. In terms of the quantity and the level of the results obtained in various fields of physics, he can be placed in the same rank of such giants of experimental physics as Faraday, Kelvin, and Kamerlingh Onnes.

Shubnikov's scientific career is linked to three cities:

Petrograd (1923–1926)

— the creation of a new method of growing single crystals (the Obreimov–Shubnikov method, *Z. Phys.* **25**, 31 (1924));

— the creation of an optical method of studying plastic deformations in crystals (I. W. Obreimow and L. W. Schubnikow, *Z. Phys.* **41**, 907 (1927)),

Leiden (1926–1930)

— discovery of magnetoresistance oscillations at low temperatures (the Shubnikov–de Haas effect, *Leiden Commun.* **207** a–d; **210** a,b; *Nature* **126**, 500 (1930)),

and Kharkov (1930–1937).

Here, at the Ukrainian Physicotechnical Institute, Shubnikov organized the first cryogenics laboratory in the Soviet Union (and the fourth in the world), which he directed until 1937.

A number of brilliant studies were done at this cryogenics laboratory, among them:

— direct experimental proof (and independent of the Meissner and Ochsenfeld results) of the ideal diamagnetism of pure superconductors (Yu. N. Rjabinin and L. W. Schubnikow, *Nature* **134**, 286 (1934));

— observation of an antiferromagnetic phase transition (jump of specific heat) in layered transition-metal chlorides (O. N. Trapeznikowa and L. W. Schubnikow, *Nature* **134**, 378 (1934));

— studies of the phase diagrams and viscosity of liquid mixtures of nitrogen, oxygen, carbon monoxide, methane, argon, and ethylene (jointly with O. N. Trapeznikowa and N. S. Rudenko);

— the experimental discovery of type-II superconductors (Yu. N. Rjabinin and L. W. Schubnikow, *Nature* **135**, 581 (1935); L. W. Schubnikow, W. I. Chotkewitsch, G. D.

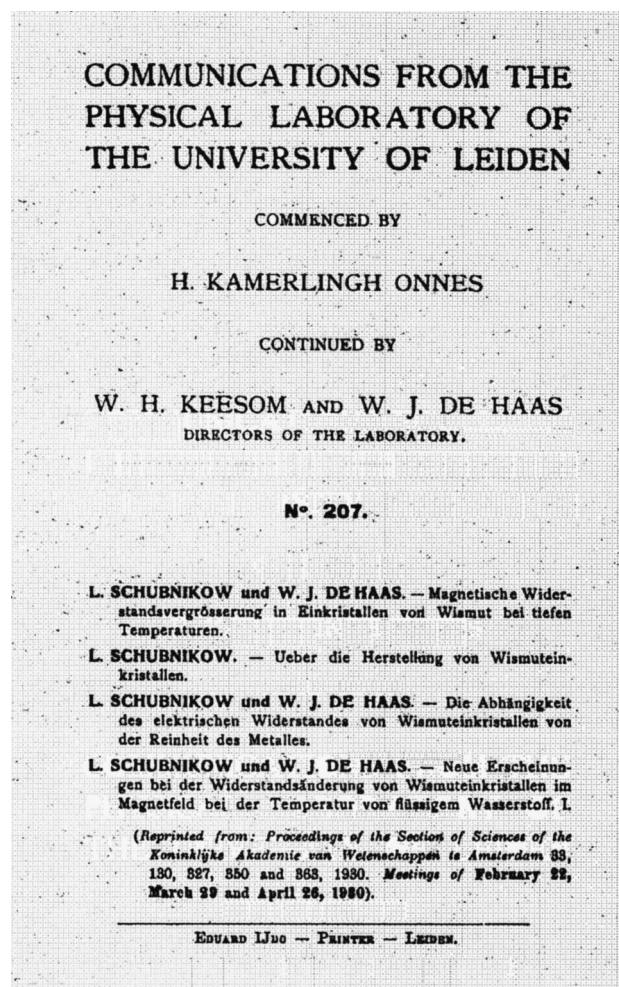


FIG. 1. Cover of the Leiden laboratory journal containing the first publication of the Shubnikov–de Haas effect.

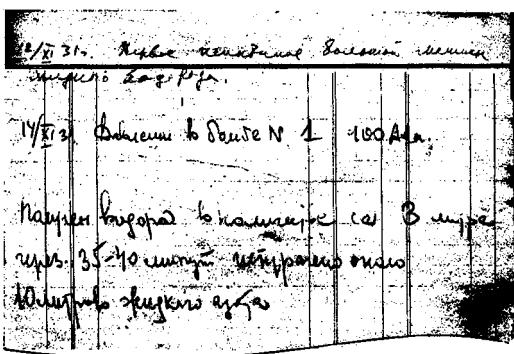


FIG. 2. Handwritten notes of L. V. Shubnikov in his laboratory journal on obtaining the first batch of liquid hydrogen (from the archive of B. G. Lazarev).

12/XI 31. First test of large liquid hydrogen machine . . .
 14/XI 31. Obtained hydrogen in the amount of ca. 3 liters . . .

Schepelew, and Yu. N. Rjabinin, Phys. Z. Sowjetunion **10**, 165 (1936));

— measurement of the magnetic moment of the proton (B. G. Lazarew and L. W. Schubnikow, Phys. Z. Sowjetunion **10**, 117 (1936); *ibid.* **11**, 445 (1937));

— optical studies of liquid helium II (A. K. Kikoin and L. W. Schubnikow, Nature **138**, 641 (1936));

— a study of neutron absorption at low temperatures in hydrogen, boron, silver, and cadmium (jointly with V. Fomin, F. Houtermans, I. V. Kurchatov, A. I. Leipunskii, L. B. Rusinov, and G. Ya. Shchepkin, Nature **138**, 326 (1936); *ibid.* **138**, 505 (1936));

— a study of the destruction of superconductivity by electric current and magnetic field (L. W. Schubnikow and N. E. Alexeyevskii, Nature **138**, 545 (1936); *ibid.* **138**, 804 (1937));

— experimental observation of an intermediate state of superconductors in magnetic field (L. W. Schubnikow and I. Nakhutin, Nature **139**, 589 (1937));

— identification of the magnetic character of a phase transition (the kink in the temperature dependence of the magnetic susceptibility in transition-metal chlorides) (L. W. Schubnikow and S. S. Schalyt, Phys. Z. Sowjetunion **11**, 566 (1937));

— a study of the thermal conductivity of solid helium (jointly with K. A. Kikoin (1936–1937));

— a study of a phase transition in solid methane under pressure (jointly with O. N. Trapeznikov and G. A. Milyutin, Nature **144**, 632 (1939)).

In 1937 L. V. Shubnikov became a victim of Stalinist terror.

In terms of the number of brilliant scientific results and extremely fruitful new directions of research begun and fostered in its six years of existence, Shubnikov's laboratory is apparently without equal in the world.

The creative explosion that marked the period 1934–1937 attested to Shubnikov's creative energy and scientific potential of the highest sort, which had only begun to be realized in the lifetime of this outstanding physicist of the twentieth century.

Yu. A. Freïman

This anniversary issue of the journal *Low Temperature Physics* is devoted to the memory of Lev Vasilievich Shubnikov. It includes articles on the physics of quantum magnetic oscillation phenomena, superconductivity, magnetism, and cryocrystals — fields of study whose creation owes much to the contributions made by Shubnikov. The Editorial Board of this journal extends its profound gratitude to all of the authors who contributed to this issue.

Editorial Board

Translated by Steve Torstveit

The Shubnikov–de Haas effect and high pressure

E. S. Itskevich*

L. F. Vereshchagin Institute of High Pressure Physics, Russian Academy of Sciences, 142190 Troitsk, Moscow District, Russia

(Submitted March 14, 2001)

Fiz. Nizk. Temp. **27**, 941–944 (September–October 2001)

[DOI: 10.1063/1.1401175]

*Dedicated to the memory of L. V. Shubnikov
and O. N. Trapeznikova*

Lev Vasilievich Shubnikov, who was born 100 years ago at the dawn of the twentieth century (September 29, 1901), would play a leading role in the development of quantum physics of the solid state. A century has also passed since the birth of his wife and co-worker, Olga Nikolaevna Trapeznikova, who was an active participant in much of Shubnikov's work. The field of solid-state physics, which arose at the end of the first quarter century, underlies all of the achievements of electronics, the principal technological base of the information revolution of the twentieth century.

Quantum oscillations of the electrical resistance in metal single crystals in a magnetic field — the so-called Shubnikov–de Haas (SdH) effect — were discovered by Shubnikov jointly with Prof. de Haas, his scientific supervisor at Leiden, Holland (1930). Perfect single crystals of bismuth, which made it possible to observe the SdH effect, were grown by Shubnikov as the first task assigned by de Haas to the young scientist who had come to him for practical training. Later these same crystals were used by de Haas and van Alphen in their discovery of analogous oscillations of the magnetic susceptibility (the de Haas–van Alphen (dHvA) effect). Both types of oscillations can be used to obtain experimental information about the energy spectrum of the charge carriers in metals and semiconductors.

Before turning to the topic stated in the title of this article, I would like to give some information about Shubnikov himself. He founded the first cryogenics laboratory in the Soviet Union, at the Kharkov Physicotechnical Institute in 1931. He did his practical training in Leiden (1926–1930) in the laboratory of Kamerlingh Onnes, who, as you know, was the first to obtain liquid helium. Shubnikov mastered the art of experimentation with liquid helium and therefore was able in a comparatively short time to set up facilities at Kharkov for obtaining “all” the liquid gases — nitrogen, hydrogen, and helium, making it possible to do research on a broad spectrum of low-temperature problems. In particular, significant work was done on superconductivity. Shubnikov's experiments gave food for thought to some of the greatest theorists of our country. His work with Trapeznikova on measurement of the low-temperature specific heat of transition-metal chlorides and with S. S. Shalyt on measurement of their magnetic susceptibility led to the discovery of transitions to an antiferromagnetic state, the theory of which was created by L. D. Landau. Skipping ahead, it may be

noted that the theory of quantum oscillation effects was created in the 1960s by I. M. Lifshits and A. M. Kosevich.

My acquaintance with the life and undertakings of L. V. Shubnikov grew out of a rather close acquaintance with O. N. Trapeznikova. It began in the 1960s during joint research on the specific heat of highly anisotropic solids and continued for many years. Shubnikov and Trapeznikova's son, Misha Shubnikov, who is also a physicist, worked for many years in Shalyt's laboratory at the Leningrad Physicotechnical Institute and did research on the properties of semiconductors under hydrostatic pressure, continuing the research on semiconductors under pressure which was begun there in 1965. The first paper was on a study of the influence of pressure on the magneto-phonon oscillations in *n*-InSb (S. S. Shalyt, E. S. Itskevich, and co-workers).

My acquaintance with Olga Trapeznikova was a multifaceted one. Her long life (she died in 1997) was filled with tragic circumstances. After the arrest and execution of her husband Shubnikov in 1937 and her trials during the Second World War, Trapeznikova found the strength to continue her scientific work at St. Petersburg University and to raise her son. She was the perfect example of the St. Petersburg intelligentsia, incorporating all the intellectual values of the early twentieth century. Not only was she widely educated, she had a love of people and displayed a sympathy that was rare in those times.

It was also my good fortune to be associated (including scientific collaboration) with other students of Shubnikov's who would gain lasting recognition in science: N. E. Alekseevskii, B. G. Lazarev, and Yu. N. Ryabinin, in addition to Trapeznikova and Shalyt. These were very productive and pleasant associations. The most important contact was with the founder and director of the Institute of High Pressure Physics of the Academy of Sciences, Leonid Fedorovich Vereshchagin, whose scientific career in physics also started at Shubnikov's laboratory (1934–1939) with research on the magnetic susceptibility of alloys. Although Vereshchagin's further activities were devoted to high-pressure research, he remembered his younger years in low-temperature studies. In 1958, when forming the Institute of High Pressure Physics (IHPP) with the main task of mastering the synthesis of diamonds at high pressure, he invited me, as a specialist in low-temperature physics and a representative of the Institute of Physical Problems, to effect another “synthesis” — to

combine high pressures and low temperatures in the study of the fundamental properties of solids. The field begun by Shubnikov was branching and developing.

THE SdH AND dHvA EFFECTS

We shall not distinguish between these two quantum effects, since in practice they give the same information about the object of study in different kinds of measurements. They arise as a result of the quantization of the energy levels of the conduction electrons in a magnetic field (Landau quantization) and are inherent to metals and semiconductors. These effects were discovered thanks to the availability of helium temperatures and the creation of methods of obtaining perfect single crystals of metals and semiconductors.

Both effects involve oscillations of certain properties in a magnetic field at low temperatures, and the possibility of observing them is contingent upon the quality of the samples, low temperatures, and a high external magnetic field.

The oscillation period in the inverse magnetic field is related to the area of the extremal (minimal or maximal) section of the Fermi surface by a plane perpendicular to the field direction, $\Delta(1/H) = eh/cS$, where S is the area of the extremal cross section of the Fermi surface, and e , c , and h are well-known global constants. By varying the field direction, one can find the shape of the Fermi surface. By measuring the temperature dependence of the amplitude of the oscillations one can determine the carrier effective mass corresponding to the given cross section of the Fermi surface, and the field dependence of this same amplitude can be used to assess the scattering of carriers on impurities, i.e., the quality of a crystalline sample. The SdH and dHvA effects have proved to be the most convenient and reliable methods of experimental determination of the Fermi surface.

ELECTRONIC–TOPOLOGICAL TRANSITIONS UNDER PRESSURE

The creation of a high-pressure chamber permitting investigation of the Fermi surface at high hydrostatic pressures by means of the oscillation effects was inspired by a paper by I. M. Lifshits (1960) in which he predicted qualitative changes in the Fermi surface of metals (a phase transition of order $2\frac{1}{2}$). Lifshits's idea can be easily understood. The Fermi surfaces of metals in momentum (wave-vector) space can be represented in the most general form as corrugated tubes (straight or curved; see Fig. 1). In the first case the extremal cross section of the tube can coincide with the boundaries (faces) of the Brillouin zone — the elementary Wigner–Seitz cell in momentum space in an extended zone scheme. In the second case the tube can have the form of a corrugated ring or system of rings placed inside the cell or on its edges (Fig. 1). One feels an irresistible urge to compress the extremal cross section of the Fermi surface (the neck) until it vanishes and thus to obtain separated closed parts of the Fermi surface. This can naturally be done by applying pressure. In principle the opposite process — the joining of disconnected parts of the Fermi surface into single “tubes” by applying pressure — is also possible, usually in the hole parts of the Fermi surface.

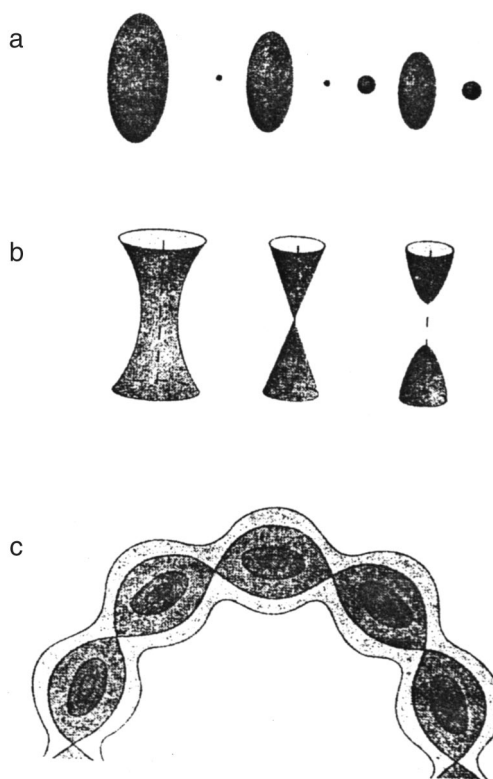


FIG. 1. Formation of a new cavity (a), the breakoff of the neck (b), and the transition of a system of corrugated tubes to ellipsoids (c).

HIGH-PRESSURE CHAMBERS

Low-temperature hydrostatic pressure chambers suitable for oscillation experiments were constructed in 1962–1963 (E. S. Itskevich). These were piston-and-cylinder systems in which a pressure medium (usually a mixture of organic liquids) was used in the working volume to transmit the pressure to the crystalline sample. The piston generating the pressure could be fixed at different degrees of compression of the medium. This technique of creating hydrostatic pressure in a volume with practically no loss of pressure is fundamentally different from the “clamped cell” technique proposed by Chester and Johnson in 1953, in which volumeless anvils are fixed in position and hydrostatic conditions are not realized.

ELECTRONIC–TOPOLOGICAL TRANSITIONS IN CADMIUM

Electronic–topological (ET) transitions are phase transitions of order $2\frac{1}{2}$ under pressure. The destruction of the connectedness of the corrugated tubes of the Fermi surface of metals at an ET transition can be observed not only by means of oscillation effects but also from the changes of the trajectories of the current carriers in a magnetic field, i.e., from the angle dependence of the magnetoresistance in a high static magnetic field.

Single-crystal cadmium samples have been investigated by both methods, and complete agreement was found for the characteristics of the ET transitions observed (S. L. Bud'ko, A. N. Voronovskii, A. G. Gapotchenko, and E. S. Itskevich). Figure 2 shows the dHvA oscillations in cadmium, and Fig. 3 shows the ET transitions that occur.

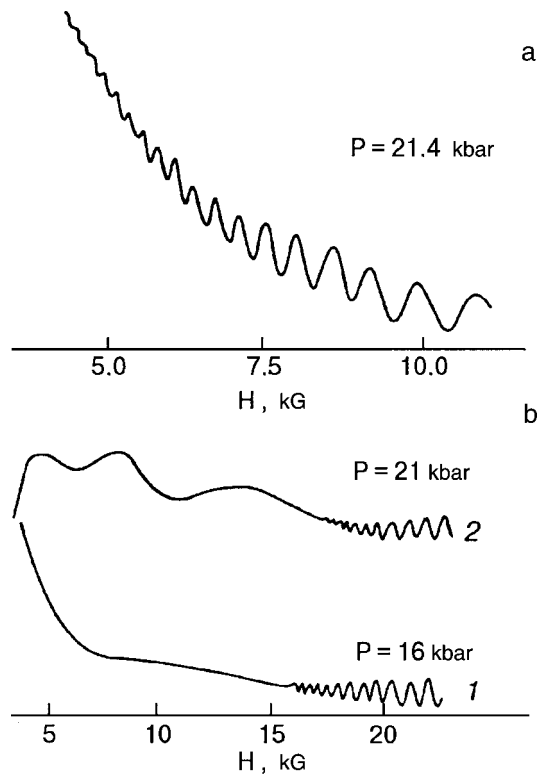


FIG. 2. De Haas–van Alphen oscillations in cadmium, due to new parts of the Fermi surface arising at phase transitions of order $2\frac{1}{2}$; a — frequency of oscillations, $\mathbf{H}||[11\bar{2}0]$; b — frequency of oscillations, $\mathbf{H}||[0001]$; before transition (1), after transition (2).

These results, together with analogous results of B. G. Lazarev and co-workers, the experiments of N. B. Brandt and Ya. G. Ponomarev, and the theory of I. M. Lifshits, were registered as a Discovery (Certificate No. 238). All of this demonstrates the direct (through the participating scientists and their followers) and conceptual links to Shubnikov as the founder of a new field of solid-state physics. The Shubnikov–de Haas effect is the principal tool used in these studies.

Using the SdH oscillations, our group has found ET transitions in bismuth and Bi–Sb alloys (E. S. Itskevich, L. M.

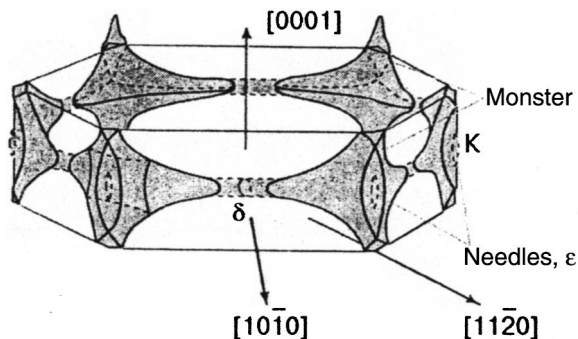


FIG. 3. Schematic illustration of the Fermi surface of cadmium. Open hole surface — the “monster” (second Brillouin zone). There are discontinuities in the basal plane, and open directions do not form along the $[11\bar{2}0]$ and $[10\bar{1}0]$ axes. At the K points there are no “needles.” The dashed lines show transitions in cadmium: necks (δ) and “needles” (ϵ) arise.

Fisher, 1967) in semiconductors, jointly with the Leningrad Physicotechnical Institute (LPTI) and the Physics Institute of the Academy of Sciences (FIAN) in tellurium, and jointly with LPTI in n - and p - Bi_2Te_3 . Successful searches for ET transitions by oscillation methods have also been carried out in other laboratories: at the Department of Low Temperature physics at Moscow State University (N. B. Brandt and co-workers) and at the Donetsk Physicotechnical Institute (A. A. Galkin and co-workers). Also noteworthy is the beautiful work of N. Ya. Minina (Moscow State University), who has discovered a whole series of ET transitions in Bi and BiSb alloys using methods she developed based on the uniaxial deformation of single crystals.

Thus a new field of solid-state physics was created: the investigation of qualitative changes (transitions) in the electronic spectra of metals and semiconductors.

In addition to ET transitions, oscillation methods under pressure have been used to study changes of the Fermi surface in magnetically ordered metals — Fe, Ni, Co, and Cr (IHPP and Institute of General Physics of the Academy of Sciences, 1977–1979). Altogether, our group has published more than 30 papers on the study of oscillation effects under pressure.

Since many laboratories in different countries have been doing research on the various changes of the Fermi surface of metals (not only ET transitions) by means of oscillation methods, the accumulated experimental data is sufficient to permit assessing the applicability of different models under conditions of hydrostatic compression. It has turned out that pseudopotential theory works rather well.

Recently the study of electronic spectra under pressure by means of the SdH oscillations has been extended to two-dimensional systems. For example, it is possible to measure the magnetoresistance and Hall emf in fields up to 7 T at $T = 4.2$ K under pressures up to 2.5 GPa for systems with GaSb/InAs/GaSb quantum wells of various widths and with different types of interfaces. The pressure dependence of the electron and hole concentrations has been determined from an analysis of the observed SdH oscillations and the dependence of the magnetoresistance tensor components in the framework of a model with two types of carriers. It has been shown that a transition from the semimetallic to the semiconductor type of conduction, accompanied by the onset of a region of negative magnetoresistance, occurs under pressure; this region persists up to pressures corresponding to a transition to the insulating state. The existence of a region of negative magnetoresistance can be explained in the framework of the concept of weak localization in a system of two-dimensional electrons. Quantitative information on the concentration and mobility of the carriers in the system has been obtained, and also on the relationship between the elastic and inelastic relaxation times for quasi-two-dimensional electrons and the pressure dependence of these times (E. M. Dizhur *et al.*, IHPP, 1998).

In closing, it can be said that L. V. Shubnikov created a research tool that can be used to study the behavior of the

conduction electrons in metals and semiconductors under pressure.

The further development of solid-state physics has led to the discovery of transitions from some states to other states, with practically no change in crystal structure, in new objects, in particular high- T_c superconducting cuprates and co-

lossal magnetoresistance manganates; these have come to be called “quantum phase transitions.”

E-mail: itskev@hppi.troitsk.ru

Translated by Steve Torstveit

Oriental effect in the magnetoresistance of organic conductors

V. G. Peschanskiĭ*

B. Verkin Institute for Low Temperature Physics and Engineering, National Academy of Sciences of Ukraine, pr. Lenina 47, 61103 Kharkov, Ukraine; V. N. Karazin Kharkov National University, pl. Svobody 4, 61077 Kharkov, Ukraine

R. Atalla

Physics Department of Bir-Zeit University, P.O. Box 28, Bir-Zeit, West Bank, Israel
(Submitted April 6, 2001)

Fiz. Nizk. Temp. **27**, 945–951 (September–October 2001)

The asymptotic behavior of the magnetoresistance of layered conductors of organic origin is discussed for different orientations of a high magnetic field \mathbf{H} relative to the layers. It is shown that when current flows along the normal \mathbf{n} to the layers, the amplitude of the Shubnikov–de Haas quantum oscillations and the smoothly varying part of the magnetoresistance increase sharply at certain angles θ between the vectors \mathbf{H} and \mathbf{n} . An experimental study of the orientational effect in a high magnetic field yields detailed information about the electron energy spectrum of quasi-two-dimensional conductors. © 2001 American Institute of Physics.
[DOI: 10.1063/1.1401176]

The oscillatory dependence of the resistance of rather perfect samples of bismuth as a function of the inverse magnetic field, discovered by Shubnikov and de Haas in Leiden in 1930,^{1,2} permitted the development of a reliable spectroscopic method^{3,4} that is still being used successfully to reconstruct the Fermi surface, a fundamental characteristic of the electron energy spectrum of degenerate conductors, from experimental data.

The Shubnikov–de Haas (SdH) effect and the oscillatory dependence of the magnetization as a function of the inverse magnetic field, discovered the same year,⁵ were long considered to be anomalous behavior of bismuth, which also has other unusual properties. However, these oscillations at low temperatures were later observed in practically all metals, and Landau showed that these effects are due to the presence of features of the density of states of the conduction electrons in a quantizing magnetic field.⁶ Quantum oscillation effects have turned out to be inherent to all degenerate conductors and are observed when the distance between the quantized levels of the electron energy $h\Omega$ exceeds the temperature-related smearing of the Fermi distribution function of the charge carriers but is considerably less than the Fermi energy.

In 1988 SdH oscillations of the magnetoresistance of the organic conductors (BEDT–TTF)₂IBr₂ and (BEDT–TTF)₂I₃ were observed at sufficiently low temperatures in a magnetic field H of several tens of tesla, when the gyration frequency Ω of the electrons is significantly higher than their collision frequency $1/\tau$.^{7–9}

Even more unexpected was the observation of periodically repeating narrow peaks in the dependence of the resistivity ρ on the angle θ between the direction of the field vector of the high magnetic field and the normal \mathbf{n} to the layers during passage of current transverse to the layers.^{7,8}

By now the SdH quantum oscillation effect has been observed in many tetrathiafulvalene salts and tetraselena-

racene halides, which have a layered structure with a pronounced anisotropy of the electrical conduction: the conductivity along the layers is significantly higher than that in the direction transverse to the layers. Consequently, the organic conductors of this family have a metallic type of conductivity with a high resistance to current flowing along the normal to the layers, apparently because of the sharp anisotropy of the velocities of the conduction electrons $\mathbf{v} = \partial\varepsilon(\mathbf{p})/\partial\mathbf{p}$ on the Fermi surface $\varepsilon(\mathbf{p}) = \varepsilon_F$, i.e., their energy

$$\varepsilon(\mathbf{p}) = \sum_{n=0}^{\infty} \varepsilon_n(p_x, p_y) \cos\left\{\frac{anp_z}{h} + \alpha_n(p_x, p_y)\right\}, \quad (1)$$

$$\alpha_n(p_x, p_y) = -\alpha_n(-p_x, -p_y)$$

is weakly dependent on the momentum projection $p_z = \mathbf{p} \cdot \mathbf{n}$ on the normal \mathbf{n} to the layers, so that the maximum values of the functions $\varepsilon_n(p_x, p_y)$ with $n \geq 1$ on the Fermi surface, $A_n = \max \varepsilon_n(p_x, p_y) = \eta_n \varepsilon_F$, are much less than the Fermi energy ε_F .

The Fermi surface of quasi-two-dimensional conductors is open, with a slight corrugation along the p_z axis; the corrugated plane may be rolled up into a cylinder whose base is positioned in the unit cell of momentum space in such a way that the Fermi surface of the layered conductors is a system of slightly corrugated cylinders or a system of planes slightly corrugated along the p_z axis. Small closed cavities associated with anomalously small groups charge carriers may also exist.

In the case of a discrete or discrete–continuous spectrum of electron energies in a magnetic field the features of their density of states repeat periodically with variation of $1/H$, and this is the cause of the quantum oscillation effects. The presence of quantum magnetoresistance oscillations of large amplitude in a magnetic field $\mathbf{H} = (0, H \sin \theta, H \cos \theta)$ in the family of tetrathiafulvalene salts indicates the existence of a rather large number of charge carriers at the Fermi energy

which execute finite motion in a plane orthogonal to the magnetic field, i.e., their orbits $\varepsilon = \text{const}$, $p_H = \mathbf{p} \cdot \mathbf{H}/H = \text{const}$ are closed, and at least one sheet of the Fermi surface is a slightly corrugated cylinder.

The quasi-two-dimensional character of the electron energy spectrum in charge-transfer complexes with a layered structure makes possible an extremely clear manifestation of the SdH effect, since a considerably greater number of conduction electrons at the Fermi energy ε_F are involved in the formation of this effect than in the case of metals, in which relatively few of the charge carriers are involved in the formation of the effect, a fraction of the order of $(h\Omega/\varepsilon_F)^{1/2}$, where $\Omega = eH/m^*c$ is their gyration frequency along the closed orbit in the magnetic field, e and m^* are the charge and cyclotron effective mass of a conduction electron, c is the speed of light, and h is Planck's constant.

The substantial dependence of the magnetoresistance of layered conductors on the orientation of the magnetic field relative to the layers is inherent only to quasi-two-dimensional conductors, and the position of the maxima of the function $\rho(\theta)$ gives detailed information about the shape of the Fermi surface.¹⁰ In contrast to the SdH effect, the orientational effect is not observed in ordinary metals.

It is easy to see that not only the smoothly varying (with H) part of the magnetoresistance but also the amplitude of the SdH oscillations also have sharp peaks at certain angles $\theta = \theta_c$.

We shall assume, solely for the sake of brevity in the calculations, that the Fermi surface of a layered conductor consists of only one corrugated cylinder of arbitrary shape. All of the sections of this cylinder by a plane $\mathbf{p} \cdot \mathbf{H} = \text{const}$ are closed if θ differs from $\pi/2$. The quantum energy levels of the conduction electrons are determined with the aid of the Schrödinger equation

$$\begin{aligned} &\varepsilon(\hat{P}_x, P_y - eHx \cos \theta/c, P_z + eHx \sin \theta/c) \\ &\quad \times \phi_N(x) \exp(iyP_y/h + izP_z/h) \\ &= \varepsilon_N(P_y, P_z) \phi_N(x) \exp(iyP_y/h + izP_z/h) \\ &= \varepsilon_N(P_y, P_z) \phi_N(x) \exp(iyP_y/h + izP_z/h). \end{aligned} \quad (2)$$

Here we have used the Landau gauge, assuming that the vector potential \mathbf{A} of the magnetic field depends only on the coordinate x , so that the Schrödinger equation (2) contains only one differential operator \hat{P}_x and the generalized momentum projections P_y and P_z are good quantum numbers. The Hamiltonian operator is obtained by replacing the kinematic momentum \mathbf{p} in formula (1) for the energy of the charge-carrying quasiparticles by the expression $\hat{\mathbf{P}} - e\mathbf{A}/c$, and the phase $\alpha_n(p_x, p_y)$ has been dropped in Eq. (2). To find the wave functions $\phi(x) \exp(iyP_y/h + izP_z/h)$ of the conduction electrons, one must specify a concrete form of the Hamiltonian, and the problem of determining the electron energy spectrum in the quasiclassical approximation can be solved for an arbitrary form of the functions $\varepsilon_n(p_x, p_y)$.

If it is assumed that the functions $\varepsilon_n(p_x, p_y)$ with $n \geq 1$ are independent of p_x , i.e., that only $\varepsilon_0(\hat{P}_x, P_y - eHx \cos \theta/c)$ contains the differentiation operator

$$\hat{P}_x = i \left(\frac{eHh \cos \theta}{c} \right)^{1/2} \frac{\partial}{\varepsilon \xi},$$

where

$$\xi = \left(\frac{eHh \cos \theta}{c} \right)^{-1/2} (P_y - eHx \cos \theta/c),$$

then the position of the energy levels of the conduction electrons is independent of the position of the center of the orbit, $x_0 = cP_y/(eH \cos \theta)$, and the eigenvalues ε_N of the operator $\varepsilon_0(\hat{P}_x, P_y - eHx \cos \theta/c)$ are also independent of the integral of the motion of the electrons in the magnetic field, $p_H = P_z \cos \theta + P_y \sin \theta$. The energy levels have an even simpler form when $\varepsilon_0(p_x, p_y)$ is a quadratic function of the momenta and all the functions $\varepsilon_n(p_x, p_y)$ with $n \geq 1$ are equal to A_n , i.e., independent of p_x and p_y . In that case the energy levels of the conduction electrons have the form

$$\begin{aligned} \varepsilon_N(p_H) &= (N + 1/2)gh\Omega + \sum_{n=1}^{\infty} A_n \cos\left(\frac{anp_H}{h \cos \theta}\right) \\ &\quad - \frac{1}{g^2 h \Omega} \sum_{n=1}^{\infty} (A_n n)^2 \alpha \sin^2\left(\frac{anp_H}{h \cos \theta}\right), \end{aligned} \quad (3)$$

where

$$\begin{aligned} \alpha &= a^2 \frac{eH \sin^2 \theta}{hc \cos \theta}, \\ g &= \left[1 - \frac{2}{h\Omega} \sum_{n=1}^{\infty} A_n n \alpha \cos\left(\frac{anp_H}{h \cos \theta}\right) \right]^{1/2}, \end{aligned} \quad (4)$$

and the gyration frequency Ω of the charge carriers in the magnetic field is the same on all cross sections of the isoenergy surface $p_H = \text{const}$. In the case of a more complicated dependence of ε_0 on p_x and p_y the energy spectrum is equidistant only at large N ($\Delta \varepsilon_N = \varepsilon_{N+1} - \varepsilon_N = h\Omega$).

The relation between the current density and the electric field E ,

$$j_i = \text{Tr}\{e\hat{v}_i \hat{f}\} = \sigma_{ik} E_k \quad (5)$$

can easily be found by solving the quantum kinetic equation for the statistical operator $\hat{f} = \hat{f}_0 + \hat{f}_1$, where \hat{f}_0 is the statistical operator describing the equilibrium state of the system of electrons and has nonzero components $\hat{f}_0^{NN'}$ only on the diagonal, where they are equal to the Fermi distribution function of the charge carriers $f_0[\varepsilon_N(P_y, P_z)]$, and the operator \hat{f}_1 describes the perturbation of the electron system by the electric field; \hat{v} is the electron velocity operator.

In the linear approximation in the weak electric field the kinetic equation has the form^{11–13}

$$\begin{aligned} &\frac{i}{h} (\varepsilon_N - \varepsilon_{N'}) f_1^{NN'} + \hat{W}_{NN'}(\hat{f}_1) \\ &= e \mathbf{E} \cdot \mathbf{v}_{NN'} \frac{f_0(\varepsilon_N) - f_0(\varepsilon_{N'})}{\varepsilon_N - \varepsilon_{N'}}, \end{aligned} \quad (6)$$

where $\hat{W}(\hat{f}_1)$ is a linear operator describing the scattering of conduction electrons on defects of the crystal and vibrations of the crystal lattice.

In calculating the oscillatory (in the field) components in the expression for the current density (5) one must take consideration that the relaxation time of the conduction electrons exhibits quantum oscillations which arise in the summation over the states of the electrons in the incoming term of the collision integral \hat{W} . Their role is extremely important in the calculation of the asymptotes of the conductivity tensor components σ_{ix} and σ_{xj} in a high magnetic field ($\Omega\tau \gg 1$). However, their contribution to the amplitude of the quantum oscillations of the remaining components of the conductivity tensor is significant only for the small corrections in the parameter $\gamma = 1/\Omega\tau$. In cases where the asymptote of the conductivity tensor components is nonzero in a high magnetic field and it is unnecessary to keep the small corrections in the parameter $1/\Omega\tau$, it is sufficient to know only the diagonal matrix elements of the nonequilibrium statistical operator.

The asymptote of the conductivity tensor component σ_{zz} for $\Omega\tau \gg 1$ has the form

$$\sigma_{zz} = \frac{2eH}{c(2\pi\hbar)^2} \sum_{N=0}^{\infty} dp_H e^2 \tau \bar{v}_z^2 \frac{\partial f_0(\varepsilon_N)}{\partial \varepsilon_N}, \quad (7)$$

where \bar{v}_z is the velocity value averaged over P_y at constant p_H , i.e., the average value of v_z on an electron orbit $\varepsilon = \text{const}$, $p_H = \text{const}$, and τ is the mean free time of the charge carriers, which is equal to their inverse collision frequency.

In calculating σ_{zz} we have made use of the solution of the kinetic equation in the τ approximation, thus giving up reliability in relatively unimportant numerical factors of order unity which do not affect ones ability to extract information about the form of the electron energy spectrum from the galvanomagnetic characteristics.

In a rather strong magnetic field, when not only $\Omega\tau \gg 1$ but also $\hbar\Omega/\varepsilon_F \gg \eta = \eta_1$, the periodic dependence of the kinetic coefficients on $1/H$ is rather complicated. However, in the opposite limiting case $\hbar\Omega/\varepsilon_F \ll \eta$, this dependence has a harmonic form and can easily be separated off in the expression for the current density with the aid of the Poisson formula:

$$\sigma_{zz} = \frac{2}{(2\pi\hbar)^3} - \sum_{k=-\infty}^{\infty} \int d\varepsilon \frac{\partial f_0(\varepsilon)}{\partial \varepsilon} \int dp_H 2\pi m^* e^2 \tau \bar{v}_z^2 \times \exp(2\pi i k N(\varepsilon, p_H)). \quad (8)$$

The drift velocity \bar{v}_H of the conduction electrons along the magnetic field for $(\pi/2 - \theta) \gg \eta$ is weakly dependent on the momentum projection p_H on the magnetic field direction. It follows that the expansion of the conductivity tensor components in power series in the quasi-two-dimensionality parameter η starts with the quadratic terms at least, provided that at least one of the indices of σ_{ij} is z . Then, for determining the resistance to current in the direction transverse to the layers it is sufficient to know only the conductivity tensor component σ_{zz} , and only in a few special cases does ρ_{zz} depend on a larger set of components σ_{ij} (Ref. 14).

For $\eta \ll 1$ and $\gamma = 1/\Omega\tau \ll 1$ the asymptotes of the oscillatory (in $1/H$) part of the conductivity σ_{zz}^{osc} and of the part σ_{zz}^{mon} which varies monotonically with the magnetic field depend substantially on the quantity $\bar{v}_z(p_H, \varepsilon)$

$= \bar{v}_H(p_H, \varepsilon) \cos \theta$, which we calculate in the quasiclassical approximation ($\Delta\varepsilon_N \ll \eta\varepsilon_F$), using the energy spectrum (1):

$$\bar{v}_z(p_H, \varepsilon) = -\frac{1}{T} \int_0^T dt \sum_{n=1}^{\infty} \frac{an}{h} \varepsilon_n(p_y(t, p_H)) \times \sin \left\{ \frac{an}{h} \left[\frac{p_H}{\cos \theta} - p_y(t, p_H) \tan \theta \right] \right\}, \quad (9)$$

where $T = 2\pi/\Omega$, and t is the time of motion of the charge in the magnetic field \mathbf{H} , according to the equations

$$\begin{aligned} \partial p_x / \partial t &= (eH/c)(v_y \cos \theta - v_z \sin \theta); \\ \partial p_y / \partial t &= -eHv_x \cos \theta / c; \\ \partial p_z / \partial t &= ev_x H \sin \theta / c. \end{aligned} \quad (10)$$

For $\tan \theta \gg 1$ the integrand in formula (9) is rapidly oscillating with t , and the main contribution to the integral is from small neighborhoods of the points of stationary phase, at which, according to Eq. (10), $v_x = 0$. We assume that all the cross sections of the Fermi surface have only two stationary phase points, t_1 and t_2 , the distance between which is equal to the diameter of the electron orbit along the p_y axis: $D_p = p_y(t_2) - p_y(t_1)$.

In the case when the angle θ is substantially different from $\pi/2$, all of the quantities appearing in the expression for σ_{zz}^{mon} except \bar{v}_z^2 depend weakly on p_H , and, dropping terms of higher order in the quasi-two-dimensionality parameter than η^2 , we obtain for

$$\sigma_{zz}^{\text{mon}} = -\frac{2}{(2\pi\hbar)^3} \int d\varepsilon \frac{\partial f_0(\varepsilon)}{\partial \varepsilon} \int dp_H 2\pi m^* e^2 \tau \bar{v}_z^2, \quad (11)$$

the following asymptotic expression:

$$\sigma_{zz}^{\text{mon}} = ae^2 \tau m^* \cos \theta / 2\pi h^4 \sum n^2 I_n^2(\theta), \quad (12)$$

where

$$I_n(\theta) = T^{-1} \int_0^T dt \varepsilon_n(t) \cos(p_y(t) an \tan \theta / h). \quad (13)$$

The functions $I_n(\theta)$ have a set of zeroes which for $\tan \theta \gg 1$ repeat periodically with period $\Delta(\tan \theta) = 2\pi\hbar/naD_p$. Of course, all of the terms in formula (12) cannot go to zero simultaneously, and the asymptotic behavior of σ_{zz}^{mon} depends substantially on the character of the falloff of the functions $\varepsilon_n(p_z, p_y)$ with increasing number n . In the tight-binding approximation, when the overlap of the wave functions is small for electrons belonging to different layers separated by a distance a much greater than the interatomic distance within a layer, A_n is proportional to the n th power of the overlap integral of the wave functions, and η_n is equal in order of magnitude to η^n . In this case for $\eta \ll 1$ and $\gamma \ll 1$ the asymptotic expression for σ_{zz}^{mon} takes the form¹⁴

$$\begin{aligned} \sigma_{zz}^{\text{mon}} &= (ae^2 \tau m^* \cos \theta / 2\pi h^4) I_1^2(\theta) \\ &+ \eta^2 \sigma_0 (\eta^2 \varphi_1 + \gamma^2 \varphi_2), \end{aligned} \quad (14)$$

where σ_0 is the conductivity along the layers in the absence of magnetic field.

The functions φ_i are of the order of unity and must be taken into account at those values $\theta = \theta_c$ at which $I_1(\theta)$ goes to zero. At $\theta = \theta_c$ the resistance along the normal to the layers, rather than saturating in high magnetic fields, increases in proportion to H^2 in the region of fields satisfying the condition $\eta \ll \gamma \ll 1$, and saturation of the resistance sets in at higher magnetic fields for $\gamma \leq \eta$. As a result, the angle dependence of the resistance to current along the normal to the layers is expected to exhibit rather sharp peaks. For $\tan \theta \gg 1$ these peaks repeat periodically with period

$$\Delta(\tan \theta) = 2\pi h / aD_p. \quad (15)$$

Although it is unclear to what extent the tight-binding approximation is valid for calculating the electron energy spectrum of an extremely complex crystal structure containing more than a hundred atoms in the unit cell, we shall nevertheless assume that the functions $\varepsilon_n(p_x, p_y)$ fall off, and quite rapidly, with increasing n .

Although the experimentally observed resistance peaks are sharp, their height is comparable in order of magnitude to, and even lower than, the resistance at the minimum of its dependence on the angle between the normal to the layers and the magnetic field direction.^{7,8} This may be because of a slow falloff of the functions $\varepsilon_n(p_x, p_y)$ with increasing n . For $aD_p \tan(\theta/2h) = -\pi/4 + \pi k$, when $I_1(\theta)$ goes to zero, all of the $I_n(\theta)$ for which $(n-1)$ is not a multiple of four are substantially nonzero. The low height of the peaks in the angle dependence of the magnetoresistance attests to a slower falloff of the functions $\varepsilon_n(p_x, p_y)$ with increasing n than in the tight-binding approximation, i.e., there are no grounds for assuming that the ratio η_2/η_1 is much less than unity, and to ignore terms with $n \geq 2$ in the dispersion relation of the charge carriers is no longer correct.

In the expression for the oscillatory (in $1/H$) part of the conductivity transverse to the layers,

$$\sigma_{zz}^{\text{osc}} = -\frac{2}{(2\pi h)^3} 2 \operatorname{Re} \sum_{k=1}^{\infty} \int d\varepsilon \frac{\partial f_0(\varepsilon)}{\partial \varepsilon} \times \int dp_H 2\pi m^* e^2 \tau \bar{v}_z^2 \exp(2\pi i k N(\varepsilon, p_H)), \quad (16)$$

there is substantial dependence on p_H not only in the factor

$$\bar{v}_z(p_H, \varepsilon) = -\sum_{n=1}^{\infty} \frac{an}{h} \sin\left(\frac{anp_H}{h \cos \theta}\right) I_n(\theta), \quad (17)$$

but also in the oscillatory (for $\hbar\Omega \ll \eta\varepsilon_F$) factor $\exp(2\pi i k N(\varepsilon, p_H))$.

In calculating σ_{zz}^{osc} in the quasiclassical approximation one should use the area quantization rule⁴

$$S(\varepsilon, p_H) = \frac{1}{\cos \theta} S_0(\varepsilon, p_H) = 2\pi h \frac{eH}{c} \left(N + \frac{1}{2}\right), \quad (18)$$

where $S_0(\varepsilon, p_H) = \oint p_y dp_x$ is the projection on the (p_x, p_y) plane of the section of the isoenergy surface $S(\varepsilon, p_H)$ by the plane $p_H = \text{const}$. The main contribution to σ_{zz}^{osc} comes from integration of small neighborhoods near the points of stationary phase, which are found from the condition

$$dN(\varepsilon, p_H) = \left(\frac{\partial S}{\partial \varepsilon} d\varepsilon + \frac{\partial S}{\partial p_H} dp_H\right) \frac{c}{2\pi h e H} = 0. \quad (19)$$

Since the cyclotron effective mass of the conduction electrons $m^* = (1/2\pi)(\partial S/\partial \varepsilon)$ is always nonzero, the condition of stationarity, when $S(\varepsilon, p_H)$ is almost constant, can only be met for $\partial \varepsilon/\partial p_H = -(\partial S/\partial p_H)(\partial S/\partial \varepsilon)$. Drift of the charge carriers is absent on the extremal cross sections of the isoenergy surface, i.e., for $\partial S/\partial p_H = 0$, and on the self-crossing orbit, when $m^* = \infty$. For $\eta \tan \theta \ll 1$ there are no self-crossing orbits on the Fermi surface, and

$$\bar{v}_z(p_H, \varepsilon_F) = \frac{\partial S/\partial p_H}{\partial S/\partial \varepsilon} \cos \theta, \quad (20)$$

goes to zero only on the extremal cross sections of the Fermi surface. After integrating expression (16) by parts with allowance for relation (20), we obtain

$$\sigma_{zz}^{\text{osc}} = \frac{2}{(2\pi h)^3} 2 \operatorname{Re} \sum_{k=1}^{\infty} \int d\varepsilon \frac{\partial f_0(\varepsilon)}{\partial \varepsilon} e^2 \tau \frac{eHh}{ikc} \times \int dp_H \exp\left(\frac{ikcS(\varepsilon, p_H)}{eHh}\right) \times \sum_{n=1}^{\infty} \left(\frac{an}{h}\right)^2 \cos\left(\frac{anp_H}{h \cos \theta}\right) I_n(\theta). \quad (21)$$

From here the calculation of σ_{zz}^{osc} by the method of stationary phase does not present any difficulty. As a result, the oscillatory part of the conductivity transverse to the layers takes the form

$$\sigma_{zz}^{\text{osc}} = \sum_{k=1}^{\infty} e^2 \tau \left(\frac{eHh}{kc}\right)^{3/2} \frac{k\lambda}{\sinh(k\lambda)} \frac{4\pi^{1/2} a^2}{(2\pi h)^3 |\partial^2 S/\partial p_H^2|^{1/2} h^2} \times \left[\sum_{n=1}^{\infty} (2n-1)^2 \sin\left(\frac{\pi}{4} - \frac{kc(S_{\max} - S_{\min})}{2eHh}\right) \times \cos\left(\frac{kc(S_{\max} + S_{\min})}{2eHh}\right) I_{2n-1}(\theta) + \sum_{n=1}^{\infty} (2n)^2 \cos\left(\frac{\pi}{4} - \frac{kc(S_{\max} - S_{\min})}{2eHh}\right) \times \sin\left(\frac{kc(S_{\max} + S_{\min})}{2eHh}\right) I_{2n}(\theta) \right], \quad (22)$$

where $\lambda = 2\pi^2 \Theta / h\Omega$, and Θ is the temperature in energy units.

If the function $\varepsilon_n(p_x, p_y)$ falls off quite rapidly with increasing index n , i.e., $\eta_{n+1} \ll \eta_n$, then the substantial decrease of σ_{zz}^{osc} sets in at the same angles $\theta = \theta_c$ as for σ_{zz}^{mon} , and the amplitude of the SdH oscillations of the magnetoresistance, ρ_{zz}^{osc} , being proportional to $\sigma_{zz}^{\text{osc}}/(\sigma_{zz}^{\text{mon}})^2$, increases rapidly at $\theta = \theta_c$. As a result, sharp peaks appear in the dependence of ρ_{zz}^{osc} on the angle θ between the vectors \mathbf{H} and \mathbf{n} . If η_2 is not much smaller than η_1 , i.e., if $I_2(\theta)$ and $I_1(\theta)$ are quantities of approximately the same order, then the peaks in the angle dependence of ρ_{zz}^{osc} will be shifted from the peaks of ρ_{zz}^{mon} . From the value of this shift one can estimate the quasi-two-dimensionality parameter of the electron energy spectrum.

The formulas for σ_{zz}^{osc} and σ_{zz}^{mon} given above are valid for not too large values of $\tan \theta$, when $\gamma \cong \gamma_0 / \cos \theta \ll 1$, and in

the oscillation amplitude one may neglect the Dingle factor $\exp(-\gamma)$, which takes into account the broadening of the quantum energy levels due to scattering of the charge carriers.¹⁵ Here $\gamma_0 = 1/\Omega_0\tau$, and Ω_0 is the gyration frequency of a conduction electron in a magnetic field directed along the normal to the layers.

When θ approaches $\pi/2$ the orbits become highly elongated, and for $\gamma_0 \tan \theta \geq 1$ the electron does not have time to complete a full revolution along the orbit in the magnetic field. In this region of angles the amplitude of the magnetoresistance oscillations decays exponentially with increasing θ , while ρ_{zz}^{mon} , on the contrary, increases sharply when θ approaches $\pi/2$ for $(\pi/2 - \theta) \ll \eta$.^{16,17} This is because a constriction along the p_x axis appears on the electron orbit with increasing θ , the value of which, Δp , tends toward zero when $\eta \tan \theta$ is of the order of unity. The time for traversing this constriction is large and diverges logarithmically as Δp approaches zero. As a result, γ increases with increasing θ more rapidly than $\tan \theta$, and the resistance transverse to the layers initially falls off with increasing θ . The drift velocity of the charge carriers along the normal to the layers, \bar{v}_z , is proportional to $\cos \theta$, and the resistance ρ_{zz} , after passing through a minimum in the region of angles where $\cos \theta$ is of the order of η , again increases, reaching its maximum value at $\theta = \pi/2$.

Thus the resistivity ρ_{zz} of a layered conductor along the “hard” direction of current flow, i.e., along the normal to the layers, is extremely sensitive to the orientation of the magnetic field, and at certain values of the angle θ it can sub-

stantially alter the asymptotic behavior at small η not only of ρ_{zz}^{mon} but also of the amplitude of the SdH oscillations of the magnetoresistance, ρ_{zz}^{osc} .

*E-mail: vpeschansky@ilt.kharkov.ua

- ¹L. V. Schubnikov and W. J. de Haas, *Leiden Commun.* **19**, 207f (1930).
- ²W. J. de Haas, J. W. Blom, and L. V. Schubnikov, *Physica* **2**, 907 (1930).
- ³L. Onsager, *Philos. Mag.* **43**, 1006 (1952).
- ⁴I. M. Lifshits and A. M. Kosevich, *Zh. Eksp. Teor. Fiz.* **29**, 730 (1955) [*Sov. Phys. JETP* **2**, 636 (1956)].
- ⁵W. J. de Haas and P. M. van Alphen, *Leiden Commun.* **19**, 208d (1930).
- ⁶L. D. Landau, *Proc. R. Soc. London, Ser. A* **170**, 341 (1939).
- ⁷M. V. Kartsovnik, V. N. Laukhin, V. N. Nizhankovskiy, and A. A. Ignat'ev, *JETP Lett.* **47**, 363 (1988).
- ⁸M. V. Kartsovnik, P. A. Kononovich, V. N. Laukhin, and I. F. Shchegolev, *JETP Lett.* **48**, 541 (1988).
- ⁹I. D. Parker, D. D. Pigram, R. H. Friend, M. Kurmo, and P. Day, *Synth. Met.* **27**, A387 (1988).
- ¹⁰V. G. Peschansky, J. A. Roldan Lopez, and Toji Gnado, *J. Phys. I* **1**, 1469 (1991).
- ¹¹I. M. Lifshits, *Zh. Éksp. Teor. Fiz.* **32**, 1509 (1957) [*Sov. Phys. JETP* **5**, 1227 (1957)].
- ¹²E. Adams and T. Holstein, *J. Phys. Chem. Solids* **10**, 254 (1959).
- ¹³A. M. Kosevich and V. V. Andreev, *Zh. Eksp. Teor. Fiz.* **38**, 882 (1960) [*Sov. Phys. JETP* **11**, 637 (1960)].
- ¹⁴V. G. Peschanskiy, *Fiz. Nizk. Temp.* **23**, 47 (1997) [*Low Temp. Phys.* **23**, 35 (1997)].
- ¹⁵Yu. A. Bychkov, *Éksp. Teor. Fiz.* **39**, 1401 (1960) [*Sov. Phys. JETP* **12**, 971 (1961)].
- ¹⁶M. V. Kartsovnik and V. G. Peschansky, *J. Low Temp. Phys.* **117**, 1717 (1999).
- ¹⁷V. G. Peschansky and M. V. Kartsovnik, *Phys. Rev. B* **60**, 11207 (1999).

Translated by Steve Torstveit

Magnetization and magnetostriction oscillations in a superconducting 2H-NbSe₂ single crystal

V. Ereminko, V. Sirenko,* and Yu. Shabakayeva

B. Verkin Institute for Low Temperature Physics and Engineering of the National Academy of Sciences of Ukraine, 47 Lenin Ave., Kharkov 61103, Ukraine

R. Schleser

Grenoble High Magnetic Field Laboratory, MPI-FKF and CNRS, BP-166, F-38042, Grenoble Cedex 09, France

P. L. Gammel

Bell Laboratories, Lucent Technologies, Murray Hill, New Jersey 07974, USA

(Submitted May 29, 2001)

Fiz. Nizk. Temp. **27**, 952–955 (September–October 2001)

The results of a comparative study of the oscillating magnetostriction and absolute magnetization components in the single crystal of the layered superconducting compound 2H-NbSe₂ are presented. The measurements were made in the temperature range 1.5–8 K in a magnetic field of 0–20 T with in-plane orientation (normal to the hexagonal axis). The mechanical stress derivative of the extremal cross-sectional area of the Fermi surface is derived from a thermodynamic analysis. The values obtained are considerably higher, by an order of magnitude, than those for other metals, which explains the observed enhancement of the magnetostriction oscillations in comparison with the magnetization oscillations. © 2001 American Institute of Physics. [DOI: 10.1063/1.1401177]

1. INTRODUCTION

L. V. Shubnikov was the first to observe oscillations of the resistivity.¹ It was this observation that led to the discovery of the de Haas–van Alphen (dHvA) oscillations of the magnetic properties. The layered dichalcogenide 2H-NbSe₂, with a transition to the charge-density-wave (CDW) state at temperature $T_{CDW}=32$ K, is the first superconducting compound (the superconducting transition temperature $T_c=7.2$ K) in which Landau oscillations of the electron spectrum have been observed.² That was the first observation of the de Haas–van Alphen and magnetothermal oscillations not only in the normal state but also in a mixed state, the so-called Shubnikov phase ($H < H_{c2}$). The measurements were made at temperatures much lower than T_c for different orientations of the external magnetic field \mathbf{H} with respect to the crystallographic axes of the single crystal under study. In that study² and in subsequent investigations^{3–7} of superconducting 2H-NbSe₂ the measurements of the magnetization oscillations were made at a temperature far below 1 K in order to eliminate the electron scattering as above the Dingle temperature ($T_D=2.5$ K, (Ref. 5), $T_D=1$ K (Ref. 6) for 2H-NbSe₂) it reduces drastically the amplitude of the oscillations, and their registration by existing techniques becomes impossible. Measurements in magnetic fields below the upper critical field H_{c2} have shown that in the mixed state the oscillations are suppressed by the scattering of normal (quantized) electrons on Abrikosov vortices, observed in other superconductors also (see the review⁸ and the references therein). The measured angular dependences of the oscillation frequency $F(\theta)$, where θ is the angle between the hexagonal axis and field direction, at $H < H_{c2}$ revealed a pro-

nounced dependence $F(\theta)$ in the angle range $0 < \theta < 20^\circ$ and a weak dependence $F(\theta)$ at $\theta > 60^\circ$.⁶ Band calculations⁵ demonstrate that the measured angular dependence of the oscillations is well described in terms of a “small, flat hole Fermi surface around the Γ point.” The above-mentioned investigation complemented the results of previous band calculations^{9–11} of the Fermi surface in 2H-NbSe₂. Existing data about the shape and peculiarities of the Fermi surface in 2H-NbSe₂ suggest its high sensitivity to pressure and stress, which has been proved by the measured pressure dependences of the superconducting parameters of this compound (Refs. 12–14 and references therein). The observed magnetostriction oscillations¹⁵ in superconducting single crystals of 2H-NbSe₂ in comparison with dHvA oscillations can be used to study the influence of mechanical stresses on the band structure of this material according to the thermodynamic approach developed in^{16–18}.

We should mention that in¹⁹ the effect of deformation on dHvA oscillations is considered. The related change of oscillation frequency is estimated. Deformations of 10^{-2} – 10^{-3} are taken into account. Here, we analyze the amplitude ratio for the magnetization and magnetostriction, the amplitude of the latter being of the order of 10^{-5} . An analysis of the frequencies will be presented elsewhere.

In this work a comparative analysis of measurements of the oscillatory magnetostriction (λ_{OSC} and absolute magnetization $\mathbf{M}=\mathbf{m}/V$ (\mathbf{m} is the magnetic moment of the sample and V is its volume) is performed. The same single crystal of 2H-NbSe₂ was studied by capacitive dilatometer and capacitive cantilever torqueometer²⁰ techniques.

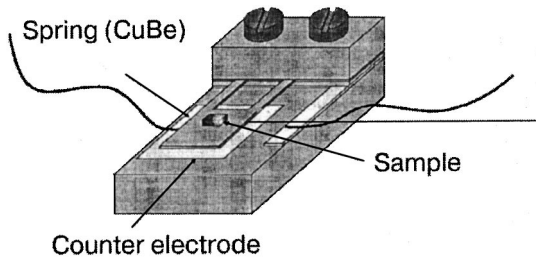


FIG. 1. Capacitive torque meter for magnetization measurements. The calibration coil is positioned in the sample area (not shown here).

2. EXPERIMENTAL TECHNIQUES

The absolute magnetization measurements were performed on single crystals of the layered compound 2H-NbSe_2 (space group $P6/mmm$ or D_{6h}^4). The high anisotropy of the crystal structure ($a = 3.45 \text{ \AA}$, $c = 12.54 \text{ \AA}$) is accompanied by anisotropy of the electronic properties, in particular, of the superconducting parameters: $H_{c2}(T = 4.2 \text{ K}) \approx 7 \text{ T}$ for $\theta = 90^\circ$ and 2.3 T for $\theta = 0^\circ$ (there is some discrepancy in the published data).^{2,15,21,22} The mass of the sample was $m = (127 \pm 0.05) \text{ mg}$. The sharp superconducting transition was observed at temperature $T_c = 7.23 \text{ K}$. The detailed information on the sample preparation technique and characterization is presented in Ref. 15. In that paper the first observation of magnetostriction oscillations in the mixed state of any superconductor was presented. The measurement of magnetostriction $\lambda^{(c,a)}$ was performed on a single crystal of 2H-NbSe_2 in the crystallographic direction (001), i.e., the c axis, in a magnetic field parallel to the a axis. The oscillatory component of $\lambda^{(c,a)}$ was defined as $\lambda_{\text{OSC}}^{(c,a)} = \lambda_{\text{rev}}^{(c,a)} - \lambda_{\text{mon}}^{(c,a)}$, where $\lambda_{\text{rev}}^{(c,a)} = (\lambda_{\text{up}} + \lambda_{\text{down}})/2$ is the reversible part of $\lambda^{(c,a)}$; $\lambda_{\text{up}}^{(c,a)}$ is $\lambda^{(c,a)}$ measured during magnetization of the sample; $\lambda_{\text{down}}^{(c,a)}$ is $\lambda^{(c,a)}$ measured during demagnetization of the sample; $\lambda_{\text{mon}}^{(c,a)}$ is the monotonic part of $\lambda_{\text{rev}}^{(c,a)}$.

In the present work the absolute magnetization measurements were performed in a temperature range 1.5–4.2 K in a magnetic field up to 20 T using a capacitive cantilever torque meter (see Fig. 1). The field sweep rate was 0.18 T/min. The torque magnetization measuring technique²² is based on the fact that in a magnetic field \mathbf{H} a magnetized sample experiences a torque \mathbf{T} proportional to the component of the sample's magnetic moment perpendicular to \mathbf{H} :

$$\mathbf{T} = \frac{V}{\mu_0} \mathbf{M} \times \mathbf{H}, \quad (1)$$

where μ_0 is the vacuum magnetic permeability.

In a sample with an anisotropic Fermi surface the magnetization component M_\perp perpendicular to the field direction is proportional to the parallel component M_\parallel :²³

$$M_\perp = -kM, \quad k = \frac{1}{\mathcal{F}} \frac{\partial \mathcal{F}}{\partial \theta} \quad (2)$$

where \mathcal{F} is the free energy.

The torque \mathbf{T} results in deflection of a Cu-Be spring joined with the sample. The change of the distance between the spring and adjacent metallic plate is measured by a capacitance technique. At $\theta = 90^\circ$ the measured signal from the torque meter disappears, as k becomes equal to zero. For this

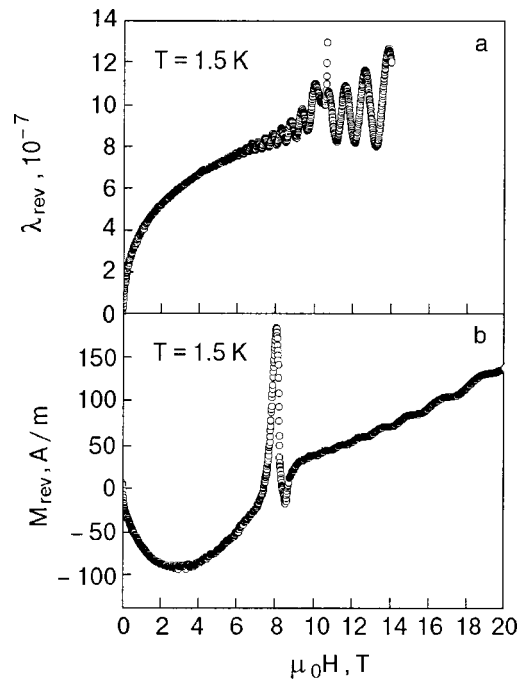


FIG. 2. The typical magnetic field dependences of λ_{rev} (a) and M_{rev} (b) for 2H-NbSe_2 single crystals.

reason the field dependence of \mathbf{M} was measured at $\theta = (77 \pm 1)^\circ$. The measurements revealed equal frequencies of the magnetization and magnetostriction oscillations, $F_M = F_{MS}$, which agrees with the weak angular dependence $F(\theta)$ at $60^\circ < \theta < 90^\circ$, measured earlier. In order to find the absolute values of \mathbf{M} , calibrations of the measuring capacitance were performed in each experiment using a calibrating coil, which was positioned in the region of the sample (Fig. 1). The volume V of the sample was determined using the density value $\rho = 6.3 \cdot 10^3 \text{ kg/m}^3$, calculated from the known⁵ atomic distribution in 2H-NbSe_2 . The oscillatory component of M was defined in the same way as the oscillatory component of the magnetostriction: $M_{\text{osc}} = 1/2(M_{\text{up}} + M_{\text{down}}) - \bar{M}$, where $M_{\text{rev}} = 1/2(M_{\text{up}} + M_{\text{down}})$ is the reversible component of M , M_{up} is the absolute magnetization of the sample measured in increasing magnetic field after zero field cooling (ZFC); M_{down} is the absolute magnetization of the sample measured in increasing magnetic field; \bar{M} is the monotonic component of M . In the oscillatory regime it was determined by averaging M_{osc} .

Analysis of M_{osc} was performed after subtracting the monotonic component according to Ref. 6.

3. EXPERIMENTAL RESULTS AND DISCUSSION

Figure 2 presents a typical magnetic-field curve of M_{rev} for a 2H-NbSe_2 single crystal, in comparison with λ_{rev} measured on the same crystal. It is clearly seen that in a region of the peak effect¹⁵ both \mathbf{M} and λ depend nonlinearly on \mathbf{H} . This means that a simple summation of the dependences measured in increased and decreased fields does not completely eliminate manifestations of the peak effect on the $M_{\text{rev}}(H)$ and $\lambda_{\text{rev}}(H)$ curves. The oscillatory behavior of the measured dependences starts near H_{c2} . Unfortunately, because of the available experimental conditions the magneto-

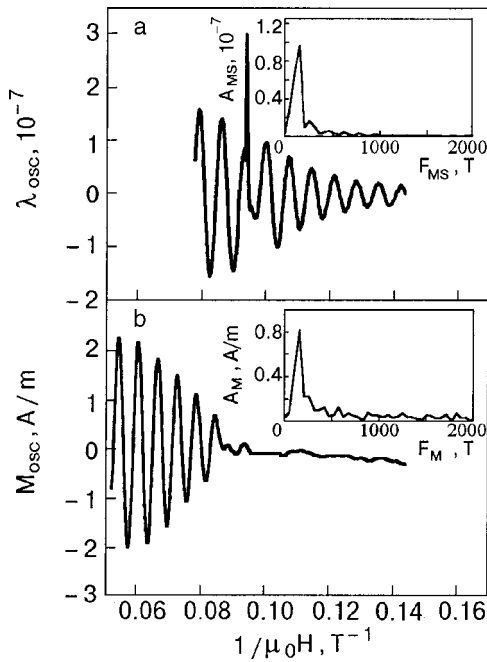


FIG. 3. The inverse field dependences of λ_{osc} (a) and M_{osc} (b) for $T = 1.5$ K. The inset shows the results of a fast Fourier transform analysis of the measurements, which was used for determination of F_M and F_{MS} .

striction measurements were restricted by an upper value of the applied field $H = 14$ T, and comparison with the magnetization measurements is possible only for this range of H . The magnetization oscillations are less pronounced than those of the magnetostriction. They appear at higher fields, and their amplitude A_M is lower than the amplitude A_{MS} of the magnetostriction oscillations. Figure 3 presents the inverse field dependences of M_{osc} and λ_{osc} for $T = 1.5$ K, which were obtained by subtracting their monotonic components from M_{rev} and λ_{rev} , respectively. The insets show the results of a fast Fourier transform analysis of the measurements, which was used for determination of F_M and F_{MS} . It is seen that these frequencies coincide. The slight phase shift may be explained by the different geometry of the experiment, explained in the previous Section. The derived values of A_M and A_{MS} were used for calculations of $\partial(\ln S_m)/\partial\sigma_\alpha$, where S_m is the extremal cross-sectional area of the Fermi surface, and σ_α is the mechanical stress arising along the \mathbf{H} direction. For that we used the expression

$$\frac{\lambda}{\mathbf{M} \cdot \mathbf{H}} = \frac{\partial(\ln S_m)}{\partial\sigma_\alpha}, \quad (3)$$

which was obtained from a thermodynamic analysis of the oscillating part of the thermodynamic potential.^{16–18} The results are presented in Table I in comparison with the data

TABLE I. Comparison of $\partial(\ln S_m)/\partial\sigma_\alpha$ values for $2H\text{-NbSe}_2$ and other metals.

Metal	$\partial(\ln S_m)/\partial\sigma_\alpha$ (in $10^{-11} \text{ m}^2/\text{N}$)
$2H\text{-NbSe}_2$	148.5 ± 11 [present work]
Cu	7.5 ± 2 [Ref. 18]
Ag	24 ± 1 [Ref. 18]
Au	8.3 ± 1 [Ref. 18]

from a review¹⁸ for common metals.

It is seen that the values of $\partial(\ln S_m)/\partial\sigma_\alpha$ obtained in the present work for $2H\text{-NbSe}_2$ are considerably, by an order of magnitude, higher than those obtained previously for the other metals. This is why the magnetostriction oscillations are enhanced in comparison with the magnetization oscillations.

CONCLUSIONS

A comparative analysis of the reversible absolute magnetization and magnetostriction as functions of the inverse magnetic field, measured on a superconducting $2H\text{-NbSe}_2$ single crystal, have shown that: 1) the oscillation periods M_{osc} and λ_{osc} coincide, which means that both effects are attributed to Landau quantum oscillations; 2) the magnetostriction oscillations are more pronounced than the magnetization oscillations: the former appear at lower fields, and their amplitude is higher (with respect to the monotonic component); 3) a thermodynamic analysis shows that the values of $\partial(\ln S_m)/\partial\sigma_\alpha$ for $2H\text{-NbSe}_2$ are much higher, by an order of magnitude, than the values of $\partial(\ln S_m)/\partial\sigma_\alpha$ for common metals. This is due to the peculiar geometry of Fermi surface in the highly anisotropic compound $2H\text{-NbSe}_2$ and explains the effect of magnetostriction “enhancement.”

The authors are indebted to P. Wyder for support of the work, to T. J. B. Janssen for some stimulating discussions, and to N. Makedonskaya for assistance in preparation of the manuscript.

*E-mail: sirenko@ilt.kharkov.ua

- ¹L. V. Schubnikov and W. J. Haas, Proc. Netherlands R. Acad. Sci. **33**, 163 (1930).
- ²J. E. Graebner and M. Robbins, Phys. Rev. Lett. **36**, 422 (1976).
- ³Y. Onuki, I. Umehara, N. Ebihara, N. Nagai, and K. Takita, J. Phys. Soc. Jpn. **61**, 692 (1992).
- ⁴Y. Onuki, I. Umehara, T. Ebihara, A. K. Albessars, K. Satoh, K. Takita, H. Aoki, S. Uji, and T. Shimuzu, Physica B **150**, 186 (1993).
- ⁵R. Corcorant, P. Meeson, Y. Onuki, P. A. Probst, M. Springford, K. Tokitani, H. Harimot, G. V. Guo, and B. L. Gyoffy, J. Phys.: Condens. Matter **6**, 4479 (1994).
- ⁶S. Rettenberger, E. Steep, F. Meyer, A. G. U. Jansen, W. Jose, P. Wyder, W. Biberacher, E. Bucher, and C. S. Oglisby, Physica B **211**, 244 (1995).
- ⁷E. Steep, S. Rettenberger, F. Meyer, A. G. U. Jansen, W. Jose, W. Biberacher, E. Bucher, and C. S. Oglisby, Physica B **204**, 162 (1995).
- ⁸T. J. B. Janssen, C. Haworth, S. M. Hayden, P. Messon, and M. Springford, Phys. Rev. B **57**, 11698 (1998).
- ⁹L. F. Matheises, Phys. Rev. B **8**, 3719 (1973).
- ¹⁰C. Y. Fong and M. L. Cohent, Phys. Rev. Lett. **32**, 720 (1974).
- ¹¹F. G. Wexler and A. Wooly, J. Phys. C **9**, 1185 (1976).
- ¹²M. A. Obolenskii, Kh. B. Chashka, V. I. Belestkii, and V. M. Gvozdikov, Fiz. Nizk. Temp. **15**, 984, (1989) [Sov. J. Low Temp. Phys. **15**, 544 (1989)].
- ¹³Kazuhiko Yamaya and Takashi Samboni, J. Phys. Soc. Jpn. **32**, 1150 (1972).
- ¹⁴V. G. Kogan, L. N. Bulaevskii, P. Miranovic, and L. Dobrosavljevic-Grujic, Phys. Rev. B **51**, 15344 (1995).
- ¹⁵V. V. Eremenko, V. A. Sirenko, R. Schleser, and P. L. Gammel, Fiz. Nizk. Temp. **27**, 412 (2001) [Low Temp. Phys. **27**, 305 (2001)].
- ¹⁶I. M. Livshits and A. M. Kosevich, Izv. Acad. Nauk **19**, 395 (1955).
- ¹⁷B. S. Chandrasekhar, J. H. Condon, E. Fawcett, and W. M. Becker, Phys. Rev. Lett. **17**, 954 (1966).
- ¹⁸B. S. Chandrasekhar and E. Fawcett, Adv. Phys. **20**, 775 (1971).
- ¹⁹A. M. Kosevich, Zh. Eksp. Teor. Fiz. **35**, 249 (1959) [Sov. Phys. JETP **35**, 171 (1959)].

²⁰P. Christ, W. Biberacher, H. Mueller, and K. Andres, *Solid State Commun.* **91**, 451 (1994).

²¹P. de Trey, Suso Gyday, and J. P. Jan, *J. Low Temp. Phys.* **11**, 421 (1973).

²²R. C. Morris, R. V. Coleman, and R. Bhandari, *Phys. Rev. B* **5**, 895 (1972).

²³D. Shoenberg, *Magnetic Oscillations in Metals*, Cambridge University (1984).

This article was published in English in the original Russian journal. Reproduced here with stylistic changes by AIP.

Shubnikov–de Haas oscillations in layered conductors with stacking faults

V. M. Gvozdkov*

*Department of Physics, Kharkov National University, 4 Svobody Sq., 61077 Kharkov, Ukraine;
Grenoble High Magnetic Field Laboratory MPI-FRF and CNRS, BP 166 F-38042, Grenoble Cedex 09,
France*

(Submitted July 9, 2001)

Fiz. Nizk. Temp. **27**, 956–962 (September–October 2001)

The Shubnikov–de Haas (SdH) oscillations of the in-plane conductivity of layered 2D electron gas are calculated. It is shown that layer stacking faults, magnetoimpurity bound states, and electron scattering modulate the SdH oscillations via the specific factors which bear the structural information. At zero temperature the 2D SdH oscillations are strongly nonsinusoidal in shape and related by a simple equation to the derivative of the de Haas–van Alphen magnetization oscillations with respect to the magnetic field. © 2001 American Institute of Physics. [DOI: 10.1063/1.1401178]

INTRODUCTION

The discovery of high- T_c superconductivity in layered cuprates and the unconventional electronic properties of layered organic superconductors make structural studies of these layered conductors of great interest. In particular, much of recent experimental effort has been devoted to de Haas–van Alphen (dHvA) and Shubnikov–de Haas (SdH) studies in organic superconductors.^{1–7} Both the dHvA and SdH measurements in these quasi-two-dimensional (Q2D) materials displayed numerous deviations from the conventional three-dimensional (3D) theory of Lifshitz and Kosevich⁸ (LK), many of which still remain not understood. For example, a sawtooth profile of the dHvA signal was predicted at zero temperature $T=0$ for a purely 2D electron gas in the canonical ensemble (i.e., for fixed number of electrons in the sample),⁹ and an inverse sawtooth was found within the grand canonical ensemble (i.e., for fixed chemical potential in the sample).¹⁰ In the first case the dHvA oscillations are due to the oscillations of the chemical potential μ . The recent analysis of this matter given in Ref. 11 shows that it is only for low electron concentrations, when it is possible to realize experimentally a regime $\hbar\Omega \approx \mu$ ($\Omega = eH/mc$ is the cyclotron frequency), that oscillations of μ with inverse magnetic field $1/H$ are important. In the case $\mu \gg \hbar\Omega$ the oscillations of the chemical potential are small, and one can use the grand canonical ensemble as it holds in the standard 3D LK theory.

Real layered conductors are far from being an ideal 2D electron gas. As a rule they consist of a stack of 2D conducting planes with an anisotropic 2D Fermi surface within them and may contain impurities as well as some amount of stacking faults appearing as a result of the intercalation. The impact of the stacking faults on the dHvA oscillations in a layered conductors was studied by the author in Ref. 12. It was shown that amplitudes of the dHvA harmonics are modulated by the layer factor

$$I_p = \int_{-\infty}^{\infty} N(\varepsilon) \exp\left(i \frac{2\pi p \varepsilon}{\hbar\Omega}\right) d\varepsilon, \quad (1)$$

which is a Fourier transform of the one-dimensional density of states (DOS) $N(\varepsilon)$ related to electron hopping across the layers (p is the number of the harmonic).

The delta peak in the $N(\varepsilon) \propto \delta(\varepsilon - \varepsilon_0)$ at some energy ε_0 makes I_p an oscillatory function of the inverse field,

$$I_p \sim \cos\left(\frac{2\pi p \varepsilon_0}{\hbar\Omega}\right),$$

with the frequency determined by ε_0 . Another modulation factors appear in the case of the magnetic field parallel to the layers¹³ and under the conditions of coherent magnetic breakdown.¹⁴

Impurities play a significant role. In the theory of the dHvA oscillations they smear the Landau levels and thereby decrease the harmonic amplitudes via the Dingle factor,¹⁰ or they may create bound electronic states which manifest themselves through beats of the dHvA oscillations,¹⁵ which are more prominent in the 2D case.¹⁶

Contrary to the dHvA effect the SdH oscillations appear as a result of the electron lifetime oscillations due to the scattering on impurities in an external magnetic field.¹⁷ Theoretically it is a much more difficult problem than the study of the thermodynamic oscillations and, consequently, the number of publications on the SdH effect in layered conductors is much less than on the dHvA effect in Q2D systems. The SdH effect in the case of a 2D electron gas was considered in a few works reviewed in Ref. 18. The anisotropy in a 2D model was considered numerically in Ref. 19 in the context of the SdH studies of the organic superconductors. Longitudinal magnetoresistance quantum oscillations due to the coherent hopping across the layers has been numerically studied in Refs. 20 and 21 for the incoherent case, i.e., when $\tau \gg \hbar/t$ (τ is the electron lifetime, and t stands for the hopping integral between the neighboring layers).

In this paper we calculate τ in a layered 2D electron gas containing a small amount of stacking faults in an external quantizing magnetic field perpendicular to the layers and then apply the results of these calculations to the theoretical consideration of the SdH oscillations in this system.

THE LIFETIME CALCULATION

A theory for the single-electron lifetime $\tau(E)$ in a 2D electron gas due to the impurity scattering in an external quantizing magnetic field was developed by Ando and Uemura.²² This theory provided a basis for further studies of different properties of a 2D electron gas in magnetic fields.¹⁸ Maniv and Vagner²³ have generalized the approach of Ando and Uemura to the case of a layered electron gas. These authors have shown that in layered conductors the interplane tunneling of electrons can significantly reduce the 2D scattering rate due to the possibility of escaping the impurity by hopping to the neighboring conducting planes. They calculated the magnetic field dependence of τ assuming the kinetic energy across the layers $\varepsilon(k_z) = k_z^2/2m$ to be limited within the band $0 \leq \varepsilon(k_z) \leq \Delta_z$. Here we generalize their approach to the case when the interlayer hopping energy is an arbitrary quantity distributed within the DOS $N(\varepsilon)$. Then the equation for the single-electron self-energy $\sigma(\omega)$ yields:²³

$$\sigma(\omega) = b_0 + c_0 \sum_{n=0}^{\infty} \int_{-\infty}^{\infty} d\varepsilon \frac{N(\varepsilon)}{\varepsilon - \gamma_n(\omega) + \sigma(\omega)}, \quad (2)$$

where

$$\gamma_n(\omega) = \omega - \hbar\Omega(n + 1/2) + \mu, \quad (3)$$

$$b_0 = U_0 n_i, \quad c_0 = \frac{U_0^2 n_i}{4\pi^2 l_H^2}, \quad (4)$$

U_0 is the impurity potential amplitude $V(\mathbf{r}) = U_0 \delta(\mathbf{r} - \mathbf{r}_i)$, n_i is the impurity concentration, and $l_H = (\hbar c / eH)^{1/2}$ is the magnetic length.

Separating the real and imaginary parts in Eq. (2) for the self-energy $\sigma(\omega) = \text{Re } \sigma(\omega) + i \text{Im } \sigma(\omega)$, we have

$$\text{Im } \sigma(\omega) = c_0 \sum_{n=0}^{\infty} \int_{-\infty}^{\infty} d\varepsilon N(\varepsilon) \times \frac{\text{Im } \sigma(\omega)}{[\gamma_n(\omega) - \text{Re } \sigma(\omega) - \varepsilon]^2 + \text{Im}^2 \sigma(\omega)}. \quad (5)$$

Since we are interested in quantum oscillations, which are relevant to the long-lifetime regime, $\hbar/\tau(\omega) = \text{Im } \sigma(\omega) \ll \hbar\Omega$, we can neglect the quantity $\text{Re } \sigma(\omega) \approx U_0 n_i \ll \mu$ as a small correction to the chemical potential μ .

Then, applying a standard summation procedure^{10,17} to Eq. (5), we can recast it in the form

$$\text{Im } \sigma(\omega) = a \left\{ 1 + 2 \text{Re} \sum_{p=1}^{\infty} (-1)^p \exp \left[-\frac{2\pi \text{Im } \sigma(\omega)}{\hbar\Omega} \right] \times I_p \cos \left[2\pi \left(\frac{\omega}{\Omega} + \delta \right) p \right] \right\}, \quad (6)$$

where $a = n_i E_0 / 2\pi$ with $E_0 = m U_0^2 / 2\hbar^2$ being the resonance energy for the δ -potential scattering, and $\delta = \Delta[1/H] / \hbar\Omega$ is a small phase shift $0 \ll \Delta[1/H] < 1/2$ arising because the ratio $\mu/\hbar\Omega$ is not exactly an integer: $\mu/\hbar\Omega = N + \Delta[1/H]$ (N stands for an integer). The factor I_p here is given by Eq. (1). This factor was studied in detail in Ref. 12, which is devoted to the dHvA effect in layered conductors. For a periodic layered system with nearest-layer hopping we have $N(\varepsilon) = 1/\pi(4t^2 - \varepsilon^2)^{1/2}$ and

$$I_p = J_0 \left(\frac{4\pi t p}{\hbar\Omega} \right), \quad (7)$$

where $J_0(x)$ is the Bessel function and t is the interlayer hopping integral.

In case when there is a small concentration $c \ll 1$ of layer stacking faults, the factor I_p was calculated in Ref. 12 to be

$$I_p = (1 - c) J_0 \left(\frac{4\pi t p}{\hbar\Omega} \right) + c \delta I_p, \quad (8)$$

where

$$\delta I_p = \exp \left(-\frac{2\pi p}{\hbar\Omega} \sqrt{t^2 - t_0^2} \right) \cos \left(\frac{4\pi t_0}{\hbar\Omega} p \right). \quad (9)$$

Because of the stacking fault, the local hopping integral t_0 relevant to the electron transition from the “defect layer” to the nearest-neighbor layers is less than t . Physically this kind of stacking faults may appear as a result of the intercalation of the layered conductor.

SHUBNIKOV-DE HAAS OSCILLATIONS

Consider now the SdH oscillations in a stack of 2D isotropic conductors with impurities in a perpendicular magnetic field. We do not assume periodicity in the layer stacking. The diagonal elements of the in-plane conductivity tensor are therefore given by¹⁸

$$\sigma_{\alpha\alpha} = -\frac{N_e e^2}{m} \int_0^{\infty} dE \left(\frac{\partial f}{\partial E} \right) \tau(E), \quad (10)$$

where N_e is the 2D density of conduction electrons within the layer and $f(E)$ is the Fermi function.

The energy-dependent lifetime $\tau(E) = \hbar / \text{Im } \sigma(E)$ can be found from Eq. (6) to a first approximation in the parameter $a/\hbar\Omega \ll 1$, which yields

$$\tau(E) \approx \frac{\hbar}{a} \left\{ 1 - 2 \sum_{p=1}^{\infty} (-1)^p \exp \left(-\frac{2\pi p a}{\hbar\Omega} \right) \times I_p \cos \left[2\pi \left(\frac{E}{\hbar\Omega} + \delta \right) p \right] \right\}. \quad (11)$$

Substituting Eq. (11) into Eq. (10) and completing the standard integration, we have

$$\sigma_{\alpha\alpha} = \sigma_0 + \tilde{\sigma}, \quad (12)$$

where $\sigma_0 = N_e e^2 \tau_0 / m$ is the smooth part of the conductivity, with $\tau_0 = \hbar/a = 4\pi^2 \hbar^3 / m U_0^2 n_i$.

The oscillating part of the conductivity $\tilde{\sigma}$ is given by

$$\tilde{\sigma} = -2\sigma_0 \sum_{p=1}^{\infty} (-1)^p \exp \left(-\frac{2\pi p}{\tau_0 \Omega} \right) R_p^T I_p \cos \left(\frac{2\pi \mu}{\hbar\Omega} p \right), \quad (13)$$

where

$$R_p^T = \frac{Z_p}{\sinh Z_p} \quad (14)$$

is the standard temperature factor, with $Z_p = 2\pi^2 T p / \hbar\Omega$. We also have neglected the small phase shift δ , since energies of the order of $E \approx \mu$ are important in the integral of Eq. (10).

Considering at first the case of a solitary layer ($I_p = 1$) and zero temperature ($R_p^T = 1$), one can perform an elementary summation in Eq. (14) to obtain

$$\tilde{\sigma} = \sigma_0 \left[1 - \frac{\sinh \nu}{\cosh \nu + \cos\left(\frac{2\pi\mu}{\hbar\Omega}\right)} \right], \quad (15)$$

where $\nu = 2\pi/\Omega\tau_0$.

On the other hand, the oscillating part of the magnetization of a 2D electron gas at zero temperature can be written as a sum¹⁰

$$\tilde{M} = M_0 \sum_{p=1}^{\infty} \frac{(-1)^p}{p} \exp\left(-\frac{2\pi p}{\tau_0\Omega}\right) \sin\left(\frac{2\pi\mu}{\hbar\Omega} p\right), \quad (16)$$

which can be completed to yield

$$\tilde{M} = M_0 \arctan \left[\frac{\sin\left(\frac{2\pi\mu}{\hbar\Omega}\right)}{\cos\left(\frac{2\pi\mu}{\hbar\Omega}\right) + e^\nu} \right]. \quad (17)$$

Here M_0 is independent of the magnetic field H .

Comparing Eqs. (15) and (17) we arrive at the relation between $\tilde{\sigma}$ and \tilde{M} for a 2D electron gas with δ -potential impurities at zero temperature:

$$\frac{\tilde{\sigma}}{\sigma_0} \approx AH^2 \frac{\partial}{\partial H} \left(\frac{\tilde{M}}{M_0} \right), \quad (18)$$

where $A = e\hbar/\pi mc\mu$. Since $AH \approx \hbar\Omega/\pi\mu \ll 1$, we see that relative amplitude of the SdH oscillation $\tilde{\sigma}/\sigma_0$ is much less than the corresponding relative oscillations of the magnetization \tilde{M}/M_0 in the dHvA effect. Nonetheless, the first observation in 1930 of the SdH oscillations by Shubnikov and de Haas preceded the discovery of the dHvA effect.²⁴

Recently, Eq. (18) was proved experimentally in a 2D organic superconductor of the ET family.⁷ The shape of the SdH oscillations observed was nonsinusoidal and very similar to that given by Eq. (15) and shown in Fig. 1. What is strange in this connection that the SdH signal was measured in a geometry in which both the magnetic field and current were directed perpendicular to the layers. The temperature was nonzero and varied within the range 0.4–1.27 K. On the other hand, it is easy to see that, strictly speaking, Eq. (18) does not hold under those conditions. First of all this is because of the anisotropy of the conductivity in the direction perpendicular to the layers. Secondly, the layer factor I_p and the factor R_p^T (as well as some other factors which we discuss below) are functions of the inverse magnetic field $1/H$, and this must be taken into account in the derivative $\partial\tilde{M}/\partial H$.

The additional degrees of freedom related to the spin of electron and bound states due to impurities (the so-called magnetoimpurity levels¹⁵) can be easily taken into consideration. In these cases the energy of an electron gains a shift $\varepsilon \rightarrow \varepsilon + \zeta$, where ζ is an energy variable related to the additional degree of freedom. If the DOS for ζ is given by $G(\zeta)$, then

$$I_p \rightarrow I_p R_p, \quad (19)$$

where

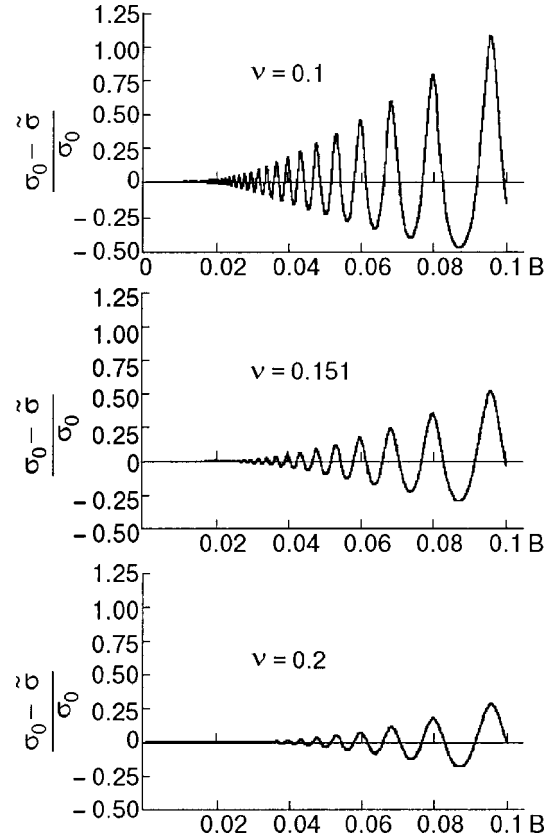


FIG. 1. Field dependence of the conductivity given by Eq. (15) (in conventional units $B = \hbar\Omega$) for $\mu = 1000$, $\nu = 0.1, 0.151, 0.2$ ($\nu = 2\pi\hbar/\tau_0$).

$$R_p = \int_{-\infty}^{\infty} d\zeta G(\zeta) \exp\left(i \frac{2\pi\zeta}{\hbar\Omega} p\right). \quad (20)$$

In the case of a spin

$$G(\zeta) = \frac{1}{2} [\delta(\zeta - \mu_e H) + \delta(\zeta + \mu_e H)], \quad (21)$$

where $\mu_e = \hbar e/2m_e c$ is the Bohr magneton. The corresponding spin factor R_p^s reads

$$R_p^s = \cos\left(\pi \frac{m}{m_e} p\right). \quad (22)$$

This is a standard spin factor, known in magnetooscillations.¹⁰ Another factor appears if impurities split bound states from the Landau levels.¹⁵ This magnetoimpurity effect is stronger in 2D systems than in the 3D case. If we denote this splitting by $\Delta_i(H)$, then the appropriate DOS is again given by the δ function

$$G^i(\zeta) = \delta(\zeta \pm \Delta_i). \quad (23)$$

The corresponding damping factor due to the magnetoimpurity bound states is

$$R_p^i = \cos\left(\frac{2\pi\Delta_i}{\hbar\Omega} p\right). \quad (24)$$

The \pm signs in Eq. (23) correspond to attractive and repulsive impurities. In the case $\Delta_i \ll \hbar\Omega$ the splitting value does not depend on p .¹⁶ Putting together all the above discussed

damping factors and taking the factor I_p in the form given by Eqs. (7)–(9), we can write the oscillating part of the in-plane conductivity in the form

$$\bar{\sigma} = \bar{\sigma}_1 + \bar{\sigma}_2 \quad (25)$$

with

$$\begin{aligned} \bar{\sigma}_1 = & -2\sigma_0(1-c) \sum_{p=1} \exp\left(-\frac{2\pi p}{\tau_0\Omega}\right) \\ & \times R_p^T R_p^i R_p^s J_0\left(\frac{4\pi t}{\hbar\Omega} p\right) \cos\left(\frac{2\pi\mu}{\hbar\Omega} p\right), \end{aligned} \quad (26)$$

$$\begin{aligned} \bar{\sigma}_2 = & -2\sigma_0 c \sum_{p=1} \exp\left(-\frac{2\pi p}{\tau_1\Omega}\right) \\ & \times R_p^T R_p^i R_p^s \cos\left(\frac{4\pi t}{\hbar\Omega} p\right) \cos\left(\frac{2\pi\mu}{\hbar\Omega} p\right). \end{aligned} \quad (27)$$

Here $\nu_1 = 2\pi/\tau_1\Omega$, where

$$\tau_1 = \frac{\hbar}{a + \sqrt{t^2 - t_0^2}} \quad (28)$$

is the renormalized (on account of the stacking faults) effective electron lifetime. At zero temperature we have

$$\begin{aligned} \bar{\sigma}_2 = & -\frac{\sigma_0 c}{8} \\ & \times \sum_{\alpha, \beta, \gamma = \pm} \left\{ \frac{\sinh \nu_1}{\cosh \nu_1 - \cos\left[(\mu + \alpha\Delta_i + \beta t) + \gamma \frac{\pi m}{m_e}\right]} - 1 \right\}. \end{aligned} \quad (29)$$

Despite the fact that $\bar{\sigma}_2$ is proportional to the stacking fault concentration c , it may be important at small $\nu_1 \ll 1$, since in this case $\bar{\sigma}_2$ has a sharp δ -like peaks, as is seen in Fig. 2.

CONCLUSIONS AND DISCUSSION

The two major experimental tools of the fermiology, the SdH and the dHvA effects, have proved to be very useful not only for studies of conventional 3D metals but also for recent analysis of the new layered organic conductors and superconductors, including the high- T_c cuprates. Though both effects are based on the Landau quantization, the SdH effect, as is well known from the textbooks on fermiology,^{10,17,25} is much more difficult to study theoretically, since it requires calculations for the transition probabilities caused by electron scattering on impurities in an external magnetic field. This scattering in turn strongly depends on the dimensionality of the system in question and manifests itself in different kinetic characteristics of organic conductors, such as the high-frequency impedance²⁶ and the SdH in quasi-2D conductors, which is the subject of the present publication. Contrary to the wide-spread opinion, even among the experts, it is the SdH oscillations, rather than the dHvA effect, which were first observed in 1930 in Leiden by Shubnikov and de Haas and thereby laid the foundation of modern fermiology. This point, as well as the dramatic history of the discovery of the SdH effect, can be found in the interesting historical essay of Ref. 24.

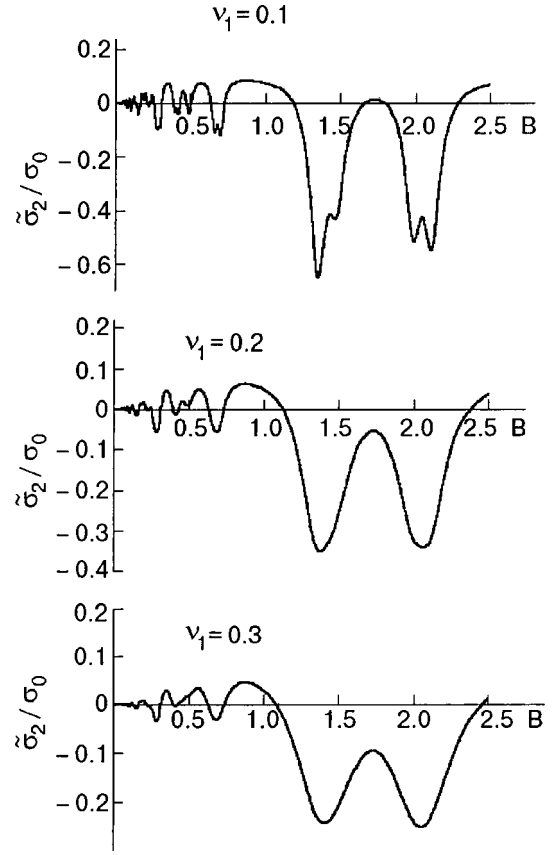


FIG. 2. Field dependence of the oscillating part of the conductivity caused by the stacking faults and given by Eq. (29) (in conventional units $B = \hbar\Omega$) for $\mu = 1000$, $c = 0.1$, $t = 0.1$, $\Delta_i = 0.5$, $m/m_e = 1.5$, $\nu_1 = 0.1, 0.2, 0.3$ ($\nu_1 = 2\pi\hbar/\tau_1$).

In this paper we have calculated the SdH oscillations within an approach which generalizes the Green function method developed by Maniv and Vagner²³ for the electron scattering problem in a quasi-2D electron gas. The calculated oscillating part of the diagonal component of the in-plane conductivity tensor $\bar{\sigma}$, Eq. (13), and the electron lifetime τ , Eq. (11), turned out to be dependent on the very same layer factor I_p , Eq. (1), which modulates the dHvA oscillations of the layered conductors¹² and depends on the layer stacking. At zero temperature and in the 2D limit a simple relation was established between the relative in-plane SdH oscillations, $\bar{\sigma}/\sigma_0$, and the corresponding relative dHvA oscillations of the magnetization \tilde{M}/M_0 . This relation is given by Eq. (18), which holds only for the 2D electron gas. The anisotropy of the 2D Fermi surface and also nonzero temperature and electron hopping across the layers bring additional terms to Eq. (18). Nonetheless, this equation has been experimentally verified by simultaneous dHvA and SdH measurements on the organic conductor $\beta''-(\text{BEDT-TTF})_2\text{SF}_5\text{CH}_2\text{SO}_3$ within the temperature range 0.4–1.27 K for the interlayer component of the conductivity tensor.⁷ The shape of these strongly nonsinusoidal oscillations is the same as given by Eq. (15) and shown in Fig. 1. The enhancement of the impurity scattering potential makes these oscillations lower in amplitude but more sinelike in form. The spin splitting and magnetoimpurity bound states yield additional factors, R_p^s and R_p^i , respectively, which modulate the SdH oscillations [see Eqs.

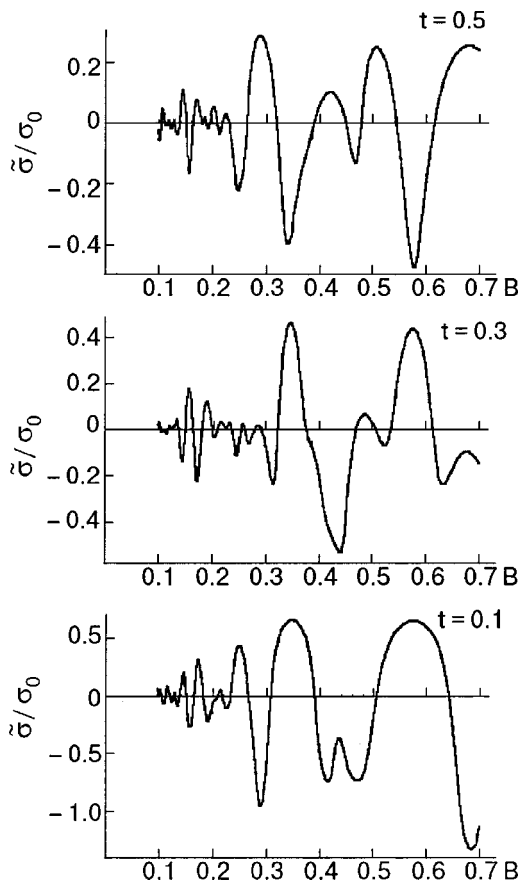


FIG. 3. Field dependence of the oscillating part of the conductivity given by Eq. (25)–(28) (in conventional units $B = \hbar\Omega$) for $\mu = 1000$, $c = 0.2$, $\Delta_i = 0.5$, $m/m_e = 1.5$, $T = 0.001$, $\nu = 0.1$, $\nu_1 = 0.2$, $t = 0.1, 0.3, 0.5$ ($\nu = 2\pi\hbar/\tau_0$, $\nu_1 = 2\pi\hbar/\tau_1$).

(25)–(27)] and result in a large variety of oscillation patterns, as displayed in Figs. 2 and 3.

The stacking faults modify the Dingle-like exponent in Eq. (27) through the effective lifetime τ_1 [Eq. (28)]. The appropriate correction to the oscillation $\bar{\sigma}_2$ arises due to the stacking faults and at zero temperature has periodic δ -like peaks when $\nu_1 \ll 1$. It is substantial even for low concentrations of stacking faults, as one can see in Fig. 2.

The oscillation patterns displayed in Figs. 1–3 are very diverse. The peaks in Figs. 2 and 3 are split because of the spin and magnetoimpurity factors and are sensitive to variations of the other parameters of the model. Some additional analysis of the SdH oscillations within this model will be published elsewhere. The results and methods of this paper will be also applied to the anisotropic 2D Fermi-surface structures typical for real organic layered (super) conductors.

The author is grateful to Tsofar Maniv and Israel Vagner for numerous stimulating discussions on the problem of electron scattering in a quasi-2D gas in magnetic field and to Peter Wyder for hospitality during his stay at the Grenoble High Magnetic Field Lab.

*E-mail: Vladimir.M.Gvozdkov@univer.kharkov.ua

- ¹F. A. Meyer, E. Steep, W. Biberacher, P. Crist, A. Lerf, A. G. M. Jansen, W. Joss, and P. Wyder, *Europhys. Lett.* **32**, 681 (1995).
- ²N. Harrison, J. Caulfield, J. Singleton, P. H. P. Reinders, F. Herlach, W. Hayes, M. Kurmoo, and P. Day, *J. Phys.: Condens. Matter* **8**, 5415 (1996).
- ³E. Steep, L. H. Nguen, W. Biberacher, H. Muller, A. G. M. Jansen, and P. Wyder, *Physica B* **259–261**, 1079 (1999).
- ⁴M. M. Honold, N. Harrison, M. S. Nam, J. Singleton, C. H. Mielke, M. Kurmoo, and P. Day, *Phys. Rev. B* **58**, 7560 (1998).
- ⁵M. Shiller, W. Schmidt, E. Balthes, D. Schwitzer, H. J. Koo, M. H. Wan-hbo, I. Heinen, T. Kalusa, P. Kircher, and W. Strunz, *Europhys. Lett.* **51**, 82 (2000).
- ⁶M. V. Kartsovnik, G. Yu. Logvenov, T. Ishiguro, W. Biberacher, H. Anzai, and N. D. Kusch, *Phys. Rev. Lett.* **77**, 2530 (1996).
- ⁷J. Wosnitzer, S. Wanka, J. Hagel, H. v. Lohneysen, J. S. Qualls, J. S. Brooks, E. Balthes, J. A. Schlueter, U. Geiser, J. Mohtasham, R. W. Winter, and G. R. Gard, *Phys. Rev. Lett.* **86**, 508 (2001).
- ⁸I. M. Lifshitz and A. M. Kosevich, *Sov. Phys. JETP* **2**, 639 (1953).
- ⁹I. D. Vagner, T. Maniv, and E. Ehrenfreund, *Phys. Rev. B* **51**, 1700 (1983); K. Jauregui, V. I. Marchenko, and I. D. Vagner, *Phys. Rev. B* **41**, 12922 (1990); P. D. Grigor'ev and I. D. Vagner, *JETP Lett.* **69**, 156 (1999).
- ¹⁰D. Shoenberg, *Magnetic Oscillations in Metals*, Cambridge University Press, Cambridge (1984).
- ¹¹T. Champel and V. P. Mineev, *Philos. Mag.* **B 81**, 55 (2001).
- ¹²V. M. Gvozdkov, *Fiz. Tverd. Tela (Leningrad)* **26**, 2574 (1984) [*Sov. Phys. Solid State* **26**, 1560 (1984)].
- ¹³V. M. Gvozdkov, *Fiz. Tverd. Tela (Leningrad)* **28**, 320 (1984) [*Sov. Phys. Solid State* **28**, 179 (1986)].
- ¹⁴V. M. Gvozdkov, *Fiz. Nizk. Temp.* **12**, 705 (1986) [*Sov. J. Low Temp. Phys.* **12**, 399 (1986)].
- ¹⁵A. M. Ermolaev and M. I. Kaganov, *JETP Lett.* **6**, 171 (1967).
- ¹⁶V. M. Gvozdkov, A. M. Ermolaev, and Yu. A. Sharapov, *Vestnik Kharkovskogo Natsional'nogo Universiteta*, 476, Ser. "Fizika," N 4, 18 (2000).
- ¹⁷A. A. Abrikosov, *Fundamentals of Theory of Metals* (in Russian) Nauka, Moscow (1987).
- ¹⁸T. Ando, A. B. Fowler, and F. Stern, *Rev. Mod. Phys.* **54**, 437 (1982).
- ¹⁹N. Harrison, R. Bogaerts, P. H. P. Reinders, J. Singleton, S. J. Blundell, and F. Herlach, *Phys. Rev. B* **54**, 9977 (1996).
- ²⁰A. E. Datars and J. E. Sipe, *Phys. Rev. B* **51**, 4312 (1995).
- ²¹R. H. Mc Kenzie and P. Moses, *Phys. Rev. Lett.* **81**, 44922 (1998).
- ²²T. Ando and Y. Uemura, *J. Phys. Soc. Jpn.* **36**, 959 (1974).
- ²³T. Maniv and I. D. Vagner, *Phys. Rev. B* **38**, 6301 (1988).
- ²⁴B. I. Verkin, S. A. Gredeskul, L. I. Pastur, and Yu. A. Freyman, *Fiz. Nizk. Temp.* **16**, 1203 (1990) [*Sov. J. Low Temp. Phys.* **16**, 696 (1990)].
- ²⁵I. M. Lifshits, M. Ya. Azbel', and M. I. Kaganov, *The Electron Theory of Metals*, Nauka, Moscow (1971).
- ²⁶V. G. Peschansky, I. V. Kozlov, and K. Jiasemides, *Fiz. Nizk. Temp.* **26**, 225 (2000) [*Low Temp. Phys.* **26**, 169 (2000)].

This article was published in English in the original Russian journal. Reproduced here with stylistic changes by AIP.

Giant magnetooscillations of the Josephson current

L. P. Gor'kov

*National High Magnetic Field Laboratory, Florida State University, Tallahassee, FL 32306, USA;
L. D. Landau Institute for Theoretical Physics, Russia*

V. Z. Kresin*

Lawrence Berkeley Laboratory, University of California, Berkeley, CA 94720

(Submitted June 19, 2001)

Fiz. Nizk. Temp. **27**, 963–966 (September–October 2001)

Josephson current flowing through an antiferromagnetic metallic barrier is studied. We consider the most interesting case of the spin-valve structure when the barrier is formed by ferromagnetic layers ordered antiferromagnetically in the direction perpendicular to the current. The most remarkable feature is the onset of giant magnetooscillations of the current amplitude. © 2001 American Institute of Physics. [DOI: 10.1063/1.1401179]

INTRODUCTION

The study of various resonance phenomena is an important area of condensed matter physics related to unique information about the spectra and properties of various materials. Measurements of such phenomena as Shubnikov-de Haas oscillations, de Haas-van Alphen effects, cyclotron resonance, etc., are well known and are described in many textbooks and monographs.

In this article we will describe the giant magnetooscillation effect. The proposed method, which combines Josephson tunneling spectroscopy and novel magnetic systems, is very sensitive to the magnetic structure of compounds.

We focus on the special case of the S–N–S junctions when the normal (N) metallic barrier is a magnetic compound. It is well known that the ferromagnetic material (F) used as a barrier frustrates the Josephson current because of the pair-breaking effect of the exchange field. Below we consider an antiferromagnetic barrier and, more specifically, the most interesting case of the so-called A-structure (S₁–A–S₂ junction). This is the situation when the barrier is formed by a multilayer system. It consists of ferromagnetic layers perpendicular to the S electrodes, with an antiferromagnetic ordering in the direction perpendicular to the current. In other words, neighboring layers have opposite magnetization.

At first, we describe the compounds and their A structure. Afterwards, we introduce the giant magnetooscillation phenomenon for the S₁–A–S₂ junction.

A-STRUCTURE. SPIN-VALVE EFFECT

There are two interesting systems which are characterized by A-structure. One of them is a mixed-valence manganite with some characteristic level of doping, and the second one is an artificial structure, a so-called giant magnetoresistance (GMR) multilayer.

As is known, the most remarkable property of manganites (see review¹) is the colossal magnetoresistance. These materials with the composition A_{1-x}Sr_xMnO₃ (A=La, Ca) have a rather complicated phase diagram.

The low-temperature phase diagram has been analyzed in our previous papers.^{2,3} The parent material, LaMnO₃, is an insulator. The region 0.17 < x < 0.5 corresponds to a metallic state. The undoped manganite (e.g., LaMnO₃ crystal) has the following cubic structure. The Mn³⁺ ions are located at the corners, and the La ion is at the center of the unit cell. In addition, the Mn³⁺ is caged by an O²⁻ octahedron; locally this forms an MnO₆ complex with the Mn ion in the central position surrounded by light O ions.

The *d* shell of the Mn ion in the cubic environment is split into a doublet and triplet. It is important that the three-fold manifold (*t*_{2g}) is occupied by three *d* electrons, whereas the upper doubly degenerate term *e*_{2g} is occupied by one electron only.

The key ingredients (interactions) are the following: 1) the strong Hund's rule coupling (this is the largest energy scale) aligns all spins in the same direction; 2) hopping, and 3) cooperative Jahn–Teller (JT) effect. As a result, the total Hamiltonian is a sum:

$$H = H_H + H_t + H_{JT}. \quad (1)$$

Here

$$H_H = J_H \sum_i \boldsymbol{\sigma} \cdot \mathbf{S}_i, \quad (2)$$

$$H_t = \sum_i t_{i,i+\delta}, \quad (3)$$

$$H_{JT} = \sum_i g(\boldsymbol{\tau}_i \cdot \mathbf{Q}_i) + \sum_i J_{el} \mathbf{Q}_i^2, \quad (4)$$

where \mathbf{Q} is a normal coordinate, $\boldsymbol{\sigma}$ is the electronic spin, \mathbf{S} is the ionic spin, J_{el} is the elastic parameter, and $\boldsymbol{\tau}$ is the pseudospin.

The Hund's coupling between the local spin \mathbf{S} ($S = 3/2$) formed by the *t*_{2g} electrons and the *e*_{2g} electron is described by the term (2); $\boldsymbol{\sigma}$ (Pauli matrices) correspond to the spin of the *e*_{2g} electron; $J_H \sim 1$ eV. Note that the unit cell

contains one e_{2g} electron, and its motion through the lattice is described (in the tight-binding picture) by the term (3).

The third term in Eq. (1) describes another important ingredient which also affects the behavior of the system, namely the Jahn–Teller instability. Indeed, the e_{2g} electron is in the doubly degenerate state, and it follows from the JT theorem that the electron–lattice coupling will lead to a static distortion and consequently, to a change in the crystal symmetry. In Eq. (4) g is the electron–phonon coupling constant, and \mathbf{Q}_i are the local active JT modes.

In a simple band picture with one electron per unit cell, the system should be metallic. This is contrary to the experimental fact that the parent compound is an insulator. Nevertheless, a more careful analysis which includes not only the hopping term, but also a strong Hund's interaction along with the cooperative Jahn–Teller effect, leads one to the picture of a peculiar band insulator.^{2,3}

As noted above, Hund's coupling corresponds to the largest energy scale ($J_H \sim 1$ eV), so that $J_H \gg t$, gQ_0 ; $t \sim gQ_0 \sim 0.1$ eV.

It is interesting that the magnetic structure of the undoped crystal belong to the A-type: antiferromagnetic (AF) ordering along the Z axis along with the ferromagnetic ordering in the XY plane. The appearance of such a structure is caused by an interplay between the Hund's interaction and the hopping energy. In other words, the A-structure is stabilized by the gain in the kinetic energy of the band electron. One can explain the underlying physics by considering the two-center problem ($\text{Mn}^{3+} - \text{Mn}^{4+}$ with spins S_1 and S_2). The low-energy electronic term has the form:

$$E = -J_H S + t \cos q/2 - O(t^2/J_H). \quad (5)$$

Therefore, at $J_H \gg t$, the main gain in the energy is due to the $-J_H S$ term. Although, because of the averaging, there is no linear contribution to the total energy, a small gain, of the order of t^2/J_H , is achieved. The relation $t^2/J_H \ll t$ sets a lower energy scale for the Néel temperature T_N , which is indeed small (~ 140 K) relative to the structural transition temperature (~ 0.1 eV). Within a single layer the electrons may be treated as ferromagnetically polarized. This ferromagnetism is provided by the double-exchange mechanism introduced by Zener⁴ and developed in Refs. 5 and 6.

As was noted above, the pure LaMnO_3 compound can be treated as a band insulator. This means that a change in the carrier concentration might lead to metallic behavior.

Consider now a doped manganite, e.g., $\text{La}_{1-x}\text{Ca}_x\text{MnO}_3$. An increase in x will lead initially to the formation of finite clusters; each of them contains itinerant polarized electrons. Eventually one can observe the formation of an infinite cluster and the transition to the metallic ferromagnetic state. Such transition can be described by percolation theory.

A very interesting observation was reported in Refs. 7–10. The presence of a *metallic* A-phase was observed. The examples are the compounds $\text{A}_{1-x}\text{Sr}_x\text{MnO}_3$ ($\text{A}=\text{La}, \text{Nd}$) with $x=0.55$, or $\text{Pr}_{0.5}\text{Sr}_{0.5}\text{MnO}_3$. This is a natural spin-valve structure.

Another case is an artificial A-structure, which is basic to the GMR phenomenon (see reviews^{11,12}). Such a multilayer system (e.g., $\text{Co}-\text{Al}_2\text{O}_3-\text{Co}$) consists of alternating ferro-

magnetic and nonmagnetic layers, with an antiferromagnetic ordering in the direction perpendicular to the layers.

Let us evaluate the energy spectrum for such a metallic A-system. This is an important step for the calculation of the Josephson current through such a barrier. For concreteness, we consider a metallic manganite in the A-phase.

The Hamiltonian for the barrier's states has the form:

$$\begin{aligned} H = & \sum_{\mathbf{p}} t(\mathbf{p}) a_{\mathbf{p}\sigma}^+ a_{\mathbf{p}\sigma'}^+ + \sum_{\mathbf{p}, \mathbf{Q}} J_H S(\mathbf{Q}) a_{\mathbf{p}\sigma'}^+ (\hat{\sigma}_z)_{\sigma' \sigma''} a_{\mathbf{p}-\mathbf{Q}; \sigma''} \\ & + \sum_{\mathbf{p}, \mathbf{Q}} J_H S(-\mathbf{Q}) a_{\mathbf{p}\sigma'}^+ (\hat{\sigma}_z)_{\sigma' \sigma''} a_{\mathbf{p}-\mathbf{Q}; \sigma''} \\ & + \sum_{\mathbf{p}} J_H M a_{\mathbf{p}\sigma'}^+ (\hat{\sigma}_x)_{\sigma' \sigma''} a_{\mathbf{p}-\mathbf{Q}; \sigma''}. \end{aligned} \quad (6)$$

Here $t = t_{\perp} + t_{\parallel}$, t_{\perp} and t_{\parallel} are electron hopping parameters for the in-plane and out-of-plane motion, J_H is the Hund's coupling, and $S(\mathbf{Q})$ is the Fourier component of the AFM ordering along the c directions; $\langle S_z \rangle = S(-1)^n$. The structural vector $\mathbf{Q} = (0, 0, \pi/a)$ reduces the Brillouin zone (a is the lattice constant). We consider the more general case of a canted structure; M is the canted magnetic moment: $S_i = (\pm \langle S_z \rangle, M_x)$, $S_z^2 + M_x^2 = S(S+1) \cong S^2$. Note that the Jahn–Teller effect is not essential for the metallic state.

With the use of the equation of motion

$$(\tilde{\varepsilon} - t_{\parallel}) a_{\mathbf{k}\sigma} = J_H S(\pm \mathbf{Q}) \hat{\sigma}_z a_{\mathbf{k}-\mathbf{Q}; \sigma} + J_H M (\hat{\sigma}_x)_{\sigma \sigma'} a_{\mathbf{k}\sigma'} \quad (7)$$

and a similar equation for $\mathbf{k} \rightarrow \mathbf{k} + \mathbf{Q}$ ($\tilde{\varepsilon} = \varepsilon - t_{\perp}$), one can determine the following energy spectrum:

$$\tilde{\varepsilon} = \pm [J_H^2 S^2 \pm 2J_H M t_{\parallel} + t_{\parallel}^2]^{1/2} \quad (8)$$

which consists of four branches. For the manganites $J_H \gg t$ (see above). As a result, for these systems, only two branches are filled:

$$\tilde{\varepsilon}_{1,2} \cong -J_H S \pm (M/S) t_{\parallel}. \quad (9)$$

JOSEPHSON CURRENT THROUGH AN ANTI-FERROMAGNETIC BARRIER. MAGNETOOSCILLATIONS

Let us evaluate the Josephson current through the A-barrier. We consider the case of a singlet pairing (s or d), i.e., the Cooper pair consists of two carriers with opposite spins and momenta. The A-barrier contains states with opposite spins; they belong to neighboring layers and, contrary to the F barrier, one should not expect any frustration for the Josephson current. Nevertheless, the calculation of the current should be carried out with considerable care. Indeed, the Josephson current is a transfer of correlated electrons, and this implies that the layers are not totally independent. The barrier should be treated as an anisotropic metal with the spectrum (8), (9). The Josephson current can be evaluated with use of the spectrum (8), (9) and the interface Hamiltonian:

$$H_{\text{pair}} = V \Delta_i \Psi(i) \Psi^+(i) \quad (10)$$

which describes the transition of a pair in the i th superconductor ($i=1,2$) into the barrier (Δ_1, Δ_2 are the order parameters, and $\Psi(i)$ and $\Psi^+(i)$ are the field operators for electrons of the barrier). With the use of Eq. (10) we find a correction to the thermodynamic potential, $\delta\Omega$, caused by the barrier; the current is obtained as $\delta\Omega/\delta\varphi$, with φ being a phase difference between two superconductors' order parameters. The Josephson current is determined by the Cooper diagram:

$$K = \pi T |V^2| \sum_{\omega_n} \Delta_1 \Delta_2 \int d\mathbf{p} d\mathbf{q} \exp(i\mathbf{q} \cdot \mathbf{L}) \Pi(i\omega_n, \mathbf{q}), \quad (11)$$

where

$$\begin{aligned} \Pi(i\omega_n, \mathbf{q}) = & \sum_{\sigma, \sigma', \sigma'', \sigma'''} (\hat{\sigma}_y)_{\sigma, \sigma'} G_{\sigma, \sigma'}(i\omega_n, \mathbf{p}) (\sigma'_y)_{\sigma'', \sigma'''} \\ & \times G_{\sigma'', \sigma'''}(-i\omega_n, \mathbf{q} - \mathbf{p}) \\ = & 2[G_{\uparrow\uparrow}(i\omega_n, \mathbf{p}) G_{\uparrow\downarrow}(-i\omega_n, \mathbf{q} - \mathbf{p}) \\ & - G_{\downarrow\downarrow}(i\omega_n, \mathbf{p}) G_{\downarrow\uparrow}(-i\omega_n, \mathbf{q} - \mathbf{p})] \end{aligned} \quad (12)$$

(we use the method of thermodynamic Green's functions; see, e.g., Ref. 13), and L is the distance between the superconductors.

The Green's function appearing in Eq. (12) can be expressed in terms of new Fermi amplitudes which correspond to the branches (8), (9). The transformation to the new amplitudes can be described by a canonical transformation $a_{\mathbf{p}\sigma} = \sum_i K_{\sigma i} \alpha_{i\mathbf{p}}$; one can show that $\sigma \equiv (\uparrow\downarrow)$, $K_{\sigma 1} = 0.5[1 - (M/S)]^{1/2}$; $K_{\uparrow 2} = -K_{\downarrow 2} = 0.5[1 + (M/S)]^{1/2}$, where the operators $\alpha_{i\mathbf{p}}$ correspond to the branches (8), (9). Then we obtain the following expression for the Cooper term:

$$\begin{aligned} j_m = & \left(1 - \frac{M}{S}\right) |V^2| |\Delta_1|^2 |\Delta_2|^2 \pi T \\ & \times \sum_{\omega_n > 0} \int dl v_{\perp} \int dp_z \exp\left(-\frac{\omega_n L}{v_{\perp}}\right) \cos\left(\frac{L t_{\parallel} M}{S v_{\perp}}\right). \end{aligned} \quad (13)$$

In the tight-binding approximation $t_{\parallel} = t_0 \cos(p_z d_c)$. Equation (13) contains the integration over the cross section of the Fermi surface (dl).

As a result, we arrive at the following expression for the amplitude of the Josephson current:

$$J_m = r [1 - (M/S)^2] f(L/\zeta_N) J_0(\beta M/S). \quad (14)$$

Here $\zeta_N = \hbar v_F / 2\pi T$ is the coherence length inside the barrier, $\beta = (t_0/T_c)(L/\xi_0)$; $\xi_0 = \hbar v_F / 2\pi T_c$, $v_F = v_F^0$ is the minimum value of the component of the Fermi velocity along L , $r \propto p \Delta_1 \Delta_2 V^2$, and $f(x) = \exp(-x)$ for $x \gg 1$ and $f(x) = x^{-1}$ for $x \ll 1$. Therefore, near $T=0$ K, the function $f = \zeta_N/L$. Note that, since $r \propto T$, the amplitude J_m in this case does not depend on T . However, near T_c and in the intermediate temperature region, the exponential dependence $f = \exp(-L/\zeta_N)$ is perfectly realistic.

DISCUSSION

Consider the junction placed in an external magnetic field, which creates the canting. For weak magnetic field the

canting is small, and the dependence of the amplitude is determined by the factor $J_0(\beta M/S)$ in Eq. (14). Since $\beta \gg 1$, one can use an asymptotic expression for the Bessel function, and we obtain:

$$\begin{aligned} J_m = & r [1 - (M/S)^2] \exp\left(-\frac{L}{\xi_N(T)}\right) \\ & \times \left(\frac{\pi \beta M}{2S}\right)^{-1/2} \cos\left(\frac{\beta M}{S} - \frac{\pi}{4}\right). \end{aligned} \quad (15)$$

The expression is valid if $L \gg \zeta_N$.

Equations (14) and (15) display a remarkable property of a junction with an A-barrier, namely, the phenomenon of giant magnetooscillations (GMO). Indeed, one can see directly from Eq. (15) that the amplitude oscillates as a function of M , and, therefore, as a function of the external field H .

The GMO effect is caused by magnetic structure (spin-valve effect) and is entirely different from the usual Fraunhofer oscillations. Note also that, because $\beta \gg 1$, the period of the GMO is much smaller. Moreover, one can choose a geometry of the Josephson contact such that the only the magnetic structure is affected by the magnetic field. An increase in magnetic field eventually leads to the situation that $M=S$; then $J_m=0$ (see Eqs. (14) and (15)). This occurs because the external field affects the magnetic ordering in the barrier. If $M=S$, then we are dealing with 3D ferromagnetic ordering. As to the the S-F contact, it frustrates the Josephson current; this is due to the pair-breaking effect of the exchange field (we are not considering some modifications caused by the spin-orbital coupling; see (Ref. 14). Therefore, the amplitude of the current can be controlled by an external magnetic field and even switched off at larger H (order of 1 T). Note that for the GMR structure the switching can be obtained with the use of a weaker magnetic field (of the order of 3–4 Oe).

In summary, we have shown that Josephson current can flow through an antiferromagnetic barrier. The most interesting case corresponds to the case of A-ordering in the direction perpendicular to the current. One can show that the amplitude of the current oscillates as a function of applied magnetic field (GMO).

Lev Vasilievich Shubnikov was a remarkable scientist who made key contributions to various areas of physics. We are pleased that this paper is published in the Special Issue devoted his memory.

*E-mail: vzkresin@lbl.gov

¹J. Coey, M. Viret, and S. von Molnar, Adv. Phys. **48**, 167 (1999).
²L. Gor'kov and V. Kresin, JETP Lett. **67**, 985 (1998).
³M. Dzero, L. Gor'kov, and V. Kresin, Eur. Phys. J. B **14**, 459 (2000).
⁴G. Zener, Phys. Rev. **82**, 403 (1951).
⁵P. Anderson and H. Hasegawa, Phys. Rev. **100**, 675 (1955).
⁶P. de Gennes, Phys. Rev. **118**, 141 (1960).
⁷H. Kawano, R. Kajimoro, H. Yoshizawa, Y. Tomioka, H. Kuwahara, and Y. Tokura, Phys. Rev. Lett. **78**, 44253 (1997).
⁸H. Fujituro, M. Ikebe, and Y. Konno, J. Phys. Soc. Jpn. **67**, 1799 (1998).
⁹M. Isumi, T. Manako, Y. Konishi, M. Kawasaki, and Y. Tokura, Phys. Rev. B **61**, 12187 (2000).

- ¹⁰Y. Morimoto, T. Akimoto, A. Nakamura, K. Ohoyama, and M. Ohashi, Phys. Rev. B **58**, 5544 (1998).
¹¹S. S. P. Parkin, Annu. Rev. Mater. Sci. **25**, 358 (1995).
¹²*Ultrathin Magnetic Structures II*, B. Heinrich and J. A. C. Bland (Eds.), Springer-Verlag, Berlin (1994).
¹³A. Abrikosov, L. Gor'kov, and I. Dzyaloshinskii, Methods of Quantum

Field Theory in Statistical Physics, Dover, New York (1975).

- ¹⁴E. Demler, G. Arnold, and M. Beasley, Phys. Rev. B **55**, 15174 (1997).

This article was published in English in the original Russian journal. Reproduced here with stylistic changes by AIP.

The critical current of superconductors: an historical review

D. Dew-Hughes*

Oxford University, Department of Engineering Science, Parks Road, Oxford OX1 3PJ, UK
(Submitted May 4, 2001)

Fiz. Nizk. Temp. **27**, 967–979 (September–October 2001)

The most important practical characteristic of a superconductor is its critical current density. This article traces the history of the experimental discoveries and of the development of the theoretical ideas that have led to the understanding of those factors that control critical current densities. These include Silsbee's hypothesis, the Meissner effect, the London, Ginsburg–Landau, and Abrikosov theories, flux pinning and the critical state, and the control of texture in high-temperature superconductors. © 2001 American Institute of Physics.
[DOI: 10.1063/1.1401180]

INTRODUCTION

The most important characteristic of any superconductor, from the viewpoint of practical applications, is the maximum electrical transport current density that the superconductor is able to maintain without resistance. This statement is equally true for large-scale applications, such as power transmission lines, electromagnets, transformers, fault-current limiters and rotating machines, as well as for small-scale electronic applications such as passive microwave devices and devices based on the Josephson effect. High lossless current densities mean that machines and devices can be made much smaller and more efficient than if made with a conventional resistive conductor. This was realized immediately upon the discovery of superconductivity; Onnes himself speculating on the possibility of magnet coils capable of generating fields of 10^5 G.¹ These early hopes were dashed by the inability of the then-known superconductors to sustain substantial currents, and applied superconductivity did not become a commercial reality until alloy and compound superconductors based on the element niobium were developed around 1960.² In the two following decades, intensive effort, primarily by metallurgists, led to the understanding of the factors that control critical currents and to the development of techniques for the fabrication of complex multifilamentary flexible conductors at economic prices. The discovery of the mixed copper oxide high-temperature superconductors initially produced a disappointment similar to that experienced by the pioneers of superconductivity. The superconducting characteristics of these materials introduced a new set of obstacles to achieving current densities of magnitudes sufficient for practical device applications. The difficulties involved in producing long lengths of high-current conductor from these materials are only just being overcome.

This article is not intended to be a review of everything that is known about critical currents in superconductors. Its aim is to trace the historical development of the understanding of the factors that control critical current density in superconductors. The significant experimental facts and theoretical ideas that have contributed to the present level of knowledge will be outlined, and the crucial contribution to the topic made by Lev Vasilievich Shubnikov will be highlighted.

THE EARLY YEARS 1911–1936

Within two years of his discovery of superconductivity in mercury, Onnes recorded that there was a “threshold value” of the current density in mercury, above which the resistanceless state disappeared.³ This critical value was temperature dependent, increasing as the temperature was reduced below the critical temperature, according to the expression⁴

$$J_c(T) = J_c(0)(T_c - T)/T_c. \quad (1)$$

A similar behavior was observed in small coils fabricated from wires of tin and lead.⁵ These represent the first-ever superconducting solenoids. Also noticed was the fact that the critical current density in the coils was less than that observed in short, straight samples of wire. This is the first instance of the phenomenon that was to plague the designers of superconducting magnets.

The following year Onnes reported on the influence of a magnetic field on the superconducting transition in lead: “The introduction of the magnetic field has the same effect as heating the conductor.”⁶ The existence of a critical magnetic field, above which superconductivity ceased to exist, was demonstrated. Surprisingly, perhaps because of the intervention of the First World War, Onnes failed entirely to make the connection between the critical current and the critical magnetic field. This connection was left to be made by Silsbee, as a consequence of his examining all of Onnes' published reports in great detail. Silsbee's hypothesis states, “The threshold value of the current is that at which the magnetic field due to the current itself is equal to the critical magnetic field.”⁷ From outside a conductor of circular cross-section, carrying a current I , the current appears to flow in a dimensionless line down the middle of the conductor. At a distance r away from a line current, there is a tangential magnetic field of strength

$$H(r) = I/2\pi r. \quad (2)$$

If the radius of the conductor is a , then the field at the surface of the conductor will be

$$H(a) = I/2\pi a \quad (3)$$

and the critical current, according to Silsbee's hypothesis, will be

$$I_c = 2\pi a H_c. \quad (4)$$

It should be noted that the critical current is thus not an intrinsic property of a superconductor, but is dependent upon the size of the conductor, increasing as the diameter of the conductor is increased. Conversely, the critical current density, also size dependent, decreases as the diameter of the conductor is increased:

$$J_c = 2H_c/a. \quad (5)$$

The experimental confirmation of Silsbee's hypothesis had to wait until after the end of the war. Both Silsbee⁸ and the Leiden laboratory⁹ carried out experiments on wires of differing diameters that did indeed confirm the correctness of the hypothesis. Tuyn and Onnes stated, "On the faith of these results obtained up till now we think we may accept the hypothesis of Silsbee as being correct." Silsbee's summary was, "It may therefore be concluded that the results of these experiments can be completely accounted for by the assumption of a critical magnetic field, without making use of the concept of critical currents."

Equation (2) is valid whatever the actual distribution of the current inside the conductor, and therefore Eq. (4) also holds for a hollow conductor of the same external radius. An ingenious extension of the Leiden experiments was to measure the critical current of a hollow conductor in the form of a film of tin deposited on a glass tube. An independent current was passed along a metal wire threaded through the tube. Depending on the direction of this current the critical current of the tin was either augmented or decreased, as the field at its surface resulted from both currents in the tin film and in the wire. This reinforced the validity of Silsbee's hypothesis.

At the same time, the Leiden laboratory was also making a study of the temperature dependence of the critical field in tin, with the result:^{9,10}

$$H_c(T) = H_c(0) \left[1 - \left(\frac{T}{T_c} \right)^2 \right]. \quad (6)$$

Also hysteresis in the superconducting transition was observed for the first time.¹¹ Hysteresis was subsequently observed in indium, lead, and thallium, and it was suggested that it might be an effect of purity, strain, or crystalline inhomogeneity.¹² It was decided that measurements on single crystals would be desirable, and in 1926 Shubnikov, who at that time was an expert in the growth of single crystals, joined the Leiden laboratory on a four-year secondment.

Meanwhile, in 1925, a new liquid helium laboratory was established at the Physikalische Technische Reichsanstalt in Charlottenberg. Chosen as the head of this laboratory was a former student of Planck, Walther Meissner. Meissner immediately instituted a program of work on superconductivity, but in order to avoid conflict with the Leiden group, this program concentrated on the superconducting transition metals, in particular tantalum and niobium.

At Leiden attention had now turned to binary alloys, one constituent of which was a superconductor and the other a nonsuperconductor. Not only did alloying often raise the

transition temperature to well above that of the superconducting element, but these alloys also exhibited very high critical fields. These investigations culminated in the discovery that the Pb–Bi eutectic had a critical field of about 20 kG at 4.2 K, and its use to generate high magnetic fields was proposed.¹³ This was actually attempted at the Clarendon laboratory in Oxford, to which Lindemann had recruited Simon, Kurti, and Mendelssohn as refugees from Nazi Germany. The attempt failed, as did a similar one by Keesom in the Netherlands. Resistance was restored at levels of magnetic field more appropriate to pure elemental superconductors. The conclusion was that the Silsbee's hypothesis was not valid for alloys.¹⁴

The studies on tin single crystals at Leiden had produced the puzzling results that, in a transverse field, resistance was restored at a value of field one-half of the critical field when the field was applied parallel to the axis of the crystal.¹⁵ Von Laue, better known for his x-ray work, realized the significance of this result and suggested that it would be profitable to explore the distribution of magnetic field in the neighborhood of a superconductor.¹⁶

Meissner had already interested himself in this problem; he and others had considered the possibility of a supercurrent being essentially a surface current. In 1933 Meissner and Ochsenfeld published the results of their experiments in which they measured the magnetic field between two parallel superconducting cylinders. The enhancement of the field as the temperature was lowered below the critical temperature of the cylinders indicated that flux was being expelled from the body of the superconductors.¹⁷

Shubnikov had left Leiden in 1930 to take up a position at the Ukrainian Physicotechnical Institute in Kharkov, where he shortly became the scientific director of the newly established cryogenic laboratory. Liquid helium became available in the laboratory in 1933, and in the following year Rjabinin and Shubnikov gave confirmation of the Meissner effect in a rod of polycrystalline lead.¹⁸

The importance of this discovery of the Meissner effect to the understanding of superconductivity cannot be overemphasised. A perfect conductor will exclude flux if placed in an increasing magnetic field, but should retain flux if cooled to below its transition temperature in a magnetic field. The Meissner effect is the expulsion of flux from the body of a superconductor when in the superconducting state. The transition from the normal state to the superconducting state is path independent, and the superconducting state is thermodynamically stable. Armed with this knowledge it was possible to develop phenomenological theories of superconductivity. Being the more stable state below the transition temperature, the superconducting state has a lower energy than the normal state. It is possible to show, from simple thermodynamics, that the energy per unit volume of the superconducting state relative to the normal state is

$$\Delta G_{ns} = -\frac{1}{2} \mu_0 H_c^2. \quad (7)$$

This is in fact just the energy required to exclude the magnetic field from the superconductor.

Two phenomenological theories followed almost immediately from the discovery of the Meissner effect. The "two-

fluids” model of Gorter and Casimir¹⁹ was able to describe the influence of temperature on the properties of the superconducting state, and it is similar to the theory for liquid helium below its lambda point. In particular, the temperature dependence of the critical magnetic field, Eq. (6), can be derived from the two-fluid model. The London theory deals with the effect of magnetic fields upon the superconducting properties, and describes the spatial distribution of fields and currents within a superconductor.²⁰ The Londons showed that flux was not totally excluded from the body of a superconductor, but that it penetrated exponentially, from the surface, decaying over a characteristic length λ , the penetration depth

$$H(r) = H(0)\exp(-r/\lambda). \quad (8)$$

Associated with the gradient in field is a current

$$J(r) = \frac{\partial H}{\partial r} = -\frac{H(0)}{\lambda}\exp(-r/\lambda). \quad (9)$$

Note that this current has a maximum value at the surface, $r=0$, equal to $H_c(0)/\lambda$. This is the maximum current density that a superconductor can tolerate, and for lead, for example, with a critical field at 4.2 K of $\sim 4.2 \times 10^4$ A/m and a penetration depth of ~ 35 nm, this maximum current density is $\sim 1.2 \times 10^{12}$ A/m². Another important result of the London theory was the conclusion that magnetic flux trapped by holes in a multiply connected superconductor, or within the body of the superconductor, must be quantized. The quantum of magnetic flux was shown to be $\Phi_0 = h/q$, where h is Planck’s constant and q is the charge of the carrier associated with superconductivity.

The groups at Oxford, Leiden, and Kharkov continued their studies on alloys. The addition of 4% Bi to Pb was sufficient to completely trap magnetic flux when an external field was reduced from above the critical field to zero.²¹ In alloys of Pb–Ti and Bi–Ti, in increasing applied fields, flux began to penetrate at fields well below those at which resistance was restored.²² Rjabinin and Shubnikov’s work on single crystals of PbTi₂ clearly demonstrated the existence of two critical fields. Below the lower critical field, H_{k1} (in their notation), the alloy behaved as a pure metal superconductor, with no flux penetration. Above H_{k1} flux began to penetrate; penetration was completed at the upper critical field H_{k2} , at which point the resistance was restored. On reducing the field some hysteresis was observed, with a small amount of flux remaining in the sample at zero field.²³ Thus was type-II superconductivity recognized. It also appeared that Silsbee’s hypothesis was obeyed by alloys, if the critical current was related to the lower critical field.

Mendelssohn essayed an ingenious explanation for the two critical fields, the hysteresis and flux trapping, with his “sponge” model.²⁴ This model postulated that a sponge or three-dimensional network of superconductor with a high critical field permeated the main body of the superconductor with a lower critical field. Flux penetration would commence once the external field exceeded the critical value for the body of the superconductor, but penetration would not be complete until the critical field of the sponge was reached. On reducing the field, the meshes of the sponge would trap flux, accounting for hysteresis. The nature of the sponge was

not specified, but it was assumed that the meshes were of a dimension small compared to the penetration depth. Gorter²⁵ produced an alternative proposal, that the alloy superconductors subdivided into extremely thin regions, rather like a stack of razor blades, parallel to the applied field. This suggestion is remarkable in the light of Goodman’s lamellar theory for type-II superconductivity.²⁶ However, even prescient was Gorter’s notion of a minimum size for the superconducting regions, foretelling the later concept of the coherence length.

Because in an ideal superconductor the flux expulsion is not complete, some surface penetration occurring, the energy required to expel the flux is less than that given by Eq. (7), and the actual critical field is slightly higher than that predicted from complete expulsion. This effect is barely noticeable in bulk superconductors, but can become appreciable when at least one dimension of the superconductor is comparable to, or smaller than, the penetration depth. H. London²⁷ showed that the critical field for a slab of superconductor, of thickness d , in an external field parallel to the faces of the slab is given by

$$H_f = H_c \left\{ 1 - \frac{\lambda}{d} \tanh \frac{d}{\lambda} \right\}^{-1/2}. \quad (10)$$

When d is small compared to λ , this reduces to

$$H_f = \sqrt{3} \frac{\lambda}{d} H_c. \quad (11)$$

Thus thin films can remain superconducting to higher fields, and carry higher currents, than can bulk superconductors. This suggestion was verified experimentally by Shalnikov in 1938.²⁸ London suggested that, if the surface energy between normal and superconducting regions was negative, the superconductor would split into alternate lamellae of normal and superconducting regions, as suggested by Gorter. Fine filaments, of diameter less than the coherence length, are expected, by similar arguments, to have a higher critical field than that of the bulk. The Mendelssohn sponge could well be a mesh of fine filaments, with superconducting properties slightly better than those of the matrix. The filaments are assumed to result from inhomogeneities in the two-phase Pb–Bi alloys under investigation.

The picture emerging by mid-1935 was that, provided they were pure and free from strain, elemental superconductors exhibited complete flux exclusion, a reversible transition at a well-defined critical field, and a final state independent of the magnetization history. Alloys, on the other hand, showed gradual flux penetration starting at a field below, and finishing at a field somewhat higher, than the critical field typical of a pure element. In decreasing fields the magnetization of alloys was hysteretic, and residual trapped flux was often retained when the applied field had returned to zero. The so-called hard elemental superconductors such as Ta and Nb showed behavior similar to that of alloys.

The research at Kharkov continued with careful magnetization measurements on single and polycrystalline pure metals, and on single alloy crystals of Pb–Bi, Pb–In, Pb–Ti, and Hg–Cd. Shubnikov’s final contribution to the critical current story was systematic magnetization measurements on a series of PbTi single crystals of differing compositions.²⁹

These showed that the change from ideal to alloy behavior occurred at a particular concentration of the alloying addition. For lesser concentrations the alloy behaved as a pure metal. As the concentration was increased above this particular value, the field at which flux began to penetrate decreased, and the field at which resistance was restored increased, with increasing concentration of alloying element. A clear picture of the change from what is now recognized as type-I superconductor to type-II superconductor was presented, although there was an absence of cross-referencing between the Ukrainian and Western European work. The theoretical explanation of the two types of superconductor was still missing, as was any understanding of what really determined the critical current density. No further progress had been made on these two problems when once again work on superconductivity was frustrated by global conflict.

THEORETICAL ADVANCES 1945–1960

With the cessation of hostilities, renewed interest was taken in superconductivity. Helium gas was now much more readily available, its production having been accelerated by the needs of the US Navy for balloons. The development of the Collins liquefier allowed many more physics laboratories to indulge in studies at liquid-helium temperatures. However, the most startling advances were made on the theoretical front.

In 1950 Ginsburg and Landau, at the Institute for Physical Problems in Moscow, published their phenomenological theory.³⁰ They ascribed to the superconductor an order parameter, Ψ , with some characteristics of a quantum-mechanical wave function. Ψ is a function of temperature and magnetic vector potential. The Gibbs function is expanded in even powers of Ψ about the transition temperature, as in Landau's theory of phase transitions, and terms to describe the magnetic energy and kinetic energy and momentum of the electrons are included in their expression for the Gibbs function of a superconductor in an external field. At an external surface their theory reproduces the results of the London theory. They introduced a new parameter, characteristic of a particular superconductor, $\kappa = \sqrt{2}\lambda^2 q \mu_0 H_c / \hbar$. The problem that they set out to solve, following the earlier speculations of H. London, was that of the surface energy between superconducting and normal regions in the same metal. Their results showed quite clearly that, if κ were to have a value greater than $1/\sqrt{2}$, then superconductivity could persist up to fields in excess of the critical field, given by $H = (\kappa/\sqrt{2})H_c$. Ignoring the pre-War work on alloys, they stated that for no superconductor was $\kappa > 0.1$, and therefore this result was of no interest!

Pippard, with wartime experience of microwave techniques, was now at Cambridge, engaged in measurements of microwave surface resistance in metals and superconductors. The anomalous skin effect in impure metals had been explained by nonlocal effects. The behavior of an electron was not influenced by the point value of the electric and magnetic fields but by the value averaged over a volume of dimensions equal to the electron mean free path l . By analogy with the explanation for the anomalous skin effect in metals, Pippard suggested that a similar nonlocality was appropriate to superconductors. In the London theory, the current density at a

point r is determined by the value of the magnetic vector potential $\mathbf{A}(r)$. In Pippard's nonlocal modification of the London theory³¹ the current density at r is determined by \mathbf{A} averaged over a volume of dimensions ξ_0 . An electron traveling from a normal to a superconducting region cannot change its wave function abruptly; the change must take place over some finite distance. This distance is called the "range of coherence," ξ_0 . Pippard estimated that, for pure (or clean) metals, $\xi_0 \approx 1 \mu\text{m}$. The Pippard theory introduces modifications to the penetration depth. For a clean superconductor, clean in this case meaning that the normal electron mean free path $l \gg \xi_0$, the penetration depth is given by

$$\lambda_\infty = [(\sqrt{3}/2\pi)\xi_0\lambda_L^2]^{1/3}, \quad (12)$$

where λ_L is the value of the penetration depth in the London theory.

For alloy, or dirty superconductors, in which $l \ll \xi_0$, the theory gives a new, much greater, value for the penetration depth,

$$\lambda = \lambda_L(\xi_0/l)^{1/2}, \quad (13)$$

and also a much reduced value for the coherence length,

$$\xi_d = (\xi_0 l)^{1/2}. \quad (14)$$

The Ginsburg–Landau κ can be shown to be approximately equal to λ/ξ , and for a dirty superconductor with l very small, i.e., high electrical resistivity in the normal state, κ can be quite large, e.g., ~ 25 for niobium-based alloys and compounds, and > 100 for mixed oxide high-temperature superconductors.

The next theoretical development was the formulation of the Bardeen–Cooper–Schrieffer (BCS) microscopic theory for superconductivity.³² This theory, for which the authors received the 1972 Nobel Prize for Physics, is now the accepted theory for conventional superconductors. In superconductors below the transition temperature, electrons close to the Fermi surface condense into pairs (Cooper pairs). These pairs are the charge carriers in superconductivity, and their charge q is equal to twice the charge on a single electron. The value of the flux quantum $\Phi_0 = h/2e = 2.07 \times 10^{-15} \text{ Wb}$. The pairs form under an attractive interaction mediated by lattice phonons. An energy gap appears in the excitation spectrum for electrons at the Fermi level. Electron pairs, lattice phonons, and energy gaps in superconductivity had been postulated previously, but Bardeen, Cooper, and Schrieffer were the first to put all of these together in one theoretical framework. The energy gap is related to the critical temperature:

$$2\Delta \approx 3.5kT_c. \quad (15)$$

This represents the energy required to break up the Cooper pairs. It is possible to derive from this another estimate of the maximum current density, the depairing current. The depairing current density is that at which the kinetic energy of the superconducting carriers exceeds the binding energy of the Cooper pairs. It is then energetically favorable for the constituent electrons in a pair to separate and cease to be superconducting. The change in energy during scattering is maximized when the momentum change is maximized. This occurs when a carrier is scattered from one point on the

Fermi surface to a diametrically opposite one, in total reversal of direction. The carrier velocity is given by the sum of the drift and Fermi velocities; $v_d + v_f$ becomes $v_d - v_f$. The resulting change in kinetic energy is

$$\delta E_n = \frac{1}{2} m(v_d - v_f)^2 - \frac{1}{2} m(v_d + v_f)^2 = -2mv_d v_f. \quad (16)$$

The breaking of a pair followed by scattering causes a change in energy

$$\delta E_s = 2\Delta - 2mv_d v_f. \quad (17)$$

For spontaneous depairing to occur, δE_s must be negative, i.e., the drift velocity must be greater than Δ/mv_f . The depairing current density J_d , which is just the drift velocity times the carrier density n and the carrier charge q , must therefore be greater than $J_d = nq\Delta/mv_f$. When appropriate substitutions are made this expression for J_d can be shown to reduce to H_c/λ , the previously quoted expression for the absolute maximum current density. Values of the depairing current density lie in the range $10^{12} - 10^{13} \text{ A/m}^2$.

Abrikosov, working in the same institute as Landau, made the fourth theoretical breakthrough in 1957.³³ He produced a mathematical solution of the Ginsburg–Landau equations for the case when $\kappa > 1/\sqrt{2}$. His solution showed that in a rising externally applied magnetic field, flux is excluded until a lower critical field, H_{c1} , is exceeded. Above H_{c1} flux penetrates in the form of flux vortices, or flux lines, each carrying a quantum of flux Φ_0 , directed parallel to the field. The structure of these flux vortices is a normal core, of radius ξ , containing the flux that is supported by supercurrents circulating over a radius λ . As the applied field is increased, more flux penetrates until the density of the flux lines is such that the normal cores begin to overlap. This occurs at the upper critical field, $H_{c2} = \sqrt{2}\kappa H_{c0} = \Phi_0/2\pi\mu_0\xi^2$. The regime between the lower and upper critical fields is known as the “mixed state.” The mutual repulsion between the flux vortices, in the absence of any other forces acting upon them, results in the formation of a triangular flux line lattice (FLL). The parameter of this lattice is $a_0 = 1.07(\Phi_0/B)^{1/2}$, where B is the local value of the magnetic induction in the superconductor. Despite being published in translation, Abrikosov’s paper took some time to be fully appreciated in the West.

In 1960 Gor’kov derived the constants in the Ginsburg–Landau theory from the BCS theory.³⁴ This trilogy of Russian theoretical work is collectively referred to as the GLAG (Ginsburg–Landau–Abrikosov–Gor’kov) theory. Superconductors with values of $\kappa > 1/\sqrt{2}$, which exhibit the mixed state, are known as type-II superconductors. For any superconductor, as the normal state mean free path of the electrons, l , is reduced, ξ gets smaller, λ gets larger, and κ increases. Alloying, by reducing l , raises κ . This explains Shubnikov’s observation that the change from type-I to type-II behavior, or the onset of the Shubnikov phase, occurs at a particular alloy concentration.²⁹

APPLIED SUPERCONDUCTIVITY 1960–1986

The experimentalists had not been idle during this period. New superconductors, showing a steady increase in critical temperature, had been discovered: the brittle com-

pounds NbN (15 K) in 1941, V_3Si (17 K) in 1951, Nb_3Sn (18 K) in 1954, and the ductile alloys Nb–Zr (~ 11 K) in 1953 and Nb–Ti (~ 10 K) in 1961. All of these were type-II superconductors, with upper critical inductions well in excess of previously known materials. B_{c2} was about 12 T for Nb–Ti and 25 T for Nb_3Sn . The pioneers in this work were the groups at Westinghouse and Bell Telephone Laboratories.² Whereas the critical temperature and critical inductions were intrinsic properties of the superconductor, the critical current density was found to be strongly dependent upon the metallurgical state of the material. In two-phase alloys J_c was influenced by the size and dispersion of the second phase particles.³⁵ In the niobium-based ductile BCC alloys, it was found³⁶ that cold deformation significantly enhanced J_c .

The problem of fabricating wire from the brittle intermetallic Nb_3Sn was solved by filling niobium tubes with a mixture of Nb and Sn powders in the appropriate proportions, drawing to a fine wire, and reacting to form the compound.³⁷ This material had a current density of 10^9 A/m^2 in an induction of 8.8 T. Similar wire was wound into a solenoid which generated an induction of 2.85 T.³⁸ If the reaction to form the compound took place at the surface of the Nb and Sn particles, the compound could have formed as a three-dimensional network, just as envisaged by Mendelssohn for his sponge. Could the two-phase microstructure in the lead alloys, or the dislocations introduced by deformation of the ductile transition metal alloys,³⁹ constitute the elements of Mendelssohn’s sponge? Or was there an alternative scenario? If the flux vortices in the mixed state were able to interact in some way with the microstructure, this interaction could impede both the ingress of flux in a rising field and the egress of flux in a falling field. This would lead to the magnetic hysteresis observed in the materials. Flux gradients resulting from nonuniform distributions of vortices can be equated with currents.

A current flowing in a superconductor in the mixed state will exert a Lorentz force on the flux vortices, $\mathbf{F}_{L(V)} = \mathbf{J} \times \mathbf{B}$ per unit volume of superconductor, or $\mathbf{F}_{L(l)} = \mathbf{J} \times \Phi_0$ per unit length of vortex, where Φ_0 is a vector of strength $|\Phi_0|$ directed along the vortex. The force acts in a direction normal to both flux and current. Unless otherwise prevented, the vortices will move in the direction of this force, and in so doing induce an electric field $\mathbf{E} = \mathbf{v} \times \mathbf{B}$, where \mathbf{v} is the velocity of the vortices. The superconductor now shows an induced resistance, the value of which approaches that of the normal state, ρ_n , as the magnetic induction rises to B_{c2} , the upper critical induction.⁴⁰ The critical current is that current at which a detectable voltage is produced across the superconductor, and is therefore that current which just causes the vortices to move. If there is no hindrance to the motion of the vortices, then above B_{c1} the critical current is zero and the magnetization is reversible. The moving vortices do experience a viscous drag, originating from dissipation in the normal cores. This force $\mathbf{F}_v = \eta \mathbf{v}$, where the coefficient of viscosity $\eta = \Phi_0 \cdot \mathbf{B} / \rho_n$ (Ref. 40). If the vortices interact with microstructural features in the body of the superconductor, such as impurities, crystal defects, and second-phase precipitates, they can be prevented from moving and become pinned. The pinning force \mathbf{F}_p is a function of the microstruc-

ture and the local value of the induction. If the current density is such that the Lorentz force is less than the pinning force, no movement of vortices will occur, and no voltage will be detected in the superconductor. If the current is increased to a value at which the Lorentz force exceeds the pinning force, vortices will move and a voltage will be detected. The critical current density is that value of the current density at which the vortices will begin to move, i.e., when $\mathbf{F}_L = \mathbf{F}_p$; thus giving $J_c = F_p/B$.

The sponge hypothesis was tested by studying an artificial sponge fabricated by impregnating porous borosilicate glass with pure metal superconductors.⁴¹ The pores were interconnected and had a diameter of 3–10 nm. At the International Conference on the Science of Superconductivity, held at Colgate University the following year, the majority opinion swung in favor of pinning of flux vortices as the origin of magnetic hysteresis and the determinant of critical currents.⁴² Nevertheless, Bean's experiments on the artificial sponge were important in leading to the concept of the critical state. Bean analyzed his results of magnetization measurements on the assumption that each filament of the sponge carried either its critical current, or no current at all. As the external field is raised, currents are induced in the outer filaments, shielding the inner filaments from the field. The field is able to penetrate only when the outer filament current attains its critical value. Filaments progressively carry the critical current until the flux has penetrated to the center of the sample. Reducing the field to zero leaves current flowing in all the filaments, and flux is trapped in the sample. Applying a field in the opposite direction causes a progressive reversal of the critical current in the filaments. Bean assumed a critical current in the filaments independent of field. The model can be modified to include a field dependence of the critical current, leading to a more realistic hysteresis curve.

The notion that the current in a superconductor is either everywhere equal to the critical current or zero transfers readily to the concept of a pinned Abrikosov vortex lattice. In terms of magnetization, as the external field is raised, vortices move into the superconductor. Their motion is resisted by the pinning forces, and local equilibrium is established. At each point on the invading flux front the Lorentz force exactly balances the pinning force, and the local current density is equal to the local value of the critical current density. The superconductor is in the critical state,⁴³ a term borrowed from soil mechanics. A heap of soil or sand, or snow on an alpine hillside, will come to equilibrium with a slope of gradient determined by gravity and friction. The addition of more material to the pile will cause a slide until equilibrium is re-established. The slope is metastable, and any disturbance will result in an avalanche. A similar situation obtains in a superconductor in the critical state. Any force acting so as to try to move a flux vortex is just opposed by an equal and opposite pinning force. An imposed disturbance, resulting from either a change in the external magnetic field or in a transport current, leads to a redistribution of flux until the critical state is restored. Spectacular flux avalanches, or jumps, have been observed in superconductors.⁴⁴ The one difference in the superconductor is that, as the pinning force is a function of the local induction, the slope of the flux front is not constant. Several em-

pirical relations have been used to describe the dependence of critical current on local magnetic induction. Surprisingly the simplest possible relation, which, as it turns out, fits the data for commercial Nb–Ti conductor, namely $J_c(B) = J_c(0)(1 - b)$, where $b = B/B_{c2}$ is the reduced induction, has been ignored.

The problem of calculating critical currents from known details of the microstructure bears some relation to that of calculating the mechanical properties of a structural alloy, or the magnetization curve of a magnetic material. In the case of structural alloys, elastic inhomogeneities impede the movement of crystal dislocations. In the case of magnetic materials, inhomogeneities in the magnetic properties impede the motion of domain walls. In superconductors the presence of inhomogeneity in the superconducting properties will impede the motion of flux vortices, and superconductors with strong pinning have been referred to as hard superconductors. The relation between microstructure, the properties of the vortex lattice, and critical currents has been the subject of several reviews, the most notable of which is that of Campbell and Evetts.⁴⁵

Three factors must be considered in calculating pinning forces: the nature of the microstructural features, or pinning centers, responsible for pinning; the size, dispersion, and topography of these pinning centers; and the rigidity of the flux-line lattice. The nature of the pinning center determines the physical basis for the pinning force. A ferromagnetic precipitate will react very strongly with a flux line.⁴⁶ In most cases the pins are either nonsuperconducting precipitates or voids,⁴⁷ or regions whose superconductivity is modified, such as dislocation tangles, grain and subgrain boundaries. By passing through these regions the flux vortices reduce their length, and hence their energy, in the superconductor. The size of pins is important, since if they have a dimension significantly less than the coherence length ξ , their effectiveness is reduced by the proximity effect.⁴⁸ If they have dimensions of the order of the penetration depth λ , then local magnetic equilibrium within the pin can be established, magnetization currents will circulate around the pin, and the vortices will interact with these currents.⁴⁹ The number of pin–vortex interactions is determined by the dispersion of the pins. The topography decides whether the vortices, once unpinned, must cut across the pins or are able to slide round them.

The lattice rigidity is important as, if the pinning centers are randomly distributed, a rigid lattice will not be pinned. In practice the lattice is not rigid, and three responses to the pinning or Lorentz forces imposed upon it can be recognized. These forces may be such as to cause local elastic distortion of the lattice; they may exceed the yield strength of the lattice, causing local plastic deformation; or they may exceed the shear strength of the lattice. Whichever of these possibilities actually occurs provides the answer to what is known as the summation problem. If the lattice undergoes elastic distortion, the situation involves collective pinning.⁵⁰ The vortices are weakly pinned and the supercurrent densities are too low to be of practical interest. This situation will not be considered further. If the pinning forces are such as to cause local plastic deformation of the vortex lattice, the vortices will position themselves so as to maximize the pinning

interaction. Each vortex can be assumed to act individually, and the global pinning force is just the direct sum of the individual forces. If the pinning forces are greater than the shear strength of the vortex lattice, some vortices may remain pinned, while the main part of the lattice shears past them.⁵¹ However, this can only happen if there are paths down which the vortices can move without traversing any pins.⁵²

If the experimental critical Lorentz force $\mathbf{J}_c \times \mathbf{B}$, determined from transport current measurements, is plotted versus the reduced value of the applied magnetic induction, b , it is found that, for a given sample, results at different temperatures lie on one master curve.⁵³ The master curve takes the form

$$J_c B = \text{const} \cdot B_{c2}^{p+q} b^p (1-b)^q, \quad (18)$$

where the temperature dependence is incorporated in the temperature dependence of the upper critical induction. This is known as a scaling law. The values of the exponents p and q are peculiar to the particular pinning mechanism. Scaling laws are fundamental to flux pinning.⁵⁴ As an example, pinning by nonsuperconducting precipitates will be considered. If an isolated vortex intersects a spherical particle of normal material of diameter D , a volume of vortex core $D\pi\xi^2$ is removed from the system. Associated with the vortex core is an energy per unit volume $B_c^2/2\mu_0$. Thus the energy of the system is lowered by an amount $D\pi\xi^2 B_c^2/2\mu_0$. The force to move the vortex from a position in which it passes through the center of the particle, to a position outside the particle, is this change in energy divided by an interaction distance, which in this case is clearly the diameter of the particle. Thus the force to depin an isolated vortex from a normal particle is $\pi\xi^2 B_c^2/2\mu_0$. The total pinning force per unit volume is the single pin force multiplied by the number of active pins per unit volume. In this case this latter quantity is approximately equal to the total length of vortices per unit volume, B/Φ_0 , multiplied by the volume fraction of particles, V_f . There is an additional effect to be taken into account. In the flux-line lattice, of reduced induction b , the density of superelectrons, and hence the superconducting condensation energy, is reduced by a factor $(1-b)$.⁴⁵ The pinning force per unit volume is thus

$$J_c B = \pi\xi^2 \frac{B_c^2}{2\mu_0} (1-b) \frac{B}{\Phi_0} V_f. \quad (19)$$

With the use of the expression for $B_{c2} = \Phi_0/2\pi\xi^2$, this becomes

$$J_c B = \frac{B_c^2}{4\mu_0} b(1-b) V_f. \quad (20)$$

The above derivation assumes only one vortex is pinned at each particle, and therefore the particle size must be less than the intervortex spacing. Based on the above expression, it is possible to make an estimate of the maximum pinning force, and hence the maximum current density. In order to maximize the pinning force, all vortices must be pinned over their entire length. This would require a microstructure consisting of continuous rods of nonsuperconductor, with diameter $\sim \xi$, parallel to the applied field, and at a spacing equal to that of the vortex lattice. In this case V_f is effectively 1, and the

interaction distance is ξ . Taking Nb₃Sn as an example, with $B_c = 1$ T and $\xi = 3.6 \times 10^{-9}$ m, and considering that $b(1-b)$ has a maximum value of 0.25 at $b = 0.5$, i.e., at $B = 12.5$ T, we find

$$J_c = \frac{b(1-b)}{4.4\pi \times 10^{-7} \cdot 3.6 \times 10^{-9} B} = \frac{5.5 \times 10^{13} \cdot 0.25}{12.5} = 10^{12} \text{ A/m}^2. \quad (21)$$

Thus the maximum possible critical current density due to pinning is about one-tenth of the depairing current density. In practice, of course, it is impossible to achieve this idealized microstructure; maximum critical current densities due to pinning are about one-hundredth of the above estimate.

The two conventional superconductors in commercial production, the ductile transition metal alloy Nb–Ti, and the intermetallic compound Nb₃Sn, will now be examined in the light of the ideas expressed in the previous paragraphs. In order to confer stability, these conductors are fabricated as many fine filaments of superconductor in a copper matrix.⁵⁵

In the case of Nb–Ti, rods of the alloy are inserted in a copper matrix, and drawn down, often with repeated bundling, drawing, and annealing schedules, to produce a multifilamentary composite wire. Extensive transmission electron microscope studies on pure Nb and V, and alloys of Nb–Ta, Nb–Zr, Nb–Ti, and Mo–Re, after cold deformation and annealing, have shown conclusively that, in these ductile metals, pinning is due to an interaction between flux lines and tangles of dislocations or cell walls, and not individual dislocations.⁵⁶ In these tangles the normal electron mean free path will be less than its value in the dislocation-free regions, and the local value of κ will be increased. This led to the idea of ΔK pinning,^{57,58} the theory for which was developed by Hampshire and Taylor.⁵⁹ The superconducting filaments in Nb–Ti have a heavily deformed microstructure, with grains, subgrains, and nonsuperconducting α -Ti particles elongated in the direction of drawing. The current flow is parallel to this elongated microstructure, and the Lorentz force acting on the flux vortices is such as to drive them across the subgrain and normal particle boundaries. Pinning occurs at these boundaries and is a mixture of normal-particle and ΔK pinning, with a pinning function in which the critical Lorentz force $J_c B$ is proportional to $b(1-b)$.⁵⁴ The critical current is associated with the unpinning of flux vortices from these boundaries. The derivation of the pinning function is along similar lines to that described above for normal particles. Theory and experiment are well matched.⁵² The above expression seems to hold whenever the critical current is determined by flux pinning with a density of pins less than the density of flux lines. The b term arises because, as the density of flux lines increases, so does the total length of line pinned. The $(1-b)$ term represents the decrease in superconducting order parameter with increasing induction.

The other commercial conductor is based on the intermetallic A15-type compound Nb₃Sn. Multifilamentary conductor is fabricated by some variant of the bronze process. In the original version of this process, rods of niobium are inserted in a copper/tin bronze ingot as matrix, and drawn, again with rebundling, to form a composite of fine niobium filaments in the bronze matrix. Reaction between the tin con-

tent of the bronze and the niobium at an elevated temperature converts the latter into Nb_3Sn filaments. This procedure is necessary, as the intermetallic compound is brittle and non-deformable. The critical Lorentz force in these materials is found to obey a scaling law similar to that postulated by Kramer,⁵¹ namely $b^{1/2}(1-b^2)$. The critical current density increases as the grain size decreases, as would be expected if the pinning occurred at the grain boundaries, and as it does in Nb–Ti. The $(1-b^2)$ term has been taken to be indicative of some flux shearing process, as the C_{66} modulus of the flux-line lattice varies as $(1-b^2)$ at high values of b . It is not immediately obvious as to why these two types of material should behave in such different fashion, as their superconducting parameters and scale of microstructure are not vastly different. However examination of the microstructure of Nb_3Sn reveals it to be very different from that of Nb–Ti. This is not at all unexpected, due to the very different ways in which two microstructure are generated. That of bronze-processed Nb_3Sn consists of columnar grains whose axes are normal to the axes of the filaments.⁶⁰ The Lorentz force will act parallel to some of these boundaries, driving the flux lines along them rather than across them. A path is thus provided down which flux can shear, and the author has put forward a mechanism of flux-lattice dislocation-assisted shear.⁵² Values of the critical Lorentz force predicted on this model are close both to the Kramer law and to observation; in addition the model predicts an inverse dependence of J_c on grain size, as is observed experimentally but not predicted on the Kramer theory. An alternative approach treats flux pinned at grain boundaries as Josephson vortices.⁶¹ Transverse unpinning, with vortices crossing grain boundaries as in Nb–Ti, leads to the $b(1-b)$ scaling law, while longitudinal unpinning, with vortices traveling along grain boundaries as proposed for Nb_3Sn , leads to the $b^{1/2}(1-b^2)$ scaling law.

HIGH-TEMPERATURE SUPERCONDUCTORS

The immediate expectation from the discovery of the high-temperature, mixed copper oxide superconductors was that these materials could be exploited at 77 K to build electromagnets that would compete with permanent magnets, offering inductions in excess of 2 T. At low temperatures, the high critical fields would allow of competition with low-temperature superconductors, and the 21 T maximum induction available from existing A15 conductor would be exceeded. These high hopes have met with disappointment; the critical current densities, especially in high magnetic fields, are much less than those in low-temperature superconductors.

Typically, the critical current density as a function of applied induction for a high-temperature superconductor shows three regimes: an initial region in which the critical current decreases rapidly as soon as the field is turned on; a region, which can be linear, falling slowly with increasing field, and a third region in which the critical current falls to zero. The middle region may appear to be perfectly horizontal, indicating no dependence of critical current on applied field. It may also extend to very high fields, especially in Bi-2212 at temperatures below 20 K. An extreme example is a sample of spray-pyrolized TI-1223, in which the critical current density at 4.2 K is constant with field up to induc-

tions of 40 T.⁶² As the temperature is increased, all regions of the curve move to lower values of field and critical current density. In particular, the cutoff field decreases and the (negative) slope of the middle region increases. The significant fundamental differences between low-temperature and high-temperature superconductors are that the latter are anisotropic and have rather small coherence lengths. Structurally the mixed oxide superconductors are tetragonal, or nearly-tetragonal, with lattice parameters a and b lying in the range 0.375–0.395 nm and the c -axis parameter 3–12 times greater. This structural anisotropy leads to anisotropy in the physical properties of the compounds. In single crystals, the critical current density in the ab plane is many times greater than that in the c direction, normal to the ab plane. The superconducting coherence length ξ is small in these compounds; that in the c direction is just a few tenths of a nanometer in length, of similar magnitude to the region of crystallographic disturbance in the boundary between two grains. The consequence of this small range of coherence is that grain boundaries in high-temperature superconductors act as weak links, i.e., the superconducting wave functions in adjacent grains are only weakly coupled to one another. The overall critical transport current density in a superconductor is determined by whichever is the lesser of the *intragrain* or the *intergrain* current densities. The *intragrain* current density is controlled by flux pinning, the *intergrain* current density is a measure of the ability of current to flow from one grain to an adjacent grain. This latter depends upon the strength of the superconducting link across the boundary, and in the case of anisotropic superconductors, upon the relative orientation between the two grains.⁶³ The initial rapid drop in J_c with field is due to many weak links between grains being progressively switched off as the field is increased.⁶⁴

The current that is left is now being carried by the few strong links that exist between the grains, and the number of these is relatively insensitive to magnetic field. The strength of supercurrent depends upon the proportion of grain boundaries that are strong links. Many models have been proposed to account for the manner in which current is transferred from grain to grain in anisotropic mixed oxide superconductors.⁶⁵ The conclusions from these models, confirmed by experience, is that the proportion of strong links between grains, and hence the intergrain current, is maximized by grain alignment. The material is textured so that the c axis of the grains is close to being normal to the direction of current flow, and that the ab planes of the grains are in near parallelism to one another. In effect, the conductor must be as close to being a single crystal as possible.

Once a degree of texture has been established, the current density is further determined by flux pinning. A fully textured material will carry no appreciable current density if the pinning is weak. Conversely, a material with strong pinning will also have a low critical current density if there is no texture. In anisotropic materials the pinning of flux is also anisotropic.⁶⁶ The pinning strength is a function of the direction of an external magnetic field relative to the ab planes of the superconductor. The critical current density is much higher with the field parallel to the ab planes than when it is perpendicular to them. The high-temperature superconducting compounds consist of groups of one, two, or three copper

oxide layers, which are responsible for the superconductivity, separated by layers of other oxides that are essentially insulating. With the field lying parallel to the *ab* planes, the vortices will tend to place themselves in the insulating layers. The pinning mechanism, known as intrinsic pinning, is similar to that by normal particles as discussed above for low-temperature superconductors. The maximum critical current density should be of the same magnitude as that estimated in Eq. (20). The density of pins is much greater than the density of flux lines, explaining the relative insensitivity of the current density to external magnetic field in the middle region of the J_c versus B curve. When the applied field is normal to the *ab* planes, the intrinsic pinning no longer acts to hinder flux-line motion; the critical current densities are much lower than when the field is parallel to the planes. The situation is made worse by the fact that flux lines normal to the *ab* planes tend to split into “pancakes.”⁶⁷ This tendency is greater the greater the ratio of nonsuperconducting oxide layer thickness to superconducting oxide layer thickness, and hence the degree of anisotropy in the material. The anisotropy can be reduced, and flux pinning can be enhanced, by chemical substitution that distorts the crystal structure, by the addition of nonsuperconducting phases, and by irradiation.

As the applied field continues to increase, a value is reached at which the critical current falls to zero. This is the irreversibility field, above which it becomes impossible to pin flux. Irreversibility in magnetization experiments also disappears. The magnitude of the irreversibility field decreases as the anisotropy and tendency to form pancake vortices increases. There is controversy as to the origin of the irreversibility field. Arguments persist as to whether it is caused by flux-lattice melting or by thermally activated depinning. What is interesting is that the critical Lorentz force in high-temperature superconductors in many cases follows scaling laws similar to those found for low-temperature superconductors. The one difference is that the reduced induction used in the scaling laws is that relative to the irreversibility field rather than the upper critical field. There are many examples of this in the literature. Scaling with the irreversibility field indicates that this field is an intrinsic property of the flux-line lattice.

The recently discovered superconductor MgB_2 , with a critical temperature of 39 K,⁶⁸ appears to be a conventional low-temperature superconductor, with well-coupled grains and strong bulk pinning.⁶⁹ Transport current densities of 10^8 A/m², measured in self-field at 4.2 K, have been reported in wires fabricated from this material.⁷⁰ The nature of the pinning sites has not yet been determined.

CONCLUSIONS

The history of the experimental facts, and the theories developed therefrom, that have defined the understanding of the factors that control critical currents in both low- and high-temperature superconductors, has been delineated. At several critical stages opportunities have been missed. Onnes failed to connect critical fields with critical currents. The Meissner effect was discovered rather later than it ought to have been. In the late 1930s there was a lack of cooperation between the Leiden and Oxford groups on the one hand, and the Kharkov group on the other hand. Ginsburg and Landau

dismissed the possibility of superconductors having values of $\kappa > 1/\sqrt{2}$. Abrikosov’s ideas were slow to be appreciated. One is tempted to ask, “Would the first proper applications of superconductivity, in high field magnets, have arisen earlier than ~ 1960 if these delays had not occurred?” The answer is almost certainly “no.” The applications were conditional upon the discovery and development of materials with the ability to carry high currents in high magnetic fields. These discoveries did not rely upon any phenomenological or theoretical developments, but were, as are so many useful discoveries, purely empirical.

The critical current density in both low-temperature and high-temperature superconductors is controlled by their microstructure. Flux pinning in the ductile alloys based on niobium occurs at dislocation tangles, subgrain boundaries, and interfaces with nonsuperconducting second phases α -Ti. Flux shear along columnar grain boundaries seems to be the controlling mechanism in the bronze-route A15 materials. In the high-temperature superconductors microstructural control must provide both a high degree of texture and flux pinning. The next challenge will be to control the microstructure of MgB_2 .

For the pre-War history of superconductivity, I have drawn heavily upon P. Dahl’s book *Superconductivity*.⁷¹

*E-mail: david.dew-hughes@eng.ox.ac.uk

- ¹H. K. Onnes, Supplements to the Communications of the Physical Laboratory of Leiden University **34b**, 55 (1913).
- ²J. K. Hulm, J. E. Kunzler, and B. T. Matthias, Phys. Today **34**(1), 34 (1981).
- ³H. K. Onnes, Communications of the Physical Laboratory of Leiden University **133a**, 3 (1913).
- ⁴H. K. Onnes, *ibid.* **133b**, 29 (1913).
- ⁵H. K. Onnes, *ibid.* **133d**, 51 (1913).
- ⁶H. K. Onnes, *ibid.* **139f**, 66 (1914).
- ⁷F. B. Silsbee, Journal of the Washington Academy of Sciences **6**, 79 (1916).
- ⁸F. B. Silsbee, Proc. Natl. Acad. Sci., USA **13**, 516 (1927).
- ⁹W. Tuyn and H. K. Onnes, Communications of the Physical Laboratory, University of Leiden, **174a**, 21 (1926).
- ¹⁰W. Tuyn and H. K. Onnes, J. Franklin Inst. **201**, 379 (1926).
- ¹¹W. J. De Haas, G. J. Sizoo, and H. K. Onnes, Physica **5**, 447 (1925).
- ¹²G. J. Sizoo, W. J. De Haas, and H. K. Onnes, in *Proceedings of the Amsterdam Akademie der Wetenschappen* **29**, 221 (1926).
- ¹³W. J. De Haas and J. Voogd, *ibid.* **32**, 874 (1929); **33**, 262 (1930).
- ¹⁴W. H. Keesom, Physica **2**, 36 (1935).
- ¹⁵W. J. De Haas and J. Voogd, in *Proceedings of the Amsterdam Akademie der Wetenschappen* **34**, 63 (1931).
- ¹⁶M. Von Laue, Phys. Z. **33**, 793 (1932).
- ¹⁷W. Meissner and R. Ochsenfeld, Die Naturwissenschaften **21**, 787 (1933).
- ¹⁸J. N. Rjabinin and L. V. Shubnikov, Nature (London) **134**, 286 (1934).
- ¹⁹C. J. Gorter and H. B. J. Casimir, Phys. Z. **35**, 963 (1934).
- ²⁰F. London and H. London, Proc. R. Soc. London, Ser. A **149**, 71 (1935).
- ²¹T. C. Keely, K. Mendelssohn, and J. R. Moore, Nature (London) **134**, 773 (1934).
- ²²W. J. De Haas and J. M. Casimir-Jonker, *ibid.* **135**, 30 (1935).
- ²³J. N. Rjabinin and L. V. Shubnikov, Phys. Z. Sowjetunion **7**, 122 (1935).
- ²⁴K. Mendelssohn and J. R. Moore, Nature (London) **135**, 826 (1935).
- ²⁵C. J. Gorter, Physica **2**, 449 (1935).
- ²⁶B. B. Goodman, IBM J. Res. Dev. **6**, 63 (1962).
- ²⁷H. London, Proc. R. Soc. London, Ser. A **152**, 650 (1935).
- ²⁸A. Shalnikov, Nature (London) **142**, 74 (1938).
- ²⁹L. V. Shubnikov *et al.*, Phys. Z. Sowjetunion **10**, 165 (1936).
- ³⁰V. L. Ginzburg and L. D. Landau, Zh. Éksp. Teor. Fiz. **20**, 1064 (1950).
- ³¹A. B. Pippard, Proc. R. Soc. London, Ser. A **216**, 547 (1953).
- ³²J. Bardeen, L. N. Cooper, and J. R. Schrieffer, Phys. Rev. **108**, 1175 (1957).

- ³³ A. A. Abrikosov, Zh. Éksp. Teor. Fiz. **5**, 1442 (1957) [Sov. Phys. JETP **5**, 1174 (1957)].
- ³⁴ L. P. Gor'kov, *ibid.* **10**, 998 (1960).
- ³⁵ J. D. Livingston, Phys. Rev. **129**, 1943 (1963); Acta Metall. **11**, 1371 (1963); J. Appl. Phys. **34**, 3028 (1963); Rev. Mod. Phys. **36**, 54 (1964).
- ³⁶ M. S. Walker, R. Stickler, and F. E. Werner, in *Metallurgy of Advanced Electronic Materials*, edited by G. E. Brock [Interscience, New York (1963), p. 49].
- ³⁷ J. E. Kunzler, E. Buehler, F. S. L. Hsu, and J. E. Wernick, Phys. Rev. Lett. **6**, 89 (1961).
- ³⁸ L. C. Salter *et al.*, in *High Magnetic Fields*, H. H. Kolm *et al.* (Eds.), John Wiley, New York (1962), p. 344.
- ³⁹ R. Schaw and D. E. Mapother, Phys. Rev. **118**, 1474 (1960).
- ⁴⁰ Y. B. Kim, C. F. Hempstead, and A. R. Strnad, Phys. Rev. **139**, A1163 (1965).
- ⁴¹ C. P. Bean, M. V. Doyle, and A. G. Pincus, Phys. Rev. Lett. **9**, 93 (1962).
- ⁴² See Rev. Mod. Phys. **36**, (1964).
- ⁴³ C. P. Bean, Phys. Rev. Lett. **8**, 250 (1962); Y. B. Kim, C. F. Hempstead, and A. R. Strnad, Phys. Rev. **129**, 528 (1963).
- ⁴⁴ J. E. Evetts, A. M. Campbell, and D. Dew-Hughes, Philos. Mag. **10**, 339 (1964).
- ⁴⁵ A. M. Campbell and J. E. Evetts, Adv. Phys. **21**, 199 (1972).
- ⁴⁶ T. H. Alden and J. D. Livingston, J. Appl. Phys. **37**, 3551 (1966).
- ⁴⁷ E. J. Kramer and H. L. Freyhardt, J. Appl. Phys. **51**, 4930 (1980).
- ⁴⁸ J. Friedel, P. G. de Gennes, and J. Matricon, Appl. Phys. Lett. **2**, 119 (1963).
- ⁴⁹ A. M. Campbell, J. E. Evetts, and D. Dew-Hughes, Philos. Mag. **18**, 313 (1968).
- ⁵⁰ A. I. Larkin and Yu. N. Ovchinnikov, J. Low Temp. Phys. **34**, 409 (1979).
- ⁵¹ E. J. Kramer, J. Appl. Phys. **44**, 1360 (1973).
- ⁵² D. Dew-Hughes, Philos. Mag. **B 55**, 459 (1987).
- ⁵³ W. A. Fietz and W. W. Webb, Phys. Rev. **178**, 657 (1969).
- ⁵⁴ D. Dew-Hughes, Philos. Mag. **30**, 293 (1974).
- ⁵⁵ M. N. Wilson, C. R. Walters, J. D. Lewin, and P. F. Smith, J. Phys. D **3**, 1518 (1970).
- ⁵⁶ A. V. Narlikar and D. Dew-Hughes, Phys. Status Solidi **6**, 383 (1964); J. Mater. Sci. **1**, 317 (1966).
- ⁵⁷ D. Dew-Hughes, Mater. Sci. Eng. **1**, 2 (1966).
- ⁵⁸ D. Dew-Hughes and M. J. Witcomb, Philos. Mag. **26**, 73 (1972).
- ⁵⁹ R. G. Hampshire and M. T. Taylor, J. Phys. F: Met. Phys. **2**, 89 (1972).
- ⁶⁰ C. S. Pande, *Metallurgy of Superconducting Materials*, edited by T. S. Luhman and D. Dew-Hughes, Academic Press, New York (1979), p. 171.
- ⁶¹ J. McDonald and E. Barzi, IEEE Trans. Appl. Supercond. **11**, 3884 (2001).
- ⁶² D. T. Ryan *et al.*, IEEE Trans. Magn. **32**, 2803 (1996).
- ⁶³ D. Dimos *et al.*, Phys. Rev. Lett. **61**, 219 (1988).
- ⁶⁴ R. L. Peterson and J. W. Ekin, Phys. Rev. B **42**, 8014 (1990).
- ⁶⁵ L. N. Bulaevskii *et al.*, Phys. Rev. B **45**, 2545 (1992); B. Hensel *et al.*, Physica C **205**, 329 (1993).
- ⁶⁶ P. H. Kes *et al.*, Phys. Rev. Lett. **64**, 1063 (1990).
- ⁶⁷ J. R. Clem, Phys. Rev. B **43**, 7837 (1991).
- ⁶⁸ J. Nagamatsu *et al.*, Nature (London) **410**, 63 (2001).
- ⁶⁹ M. Kambara *et al.*, Semicond. Sci. Technol. **14**, L5 (2001).
- ⁷⁰ B. A. Glowacki *et al.*, *ibid.* **14**, 193 (2001).
- ⁷¹ P. F. Dahl, *Superconductivity, its Historical Roots and Development from Mercury to the Ceramic Oxides*, American Institute of Physics, New York (1992).

This article was published in English in the original Russian journal. Reproduced here with stylistic changes by AIP.

Geometric edge barrier in the Shubnikov phase of type-II superconductors

E. H. Brandt*

Max-Planck-Institut für Metallforschung, D-70506 Stuttgart, Germany; Institute for Superconducting and Electronic Materials, University of Wollongong, NSW 2522 Australia
(Submitted April 25, 2001)

Fiz. Nizk. Temp. **27**, 980–990 (September–October 2001)

In type-II superconductors the magnetic response can be irreversible for two different reasons: vortex pinning and barriers to flux penetration. Even without bulk pinning and in the absence of a microscopic Bean–Livingston surface barrier for vortex penetration, superconductors of nonellipsoidal shape can exhibit a large geometric barrier for flux penetration. This edge barrier and the resulting irreversible magnetization loops and flux-density profiles are computed from continuum electrodynamics for superconductor strips and disks of constant thickness, both without and with bulk pinning. Expressions are given for the field of first flux entry H_{en} and for the reversibility field H_{rev} above which the pin-free magnetization becomes reversible. Both fields are proportional to the lower critical field H_{c1} but otherwise depend only on the specimen shape. These results for rectangular cross section are compared with the well-known reversible magnetic behavior of ideal ellipsoids. © 2001 American Institute of Physics. [DOI: 10.1063/1.1401181]

1. SHUBNIKOV PHASE WITH ABRIKOSOV'S FLUX-LINE LATTICE

Many metals, alloys, and compounds become superconducting when they are cooled below a transition temperature T_c . This critical temperature ranges from $T_c < 1$ K for Al, Zn, Ti, U, and W and $T_c = 4.15$ K for Hg (the first superconductor discovered, in 1911),¹ through $T_c = 9.2$ K for Nb (the elemental metal with the highest T_c) and $T_c \approx 23$ K for Nb₃Ge (the highest value from 1973 to 1986; see the overview in Ref. 2), to the large T_c values of the high- T_c superconductors (HTSCs) discovered in 1986,³ e.g., YBa₂Cu₃O_{7- δ} (YBCO, $\delta \leq 1$),⁴ with $T_c \approx 92.5$ K, and Bi₂Sr₂Ca₂Cu₃O_{10+ δ} (BSCCO),^{5,6} with T_c up to 120 K, and on up to Tl₂Ba₂Sr₂Ca₂Cu₃O₁₀, with maximum $T_c = 127$ K,⁷ and some Hg compounds which under pressure have reached $T_c \approx 164$ K,^{8,9} the just recently discovered “simple” superconductor MgB₂ has $T_c = 39$ K.¹⁰

The superconducting state is characterized by the vanishing of the electric resistivity $\rho(T)$ of the material and by the complete expulsion of magnetic flux, irrespective of whether the magnetic field B_a was applied before or after cooling the superconductor below T_c . The existence of this Meissner effect proves that the superconducting state is a thermodynamic state, which uniquely depends on the applied field and temperature but not on previous history. As opposed to this, an ideal conductor expels the magnetic flux of a suddenly switched on field B_a but also “freezes” in its interior the magnetic flux which was there before the conductivity became ideal.

Lev Shubnikov realized that some superconductors do not exhibit complete expulsion of flux, but the applied field partly penetrates and the magnetization of the specimen depends on the magnetic history in a complicated way.^{11,12} Early theories tried to explain this by a “spongelike” nature of the material, which could trap flux in microscopic current

loops that may become normal conducting when the circulating current exceeds some critical value. The true explanation of partial flux penetration was given in a pioneering work by Alexei Abrikosov in 1957.¹³ Abrikosov, a student of Lev Landau in Moscow, discovered a periodic solution of the phenomenological theory of superconductivity conceived a few years earlier by Ginzburg and Landau.¹⁴ Abrikosov interpreted his solution as a lattice of parallel flux lines, now also called flux tubes, fluxons, or Abrikosov vortex lines. These flux lines thread the specimen, each carrying a quantum of magnetic flux $\phi_0 = h/2e = 2.07 \times 10^{-15}$ T·m². At the center of a flux line the superconducting order parameter $\psi(\mathbf{r})$ (the complex Ginzburg–Landau (GL) function) vanishes. The line $\psi = 0$ is surrounded by a tube of radius $\approx \xi$, the vortex core, within which $|\psi|$ is suppressed from its superconducting value $|\psi| = 1$ that it attains in the Meissner state. The vortex core is surrounded by a circulating supercurrent $\mathbf{J}(\mathbf{r})$ which generates the magnetic field $\mathbf{B}(\mathbf{r})$ of the flux line. In bulk specimens the vortex current and field are confined to a flux tube of radius λ , the magnetic penetration depth; at large distances $r \gg \lambda$, the current and field of an isolated vortex decay as $\exp(-r/\lambda)$.

In thin films of thickness $d \ll \lambda$ the current and magnetic field of a vortex extend to the larger distance $\lambda_{\text{film}} = 2\lambda^2/d$, the circulating current and the parallel magnetic field at large distances $r \gg \lambda_{\text{film}}$ decrease only as $1/r^2$ and the perpendicular field as $1/r^3$, and the vortex core has a wider radius $\approx (12\lambda_{\text{film}}\xi^2)^{1/3}$ (Refs. 15 and 16). These thin-film results have been applied to the high- T_c superconductors with layered structure, defining the vortex lines as stacks of vortex disks (“pancake vortices”) in the superconducting CuO layers.¹⁷ The coherence length $\xi(T)$ and magnetic penetration depth $\lambda(T)$ of the GL theory diverge at temperature T_c as $(1 - T/T_c)^{-1/2}$.

The ratio $\kappa = \lambda/\xi$ is the GL parameter of the supercon-

ductor. Within GL theory, which was conceived for temperatures close to the transition temperature T_c , κ is independent of T . Abrikosov's flux-line lattice (FLL) exists only in materials with $\kappa > 1/\sqrt{2}$; these are called type-II superconductors as opposed to type-I superconductors, which have $\kappa < 1/\sqrt{2}$. Type-I superconductors in a parallel applied field $H_a < H_c(T)$ are in the Meissner state, i.e., flux penetrates only into a thin surface layer of depth $\lambda(T)$, and at $H_a > H_c(T)$ they become normal conducting. Here $H_c(T)$ is the thermodynamic critical field. Type-II superconductors in a parallel applied field $B_a < B_{c1}(T) \leq B_c(T)$ are in the Meissner state, i.e., no magnetic flux has penetrated, and their inner induction is thus $B=0$; in the field range $H_{c1}(T) < H_a < H_{c2}(T)$ the magnetic flux penetrates partly in the form of flux lines (Shubnikov phase or mixed state with $0 < B < \mu_0 H_a$); and at $H_a > H_{c2}(T) \geq H_c(T)$ the material is in the normal conducting state, and thus $B = \mu_0 H_a$. H_{c1} and H_{c2} are the lower and upper critical fields. One has

$$H_{c1} \approx \frac{\phi_0}{4\pi\lambda^2\mu_0} (\ln \kappa + 0.5),$$

$$H_c = \frac{\phi_0}{2\sqrt{2}\pi\xi\lambda\mu_0}, \quad H_{c2} = \frac{\phi_0}{2\pi\xi^2\mu_0} = \sqrt{2}\kappa H_c.$$

All three critical fields vanish for $T \rightarrow T_c$ as $T_c - T$ and have an approximate temperature dependence $\propto 1 - T^2/T_c^2$.

If the superconductor is not a long specimen in a parallel field, then demagnetization effects come into play. For ellipsoidal specimens with homogeneous magnetization the demagnetizing field is taken into account by a demagnetization factor N with $0 < N < 1$. If $N > 0$, flux penetration starts earlier, namely, into type-II superconductors at $H'_{c1} = (1 - N)H_{c1}$ in the form of a FLL, and into type-I superconductors at $H'_c = (1 - N)H_c$ in the form of normal conducting lamellae; this "intermediate state" is described by Landau and Lifshitz,¹⁸ see also Refs. 19 and 20. GL theory yields that the wall energy between normal and superconducting domains is positive (negative) for type-I (type-II) superconductors. Therefore, at $H_a = H_c$ the homogeneous Meissner state is unstable in type-II superconductors and tends to split into normal and superconducting domains in the finest possible way; this means a FLL appears with normal cores of radius $\approx \xi$. With allowance for demagnetization effects, the field of first penetration of flux lines into type-II superconductors is thus $H'_{c1} = (1 - N)H_{c1} < (1 - N)H_c$, and into type-I superconductors²¹ $H_p = [(1 - N)^2 H_c^2 + K^2]^{1/2} > (1 - N)H_c$, with K proportional to the wall energy. Superconductivity disappears when the applied field H_a reaches the critical field H_{c2} (type-II) or H_c (type-I), irrespective of demagnetization effects, since the magnetization vanishes at this transition.

The order parameter $|\psi(\mathbf{r})|^2$ and microscopic field $B(\mathbf{r})$ of an isolated flux line oriented along z for $2\kappa^2 \gg 1$ are given approximately by^{22,23}

$$|\psi(\mathbf{r})|^2 \approx 1/(1 + 2\xi^2/r^2),$$

$$B(\mathbf{r}) \approx \frac{\phi_0}{2\pi\lambda^2} K_0 \left(\frac{\sqrt{r^2 + 2\xi^2}}{\lambda} \right),$$

with $r = (x^2 + y^2)^{1/2}$ and $B\|\mathbf{z}$; $K_0(x)$ is a modified Bessel function with the limits $-\ln(x)$ ($x \ll 1$) and $(\pi/2x)^{1/2} \exp(-x)$ ($x \gg 1$). This field $B(\mathbf{r})$ exactly minimizes the GL free energy if the above variational ansatz $|\psi(r)|^2$ is inserted. The maximum field occurs in the vortex core, $B_{\max} = B(0) \approx (\phi_0/2\pi\lambda^2) \ln \kappa \approx 2B_{c1}$ (still for $2\kappa^2 \gg 1$). From this $B(r)$ one obtains the current density circulating in the vortex $J(r) = \mu_0^{-1} |B'(r)| = (\phi_0/2\pi\lambda^2\mu_0)(r/\lambda\bar{r})K_1(\bar{r}/\lambda)$, with $\bar{r} = (r^2 + 2\xi^2)^{1/2}$. Inserting for the modified Bessel function $K_1(x)$ the approximation $K_1(x) \approx 1/x$ valid for $x \ll 1$, one obtains the maximum current density $J_{\max} = J(r = \sqrt{2}\xi) \approx \phi_0/(4\sqrt{2}\pi\lambda^2\xi\mu_0) = (27/32)^{1/2} J_0$ where $J_0 = \phi_0/(3\sqrt{3}\pi\lambda^2\xi\mu_0)$ is the "depairing current density," i.e., the maximum supercurrent density which can flow within the GL theory in planar geometry (see, e.g., Tinkham²⁴). Thus, for large $\kappa \gg 1$ the field in the flux-line center is twice the lower critical field, and the maximum vortex current is the depairing current.

A curious property of the flux-line lattice is its softness, which is due to the long range interaction between the flux lines over several penetration lengths λ , a distance which typically is much larger than the flux-line spacing. This leads to "nonlocal" elastic behavior and to highly dispersive elastic moduli for compression [$c_{11}(\mathbf{k})$] and tilt [$c_{44}(\mathbf{k})$], while the very small shear modulus [$c_{66} \ll c_{11}(0) \approx c_{44}(0) \approx B^2/\mu_0$ for $B > \mu_0 H_{c1}$] does not depend on the wave vector \mathbf{k} of the strain field.²⁵ For more properties of the ideal and pinned FLL, also in the highly anisotropic or layered high- T_c superconductors, see the reviews on Refs. 26 and 27, and for the rather complex statistical theory of pinning and thermally activated depinning of vortex lines and pancake vortices, see the review in Ref. 28. The properties of the ideally periodic FLL have recently been computed with high accuracy for the entire ranges of the induction $0 < B < \mu_0 H_{c2}$ and of the GL parameter $1/\sqrt{2} < \kappa < \infty$ by an iteration method.²⁹

The present paper considers the magnetic behavior of superconductors which are not long cylinders or ideal ellipsoids but have a more realistic constant thickness, i.e., they have rectangular cross section in the planes containing the direction of the magnetic field. For such realistic geometries, the concept of a demagnetization factor does not work. Moreover, a new type of magnetic irreversibility occurs, which is not related to flux-line pinning but to the nonellipsoidal cross section that causes a "geometric barrier." This barrier delays the penetration of flux lines at the four edges of the rectangular cross section of the specimen. It will be shown that this problem can be treated within a continuum approach, which considers the induction and current density averaged over a few cells of the FLL.

2. MAGNETIC IRREVERSIBILITY

The irreversible magnetic behavior of type-II superconductors usually is caused by pinning of the Abrikosov vortices at inhomogeneities in the material.³⁰ However, similar hysteresis effects have also been observed³¹ in type-I superconductors, which do not contain flux lines, and in type-II superconductors with negligible pinning. In these two cases the magnetic irreversibility is caused by a geometric (specimen-shape dependent) barrier which delays the penetration of magnetic flux but not its exit. In this respect the

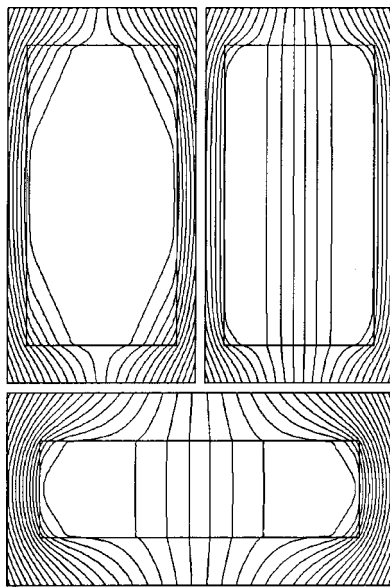


FIG. 1. Field lines of the induction $\mathbf{B}(x,y)$ in strips with aspect ratio $b/a = 2$ (top) and $b/a = 0.3$ (bottom) in a perpendicular magnetic field H_a . Top left: $H_a/H_{c1} = 0.66$, in increasing field shortly before the entry field $H_{en}/H_{c1} = 0.665$. Top right: $H_a/H_{c1} = 0.5$, decreasing field. Bottom: $H_a/H_{c1} = 0.34$ in increasing field just above $H_{en}/H_{c1} = 0.32$. Note the nearly straight field lines in the corners, indicating the tension of the flux lines. The field lines of cylinders look very similar.

macroscopic geometric barrier behaves in a manner similar to the *microscopic* Bean–Livingston barrier³² for straight vortices penetrating at a parallel surface. In both cases the magnetic irreversibility is caused by the asymmetry between flux penetration and exit. The geometric irreversibility is most pronounced for thin films of constant thickness in a perpendicular field. It is absent only when the superconductor is of exactly ellipsoidal shape or is tapered like a wedge with a sharp edge where flux can penetrate easily due to the large local enhancement of the external magnetic field at this edge in a diamagnetic material.

Ellipsoids are a particular case. In superconducting ellipsoids the inward directed driving force exerted on the vortex ends by the surface screening currents is exactly compensated by the vortex line tension.^{27,33} An isolated vortex line is thus in an indifferent equilibrium at any distance from the specimen center. The repulsive vortex interaction therefore yields a uniform flux density, and the magnetization is reversible. However, in specimens of constant thickness (i.e., of rectangular cross section) this line tension opposes the penetration of flux lines at the four corner lines, thus causing an edge barrier; but as soon as two penetrating vortex segments join at the equator, they contract and are driven to the specimen center by the surface currents; see Figs. 1 and 2. As opposed to this, when the specimen profile is tapered and has a sharp edge, the driving force of the screening currents even in very weak applied fields exceeds the restoring force of the line tension, so that there is no edge barrier. The resulting absence of hysteresis in wedge-shaped samples was clearly shown by Morozov *et al.*³⁴

For thin superconductor strips with an edge barrier an elegant analytical theory of the field and current profiles has been presented by Zeldov *et al.*³⁵ using the theory of complex functions; see also the calculations in Refs. 36 and 37.

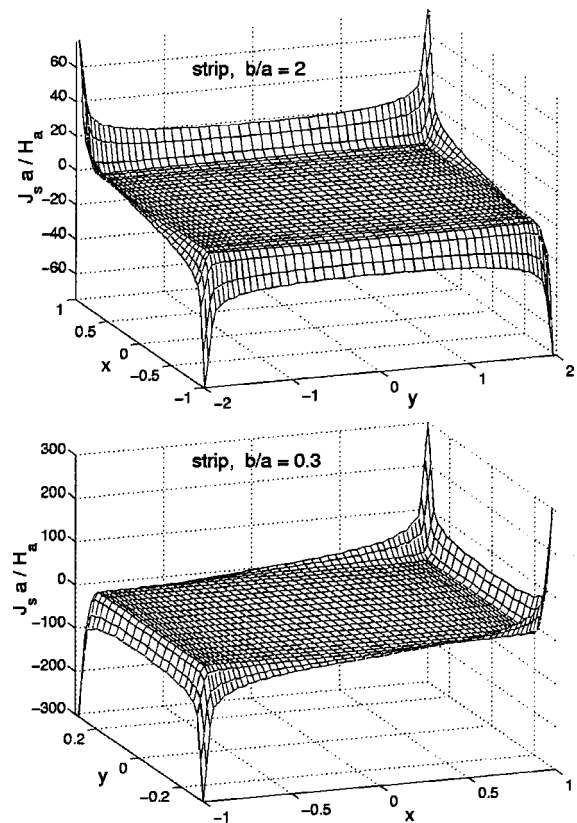


FIG. 2. 3D plots of the screening current density $J_s(x,y)$, Eq. (11), in superconductor strips with $b/a = 2$ (top) and $b/a = 0.3$ (bottom) as in Fig. 1. Shown is the limit of small applied field $H_a \ll H_{c1}$ before magnetic flux has penetrated. For better presentation the depicted $J_s(x,y)$ is smeared over a few grid cells.

With increasing applied field H_a , the magnetic flux does not penetrate until an entry field H_{en} is reached; at $H_a = H_{en}$ the flux immediately jumps to the center, from where it gradually fills the entire strip or disk. This behavior in increasing H_a is similar to that of thin films with artificially enhanced pinning near the edges,^{36,38} but in decreasing H_a the behavior is different: In films with enhanced edge pinning (critical current density J_c^{edge}) the current density J at the edge immediately jumps from $+J_c^{edge}$ to $-J_c^{edge}$ when the ramp rate reverses its sign, while in pin-free films with a geometric barrier the current density at the edge first stays constant or even increases and then gradually decreases and reaches zero at $H_a = 0$. For pin-free thin strips the entry field H_{en} was estimated in Refs. 35, 39, and 40.

The outline of the present work is as follows. Section 3 discusses the reversible magnetic behavior of pin-free superconductor ellipsoids. The effective demagnetization factor of long strips (or slabs) and circular disks (or cylinders) with rectangular cross section $2a \times 2b$ is given in Sec. 4. In Sec. 5 appropriate continuum equations and algorithms are presented that allow one to compute the magnetic irreversibility caused by pinning and/or by the geometric barrier in type-II superconductors of arbitrary shape, in particular, strips and disks of finite thickness. Results for thick long strips and disks or cylinders with arbitrary aspect ratio b/a are given in Sec. 6 for pin-free superconductors and in Sec. 7 for superconductors with arbitrary bulk pinning. In particular, explicit expressions are given for the field of first flux entry H_{en} and

for the reversibility field H_{rev} above which the magnetization curve is reversible and coincides with that of an ellipsoid.

3. ELLIPSOIDS

First consider the known magnetization of ideal ellipsoids. If the superconductor is homogeneous and isotropic, the magnetization curves of ellipsoids $M(H_a; N)$ are reversible and may be characterized by a demagnetizing factor N . If H_a is along one of the three principal axes of the ellipsoid then N is a scalar with $0 < N \leq 1$. One has $N=0$ for long specimens in a parallel field, $N=1$ for thin films in a perpendicular field, $N=1/2$ for transverse circular cylinders, and $N=1/3$ for spheres. For general ellipsoids with semi-axes a, b, c along the Cartesian axes x, y, z , the three demagnetizing factors along the principal axes satisfy $N_x + N_y + N_z = 1$. For ellipsoids of revolution with $a=b$ one has $N_x = N_y = (1 - N_z)/2$, where for “cigars” with $a=b < c$ and for disks with $a=b > c$ with eccentricity $e = |1 - c^2/a^2|^{1/2}$ one obtains¹⁸

$$N_z = \frac{1 - e^2}{e^3} (\operatorname{arctanh} e - e), \quad (\text{cigar}),$$

$$N_z = \frac{1 - e^2}{e^3} (e - \arctan e), \quad (\text{disk}). \quad (1)$$

For thin ellipsoidal disks with $a > b \gg c$ one has⁴¹

$$N_z = 1 - \frac{c}{b} E(k), \quad (2)$$

where $E(k)$ is the complete elliptic integral of the second kind with $k^2 = 1 - b^2/a^2$.

When the magnetization curve in parallel field is known, $M(H_a; 0) = B/\mu_0 - H_a$, where B is the flux density inside the ellipsoid, then the homogeneous magnetization of the general ellipsoid, $M(H_a; N)$, follows from the implicit equation

$$H_i = H_a - NM(H_i; 0). \quad (3)$$

Solving Eq. (3) for the effective internal field H_i , one obtains $M = M(H_a; N) = M(H_i; 0)$. In particular, for the Meissner state ($B=0$) one finds $M(H_a; 0) = -H_a$ and

$$M(H_a; N) = -\frac{H_a}{1-N} \quad \text{for } |H_a| \leq (1-N)H_{c1}. \quad (4)$$

At the lower critical field H_{c1} one has $H_i = H_{c1}$, $H_a = H'_{c1} = (1-N)H_{c1}$, $B=0$, and $M = -H_{c1}$. Near the upper critical field H_{c2} one has an approximately linear $M(H_a; 0) = \gamma(H_a - H_{c2}) < 0$ with $\gamma > 0$, yielding

$$M(H_a; N) = \frac{\gamma}{1 + \gamma N} (H_a - H_{c2}) \quad \text{for } H_a \approx H_{c2}. \quad (5)$$

Thus, if the slope $\gamma \ll 1$ is small (and in general, if $|M/H_a| \ll 1$ is small), demagnetization effects may be disregarded, and one has $M(H_a; N) \approx M(H_a; 0)$.

The ideal magnetization curve of type II superconductors with $N=0$, $M(H_a; 0)$ or $B(H_a; 0)/\mu_0 = H_a + M(H_a; 0)$ may be calculated from Ginzburg–Landau theory,²⁹ but to illustrate the geometric barrier any other model curve may be used provided $M(H_a; 0) = -M(-H_a; 0)$ has a vertical slope at $H_a = H_{c1}$ and decreases

monotonically in size for $H_a > H_{c1}$. Below for simplicity I shall assume $H_{c1} \ll H_{c2}$ (i.e., large GL parameter $\kappa \gg 1$) and $H_a \ll H_{c2}$. In this case one may use the model $M(H_a; 0) = -H_a$ for $|H_a| \leq H_{c1}$ and

$$M(H_a; 0) = (H_a/|H_a|)(|H_a|^3 - H_{c1}^3)^{1/3} - H_a \quad (6)$$

for $|H_a| > H_{c1}$, which well approximates the pin-free GL magnetization.

4. THICK STRIPS AND DISKS IN THE MEISSNER STATE

In nonellipsoidal superconductors the induction $\mathbf{B}(\mathbf{r})$ in general is not uniform and so the concept of a demagnetizing factor does not work. However, when the magnetic moment $\mathbf{m} = 1/2 \int \mathbf{r} \times \mathbf{J}(\mathbf{r}) d^3 r$ is directed along H_a , one may define an effective demagnetizing factor N which in the Meissner state ($B=0$) yields the same slope $M/H_a = -1/(1-N)$, Eq. (2), as an ellipsoid with this N . Here the definition $M = m/V$ with $m = \mathbf{m} \cdot \mathbf{H}_a/H_a$ and specimen volume V is used. In particular, for long strips or slabs and circular disks or cylinders with rectangular cross section $2a \times 2b$ in a perpendicular or axial magnetic field along the thickness $2b$, approximate expressions for the slopes $M/H_a = m/(VH_a)$ are given in Refs. 42 and 43. Using this and defining $q = (|M/H_a| - 1)(b/a)$, one obtains the effective N for any aspect ratio b/a in the form

$$N = 1 - 1/(1 + qa/b),$$

$$q_{\text{strip}} = \frac{\pi}{4} + 0.64 \tanh \left[0.64 \frac{b}{a} \ln \left(1.7 + 1.2 \frac{a}{b} \right) \right],$$

$$q_{\text{disk}} = \frac{4}{3\pi} + \frac{2}{3\pi} \tanh \left[1.27 \frac{b}{a} \ln \left(1 + \frac{a}{b} \right) \right]. \quad (7)$$

In the limits $b \ll a$ and $b \gg a$, these formulas are exact, and for general b/a the relative error is $< 1\%$. For $a=b$ (square cross section) they yield for the strip $N=0.538$ (while $N=1/2$ for a circular cylinder in a perpendicular field) and for the short cylinder $N=0.365$ (while $N=1/3$ for a sphere).

5. COMPUTATIONAL METHOD

To obtain the full, irreversible magnetization curves $M(H_a)$ of nonellipsoidal superconductors one has to resort to numerics. Appropriate continuum equations and algorithms have been proposed recently by Labusch and Doyle⁴⁴ and by the author,⁴⁵ based on the Maxwell equations and on constitutive laws which describe flux flow and pinning or thermal depinning, and the equilibrium magnetization in absence of pinning, $M(H_a; 0)$. For arbitrary specimen shape these two methods proceed as follows.

While the method of Ref. 44 considers a magnetic charge density on the specimen surface which causes an effective field $\mathbf{H}_i(\mathbf{r})$ inside the superconductor, our method⁴⁵ couples the arbitrarily shaped superconductor to the external field $\mathbf{B}(\mathbf{r}, t)$ via surface screening currents: In a first step the vector potential $\mathbf{A}(\mathbf{r}, t)$ is calculated for given current density \mathbf{J} ; then this linear relation (a matrix) is inverted to obtain \mathbf{J} for given \mathbf{A} and given \mathbf{H}_a ; next the induction law is used to obtain the electric field [in our symmetric geometry one has $\mathbf{E}(\mathbf{J}, \mathbf{B}) = -\partial \mathbf{A} / \partial t$], and finally the constitutive law $\mathbf{E} = \mathbf{E}(\mathbf{J}, \mathbf{B})$ is used to eliminate \mathbf{A} and \mathbf{E} and obtain one single integral equation for $\mathbf{J}(\mathbf{r}, t)$ as a function of $\mathbf{H}_a(t)$, without

having to compute $\mathbf{B}(\mathbf{r}, t)$ outside the specimen. This method in general is fast and elegant; but so far the algorithm is restricted to aspect ratios $0.03 < b/a < 30$, and to a number of grid points not exceeding 1400 (on a personal computer). Improved accuracy is expected by combining the methods of Refs. 44 (working best for small b/a) and 45. Here I shall use the method of Ref. 45 and simplify it to the two-dimensional (2D) geometry of thick strips and disks.

In the 2D geometry of thick strips⁴² or short cylinders⁴³ in an applied magnetic field $\mathbf{B}_a = \mu_0 \mathbf{H}_a = \nabla \times \mathbf{A}_a$ along y , one writes $\mathbf{r} = (x, y)$ or $\mathbf{r} = (\rho, y)$ (in cylindrical coordinates ρ, φ, y). For a uniform applied field the applied vector potential in these two geometries reads $A_a = -xB_a$ or $A_a = -\rho B_a/2$. The current density $\mathbf{J}(\mathbf{r}, t)$, electric field $\mathbf{E}(\mathbf{r}, t)$, and vector potential $\mathbf{A}(\mathbf{r}, t)$ now have only one component oriented along z or φ and denoted by J, E, A . The method^{42,43,45} describes the superconductor by its current density $J(\mathbf{r}, t)$, from which the magnetic field $\mathbf{B}(x, y, t) = (B_x, B_y)$ or $\mathbf{B}(\rho, y, t) = (B_\rho, B_y)$, the magnetic moment $m(t)$ (along y), and the electric field $E(\mathbf{r}, t) = E(J, \mathbf{B}, \mathbf{r}')$ follow directly or via the constitutive law $E = E(J, \mathbf{B})$. For high inductions $B \gg \mu_0 H_{c1}$ one has $\mathbf{B} \approx \mu_0 \mathbf{H}$ everywhere and $J = -\mu_0^{-1} \nabla^2 (A - A_a)$. The current density J is then obtained by time-integrating the following equation of motion:

$$\mathbf{J}(\mathbf{r}, t) = -\frac{1}{\mu_0} \int_V d^2 r' K(\mathbf{r}, \mathbf{r}') [E(J, \mathbf{B}) + \dot{A}_a(\mathbf{r}', t)]. \quad (8)$$

Here $K(\mathbf{r}, \mathbf{r}') = Q(\mathbf{r}, \mathbf{r}')^{-1}$ is an inverse integral kernel obtained by inverting a matrix; see Refs. 42 and 43 for details. The kernels Q and K apply to the appropriate geometry and relate J to the current-caused vector potential $A - A_a$ in the (here trivial) gauge $\nabla \cdot \mathbf{A} = 0$ via integrals over the specimen volume V ,

$$A(\mathbf{r}) = \mu_0 \int_V d^2 r' Q(\mathbf{r}, \mathbf{r}') J(\mathbf{r}') + A_a(\mathbf{r}), \quad (9)$$

$$J(\mathbf{r}) = \frac{1}{\mu_0} \int_V d^2 r' K(\mathbf{r}, \mathbf{r}') [A(\mathbf{r}') - A_a(\mathbf{r}')]. \quad (10)$$

The Laplacian kernel Q is universal, e.g., $Q(\mathbf{r}, \mathbf{r}') = -(1/2\pi) \ln|\mathbf{r} - \mathbf{r}'|$ for long strips with arbitrary cross section, but the inverse kernel K depends on the shape of the specimen cross section. Putting $A(\mathbf{r}') = 0$ in Eq. (10) (Meissner state), one sees that

$$J_s(\mathbf{r}) = -\frac{1}{\mu_0} \int_V d^2 r' K(\mathbf{r}, \mathbf{r}') A_a(\mathbf{r}') \quad (11)$$

is the surface screening current caused by the applied field. In particular, one has $J_s(\mathbf{r}) = 0$ inside the superconductor. In our above method J_s automatically is restricted to the layer of grid points nearest to the surface; see Fig. 2. Analytical expressions for the current J_s in thick rectangular strips with applied field H_a and/or applied current I_a were recently given⁴⁶ for this limit of vanishing magnetic penetration depth $\lambda \rightarrow 0$. Finite $\lambda > 0$ may be introduced into these computations by modifying the integral kernel according to Ref. 47: $K(\mathbf{r}, \mathbf{r}') = [Q(\mathbf{r}, \mathbf{r}') + \lambda^2 \delta(\mathbf{r} - \mathbf{r}')]^{-1}$. The resulting screening current then flows in a surface layer of finite thickness λ .

If one is interested also in low inductions one has to generalize Eq. (8) to general reversible magnetization $\mathbf{H} = \mathbf{H}(\mathbf{B})$. This is achieved by replacing in the constitutive law $\mathbf{E}(\mathbf{J}, \mathbf{B})$ the actual current density $\mathbf{J} = \mu_0^{-1} \nabla \times \mathbf{B}$ by the effective current density $\mathbf{J}_H = \nabla \times \mathbf{H}$ which drives the vortices and thereby generates an electric field \mathbf{E} . That $\mathbf{J}_H = \nabla \times \mathbf{H}(\mathbf{B}, \mathbf{r})$ enters the Lorentz force is rigorously proven by Labusch.⁴⁴ Within the London theory this important relation may also be inferred from the facts that the force on a vortex is determined by the *local* current density at the vortex center, while the energy density F of the vortex lattice is determined by the magnetic field at the vortex centers. Thus, $\mathbf{J}_H = \nabla \times (\partial F / \partial \mathbf{B})$ is the average of the current densities at the vortex centers, which in general is different from the current density $\mathbf{J} = \mu_0^{-1} \nabla \times \mathbf{B}$ averaged over the vortex cells. In our 2D geometry one thus has to replace in Eq. (8)

$$E[J(\mathbf{r}'), \mathbf{B}(\mathbf{r}')] \rightarrow E[J_H(\mathbf{r}'), \mathbf{B}(\mathbf{r}')], \quad (12)$$

where $J_H = \partial H_y / \partial x - \partial H_x / \partial y$ depends on the reversible constitutive law $H(B) = \partial F / \partial B$ with $H_x = H(B) B_x / B$, $H_y = H(B) B_y / B$, and $B = (B_x^2 + B_y^2)^{1/2}$.

The boundary condition on $\mathbf{H}(\mathbf{r})$ is simply that one has $\mathbf{H} = \mathbf{B} / \mu_0$ at the surface (and in the vacuum outside the superconductor, which does not enter our calculation). This boundary condition may be forced by an appropriate space-dependent constitutive law $\mathbf{H} = \mathbf{H}(\mathbf{B}, \mathbf{r})$, which outside and at the surface of the superconductor is trivially $\mathbf{H} = \mathbf{B} / \mu_0$. The specimen shape thus enters in two places: via the integral kernel $K(\mathbf{r}, \mathbf{r}')$ and via the constitutive law $\mathbf{H} = \mathbf{H}(\mathbf{b}, \mathbf{r})$.

To compute the induction $\mathbf{B}(\mathbf{r})$ entering $\mathbf{H}(\mathbf{B})$, for maximum accuracy one should not use the derivative $\mathbf{B} = \nabla \times \mathbf{A}$ but the Biot–Savart integral

$$\mathbf{B}(\mathbf{r}) = \int_V d^2 r' \mathbf{L}(\mathbf{r}, \mathbf{r}') J(\mathbf{r}') + \mathbf{B}_a(\mathbf{r}) \quad (13)$$

with a suitable kernel $\mathbf{L}(\mathbf{r}, \mathbf{r}')$. The accuracy of the method then depends mainly on the algorithm used to compute the derivative $\mathbf{J}_H = \nabla \times \mathbf{H}$. A useful trick is to compute \mathbf{J}_H as $\mathbf{J}_H = \mathbf{J} + \nabla \times (\mathbf{H} - \mathbf{B} / \mu_0)$, where $\mathbf{H} - \mathbf{B} / \mu_0$ is typically small and vanishes at the surface.

For the following computations I use simple models for the constitutive laws of an isotropic homogeneous type-II superconductor without the Hall effect, though our method⁴⁵ is more general. With Eq. (6) and $H = B / \mu_0 - M$ one has

$$H(B) = \mu_0^{-1} [B_{c1}^3 + B^3]^{1/3} \quad (14)$$

with $B_{c1} = \mu_0 H_{c1}$. A simple B -dependent current–voltage law which describes pinning, thermal depinning, and flux flow is $\mathbf{E}(\mathbf{J}, \mathbf{B}) = \rho(J, B) \mathbf{J}$, with

$$\rho(J, B) = \rho_0 B \frac{(J/J_c)^\sigma}{1 + (J/J_c)^\sigma}. \quad (15)$$

This model has the correct limits $\rho \propto J^\sigma$, ($J \ll J_c$, flux creep) and $\rho = \rho_0 B = \rho_{FF}$ ($J \gg J_c$, flux flow, $\rho_0 = \text{const}$), and for large creep exponent $\sigma \gg 1$ it reduces to the Bean critical state model. In general the critical current density $J_c = J_c(B)$ and the creep exponent $\sigma(B) \geq 0$ will depend on B . For pin-free superconductors ($J_c \rightarrow 0$) this expression de-

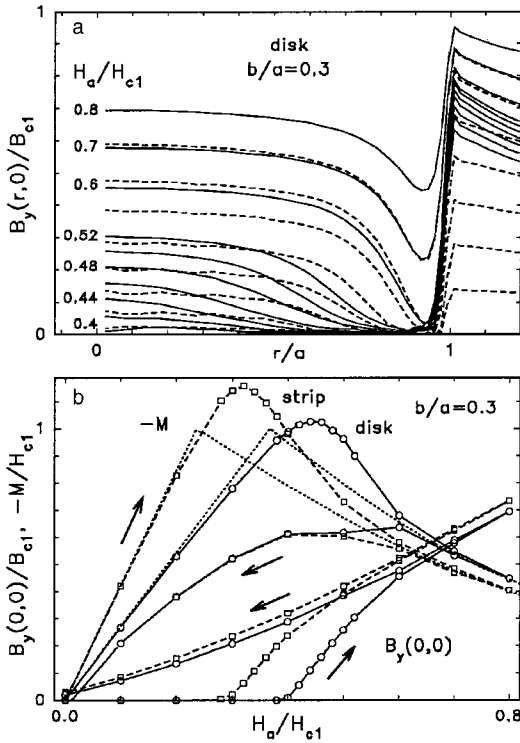


FIG. 3. The axial magnetic induction $B_y(r,y)$ in the midplane $y=0$ of a pin-free superconductor disk with aspect ratio $b/a=0.3$ in increasing field (solid lines) and then decreasing field (dashed lines), plotted at $H_a/H_{c1}=0.4, 0.42, \dots, 0.5, 0.52, 0.6, 0.7, 0.8, 0.7, 0.6, \dots, 0.1, 0$ (a). The induction $B_y(0,0)$ as the center of the same disk (solid line) and of a strip (dashed line), both with $b/a=0.3$. The symbols mark the field values at which the profiles are taken. Also shown are the magnetization loops for the same disk and strip and the corresponding reversible magnetization (dotted lines) (b).

scribes usual flux flow, i.e., viscous motion of vortices, $\mathbf{E} = \rho_{FF}(\mathbf{B})\mathbf{J}$, with the flux-flow resistivity $\rho_{FF} \propto B$, as it should be.

6. PIN-FREE SUPERCONDUCTORS

The penetration and exit of flux computed from Eqs. (8)–(15) is visualized in Figs. 1–3 for isotropic strips and disks without volume pinning, using a flux-flow resistivity $\rho_{FF} = \rho_0 B(\mathbf{r})$ with $\rho_0 = 140$ (strip) or $\rho_0 = 70$ (disk), in units where $H_{c1} = a = \mu_0 = |dH_a/dt| = 1$. Figure 1 shows the field lines of $\mathbf{B}(x,y)$ in two pin-free strips with aspect ratios $b/a = 2$ and $b/a = 0.3$; Fig. 2 shows the surface screening currents in the same strips before flux has penetrated; and Fig. 3 plots some induction profiles in a strip and some hysteresis loops of the magnetization and of the induction at the center of a strip and disk.

The profiles of the induction $B_y(r,y)$ taken along the midplane $y=0$ of the thick disk in Fig. 3 have a pronounced minimum near the edge $r=a$, which is the region where strong screening currents flow. Away from the edges, the current density $\mathbf{J} = \nabla \times \mathbf{B}/\mu_0$ is nearly zero; note the parallel field lines in Fig. 1. The quantity $\mathbf{J}_H = \nabla \times \mathbf{H}(\mathbf{B})$, which enters the Lorentz force density $\mathbf{J}_H \times \mathbf{B}$, is even exactly zero, since we assume the absence of pinning and the viscous drag force is small. Our finite flux-flow parameter ρ_0 and finite ramp rate $dH_a/dt = \pm 1$ mean a dragging force which, simi-

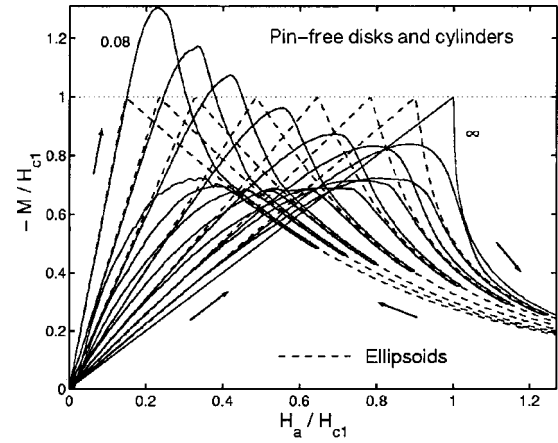


FIG. 4. The irreversible magnetization curves $-M(H_a)$ of pin-free circular disks and cylinders with aspect ratios $b/a=0.08, 0.15, 0.25, 0.5, 1, 2, 5, \infty$ in an axial field H_a . Here the irreversibility is due only to a geometric edge barrier for flux penetration. The reversible magnetization curves of the corresponding ellipsoids defined by Eqs. (3), (6), and (7) are shown as dashed lines.

lar to pinning, causes a weak hysteresis and a small remanent flux at $H_a=0$; this artifact is reduced by choosing a larger resistivity or a slower ramp rate.

In Fig. 3 the induction $B_0 = B_y(0,0)$ in the specimen center performs a hysteresis loop very similar to the magnetization loops $M(H_a)$ shown in Figs. 3 and 4. Both loops are symmetric, $M(-H_a) = -M(H_a)$ and $B_0(-H_a) = -B_0(H_a)$. The maximum of $M(H_a)$ defines a field of first flux entry H_{en} , which closely coincides with the field H'_{en} at which $B_y(0,0)$ starts to appear. The computed entry fields are well fitted by

$$H_{en}^{\text{strip}}/H_{c1} = \tanh \sqrt{0.36b/a},$$

$$H_{en}^{\text{disk}}/H_{c1} = \tanh \sqrt{0.67b/a}. \quad (16)$$

These formulas are good approximations for all aspect ratios $0 < b/a < \infty$; see also the estimates of $H_{en} \approx \sqrt{b/a}$ for thin strips in Refs. 35 and 39.

The virgin curve of the irreversible $M(H_a)$ of strips and disks at small H_a coincides with the ideal-Meissner straight line $M = -H_a/(1-N)$ of the corresponding ellipsoid, Eqs. (4), (7). When the increasing H_a approaches H_{en} , flux starts to penetrate into the corners in the form of almost straight flux lines (Fig. 1), and thus $|M(H_a)|$ falls below the Meissner line. At $H_a = H_{en}$ flux penetrates and jumps to the center, and $|M(H_a)|$ starts to decrease. In decreasing H_a , this barrier is absent. As soon as flux exit starts, all our calculated $M(H_a)$ exhibit strong “numerical noise,” which reflects the instability of this state. Similar but weaker noise occurs at the onset of flux penetration.

As can be seen in Fig. 4, above some field H_{rev} , the magnetization curve $M(H_a)$ becomes reversible and exactly coincides with the curve of the ellipsoid defined by Eqs. (3), (6), and (7) (in the quasistatic limit with $\rho_0^{-1} dH_a/dt \rightarrow 0$). The irreversibility field H_{rev} is difficult to compute since it depends slightly on the choices of the flux-flow parameter ρ_0 (or ramp rate) and of the numerical grid, and also on the model for $M(H_a; 0)$. In the interval $0.08 \leq b/a < 5$ we find, with relative error of 3%,

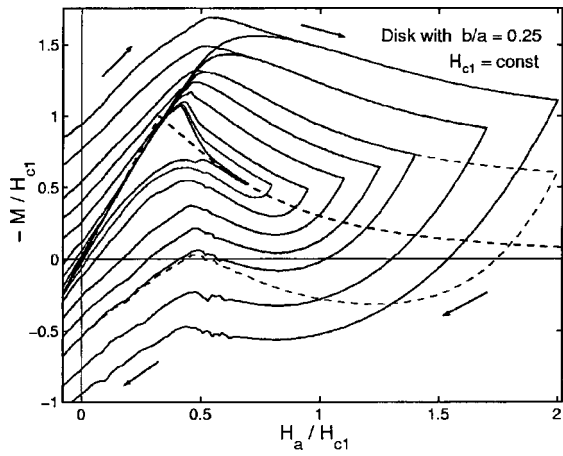


FIG. 5. The magnetization curves $M(-H_a) = -M(H_a)$ of a thick disk with aspect ratio $b/a=0.25$ and constant H_{c1} for various pinning strengths, $J_c = 0, 0.25, 0.5, 1, 1.5, 2, 3, 4$ in units of H_{c1}/a , and various sweep amplitudes. Bean model. The inner loop belongs to the pin-free disk ($J_c=0$), the outer loop to strongest pinning. The reversible magnetization curve of the corresponding ellipsoid is shown as a dashed curve.

$$H_{rev}^{strip}/H_{c1} = 0.65 + 0.12 \ln(b/a),$$

$$H_{rev}^{disk}/H_{c1} = 0.75 + 0.15 \ln(b/a). \quad (17)$$

This fit obviously does not apply to very small $b/a \ll 1$ (since H_{rev} should exceed $H_{rev} > 0$) nor to very large $b/a \gg 1$ (where H_{rev} should be close to H_{c1}). The limiting value of H_{rev} for thin films with $b \ll a$ is thus not yet known.

Remarkably, the irreversible magnetization curves $M(H_a)$ of pin-free strips and disks fall on top of each other if the strip is chosen twice as thick as the disk, $(b/a)_{strip} \approx 2(b/a)_{disk}$. This striking coincidence holds for all aspect ratios $0 < b/a < \infty$ and can be seen from each of Eqs. (7), (16), and (17). The effective N [or virgin slope $1/(1-N)$], the entry field H_{en} , and the reversibility field H_{rev} are nearly equal for strips and disks with half thickness, or for slabs and cylinders with half length.

Another interesting feature of the pin-free magnetization loops is that the maximum of $|M(H_a)|$ exceeds the maximum of the reversible curve (equal to H_{c1}) when $b/a < 0.8$ for strips and $b/a < 0.4$ for disks, but at larger b/a it falls

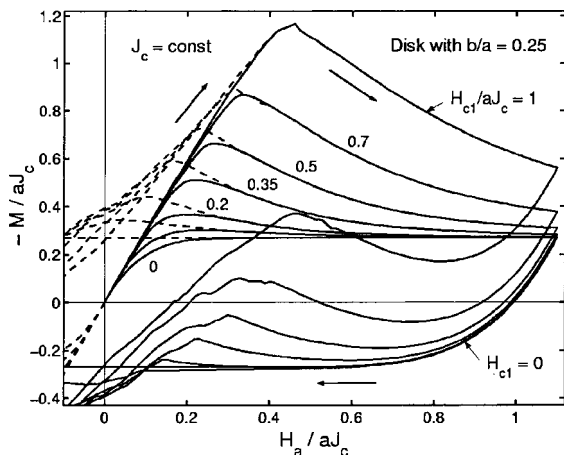


FIG. 6. Magnetization curves of a disk as in Fig. 5 but with $J_c = \text{const}$ and for various lower critical fields H_{c1} in units of aJ_c . Bean model.

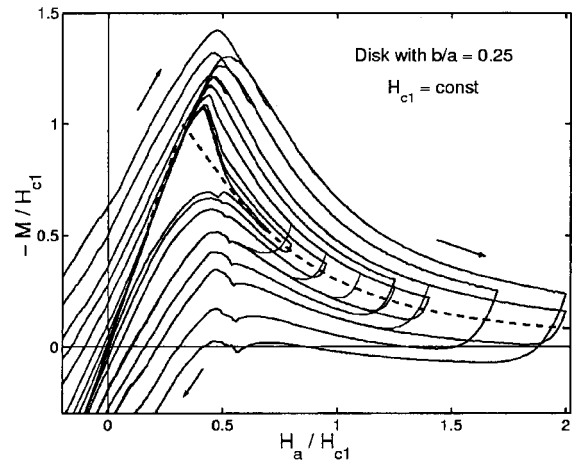


FIG. 7. Magnetization curves of the same disk as in Fig. 5 but for the Kim model, $J_c(B) = J_{c0}/(1+3|B|/B_{c1})$ for various pinning strengths $J_{c0} = 0, 0.25, 0.5, 1, 1.5, 2, 3, 4$ in units of H_{c1}/a . Presentation as in Fig. 5.

below H_{c1} . The maximum magnetization may be estimated from the slope of the virgin curve $1/(1-N)$, Eq. (7), and from the field of first flux entry, Eq. (16).

Formulas (7), (16), and (17) are derived essentially from first principles, with no assumptions but the geometry and finite H_{c1} . They should be used to interpret experiments on superconductors with no or very weak vortex pinning. At present it is not clear how the presence of a microscopic Bean–Livingston barrier may modify these continuum theoretical results.

7. SUPERCONDUCTORS WITH PINNING

Figures 5–8 show how the irreversible magnetization loops of disks with $b/a=0.25$ (and in Fig. 9 for a thinner disk with $b/a=0.125$) are modified when volume pinning is switched on. In Figs. 5, 6, and 9, pinning is described by the Bean model with constant critical current density J_c , while in Figs. 7 and 8 the Kim model is used with an induction-dependent $J_c(B) = J_{c0}/(1+3|B|/B_K)$, with $B_K = \mu_0 H_{c1}/3$

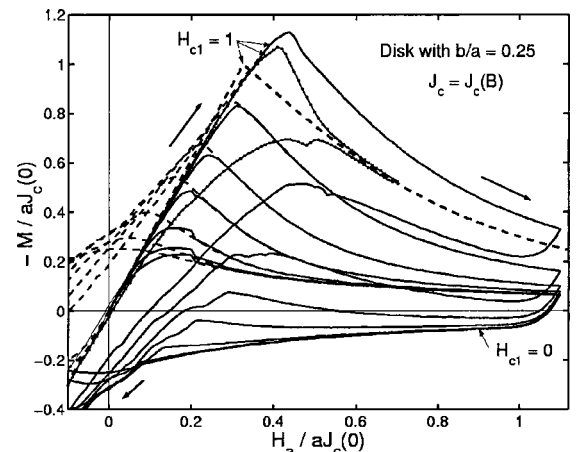


FIG. 8. Magnetization curves as in Fig. 6 but for the Kim model $J_c(B) = J_{c0}/(1+3|B|/aJ_{c0})$ with $J_{c0} = \text{const}$ for various $H_{c1} = 0, 0.1, 0.2, 0.35, 0.5, 0.7, 1$ in units of aJ_{c0} . Also depicted are the pin-free magnetization (line with dots; M and H_a here are in units H_{c1} since $J_{c0}=0$) and the irreversible magnetization of the corresponding ellipsoid.

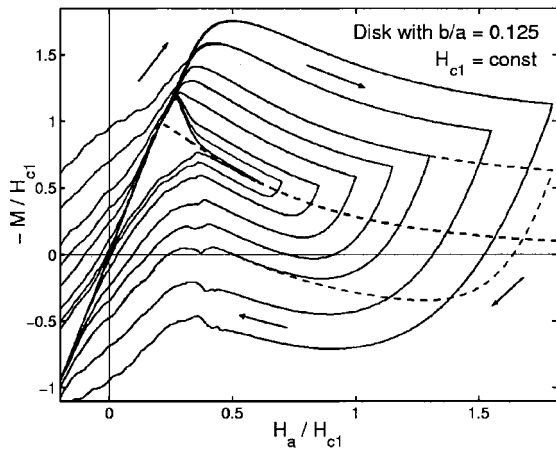


FIG. 9. Same magnetization curves as in Fig. 5 but for a thinner disk with aspect ratio $b/a=0.125$ for various degrees of pinning $J_c/H_{c1}=0, 0.25, 0.5, 1, 1.5, 2, 3, 4$ and constant H_{c1} .

(Fig. 8) or $B_K = \mu_0 a J_{c0}/3$ (Fig. 9). In Figs. 5, 7, and 9, H_{c1} is held constant; with increasing J_c or J_{c0} (in natural units H_{c1}/a) the magnetization loops are inflated nearly symmetrically about the pin-free loop or about the reversible curve (above H_{rev}), and the maximum of $|M(H_a)|$ shifts to higher fields. Above H_{rev} the width of the loop is nearly proportional to J_c , as expected from theories^{42,43} which assume $H_{c1}=0$, but at small fields the influence of finite H_{c1} is clearly seen up to rather strong pinning.

In Figs. 6 and 8, J_c or J_{c0} is held constant and H_{c1} increased from zero (in the natural units aJ_c). As expected, the influence of finite H_{c1} is most pronounced at small applied fields H_a , where it causes a peak in $-M$ even in the Bean magnetization curves, which without consideration of H_{c1} consist of two monotonic branches and a monotonic virgin curve. Within the Kim model, or with any decreasing $J_c(B)$ dependence, the magnetization loops exhibit a maximum even when $H_{c1}=0$ is assumed.⁴⁸ With increasing H_{c1} this maximum becomes sharper and shifts to larger fields (cf. Fig. 8). Comparing Figs. 5 and 9, one sees that for superconductor disks with pinning and with $H_{c1}>0$, the peak in $-M(H_a)$ becomes more pronounced and shifts towards smaller applied fields when the disk thickness is decreased.

In the classical Bean model, i.e., if the lower critical field H_{c1} and the B dependence of $J_c(B)$ are disregarded (both conditions are satisfied when B is sufficiently high), there exist analytical solutions for the critical state not only for the simple longitudinal geometry³² but also for the more realistic geometries of thin disks in an axial field⁴⁹ and for long thin strips in a perpendicular field.⁵⁰ Interestingly, the expressions for the profiles of the current density, $J(\rho)$ and $J(x)$, have identical form in these two geometries, but an analytical expression for the magnetic field profiles, $B_y(\rho)$ and $B_y(x)$, exists only for the strip geometry but not for the disk. Recently the critical-state problem has been solved also for thin ellipsoidal disks in a perpendicular magnetic field;⁴¹ this general solution contains the circular disk and long strip as limiting cases. Exact solutions were also obtained when the critical current density in thin films depends on the orientation of the local magnetic field with respect to the film plane, i.e., on the inclination angle of the flux lines.⁵¹ This out-of-

plane anisotropy of pinning occurs, e.g., in high- T_c superconductors with layered structure.

*E-mail: ehb@physix.mpi-stuttgart.mpg.de

- ¹H. Kamerlingh Onnes, Leiden Comm. **120b**, **122b**, **124c**, (1911).
- ²J. K. Hulm and B. T. Matthias, Science **208**, 881 (1980).
- ³J. G. Bednorz and K. A. Müller, Z. Phys. **B64**, 189 (1986).
- ⁴M. K. Wu, J. R. Ashburn, C. J. Torng, P. H. Hor, R. L. Meng, L. Gao, Z. J. Huang, Y. Q. Wang, and C. W. Chu, Phys. Rev. Lett. **58**, 908 (1987).
- ⁵H. Maeda, Y. Tanaka, M. Fukutomi, and T. Asano, Jpn. J. Appl. Phys. **27**, L206 (1988).
- ⁶S. X. Dou, X. L. Wang, Y. C. Guo, Q. Y. Hu, P. Mikheenko, J. Horvath, M. Ionescu, and H. K. Liu, Supercond. Sci. Technol. **10**, A52–A67 (1997).
- ⁷Z. Z. Sheng and A. M. Hermann, Nature (London) **332**, 55 (1988).
- ⁸L. Gao, Y. Y. Xue, F. Chen, Q. Xiong, R. L. Meng, D. Ramirez, C. W. Chu, J. H. Eggert, and H. K. Mao, Phys. Rev. B **50**, 4260 (1994).
- ⁹Y. C. Kim, J. R. Thompson, J. G. Ossandon, D. K. Christen, and M. Paranthaman, Phys. Rev. B **51**, 11767 (1995).
- ¹⁰J. Nagamatsu, N. Nakagawa, T. Muranaka, Y. Zenitani, and J. Akimitsu, Nature (London) **410**, 63 (2001).
- ¹¹*Magnetic Properties and Critical Currents of Superconducting Alloys*, J. N. Rjabinin and L. W. Schubnikow, Phys. Z. Sowjetunion **7**, N1, 122 (1935); Nature (London) **135**, 581 (1935).
- ¹²L. W. Schubnikow, W. I. Chotewitsch, J. D. Schepelew, and J. N. Rjabinin, Phys. Z. Sowjetunion **10**, N2, 39 (1936); Zh. Éksp. Teor. Fiz. **7**, 221 (1937).
- ¹³A. A. Abrikosov, Zh. Éksp. Teor. Fiz. **32**, 1442 (1957) [Sov. Phys. JETP **5**, 1174 (1957)].
- ¹⁴V. L. Ginzburg and L. D. Landau, Zh. Éksp. Teor. Fiz. **20**, 1064 (1950) [English translation in *Men of Physics*], edited by L. D. Landau and D. ter Haar, New York: Pergamon (1965), Vol. 1, p. 138.
- ¹⁵J. Pearl, Appl. Phys. Lett. **5**, 65 (1964).
- ¹⁶A. L. Fetter and P. C. Hohenberg, Phys. Rev. **159**, 330 (1967).
- ¹⁷J. R. Clem, Phys. Rev. B **43**, 7837 (1991).
- ¹⁸L. D. Landau and E. M. Lifshitz, *Electrodynamics of Continuous Media*, Vol. 8, in Theoretical Physics, Pergamon Press, London (1959).
- ¹⁹A. Hubert, Phys. Status Solidi **24**, 669 (1967).
- ²⁰A. Fortini and E. Paumier, Phys. Rev. B **5**, 1850 (1972).
- ²¹H. Kronmüller and H. Riedel, Phys. Status Solidi **77**, 581 (1976).
- ²²J. R. Clem, J. Low Temp. Phys. **18**, 427 (1975).
- ²³Z. Hao, J. R. Clem, M. W. McElfresh, L. Civale, A. P. Malozemoff, and F. Holtzberg, Phys. Rev. B **43**, 2844 (1991).
- ²⁴M. Tinkham, *Introduction to Superconductivity*, McGraw-Hill, New York (1975).
- ²⁵E. H. Brandt, J. Low Temp. Phys. **26**, 709 (1977); *ibid.*, 735 (1977); *ibid.* **28**, 263 (1977); Phys. Rev. B **34**, 6514 (1986).
- ²⁶E. H. Brandt and U. Essmann, Phys. Status Solidi B **144**, 13 (1987).
- ²⁷E. H. Brandt, Rep. Prog. Phys. **58**, 1465 (1995).
- ²⁸G. Blatter, M. V. Feigel'man, V. B. Geshkenbein, A. I. Larkin, and V. M. Vinokur, Rev. Mod. Phys. **66**, 1125 (1994).
- ²⁹E. H. Brandt, Phys. Rev. Lett. **78**, 2208 (1997).
- ³⁰P. W. Anderson, Phys. Rev. Lett. **9**, 309 (1962).
- ³¹J. Provost, E. Paumier, and A. Fortini, J. Phys. F: Met. Phys. **4**, 439 (1974); A. Fortini, A. Haire, and E. Paumier, Phys. Rev. B **21**, 5065 (1980).
- ³²C. P. Bean and J. D. Livingston, Phys. Rev. Lett. **12**, 14 (1964); L. Burlachkov, Phys. Rev. B **47**, 8056 (1993).
- ³³M. V. Indenborn, H. Kronmüller, T. W. Li, P. H. Kes, and A. A. Menovsky, Physica C **222**, 203 (1994); M. V. Indenborn and E. H. Brandt, Phys. Rev. Lett. **73**, 1731 (1994).
- ³⁴N. Morozov, E. Zeldov, D. Majer, and B. Khaykovich, Phys. Rev. Lett. **76**, 138 (1996); N. Morozov, E. Zeldov, V. Konczykowski, and R. A. Doyle, Physica C **291**, 113 (1997).
- ³⁵E. Zeldov, A. I. Larkin, V. B. Geshkenbein, M. Konczykowski, D. Majer, B. Khaykovich, V. M. Vinokur, and H. Strikhman, Phys. Rev. Lett. **73**, 1428 (1994).
- ³⁶E. Zeldov, A. I. Larkin, M. Konczykowski, B. Khaykovich, D. Majer, V. B. Geshkenbein, and V. M. Vinokur, Physica C **235–240**, 2761 (1994); B. Khaykovich, E. Zeldov, M. Konczykowski, D. Majer, A. I. Larkin, and John R. Clem, *ibid.* **235–240**, 2757 (1994).

- ³⁷I. L. Maksimov and A. A. Elistratov, JETP Lett. **61**, 208 (1995); I. L. Maksimov and A. A. Elistratov, Appl. Phys. Lett. **72**, 1650 (1998).
- ³⁸Th. Schuster, M. V. Indenborn, H. Kuhn, E. H. Brandt, and M. Konczykowski, Phys. Rev. Lett. **73**, 1424 (1994).
- ³⁹M. Benkraouda and J. R. Clem, Phys. Rev. B **53**, 5716 (1996); *ibid.* **58**, 15103 (1998).
- ⁴⁰A. V. Kuznetsov, D. V. Eremenko, and V. N. Trofimov, Phys. Rev. B **56**, 9064 (1997); *ibid.* **57**, 5412 (1998).
- ⁴¹G. P. Mikitik and E. H. Brandt, Phys. Rev. B **60**, 592 (1999).
- ⁴²E. H. Brandt, Phys. Rev. B **54**, 4246 (1996).
- ⁴³E. H. Brandt, Phys. Rev. B **58**, 6523 (1998).
- ⁴⁴R. Labusch and T. B. Doyle, Physica C **290**, 143 (1997); T. B. Doyle, R. Labusch, and R. A. Doyle, *ibid.* **290**, 148 (1997).
- ⁴⁵E. H. Brandt, Phys. Rev. B **59**, 3369 (1999).
- ⁴⁶E. H. Brandt and G. P. Mikitik, Phys. Rev. Lett. **85**, 4164 (2000).
- ⁴⁷E. H. Brandt, Phys. Rev. B **64**, 24505 (2001).
- ⁴⁸D. V. Shantsev, M. R. Koblichka, Y. M. Galperin, T. H. Johansen, L. Pust, and M. Jirsa, Phys. Rev. Lett. **82**, 2947 (1999).
- ⁴⁹P. N. Mikheenko and Yu. E. Kuzovlev, Physica C **204**, 229 (1993).
- ⁵⁰E. H. Brandt, M. V. Indenborn, and A. Forkl, Europhys. Lett. **22**, 735 (1993).
- ⁵¹G. P. Mikitik and E. H. Brandt, Phys. Rev. B **62**, 680 (2000).

This article was published in English in the original Russian journal. Reproduced here with stylistic changes by AIP.

Vortex matter in superconductors

V. M. Pan*

G. V. Kurdyumov Institute of Metal Physics, National Academy of Sciences of Ukraine, bul'var Vernadskogo 36, 03142 Kiev, Ukraine

A. V. Pan**

G. V. Kurdyumov Institute of Metal Physics, National Academy of Sciences of Ukraine, bul'var Vernadskogo 36, 03142 Kiev, Ukraine; Institute for Superconducting and Electronic Materials, University of Wollongong, New South Wales 2522, Australia

(Submitted May 18, 2001)

Fiz. Nizk. Temp. **27**, 991–1011 (September–October 2001)

The behavior of the ensemble of vortices in the Shubnikov phase in biaxially oriented films of the high-temperature superconductor $\text{YBa}_2\text{Cu}_3\text{O}_{7-\delta}$ (YBCO) in an applied magnetic field is investigated for different orientations of the field. The techniques used are the recording of the current–voltage characteristics in the transport current and of resonance curves and damping of a mechanical oscillator during the passage of a transport current. It is shown that the behavior of the vortex ensemble in YBCO films, unlike the case of single crystals, is determined by the interaction of the vortices with linear defects—edge dislocations, which are formed during the pseudomorphic epitaxial growth and are the dominant type of defect of the crystal lattice, with a density reaching 10^{15} lines/m². The effective pinning of the vortices and the high critical current density ($J_c \geq 3 \times 10^{10}$ A/m² at 77 K) in YBCO films are due precisely to the high density of linear defects. New phase states of the vortex matter in YBCO films are found and are investigated in quasistatics and dynamics; they are due to the interaction of the vortices with crystal defects, to the onset of various types of disordering of the vortex lattice, and to the complex depinning process. A proposed H – T phase diagram of the vortex matter for YBCO films is proposed. © 2001 American Institute of Physics. [DOI: [DOI: 10.1063/1.1401182]

INTRODUCTION

It was first shown by the Ukrainian physicist L. V. Shubnikov back in 1936¹ that in superconducting alloys there exists a wide range of magnetic fields at which the Meissner effect gradually diminishes and the magnetic flux penetrates into the volume of the superconductor. In that case the response of the superconductor to an increase in the external magnetic field (i.e., the magnetization curves) have a completely different form than in the case of pure metals, i.e., type-I superconductors. The term “type-II superconductor” was first used for alloys and compounds by Abrikosov in 1957 in developing a consistent theory of type-II superconductors.² This theory made it possible to understand the experimental results of Shubnikov on the basis of the concepts of flux quantization and the penetration of magnetic field into type-II superconductors in the form of a lattice of Abrikosov vortices. On the H – T phase diagram (i.e., the diagram in magnetic field versus temperature) the phase in which a type-II superconductor is threaded by vortices—magnetic flux quanta—has ever since that time been called the Shubnikov phase. As time went on, it became clear that vortex states in superconductors are very complex and diverse while at the same time being exceedingly important for understanding the behavior of superconductors in an electromagnetic field and under current loading. A new field of physics has arisen, which might be called vortex-matter physics. In this article we examine the features of the vortex

state in films of the moderately anisotropic high-temperature superconductor (HTSC) $\text{YBa}_2\text{Cu}_3\text{O}_{7-\delta}$ (YBCO).

1. QUANTIZED VORTICES IN A SUPERCONDUCTOR

The penetration of magnetic field into a type-II superconductor occurs in the form of quantized vortex lines or flux lines. Each such flux line carries a quantum of magnetic flux, $\Phi_0 = hc/2e = 2.07 \times 10^{-15}$ T·m², and has a normal core, which in an isotropic superconductor is a thin normal cylinder along the magnetic field. The radius of this cylinder, the vortex core, is equal to the coherence length ξ (an important scale length in a superconductor, which in the microscopic theory is defined as the distance between interacting electrons in a Cooper pair and in the Ginzburg–Landau (GL) phenomenological theory, as the distance at which the superconducting order parameter varies from its maximum to zero at a superconductor/normal metal boundary).³ Around the normal core flows an undamped supercurrent, which in isotropic type-II superconductors is oriented in such a way that the magnetic field induced by it is directed along the core and coincides with the direction of the external field. The vortex current flows in a region with a radius of the order of λ , the London penetration depth of a weak magnetic field. For a type-II superconductor this region is much larger than ξ , and this is a consequence of the fact that $\sigma_{ns} < 0$ in a type-II superconductor, i.e., $\lambda \gg \xi$. The penetration of vortices into a type-II superconductor becomes energetically fa-

avorable in an external field $H_{\text{ext}} > H_{c1}$ (H_{c1} is the first, or lower, critical field). Penetrating into the volume of the type-II superconductor, the vortices are spaced a distance $a_0 \propto (\Phi_0/H)^{1/2}$ apart, and when $a_0 \leq \lambda$ they begin to interact (repelling each other) owing to the Lorentz force $\mathbf{f}_L = 1/c [\mathbf{j} \times \Phi_0]$, forming a regular triangular lattice in the transverse cross section.^{3,4}

2. VORTEX STATE—A NEW FORM OF CONDENSED MATTER

A powerful impulse for the further development of the physics of the vortex state was obtained after the discovery of high- T_c superconductors in 1986. This was because of two important circumstances: first, the critical temperature of HTSC cuprates is so high that they become superconducting at temperatures where thermal fluctuations play an appreciable role, since their energy becomes comparable to the elastic energy of a vortex and/or of the vortex lattice and also to the pinning energy, thus creating the necessary conditions for the appearance of unusual new regions on the H – T phase diagram of the superconductor—different states of the vortex matter and phase transitions between them; second, owing to the layered crystal structure and the anisotropy inherent to HTSC metal-oxide cuprates, favorable conditions are created for the appearance on the H – T diagram of phase regions and phase transitions involving changes in the dimensionality in the vortex ensemble from three-dimensional to two-dimensional and vice versa.

The vortex matter in type-II superconductors is a unique example of a condensed state with controllable parameters.⁵ Unlike ordinary condensed-matter systems the density of the constituent particles (magnetic vortices) and their interaction can be changed by several orders of magnitude in a controllable way by simply varying the external magnetic field. In addition, extremely important thermal fluctuation effects in experiments with HTSC cuprates can be observed over a wide temperature range, and these effects are reflected on the H – T phase diagram. Finally, vortex matter is the most convenient tool for studying disordered media—one of the central problems of condensed-matter physics.

In a conventional treatment of the Shubnikov vortex state without allowance for thermal fluctuation and pinning effects, it is assumed that a homogeneous solid vortex-lattice phase exists in the field interval between the lower critical field H_{c1} , where the vortices begin to penetrate into the superconductor, and the mean-field upper critical field H_{c2} , above which the superconductivity vanishes.

The upper critical field $H_{c2}(T)$ of a type-II superconductor is defined as the field at which, at a temperature T , the normal cores of the vortices begin to overlap, and the superconductor becomes “normal.” If one ignores thermal fluctuations, then $H_{c2} = \Phi_0 / (2\pi\xi^2)$, and this means that a small coherence length is conducive to an increase in H_{c2} .

For high- T_c cuprate superconductors the small value of ξ is the reason why H_{c2} far exceeds 100 T at low temperatures. The well-known H – T phase diagram for a “clean” or ideal type-II superconductor can be obtained using the “mean field approximation” in the GL theory. However, taking thermal fluctuations and disordering effects into account has been

shown to strongly alter the form of this phase diagram, adding new features and new phase regions.

3. THE H – T PHASE DIAGRAM IN THE PRESENCE OF CORRELATED DISORDERING

The presence of linear defects, which by their nature are capable of pinning vortices most strongly along their entire length and whose density is comparable to the density of vortices will give rise to a special state, the so-called “Bose glass,” when the vortices are localized in a random manner by linear defects lying parallel to one another. The mechanism of formation of the two-dimensional (or correlated) Bose glass is reminiscent of the mechanism of formation of the three-dimensional vortex glass (which is another disordered state of the vortex lattice, in which it interacts with a set of random pointlike defects of the crystal):^{6–10} the linear defects also generate additional low-lying vortex states which differ from those already existing in the perfect lattice, and the vortices are trapped by these states if the potential wells induced by the disorder are sufficiently deep in comparison with the energy of thermal fluctuations. The character of the H – T phase diagram, as in the case of pointlike disorder, is determined by the compensation and competition of the elastic, pinning, and thermal characteristic energies and also by the use of the corresponding Lindemann criterion.⁵

The upward shift of the melting line on the H – T diagram in the presence of linear defects can be estimated, keeping in mind that the modulation of the parabolic elastic potential of the vortex lattice by the linear pinning potential causes an increase in its effective depth. Therefore, in order to remove a given vortex from the confines of the “box,” the thermal fluctuations must overcome not only the elastic barrier but also additional pinning barriers. Thus the condition for the loss of stability of the vortex lattice can be determined from the equation

$$k_B T = E_{\text{elastic}} + E_{\text{pin}}, \quad (1)$$

where $k_B T$, E_{elastic} , and E_{pin} are the characteristic energies of thermal fluctuations, the elastic interaction, and pinning. The form of Eq. (1) shows that linear defects are the cause of the shift of the solid↔liquid transition, which in this case is called the Bose glass transition, $H_{BG}(T)$, to higher temperatures in comparison with the melting temperature of the perfect crystal in the absence of these linear defects, $H_{BG}(T) > H_m(T)$.¹¹ In the case of a fairly low density of linear defects, when the main contribution is given by the elastic energy and the disordering leads only to small shifts of the melting line, the melting of the Bose glass still preserves the features of a first-order transition. Such a transition occurs in low magnetic fields $H < H_\Phi$, where $H_\Phi = \Phi_0/D^2$ is the so-called “matching” field, at which the density of linear defects equals the density of vortices (D is the average distance between linear defects). At higher fields $H > H_\Phi$ the corrections to the melting temperature rapidly decrease, and the melting line of the Bose glass returns to its original position. Thus the greatest deviation of the melting line of the Bose glass from its original position in perfect crystals is expected to occur near $H \cong H_\Phi$.

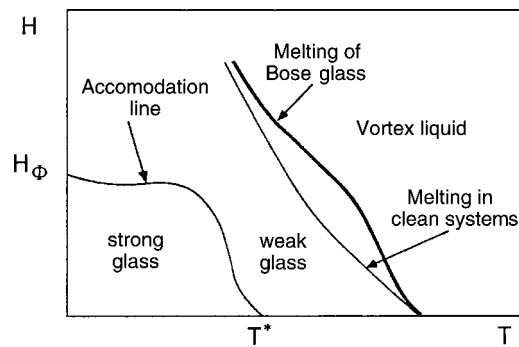


FIG. 1. Schematic H - T phase diagram of the vortex matter in the presence of statistically distributed extended linear (columnar) defects.⁵

Figure 1 shows a schematic phase diagram of a vortex system with correlated disorder arising because of the presence of defects. According to Ref. 5, an accommodation line separates two regimes of behavior of the vortex matter: the regime of individual pinning, and the regime of collective pinning with the participation of linear defects.¹¹ The position of the accommodation line is determined by the competition and compensation of the characteristic elastic energy arising because of the interaction with the remaining vortex lattice (the potential box) and the pinning energy. Below the accommodation line the pinning force dominates, and the vortices can therefore be shifted substantially from their equilibrium positions in the perfect lattice. To emphasize the particularly strong individual pinning in such a state, it has been proposed⁵ to call this state of the vortex lattice a “strong Bose glass.” It was proposed⁵ that the state that is formed in the collective pinning regime be considered a quasilattice or “weak Bose glass.” A very important distinction between the effect of linear and point defects is that, unlike point defects, which stimulate lateral (bending) deformations of the vortices, linear pinning centers *stabilize* the residence of a given vortex line in the potential box formed by the elastic interaction with the neighbors against thermal fluctuations and against bending displacements caused by point defects (as is shown schematically in Fig. 2), thereby preventing the formation of a three-dimensionally disordered solid state of the vortex lattice. It is particularly important to emphasize that in the case of linear crystal defects—pinning centers—the “strong” glass phase, with a highly two-dimensional distorted structure of the vortex lattice and the highest critical current density, occupies the low-field part of the H - T phase diagram. Of course, such behavior contrasts with the effects of point disorder, when the more strongly pinned three-dimensionally disordered solid vortex phase appears in higher fields.^{12–18}

Thus it turns out that the contributions of linear and point defects to the volume pinning force not only do not add together but they may even subtract, i.e., the point disorder promotes the depinning (breakaway) of vortex lines from linear defects. This conjecture has been shown experimentally^{12–18} to be well confirmed for configurations in which the linear defects are oriented parallel to the magnetic field (or, more precisely, to the direction of the vortex lines). Since all real HTSC materials unavoidably contain pointlike defects (e.g., oxygen vacancies), the question of the dominant pinning mechanism is one of paramount impor-

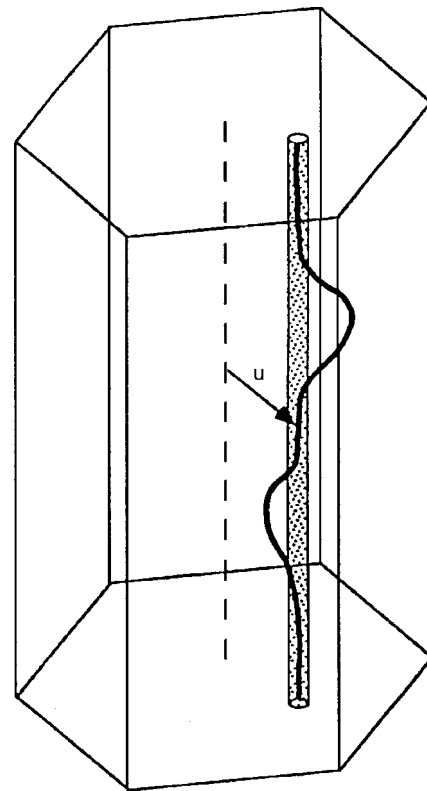


FIG. 2. Vortex line in a potential “box” containing an extended linear defect,^{5,10,11} which modulates the parabolic potential well, creating new minima and displacing the vortex from its equilibrium position in the box. Also shown are the short-wavelength lateral displacements that arise due to the simultaneous action of a random point potential. These displacements promote depinning of the vortex from the linear defect.

tance for the controlled creation of desired transport current-carrying properties of a material. The competition of these two types of disorder was first studied experimentally in Refs. 12–18 and theoretically in Ref. 19. In particular, it was shown in Ref. 19 that in the real cases the influence of the correlated disorder is dominant in the behavior of the vortex matter, even when the density of defects is lower than the density of vortices.

Up till now, however, the discussions and calculations of theorists have been based exclusively on the hypotheses of structures with linear defects obtained in HTSCs subjected to irradiation by heavy ions with high energies (around 1 GeV and higher). Very recently it has become clear that dislocation ensembles in strongly biaxially textured epitaxial films of YBCO play the role of strongly-pinning correlated linear defects.

4. PINNING CENTERS IN EPITAXIAL YBCO FILMS

As we have said, the fact that the highest J_c ($\geq 10^{10}$ A/m² at 1 T and 77 K) can be obtained relatively easily in YBCO epitaxial films while remaining unachievable for any YBCO bulk materials should be attributed to features of the defect structure of the films and, accordingly, to the formation of a volume pinning force in them due to the most effective interaction, primarily with linear defects. Many attempts have been made to establish a linkage of the pinning force to the screw dislocations that initiate the corresponding three-dimensional mode of film growth during

deposition (by the appearance and propagation of screw dislocations)—the so-called “screw-mediated” growth^{20,21}—and to the growth steps on the surface of the film in the two-dimensional, “layer-by-layer,” growth mode. However, these attempts have been futile: for example, one can prepare films in which the concentration of screw dislocations will differ by an order of magnitude or more (from 5×10^7 to 10^9 cm^{-2}) while the critical current density will be the same, and vice versa. Moreover, the cores of the growth screw dislocations in YBCO films have been shown by electron microscope studies to have a characteristic transverse size that is much greater than the coherence length.²² Therefore, they can hardly be effective pinning centers. The experimental evidence^{13,14,23–25} of a very high density of edge dislocations in YBCO epitaxial films is also not very convincing, since the investigators could scarcely believe that a dislocation line (i.e., the core of a dislocation) could in itself serve as a strong pinning center providing effective “core pinning.” Indeed, on the one hand, back in the early papers of Dew-Hughes²⁶ it was shown that dislocations pin only when they comprise an ensemble which forms “walls” of a cellular structure in metallic bcc alloys owing to the long-range stress fields, which can lead to both δl and δT_c pinning.⁶ As to an isolated linear defect, in the papers by Dew-Hughes and his followers it was clearly stated that “isolated dislocations lead to a negligibly small change in κ_{GL} ” (the parameter of the Ginzburg–Landau theory). And, on the other hand, it is known from the theory of dislocations that the transverse cross section of the core can have an area of the order of the square of the Burgers vector, which is clearly much smaller than the square of the coherence length, even for HTSCs ($\xi_{ab} \approx 1.5 \text{ nm}$ for YBCO in comparison with the value of the Burgers vector $B \approx 0.4 \text{ nm}$). Thus it appears that, as in the case of point defects, dislocations can pin only collectively, since the depth of the pinning potential well U_p is small, and the experimental pinning force of an individual dislocation, $f_p = dU_p/dr$, is small. Two new important results have played a most important role in the further development of the concepts of dislocation pinning in HTSCs, presenting unambiguous evidence in favor of strong pinning on dislocation lines. The first of these was obtained by Chisholm and Smith,²⁷ and then, more convincingly, by Merkle and co-workers.^{28,29} A high-resolution transmission electron microscope (HRTEM) was used to obtain pictures of the real distribution of atoms inside and in a neighborhood around the core of a complete [001] edge dislocation. It was found that the core of an edge dislocation is a highly distorted structure on a characteristic scale length of the order of 5–10 interatomic distances, i.e., around 3 nm.^{28,29} In addition, it was found that in the core region there is an excess of copper above stoichiometry (see, e.g., Ref. 28). Thus it turns out that the cores of dislocation lines have a structure that resembles that of artificial defects introduced by irradiation with heavy ions of high energy; those defects act as exceedingly strong one-dimensional linear pinning centers. This has been shown convincingly in many studies (see, e.g., Refs. 30–32).

It remained to show whether a structure state providing a very high average dislocation density is formed in YBCO epitaxial films during their deposition and growth. It appears

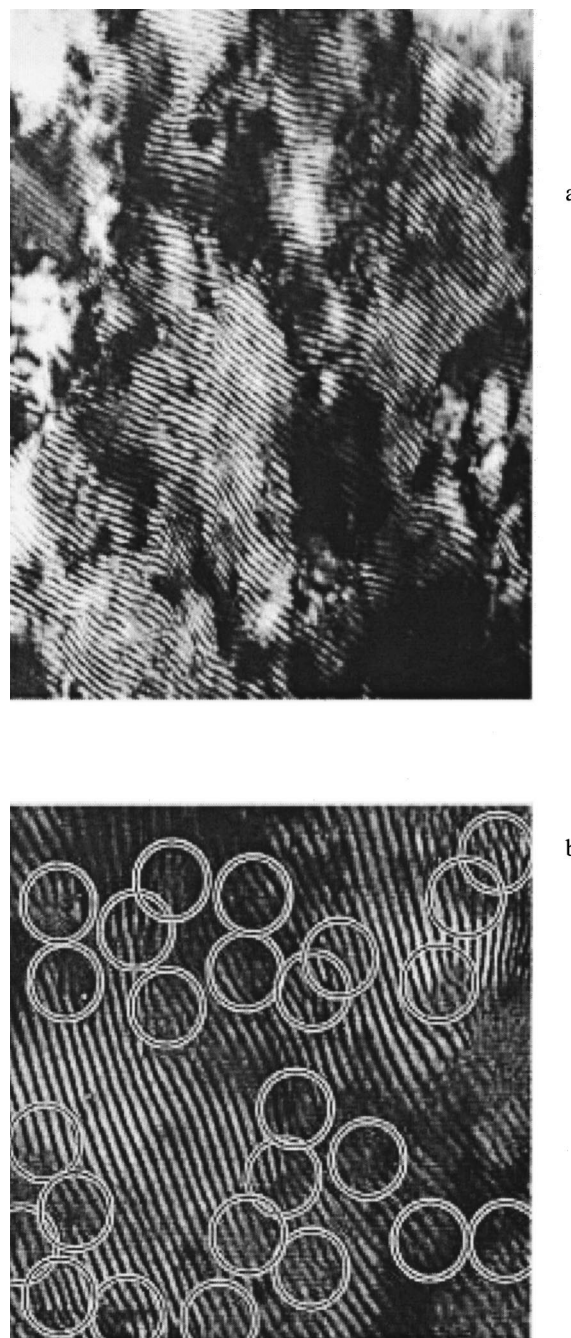


FIG. 3. a—Moiré pattern showing edge dislocations with the aid of a transmission electron microscope (TEM); the dislocation lines are perpendicular to the cuprate planes. The dislocations, which are additional crystallographic half planes in the structure are clearly revealed by the Moiré fringes, the distance between which is 2.2–2.3 nm.^{13,14,18,25,35} b—TEM Moiré pattern showing the distribution of edge dislocations (in a YBCO film 10–12 nm thick, deposited on a single-crystal MgO substrate); the dislocation lines are perpendicular to the ab plane. The arrangement of the dislocations corresponds to an averaged misorientation angle of 1.2° between neighboring domains (subgrains).^{13,14,18,25,35}

that our recent HRTEM results (some of which are shown in Fig. 3) unambiguously confirm the formation of such a dislocation structure in YBCO films exhibiting record values of $J_c(H)$. These results also make it possible to understand the mechanism of formation of linear defects during deposition and growth of the films. The problem of the formation of a dislocation substructure during epitaxial growth of films in general and YBCO films in particular goes beyond the scope

of the present paper, and for an introduction to this topic the reader is referred to the recent papers cited as Refs. 13, 14, 18, 20–25, 27–29, 33, and 34.

5. DYNAMICS OF VORTICES IN A YBCO SUPERCONDUCTOR WITH LINEAR PINNING CENTERS

It follows from the results of structural studies^{13,14,18,20–25,27–29} that the most interesting type of defects in YBCO thin epitaxial films and bicrystals in respect to their contribution to the pinning and dynamics of vortices are low-angle tilt dislocation boundaries. Of course, point defects (oxygen vacancies) distributed in a random manner, dislocation loops due to stacking faults and lying parallel to the ab plane, and $\{110\}$ microtwins are present in the films, and in certain cases make an appreciable contribution to the behavior of the vortices and to the magnetic-field dependence of the critical current density.

As we have said, recent transport measurements in combination with a scaling analysis provide substantial arguments in favor of the existence of a Bose glass phase in YBCO crystals and thin films irradiated by heavy ions at high energy (1 GeV and higher). The formation of a Bose glass phase is initiated by randomly distributed correlated extended defects—columnar tracks made by the heavy ions. However, as we have seen above, correlated linear defects in deposited YBCO thin films are actually distributed nonuniformly: they form more or less well-formed rows or walls of edge dislocation lines lying parallel to one another, with non-superconducting cores of transverse size $D \approx \xi_{ab}$. The dislocation walls frame domains of mosaicity, azimuthally misoriented by approximately 1° with respect to the neighboring domains. Inside the domains the dominant pinning defects are pointlike (oxygen vacancies). For such a spatial distribution of correlated linear pinning centers the Bose glass phase exists only at sufficiently low applied magnetic fields, for which $a_0 \propto (\Phi_0/H)^{1/2}$ remains much larger than the transverse domain size L_{domain} . When the magnetic field is increased to a certain critical value $H_{B \rightarrow F}$ there is a crossover to a distinctive new correlated glassy state, the “Fermi glass,” in which the vortices are located both in dislocation walls and in the interior of the domains. The vortices inside the domains interact with random point defects, and their behavior is therefore similar to that in single crystals.

At a certain value of the applied magnetic field the linear tension of the vortex “softens” as a result of dispersion of the elastic constant $C_{44}(\mathbf{k})$, and then the picture arises that is described below in an analysis of the concrete results of our recent experimental measurements of $J_c(H, T, \theta)$ for YBCO films (θ is the angle between the cuprate planes and the applied magnetic field H). For an idealized case, i.e., when the low-angle boundary is formed by a regular row of equally spaced edge dislocations parallel to one another and with no other disruptions of the crystalline order in neighboring subgrains (domains), one can use the model of vortex dynamics. For this case Kasatkin^{35–37} examined the transport of vortices along low-angle domain walls (or more precisely, bicrystal boundaries). In the framework of this model it was shown that despite the strong single-particle core pinning by lines of edge dislocations, the motion of the vortices occurs along the domain walls in accordance with the conventional

ideas.^{32,38,39} The model is actually completely adequate for treating the electrodynamics of bicrystals with this sort of tilt boundaries and with small values of the misorientation angle. The model does not require making any sort of assumptions as to the transmissivity for supercurrent or to Josephson properties of the bicrystals with such a tilt dislocation boundary, as must be made for the models proposed in Refs. 40–43. Most importantly, in the framework of the model one can consistently explain the strong dependence of the critical current J_c through the boundary on the misorientation angle θ between the adjacent domains (“banks” of the junction), as has been observed for YBCO bicrystals and films.^{35–37,44} In order to apply this model for describing polydomain mosaic films containing this sort of low-angle boundaries, one must take into account the additional effects in the motion of vortices in both the direction transverse to the domains and along the curved domain walls, with spatial variation of the misorientation and also of the distance between adjacent dislocations.

The model of vortex transport along a row of edge dislocations lying parallel to the c axis and forming, as we have said, a low-angle boundary between slightly misoriented subgrains (domains) is based on the above treatment of the pinning and dynamics of vortices in superconductors with extended linear (columnar) defects.^{11,32,35–38} It is important to note that collective effects were not taken into account, at least not in Refs. 35–37. According to the results of those papers, the depinning of vortices residing at linear pinning centers and their subsequent dynamics in the presence of transport current occur owing to the spontaneous formation of vortex excitations caused by thermal fluctuations in the volume of the superconductor. A vortex excitation has the form of a partially depinned vortex loop (Fig. 2). When the size of the depinned part of such a loop exceeds a certain critical value for a given superconducting transport current (see Refs. 35 and 36), the loop becomes unstable and begins to expand until it touches the neighboring linear defect. After that, the motion of the remaining part of the given vortex will occur through the motion of two vortex “steps” (kinks) moving apart in opposite directions along the c axis under the influence of the Lorentz force. The model of vortex motion along an equidistant row of mutually parallel dislocations can be extended to the case of a real polydomain (mosaic) structure of a film with a low-angle-boundary network formed by ensembles of edge dislocations, as appears to be the case in an actual image similar to that shown in Fig. 3. These dislocations are found in a more or less disordered state and are not equidistant, as was proposed above. Nevertheless, using a percolation approach, as was done by Gurevich in a treatment of flux creep,^{45,46} one expects that the low-angle boundaries will serve as percolation channels for the thermally activated motion of vortices. This is apparently the case, since the activation energy $U_c(D)$ for the transition of a vortex from one edge dislocation to a neighboring one [i.e., at a distance $D(\theta)$] is much less than the corresponding value U_{c0} for the traversal of a vortex across a domain. Thus the network of low-angle boundaries can be formed by a spatial landscape of U_c , in the more or less pronounced “valleys” of the vortex activation energy $U_c(r)$. Considering the thermally activated flux flow (TAFF) regime

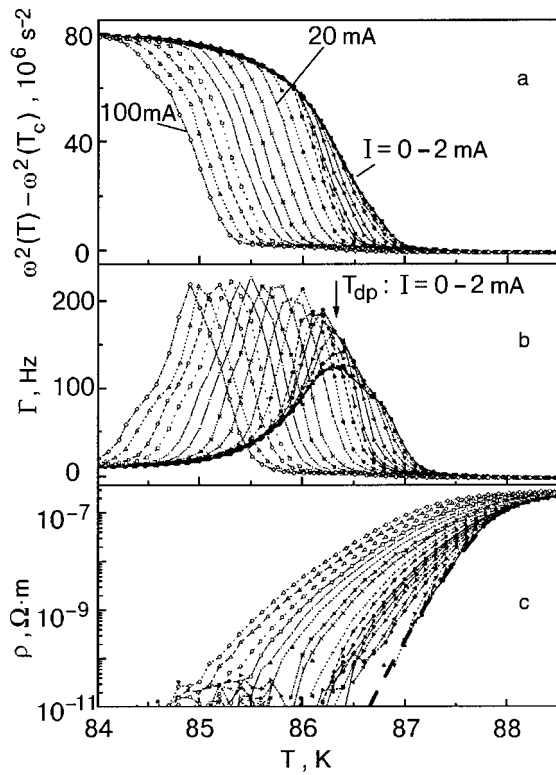


FIG. 4. Square of the resonance frequency (a), of the corresponding damping (b), and of the resistivity (c) as functions of temperature for different values of the transport current at a field $H=2$ T and $\theta=0^\circ$. The dashed curve in part (c) is an example of a resistivity curve rescaled by means of Eq. (2) to the diffusion constant, which was taken for calculation of the damping curve (see Fig. 5) according to Eq. (3).

of vortex motion along these percolation channels, one expects that the average distance between nearest dislocations is nevertheless related to the angle of misorientation of neighboring domains. Then at small values of the angle one has $\vartheta \langle U_c(D) \rangle \propto \langle (\sin \vartheta)^{-1} \rangle$, and, hence, the strong dependence $J_c(\vartheta)$ obtained for a straight row of equidistant dislocations will hold for the percolation situation with $\sin \vartheta$ replaced by its value averaged over the whole film.

A strong dependence $J_c(\vartheta)$ for polydomain epitaxial films of YBCO with low-angle boundaries was observed experimentally in Ref. 47.

5.1. Dynamic depinning of the vortex lattice in YBCO films

An extremely informative method for describing the behavior of the vortex ensemble in YBCO films in the dynamic regime utilizes a mechanical oscillator with a high Q factor under passage of a dc transport current. Such measurements have been done using miniature current and potential contacts on a vibrating YBCO film sample.⁴⁸ The technique permits making the following simultaneous measurements: 1) the change in the square of the resonance frequency, $\omega^2(B_a, T) - \omega^2(0, T)$, of a mechanical oscillator with a film sample of the HTSC YBCO attached to it, executing vibrational motion in a magnetic field, which yields information about the pinning force^{49,50} (Fig. 4a); 2) the damping Γ , which characterizes dissipative processes in the sample in connection with the motion of the vortices^{49,50} (Fig. 4b); 3) the resistivity of YBCO films (Fig. 4c). Using this technique we were able to study the dynamic behavior of vortices in

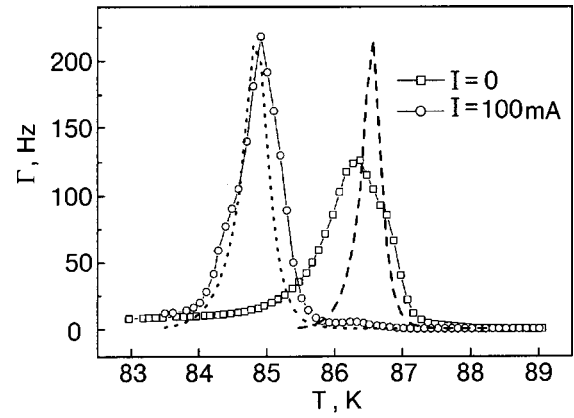


FIG. 5. Damping curves for $I=0$ and 100 mA at $H=2$ T. The dotted and dashed curves were calculated according to Eq. (3), following the procedure described in Refs. 48, 52, and 58.

YBCO films in the region of their depinning at angles $\theta=90^\circ$ (which is equivalent to a parallel orientation of the applied field relative to the cuprate planes), 75° , and 60° , with the transport current always flowing perpendicular to the applied field.

The dynamic behavior of the vortices in such an oscillator is well described by a *diffusion model* for the thermally activated vortices.⁵⁰ In this model the diffusion constant is given by

$$D = \mathcal{D}(H, T) = \rho(H, T) / \mu_0, \quad (2)$$

where ρ is the resistivity of flux flow. In the framework of this model, in accordance with Refs. 48, 51, and 52, the damping of the vibrating superconductor has the form

$$\Gamma = \frac{1}{2I_i \omega} \left(\frac{\mu_0 H^2}{2} \right) V_p \chi''(D), \quad (3)$$

where I_i is the effective moment of inertia of the oscillator, which can be found experimentally,⁴⁸ ω is the resonance frequency of the oscillator, V_p is the volume of the sample, and χ'' is the imaginary part of the ac susceptibility of the sample: χ'' as a function of temperature has a maximum $\chi''_{\max} = 0.41723$.⁵¹ This result is valid for any value of the transport current density J , i.e., χ''_{\max} is independent of the current load. Changing the diffusion parameter \mathcal{D} by the passage of current only shifts the position of the damping peak (e.g., on account of the dependence of the effective activation barrier U_p on the current), but it does not introduce any changes in its absolute value. It should be noted that the top of the damping peak determines the position of the depinning temperature T_{dp} or the irreversibility point.

If the measured value of the resistivity $\rho(T, H, J)$ is used for $\mathcal{D} = \rho / \mu_0$ according to the procedure described in Ref. 48, then it becomes possible to apply the theory quantitatively to the discussion of the experimental results, through the use of Eq. (3). Figure 5 shows the the calculated damping curves for two values of the current $I=0$ mA ($J=0$ A/m²) and $I=100$ mA ($J \approx 2 \times 10^8$ A/m²). The calculated temperature dependence for $\Gamma(I=100$ mA), its absolute value, and the width of the transition turn out to be in good agreement with experiment. Furthermore, it is clear that richer information about the depinning transition of the vortex lattice can

be obtained from the damping of a vibrating superconductor than from the value of the electric field induced by the motion of the vortex lattice. The broadening and asymmetry of the damping peak are evidence of a diverse character of the depinning of the vortex lattice.

Of course, from the present investigations it is difficult to reconstruct the microscopic picture of the dynamics of the moving vortices, but, considering the known results from observations of the motion of an almost ordered vortex lattice in superconducting crystals,⁵³ the results of theoretical papers on moving disordered vortex lattices,^{54,55} and the aforementioned complex “valley” spatial landscape of the pinning potential U_p in real YBCO superconducting films, we propose a scenario that will lead to the observed effects (Fig. 4b): 1) a narrowing and symmetrizing of the damping peak upon application of a current load; 2) a rise of the peak value of the damping for $J > 2 \times 10^6$ A/m². We note that at high values of the transport current density the height of the damping peak becomes independent of the current density, and only the position of the peak changes, shifting to lower temperatures with increasing current.

In the YBCO films under study there is a chaotic distribution of the pinning potential, the interaction with which leads to disordering of the vortex lattice. The situation becomes even more complicated when one takes into account that rather complex vortex configurations can arise for field orientations close to parallel with respect to the ab planes, when two mutually perpendicular vortex subsystems can coexist simultaneously in the superconducting films on account of the two components of the field vector penetrating into the film.^{56–58} Then for vortices parallel to the ab plane the majority of linear defects are dislocation loops distributed chaotically in the interior of the film. Their characteristic size is 5–7 nm, but then their pinning force hardly decreases with temperature because of the weak stress–strain fields near the core (see Sec. 7) and also because in this orientation the bending modulus C_{44} does not “soften” along the field, as it does in the case $H \parallel c$ on account of the anisotropy and layered nature of the atomic structure. In the case of vortices parallel to the c axis there exists a hierarchy of pinning centers, with a spatial distribution: 1) the strongest obstacles for the transverse motion of the vortices are close-packed dislocation walls with vortices already residing on them and with shielding currents flowing along these walls; 2) individual “standing” or “threading” dislocations, which are also strongly pinning if $H \parallel c$; 3) point defects inside the domains, which can rapidly decrease the net pinning force and current density, as follows from the arguments given above (see Sec. 3) and the experimental data presented below (Sec. 8).

The larger-scale topological defects existing in YBCO films, such as shaped (polygonized) domain dislocation walls, can lead to plastic flow of vortex rows but not to displacement of an elastically deformable vortex lattice. A mechanism for the motion of vortices along so-called “easy-slip channels” has been proposed previously (see, e.g., Ref. 59). However, this mechanism requires a small shear modulus C_{66} in the vortex lattice, and that ordinarily takes place in fields approaching H_{irr} . Thus the thermally activated depinning of the vortex lattice under the influence of a small driving force can occur near $H_{irr}(T)$ along “plastic flow

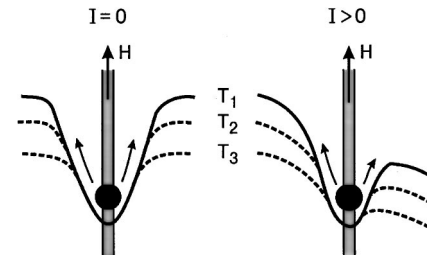


FIG. 6. Pinning potential with a vibrating vortex at different temperatures ($T_1 < T_2 < T_3$) during the passage of current and with no current.

valleys,” i.e., the easy-slip channels, when they are oriented parallel to the driving force (see also Ref. 60). This behavior, as we have said, can be treated as percolational.^{45,46} If the initial breakaway of the vortices when depinning is achieved is interpreted as vortex rows moving along “channels,” then one expects that the vortex lattice inside the domains remains pinned on account of the strong pinning on domain walls perpendicular to the driving force, i.e., it remains practically immobile at temperatures $T < T_{dp}$. As the temperature is raised, the observed damping peak at $T_{dp}(J=0)$ is indicative of depinning of strongly pinned regions. Under the influence of the aforementioned factors, this peak, which characterizes the depinning of the vortex lattice, becomes broad and asymmetric.

Phenomenologically, without specifying the type of pinning defects, one can describe the behavior of the damping peak of a vibrating sample at $J=0$ by introducing a distribution of the potential energy of the activation barriers. Such a distribution will lead to two main effects: broadening of the transition with respect to temperature, and, consequently, decreasing the height of the damping peak at the depinning temperature. Indeed, the use of a single-barrier approximation in the framework of the diffusion model leads to an unavoidable difference between theory and experiment, as is usually observed in practice.^{48,52}

One can give a simple picture in which the loading of the sample by current leads to tilting of the whole pinning potential⁶¹ and in which the depth of the potential is temperature dependent (Fig. 6). By scanning the pinning potential with the aid of low-amplitude mechanical vibrations of the superconducting sample, one can record the tiniest changes in the height of this well at very low transport currents. This effect is observed at current densities as low as $J < 10^6$ A/m². The decrease and shift of the high-temperature part of the transition (Fig. 4) indicates that the upper part of the potential distribution (high U_p) is shifted to lower values of U_p . It is possible that a decrease and shift to higher values of U_p occurs in the low-lying part of the U_p distribution (i.e., at lower temperatures). This effect can scarcely be observed by the technique used, since the flux bundles remain pinned by the highest potential barriers until the temperature becomes high enough to provoke depinning.

At large values of the driving force ($J \gg 10^6$ A/m²) the velocity of the vortices is expected to play the role of an order parameter. The observed motional narrowing of the damping peak upon increasing current loading (i.e., driving force) means that a new “instrument” for the ordering of the vortex lattice has appeared. We again note the explicit satu-

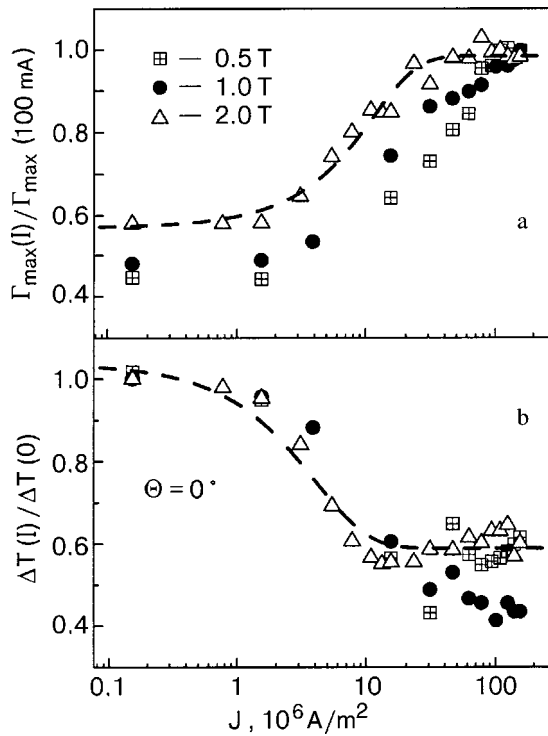


FIG. 7. Normalized damping peak (a) and the half-width of the damping peak (b) of a vibrating YBCO film as functions of the transport current density at different values of the external magnetic field. The dashed curves were calculated with the use of the function $a + b \tanh(J/c)$, where $a = 0.57$ (1.03), $b = 0.42$ (0.44), and $|c| = 15 \times 10^6$ (5.5×10^6) A/m^2 for the upper (lower) panel.

ration effect at high values of the transport current (Fig. 7). In terms of the picture of a distribution of effective potential barriers, this result indicates that the moving elastic vortex lattice becomes increasingly dominant over the pinning disorder and approaches a delta-function distribution of barriers. In other words, the thermally activated depinning behaves as if all the barriers have equal depth. It can also be assumed that the vortex lattice begins to behave like an elastically deformable continuum whose motion is insensitive to the individual pinning centers. An important circumstance is that the damping $\Gamma(T)$ of the vibrating film can be described quantitatively with the help of formula (3) without any free parameters by using the experimentally determined resistivity of the flux flow as the diffusion constant (2).

5.2. Vortex glass or depinning?

Simultaneous measurements of the resonance frequency and damping of a vibrating sample of a superconducting YBCO film together with the resistivity curves $\rho(T, J)$ (Fig. 4) permit a direct comparison of the so-called “glass temperature” T_g and the depinning temperature T_{dp} . Figure 8a shows the dependence of the resistivity on the transport current density. It is seen that the $\rho(J)$ curves are clearly separated into two groups by the dotted line $T_g = 86.35 \text{ K}$. Behavior of this type is often used as an argument in favor of the possibility of a “vortex glass” state.^{7,8,62} In other words, it is assumed that the vortex lattice undergoes a second-order phase transition to a “vortex glass” state at a temperature T_g .

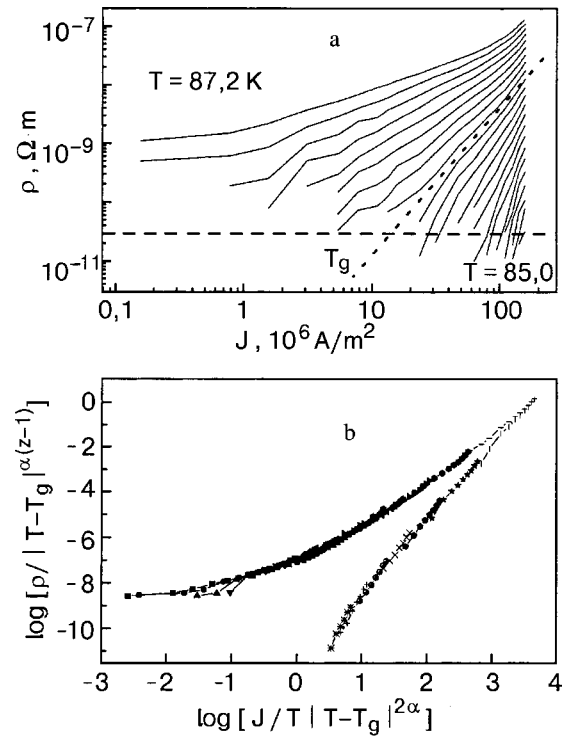


FIG. 8. a—Resistivity of a YBCO film versus the transport current density, measured at $H = 2 \text{ T}$ and various temperatures with a step of 0.1 K . The dotted line is the so-called “vortex glass” transition at a temperature $T_g = 86.35 \text{ K}$. b—Scaling behavior of the $\rho(J)$ curves as described in the text; here $z \approx 1.7$ and $\alpha = 4.7 \pm 1$.

The “vortex glass” model predicts that the typical scaling procedure can be applied to the $\rho(J)$ curves to give two groups of lines with different signs of the curvature. Indeed, the experimental curves can be subjected to a scaling analysis in the coordinates $\rho_{ab}/|T - T_g|^{\alpha(z-1)}$ versus $J/T |T - T_g|^{2\alpha}$, where $z = 1.7 \pm 0.15$ and $\alpha = 4.7 \pm 1$ (Fig. 8b). Both parameters agree with the values given in Refs. 63 and 64.

A particularly interesting fact that emerges from these measurements is that for $I = 0$ and angles $\theta = 90^\circ$, 75° , and 60° in magnetic fields of $0.5 \text{ T} \leq H \leq 2 \text{ T}$ the depinning temperature and the temperature of the proposed formation of the “vortex glass” coincide: $T_g \cong T_{\text{dp}}$. Since the behavior observed with the use of the mechanical oscillator can be described by a depinning transition in the framework of diffusion concepts, it is necessary to understand to what extent the result obtained from the scaling analysis can be taken as evidence of a second-order phase transition in the vortex lattice. In contrast to the experimentally proven melting of the vortex lattice, which has been observed in clean high-temperature superconductors by different techniques, the “vortex glass” transition is determined solely by means of the scaling analysis shown in Fig. 8b. One wonders whether the result of this scaling analysis can be described using a different model without invoking the concepts of a “vortex glass” and a phase transition of the vortex lattice into such a state.

Indeed, a serious alternative interpretation of the results of the scaling analysis of the experimental data is the percolation model of vortex motion proposed by a number of authors over the past few years.^{65–67} According to the percolation model, a superconductor found in the mixed state con-

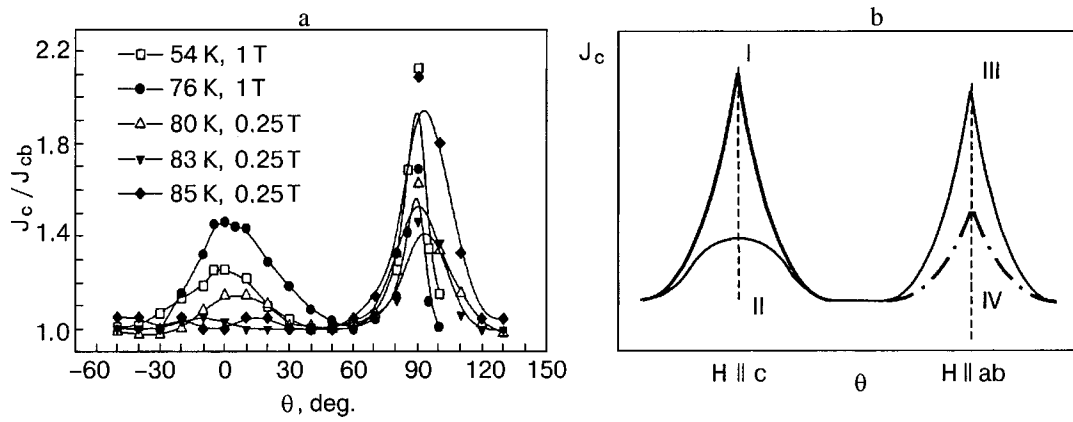


FIG. 9. a—Angle dependence of $J_c(H)$ measured by the four-probe transport method for YBCO films deposited by a pulsed laser technique on a LaAlO_3 substrate. b—Schematic representation of the angle dependence of $J_c(H)$ for the case when both dislocation ensembles perpendicular and parallel to the ab plane contribute to the two-peak curves: the contributions from linear defects (I), from the intersection of vortices with dislocations (II), from pinning centers lying in the ab plane (III), and from the anisotropy of H_{irr} (IV).

sists of percolation regions with different resistivities, which correspond to pinned and free (depinned) vortex lines. When the percolation threshold is reached there is a transition from the depinned state to a pinned state with an insignificant linear resistivity. In the framework of the percolation picture the disorder and the distribution of percolation regions also leads to a broader pinning transition. Consequently, the narrowing of the depinning transition when a current load is applied, as we have said, can be interpreted as a decrease of the disorder (or the pinning) of the vortex lattice as a result of its motion. In the “microscopic” picture of this process, the vortex lattice, as its velocity increases, ceases to “notice” the point and pointlike defects (e.g., the crossing of dislocation lines by vortices), through which a vortex passes in a very short time. There is insufficient time for the vortex to interact with them, since the pinning time is shorter than the

relaxation time of the vortex lattice (the increasing velocity the lattice becomes “stiffer”). On the whole, this process leads to an average viscosity η of the vortex lattice which is related to the diffusion constant as $D = \mu_0 H^2 / \eta$.

6. THE $J_c(H, T, \theta)$ CURVES FOR YBCO FILMS. RELATION TO THE CHARACTERISTIC ENSEMBLE OF LINEAR DEFECTS

Saemann-Ischenko⁶⁸ was the first to show that when the magnetic field vector is rotated with respect to the c axis (while maintaining constancy of the Lorentz force) in a biaxially textured epitaxial YBCO film the $J_c(H, T, \theta)$ curves have two characteristic peaks at $H \parallel c$ ($\theta = 0^\circ$) and $H \parallel ab$ ($\theta = 90^\circ$), which are shown in Fig. 9 (our data). The prop-

TABLE I. Properties, characteristics, and behavior of the $J_c(\theta)$ peaks.

Experimentally measured parameter	$J_c(\theta)$ peak for $H \parallel c$	$J_c(\theta)$ peak for $H \parallel ab$
1. Temperature change during measurements	Relative height grows with increasing T for 40–80 K, then the peak is suppressed for $T \rightarrow T_{\text{irr}}(H)$.	Relative height decreases with increasing T , but for $T \rightarrow T_{\text{irr}}(H)$ the peak becomes dominant.
2. Influence of the strength of the applied magnetic field	Practically vanishes in fields above 2–3 T.	The higher the field, the sharper the peak. For $T \rightarrow T_{\text{irr}}(H)$ only this peak remains.
3. Rate and method of deposition of the film	Low-rate off-axis magnetron sputtering tends to enhance the peak (e.g., for sapphire/ CeO_2 /YBCO films).	High-rate pulsed laser deposition substantially enhances this peak.
4. Effects of the substrate and buffer layers	The greater the misfit of the crystal lattices between the materials of the substrate, buffer layers(s), and YBCO film, the stronger the peak.	This peak is sharper and more significant if the misfit is small, as, e.g., for substrates of SrTiO_3 or LaAlO_3 .
5. Influence of deposition temperature of YBCO film	Height increases with increasing T (up to 745–750 °C) for sapphire/ CeO_2 /YBCO films.	Substantially suppressed with increasing T (up to 745–750 °C) in the case of sapphire/ CeO_2 /BCO films.
6. Effect of a change in thickness of the YBCO film	The thicker the YBCO film (at least on a LaAlO_3 substrate), the higher the peak.	Practically independent of the thickness of the YBCO film.
7. Effect of a change in the growth mode of the YBCO film	2D growth mode suppresses the peak and 3D mode enhances it.	3D growth mode leads to substantial suppression of the peak.

erties, characteristics, and behavior of the two peaks are described below and listed in Table I.

It can be seen from Table I that the relative height of these peaks depends on the conditions of measurement of the current–voltage characteristics and determination of the value of the critical current, specifically, on the temperature of the measurements, the applied magnetic field, and the value of the electric field E_c . Indeed, the $J_c(H)$ peak for $H\parallel c$ initially grows with increasing temperature approximately from 40 to 80 K and then, when the temperature approaches the line of irreversibility, the J_c peak is substantially suppressed and can even vanish in the case of YBCO films deposited by pulsed laser sputtering on LaAlO_3 substrates. On the contrary, the $J_c(H)$ peak for $H\parallel ab$ survives at all temperatures, magnetic fields, and velocities of the vortex lattice under the influence of the Lorentz force.

As is now known from the high-resolution electron microscopy data, there are several types of dislocation ensembles that can form in YBCO films during their growth:

1. Misfit edge dislocations at the boundary due to the usual mismatch of the interatomic spacings in the crystal lattices of the substrate and growing film.

2. Dislocation loops due to the existence of stacking faults (i.e., the local appearance of “extra” or “missing” segments of CuO_2 planes, usually up to 10 nm in size, during growth); these are edge dislocations, the dislocation lines being parallel to the ab plane.⁶⁹

3. “Threading” edge dislocations, whose dislocation lines, being parallel to the c axis and perpendicular to the surface of the film, as a result of the polygonization process partially or completely form low-angle tilt boundaries of domains of azimuthal mosaicity in the film. The average density of such dislocation lines can reach 10^{11} lines/cm² and even higher.^{13,14,18,23–25,31} These dislocations are formed mainly as a result of the realization of a two-dimensional heteroepitaxial growth mode in which a so-called “rotational” relaxation of the misfit at the boundary occurs. In particular, this mechanism can be enhanced further on account of specific growth conditions, e.g., as a consequence of their rotational misfit on the R plane of sapphire and the (001) plane of CeO_2 (for details see, e.g., Refs. 70 and 71).

4. Screw dislocations at the boundary in low-angle twist boundaries, which are a source of screw dislocations in the low-angle domain walls, making them increasingly more complex tilt–rotational boundaries the higher the degree of mismatch of the crystal lattices at the boundary. Screw dislocation sources emerging on the surface of the film at higher deposition temperatures (above 740 °C for YBCO) can initiate a three-dimensional growth mechanism with the formation of polygonal spirals.^{20,25,35,72}

Analysis of the data obtained as a result of measurements of the angle dependence of $J_c(H)$ for a large number of perfect biaxially textured YBCO films with high $J_c(H)$ shows convincingly that the maxima of the critical current and hence the orientation of the dislocation ensemble correspond to two directions: parallel to the c axis, and parallel to the ab plane. This conclusion is equivalent to the assumption that the effective pinning of vortices in YBCO films is due to extended linear defects oriented along the given directions, i.e., dislocation ensembles **a** [100] and dislocations and loops

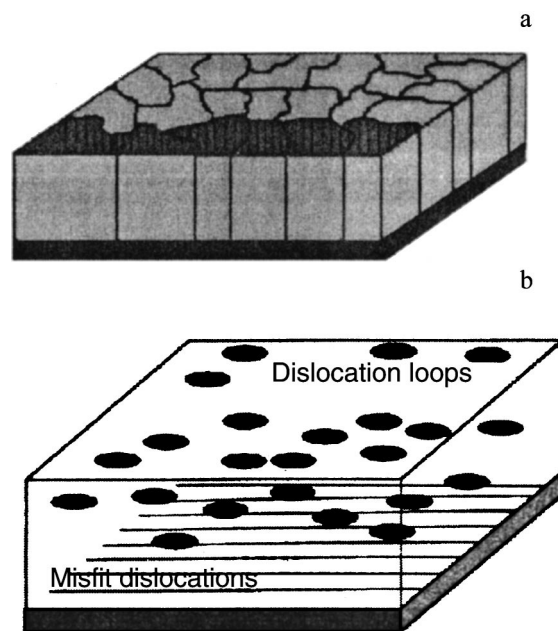


FIG. 10. Schematic illustrations of ensembles of edge dislocations, which are formed in YBCO films during growth in different modes: a—ensembles of “threading” dislocations perpendicular to the cuprate planes and lying in low-angle tilt domain boundaries (substrate with large misfit (MgO , YSZ , sapphire+ CeO_2)); b—ensembles of dislocations parallel to the cuprate planes and consisting of misfit dislocations at the boundaries and dislocation loops induced by local stacking faults (substrate with small misfit (SrTiO_3 , LaAlO_3)).

lying in the ab plane. It is important to note that these latter dislocations and loops also contribute to the maximum $J_c(H\parallel c)$, since, as was first shown in Ref. 73 and then confirmed by the present authors in Refs. 12–14, 74, and 75, when the vortices are parallel to the c axis they can interact with transverse dislocation lines as with pointlike defects. Then the function $J_c(H, \theta)$ has a domelike character of the type $J_c(\theta) \propto (\cos \theta)^{1/2}$. It can also be assumed that some contribution to the volume pinning force is made by point defects such as oxygen vacancies. At the peak $J_c(H\parallel c)$ the two contributions from point and quasi-point pinning centers create the pedestal that vanishes as the line of irreversibility is approached, i.e., for $T \rightarrow T_{\text{irr}}(H)$, as the magnetic field is increased, and as the velocity of the vortices (i.e., the dimensionless number E_c) increases.^{12–14,18} As to the peak $J_c(H\parallel ab)$, since it survives at all temperatures, fields, and velocities of the vortex lattice, we may assume that it is due to dislocation pinning on dislocations and loops lying in the ab plane and also to anisotropy of $H_{\text{irr}}(T)$. As was discussed above, anisotropy of $H_{\text{irr}}(T)$ leads to anisotropy of the resistivity due to the motion of the vortex lattice under the influence of the Lorentz force. This means that at a given value of E_c the value of J_c determined from the current–voltage characteristics for $H\parallel ab$ and $H\parallel c$ will be substantially different.

Thus, in considering the behavior of YBCO films one should keep in mind that there are two ensembles of edge dislocations: 1) with dislocation lines along the c axis, and 2) in the ab plane. This was confirmed in our recent papers^{74–77} by means of transmission and high-resolution electron microscopy and also by electronic transport measurements of the angle dependence of the critical current density in a magnetic field. Such measurements have also been made by other

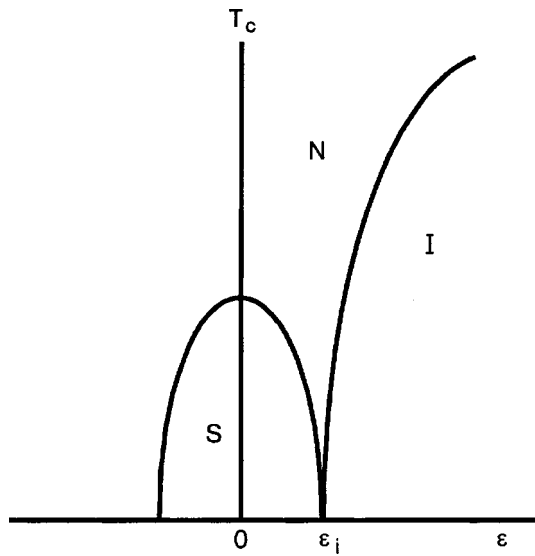


FIG. 11. Schematic phase diagram of an anisotropic metal-oxide cuprate of the YBCO type with a high T_c . This diagram was obtained by Gurevich and Pashitskii⁸² from the well-known $T_c(x)$ phase diagram, where x is the doping level, with the use of Eq. (4).

groups.^{68,78} For a clearer and more convincing demonstration of the real nonuniform distribution of dislocation ensembles in YBCO films prepared under different conditions of nucleation and growth and by different growth mechanisms, in Fig. 10 we show schematic illustrations of the fine structure of the films: with a set of mosaic domains differing from one another by low-angle tilt dislocation boundaries (a typical misorientation angle of around $1-2^\circ$, typical domain size of 20–50 nm, average distance between dislocations in the boundary 10–20 nm, and average dislocation density around 10^{11} lines/cm² (Fig. 10a); with misfit dislocations at the boundary and dislocation loops due to stacking faults, i.e., with extra or missing segments of the copper–oxygen layers of the CuO₂ type,⁶⁹ with the dislocation lines lying in the ab plane and an extremely high average dislocation density (Fig. 10b). It is surprising that in YBCO films such a dislocation structure with a high density can coexist with a very high degree of perfection of the crystal structure, as characterized by transmission and high-resolution electron microscopy^{23–25,27–29} and x-ray diffractometry.⁷⁴ However, the most reliable tool for experimental observation of these two different dislocation ensembles is measurement of the angle dependence of $J_c(H, \theta)$ at a constant value of the Lorentz force^{74–77} (see Fig. 9).

7. ELASTIC STRAIN FIELDS IN THE NEIGHBORHOOD OF LINEAR DEFECTS AND THE FEATURES OF THE PINNING POTENTIAL IN YBCO FILMS

It has been shown experimentally^{79–81} that layered anisotropic HTSC metal-oxide cuprates have an anomalously strong anisotropic dependence of the critical temperature T_c on the pressure in the case of uniaxial compression. For example,⁸⁰ for the optimally doped YBa₂Cu₃O_{7- δ} single crystal the derivatives $\partial T_c / \partial P_i$ measured along the principal crystallographic axes are: $\partial T_c / \partial P_a \approx -(1.9-2)$ K/GPa, $\partial T_c / \partial P_b \approx (1.9-2.2)$ K/GPa, and $\partial T_c / \partial P_c \approx -(0-0.3)$ K/GPa. This means that the pressure dependence $T_c(P)$ for

an isotropically, hydrostatically compressed crystal is very weak. However, in regions of the crystal with a local anisotropic deformation the changes of T_c can be significant. In the linear approximation this dependence can be written as

$$T_c(\mathbf{r}) = T_{c0} - C_{ik}\varepsilon_{ik}(\mathbf{r}). \quad (4)$$

Here T_{c0} is the critical temperature of the undeformed crystal, ε_{ik} is the strain tensor, and the coefficients $C_{ik} = -\partial T_c / \partial \varepsilon_{ik}$ are related to the derivatives $\partial T_c / \partial P_a$ (Fig. 11). According to Refs. 79 and 81, the diagonal coefficients C_{ii} in the ab basal plane of the crystal are $C_a = -\partial T_c / \partial \varepsilon_{aa} \approx -220$ K, $C_b = \partial T_c / \partial \varepsilon_{bb} \approx 320$ K, and $\partial T_c / \partial \varepsilon_{cc} \approx 0$.

Based on the experimental data,^{79–81} a theoretical calculation by Gurevich and Pashitskii⁸² showed that the elastic deformations created by a single edge dislocation or a dislocation ensemble (e.g., a “wall” of dislocations) in an anisotropic crystal can cause a local elevation or depression of T_c and can even suppress the superconducting state completely at a given temperature (e.g., at 77 K). Consequently, the region of the normal (nonsuperconducting) phase should exist around a dislocation core, which, as described above in accordance with the data of Refs. 28 and 29, is (for a “threading” edge dislocation \mathbf{a} [100]) a cylindrical channel of highly plastically deformed medium with a diameter of around 2 nm. The normal regions surrounding the core should also play an important role in the formation of the pinning potential of the superconductor. Therefore it is necessary to examine in more detail the deformation mechanism of suppression of superconductivity in the neighborhood of a dislocation core, i.e., of the effect of an elastic strain field in the anisotropic crystal YBa₂Cu₃O_{7- δ} .

An edge dislocation perpendicular to the ab plane gives rise to elastic strains in the ab plane and to corresponding local changes in T_c . Under certain conditions, if the Burgers vector \mathbf{B} is directed at an angle ϑ to either the a or b axis, the change of T_c is given by the expression

$$\delta T_c = -C[\varepsilon + \beta(\varepsilon_{xx} - \varepsilon_{yy})\cos 2\vartheta + 2\beta\varepsilon_{xy}\sin 2\vartheta], \quad (5)$$

where

$$\varepsilon = \varepsilon_{xx} + \varepsilon_{yy}; C = \frac{C_a + C_b}{2}; \beta = \frac{C_a - C_b}{C_a + C_b}. \quad (6)$$

Using the well-known⁸³ components of the strain tensor ε_{ik} under the condition $\mathbf{B} \parallel \mathbf{a}$, Pashitskii⁷⁴ obtained an expression for the variation of the critical temperature in cylindrical coordinates:

$$\delta T_c(r, \varphi) = -\frac{CB}{2\pi(1-\sigma)} \frac{\sin \varphi}{2} [(1-2\sigma) + 2\beta \cos^2 \varphi]. \quad (7)$$

Here φ is the azimuthal angle in the ab plane, measured from the a or b axis, $\sigma \approx 0.28$ is Poisson’s ratio,⁸⁴ and B is the modulus of the Burgers vector, which is approximately equal to the lattice constant $a \approx 0.4$ nm in the ab plane. Thus Pashitskii⁷⁴ determined the boundary of the region of the normal phase around a dislocation core, i.e., the region in which the local value of T_c is lower than the characteristic average level:

$$r_N(\varphi, T) = R_0(T) \sin \varphi [1 + \beta_0 \cos^2 \varphi] \geq 0, \quad (8)$$

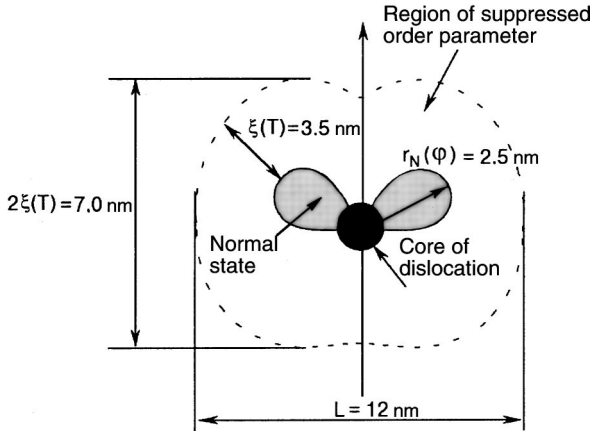


FIG. 12. Shape and size of the region of the normal state at 77 K, and also the region partially suppressed superconducting order parameter in the neighborhood of a dislocation core for a “threading” dislocation whose dislocation line is perpendicular to the *ab* plane of the YBCO crystal; calculated by Pashitskii⁷⁴ with the use of Eqs. (4), (7), and (8).

where

$$R_0(T) = \frac{CB(1-2\sigma)}{2\pi(1-\sigma)T_{c0}\tau}, \quad \tau = 1 - \frac{T}{T_{c0}}, \quad \beta_0 = \frac{2\beta}{1-2\sigma}. \quad (9)$$

For $T_{c0} = 90$ K and for the values of the coefficients $C_{a,b}$ mentioned above, the parameter $R_0(T) \approx 0.042/\tau(\text{nm})$, and $\beta_0 \approx -24$. At $T = 77$ K we have $R_0 \approx 0.3$ nm and the maximum of r_N occurs in the direction $\varphi = -\pi/4$ and has the value $r_{N \max} \approx 2.5$ nm (Fig. 12).

If now we take into account the proximity effect, then it becomes clear that the region with a suppressed superconducting order parameter extends in all directions to a distance of the order of the coherence length $\xi(T) = \xi_0/\tau^{1/2}$ (where $\xi_0 \approx 1.3$ nm is the coherence length at $T = 0$).

At 77 K we have $\xi(T) \approx 3.5$ nm, and the maximum width of the normal region is $L(T) = 2[r_{N \max} + \xi(T)] \geq 12$ nm. The area of the region of suppressed order parameter per dislocation parallel to the *c* axis can be estimated as $S_N(T) \approx 2\xi(T)L(T) \approx 8 \times 10^{-13}$ cm² at 77 K. This means that at a concentration of edge dislocations of around 10^{11} lines/cm² the fraction of the normal phase is approximately equal to 10%. Each component of the function $L(T)$ increases at a different rate as $T \rightarrow T_{c0}$: $r_N(T) \propto \tau^{-1}$, and $\xi(T) \propto \tau^{-1/2}$. Consequently, the width and shape of the pinning potential well change with increasing temperature faster than τ^{-1} , the dependence approaching $\tau^{-3/2}$ as $T \rightarrow T_{c0}$. Although a detailed analysis of the consequences of this situation goes beyond the scope of this paper, there are sufficient grounds for assuming that the pinning force arising in the interaction of vortices with dislocations of this ensemble should decrease appreciably with increasing temperature, as is observed in the measurement of the temperature dependence of $J_c(H\parallel c)$ (Fig. 13).

We conclude this Section by noting that the anisotropy parameter β_0 in Eq. (8) for dislocation lines parallel to the *ab* plane is smaller by many times than that for perpendicular “threading” dislocations, because of the negligibly small value of C_c . In this case $\beta = 2/(1-2\sigma) \approx 4.5$. Thus one can assume that the dislocations and dislocation loops lying par-

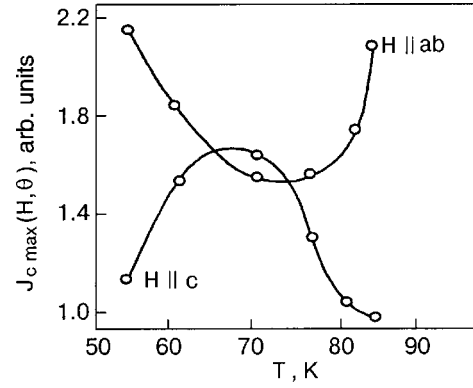


FIG. 13. Temperature dependence of the height of the $J_c(H, \theta)$ peaks for orientations of the magnetic field $H\parallel c$ and $H\parallel ab$, shown in relative units in relation to the position of the pedestal (or “background”).

allel to the *ab* plane, unlike the perpendicular ones, have insignificant strain fields in the neighborhood of the core. This means that the corresponding pinning potential wells are much narrower and steeper. The elementary pinning force for these dislocations is larger. In addition, their shape is apparently weakly dependent on temperature, and hence the pinning force is independent of temperature, as is confirmed in experiment (Fig. 13). The opposite forms of the temperature dependence of the relative height of the J_c peaks for $H\parallel ab$ and $H\parallel c$ is evidently due in large measure to the fact that the pinning potential wells have a different shape and different temperature behavior: steeper slopes and weak temperature dependence for $H\parallel ab$, and more gradual slopes and strong temperature dependence for $H\parallel c$.

8. MAGNETIC FIELD DEPENDENCE OF $J_c(H)$ AND THE $H-T$ PHASE DIAGRAM FOR AN ISOTROPIC HTSC WITH LINEAR DEFECTS FOR $H\parallel c$

The typical $J_c(H)$ curves of YBCO films for $H\parallel c$, as was shown in Refs. 74–77, 85, and 86 have three different segments (Fig. 14). The low-field part is a plateau or a weakly field-dependent part up to the point $H = H_A$, which corresponds to $a_0 \approx (\Phi_0/H_A)^{1/2} \approx \lambda_L$ (~ 0.1 T at 77 K), where the position of the points H_A must be determined as the intersection of the horizontal part of the curve $J_c(H) \approx \text{const}$ with the extrapolated part $J_c \propto H^{-0.5}$, but on our curves (Fig. 14) this cannot always be done because of the lack of measurements in sufficiently low fields. Undoubtedly

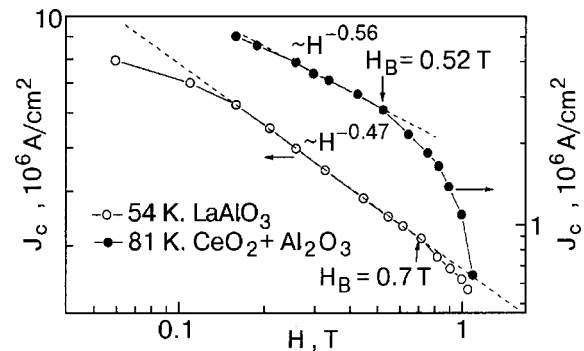


FIG. 14. Magnetic-field dependence for biaxially oriented epitaxial YBCO films for $H\parallel c$.

here we are dealing with a regime of individual or single-particle pinning, in which the vortices are far apart and non-interacting, and a vortex lattice is not formed. This effect was also mentioned in Refs. 85 and 86, but the authors explained it as a transition through a so-called “matching” field $H = H_\Phi$, at which the density of vortices becomes equal to the density of linear pinning defects parallel to them. This is clearly incorrect for two reasons: first the authors of Refs. 85 and 86 incorrectly determined the density of defects from the etch pits, obtaining a value too low by one or two orders of magnitude (10^8 – 10^9 lines/cm² instead of the actual 10^{10} – 10^{11} lines/cm², as is shown in Refs. 23–25); second, as the “matching” field is approached in YBCO, it is known⁸⁷ that $J_c(H\parallel c)$ increases rather than remaining constant.

The intermediate part of the field dependence of $J_c(H\parallel c)$ turns out to be practically linear on a log–log scale: $J_c \propto H^{-q}$, where the exponent q is close to 0.5. Such a dependence can be the result of the presence of a two-dimensional correlated “quenched” disorder in the vortex lattice, apparently of the Bose glass type, in this interval of fields ($H_A < H < H_B$). At higher fields ($H > H_B$) the $J_c(H)$ curve begins to decrease faster, viz., as H^{-q} with $q = 1.0$ – 1.5 .

A tentative explanation for this is that the vortex lattice begins to interact with random pointlike defects as well. Indeed, at the crossover field H_B the intervortex distance $a_0 \approx (\Phi_0/H_B)^{1/2}$ becomes comparable to the transverse size L_d of the domains of mosaicity, which are slightly misoriented with respect to one another and are separated by low-angle dislocation boundaries. This is the most important point in this treatment, since at low fields ($H_A < H < H_B$) the vortex lattice “perceives” the network of threading dislocations as a random, chaotic system which induces a quasi-two-dimensional correlated state of the vortex lattice of the Bose glass type with a high value of the bending modulus C_{44} . When the field increases to H_B , some of the vortices no longer have a chance to become pinned on the dislocation lines in the low-angle boundaries, since the benefit in terms of the pinning energy would be much smaller than the energy cost due to the 2D deformation of the vortex lattice. As a result, a significant number of vortices are inside the domains, being only weakly pinned by pointlike defects. Since the magnetic field in this case is already quite high, one expects that a substantial change in behavior will occur, much as in the case of single crystals. Thus one expects an intradomain crossover from 2D to 3D behavior of the vortex lattice due to wave-vector dispersion of the bending modulus $C_{44}(\mathbf{k})$ of the vortex lattice, which is interacting with a random pointlike pinning potential. However, because of this the phenomena that occur are radically different from that which occurs in a single crystal. In a single crystal the vortices, by “softening,” more easily adjust to the chaotically distributed point centers, and the resulting bulk pinning force increases, and $J_c(H)$ also increases from 10^8 to 5×10^8 A/m² (Refs. 12–18). In this case the vortices are pinned (while $H \leq H_B$) on linear defects, and $J_c(H) = 5 \times 10^9$ – 10^{10} A/m². Therefore, when some vortices are found inside the domains and become unstable to lateral deformations owing to the sharp decrease of their effective linear tension, $J_c(H)$ does not increase but instead begins to fall.

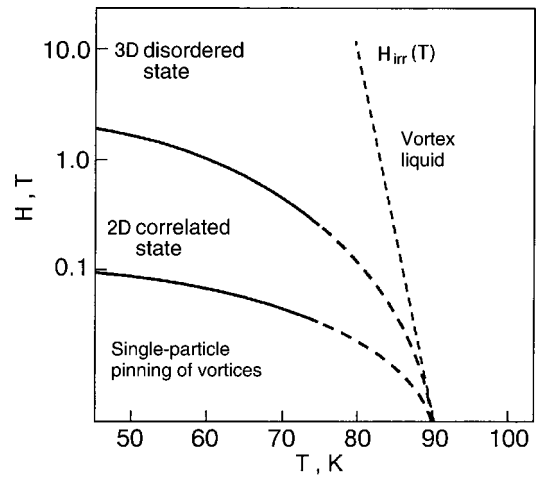


FIG. 15. Proposed H – T phase diagram of the vortex matter in a YBCO epitaxial film for $H\parallel c$.

This crossover in the behavior of the vortex system can be classified as a manifestation of a change in dimensionality in the nonuniform ensemble. We denote the nonuniform state of the vortex ensemble, interacting with the 2D pinning potential parallel to equidistant linear centers forming a polygonal 2D lattice (if the field is applied parallel to the c axis),^{74–77} as a correlated inhomogeneous Bose glass (CIBG). This state differs substantially from the usual state of a triangular vortex lattice and a random Bose glass, in which the linear pinning centers are distributed chaotically. The CIBG state (which is realized for $H_A < H < H_B$) also differs from the nonuniform state of the vortex lattice formed for $H > H_B$, where the vortices interact with both linear and planar defects. The latter can be called a Fermi glass, since the relation between the number of vortices resident on dislocations and the number of vortices inside the domains can be found by introducing a distribution of the Fermi type, much as was done by Gurevich.^{45,46} Figure 15 shows the proposed H – T phase diagram of the states of the vortex lattice in a YBCO film for a magnetic field direction $H\parallel c$.

CONCLUSIONS

—Several type of dislocations and dislocation ensembles are formed in YBCO films during their growth: 1) edge dislocations of nonregistry at the boundary; 2) dislocation loops due to stacking faults (i.e., with extra or missing segments of the CuO_2 planes), the lines of which are parallel to the ab plane; 3) edge dislocations in low-angle boundaries of mosaic domains with a density of up to 10^{11} lines/cm² and higher.

—The efficient pinning of vortices and high critical current densities ($J_c \geq 3 \times 10^{10}$ A/m² at 77 K) in epitaxial YBCO films are due to the high density of linear defects formed in the process of nucleation and growth of the film.

—The “motional narrowing” of the damping peak is indicative of ordering of the vortex lattice upon the passage of current. The remarkable agreement between the measured damping peak and the theoretical curve obtained in the framework of the diffusion model attests to preservation of a

gradual transition (*the absence of sharp phase transformations*) upon the depinning of the vortices in systems with strong disorder.

—The “*vortex glass*” transition temperature obtained by means of scaling of the resistivity coincides with the depinning temperature measured at zero current, indicating that the interpretation of this transition is ambiguous and might be explained in terms of a model of vortex depinning.

—Linear defects oriented along the c axis, i.e., dislocation ensembles \mathbf{a} [100], are the reason for the appearance of the $J_c(H\parallel c)$ peak, while dislocations and loops lying in the ab plane contribute to the peak $J_c(H\parallel ab)$ and also to the peak $J_c(H\parallel c)$ as a result of the interaction of vortices with transverse dislocation lines as with pointlike defects.

—Opposite temperature behavior of the peaks of $J_c(H, \theta)$ for $H\parallel c$ and $H\parallel ab$ is found experimentally. The peak $J_c(H\parallel c)$ initially grows with increasing temperature and then is suppressed when T approaches $T_{\text{irr}}(H)$. In contrast, the relative height of the peak $J_c(H\parallel ab)$ becomes larger and larger as the temperature increases. This behavior is due to the different temperature dependence of the different contributions to $J_c(H\parallel c)$ and $J_c(H\parallel ab)$: pinning on dislocations, pinning on pointlike defects, and the effect of the anisotropy of the strain fields near the dislocation cores.

—In the neighborhood of the cores of edge dislocations whose lines are parallel to the c axis a strain field arises which plays an important role in the formation of the pinning potential and the local suppression of the superconducting order parameter and T_c . For $T < T_c$ this will give rise to anisotropic regions of the normal phase near the dislocation core.

—In the neighborhood of dislocation lines parallel to the ab plane no appreciable strain fields appear. It can be assumed that this is the cause of the opposite behavior of the pinning force and critical current density in the case $J_c(H\parallel ab)$.

—The measured $J_c(H)$ curves for $H\parallel c$ in YBCO films demonstrate two clear crossovers, corresponding to transitions from $J_c(H) \sim \text{const}$ at low fields, in which the vortex lattice has not yet formed and the interaction of vortices with linear centers occurs in the regime of individual pinning, to $J_c \propto H^{-0.5}$ at intermediate fields (the motion of the vortex lattice as a deformable 2D continuum) and, finally, to $J_c \propto H^{-q}$ (where $q \sim 1-1.5$) at higher fields.

—The inhomogeneous state of a vortex ensemble interacting with an ensemble of parallel equidistant linear centers which are arranged in a network substantially differs from the state of a random 2D Bose glass.

This study was done with the support of the State fund for Basic Research of the Ministry of Education and Science of Ukraine, project No. 2–4/349 (contract No. F4/147–97), the International Program for Support of Science and Education (ISSEP), grants SPU 062044 and SPU 072046, the international association INTAS, grant No. 99-00585, the Federal Ministry of Education, Science, Research, and Technology of Germany (BMBF FKZ TRANSFORM), grant 13 N 7218/7 through the Institute of Experimental Physics II of the University of Leipzig, and also the Department of Energy of the USA through Brookhaven National Laboratory, contract No. 851924. The authors express their pro-

found gratitude to their colleagues and friends E. A. Pashitskii, A. L. Kasatkin, V. F. Solov'ev, V. L. Svechnikov, V. S. Flis, V. A. Komashko, H. W. Zandbergen, G. W. Crabtree, P. Esquinazi, C. L. Snead, M. Suenaga, and M. Lorenz, who all contributed immeasurably to the development of this paper. The authors are grateful to T. H. Geballe, J. R. Clem, E. H. Brandt, D. Dew-Hughes, D. Larbalestier, H. Küpfer, and A. A. Zhukov for helpful discussions.

*E-mail: pan@imp.kiev.ua

**E-mail: pan@uow.edu.au

- ¹L. V. Shubnikov, V. I. Khotkevich, Yu. D. Shepelev, and Yu. N. Ryabinin, *Zh. Éksp. Teor. Fiz.* **7**, 221 (1937).
- ²A. A. Abrikosov, *Zh. Éksp. Teor. Fiz.* **32**, 1442 (1957) [*Sov. Phys. JETP* **5**, 1174 (1957)].
- ³V. V. Shmidt, *Introduction to the Physics of Superconductors* [in Russian], Nauka, Moscow (1982), p. 240.
- ⁴U. Essman and H. Träuble, *Phys. Lett. A* **24**, 526 (1967).
- ⁵V. Vinokur, B. Khaykovich, E. Zeldov, M. Konezykowski, R. A. Doyle, and P. H. Kes, *Physica C* **295**, 209 (1998).
- ⁶G. Blatter, M. V. Feigel'man, V. B. Geshkenbein, A. I. Larkin, and V. M. Vinokur, *Rev. Mod. Phys.* **66**, 1125 (1994).
- ⁷M. P. A. Fisher, *Phys. Rev. Lett.* **62**, 1415 (1989).
- ⁸D. S. Fisher, M. P. A. Fisher, and D. A. Huse, *Phys. Rev. B* **43**, 130 (1991).
- ⁹A. E. Koshelev and V. M. Vinokur, Preprint cond-mat/9801144 (January 14, 1998).
- ¹⁰G. W. Crabtree and D. R. Nelson, *Phys. Today* **50**, 38 (1997).
- ¹¹D. R. Nelson and V. M. Vinokur, *Phys. Rev. B* **48**, 13060 (1993).
- ¹²V. F. Solovjov, V. M. Pan, and H. C. Freyhardt, *Phys. Rev. B* **50**, 13724 (1994).
- ¹³V. M. Pan, V. F. Solovjov, A. L. Kasatkin *et al.*, in *Physics and Materials Science of High Temperature Superconductivity IV*, Vol. 26 of NATO ASI Series, edited by R. Kossowsky *et al.*, Kluwer Academic Publ., Dordrecht, Boston, London (1997), p. 3.
- ¹⁴V. M. Pan, in *Physics and Materials Science of Vortex States, Flux Pinning and Dynamics*, Vol. 356 of NATO ASI Series, edited by R. Kossowsky *et al.*, Kluwer Academic Publ., Dordrecht, Boston, London (1999), p. 1.
- ¹⁵V. M. Pan, V. F. Solovjov, and H. C. Freyhardt, in *Advances in Cryogenic Engineering, Materials*, Vol. 42, edited by L. T. Summers, Plenum Press, New York (1997), p. 663.
- ¹⁶V. M. Pan, V. F. Solovjov, and H. C. Freyhardt, *Physica C* **279**, 18 (1997).
- ¹⁷V. M. Pan, V. F. Solovjov, and H. C. Freyhardt, *Czech. J. Phys.* **46**, 1643 (1996).
- ¹⁸V. M. Pan, *Usp. Fiz. Met.* **1**, 49 (2000).
- ¹⁹T. Hwa, D. R. Nelson, and V. M. Vinokur, *Phys. Rev. B* **48**, 1167 (1993).
- ²⁰J. Mannhart, D. Anselmetti, J. G. Bednorz *et al.*, *Semicond. Sci. Technol.* **5**, 125 (1992).
- ²¹D. G. Schlom, D. Anselmetti, J. G. Bednorz *et al.*, *Z. Phys. B: Condens. Matter* **86**, 163 (1992).
- ²²V. L. Svetchnikov, *Met. Phys. Adv. Tech.* (2001), in press.
- ²³S. K. Streiffer, B. M. Lairson, C. B. Eom *et al.*, *Phys. Rev. B* **43**, 13007 (1991).
- ²⁴S. J. Pennycook, M. F. Chisholm, D. E. Jensen *et al.*, *Physica C* **202**, 1 (1992).
- ²⁵V. Svetchnikov, V. Pan, Ch. Traeholt, and H. Zandbergen, *IEEE Trans. Appl. Supercond.* **AS-7**, 1396 (1997).
- ²⁶V. Narlikar and D. Dew-Hughes, *Phys. Status Solidi* **6**, 383 (1964).
- ²⁷M. F. Chisholm and D. A. Smith, *Philos. Mag. A* **59**, 181 (1989).
- ²⁸Y. Gao, K. L. Merkle, G. Bai, H. L. M. Chang, and D. J. Lam, *Physica C* **174**, 1 (1991).
- ²⁹K. Merkle, *Interface Sci.* **2**, 311 (1995).
- ³⁰V. Hardy, J. Provost, D. Groult *et al.*, *J. Alloys Compd.* **195**, 395 (1993).
- ³¹S.-W. Chan, *J. Phys. Chem. Solids* **55**, 1415 (1994).
- ³²D. R. Nelson and V. M. Vinokur, *Phys. Rev. Lett.* **68**, 2398 (1992).
- ³³A. Gervais and D. Keller, *Physica C* **246**, 29 (1995).
- ³⁴Z. L. Wang, D. H. Lowndes, D. H. Christen, D. K. Kroeger, C. E. Klabunde, and D. P. Norton, *Physica C* **252**, 125 (1995).
- ³⁵V. M. Pan, A. L. Kasatkin, V. L. Svetchnikov, and H. W. Zandbergen, *Cryogenics* **33**, 21 (1993).

- ³⁶V. M. Pan, A. L. Kasatkin, and H. C. Freyhardt, IEEE Trans. Appl. Supercond. **AS-7**, 1588 (1997).
- ³⁷A. L. Kasatkin and V. M. Pan, *The Ninth International Workshop on Critical Currents*, IWCC 9-99, Extended Program Book, July 7–10, 1999, The Pyle Center, University of Wisconsin-Madison, USA (1999), p. 14.
- ³⁸E. H. Brandt, Phys. Rev. Lett. **69**, 1105 (1992).
- ³⁹V. M. Pan, V. A. Komashko, V. S. Flis, A. L. Kasatkin, V. L. Svetchnikov, O. P. Karasevskaja, A. G. Popov, A. V. Pronin, C. L. Snead, M. Suenaga, and H. W. Zandbergen, Physica B **284–288**, 831 (1999).
- ⁴⁰J. Mannhart, J. Supercond. **3**, 281 (1990).
- ⁴¹R. Gross and B. Mayer, Physica C **180**, 235 (1991).
- ⁴²P. A. Nilsson, D. Winkler, J. A. Alarco *et al.*, Appl. Phys. Lett. **59**, 3030 (1991).
- ⁴³D. Shi, Appl. Supercond. **1**, 61 (1993).
- ⁴⁴D. Dimos, P. Chaudhari, and J. Mannhart, Phys. Rev. B **41**, 4038 (1990).
- ⁴⁵A. Gurevich, H. Kuepfer, and C. Keller, Semicond. Sci. Technol. **4**, 91 (1991).
- ⁴⁶A. Gurevich, Phys. Rev. B **42**, 4857 (1990).
- ⁴⁷M. Strikovsky, G. Linker, S. V. Gaponov *et al.*, Phys. Rev. B **45**, 12522 (1992).
- ⁴⁸A. V. Pan, F. Ciovacco, P. Esquinazi, and M. Lorenz, Phys. Rev. B **60**, 4293 (1999).
- ⁴⁹P. Esquinazi, J. Low Temp. Phys. **85**, 139 (1991).
- ⁵⁰M. Ziese, P. Esquinazi, and H. F. Braun, Semicond. Sci. Technol. **7**, 869 (1994).
- ⁵¹E. H. Brandt, Phys. Rev. Lett. **68**, 3769 (1992).
- ⁵²M. Ziese, P. Esquinazi, Y. Kopelevich, and A. B. Sherman, Physica C **224**, 79 (1994).
- ⁵³F. Pardo, F. de la Cruz, P. Gammel, E. Bucher, and D. J. Bishop, Nature (London) **396**, 348 (1998).
- ⁵⁴P. Le Doussal and T. Giamarchi, Phys. Rev. B **57**, 11356 (1998).
- ⁵⁵S. Scheidel and V. Vinokur, Phys. Rev. B **57**, 2574 (1998).
- ⁵⁶L. N. Bulaevskii, M. Ledvij, and V. G. Kogan, Phys. Rev. B **46**, 366 (1992).
- ⁵⁷A. V. Pan, R. Hohne, M. Ziese, P. Esquinazi, and C. Assmann, in *Physics and Materials Science of Vortex States, Flux Pinning and Dynamics*, Vol. 356 of NATO Science Series, edited by R. Kossowsky *et al.*, Kluwer Academic Publ., Dordrecht, Boston, London (1999), p. 545.
- ⁵⁸A. V. Pan, PhD thesis, University of Leipzig, Leipzig (2000).
- ⁵⁹V. M. Pan, G. G. Kaminsky, A. L. Kasatkin, M. A. Kuznetsov *et al.*, Supercond. Sci. Technol. **5**, 48 (1992).
- ⁶⁰H. Jensen *et al.*, Phys. Rev. Lett. **60**, 1676 (1988); Phys. Rev. B **38**, 9235 (1988).
- ⁶¹A. V. Pan, P. Esquinazi, and M. Lorenz, Phys. Status Solidi B **215**, 573 (1999).
- ⁶²E. H. Brandt, Rep. Prog. Phys. **58**, 1465 (1995).
- ⁶³R. H. Koch, V. Foglietti, W. J. Gallagher, G. Koren, A. Gupta, and M. P. A. Fisher, Phys. Rev. Lett. **63**, 1511 (1989); **64**, 2586 (1990).
- ⁶⁴J. R. Thompson, Y. R. Sun, L. Civale, A. P. Malozemoff, M. W. McElfresh, A. D. Marwick, and F. Holtzberg, Phys. Rev. B **47**, 14440 (1993).
- ⁶⁵K. Yamafuji and T. Kiss, Physica C **258**, 197 (1996).
- ⁶⁶T. Matsushita, T. Tohdoh, and N. Ihara, Physica C **259**, 321 (1991).
- ⁶⁷M. Ziese, Phys. Rev. B **53**, 12422 (1996); **55**, 8106 (1997); Physica C **269**, 35 (1996).
- ⁶⁸B. Roas, L. Schultz, and G. Saemann-Ischenko, Phys. Rev. Lett. **64**, 479 (1990).
- ⁶⁹M. Fendorf, C. P. Burmester, L. T. Wille, and R. Gronsky, Appl. Phys. Lett. **57**, 2481 (1990).
- ⁷⁰V. Svetchnikov, A. Palti, and V. Pan, Met. Phys. Adv. Tech. **17**, 257 (1998).
- ⁷¹V. Svetchnikov, V. Vysotskii, and V. Pan, Met. Phys. Adv. Tech. **17**, 1235 (1999).
- ⁷²V. M. Pan, A. L. Kasatkin, V. L. Svetchnikov, V. A. Komashko, A. G. Popov, A. Yu. Galkin, H. C. Freyhardt, and H. W. Zandbergen, IEEE Trans. Appl. Supercond. **AS-9**, 1532 (1999).
- ⁷³V. Selvamanickam, M. Mironova, S. Son, and K. Salama, Physica C **208**, 238 (1993).
- ⁷⁴V. M. Pan, V. S. Flis, O. P. Karasevskaja, V. I. Matsui, I. I. Peshko, V. L. Svetchnikov, M. Lorenz, A. N. Ivanyuta, G. A. Melkov, E. A. Pashitskii, and H. W. Zandbergen, J. Superconductivity and Incorporated Magnetism **14**, 109 (2001).
- ⁷⁵V. M. Pan, V. S. Flis, V. A. Komashko, O. P. Karasevskaja, V. L. Svetchnikov, M. Lorenz, A. N. Ivanyuta, G. A. Melkov, E. A. Pashitskii, and H. W. Zandbergen, IEEE Trans. Appl. Supercond. **AS-11**, 3960 (2001).
- ⁷⁶V. M. Pan, A. L. Kasatkin, V. S. Flis, V. A. Komashko, V. L. Svetchnikov, A. G. Popov, A. V. Pronin, O. P. Karasevskaja, C. L. Snead, M. Suenaga, and H. W. Zandbergen, Institute of Physics Conference Series No. 167, *Applied Superconductivity* (2000), p. 699.
- ⁷⁷V. A. Komashko, A. G. Popov, V. L. Svetchnikov, A. V. Pronin, V. S. Melnikov, A. Yu. Galkin, V. M. Pan, C. L. Snead, and M. Suenaga, Semicond. Sci. Technol. **13**, 209 (2000).
- ⁷⁸H. Safar, J. Y. Coulter, M. P. Maley *et al.*, Phys. Rev. B **52**, 9875 (1995).
- ⁷⁹B. Meingast, O. Krant, T. Wolf, H. Wuehl, A. Erb, and G. Mueller-Vogt, Phys. Rev. Lett. **67**, 1639 (1991).
- ⁸⁰U. Welp, M. Grimsditch, S. Fleshler, W. Nessler, B. Veal, and G. W. Crabtree, J. Supercond. **7**, 159 (1994).
- ⁸¹B. Meingast, A. Junod, and E. Walker, Physica C **272**, 106 (1996).
- ⁸²A. Gurevich and E. A. Pashitskii, Phys. Rev. B **56**, 6213 (1997).
- ⁸³J. B. Hirth and J. Lothe, *Theory of Dislocations*, McGraw-Hill, New York (1988).
- ⁸⁴H. Ledbetter and M. Lei, J. Mater. Res. **6**, 2253 (1991).
- ⁸⁵B. Dam, J. M. Huijbregtse, F. C. Klaassen, R. C. F. van der Geest, G. Doornbos, J. H. Rector, A. M. Testa, S. Freisem, J. C. Martinez, B. Staeuble-Puempin, and R. Griessen, Nature (London) **399**, 439 (1999).
- ⁸⁶J. M. Huijbregtse, F. C. Klaassen, R. C. F. van der Geest, B. Dam, and R. Griessen, J. Low Temp. Phys. **32**, 114 (1999).
- ⁸⁷L. Civale, A. D. Marwick, T. K. Worthington, M. A. Kirk, J. R. Thompson, L. Krusin-Elbaum, Y. Sun, J. R. Clem, and F. Holtzberg, Phys. Rev. Lett. **65**, 648 (1991).

Translated by Steve Torstveit

Magnetic properties of irradiated quasi-2D type-II superconductors

G. M. Braverman

Max Planck Institut für Kernphysik, Heidelberg, Germany

S. A. Gredeskul* and Y. Avishai

Department of Physics, Ben-Gurion University of the Negev, Beer-Sheva 84105, Israel

(Submitted April 3, 2001)

Fiz. Nizk. Temp. **27**, 1012–1018 (September–October 2001)

Persistent scaling behavior of magnetization in layered high T_c superconductors with short-range columnar defects is explained within the Ginzburg–Landau theory. In the weak field region, the scaling function differs from that of a clean sample and the critical temperature is renormalized due to defects. In the strong field region, defects are effectively suppressed and the scaling function and critical temperature are the same as in a clean superconductor. This picture is consistent with recent experimental results. © 2001 American Institute of Physics. [DOI: 10.1063/1.1401183]

1. INTRODUCTION

Layered high-temperature superconducting (HTSC) materials, such as $\text{Bi}_2\text{Sr}_2\text{CaCu}_2\text{O}_{8+\delta}$ and $\text{Bi}_2\text{Sr}_2\text{Ca}_2\text{Cu}_3\text{O}_{10}$, are known experimentally to exhibit 2D scaling of magnetic properties^{1,2} around the mean-field transition line $H_{c2}(T)$. It is manifested by inspecting the magnetization M_0 as a function of temperature T and the (external) magnetic field H :

$$\frac{s\Phi_0}{A\sqrt{k_B TH}} M_0(T, H) = -2\gamma_0(x), \quad (1)$$

where s is an effective interlayer spacing, Φ_0 is the flux quantum, $x = AH'_{c2}[T - T_{c2}(H)]/\sqrt{k_B TH}$ is the scaling variable, $2\gamma_0(x)$ is so called scaling function, $H'_{c2} \equiv -dH_{c2}(T)/dT|_{T=T_{c0}}$, and T_{c0} is the zero-field critical temperature. For a superconductor with Ginzburg–Landau (GL) parameter κ and Abrikosov geometric factor³ β_A the constant $A = \sqrt{s\Phi_0/p}$, where $p = 16\pi\kappa^2\beta_A$.

The scaling function $\gamma_0(x)$ was first evaluated in the perturbative regime^{4,5} for $x \ll 1$. A nonperturbative result for it was obtained later using the following arguments. The compounds mentioned above are strongly type-II superconductors with large GL parameters $\kappa \approx 100$. Their effective interlayer separation $s = 1.5$ nm is larger than the effective superconducting coherence length $\xi(H, T)$ (if the magnetic field is not extremely close to the mean field transition field $H_{c2}(T)$), but is much smaller than the magnetic penetration depth. Hence the problem of fluctuations near $H_{c2}(T)$ becomes effectively two dimensional and can be represented theoretically in terms of the 2D GL mean-field theory projected onto the lowest Landau level (LLL).⁶ Such an approximation remains valid at least for $H > H_{c2}(T)/3$, when higher Landau levels are obviously irrelevant. Moreover, recent results⁷ show that LLL projection is valid even for $H > H_{c2}(T)/13$. Tesanović⁶ emphasized the crucial role played by the total amplitude of the order parameter in the critical region. Integration of the partition function over this amplitude, assuming that the Abrikosov factor β_A depends weakly on the vortex configuration, leads⁸ to the scaling law (1).

Moreover, putting this factor equal to a constant from the very beginning, Tesanović *et al.* obtained an explicit form of the scaling function,⁹

$$\gamma_0(x) = \frac{1}{2}(\sqrt{x^2 + 2} - x) \quad (2)$$

which agrees, to good accuracy, with the experimental magnetization data for $\text{Bi}_2\text{Sr}_2\text{Ca}_2\text{Cu}_3\text{O}_{10}$. Such a form of the scaling function (2) implies the existence of a crossing point: at some temperature $T_0^* = T_{c0}(1 + k_B/(2A^2 H'_{c2}))^{-1}$ the sample magnetization is independent of H , $M_0^* \equiv M_0(T_0^*, H) = -k_B T_0^*/(s\Phi_0)$. Later on, Tesanović and Andreev¹⁰ took the fluctuations of β_A into account and generalized the approach developed in Ref. 9 to arbitrary type-II superconductors.

Recently the influence of columnar defects on the magnetic properties of superconductors has been studied experimentally^{11,12} and theoretically.^{13–17} Columnar defects emerge after heavy ion irradiation of the superconducting sample.¹¹ They serve as strong pinning centers: each one is able to pin a single vortex. The radius of a columnar defect can be larger or smaller than the coherence length (long-range or short-range defects, respectively). Strong columnar defects lead to the formation of multiquantum vortices in high-temperature superconductors^{13,14} and in conventional ones as well.¹⁶ They also lead to additional magnetization jumps in mesoscopic samples.¹⁷ Therefore it is interesting to understand how such defects influence both the scaling behavior and the existence of the crossing point.

Specifically we refer to experiments performed by van der Beek *et al.*,¹² who studied the thermodynamic properties of single crystals of $\text{Bi}_2\text{Sr}_2\text{CaCu}_2\text{O}_{8+\delta}$. The samples were irradiated with 5.8-GeV ions that produced columnar defects with radius $L = 3.5$ nm and 2D density $n_d = 5 \times 10^{10} \text{ cm}^{-2}$. This density is small in the sense that the matching field $H_\Phi = n_d \Phi_0$, at which the number of vortices becomes equal to the number of defects, is much smaller than $H_{c2}(T)$. The magnetization was measured in the region of magnetic fields 0.2–5 T (which are also smaller than $H_{c2}(T)$) and tempera-

tures 72–86 K. Within this interval of fields the defect radius is the smallest length scale in the problem, and the defects can be treated as short-range. Measurements showed that columnar defects drastically change the reversible magnetization of the sample: there are now two scaling regimes, pertaining to relatively weak ($H < H_\Phi$) and strong ($H > H_\Phi$) magnetic fields. These two regimes are described by the same form (2) of the scaling function as for clean sample but they correspond to two different zero-field critical temperatures (used in Ref. 12 as fitting parameters) and two crossing points.

In this paper we propose an explanation of these results. Our arguments are based on the observation that the magnetic field serves as a control parameter for tuning an effective concentration $c = H_\Phi/H$ of defects (the number of defects divided by the number of vortices). In the weak field region the concentration is large ($c = 5$ for $\mu_0 H = 0.2$ T and n_d from Ref. 12), and each vortex is affected by a force emanating from many defects. On the average, this force leads to renormalization of the critical temperature T_c . Short-range defects are effectively weak and can be taken into account perturbatively. In first order they retain the same form of the scaling function (2) as that of a clean sample, up to the aforementioned renormalization of the critical temperature. Second-order corrections indeed destroy the scaling behavior, but in the vicinity of the crossing temperature scaling is approximately maintained. In the strong field region the concentration is small ($c = 0.2$ for $\mu_0 H = 5$ T and n_d from Ref. 12), renormalization is not needed, and the standard concentration expansion¹⁸ can be used. Here, strictly speaking, even the first-order correction (with respect to small concentration) destroys the scaling behavior. However, a strong field effectively suppresses the defects, thus restoring the scaling behavior of a clean superconductor with the initial critical temperature T_{c0} . Identifying the two fitting temperatures of Ref. 12 with the renormalized and initial critical temperatures T_c and T_{c0} , respectively, one finds for the dimensionless defect strength $\theta_1 = 0.49$, well within its allowed range $0 \leq \theta_1 \leq 1$. This indicates complete consistency between the description constructed below and the experimental results of Ref. 12.

Our quantitative approach follows the one proposed and successfully used within the critical region in clean superconductors^{8–10} and at low fields in disordered superconductors.¹⁵ This approach is based on the LLL projection and on the assumption that the Abrikosov factor is almost independent of the magnetic field. The latter assumption is evidently not valid in the vicinity of the matching field, but it is valid for fields much smaller or much larger than H_Φ . Indeed, columnar defects are strong pinning centers. Then, if the number of vortices is much less than or much greater than the number of defects, configurations close to the triangular Abrikosov lattice are always simultaneously compatible with any typical configuration of defects and with the condition of complete (as possible) pinning. This assumption is supported by noticing the remarkable difference between the number of vortices and the number of defects in both regions of fields. This enables us to take into account only these Abrikosov-like vortex configurations and fluctuations around them.¹⁾ But for these configurations the

Abrikosov factor almost coincides with its “triangular” value $\beta_A = 1.16$.

The next Section contains the main body of the paper. First we formulate the model (subsection 2.1) and then obtain the magnetization in the weak field region (subsection 2.2) and in the strong field region (subsection 2.3). Relation of our calculations to the experiment¹² is discussed in Sec. 3. Finally, the results obtained in this work are summarized in Sec. 4.

2. SCALING BEHAVIOR OF THE IRRADIATED SUPERCONDUCTOR

2.1. The model

Consider an irradiated thin superconducting film (or one layer in a layered superconductor) with area S subject to a perpendicular magnetic field (thus parallel to the defects). Columnar defects can be described as a local reduction of the critical temperature $\delta T_c(\mathbf{r}) = T_{c0} \sum_j t_j \exp(-(\mathbf{r} - \mathbf{r}_j)^2/2L^2)$. Here \mathbf{r} is a two-dimensional vector in the film plane, L is the defect radius, and the positions \mathbf{r}_j of defects are uniformly and independently distributed over the film plane with density n_d . The value of n_d is assumed to be moderate, so that for the pertinent region of temperature the matching field H_Φ is always much smaller than $H_{c2}(T)$. The dimensionless amplitudes of the defects $0 \leq t_j \leq 1$ are also independent random quantities distributed with some probability density $p(t)$ whose first two moments θ_1 and θ_2 satisfy $0 \leq \theta_{1,2} \leq 1$. On average, the defects lead to renormalization of the critical temperature

$$T_c = T_{c0} - \delta T_c, \quad (3)$$

where

$$\delta T_c \equiv \langle \delta T_c(\mathbf{r}) \rangle = 2\pi n_d L^2 \theta_1 T_{c0}.$$

The fluctuation of the shift of the critical temperature has zero mean value and a variance

$$\langle (\delta T_c(\mathbf{r}) - \delta T_c)^2 \rangle = \pi n_d L^2 \theta_2 T_{c0}^2.$$

The thermodynamic properties of a type-II superconductor are described by its partition function

$$\mathcal{Z} \propto \int \mathcal{D}\{\Psi\} \exp\left(-\frac{G}{k_B T}\right), \quad (4)$$

where Ψ is the order parameter and G is the standard GL functional

$$G = s \int \left\{ \alpha(\mathbf{r}) |\Psi|^2 + \frac{\beta}{2} |\Psi|^4 + \gamma \left| \partial_- \Psi \right|^2 + \frac{1}{8\pi} (\mathbf{B} - \mathbf{H})^2 \right\} d^2 \mathbf{r}, \quad (5)$$

$$\partial_- = \frac{\hbar}{i} \nabla + \frac{2e}{c} \mathbf{A}, \quad \mathbf{B} = \nabla \times \mathbf{A},$$

with the first GL coefficient $\alpha(\mathbf{r})$ depending on coordinate through a local change of the critical temperature.

Further simplifications will be done for the case of weak fields (in the case of strong fields slightly different simplifications are required—see subsection 2.3 below). Let us take into account the large value of the GL parameter, project the

system on the LLL corresponding to the external field, introduce the scaling variable x as mentioned above, a scaled order parameter $\varphi \propto \Psi$, and dimensionless temperature fluctuations

$$\tau(\mathbf{r}) = \left(\frac{s\Phi_0}{p} \right)^{1/2} \frac{H_{c2}(T)}{\sqrt{k_B T H}} \frac{\delta T_c(\mathbf{r}) - \delta T_c}{T_c - T}.$$

(We emphasize that for the case of weak fields it is the renormalized critical temperature which enters the expression for the upper critical field as well as the definition of the scaling variable x .) This results in the following expression for the partition function:

$$\mathcal{Z} \propto \int \mathcal{D}\{\varphi\} \exp \left\{ -N_v \left(x |\varphi|^2 + \frac{1}{4\beta_A} |\varphi|^4 + \overline{\tau(\mathbf{r})} |\varphi|^2 \right) \right\}, \quad (6)$$

where N_v is the total number of vortices (i.e., the total number of flux quanta through the sample area S) and the bar denotes averaging over the sample area. The expression for the magnetization has the form

$$\frac{s\Phi_0}{A\sqrt{k_B T H}} M(T, H) = \frac{1}{N_v} \frac{\partial \ln \mathcal{Z}}{\partial x}. \quad (7)$$

These two formulas (6), (7) form the basis for the further calculation and analysis.

2.2. Magnetization: weak fields

The assumption that the Abrikosov factor is a constant enables us, following Ref. 15, to replace $|\varphi(\mathbf{r})|^4$ in Eq. (6) by $\beta_A (|\varphi(\mathbf{r})|^2)^2$. This replacement, together with the simplest version of the Hubbard-Stratonovich transformation (introduction of an additional integration over some auxiliary field γ) turns the problem to be an exactly solvable one.¹⁵ Indeed, we expand the order parameter on the LLL subspace,

$$\varphi(\mathbf{r}) = \sum_{m=0}^{N_v} C_m L_m(\mathbf{r}), \quad (8)$$

where $L_m(\mathbf{r})$ are normalized LLL eigenfunctions with orbital momentum m . Then after integration over the expansion coefficients C_m , the partition function (6) reads

$$\mathcal{Z} \propto \int_{\Gamma} \exp\{-N_v \mathcal{L}(\gamma, x)\} d\gamma, \quad (9)$$

where

$$\mathcal{L}(\gamma, x) = -\gamma^2 + N_v^{-1} \text{tr} \ln[(x + \gamma)\hat{I} + \hat{\tau}] \quad (10)$$

and $\hat{\tau}$ is a random matrix with elements

$$\tau_{mn} = \int_S L_m^*(\mathbf{r}) \tau(\mathbf{r}) L_n(\mathbf{r}) d^2\mathbf{r}. \quad (11)$$

The contour Γ in Eq. (9) is parallel to the imaginary axis and stretches from $\gamma^* - i\infty$ to $\gamma^* + i\infty$. To assure convergence of the integrals over the coefficients $\{C_m\}$ the real constant γ^* should satisfy the inequality $\gamma^* + x + \min \tau_n > 0$, where τ_n is the n th eigenvalue of the matrix τ_{mn} .

In the thermodynamic limit $S \rightarrow \infty$ with n_d and N_v/S fixed, the partition function (9) could be calculated in a saddle-point approximation. This results in the following form for the magnetization:

$$\frac{s\Phi_0}{A\sqrt{HT}} M(T, H) = -2\gamma(x), \quad (12)$$

where $\gamma(x)$ is the solution of the saddle-point equation

$$\partial \mathcal{L}(\gamma, x) / \partial \gamma = 0. \quad (13)$$

In the case $\hat{\tau} = 0$ the two possible saddle points satisfy the equation

$$-2\gamma + \frac{1}{x + \gamma} = 0,$$

but only one of them

$$\gamma_0(x) = \frac{1}{2} (\sqrt{x^2 + 2} - x) \quad (14)$$

can be reached by an allowed deformation of the contour Γ . Substitution of Eq. (14) into (12) yields the magnetization $M_0(T, H)$ of a clean sample (up to renormalization of the critical temperature (1), (2)) obtained in Ref. 9. The saddle point $\gamma_0(x)$ serves as the scaling function.

Returning to the disordered case, we note that in the thermodynamic limit the last term on the right-hand side of Eq. (10) has an explicit self-averaged structure $N_v^{-1} \text{tr}(\dots)$ and can therefore be replaced by its average. This procedure modifies the saddle-point equation to

$$2\gamma = \frac{1}{x + \gamma} + \frac{\varepsilon(T)}{(x + \gamma)^3} \quad (15)$$

and results in a magnetization

$$M(T, H) = M_0(T, H) \left(1 + \varepsilon(T) \frac{2\gamma_0(x)}{\sqrt{x^2 + 2}} \right), \quad (16)$$

where

$$\varepsilon(T) = \left\langle \frac{\text{tr} \hat{\tau}^2}{N_v} \right\rangle = \frac{\theta_2}{p} n_d L^2 \frac{(2\pi H'_{c2} T_{c0})^2 s L^2}{k_B T}. \quad (17)$$

Note that the parameter $\varepsilon(T)$ is proportional to the fourth power of the defect radius L , thus justifying the perturbation approach for short-range defects.

In the zeroth-order approximation with respect to $\varepsilon(T)$ the magnetization has exactly the same form as for a clean sample, thus retaining both the scaling property and the existence of a crossing point. However, due to renormalization of the critical temperature, the crossing temperature $T^* = T_0^* - \delta T^*$ differs from its value T_0^* for a clean sample without defects: $\delta T^* = \delta T_c (1 + (2A^2 H'_{c2})^{-1})^{-1}$. In the next order, scaling is virtually destroyed since the correction term (within the parenthesis in Eq. (16)) depends not only on the scaling variable x but also on temperature. But at the crossing temperature T^* the magnetization reads

$$M(T^*, H) = M_0(T^*) \left(1 + \varepsilon(T^*) \frac{2H^*}{H + H^*} \right), \quad (18)$$

where $H^* = H_{c2}(T^*) = k_B T^* / (2A^2)$. Therefore if the field is weak enough, $H \ll H^*$, then the crossing point is restored,

T^* serves as a true crossing temperature, and the magnetization at the crossing temperature differs from its unperturbed form $-2\gamma_0(x)$ merely by a multiplicative constant $1+2\varepsilon(T^*)$.

2.3. Magnetization: strong fields

When the magnetic field increases, the approach used above becomes inapplicable. First, it fails in the vicinity of the matching field, where the Abrikosov factor becomes very sensitive to the details of the defect configuration. Secondly, higher-order terms in the perturbation expansion for the saddle-point equation [which were omitted in Eq. (16)] grow with magnetic field. Fortunately, we have here a new small parameter, because the dimensionless concentration c of defects in the strong field region is small. Therefore there is no sense in renormalizing the critical temperature, and it is natural to use the concentration expansion.¹⁸ Then in this region the dimensionless temperature fluctuation $\tau(\mathbf{r})$ is now defined as

$$\tau(\mathbf{r}) = \left(\frac{s\Phi_0}{p} \right)^{1/2} \frac{H_{c2}(T)}{\sqrt{k_B T H}} \frac{\delta T_c(\mathbf{r})}{T_{c0} - T}. \quad (19)$$

As mentioned above, the second term in the right-hand side of Eq. (10) is self-averaging and can be calculated using the limiting form of the density of states $\rho(\tau)$ of the matrix (11). For short-range defects in the linear approximation with respect to c , this density of states reads

$$\rho(\tau) = (1-c)\delta(\tau) + \frac{c}{\lambda} p \left(\frac{\tau}{\lambda} \right), \quad (20)$$

where $\lambda = 2\pi L^2 T_{c0} A H'_{c2} \sqrt{H} (\Phi_0 \sqrt{k_B T})^{-1}$ and $p(t)$ is the probability distribution of the dimensionless temperature t_j . Indeed, the matrix τ_{mn} is nothing but the Hamiltonian of a particle with charge $2e$ in a 2D system subject to a perpendicular magnetic field and containing short-range defects (projected on the LLL). The first and second terms in Eq. (20) correspond, respectively, to those states whose energy is stuck to the LLL (despite the presence of zero-range defects (see, e.g., Ref. 19)) and those states whose energies are lifted from the LLL by these defects. For sufficiently narrow distribution $p(t)$, the corresponding saddle-point equation leads to the magnetization

$$M = M_0 \left[- \frac{c\lambda\theta_1}{(1+2\lambda\theta_1\gamma_0(x))\sqrt{x^2+2}} \right], \quad (21)$$

where $M_0(T, H)$ is given by Eq. (1) with an initial critical temperature T_{c0} .

Rigorously speaking, scaling is destroyed since both the concentration c and the shifted eigenvalue $\lambda\theta_1$ depend explicitly on H and T . However, at strong field the correction term in Eq. (21) becomes negligibly small. This implies a restoration of the crossing point. Indeed, at temperature T_0^* the magnetization $M^* = M(T^*, H)$ assumes the form

$$M^* = M_0^* \left(1 - \frac{1}{1+\eta} \frac{H_\Phi}{H+H^*} \right), \quad (22)$$

with $\eta^{-1} = 2\pi L^2 H'_{c2} T_{c0} \theta_1 / \Phi_0$. Therefore in the entire

strong field region $H_\Phi \ll H \ll H^*$ the crossing temperature coincides with its initial value T_0^* and the magnetization in the crossing point practically coincides with its value M_0^* in a clean superconductor.

3. DISCUSSION

According to the results obtained above, within the main approximation, the magnetization indeed manifests two separate scaling regimes in the regions of weak and strong magnetic fields. These regimes are described by the same scaling function that characterizes a clean sample, but with a renormalized critical temperature in the weak region and with the initial critical temperature at high fields. These results are in complete qualitative correspondence with the experimental observations of van der Beek *et al.* Without pretending to account for a complete quantitative description of the above mentioned experiments, we nevertheless will show that some quantitative agreement can also be achieved.

Let us discuss the limits of applicability of our results and their relation to the experiment of Ref. 12.

1. In the weak field region, the important small parameters are $\varepsilon(T)$ (which enters the magnetization (18)) and $\varepsilon(T)/(x+\gamma_0(x))^2$ (which enters the saddle-point equation). Using the parameters which were employed in the experimental work¹² ($k_B\mu_0 H'_{c2} = 1.15 \text{ T}\cdot\text{K}^{-1}$, $T^* = 78.9 \text{ K}$, and the rest of parameters which were already mentioned in Sec. 1), we find from Eq. (17) $\varepsilon(T^*) = 0.5\theta_2$ and $\varepsilon(T^*)/(x^* + \gamma_0(x^*))^2 \approx 0.25$ (the latter figure is obtained for $\mu_0 H = 0.2 \text{ T}$). For the quite plausible value $\theta_2 = 0.5$ one then finds $\varepsilon(T^*) = 0.5\theta_2 = 0.25$.

2. The condition of convergence of the integral over the expansion coefficients $\{C_m\}$ can be written as $H > 0.25H_\Phi\theta_1^2/\theta_2$, and even in the worst case $\theta_1^2 = \theta_2$ it reads $\mu_0 H \approx 0.25 \text{ T}$.

3. Then, one has $\mu_0 H^* \approx 6.4 \text{ T}$, and applicability of the LLL projection requires $\mu_0 H > 0.5 \text{ T}$. The weak field region of Ref. 12 corresponds to $\mu_0 H = 0.2\text{--}0.02 \text{ T}$. Thus, in the weak field region, only the condition for applicability of the LLL projection is violated slightly, but the deviation is not dramatic.

4. In the strong field region we find $\eta \approx 2.9$, and therefore the correction term in parenthesis in Eq. (22) is less than three percent, so that in this region our assumptions are fully satisfied.

Hence, up to an insignificant mismatch for very weak fields our theoretical assumptions and simplifications are completely consistent with the experimental parameters of Ref. 12. Using the same set of parameters, we display in Fig. 1 the quantity M/\sqrt{TH} as a function of the scaling variable for weak field (inset) and strong field (main part). We used here the maximal value $\theta_1 = 1$. In the strong field region, the deviation from clean-sample scaling behavior is negligibly small for all three values of the strong magnetic field, in complete agreement with our results. In the weak field region, the scaling functions for three different fields can hardly be distinguished. This means that scaling is undoubtedly valid in a neighborhood of the crossing temperature. At the same time the scaling function differs from its form in a clean sample (1) by a multiplicative constant (see the parenthesis in Eq. (16)). Note that scaling in the weak field region

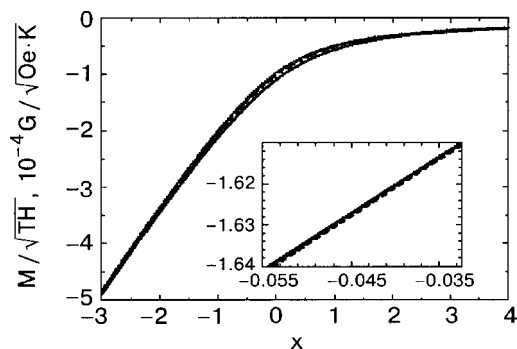


FIG. 1. The quantity M/\sqrt{HT} as a function of the scaling variable x . The dashed, dotted, and dot-dashed lines correspond to $\mu_0 H = 3, 4,$ and 5 T (main figure) and to $\mu_0 H = 0.02, 0.1,$ and 0.2 T (inset). The solid line corresponds to the clean-sample scaling function (strong field region only).

(which was experimentally established) is less pronounced than that in the strong field region. Apparently, the reason is that the experimental data are fitted to account for the clean-sample scaling function. Nevertheless, if we identify the fitted temperature 82.6 K (found in Ref. 12 in the weak field region) with the renormalized critical temperature $T_c = T_{c0} - \delta T_c$, and the fitted critical temperature 84.2 K in the strong field region¹² with T_{c0} , then, even within such a rough approximation, we obtain $\theta_1 \approx 0.5$. Recalling that θ_1 should be positive and less than unity, the above result strongly supports the applicability of our theory to the pertinent experiment.¹²

4. SUMMARY

In summary, we have calculated the magnetization of an irradiated superconductor below the mean-field transition line $H_{c2}(T)$, using the approach developed in Refs. 8–10 and 15. It was shown that, from a rigorous point of view, disordered short-range defects are expected to destroy the scaling behavior and prevent the existence of crossing point in both regions of weak and strong magnetic fields (with respect to matching field H_Φ). And yet, within the framework of the parameters which were employed in the experimental work,¹² the deviation from scaling behavior appears to be negligibly small, and crossing points exist in both field regions, in complete agreement with the experimental findings. The two fitting critical temperatures introduced in Ref. 12 for the strong and weak field regions correspond, in our formalism, to the initial and renormalized critical temperatures.

This paper is devoted to the memory of Lev Shubnikov, whose outstanding contributions to many branches of low-temperature physics have shaped its development ever since.

This work was supported by the MINERVA Foundation (G. B.), by grants from Israel Academy of Science “Mesoscopic effects in type II superconductors with short-range pinning inhomogeneities” (S. G.), and “Center of Excellence” (Y. A.), and by a DIP grant for German-Israel collaboration (Y. A.). We would like to thank E. Zeldov, who drew our attention to the paper of van der Beek *et al.*,¹² Z. Tesanović for helpful discussions, and P. H. Kes, who advised us about some parameters of the experimental setup of Ref. 12.

*E-mail: sergeyg@bgumail.bgu.ac.il

¹¹However, the field could not be very strong: if the order parameter is close to zero, vortices could collapse onto a single defect.¹⁶ But in the case $H_\Phi \ll H_{c2}(T)$ there exists a finite region of strong fields $H_\Phi < H < H_{c2}(T)$ where the distribution of the vortices does not feel the presence of defects.

- ¹P. H. Kes, C. J. van der Beek, M. P. Maley, M. E. McHenry, D. A. Huse, M. J. V. Menken, and A. A. Menovsky, *Phys. Rev. Lett.* **67**, 2382 (1991).
- ²Q. Li, M. Suenaga, J. Gohng, D. K. Finnemore, T. Hikata, and K. Sato, *Phys. Rev. B* **46**, 5857 (1992).
- ³A. A. Abrikosov, *Zh. Éksp. Teor. Fiz.* **5**, 1442 (1957) [*Sov. Phys. JETP* **27**, 1174 (1957)].
- ⁴E. Brezin, A. Fujita, and S. Hikami, *Phys. Rev. Lett.* **65**, 1949 (1990).
- ⁵R. Ikeda, T. Ohmi, and T. Tsuneto, *J. Phys. Soc. Jpn.* **60**, 1051 (1991).
- ⁶Z. Tesanović, *Phys. Rev. B* **44**, 12635 (1991).
- ⁷D. Li and B. Rosenstein, *Phys. Rev. B* **60**, 9704 (1999).
- ⁸Z. Tesanović and L. Xing, *Phys. Rev. Lett.* **67**, 2729 (1991).
- ⁹Z. Tesanović, Lei Xing, L. Bulaevskii, Q. Li, and M. Suenaga, *Phys. Rev. Lett.* **69**, 3563 (1992).
- ¹⁰Z. Tesanovich and A. V. Andreev, *Phys. Rev. B* **49**, 4064 (1994).
- ¹¹L. Civale, A. D. Marwick, M. W. McElfresh, T. K. Worthington, A. P. Malozemoff, F. H. Holtzberg, J. R. Thompson, and M. A. Kirk, *Phys. Rev. Lett.* **65**, 1164 (1990); L. Civale, A. D. Marwick, T. K. Worthington, M. A. Kirk, J. R. Thompson, L. Krusin-Elbaum, Y. Sun, J. R. Clem, and F. H. Holtzberg, *ibid.* **67**, 648 (1991).
- ¹²C. J. van der Beek, M. Konczykowski, T. W. Li, P. H. Kes, and W. Benoit, *Phys. Rev. B* **54**, R792 (1996).
- ¹³I. B. Khalfin and B. Ya. Shapiro, *Physica C* **202**, 393 (1992).
- ¹⁴A. I. Buzdin, *Phys. Rev. B* **47**, 11416 (1993).
- ¹⁵Z. Tesanović and I. F. Herbut, *Phys. Rev. B* **50**, 10389 (1994).
- ¹⁶G. M. Braverman, S. A. Gredeskul, and Y. Avishai, *Phys. Rev. B* **57**, 13899 (1998).
- ¹⁷G. M. Braverman, S. A. Gredeskul, and Y. Avishai, *Phys. Rev. B* **59**, 12039 (1999).
- ¹⁸I. M. Lifshits, *Nuovo Cimento* **3**, Suppl., No. 4 (1956).
- ¹⁹S. A. Gredeskul, M. Zusman, Y. Avishai, and M. Ya. Azbel', *Phys. Rep.* **288**, 223 (1997).

This article was published in English in the original Russian journal. Reproduced here with stylistic changes by AIP.

Commensurate vortex lattices in thin vanadium films and in V/Si superconducting superlattices

N. Ya. Fogel* and E. I. Buchstab

Department of Physics, Solid State Institute Technion, Haifa 32100, Israel

V. G. Cherkasova, O. I. Yuzepovich, and M. Yu. Mikhailov

B. Verkin Institute for Low Temperature Physics and Engineering, National Academy of Sciences of Ukraine, pr. Lenina 47, 61103 Kharkov, Ukraine

A. N. Stetzenko

Kharkov State Polytechnical University, ul. Frunze 21, 61002 Kharkov, Ukraine

(Submitted March 21, 2001)

Fiz. Nizk. Temp. **27**, 1019–1029 (September–October 2001)

The features of the Shubnikov phase in thin films of type-II superconductors are investigated in the case when the magnetic field is parallel to the surface of the film. Measurements of the nonmonotonic dependence of the critical current I_c on the magnetic field H_{\parallel} reveal commensurate vortex lattices with different numbers of vortex chains in the film. It is proved experimentally that in homogeneous films the commensurability effect between the vortex lattice parameter and the thickness of the film can be observed only for the ideal state of the film boundaries, admitting the formation of an infinite lattice of the vortices and their images. Worsening of the film surface smoothness and of the plane-parallel precision of the two surfaces of the film leads to vanishing of the oscillations of I_c and to a sharp decrease of the critical current. The lock-in transition due to the influence of the surface barrier is observed in the films for the first time. It is found that a thin-film layered sample exhibits an interplay between two types of commensurability effects: with the period of the superstructure and with the total thickness of the sample. The H – T phase diagram is considered for a homogeneous film in a parallel magnetic field. © 2001 American Institute of Physics.
[DOI: [DOI: 10.1063/1.1401184]

Recently, commensurability effects in type-II superconductors (meaning commensurability of the lattice parameter a_0 of the vortex lattice and the period of the regular structure of the inhomogeneities) have become a focus of research attention as substantial progress has been achieved in the creation of nanostructures and periodic systems of pinning centers at extremely small length scales.¹ Of no less interest for the study of the commensurability effect are natural materials with regular periodic inhomogeneities. These materials include transition-metal dichalcogenides and high-temperature metal oxides. Many materials of this type—superconducting superlattices of different kinds—have also been created artificially. In the case when the intervortex distance is equal to or a multiple of the period of the superstructure of inhomogeneities, all of the vortices are pinned in the pinning potential. This situation, as a rule, corresponds to the maximum critical current I_c , and the corresponding vortex structure is called commensurate. In the incommensurate phase, if no other types of pinning centers are present, the critical current should be equal to zero.² Such an ideal structure of a superconductor is not achievable in practice, and the critical current is nonzero even in the incommensurate phase. Experimentally one observes oscillatory dependence of the critical current I_c ,^{3–8} magnetic moment \mathbf{M} ,^{9,10} and energy dissipation^{11,12} as functions of magnetic field.

As far as we know, the commensurability effect in su-

perconductors was first studied by Guyon's and Martinolli's groups.^{3,4} In one of the cases the objects of study were artificial periodic superlattices consisting of a PbBi alloy with a periodic modulation of the concentration of the components, while in the other case they were thin films with an artificially created periodic modulation of the thickness. In the the aforementioned superlattices the curves of the critical current I_c as a function of H exhibit oscillations when the magnetic field \mathbf{H} is parallel to the plane of the layers. In the films with modulated thickness the oscillations of I_c were observed in a magnetic field perpendicular to the layers. In both cases the oscillations were observed for a mutually perpendicular orientation of the vortices and the modulation direction. At certain values of the magnetic field the period of the vortex lattice turns out to be commensurate⁴ with the period of the modulation potential, and maxima of I_c appear namely at these fields. Later the effect under discussion was also studied in other layered systems: artificial superlattices of different types and high- T_c superconductors.^{5–12} A theoretical explanation for the results mentioned can be found in Refs. 2, 13, and 14. The oscillatory dependence of the critical current I_c and resistance R as functions of H_{\parallel} has also been observed in the situation when, because of strong intrinsic pinning, only commensurate vortex lattices can exist.^{5,6,15} In that case the maxima of I_c (and minima of R) correspond to stable states of the commensurate vortex lattice or to phase transi-

tions between lattices with different orders of commensurability.^{5,6}

An interesting cycle of studies was done on superconducting films with an artificial two-dimensional lattice of submicron pores or ferromagnetic particles (see, e.g., Refs. 16–18). In those experiments the configuration, size of the elements, and periodicity of the artificial lattice were varied, and the critical current, magnetization, magnetic relaxation, and current–voltage characteristics were measured. The field dependences of all these parameters exhibited distinct features in fields corresponding to commensurability conditions.

Of particular interest is the case in which the commensurability effect is manifested in superconducting samples in which no periodic pinning potential is present. We are referring to homogeneous superconducting thin films, for which oscillatory $I_c(H)$ curves in a parallel magnetic field have also been observed.^{19–24} In films whose thickness satisfies the conditions $\lambda > d > \xi$ (λ is the penetration depth of the magnetic field, d is the thickness of the film, and ξ is the coherence length), the transition from the Meissner to the mixed state starts with the penetration of a single vortex chain. As the external magnetic field is increased, the density of vortex lines in the chain grows, and at a certain critical density an instability arises, causing the single row of vortices to split into two. Further increase of the field gives rise to a vortex lattice consisting of three chains, and so on. Owing to the interaction of the vortices with the boundaries of the film, a symmetric arrangement of the vortex chains with respect to the two surfaces of the film corresponds to the most stable state of the vortex lattice. When the distances between vortex chains are commensurate with the total thickness of the sample, extrema of I_c are observed. This is the basic explanation offered for the oscillatory dependence of the film parameters as functions of H_{\parallel} in Refs. 12, 25, and 26. In Refs. 22 and 23 a somewhat different interpretation was proposed. The interaction of the vortices with the boundaries of the superconductor as a rule is treated by taking the image vortices into account. In the case of a thin film the system of vortices and their images form an infinite lattice.²⁷ The period of this lattice along the direction orthogonal to the film is determined by the thickness of the film and the number of vortex rows, and the lattice period along the film is determined by the external magnetic field. These two periods coincide or are multiples of each other only at certain values of the magnetic field.^{22,23}

$$H_n = (n^2 \sqrt{3} \Phi_0) / 2d^2, \quad n = 1, 2, 3, \dots \quad (1)$$

Here n is the order of commensurability or the number of vortex rows in the film, and Φ_0 is the magnetic flux quantum. Thus in order for oscillatory effects to appear it is important to have commensurability in the two-dimensional (2D) lattice of vortices and image vortices. Under the condition of commensurability this 2D lattice has high symmetry, and the lattice of the real vortices inside the film corresponds to an Abrikosov vortex lattice (for $n > 1$). For the formation of a regular periodic lattice of vortices and their images it is necessary that the surfaces of the film be smooth and parallel to each other. Even a slight misorientation between the vortex-reflecting surfaces will preclude the formation of an

infinite regular lattice of images. Furthermore, such a lattice cannot be formed if the surface has noticeable roughness. The latter, as we know, suppresses the effectiveness of the Bean–Livingston surface barrier.

It should be noted that the oscillations of I_c and M also take place in multilayered films of finite thickness.^{12,25,26,28} However those data were obtained for Nb/Cu and Nb/Ti superlattices with a small anisotropy parameter ($\gamma = 1.2–1.8$),^{12,28} which corresponds to a weak periodic potential that has little influence on the properties of the film. Indeed, for homogeneous films of different materials and Nb/Cu and Nb/Ti layered films there is no qualitative difference in the behavior of $I_c(H_{\parallel})$. In the case of thin-film superlattices there is only a renormalization of the values of the commensurability fields. This question will be discussed in more detail below.

Our proposed interpretation for homogeneous films has found support in the paper by Carneiro,²⁷ where the equilibrium configuration of the vortex lines in films was determined numerically by the Monte Carlo method on the basis of London theory with allowance for an infinite system of image vortices.

Since, in our view, the influence of the surface barrier is exceedingly important and the commensurability effect in homogeneous thin films can be observed only when the film has ideal boundaries, we undertook experiments expressly designed to permit unambiguous confirmation of this hypothesis as to the origin of the oscillations of I_c in films in a parallel magnetic field.

In addition, we obtained data on a superlattice sample of finite thickness with larger anisotropy than in the multilayered films investigated previously. A comparison of these data with the results for homogeneous films leads to some interesting conclusions. On the one hand, in layered films it is possible to have commensurability effects simultaneously with respect to the total thickness of the sample and the period of the superstructure. On the other hand, because of the competing influence of the two different commensurability effects an additional selection rule arises, so that the extrema corresponding to the successive values of n do not all appear.

The H – T phase diagram for a homogeneous superconducting film in a parallel magnetic field, is also discussed.

SAMPLES AND EXPERIMENTAL TECHNIQUE

As the objects of study we chose homogeneous vanadium films. These films were condensed by electron-beam evaporation of the metal in a vacuum chamber at residual gas pressures of $\sim 10^{-6}$ Torr. The sharp-focus electron gun used had a power of 5 kW. The material used for the deposition was VEL-2 (99.9% vanadium).

The substrates used were especially smooth glass. The films were deposited on substrates heated to 300 °C. The rate of deposition of the vanadium was held constant at a value from 40 to 60 Å/s. Together with the correctly chosen substrate temperature, the electron-beam evaporation method made it possible to obtain fine-grained films with an average crystallite size of 150–200 Å. We did not observe texture in the films. Studies on a scanning electron microscope did not reveal any noticeable flaws of the surface relief of the film.

The samples were deposited through special heat-resistant masks of molybdenum foil 0.3 mm thick, prepared by an electroerosion method. The distance between the mask and substrate was 0.1–0.3 mm. The geometry of the deposited samples facilitated the use of the four-probe method for studying their electrical characteristics. The characteristic dimensions of the samples were as follows: distance between potential contacts 5 mm, width 0.5 mm.

The thickness of the films during deposition was determined by both a quartz oscillator and from the deposition time at a known rate. The thickness of the vanadium films was varied in the range 600–1600 Å. After preparation of the samples their thickness was monitored by the Talansky method to an accuracy of ± 20 Å.

Besides the films, we also investigated V/Si superlattices formed by the successive programmed deposition of vanadium and silicon layers on a fluorophlogopite substrate by the method of dc magnetron sputtering in an argon medium. The working pressure of the argon in the vacuum chamber was 3×10^{-3} Torr. The initial vacuum was 10^{-6} Torr or better. The substrate temperature was maintained at 100 °C. The deposition, as in the case of the thin films, was done through a special heat-resistant mask with a specified geometry. The thicknesses of the layers were determined by means of quartz sensors from the masses of the deposited substances. The error in the determination of the layer thicknesses was 1–2 Å. The number of bilayers of the superlattice was 10. An electron microscope study “in transmission” showed that the Si films are amorphous, while the V film is fine-grained polycrystalline, with a grain size of the order of 100 Å.

Measurements of the superconducting characteristics were done on an apparatus equipped with a superconducting solenoid. The samples were placed in liquid helium, and no heating was observed in the interval of currents used in the experiments. The stabilization of the temperature at the chosen point and the accuracy of its measurement were 0.003 K or better. To change the orientation of the films in the external magnetic field the samples were placed on a rod equipped with a special rotating device. The samples on the rotating table could be arranged in two different ways: in the first case the angle between the transport current and the magnetic field direction remained unchanged at 90° during the rotation, while in the second case changing the angle between the plane of the film and the magnetic field simultaneously changed the angle between \mathbf{H} and \mathbf{I} as well. The parallel orientation was set according to the resistivity minimum to an accuracy of 0.1° or better. The critical current I_c was determined from the current–voltage characteristics according to the points at which the voltage reached a fixed value of 1 μ V.

EXPERIMENTAL RESULTS AND DISCUSSION

Figure 1 shows the dependence of the critical current I_c on the parallel magnetic field H_{\parallel} for vanadium sample No. 1 ($d=750$ Å) at various temperatures. The curves exhibit two features: 1) at magnetic fields lower than H^* , which increases with decreasing temperature (its values are indicated by arrows in Fig. 1) the value of I_c remains practically unchanged as the field is increased; at the field H^* the value of I_c starts to decrease sharply; 2) I_c has a minimum that does

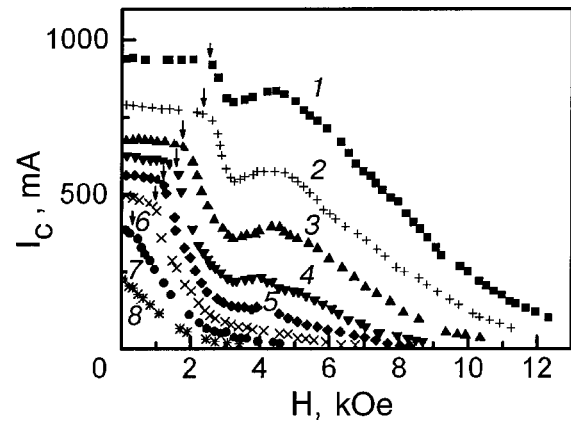


FIG. 1. Dependence of the critical current I_c on the parallel magnetic field H_{\parallel} for sample No. 1 ($d=750$ Å) at different temperatures T [K]: 1.980 (1), 2.384 (2), 2.749 (3), 3.125 (4), 3.368 (5), 3.618 (6), 3.819 (7), and 3.989 (8).

not shift in field as the temperature is varied. It has been shown previously²⁹ that the field H^* corresponds to either the first critical field H_{c1} or to the surface barrier field $H_s > H_{c1}$, depending on the state of the film surface. As we have said, penetration of vortices into the film in the field of the surface barrier occurs in the case of smooth boundaries of the film. The experiments done demonstrate a clear correlation: if the field H^* is equal to the first critical field³⁰

$$H_{c1} = \frac{2\Phi_0}{\pi d^2} \left[\ln \frac{\zeta d}{\pi \xi(T)} + 0.081 \right], \quad (2)$$

then there are no oscillations¹⁾ of $I_c(H_{\parallel})$ (Ref. 29; here $\zeta = 1.78$ is Euler’s constant); if H^* is equal to H_s , then the $I_c(H_{\parallel})$ curves are nonmonotonic, like those shown in Fig. 1. These data attest to the important role of the surface barrier in the appearance of oscillation effects.

Oscillations of the critical current are observed not only in a parallel field but also in inclined magnetic fields in a certain region of angles near the parallel orientation. For relatively small misorientations between the direction of the external magnetic field and the surface of the film the minimum of I_c on these curves coincides (Fig. 2). However, start-

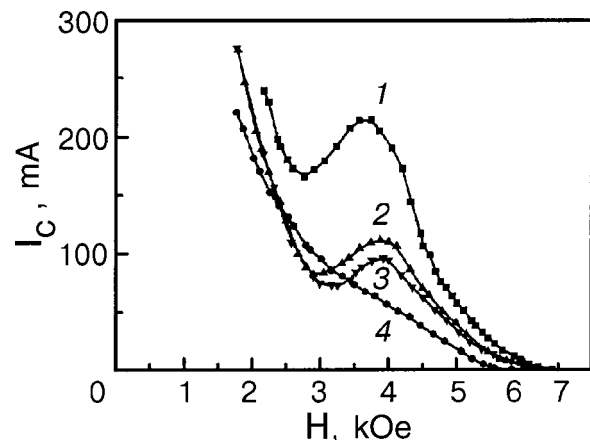


FIG. 2. Dependence of the critical current I_c on the magnetic field H for sample No. 3 ($d=1590$ Å) at different angles θ between the direction of the external magnetic field and the plane of the sample: $\theta=0^\circ$ (1), 5° (2), 8° (3), and 11° (4). The angle θ is measured from the parallel orientation; $T=3.614$ K.

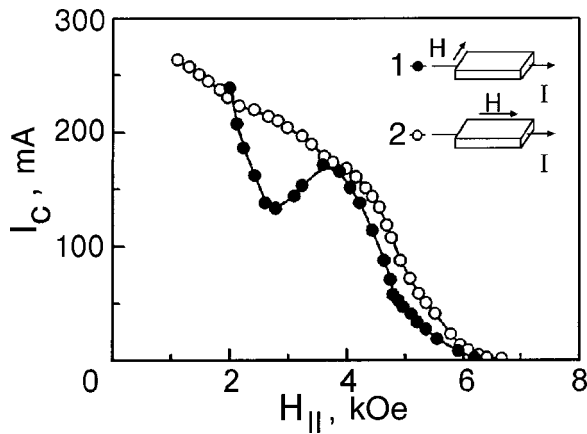


FIG. 3. Dependence of the critical current I_c on the parallel magnetic field H_{\parallel} for two different mutual orientations of the external magnetic field and the transport current for sample No. 3: $\perp H$ (1), $\parallel H$ (2). $T=3.614$ K.

ing at a certain critical angle θ_c (for sample No. 3 it is $\approx 9^\circ$) the minimum vanishes, and the $I_c(H)$ curves become monotonic. The existence of a critical angle for observation of oscillations in the case of thin-film layered samples has also been reported previously in a number of papers (see, e.g., Refs. 12 and 32). A more preferable explanation for the presence of a critical angle is in terms of the lock-in transition³³ proposed in Ref. 32. Such a transition was predicted by Feinberg and Villard³³ for layered superconductors with strong intrinsic pinning. The essence of this phenomenon is that in a field inclined at small angles θ the minimum of the free energy corresponds to vortices oriented along extended planar inhomogeneities (including the boundaries of the film) and not along the field. A difference appears between the directions of the magnetic induction in the sample and the external magnetic field; this difference vanishes only for $\theta > \theta_c$. The authors of the cited papers did not rule out that in slightly inclined fields the state of the vortex system does not completely correspond to the picture described in Ref. 32. An alternative considered is a system of stepwise-inclined vortices, in which the main orientation coincides with the parallel one and those parts of the vortex lines which are parallel to the layers are connected together by so-called kinks oriented along the normal to the layers.

Since our experiments have been done on homogeneous films, where stepwise inclined vortices cannot appear, their results permit us to state that for the first time a lock-in transition is observed which is due to the influence of a surface barrier rather than a periodic pinning potential.

It follows from Fig. 3 that the presence or absence of minima in a parallel field is critically dependent on the geometry of the experiment. The minimum is observed in the case when the vectors of the magnetic field and current, which lie in a plane parallel to the surface of the film, are mutually perpendicular (geometry 1 in Fig. 3). Here a Lorentz force arises which causes the vortices to move in the direction perpendicular to the surface of the film, overcoming the strong surface barrier. In the forceless configuration (geometry 2 in Fig. 3) there are no such features on the $I_c(H_{\parallel})$ curves. Thus the surface barrier again emerges as a phenomenon directly involved in the origin of the oscillations.

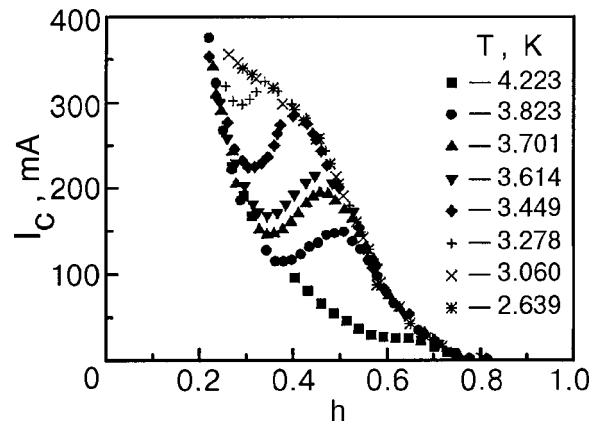


FIG. 4. Dependence of the critical current I_c on the reduced magnetic field $h=H/H_{\parallel}(T)$ for sample No. 3 at different temperatures.

The curves of I_c as a function of the reduced magnetic field $h=H/H_{\parallel}(T)$ obtained at different temperatures form a cigar-shaped family of curves, as follows from Figs. 4 and 5. The values of I_c on those parts of the curves that bound the cigar coincide for different temperatures, i.e., there is no temperature dependence of I_c in a certain region of reduced fields and temperatures. In the region of fields h corresponding to the interior of the cigar, where the minima and maxima of I_c are located, one observes the usual type of temperature dependence of I_c . For the region inside the cigar (and only for that region), as is shown in Fig. 6, there is a characteristic hysteresis of I_c . Hysteresis in the neighborhood of the fields H_n was also reported in Ref. 19.

As we have said, the minima on the $I_c(H_{\parallel})$ curves should correspond to the conditions of commensurability between the intervortex distance and the film thickness. The corresponding fields for a homogeneous film are determined

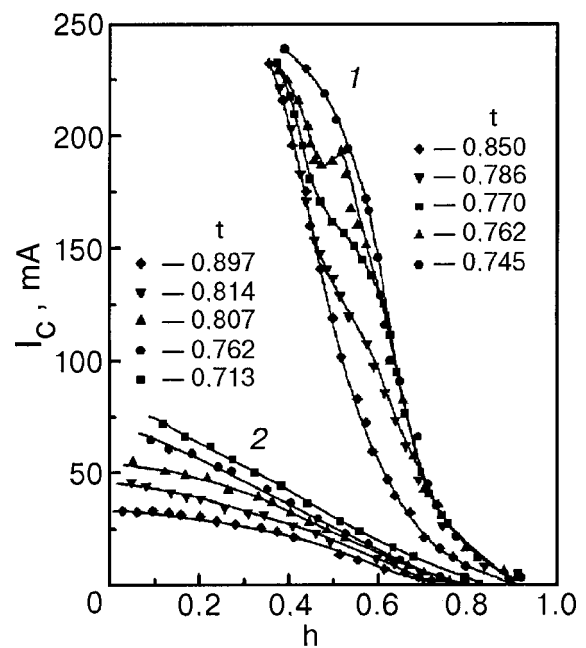


FIG. 5. Dependence of the critical current I_c on the reduced magnetic field $h=H/H_{\parallel}(T)$ at different temperatures for sample No. 4 ($d=1590$ Å) before (1) and after (2) etching; $t=T/T_c$.

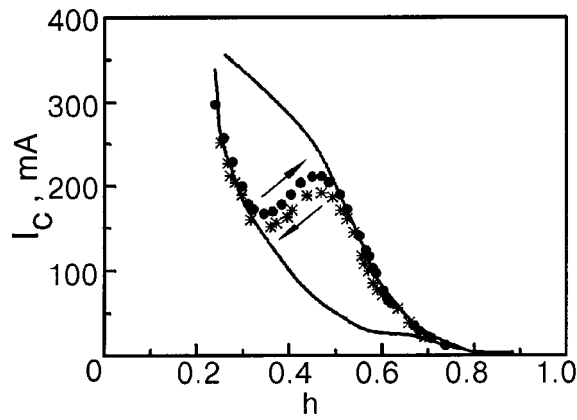


FIG. 6. Dependence of the critical current I_c on the reduced magnetic field $h = H/H_0(T)$ for sample No. 3 for increasing and decreasing magnetic field; $T = 3.614$ K.

by formula (1). If the film is a layered system, then formula (1) transforms into the following form with allowance for the anisotropy parameter γ :²⁶

$$H_n = n^2 \sqrt{3} \Phi_0 / 2 \gamma d^2, \quad n = 1, 2, 3, \dots \quad (3)$$

The experimental data obtained in the present study are in good agreement with formula (1). For example, for sample No. 1 ($d = 750$ Å) the field $H_{\min} = 3.1$ kOe, and a calculation according to formula (1) gives the value $d_{\text{calc}} = 760$ Å for $n = 1$. For sample No. 2 ($d = 780$ Å) one has $H_{\min} = 3.25$ kOe and $d_{\text{calc}} = 740$ Å. For the identical samples Nos. 3 and 4 ($d = 1590$ Å) the field $H_{\min} = 2.6$ kOe, and the calculated value of d for $n = 2$ is 1660 Å. Good agreement with formula (1) has also been noted¹⁹ for homogeneous films of the alloy PbIn with thicknesses $d = 650 - 3500$ Å.²¹ It is easy to see that for Nb/Cu layered films the position of the minima on the $M(H_{\parallel})$ curves³ correspond to the calculated fields H_n found using formula (3). Good agreement with this formula has also been observed in the case of Nb/Ti thin-film superlattices.²⁸

It is of interest to compare the data for homogeneous thin films and films of the same material with a periodic system of planar inhomogeneities. In the case of layered thin-film samples with sufficiently large values of the anisotropy parameter γ an “interference” between the two different commensurability effects can arise. The vortex lattice parameter can be commensurate with both the sample thickness d and with the period s of the layered structure. The available experimental results for Nb/Cu and Nb/Ti (with values $\gamma = 1.2 - 1.8$) attest to the fact that in the case of a comparatively weak modulation of the order parameter the presence of anisotropy leads to renormalization of the values of H_n [see formula (3)], but the surface barrier exerts the dominant influence on oscillation effects, as in the case of homogeneous films. Here we present the results for a V/Si superlattice (vanadium layer thickness 240 Å, silicon spacer thickness 30 Å) with a comparatively large value of the anisotropy parameter, $\gamma = 5.2$. This sample consists of the same number of bilayers, $m = 10$, as the Nb/Cu and Nb/Ti samples studied previously.^{12,25,28} The total thickness of the sample is 2700 Å. The dependence of the critical current I_c on the parallel magnetic field for this sample is shown in Fig. 7.

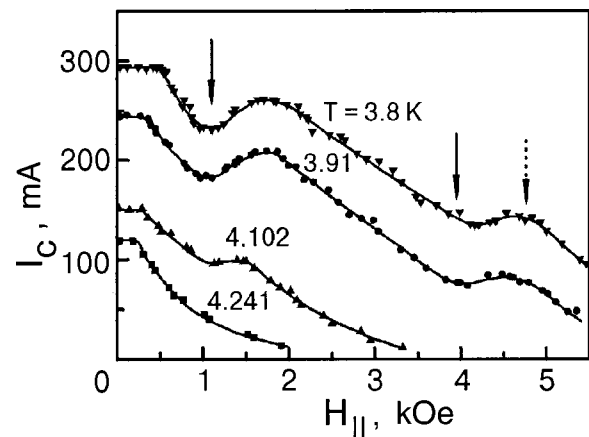


FIG. 7. Dependence of the critical current I_c on the parallel magnetic field H_{\parallel} for a 240/30 V/Si superlattice. The solid arrows indicate the calculated values of H_n , and the dotted arrow the calculated value of H_N .

In multilayer superlattices in which the boundary effects can be neglected, the fields H_N at which the vortex lattice parameter is commensurate with the period of the superstructure of the superlattice are determined by the expression³⁴

$$H_N = \sqrt{3} \Phi_0 / 2 N^2 s^2 \gamma. \quad (4)$$

Here N is the order of commensurability for the effect under study. The ratio of the fields H_N and H_n for the two type of commensurability effect, as can be seen from formulas (3) and (4), does not depend on any of the parameters of the system except the number of bilayers:

$$\frac{H_N}{H_n} = \frac{m^2}{n^2 N^2}. \quad (5)$$

It follows from formula (5) that it is possible to observe a large number of extrema of I_c . We recall that upon commensurability of the vortex lattice parameter a_0 with the total thickness of the film one should observe minima of the critical current I_c , while commensurability with s corresponds to maxima of I_c .

It follows from an analysis of Fig. 7 that the first minimum of I_c for $H_{\parallel} = 1.17$ kOe corresponds to the calculated value of H_n at $n = 5$, while the second at $H_{\parallel} = 3.8$ kOe corresponds to the value $n = 9$. The minima with commensurability orders $n = 1 - 4$ cannot be observed because the fields corresponding to them are less than or of the order of the field at which the initial penetration of vortices into the film occurs. Such an explanation will of course not work for the commensurability orders $n = 6 - 8$, for which the extrema also fail to appear on the $I_c(H_{\parallel})$ curves. It is important to note, however, that, since for the given sample $m = 10$, it is only for $n = 5$ and 9 that all the vortex chains can lie in the Si spacers, where their position is energetically most favorable. At $n = 9$ all of the Si spacers in the sample are occupied, and the distance between vortex rows is equal to s . At $n = 5$ the distance between vortex rows is equal to $2s$. On the other hand, the position of the maximum of I_c at 4.7 kOe corresponds, according to formula (4), to commensurability order $N = 1$. The position of H_N for $N = 2$ coincides with that for $n = 5$, and there a minimum of I_c is observed. A curious picture emerges. Instead of the large number of oscillations expected one observes only a few, and the reason for this is

apparently the additional selection rule that arises in the case of a competition between two different commensurability effects. Of the set of vortex lattices that can exist in homogeneous films, in a superlattice sample of the *S/I* type (*S* is a superconductor and *I* is a semiconductor) only those which correspond to an ordered arrangement of vortex rows in the semiconductor spacer layers are realized. In relatively weak fields the dominant effect is that of commensurability with the total thickness of the film (we recall that the fields H_n for $n=5$ and H_N for $N=2$ are numerically equal, but at that value of the field a minimum of I_c is observed). In the case of high fields both commensurability effects are manifested: a minimum of I_c at $H_n=3.8$ kOe ($n=9$) and a maximum of I_c at $H_N=4.7$ kOe ($N=1$). In both cases the distance between vortex chains is the same, equal to s , but the number of vortices in the chains is different. The appearance of the maximum after the minimum of I_c is explained by the fact that in fields $H_{\parallel} > H_n$ the depth of the potential well for the vortices increases.^{32,35} However, the theory does not determine the field values up to which this occurs. For the given sample the maximum at 4.7 kOe corresponds exactly to the condition of commensurability between the superlattice period and a_0 . It follows from the experiment under discussion that in a superlattice of finite thickness the character of the oscillation effects at large values of the parameter γ will differ considerably from those for homogeneous films.

Let us now return to the case of homogeneous films and present the results of direct experiments which indicate that the smoothness and plane-parallel precision of the two surfaces of the films are the main factors determining the appearance of the oscillatory dependence of $I_c(H_{\parallel})$. The surface of sample No. 4 after the measurements of the $I_c(H_{\parallel})$ curves (the series of curves 1 in Fig. 5) was subjected to chemical etching. After the etching its thickness had changed only slightly ($\Delta d/d \approx 5\%$). An examination with a scanning electron microscope (resolution ~ 200 Å) showed that the state of the surface had been modified by the chemical etching. Whereas before etching it had been practically smooth (within the resolution of the device), after the etching there were shallow “pits” of arbitrary shape, with dimensions of 0.1–1 μm . After the etching the values of I_c and the form of the $I_c(H_{\parallel})$ curves were radically altered (series of curves 2 in Fig. 5). The values of the critical current in the same interval of reduced temperatures and fields decreased by a factor of 3–7 (while T_c and $H_{c\parallel}$ changed insignificantly, by not more than 2–4%). The $I_c(H_{\parallel})$ curves became monotonic: the “cigar” vanished. The artificially created roughness of the sample surface led to suppression of the surface barrier and, accordingly, to an overall decrease of the critical current. The features characteristic of the commensurability effect also vanished.

In the same deposition session as for sample No. 1 we also prepared a sample (No. 5) with variable thickness by the technique proposed in Ref. 36. For this wedge-shaped sample with a difference in thicknesses at the edges of $\sim 7\%$ and a misorientation of the two surfaces amounting to only a few minutes of arc, the values of I_c at the same values of t and h are smaller by a factor of 2–3.5 than for sample No. 1, and the $I_c(H_{\parallel})$ curves are smooth (the average thickness of film No. 5 was close to the thickness of sample No. 1).

Thus, from the last two experiments and also from the correlation between the appearance of the minimum of I_c and the penetration of vortices into the film in the surface barrier field H_s it follows unambiguously that commensurability between the film thickness and the interchain distance in the vortex lattice is by itself insufficient for observation of oscillation effects. On the other hand, the same experiments give evidence in favor of the previously stated hypothesis that an important role is played by the formation of a regular lattice of vortices and their images and the conditions of commensurability in that lattice.

Having proved experimentally that the presence of a lattice of vortices and vortex images vortices is critically important for observation of the commensurability effect, we can repeat the previous arguments^{22,23} concerning the nature of the oscillatory critical current in thin-film samples. It can be assumed that in accordance with the general concepts about phase transitions between commensurate and incommensurate phases,^{37,38} in the neighborhood of the points of commensurability (i.e., in a certain interval of variation of the vortex lattice parameter or the external field H) there exists a commensurate (*C*) phase. In the *C* phase the vortices behave in the usual way, and the critical current is determined by the mechanism of interaction of the vortices with the boundaries of the film. According to the calculations of Shmidt,³⁵ in this region one should observe a minimum of the critical current, corresponding to the entry of a monolayer of vortices, and a maximum due to fact that the depth of the potential well for the chain of vortices increases with increasing field. Of course, in this case the critical current should depend on temperature.³⁵ Just such behavior is observed inside the region bounded by the “cigar” (see Fig. 4).

For each system there exists an incommensurability parameter δ , at the critical value of which a transition should occur to an incommensurate (*I*) phase. In the *I* phase, in accordance with the same concepts,^{37,38} one typically sees the formation of static periodically repeating solitons (domain walls). In our case these solitons or domain walls can separate regions with two different commensurate lattices.

The critical current on the envelope of the “cigar” is independent of temperature and can apparently be interpreted as the critical current due to the transition from the *I* phase to the *C* phase, or as the current at which the solitons are destroyed. Inside the *C* phase the critical current is determined by the relationships governing the interaction of individual vortices with the boundaries of the film.

The results of the above experiments allow us to state with certainty that the oscillations of the superconducting parameters of homogeneous films in a parallel magnetic field are due to the commensurability effect occurring in the lattice of vortices and vortex images vortices arising in the case of an ideal state of the boundaries of the sample. These results are consistent with the results of previous experiments which established that for observation of oscillations it is necessary to have commensurability between the vortex lattice parameter in the film and the total thickness of the sample, since the conditions of commensurability are the same in both cases. For our hypothesis, however, one must impose more stringent requirements on the samples in order to be able to observe the effects under discussion. These

conditions undoubtedly must be met in the case of homogeneous samples. If the film has a layered structure, then one can observe oscillations of the physical parameters due to the commensurability between the interchain distance and the period of the superstructure, and therefore the state of the surface is not so important.

Let us conclude with a discussion of the H - T phase diagram of a homogeneous superconducting film in a parallel magnetic field and the necessary conditions for observation of the commensurability effect due to the influence of the sample boundaries. One of the obvious conditions, a restriction on the film thickness, $\lambda \gg d \gg \xi$, has already been mentioned above. It follows from this condition that the materials used for preparation of the films should have rather large values of the Ginzburg–Landau parameter κ . This condition is met for transition metals, superlattices based on them, and certain superconducting alloys. The inequality $d \gg \xi(T)$ presupposes the possibility of penetration of one, two, etc. chains of vortices into the film in a parallel magnetic field. This inequality, which, with allowance for the critical thickness $d_c = \sqrt{5/2}\xi(T)$ (Ref. 39), determines the condition under which the homogeneous film undergoes a transition to a one-dimensional mixed state at the upper critical field, can be reduced to the less stringent restriction $d \gg \sqrt{5/2}\xi(T_0)$. If this condition is not met, then the uniform distribution of the order parameter will persist in the film all the way down to $T=0$ K. If $d \gg \xi(0)$, then the upper boundary for the existence of the mixed state is determined, as in the case of a bulk superconductor, by the field $H_{c3} = 1.7H_{c2} = 1.7\Phi_0/(2\pi\xi^2)$. From the field ratio $H_{c3}(0)/H_n \approx 0.2d^2/[n^2\xi^2(0)]$ it follows that the maximum number of commensurate vortex phases with different n which can be observed at $T=0$ in a given film is determined by the ratio $d/\xi(0)$: $n_{\max} < 0.47d/\xi(0)$. This definition of n_{\max} is valid for those film thicknesses for which the condition $d/\xi(0) \leq 4$ is met. If this inequality does not hold, then the commensurate lattice with $n=1$ at $T=0$ or at low temperatures cannot be detected experimentally, since the field H_{c1} turns out to be less than the field of overheating of the Meissner state, $H_s = \Phi_0/(\sqrt{2}\pi\xi d)$, at $T=0$.³⁵ Accordingly, the number of commensurate vortex lattices will be equal to $n_{\max} - 1$. An example of the H - T phase diagram for a homogeneous film is shown in Fig. 8.

At nonzero temperatures the number of observable commensurate vortex phases depends on T , since the fields bounding the existence region of the mixed state are temperature dependent. For this reason there exists a region near T_c in which one can observe a commensurate phase with $n=1$, which at lower temperatures is “hidden” in the region of the Meissner state. As T is lowered, this phase vanishes, but the phase with $n=2$ becomes observable. At still lower temperatures one can observe two or more commensurate phases. The larger the film thickness, the larger the number of commensurate phases there are in the region of the mixed state. However, there is a limit to the film thickness, above which the neighboring commensurate phases turn out to be located so close to each other in magnetic field that the existence regions of the individual phases begin to overlap. The maximum number of commensurate vortex phases that have been observed in thin films by measurement of the magnetic

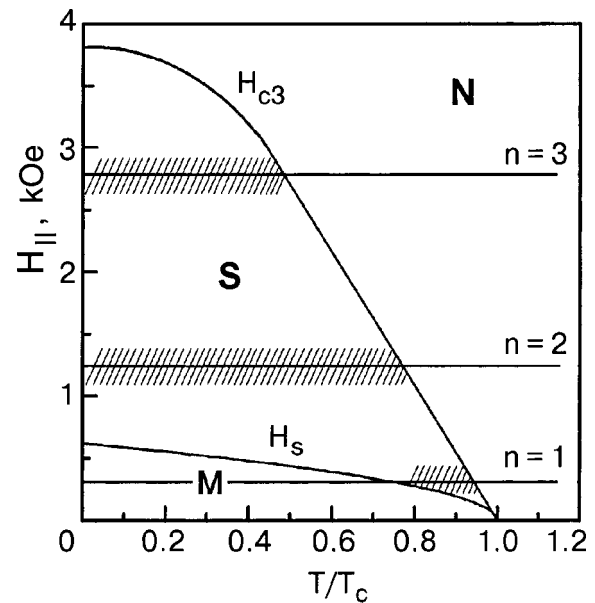


FIG. 8. H - T phase diagram for sample No. 1: M, S, and N are the Meissner, mixed, and normal states. The horizontal lines with $n=1,2,3$ indicate the positions of the commensurate phases, and the shading indicates the existence region of each of these phases.

moment is six.¹² In the case when measurements of the critical current are used to study the commensurate phases, one ordinarily sees fewer of them. To a large degree this is due to a purely “technical” limitation: at large values of the critical current density the samples can become overheated (e.g., in sample No. 1 at $t \approx 0.5$ the critical current density in low fields already exceeds 10^6 A/cm²). Measurements of the magnetic moment, which are free of this limitation, can give more complete information about commensurate vortex lattices in thin films.

This study was supported in part by the Israel Academy of Sciences (Grant 359/99) and the Center for Absorption in Science of the Ministry of Immigrant Absorption of the State of Israel.

*E-mail: nfogel@technion.technion.ac.il or fogel@ilt.kharkov.ua

¹Oscillations can be absent for a completely trivial reason as well (see, e.g., Ref. 31). The critical current in that study was measured with such a large step in magnetic field that it was not possible to register oscillations.

²Sutton’s formula,¹⁹ which is based on a calculation of close packing of spheres, is practically the same as formula (1).

³Some authors^{25,26} have held the opinion that the commensurability conditions correspond to maxima rather than minima of I_c and M , but apparently this point of view has changed, since a more recent paper¹² by some of the same authors spoke of minima.

¹V. V. Moshchalkov, Physica C 332, 1 (2000).

²S. E. Burkov and V. L. Pokrovsky, J. Low Temp. Phys. 44, 423 (1981).

³H. Raffi, J. C. Renard, and E. Guyon, Solid State Commun. 11, 1679 (1972).

⁴O. Daldini, P. Martinolli, T. L. Olsen, and G. Berner, Phys. Rev. Lett. 22, 218 (1974).

⁵N. Ya. Fogel, M. Yu. Mikhailov, Yu. B. Bomze, and O. I. Yuzepovich, Phys. Rev. B 59, 3365 (1999).

⁶N. Ya. Fogel, M. Yu. Mikhailov, Yu. B. Bomze, and O. I. Yuzepovich, Physica B 284–288, 731 (2000).

⁷P. R. Broussard and T. H. Geballe, Phys. Rev. B 37, 68 (1988).

⁸C. Coccoresse, C. Attanasio, L. V. Mercaldo, M. Salvato, L. Maritato, J. M.

- Slaughter, C. M. Falco, S. L. Prischepa, and B. I. Ivlev, *Phys. Rev. B* **57**, 7922 (1998).
- ⁹M. Oussena, P. A. J. de Groot, R. Gagnon, and L. Taillefer, *Phys. Rev. Lett.* **72**, 3606 (1994).
- ¹⁰A. A. Zhukov, H. Kupfer, G. K. Perkins, A. D. Caplin, K. I. Kugel, A. L. Rakhmanov, M. G. Mikheev, V. I. Voronkova, M. Klaser, and H. Wuhl, *Phys. Rev. B* **59**, 11213 (1999).
- ¹¹C. Hunnekes, H. G. Bohn, W. Shilling, and H. Schulz, *Phys. Rev. Lett.* **72**, 2271 (1994).
- ¹²M. Ziese, P. Esquinazi, P. Wagner, H. Adrian, S. H. Brongersma, and R. Griessen, *Phys. Rev. B* **53**, 8658 (1996).
- ¹³S. Ami and K. Maki, *Prog. Theor. Phys.* **53**, 1 (1997).
- ¹⁴S. E. Burkov and V. L. Pokrovskii, *JETP Lett.* **32**, 263 (1980).
- ¹⁵B. I. Ivlev, N. B. Kopnin, and V. L. Pokrovsky, *J. Low Temp. Phys.* **80**, 187 (1990).
- ¹⁶E. Rossel, M. Van Bael, M. Baert, R. Jonckheere, V. V. Moshchalkov, and Y. Bruynseraede, *Phys. Rev. B* **53**, R2983 (1996).
- ¹⁷M. Baert, V. V. Metlushko, C. D. Potter, E. Rossel, K. Temst, R. Jonckheere, A. Gilibert, V. V. Moshchalkov, and Y. Bruynseraede, *Physica C* **235–240**, 2791 (1994).
- ¹⁸M. J. Bael, K. Temst, L. V. Look, J. Bekaert, V. V. Moshchalkov, and Y. Bruynseraede, *Physica B* **284–288**, 893 (2000).
- ¹⁹J. Sutton, *Proc. Phys. Soc.* **67**, 791 (1966).
- ²⁰T. Yamashita and Y. Onodera, *Solid State Commun.* **13**, 1289 (1973).
- ²¹T. Yamashita and L. Rinderer, *J. Low Temp. Phys.* **24**, 695 (1976).
- ²²N. Ya. Fogel and V. G. Cherkasova, *Physica B* **107**, 291 (1981).
- ²³N. Ya. Fogel' and V. G. Cherkasova, *Fiz. Nizk. Temp.* **7**, 268 (1981) [*Sov. J. Low Temp. Phys.* **7**, 131 (1981)].
- ²⁴L. P. Ichkitidze and V. I. Skobelkin, *Fiz. Nizk. Temp.*, **7**, 117 (1981) [*Sov. J. Low Temp. Phys.* **7**, 58 (1981)].
- ²⁵S. H. Brongersma, E. Verweij, N. Y. Koeman, D. G. de Groot, R. Griessen, and B. I. Ivlev, *Phys. Rev. Lett.* **71**, 2319 (1993).
- ²⁶S. H. Brongersma, E. Verweij, N. Y. Koeman, D. G. de Groot, and R. Griessen, *Thin Solid Films* **228**, 201 (1993).
- ²⁷G. Carneiro, *Phys. Rev. B* **57**, 6077 (1998).
- ²⁸P. Lobotka, I. Varva, R. Senderak, D. Machajdik, M. Jergel, S. Gazi, E. Rossel, M. Baert, Y. Bruynseraede, M. Forsthuber, and G. Hilscher, *Physica C* **229**, 231 (1994).
- ²⁹V. G. Cherkasova and N. Ya. Fogel', *Fiz. Nizk. Temp.* **15**, 383 (1989) [*Sov. J. Low Temp. Phys.* **15**, 216 (1989)].
- ³⁰A. A. Abrikosov, *Zh. Éksp. Teor. Fiz.* **47**, 720 (1964) [*Sov. Phys. JETP* **20**, 480 (1965)].
- ³¹G. Stejic, A. Gurevich, E. Kadyrov, D. Christen, R. Joyat, and D. C. Larbalestier, *Phys. Rev. B* **49**, 1274 (1994).
- ³²A. J. Vermeer, D. J. de Groot, N. J. Koeman, R. Griessen, and C. van Hasendonck, *Physica C* **185–189**, 2345 (1991).
- ³³D. Feinberg and C. Villard, *Phys. Rev. Lett.* **65**, 919 (1990).
- ³⁴B. I. Ivlev and N. B. Kopnin, *J. Low Temp. Phys.* **80**, 161 (1990).
- ³⁵V. V. Schmidt, *Zh. Éksp. Teor. Fiz.* **57**, 2095 (1969) [*Sov. Phys. JETP* **30**, 1137 (1970)].
- ³⁶Yu. F. Komnik and E. I. Bukhshtab, *Zh. Éksp. Teor. Fiz.* **54**, 34 (1968) [*Sov. Phys. JETP* **27**, 34 (1968)].
- ³⁷P. Bak, *Rep. Prog. Phys.* **45**, 587 (1982).
- ³⁸V. L. Pokrovskii and A. L. Talapov, *Zh. Éksp. Teor. Fiz.* **78**, 269 (1980) [*Sov. Phys. JETP* **51**, 134 (1980); Erratum, **51**, 654 (1980)].
- ³⁹I. O. Kulik, *Zh. Éksp. Teor. Fiz.* **52**, 1632 (1967) [*Sov. Phys. JETP* **25**, 1085 (1967)].

Translated by Steve Torstveit

Triplet superconducting proximity effect in inhomogeneous magnetic materials

A. Kadigrobov*

Department of Applied Physics, Chalmers University of Technology and Göteborg University, SE-412 96 Göteborg, Sweden and B. Verkin Institute for Low Temperature Physics and Engineering, National Academy of Science of Ukraine, 47 Lenin Ave., Kharkov, 61103, Ukraine

R. I. Shekhter and M. Jonson

Department of Applied Physics, Chalmers University of Technology and Göteborg University, SE-412 96 Göteborg, Sweden
(Submitted May 14, 2001)

Fiz. Nizk. Temp. **27**, 1030–1038 (September–October 2001)

We show that quantum spin fluctuations in inhomogeneous conducting ferromagnets drastically affect the Andreev reflection of electrons and holes at a ferromagnet–superconductor interface. As a result, a strong long-range proximity effect appears, associated with electron–hole spin triplet correlations and persisting on a length scale typical for nonmagnetic materials but anomalously large for ferromagnets. For applications, an important consequence is that this long-range proximity effect permits the creation of superconducting quantum interference devices with magnetic Josephson junctions of anomalously large length. © 2001 American Institute of Physics. [DOI: 10.1063/1.1401185]

1. INTRODUCTION

In recent years much attention has been paid to normal conductor-superconductor (N/S) structures (for a review, see, e.g., Ref. 1). Transport of electric charge in such systems is much affected by the existence of an energy gap in the spectrum of elementary excitations in the superconductor. As a result of the existence of the gap, electronic elementary excitations which freely propagate in the nonsuperconducting material cannot penetrate into the superconductor to a sufficient distance if their energy ε (measured from the Fermi level ε_F) is less than the superconductor energy gap Δ . A correlated transfer of two electrons accompanied by their pairing inside the superconductor is the only mechanism that provides a direct transmission of the charge into the superconducting condensate that is the ground state of the superconductor. The above-mentioned two-electron transfer may be considered in terms of the conventional scattering scheme as a process of an electron-hole transformation of excitations inside the normal conductor that takes place at the boundary with the superconductor. This scattering (which is known as Andreev reflection) couples the incident electron and the reflected hole in such a way that their spins are oriented in opposite directions and their energies ($\pm\varepsilon$) are symmetrically positioned with respect to the Fermi energy (“Andreev hybrid”). Such a two-electron correlation which arises at the boundary with the superconductor persists inside the normal conductor to a distance \mathcal{L}_e from the superconductor, $\mathcal{L}_e = \min(\hbar/\Delta p, \sqrt{\hbar D/\Delta p v_F})$, where $\Delta p = \varepsilon/v_F$, v_F is the Fermi velocity, and D is the diffusion coefficient. The destruction of the phase coherence arises due to the difference between the momenta of the electron (ε/v_F) and hole ($-\varepsilon/v_F$) components in the Andreev hybrid. The other peculiar feature of the Andreev hybrid, which is that the electron and hole spins have opposite directions, makes for sensitivity of the Andreev correlation to a magnetic field H

controlling the spin splitting $\Delta E = \mu_B H$ (μ_B is the Bohr magneton) of the electron and hole energies in the hybrid.

It becomes necessary to take this splitting into account in the case of a ferromagnet-superconductor structure, where the interaction of the quasiparticle spin with the magnetization is of an exchange character and hence can be extremely large. Conservation of the electron-hole symmetry (that is, the symmetric positioning of their energies with respect to the Fermi level) causes an additional difference $\Delta p = I_0/v_F$ (I_0 is the exchange energy of the ferromagnet) in the momenta of the electron and hole components of the hybrid that drastically decreases the penetration length \mathcal{L}_e by orders of magnitude (in this case the penetration length is $L_{I_0} = \sqrt{\hbar D/I_0}$; Ref. 2). Such a shortening of the proximity effect has been actually observed in magnetic materials.^{3–7} On the other hand, measurements carried out in recent works^{8–11} demonstrate a long-range proximity effect in magnetic materials that is in an obvious contradiction with the general considerations discussed above. It has been pointed out⁹ that spin triplet fluctuations in the electron-hole correlations caused by the spin-orbit interaction and electron-impurity scattering¹² cannot (by two orders of magnitude) explain the large effect observed in Refs. 8–11.

The main message of this paper is that in magnetically inhomogeneous materials (such as multidomain ferromagnets (F), inhomogeneous “cryptoferromagnetic” states imposed by the superconductor,¹³ or F/S interfaces inducing electronic spin-flip processes),¹⁴ strong quantum fluctuations of the electron and hole spins make the proximity effect less sensitive to the spin selection rule that applies to Andreev reflections. As a result, a strong long-range, spin-triplet proximity effect in F/S structures persists on a length scale typical for nonmagnetic materials.¹ We estimate the conductance of such an F/S structure to be of the same order of magnitude as the conductance measured in experiments.^{8–11} Additional ex-

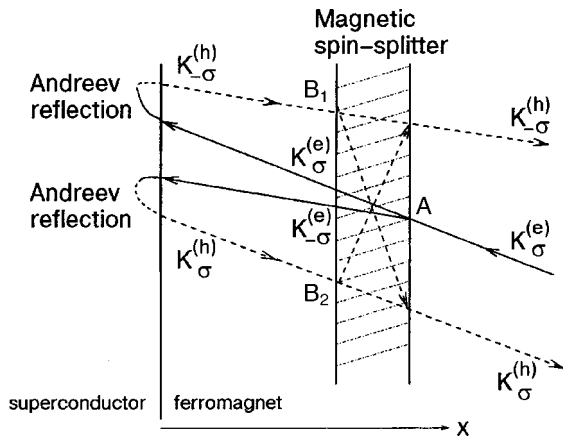


FIG. 1. Sketch of the composite scattering of an electron impinging on the interface between a magnetically inhomogeneous ferromagnet and a superconductor: Andreev reflection at the F/S interface is accompanied by spin-splitting scattering in the region of inhomogeneity (for clarity here assumed to be confined to a finite-width layer). As a result, the reflected hole is in a mixed state with both spin up and spin down components.

periments with intentionally introduced magnetic inhomogeneities are needed to check the predicted effect quantitatively.

A schematic illustration of Andreev reflection in the presence of a magnetic inhomogeneity is presented in Fig. 1. For convenience we consider the inhomogeneous magnetization of the material to be confined to a layer of finite width located close to the superconductor-ferromagnet interface. Such a layer serves as a magnetic spin-splitter for the incident electron (see Fig. 1). The composite scattering produced by the F/S boundary and the spin-splitter can then be separated into three scattering events: an incident electron with spin up crosses the inhomogeneous magnetic layer at point A and splits up into a coherent mixture of spin up (e, \uparrow) (see Fig. 1) and spin down (e, \downarrow) electronic states. These are subject to Andreev reflection at the F/S interface and are transformed into spin down (h, \downarrow) and spin up (h, \uparrow) hole states (see the dashed lines in Fig. 1). These two states encounter the magnetic scatterer again at points B_1 and B_2 , respectively, and experience further “spin-splitting.” The final result of the composite scattering process is that the incoming electron is reflected in two hole channels, one with spin up (h, \uparrow) and the other with spin down (h, \downarrow). One of the reflected hole channels has the same spin orientation as the incident electron.

Taking an alternative point of view, one may consider the time-reversed process wherein a Cooper pair propagates from the superconductor to the ferromagnet. Being in the singlet state at the moment of injection, the pair is then scattered into the triplet configuration by an inhomogeneously oriented magnetization in the ferromagnet. This singlet-triplet scattering is effective if the length scale of the inhomogeneity is of the order of L_{l_0} , the separation between the two Cooper pair electrons in the ferromagnet.

The above result of the two-channel magneto-Andreev scattering implies that the electron-hole correlation has a contribution that is unaffected by the magnetic exchange energy, which leads to a long-range “spin-triplet” proximity effect.

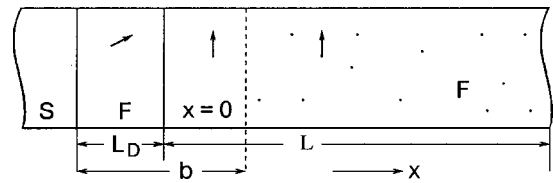


FIG. 2. Schematic view of an S/F structure with a magnetic domain wall at $x=0$, a distance L_D from the S/F interface. Impurity scattering is assumed to occur out of the ballistic region (to the right of the vertical dashed line).

2. FORMULATION OF THE PROBLEM

We consider the conductance of a ferromagnet-superconductor structure schematically shown in Fig. 2 for a special case when magnetic spin scattering occurs within a distance, L_D , from the S/F interface that is shorter than the electronic mean free path l_0 (that is, $L_D \ll l_0$). This allows us to consider the Andreev reflection at the interface to occur with unit probability and to describe the magnetic spin scattering using the semiclassical Eilenberger equation,¹⁷ which can be readily solved in the ballistic transport regime. Proper boundary conditions for matching the solution of the Eilenberger equation to the appropriate solution in the diffusive part of the ferromagnet can also be formulated in this model and used to solve the Usadel equation,¹⁸ which is the appropriate equation in the diffusive transport regime. In this way, the excess conductance of the F/S boundary can be calculated.

Solving the model problem described, we find that a new type of superconducting ordering, corresponding to the triplet spin correlations

$$F_{\sigma,\sigma}(\mathbf{r}; \varepsilon) = \int \langle \psi_{\sigma}(\mathbf{r}, t) \psi_{\sigma}(\mathbf{r}, 0) \rangle \exp\left(\frac{i\varepsilon t}{\hbar}\right) dt \quad (1)$$

(here $\sigma = \uparrow, \downarrow$), is the source of the proximity effect at distances of order $\mathcal{L}_T \gg L_{l_0}$, $\mathcal{L}_T \equiv \mathcal{L}_{\varepsilon} |_{\varepsilon = kT}$.

The Hamiltonian describing the system is written as follows:

$$\begin{aligned} \hat{H} = & \int d\mathbf{r} \{ \psi_{\alpha}^{+}(\mathbf{r}) (\hat{\mathbf{p}}^2/2m - eV(\mathbf{r})) \psi_{\alpha}(\mathbf{r}) \\ & + \Delta(\mathbf{r}) \psi_{\uparrow}^{+}(\mathbf{r}) \psi_{\downarrow}^{+}(\mathbf{r}) + \Delta^{*}(\mathbf{r}) \psi_{\downarrow}(\mathbf{r}) \psi_{\uparrow}(\mathbf{r}) \} \\ & + \mathbf{h}(\mathbf{r}) \sigma_{\alpha\beta} \psi_{\alpha}^{+}(\mathbf{r}) \psi_{\beta}(\mathbf{r}) \end{aligned} \quad (2)$$

where $V(\mathbf{r})$ is the electrical potential; $\hat{\sigma}$ are Pauli matrices; $\alpha, \beta = (\uparrow, \downarrow)$ and summation with respect to double indices is assumed; $\mathbf{h}(\mathbf{r}) = I_0 \mathbf{e}(\mathbf{r})$ is the inhomogeneous exchange energy in the ferromagnet ($\mathbf{e}(\mathbf{r})$ is a unit vector along the magnetization at point \mathbf{r}); the superconductor energy gap Δ and the ferromagnet exchange field \mathbf{h} have nonzero values in complementary space regions: $\Delta \neq 0, \mathbf{h} = 0$ in the superconductor and $\mathbf{h} \neq 0, \Delta = 0$ in the ferromagnet.

We start with the 4×4 correlation functions

$$\begin{aligned} \hat{G}^{<}(1, 1') &= i \langle \hat{\psi}^{+}(1) \hat{\psi}(1') \rangle; \hat{G}^{>}(1, 1') \\ &= -i \langle \hat{\psi}(1) \hat{\psi}^{+}(1') \rangle \end{aligned} \quad (3)$$

where $\hat{\Psi}^{+}(1) = (\Psi_{\uparrow}^{+}(1), \Psi_{\downarrow}(1), \Psi_{\downarrow}^{+}(1), \Psi_{\uparrow}(1))$ is the Nambu pseudo-spinor field (its variable is $1 \equiv (\mathbf{r}, t)$). Using the correlation functions Eq. (3) in the standard way (see,

e.g., the review article),¹⁹ one constructs the 8×8 Green's function in the 2×2 Keldysh and 4×4 Nambu spaces as follows:

$$\check{G} = \begin{pmatrix} \hat{G}^R & \hat{G}^K \\ \hat{0} & \hat{G}^A \end{pmatrix} \quad (4)$$

where $\hat{G}^{R,A,K}$ are retarded (R), advanced (A), and Keldysh (K) 4×4 matrix Green's functions which include both the singlet $\hat{G}_{\sigma,-\sigma}$ and triplet $\hat{G}_{\sigma,\sigma}$ components of the normal as well as anomalous Green's functions:

$$\hat{G}^R = \Theta(t_1 - t_1') (\hat{G}^>(1,1') - \hat{G}^<(1,1'))$$

$$\hat{G}^A = -\Theta(t_1' - t_1) (\hat{G}^>(1,1') - \hat{G}^<(1,1')) \quad (5)$$

$$\hat{G}^K = \hat{G}^>(1,1') + \hat{G}^<(1,1').$$

Using Eqs. (2)–(5), one gets the Eilenberger equation for the matrix quasi-classical Green's function in the Wigner representation,

$$\check{g}(\mathbf{n}, \mathbf{R}; \varepsilon) = (i/\pi) \check{\tau}_3 \int d\xi \check{G}(\mathbf{p}, \mathbf{R}; \varepsilon), \quad (6)$$

where the 8×8 matrix $\check{\tau}_3$ is represented in a compact notation of the tensorial product of Pauli matrices as $\check{\tau}_3 = \check{\sigma}_0 \otimes \hat{\sigma}_z \otimes \hat{\sigma}_0$; the integrand $\check{G}(\mathbf{p}, \mathbf{R}; \varepsilon)$ is the Fourier transform of the Green's function of Eq. (4) with respect to the coordinate and time differences; the space variable in the center-of-mass system is $\mathbf{R} = \mathbf{r} + \mathbf{r}'$; the vector \mathbf{n} is the unit vector along the momentum \mathbf{p} , and $\xi = p^2/2m - \varepsilon_F$. For reference we write out \hat{g}^α in full as follows:

$$\hat{g}^\alpha \equiv \begin{pmatrix} g_{\uparrow\uparrow}^\alpha & f_{\uparrow\downarrow}^\alpha & g_{\downarrow\downarrow}^\alpha & f_{\uparrow\uparrow}^\alpha \\ \bar{f}_{\uparrow\uparrow}^\alpha & \bar{g}_{\downarrow\downarrow}^\alpha & \bar{f}_{\downarrow\downarrow}^\alpha & \bar{g}_{\uparrow\uparrow}^\alpha \\ g_{\downarrow\uparrow}^\alpha & f_{\downarrow\downarrow}^\alpha & g_{\downarrow\downarrow}^\alpha & f_{\downarrow\uparrow}^\alpha \\ \bar{f}_{\uparrow\uparrow}^\alpha & \bar{g}_{\uparrow\downarrow}^\alpha & \bar{f}_{\downarrow\uparrow}^\alpha & \bar{g}_{\downarrow\uparrow}^\alpha \end{pmatrix} \quad (7)$$

where $\alpha = R, A, K$. The Eilenberger equation for $\check{g}(\mathbf{n}, \mathbf{R}; \varepsilon)$ reads

$$i v_F \mathbf{n} \frac{\partial}{\partial \mathbf{R}} \check{g} + [\varepsilon \check{\tau}_3 + \check{\Delta} + i \check{\sigma} - \check{h}, \check{g}] = 0, \quad (8)$$

where $[\check{A}, \check{B}] = \check{A}\check{B} - \check{B}\check{A}$; the impurity-induced self-energy $\check{\sigma}$ in the Born approximation is

$$\check{\sigma} = \frac{\pi}{2t_0} \int \frac{d\mathbf{n}}{4\pi} \check{g}(\mathbf{n}, \mathbf{R}, \varepsilon), \quad (9)$$

t_0 is the impurity scattering time; the pairing potential $\check{\Delta}$ that determines the electron-hole correlations and the operator $\check{h} = \check{h}_\perp + \check{h}_z$ that describes the effect of the inhomogeneous magnetic moment on the spins of electrons and holes can be written as

$$\begin{aligned} \check{\Delta} &= \hat{\sigma}_0 \otimes \hat{\sigma}_3 \otimes (\Delta^* \hat{\sigma}_- - \Delta \hat{\sigma}_+); \quad \hat{\sigma}_\pm = \hat{\sigma}_1 \pm i \hat{\sigma}_2; \\ \check{h}_\perp &= \hat{\sigma}_0 \otimes (h_x \hat{\sigma}_1 \otimes \hat{\sigma}_0 + h_y \hat{\sigma}_2 \otimes \hat{\sigma}_0); \\ \check{h}_z &= h_z \hat{\sigma}_0 \otimes \hat{\sigma}_3 \otimes \hat{\sigma}_3. \end{aligned} \quad (10)$$

In the ferromagnet at distances much greater than the mean free path l_0 (the dirty limit) the Eilenberger equation (8) reduces to the Usadel equation for the symmetric part of the Green's function $\check{G} \equiv \langle \check{g} \rangle$ ($\langle \dots \rangle$ denotes an average over the directions of the electron/hole momenta):

$$\check{G}^\alpha \equiv \begin{pmatrix} G_{\uparrow\uparrow}^\alpha & F_{\uparrow\downarrow}^\alpha & G_{\downarrow\downarrow}^\alpha & F_{\uparrow\uparrow}^\alpha \\ \bar{F}_{\uparrow\uparrow}^\alpha & \bar{G}_{\downarrow\downarrow}^\alpha & \bar{F}_{\downarrow\downarrow}^\alpha & \bar{G}_{\uparrow\uparrow}^\alpha \\ G_{\downarrow\uparrow}^\alpha & F_{\downarrow\downarrow}^\alpha & G_{\downarrow\downarrow}^\alpha & F_{\downarrow\uparrow}^\alpha \\ \bar{F}_{\uparrow\uparrow}^\alpha & \bar{G}_{\uparrow\downarrow}^\alpha & \bar{F}_{\downarrow\uparrow}^\alpha & \bar{G}_{\downarrow\uparrow}^\alpha \end{pmatrix}. \quad (11)$$

This equation reads as follows:

$$D \frac{d}{dx} \left(\check{G} \frac{d\check{G}}{dx} \right) + [(\varepsilon \check{\tau}_3 - \check{I}_0), \check{G}] = 0, \quad (12)$$

where $\check{I}_0 = I_0 \hat{\sigma}_0 \otimes \hat{\sigma}_3 \otimes \hat{\sigma}_3$; when writing Eq. (12) we took into account the fact that at distances $x \geq l_0$ from the boundary the ferromagnet is assumed to be homogeneous, with the magnetic moment parallel to the z axis ($h_z = I_0$). Here and below we also assume all quantities in the structure to vary only along the x axis which is perpendicular to the F/S interface.

3. BOUNDARY CONDITIONS FOR THE USADEL EQUATION

In order to find boundary conditions for the Usadel equation in the diffusive region we solve the Eilenberger equation (8) at distances $x \lesssim b \leq l_0$ (see Fig. 2), where the impurity scattering term ($\propto \check{\sigma}$) is negligible (we assume the superconductor to be pure as well; that is, $\xi_0 = \hbar v_F / |\Delta| \ll l_0$). In this case Eq. (8) reduces to the following linear equation:

$$i v_F n_x \frac{d}{dx} \check{g} + [(\varepsilon \check{\tau}_3 + \check{\Delta}(x) - \check{h}(x)), \check{g}] = 0. \quad (13)$$

Deep inside the superconductor ($x \rightarrow -\infty$) we use the conventional boundary conditions for the Eilenberger equation (8):

$$\begin{aligned} g_{\sigma,\sigma} &= \frac{\varepsilon}{\sqrt{\varepsilon^2 - |\Delta|^2}}, \quad f_{\sigma,-\sigma} = \frac{\Delta}{\sqrt{\varepsilon^2 - |\Delta|^2}}, \\ \bar{f}_{\sigma,-\sigma} &= -\frac{\Delta^*}{\sqrt{\varepsilon^2 - |\Delta|^2}}, \quad \bar{g}_{-\sigma,-\sigma} = -\frac{\varepsilon}{\sqrt{\varepsilon^2 - |\Delta|^2}}, \end{aligned} \quad (14)$$

$$g_{\sigma,-\sigma} = \bar{g}_{\sigma,-\sigma} = f_{\sigma,\sigma} = \bar{f}_{\sigma,\sigma} = 0.$$

As we consider the case that the transparency of the superconductor-ferromagnet interface is equal to 1 (that is the Andreev reflection takes place in the absence of the normal reflection) the boundary condition at the F/S interface $x = -L_D$ (see Fig. 2) is the continuity of Green's functions, that is

$$\check{g}(-L_D - 0) = \check{g}(-L_D + 0). \quad (15)$$

We solve the ballistic linear Eilenberger equation (13) in the superconductor, where $\mathbf{h} = 0$, $\Delta = \Delta_0$, and in the ferromagnet, where $\Delta = 0$, $\mathbf{h} = \mathbf{h}(x)$, matching the solutions at the F/S interface.

In order to find the solution in the ferromagnet one needs to know the detailed character of the magnetic inhomogene-

ity. A quantitative theory can be formulated only in case the magnetic structure is known in the experiment of interest. In the absence of any precise information about the magnetic structure of the samples used in existing experiments, we turn to illustrative examples of magnetic disorder and restrict ourselves to making only qualitative comparisons with experiments. We will consider two such examples.

1. The spin-splitting magnetic scattering is due to a multidomain structure with the magnetizations in the magnetic domain near the F/S interface (L_D region in Fig. 2) and in the rest of the ferromagnet being collinear but of opposite directions; the width L_{DW} of the domain wall between them is small compared with the ballistic magnetic length $L_h = \hbar v_F / I_0$. In this case the spin-flip takes place inside the domain wall with a probability amplitude proportional to the parameter $\lambda_D = L_{DW} / L_h$.

2. The magnetizations in the magnetic domain near the F/S interface and in the rest of the ferromagnet are noncollinear, with the domain wall between them of a negligible width. In this case the spin flip takes place due to Rabi oscillations in the L_D region, the probability amplitude of that being proportional to the noncollinearity of the magnetizations in the neighboring domains, $\lambda_R = \sqrt{h_x^2 + h_y^2} / I_0$.

Inserting dimensionless variables into Eq. (13), one sees that solutions of this equation in the ferromagnet region are controlled by the parameter λ_D for case 1 and by λ_R for case

2; this allows us to develop a perturbation theory in $\lambda_D \ll 1$ and $\lambda_R \ll 1$. Therefore, while solving this equation inside the ferromagnet we assume the probability of the spin-flip scattering to be small.

For both cases, rather simple but cumbersome perturbation-theory calculations show that far inside the ferromagnet, where the magnetization is already homogeneous but one is still in the ballistic region (at the distance b in Fig. 2), the retarded and advanced parts of the Green's function $\hat{g}^{(\alpha)}$, $\alpha = (R, A)$ can be written as follows:

$$\begin{aligned} \hat{g}_a^{(\alpha)}(b) &= \hat{\tau}_a \tilde{g}_s^\alpha(b) + \hat{\tau}_s \tilde{g}_a^\alpha(b) + (\hat{\tau}_s - \hat{1}) \text{sign } p_x \\ \hat{g}_s^{(\alpha)}(b) &= \hat{\tau}_s \tilde{g}_s^\alpha(b) + \hat{\tau}_a \tilde{g}_a^\alpha(b) + \hat{\tau}_a \text{sign } p_x \end{aligned} \quad (16)$$

where $\hat{g}_{a,s}^{(\alpha)} = \hat{g}^{(\alpha)}(p_x) \mp \hat{g}^{(\alpha)}(-p_x)$ are the antisymmetric and symmetric parts of the Green's functions:

$$\tilde{g}_{a,s}^\alpha = \begin{pmatrix} g_{\uparrow\uparrow}^{(a,s)} & 0 & g_{\uparrow\downarrow}^{(a,s)} & 0 \\ 0 & \bar{g}_{\downarrow\downarrow}^{(a,s)} & 0 & \bar{g}_{\downarrow\uparrow}^{(a,s)} \\ g_{\downarrow\uparrow}^{(a,s)} & 0 & g_{\downarrow\downarrow}^{(a,s)} & 0 \\ 0 & \bar{g}_{\uparrow\downarrow}^{(a,s)} & 0 & \bar{g}_{\uparrow\uparrow}^{(a,s)} \end{pmatrix},$$

where $g_{\sigma\sigma'}^{(a,s)} = 1/2(g_{\sigma\sigma'}(p_x) \pm g_{\sigma\sigma'}(-p_x))$; for the case $\varepsilon \ll |\Delta|$ the antisymmetric $\hat{\tau}_a$ and symmetric $\hat{\tau}_s$ matrices (which match the normal and anomalous components of the Green's function $\hat{g}^\alpha(b; p_x)$) are as follows:

$$\hat{\tau}_a = i \text{sign } p_x \begin{pmatrix} 0 & t_a \exp(i\varphi) & 0 & r_a \exp(i\varphi) \\ t_a \exp(-i\varphi) & 0 & -r_a \exp(-i\varphi) & 0 \\ 0 & -r_a^* \exp(i\varphi) & 0 & -t_a \exp(-i\varphi) \\ r_a^* \exp(-i\varphi) & 0 & -t_a \exp(-i\varphi) & 0 \end{pmatrix} \quad (17)$$

and

$$\hat{\tau}_s = \begin{pmatrix} 1 & t_s \exp(i\varphi) & 0 & r_s \exp(i\varphi) \\ -t_s \exp(-i\varphi) & 1 & r_s \exp(-i\varphi) & 0 \\ 0 & -r_s^* \exp(i\varphi) & 1 & t_s \exp(i\varphi) \\ -r_s^* \exp(-i\varphi) & 0 & -t_s \exp(-i\varphi) & 1 \end{pmatrix}. \quad (18)$$

Here $t_{sf} = it_a + t_s$ and $r_{sf} = ir_a + r_s$ are the probability amplitudes for an electron incident on the magnetically inhomogeneous region to be reflected back as a hole with the same and with the opposite direction of its spin, respectively ($|t_{sf}|^2 + |r_{sf}|^2 = 1$; see Fig. 1).

For the domains with collinear magnetization (case 1) one has

$$t_a \approx 1 - \frac{1}{2} \left(\frac{\pi L_{DW}}{L_h n_x} \right)^2, \quad r_a \approx 0; \quad t_s \approx 0, \quad r_s = \frac{\pi L_{DW}}{L_h |n_x|}. \quad (19)$$

For the domains with noncollinear magnetization (case 2) one has

$$t_a = -\cos \frac{2L_D}{|n_x| L_h}, \quad r_a \approx 0; \quad t_s = \frac{h_z^{(0)}}{l_0} \sin \frac{2L_D}{|n_x| L_h},$$

$$r_s = -\frac{h_+^{0*}}{l_0} \sin \frac{2L_D}{|n_x| L_h} \quad (20)$$

(Eqs. (19) and (20) are written for $1 \geq |n_x| \geq \pi L_{DW} / L_h$).

Equation (16) together with Eqs. (19), (20) show that spin-flip scattering at the magnetization inhomogeneity accompanied by Andreev reflection at the F/S interface produces a new triplet order parameter (Eq. (1) and a new normal singlet correlation function $G_{\sigma,-\sigma}$ proportional to the spin-flip probability amplitude r_{sf} . In contrast to the conventional singlet order parameter, this triplet order parameter does not decay exponentially at distances from the F/S interface greater than the magnetic length L_{I_0} in the diffusive ferromagnet. This fact can be proved for two cases: 1) $l_0 \ll L_h$, and 2) $l_0 \gg L_h$. In case 1) one neglects the terms quadratically small in $|r_{sf}| \ll 1$ in the Usadel equation (12) (that

is, if one neglects the terms quadratic in $F_{\sigma,\sigma}$ and $G_{\sigma,-\sigma}$ and their derivatives). In this case, for the “usual” components $F_{\sigma,-\sigma}^\alpha$ and $G_{\sigma,\sigma'}^\alpha$ one gets the conventional Usadel equation that shows exponential decay of $F_{\sigma,-\sigma}^\alpha$ at distances greater than L_{I_0} (Ref. 2). As for the $F_{\sigma,\sigma}^\alpha$ components, the equations for them show a slow variation of these components at such distances because these equations have no terms proportional to I_0 . The latter is a mathematical manifestation of the fact that these correlation functions are associated with such a scattering process under which the incident electron is transformed into a hole without changing the direction of the spin, and hence this electron-hole transformation requires no change in the magnetic energy (I_0) of the quasiparticles, as is qualitatively explained in the Introduction.

In case 2) ($l_0 \gg L_h$) at distances $x \gg l_0$ the Green's functions behave in the same way. In order to see this we start with solving the Eilenberger equation at distances $L_D \ll x \ll l_0$, where the equation is linear with constant coefficients. It is straightforward to see that the Green functions $F_{\sigma,-\sigma}^\alpha \propto \exp(ix/(L_h n_x))$, $G_{\sigma,-\sigma}^\alpha \propto \exp(ix/(L_h n_x))$, and hence they are rapidly oscillating functions of the momentum direction n_x at distances $x \gg L_h$. This means that the averaging with respect to the momentum direction results in their decay proportional to $L_h/x \ll 1$.² As to the Green's functions with the same direction of the spin variables ($G_{\sigma,\sigma}^\alpha$ and $F_{\sigma,\sigma}^\alpha$), they are slowly varying functions of the momentum direction, and they survive at such distances. Neglecting the rapidly oscillating components of the Green's function $\langle \hat{g}^{(\alpha)} \rangle$ averaged over the momentum direction (which are small in the parameter $L_h/x \ll 1$), one finds that only the triplet components are nonzero:

$$\langle \hat{g}^{(\alpha, \text{tr})} \rangle \equiv \hat{G}^{(\alpha, \text{tr})} = \begin{pmatrix} G_{\uparrow\uparrow}^{(\alpha)} & 0 & 0 & F_{\downarrow\downarrow}^{(\alpha)} \\ 0 & \bar{G}_{\downarrow\downarrow}^{(\alpha)} & \bar{F}_{\downarrow\downarrow}^{(\alpha)} & 0 \\ 0 & F_{\downarrow\downarrow}^{(\alpha)} & G_{\downarrow\downarrow}^{(\alpha)} & 0 \\ \bar{F}_{\uparrow\uparrow}^{(\alpha)} & 0 & 0 & \bar{G}_{\uparrow\uparrow}^{(\alpha)} \end{pmatrix}. \quad (21)$$

Using Eq. (21), one sees that nonlinear Eilenberger equation (8) splits into two sets of equations for the slowly varying components of the Green's function and the rapidly oscillating ones in the region $L_h/x \ll 1$. The latter are not of interest to us as at distances $x \gg l_0$ they decay exponentially; the matrix Eilenberger equation for the slowly varying components is as follows:

$$i v_F \mathbf{n} \frac{\partial}{\partial \mathbf{R}} \check{g}^{\text{tr}} + \left[\varepsilon \check{\tau}_3 + \frac{i}{t_0} \langle \check{g}^{\text{tr}}, \check{g}^{\text{tr}} \rangle \right] = 0, \quad (22)$$

where the reduced matrix Green function (see Eq. (7)) is

$$\hat{g}^{(\alpha, \text{tr})} = \begin{pmatrix} g_{\uparrow\uparrow}^{(\alpha)} & 0 & 0 & f_{\downarrow\downarrow}^{(\alpha)} \\ 0 & \bar{g}_{\downarrow\downarrow}^{(\alpha)} & \bar{f}_{\downarrow\downarrow}^{(\alpha)} & 0 \\ 0 & f_{\downarrow\downarrow}^{(\alpha)} & g_{\downarrow\downarrow}^{(\alpha)} & 0 \\ \bar{f}_{\uparrow\uparrow}^{(\alpha)} & 0 & 0 & \bar{g}_{\uparrow\uparrow}^{(\alpha)} \end{pmatrix}. \quad (23)$$

In the dirty limit, Eq. (22) reduces to a set of Usadel equations for the Green's functions $\check{G}^{(\alpha, \text{tr})}$ [see Eq. (21)] that reads

$$D \frac{d}{dx} \left(\check{G}^{(\text{tr})} \frac{d\check{G}^{(\text{tr})}}{dx} \right) + [\varepsilon \check{\tau}_3, \check{G}^{(\text{tr})}] = 0. \quad (24)$$

From the above considerations it follows that Eq. (22) and Eq. (24) are valid for the both cases $l_0 \ll L_h$ and $l_0 \gg L_h$.

We obtain the boundary conditions for Eq. (24) at distances from the F/S interface of the order of l_0 ($l_0 \gg L_D$) for the case $\hbar v_F / \varepsilon \gg l_0$ that permits us to neglect the term proportional to ε in the Eilenberger equation (22) and rewrite it as the following equation:²⁰

$$v_F t_0 \mathbf{n} \frac{\partial}{\partial \mathbf{R}} \check{g}_a^{\text{tr}} = \check{g}_a^{\text{tr}} \langle \check{g}_s^{\text{tr}} \rangle - \check{g}_s^{\text{tr}} \langle \check{g}_a^{\text{tr}} \rangle, \quad (25)$$

where

$$\check{g}_{s(a)}^{\text{tr}} = \frac{1}{2} (\check{g}^{\text{tr}}(p_x) \pm \check{g}^{\text{tr}}(-p_x)).$$

Averaging Eq. (25) over the momentum direction, one sees that $C = \langle n_x \check{g}^{\text{tr}} \rangle$ does not depend on x .²⁰ Using this fact, Eqs. (16), (18), and (21), and the relation $\check{g}^{\text{tr}} = l_0 \check{G}^{(\text{tr})} \nabla \check{G}^{(\text{tr})}$ which couples the isotropic Usadel functions and the anisotropic one at distances greater than l_0 , one gets the desired effective boundary conditions for the Usadel equation (24) at $x \approx 0$ (that is in the vicinity of the magnetically inhomogeneous region adjacent to the F/S interface) as follows:

$$\frac{d}{dx} F_{\sigma,\sigma}^{(\alpha, \text{tr})} \Big|_{x=0} = \sigma \frac{v_F}{D} e^{i\varphi} \langle |n_x| r^s \rangle. \quad (26)$$

The exchange energy I_0 does not appear in Eqs. (22), (24) as these equations contain only triplet normal and anomalous Green's functions: formally this set of equations is the same as for a nonmagnetic conductor-superconductor diffusive structure if one changes the triplet anomalous Green's functions to the singlet ones and uses the boundary conditions (26). From here it obviously follows that the spin-flip scattering due to magnetic inhomogeneity accompanied by Andreev reflection produces a new (triplet) order parameter (1) (see also Eq. (7)) that decays at distances from F/S interface of the same order of magnitude as in nonmagnetic metal-superconductor structures, $L_\varepsilon = \sqrt{\hbar D / \varepsilon}$, producing a long-range proximity effect in the ferromagnet. In the next Section we solve the Usadel equation (24) using boundary conditions (26) and find the conductance of such a structure.

4. SOLUTION OF THE EFFECTIVE USADEL EQUATION AND THE CONDUCTANCE OF THE STRUCTURE

The current flowing through the structure under consideration can be written as follows (see, e.g., Refs. 22, and 23)

$$j = \frac{\sigma_N}{2e} \int \text{Tr} \hat{\sigma}_z \left(\hat{G}^{(R, \text{tr})} \frac{d\hat{G}^{(K, \text{tr})}}{dx} + \hat{G}^{(K, \text{tr})} \frac{d\hat{G}^{(A, \text{tr})}}{dx} \right) d\varepsilon \quad (27)$$

where σ_N is the conductivity of the normal metal; $\hat{\sigma}$ is a 4×4 matrix $\hat{\sigma}_0 \otimes \sigma_z$.

According to the relation^{17,21}

$$\check{G}^{(\text{tr})} \check{G}^{(\text{tr})} = \check{I} \quad (28)$$

the Keldysh function $\hat{G}^{(K, \text{tr})}$ reads

$$\hat{G}^{(k, \text{tr})} = \hat{G}^{(R, \text{tr})} \hat{q} - \hat{q} \hat{G}^{(A, \text{tr})} \quad (29)$$

where \hat{q} is a diagonal matrix

$$\hat{q} = \begin{pmatrix} q_{\uparrow 1} & 0 & 0 & 0 \\ 0 & q_{\downarrow 2} & 0 & 0 \\ 0 & 0 & q_{\downarrow 3} & 0 \\ 0 & 0 & 0 & q_{\uparrow 4} \end{pmatrix}, \quad (30)$$

while the components of retarded and advanced Green's functions (21) satisfy the relations

$$G_{\sigma, \sigma}^{(\gamma, \text{tr})} G_{\sigma, \sigma}^{(\gamma, \text{tr})} + F_{\sigma, \sigma}^{(\gamma, \text{tr})} \bar{F}_{\sigma, \sigma}^{(\gamma, \text{tr})} = 1; \quad (31)$$

$$G_{\sigma, \sigma}^{(\gamma, \text{tr})} = -\bar{G}_{\sigma, \sigma}^{(\gamma, \text{tr})}$$

($\gamma = R, A$). Matrix \hat{q} together with $\hat{G}^{(R, \text{tr})}$ satisfies matrix equation (24).

Following the reasoning of Ref. 1 and using Eqs. (27)–(30), one can rewrite Eq. (27) for the current as follows:

$$j = \frac{\sigma_N}{32} \int d\varepsilon \sum_{\sigma} (f_{\sigma}(L) - f_{\sigma}(0)) \frac{1}{m_{\sigma}(L)}, \quad (32)$$

where $f_{\sigma}(x)$ is the distribution function for electrons with spin $\sigma = (\uparrow, \downarrow)$, and

$$m_{\sigma}(\varepsilon) = \int_0^L \frac{dx}{1 - G_{\sigma}^{(R, \text{tr})} \hat{G}_{\sigma}^{(A, \text{tr})} - F_{\sigma}^{(R, \text{tr})} \bar{F}_{\sigma}^{(A, \text{tr})}}. \quad (33)$$

Therefore, the current is determined by $\hat{G}^{(R, \text{tr})}$, the triplet Green's functions of which for normal pairing $G_{\sigma, \sigma}^R, \bar{G}_{\sigma, \sigma}^R$ and anomalous pairing $F_{\sigma, \sigma}^R, \bar{F}_{\sigma, \sigma}^R$ can be parameterized (see Eq. (31)) in the standard way as follows:

$$\hat{G}_{\sigma, \sigma}^R = \begin{pmatrix} \cosh(\Theta_{\sigma}) & \sinh(\Theta_{\sigma}) \exp(i\chi_{\sigma}) \\ -\sinh(\Theta_{\sigma}) \exp(-i\chi_{\sigma}) & -\cosh(\Theta_{\sigma}) \end{pmatrix}, \quad (34)$$

where Θ_{σ} and χ_{σ} are complex functions; the function χ_{σ} does not contribute to the conductance (see Eq. (37) below).

Using the parameterization (34) and Eqs. (24) and (26), one gets both the Usadel equation and its boundary conditions as

$$\hbar D \frac{d^2 \Theta_{\sigma}}{dx^2} - 2i\varepsilon \Theta_{\sigma} = 0, \quad (35)$$

$$\left. \frac{d}{dx} \Theta_{\sigma} \right|_{x=0} = \sigma \frac{v_F}{D} |\langle |n_x| r_s \rangle|. \quad (36)$$

Here r_s is the magnetic spin-flip scattering amplitude [see Eq. (19), (20)]. Equations (35) and (36) are linear due to the smallness of the amplitude for magnetic spin-flip scattering, $|r_s| \ll 1$, and are valid in the temperature interval $k_B T \ll \Delta$, which includes the Thouless energy $k_B T_{\text{Th}} = \hbar D / L^2 \ll \Delta$.

In order to calculate the conductance we follow Ref. 1 and find that the excess conductance can be written as

$$\frac{\delta G}{G_0} = -\frac{1}{16T} \sum_{\sigma=-1}^1 \int_{-\infty}^{\infty} d\varepsilon \frac{\partial f_0}{\partial \varepsilon} \left[\frac{1}{L} \int_0^L dx (\text{Re } \Theta_{\sigma})^2 \right], \quad (37)$$

where G_0 is the conductance of the ferromagnetic part of the structure; $f_0(\varepsilon)$ is the Fermi distribution.

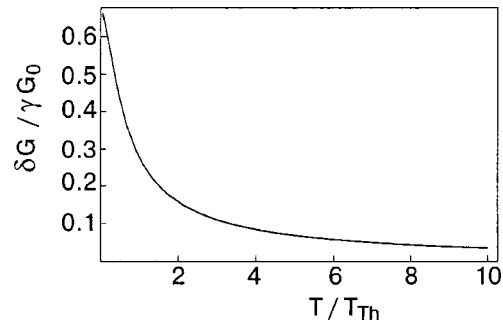


FIG. 3. Temperature dependence of the normalized excess conductance (see Eqs. (39) and (40)).

The solution of the Usadel equation (35) with the boundary condition given by Eq. (36) at $x=0$ and by $\Theta_{\sigma}=0$ at $x=L$, is

$$\Theta_{\sigma} = \sigma \frac{v_F |\langle |n_x| r_s \rangle| \sinh[k(\varepsilon)(x-L)]}{Dk(\varepsilon) \cosh(k(\varepsilon)L)}, \quad (38)$$

$$k(\varepsilon) = (1+i) \sqrt{\varepsilon / \hbar D}.$$

Equation (38) shows that the superconducting correlations due to the spin-splitting processes in the magnetic inhomogeneous region decay exponentially in the ferromagnet and vanish at distances of order $L_T = \sqrt{\hbar D / k_B T}$ (for energies $\varepsilon \sim k_B T$), corresponding to the superconducting correlation length in nonmagnetic materials.

Inserting Eq. (38) into Eq. (37), one obtains an excess conductance that can be expressed as

$$\delta G / G_0 = \gamma f(T / T_{\text{Th}}), \quad (39)$$

where

$$\gamma = |\langle |n_x| r_s \rangle|^2 (L / l_0)^2$$

and $f(T / T_{\text{Th}})$ is a dimensionless function, the temperature dependence of which is presented in Fig. 3:

$$f(x) = \frac{1}{x} \int_0^{\infty} dt \cosh^{-2}(t^2 / 2x) \times \left(\text{Re} \frac{\sinh[2(1+i)t] - 2(1+i)t}{4(i-1)t^2 \cosh^2[(1+i)t]} + \frac{\sinh 2t - \sin 2t}{4t^2 |\cosh(1+i)t|^2} \right). \quad (40)$$

Using experimental values of the parameters taken from Ref. 10, $D = 100 \text{ nm}^2/\text{s}$ and $T / T_{\text{Th}} = 50$, and making the reasonable assumption that $r_{sf} \sim 0.1$, we find that our result for the excess resistance, $\delta R \approx -10 \Omega$, is in agreement with the experiment. The temperature dependence of the excess conductance in the range $T \sim T_{\text{Th}}$ is shown in Fig. 3. For higher temperatures, $T \sim \Delta / k_B \gg T_{\text{Th}} = \hbar D / (k_B L^2)$, our theory is not valid, and contributions of order $k_B T / \Delta \sim 1$ can modify the temperature dependence of the resistance. Additional measurements around the Thouless temperature (where the proximity effect is most pronounced) would permit a comparison with the temperature dependence coming from the long-range proximity effect described by our theory. However, additional investigations of the magnetic structure of the F/S interface are needed to carry out a complete comparison with

the theory. Multidomain ferromagnets suitable for these studies can be created in various ways. It was recently demonstrated²⁴ that grain boundaries, magnetic inhomogeneities (including domains with nonparallel magnetization) can be introduced in a predetermined position in a ferromagnet film by controlling the epitaxial growth. Experiments in which such magnetic inhomogeneities are intentionally created would permit long-range proximity effects to be studied in well-characterized ferromagnet—superconductor structures.

In conclusion, we have shown that spin-splitting scattering related to magnetic inhomogeneities modifies the spin-selection rule governing Andreev reflections at a ferromagnetic normal metal-superconductor interface. As a result a long-range proximity effect, due to correlations between spin-aligned electrons and holes, appears (a spin-triplet proximity effect). Estimations of the value of the excess conductance are consistent with experiments.^{8–11} For applications, an important consequence of this phenomenon is that the proximity effect can be stimulated by orders of magnitude by intentionally produced magnetic inhomogeneity in the sample.

We acknowledge useful discussions with E. V. Bezuglyi and Z. G. Ivanov. We are grateful to Z. G. Ivanov for calling to our attention experimental possibilities for observing the effect predicted by our theory.

*E-mail: kadig@kam.kharkov.ua

¹⁾A short formulation of this prediction was published as a Letter in Ref. 15. Analogous prediction based on a somewhat different approach was simultaneously made in Ref. 16.

¹C. J. Lambert and R. Raimondi, *J. Phys.: Condens. Matter* **10**, 901 (1998).

²E. A. Demler, G. B. Arnold, and M. R. Beasley, *Phys. Rev. B* **55**, 15174 (1997).

³K. Kawaguchi and M. Sohma, *Phys. Rev. B* **46**, 14722 (1992).

⁴J. S. Jiang, D. Davidovic, D. H. Reich, and C. L. Chien, *Phys. Rev. Lett.* **74**, 314 (1995).

⁵R. J. Soulen Jr., J. M. Byers, M. S. Osofsky, B. Nadgorny, T. Ambrose, S. F. Cheng, P. R. Broussard, C. T. Tanaka, J. Nowak, J. S. Moodera, and J. M. D. Coey, *Science* **282**, 85 (1998).

⁶A. M. Goldman, V. Vas'ko, P. Kraus, and K. Nikolaev, *J. Magn. Magn. Mater.* **200**, 69 (1999).

⁷L. Lazar, K. Westerholt, H. Zabel, L. R. Tagirov, Yu. V. Goryunov, N. N. Garif'yanov, and I. A. Garifulin, *Phys. Rev. B* **61**, 3711 (2000).

⁸V. T. Petrashov, I. A. Sosnin, I. Cox, A. Parson, and C. Troadec, *Phys. Rev. Lett.* **83**, 3281 (1999).

⁹V. T. Petrashov, I. A. Sosnin, I. Cox, A. Parson, and C. Troadec, *J. Low Temp. Phys.* **118**, 689 (2000).

¹⁰M. D. Lawrence and N. Giordano, *J. Phys.: Condens. Matter* **8**, L563 (1996).

¹¹M. Giroud, H. Courtois, K. Hasselbach, D. Maily, and B. Pannetier, *Phys. Rev. B* **58**, R11872 (1998).

¹²F. Zhou and B. Spivak, *cond-mat/9906177*.

¹³F. S. Bergeret, K. B. Efetov, and A. I. Larkin, *Phys. Rev. B* **62**, 11872 (2000).

¹⁴J.-X. Zhu and C. S. Ting, *Phys. Rev. B* **61**, 1456 (2000).

¹⁵A. Kadigrobov, R. I. Shekhter, and M. Jonson, *Europhys. Lett.* **54**, 394 (2001); *cond-mat/00124347*.

¹⁶F. S. Bergeret, A. F. Volkov, and K. B. Efetov, *Phys. Rev. Lett.* **86**, 4096 (2001); *cond-mat/0011425*.

¹⁷G. M. Eilenberger, *Z. Phys.* **214**, 195 (1968).

¹⁸K. D. Usadel, *Phys. Rev. Lett.* **25**, 507 (1970).

¹⁹J. Rammer and H. Smith, *Rev. Mod. Phys.* **58**, 323 (1986).

²⁰M. Yu. Kuprianov and V. F. Lukichev, *Zh. Éksp. Teor. Fiz.* **94**, 139 (1988) [*Sov. Phys. JETP* **67**, 1163 (1988)].

²¹A. I. Larkin and Yu. N. Ovchinnikov, *Zh. Éksp. Teor. Fiz.* **68**, 1915 (1975); **73**, 299 (1977) [*Sov. Phys. JETP* **41**, 960 (1975); *ibid.* **46**, 155 (1977)].

²²W. Belzig, F. K. Wilhelm, C. Bruder, G. Schön, and A. D. Zaikin, *Superlattices Microstruct.* **25**, 1252 (1999).

²³E. V. Bezuglyi, E. N. Bratus' and V. P. Galaiko, *Fiz. Nizk. Temp.* **25**, 230 (1999) [*Low Temp. Phys.* **25**, 167 (1999)].

²⁴R. Mathieu, P. Svedlindh, R. A. Chakalov, and Z. G. Ivanov, *Phys. Rev. B* **62**, 3333 (2000).

This article was published in English in the original Russian journal. Reproduced here with stylistic changes by AIP.

Formation of *d*-wave superconducting order in a randomly doped lattice

V. M. Loktev* and Yu. G. Pogorelov

Bogolyubov Institute for Theoretical Physics of the National Academy of Science of Ukraine, 14b, Metrologichna Str., Kiev, 03143, Ukraine; CFP and Departamento de Física da Faculdade de Ciências da Universidade do Porto, Rua do Campo Alegre, 687, 4169-007 Porto, Portugal

(Submitted May 14, 2001)

Fiz. Nizk. Temp. **27**, 1039–1052 (September–October 2001)

We consider the interplay between superconducting coupling and dopant impurity scattering of charge carriers in planar square lattice systems and examine the physical conditions (doping level, temperature, local symmetry of coupling and scattering potentials) necessary in this model system to obtain a *d*-wave superconducting order, like that observed in real doped cuprate HTSC materials. Using the Lifshitz model for the disorder introduced into the system by dopants, we analyze also the nonuniform structure of such a *d*-wave parameter, including both its magnitude and phase variation. The results indicate that *d*-wave superconductivity becomes possible in a doped metal until it is destroyed at too high doping levels. © 2001 American Institute of Physics. [DOI: 10.1063/1.1401186]

1. INTRODUCTION

Studies of the effect of impurities and defects on superconducting (SC) properties of metals (including SC alloys) began practically as early as the BCS theory had been constructed. In particular, the classical papers by Anderson¹ and by Abrikosov and Gor'kov² indicated a substantial difference between magnetic and nonmagnetic impurities in superconductors. While the addition of nonmagnetic impurities has practically no effect on the value of the transition critical temperature T_c , the presence of spin on the impurity atom (leading to the Kondo effect in a normal metal) results in pair-breaking, that is, it transforms a singlet Cooper pair into an unstable triplet and rapidly suppresses T_c . All of the known studies have considered the *s*-type, or isotropic, SC order (apart from heavy-fermion systems, where it is the *p*-type order and T_c is extremely low) and, correspondingly, an isotropic gap near the Fermi level.

The discovery of high- T_c superconductivity (HTSC) in copper oxides confronted physicists with a number of problems which still remain a challenge for the theory. Undoubtedly, this includes the issue of the HTSC mechanism, the strong dependences of many (both SC and normal) properties of copper oxides on the charge-carrier concentration, the specifics of weakly doped systems (first of all, the existence of a pseudogap at temperatures above T_c), the formation of stripe structures, etc. (see, e.g., the review articles).^{3–6} Such a problem is also presented by the impurity effect on the SC properties of HTSC systems. These differ from the “old” or “conventional” superconductors not only in their higher T_c and the *d*-wave anisotropy of their order parameter but also in the fact that here magnetic and nonmagnetic impurities change their roles: the former are weak suppressors of T_c (Refs. 7 and 8), while the latter (in particular, Zn substituting for Cu in cuprate layers) lead to a fast decay of HTSC.^{7,10,11} Many aspects of impurity effects in superconductors with anisotropic (including *d*-wave) pairing have already been studied theoretically in Refs. 12–17, using a range of models and approximations. However, these (and many other) papers

did not include one of the most essential features of HTSC systems: the fact that they cannot be non-impure.

In other words, most of theoretical approaches to HTSC are based on the concept formulated and applied in the aforementioned pioneering works:^{1,2} one starts from an ideal (2D or quasi-2D) metal with a given Fermi energy ε_F , defined by the density of free carriers, and then considers the perturbation of an independently existing SC condensate by some extrinsic (magnetic or nonmagnetic) impurities. Their action, local or global, affects the preformed and condensed singlet pairs. Of course, this formulation is reasonable but it lacks an essential element for the conductance in copper oxides: almost all HTSCs are doped metals, where (like the doped semiconductors) each carrier is provided by insertion of a donor or acceptor into the system. In turn, this implies that HTSCs are intrinsically impure systems with an inherent disorder,¹⁾ and the number of impurity (“foreign” included) atoms can not be less than the number of charge carriers, at least. While in normal metals one has the condition $k_F l \gg 1$ (k_F is the Fermi momentum, and l is the carrier mean free path between collisions with impurity atoms),¹⁸ it turns to $k_F l \sim 1$ in HTSCs, and they belong to the family of “bad” metals with both k_F and l determined by the doping.

Perhaps the first attempt to consider in a self-consistent way the characteristic tendencies for HTSC, pairing of the carriers and their localization on impurity atoms, was made in the authors' previous paper.¹⁹ It discussed the phase diagram of doped 2D metal in presence of *s*-wave pairing and showed that SC is possible neither at low impurity concentrations $c < c_0 \sim \varepsilon_0/W$ (when all the carriers are localized near impurities with localization energies ε_0 much less than the bandwidth W , so that c_0 is typically few percent) nor at too high c (when the pair inverse lifetime times \hbar exceeds the SC gap). There, in general, the self-consistency is related either to the SC order parameter (like the common Bardeen-Cooper-Schrieffer or Bogolyubov-de Gennes treatments) and to the chemical potential.

The present work is aimed at extending the approach of

Ref. 19 to the case of d -wave SC coupling and to trace the formation of the corresponding order parameter. It is motivated, not least, by an apparent controversy between the experimental evidence for d -symmetry of the order parameter in HTSCs^{20–22} and the theoretical claim that anisotropic pairing should not survive in the presence of chaotically distributed isotropic scatterers.²³ For the sake of simplicity, we restrict consideration to the doping range $c > c_0$, where the self-consistency is only relevant for the SC order parameter, while the chemical potential can be put in the form²⁾ $\mu \approx \varepsilon_F \approx 3cW/4$. Then we distinguish between two types of impurity effects by doping. The first, the so-called *homogeneous effects*, are displayed by translationally invariant *single-particle* Green functions (SPGFs). They have been studied earlier by various means²⁴ but, as a rule, by introducing the disorder through a single parameter V_A of Anderson's model.²⁴ In contrast, we employ Lifshitz's model of disorder,²⁵ characterized by two independent parameters: c and the impurity potential V_L . They produce an equivalent $V_A \sim \sqrt{c(1-c)}V_L$, but not vice versa. Within this model, more adequate for doped HTSC systems, we conclude the persistence of the d -wave order parameter under homogeneous impurity effects. Also we explicitly consider the other type of effects, *inhomogeneous*, due to local variations of the order parameter near impurity centers. This involves *two-particle* Green functions (TPGFs) besides the usual SPGFs, and yields a possible limitation on SC at high enough dopant concentrations.

At least, we would like to acknowledge the great honor and pleasant opportunity for us to publish this paper in the Low Temperature Physics issue dedicated to the memory of the outstanding physicist L. V. Shubnikov, whose contribution to low-temperature physics in general and to superconductivity in particular cannot be overestimated.

2. HAMILTONIAN AND GREEN FUNCTIONS

We start from the model electronic Hamiltonian in the band representation,

$$H = \sum_{\mathbf{k}} \left\{ \sum_{\sigma} \varepsilon_{\mathbf{k}} c_{\mathbf{k},\sigma}^+ c_{\mathbf{k},\sigma} - \frac{1}{N} \sum_{\mathbf{k}'} \left[V \gamma_{\mathbf{k}} \gamma_{\mathbf{k}'} c_{\mathbf{k},\uparrow}^+ n_{-\mathbf{k},\downarrow}^+ c_{-\mathbf{k}',\downarrow} c_{\mathbf{k}',\uparrow} - V_L \sum_{\mathbf{p},\sigma} e^{i(\mathbf{k}'-\mathbf{k})\cdot\mathbf{p}} c_{\mathbf{k}',\sigma}^+ c_{\mathbf{k},\sigma} \right] \right\}, \quad (1)$$

where $c_{\mathbf{k},\sigma}$ and $c_{\mathbf{k},\sigma}^+$ the Fermi operators for a charge carrier with wave vector \mathbf{k} and spin σ . The simplest band energy $\varepsilon_{\mathbf{k}} = 4t - 2t(\cos ak_x + \cos ak_y)$, with full bandwidth $W = 8t$, is expressed through the amplitude t of carrier hopping between nearest-neighbor sites.³⁾ (of the total N in the lattice, with a lattice constant a). The parameter V models the attraction between two carriers with opposite spins on such sites, the factor $\gamma_{\mathbf{k}} = (\cos ak_x - \cos ak_y)\theta(\varepsilon_D^2 - \xi_{\mathbf{k}}^2)$ has d -wave symmetry and is effective only for quasiparticle energies $\xi_{\mathbf{k}} = \varepsilon_{\mathbf{k}} - \varepsilon_F$ smaller than the “Debye energy” ε_D . The latter is understood as a characteristic energy of the intermediate (Frölich) boson, and in what follows we suppose the condi-

tion $\varepsilon_D < \mu$ to hold and a BCS shell to exist (the alternative $\mu < \varepsilon_D$, possible for underdoped HTSC systems, will be considered elsewhere). The impurity perturbation V_L expresses the shift of the on-site electronic energy at a random dopant site \mathbf{p} , where the negative sign takes explicit account of the carrier attraction to the ionized dopant, and, for simplicity, we consider this perturbation localized on a single site. With the usual BCS ansatz: $c_{-\mathbf{k},\downarrow} c_{\mathbf{k},\uparrow} = \langle c_{-\mathbf{k},\downarrow} c_{\mathbf{k},\uparrow} \rangle + \varphi_{\mathbf{k}}$, and in neglect of terms quadratic in the pair fluctuations $\varphi_{\mathbf{k}}$, Eq. (1) leads to a bilinear form $H' = H - \mu N$:

$$H' = \sum_{\mathbf{k}} \left[\sum_{\sigma} \xi_{\mathbf{k}} c_{\mathbf{k},\sigma}^+ c_{\mathbf{k},\sigma} - (\Delta_{\mathbf{k}} c_{-\mathbf{k},\downarrow} c_{\mathbf{k},\uparrow} + \text{h.c.}) - \frac{V_L}{N} \sum_{\mathbf{p},\mathbf{k}',\sigma} e^{-i(\mathbf{k}'-\mathbf{k})\cdot\mathbf{p}} c_{\mathbf{k}',\sigma}^+ c_{\mathbf{k},\sigma} \right]. \quad (2)$$

Here the gap function is defined by the self-consistency relation

$$\Delta_{\mathbf{k}} = \frac{V\gamma_{\mathbf{k}}}{N} \sum_{\mathbf{k}'} \gamma_{\mathbf{k}'} \langle c_{\mathbf{k}',\uparrow} c_{-\mathbf{k}',\downarrow} \rangle, \quad (3)$$

extending the common BCS gap equation to the d -wave case. A nonuniform system can be treated within the formalism used formerly for impurity problems in SC^{14,19} by passing to the Nambu spinors $\psi_{\mathbf{k}}^+ = (c_{\mathbf{k},\uparrow}^+, c_{-\mathbf{k},\downarrow})$ and $\psi_{\mathbf{k}}$ and defining the Fourier-transformed matrix Green function (GF)

$$\hat{G}_{\mathbf{k},\mathbf{k}'}(\varepsilon) \equiv \langle\langle \Psi_{\mathbf{k}} | \Psi_{\mathbf{k}'}^+ \rangle\rangle_{\varepsilon} = \int_{-\infty}^0 e^{i(\varepsilon-i0)t} \langle\langle \Psi_{\mathbf{k}}(t) | \Psi_{\mathbf{k}'}^+(0) \rangle\rangle dt. \quad (4)$$

Here \hat{A} denotes a 2×2 matrix in Nambu indices, $\langle\langle \dots \rangle\rangle$ is the quantum statistical average, and $\{a(t), b(0)\}$ is the anticommutator of Heisenberg operators. In the GFs below we omit their explicit dependence on energy ε but distinguish between their diagonal and nondiagonal forms in the Nambu (N) and momentum (M) indices. Then, applying the Heisenberg equation of motion $i\hbar \partial \psi_{\mathbf{k}} / \partial t = [H', \psi_{\mathbf{k}}]$ in Eq. (4), we arrive at an equation of motion of the Dyson type for the SPGFs:

$$\hat{G}_{\mathbf{k},\mathbf{k}'} = \hat{G}_{\mathbf{k}}^{(0)} \delta_{\mathbf{k},\mathbf{k}'} - \hat{G}_{\mathbf{k}}^{(0)} \hat{V} \sum_{\mathbf{p},\mathbf{k}''} e^{i(\mathbf{k}-\mathbf{k}'')\cdot\mathbf{p}} \hat{G}_{\mathbf{k}'',\mathbf{k}'} \quad (5)$$

where the unperturbed SPGF $\hat{G}_{\mathbf{k}}^{(0)} = (\varepsilon - \xi_{\mathbf{k}} \hat{\tau}_3 - \Delta_{\mathbf{k}} \hat{\tau}_1 + i0)^{-1}$, and the scattering matrix $\hat{V} = V_L \hat{\tau}_3$ includes the Pauli matrices $\hat{\tau}_i$.

For a disordered system, the relevant (observable) characteristics are described by the so-called self-averaging GFs, whose values for all particular realizations of disorder turn practically nonrandom, equal to those averaged over disorder.²⁶ The most important example of such a function is the M-diagonal SPGF, $\hat{G}_{\mathbf{k}} \equiv \hat{G}_{\mathbf{k},\mathbf{k}}$. The general solution for Eq. (5) in this case can be written (see Appendix E) as

$$\hat{G}_{\mathbf{k}} = \{[\hat{G}_{\mathbf{k}}^{(0)}]^{-1} - \hat{\Sigma}_{\mathbf{k}}\}^{-1}, \quad (6)$$

where the self-energy matrix $\hat{\Sigma}_{\mathbf{k}}$ is given by the so-called fully renormalized group expansion (GE)^{14,19,27,28}

$$\hat{\Sigma}_{\mathbf{k}} = -c \hat{V} [1 + \hat{G} \hat{V}]^{-1} \times \left\{ 1 + c \sum_{\mathbf{n} \neq 0} [\hat{A}_{0\mathbf{n}} e^{-i\mathbf{k} \cdot \mathbf{n}} + \hat{A}_{0\mathbf{n}} \hat{A}_{\mathbf{n}0}] [1 - \hat{A}_{0\mathbf{n}} \hat{A}_{\mathbf{n}0}]^{-1} + \dots \right\}. \quad (7)$$

Here the integrated SPGF matrix $\hat{G} = N^{-1} \sum_{\mathbf{k}} \hat{G}_{\mathbf{k}}$, and the matrices $\hat{A}_{0\mathbf{n}}$ of indirect interaction between scatterers at sites 0 and \mathbf{n} are

$$\hat{A}_{0\mathbf{n}} = -\hat{V} \sum_{\mathbf{k}' \neq \mathbf{k}} e^{i\mathbf{k}' \cdot \mathbf{n}} \hat{G}_{\mathbf{k}'} [1 + \hat{G} \hat{V}]^{-1}. \quad (8)$$

The restriction to $\mathbf{k}' \neq \mathbf{k}$ in the single summation in $\hat{A}_{0\mathbf{n}}$ should be complemented by $\mathbf{k}'' \neq \mathbf{k}, \mathbf{k}'$ for double summation in the product $\hat{A}_{0\mathbf{n}} \hat{A}_{\mathbf{n}0}$, but such restrictions can be ignored in $\hat{A}_{0\mathbf{n}} \hat{A}_{0\mathbf{n}} \hat{A}_{\mathbf{n}0}$ and the higher-degree terms²⁷ resulting from expansion of the right-hand side of Eq. (7).

Many observable characteristics of the SC state follow from the GFs, in the spectral theorem representation

$$\langle ab \rangle = \int_{-\infty}^{\infty} \frac{d\varepsilon}{e^{\beta(\varepsilon - \mu)} + 1} \text{Im} \langle \langle b|a \rangle \rangle_{\varepsilon}, \quad \beta = \frac{1}{T}, \quad (9)$$

where the chemical potential μ is defined by the overall electron concentration

$$c = \frac{1}{N} \sum_{\mathbf{k}} \int_{-\infty}^{\infty} \frac{d\varepsilon}{e^{\beta(\varepsilon - \mu)} + 1} \text{Im Tr} \hat{\tau}_3 \hat{G}_{\mathbf{k}}. \quad (10)$$

On the other hand, c is just the concentration of dopant centers which give rise to carrier scattering: $c = N^{-1} \sum_{\mathbf{p}} 1$ and the carrier concentration only gets close to (but never exceeds) c in the regime of the doped metal, for c above a certain metallization threshold c_0 (for a quasi-2D dispersed $\varepsilon_{\mathbf{k}}$ it is $c_0 \sim \exp(-\pi W/4V_L) \ll 1$).¹⁹ Under this condition, the self-consistency implied by Eq. (10) is not necessary, and a good approximation⁴ for the chemical potential is $\mu \approx 3cW/4$ (see Appendix A). Then the gap equation (3) takes the form

$$\Delta_{\mathbf{k}} = \frac{V\gamma_{\mathbf{k}}}{2N} \sum_{\mathbf{k}'} \gamma_{\mathbf{k}'} \int_{-\infty}^{\infty} \frac{d\varepsilon}{e^{\beta(\varepsilon - \mu)} + 1} \text{Im Tr} \hat{\tau}_1 \hat{G}_{\mathbf{k}}, \quad (11)$$

and its solution, discussed in Appendix C for the uniform case ($V_L = 0$), is simply $\Delta_{\mathbf{k}} = \Delta \gamma_{\mathbf{k}}$, with the ratio $r = 2\Delta/k_B T_c$ being $e^{1/3}$ times the s -wave BCS value $r_{BCS} \approx 3.52$.

Another important self-averaging quantity is the integrated SPGF matrix \hat{G} itself, since the density of states $\rho(\varepsilon)$ is just

$$\rho(\varepsilon) = \frac{1}{\pi} \text{Im Tr} \hat{G}. \quad (12)$$

For an unperturbed system $V_L \rightarrow 0$, $\hat{G} \rightarrow \hat{G}^{(0)} = N^{-1} \sum_{\mathbf{k}} \hat{G}_{\mathbf{k}}^{(0)}$, and calculation of the imaginary part of $\hat{G}^{(0)}$ within the nodal point approximation (Appendix B) leads to the standard d -wave density of states:

$$\rho(\varepsilon) \rightarrow \rho^{(0)}(\varepsilon) = \frac{1}{\pi} \text{Im Tr} \hat{G}^{(0)} = \frac{2\varepsilon\rho_0}{\Delta} \arcsin \left[\min \left(1, \frac{\Delta}{\varepsilon} \right) \right], \quad (13)$$

where $\rho_0 \approx 4/(\pi W)$ is the normal Fermi density of states of a doped (quasi-2D) metal with $\varepsilon_F < W/2$. Accordingly, the real part of $\hat{G}^{(0)}$ is

$$\text{Re} \hat{G}^{(0)} = \varepsilon \rho_0 \left[\frac{W}{\mu(W - \mu)} - \frac{\pi}{\Delta} \theta(\Delta - \varepsilon) \text{arccosh} \frac{\Delta}{\varepsilon} \right]. \quad (14)$$

Then Eqs. (13) and (14) can be unified into a single analytic form:

$$\hat{G}^{(0)} = \varepsilon \rho_0 \left[\frac{W}{\mu(W - \mu)} - \frac{\pi}{\Delta} \left(\text{arccosh} \frac{\Delta}{\varepsilon} - i \frac{\pi}{2} \right) \right], \quad (15)$$

since at $\varepsilon > \Delta$ one has $\arccos(\Delta/\varepsilon) = i[\pi/2 - \arcsin(\Delta/\varepsilon)]$, thus restoring Eq. (13). But it is just the growth of the (real) arccosh term at $\varepsilon < \Delta$ that permits the existence of a low-energy ($\varepsilon_{\text{res}} \ll \Delta$) resonance feature in $\text{Re}(1 + \hat{G} \hat{V})^{-1}$ and hence in $\rho(\varepsilon)$. Such a resonance was discussed previously¹⁴ for a d -wave SC with low enough concentration c (so that $\hat{G} \approx \hat{G}^{(0)}$) of “foreign” impurities producing a strong enough perturbation V_L , and it is similar to the known low-frequency resonance by heavy impurities in acoustic phonon spectra.²⁹ However, in the situation of interest here, when both V_L and c are not small, \hat{G} can be substantially modified compared to $\hat{G}^{(0)}$, and this is expressed in a very complicated way by Eq. (7). To simplify the task, certain self-consistent procedures, like the CPA method, quite useful in the theory of normal metals,³⁰ can be employed. A similar approach was previously proposed for an s -wave SC doped system,¹⁹ and here we begin with the analysis of a self-consistent solution for Eq. (5) in the d -wave case.

3. UNIFORM DOPING EFFECTS IN THE SELF-CONSISTENT APPROACH

If the GE series (7) is restricted to its first term, the self-energy matrix $\hat{\Sigma}_{\mathbf{k}}$ in fact becomes independent of \mathbf{k} :

$$\hat{\Sigma}_{\mathbf{k}} \rightarrow \hat{\Sigma} = -c \hat{V} [1 + \hat{G} \hat{V}]^{-1}, \quad (16)$$

and substitution of Eq. (16) into Eq. (6) defines the self-consistent approximation $\hat{G}_{\mathbf{k}}^{(sc)}$ for the M-diagonal SPGF:

$$\hat{G}_{\mathbf{k}}^{(sc)} = \{ [\hat{G}_{\mathbf{k}}^{(0)}]^{-1} - \hat{\Sigma}^{(sc)} \}^{-1}, \quad (17)$$

$$\hat{\Sigma}^{(sc)} = -c \hat{V} [1 + \hat{G}^{(sc)} \hat{V}]^{-1}, \quad (18)$$

$$\hat{G}^{(sc)} = \frac{1}{N} \sum_{\mathbf{k}} \hat{G}_{\mathbf{k}}^{(sc)}. \quad (19)$$

To solve this system, we first parametrize the self-energy matrix (18):

$$\hat{\Sigma}^{(sc)} = \Sigma_0 + \Sigma_1 + \hat{\tau}_1 + \Sigma_3 \hat{\tau}_3, \quad (20)$$

where the Σ_i are some complex-valued functions of energy. Then the integration in Eq. (19) within the nodal-point approximation (Appendix D) results in

$$\hat{G}^{(sc)} = G_0 + G_1 \hat{\tau}_1 + G_3 \hat{\tau}_3 \quad (21)$$

with the coefficients

$$G_0 = (\varepsilon - \Sigma_0) \rho_0 \times \left[-\frac{\pi}{2\Delta} \left(\operatorname{arccosh} \frac{\Delta + \Sigma_1}{\varepsilon - \Sigma_0} + \operatorname{arccosh} \frac{\Delta - \Sigma_1}{\varepsilon - \Sigma_0} - i\pi \right) + \frac{W}{\mu(W - \mu)} \right], \quad (22)$$

$$G_1 = \Sigma_1 \rho_0 \left[-\frac{2i\pi}{\sqrt{(\varepsilon - \Sigma_0)^2 - (\Delta + \Sigma_1)^2} + \sqrt{(\varepsilon - \Sigma_0)^2 - (\Delta - \Sigma_1)^2}} + \frac{W}{\mu(W - \mu)} \right], \quad (23)$$

$$G_3 = \rho_0 \left[\ln \frac{\mu}{W - \mu} + 2\Sigma_3 \frac{(\varepsilon - \Sigma_0)^2 - \Delta^2/3 - \Sigma_1^2}{\varepsilon_D^3} \right]. \quad (24)$$

Substituting Eq. (21) into Eq. (18), we arrive at

$$\hat{\Sigma}^{(sc)} = \frac{cV_L[V_L(G_0 + G_1\hat{\tau}_1) - (1 + V_L G_3)\hat{\tau}_3]}{(1 + V_L G_3)^2 - V_L^2(G_0^2 - G_1^2)}. \quad (25)$$

Comparing Eqs. (25), and (22)–(24) with Eq. (20), we immediately conclude that $\Sigma_1 = G_1 = 0$, or that $\hat{\Sigma}^{(sc)}$ is in fact *N-diagonal*, which is extremely important. Physically, this means that (within the self-consistent approximation linear in c) the scattering by dopants does not influence the d -wave order parameter, and this can be directly related to the fact that the s -symmetry of the impurity perturbation V_L is orthogonal to the d -symmetry of the SC pairing V . It also applies to more realistic models of dopant perturbation in HTSC (e.g., with plaquette- or dumbbell-like anisotropy),³¹ provided that their symmetries do not coincide with that of the order parameter. Complications arise when they do coincide, as was found for an isotropic perturbation on s -wave order with all three Σ_i being nonzero;¹⁹ hence the apparently “harder” d -wave system in fact turns “easier”!

By using the fact that $\Sigma_1 = 0$ and the relation $\cosh(x + i\pi/2) = \sin x$, Eq. (22) is brought to a very simple form:

$$\frac{\Delta}{\varepsilon - \Sigma_0} = \sin \left(\alpha - \frac{G_0}{\pi \rho_0} \frac{\Delta}{\varepsilon - \Sigma_0} \right), \quad (26)$$

with $\alpha = W\Delta/[\pi\mu(W - \mu)] \ll 1$, while the same comparison for the two nonzero components of $\hat{\Sigma}^{(sc)}$: Σ_0 and Σ_3 , gives:

$$\Sigma_0[(1 + V_L G_3)^2 - V_L^2 G_0^2] = cV_L^2 G_0, \quad (27)$$

$$\Sigma_3[(1 + V_L G_3)^2 - V_L^2 G_0^2] = -cV_L(1 + V_L G_3). \quad (28)$$

From Eq. (28) we estimate $|\Sigma_3| \sim cV_L$; hence, within the relevant energy region $|\varepsilon| \ll \varepsilon_D$ the function G_3 from Eq. (24) is reasonably well approximated by a (negative) constant $g_3 = \rho_0 \ln[\mu/(W - \mu)]$. Then Eq. (27) turns quadratic for G_0 :

$$G_0^2 + \frac{c}{\Sigma_0} G_0 - \left(\frac{1}{\tilde{V}} \right)^2 = 0, \quad (29)$$

with $\tilde{V} = V_L/(1 + V_L g_3) \approx V_L \ln(1/c_0)/\ln(3c/4c_0)$. The system of equations (26), (29) fully determines the self-energy Σ_0 and other uniform physical properties of a disordered d -wave system, and its solution can be found (in principle,

numerically) within the whole relevant energy range. It turns especially simple if $|\Sigma_0| \ll c\tilde{V}$ (this proves to hold at least for $\varepsilon \ll \varepsilon_{\text{res}}$); then the proper solution to Eq. (29) is $G_0 \approx \Sigma_0/c\tilde{V}^2$, and from Eq. (26) we obtain the following equation for a single important function Σ_0 :

$$\frac{\Delta}{\varepsilon - \Sigma_0} = \sin \left(\alpha - \frac{\tilde{\alpha}\Sigma_0}{\varepsilon - \Sigma_0} \right) \quad (30)$$

with $\tilde{\alpha} = \Delta/[\pi c\tilde{V}^2 \rho_0] \gg 1$. It defines the self-consistent density of states

$$\rho^{(sc)}(\varepsilon) = \frac{1}{\pi} \operatorname{Im} \operatorname{Tr} \hat{G}^{(sc)}(\varepsilon) = \frac{2 \operatorname{Im} \Sigma_0(\varepsilon)}{\pi c \tilde{V}^2}, \quad (31)$$

at lowest energies. The results of this approach are free of the infrared logarithmic divergences that appear in the integrals of perturbation theory³² and thus allow one to avoid applying heavy field-theoretic methods for a white-noise scattering potential,¹⁵ whose adequacy to the case of discrete random dopants is not clear.

The exact value of the density of states at the very center of the gap, $\rho(0) = \rho(\varepsilon \rightarrow 0)$, is also of a particular interest in view of the known claim about existence of a nonzero “universal” value $\rho(0) \sim c/\ln(1/c)$ if V_L is sufficiently strong.^{12,17} However, we conclude from Eq. (30) that in the limit $\varepsilon \rightarrow 0$:

$$\Sigma_0 \rightarrow \varepsilon \left[1 + i \frac{\tilde{\alpha}}{\ln(2\Delta/\tilde{\alpha}|\varepsilon|)} \right],$$

and hence of the self-consistent density of states at $\varepsilon \rightarrow 0$:

$$\rho^{(sc)}(\varepsilon) \rightarrow \frac{4\tilde{\alpha}^2 \rho^{(0)}(\varepsilon)}{\pi \ln(2\Delta/\tilde{\alpha}|\varepsilon|)}, \quad (32)$$

vanishes even faster than the unperturbed function $\rho^{(0)}(\varepsilon)$ of Eq. (13). This produces a certain narrow “quasi-gap” (not to be confused with the pseudogap observed at $T > T_c$ in the underdoped regime) around the center. For comparison, the estimated $\rho(\varepsilon)$ from the two first terms of Eq. (7) tends to zero linearly in ε with corrections $\sim \varepsilon^2$ (Ref. 14), while the field-theoretical analysis¹⁵ predicts $\rho(\varepsilon) \rightarrow \varepsilon^\omega$, with the nonuniversal exponent being (in our notation) $\omega = \tanh \ln \sqrt{\pi^2 \Delta W/2cV_L^2}$, which is always < 1 and can even be < 0 .

The discrepancy between our results and the aforementioned “universal” behavior originates in the improper use of the unitary limit $V_L \rightarrow \infty$ in neglect of the $1 + V_L G_3$ term in Eq. (27), leading to the relation $\Sigma_0 = -c/G_0$. But the true limiting relation is inverse: $\Sigma_0 = c\tilde{V}^2 G_0$, with \tilde{V} finite for $V_L \rightarrow \infty$, and also the unitary limit fails at any⁵ finite V_L when $\varepsilon \rightarrow 0$. Finally, the existing experimental data do not confirm the “universal” $\rho(0)$ value but seem to favor the conclusion that there exists a strong low-energy resonance in $\rho(\varepsilon)$,¹¹ with a possible quasi-gap at the very center,³³ though experimental observations at such low energies of course require extremely low temperatures.

Note, however, that the self-consistent treatment of the low-energy resonance, at $\varepsilon_{\text{res}} \sim \Delta \ln(3c/4c_0)/(\pi \ln 2\pi)$ for the case of self-impurities (Fig. 1), already requires solution of the full system of equations (26), (29), and, in view of a

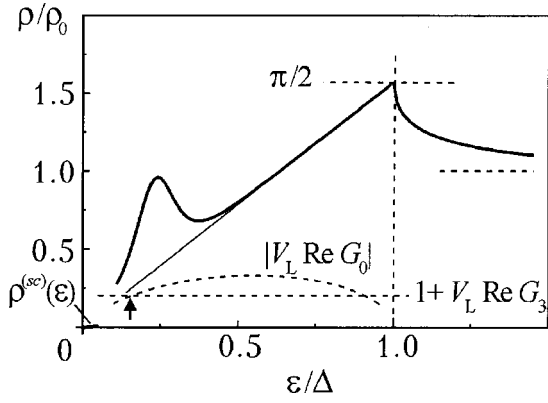


FIG. 1. Density of states in a d -wave SC system (heavy solid line). The thin solid line shows the unperturbed $\rho^{(0)}(\varepsilon)$, and the arrow indicates the solution for $\text{Re}[(1 + V_L G_3)^2 - V_L^2 G_0^2] = 0$, corresponding to the low-energy resonance (the other solution at $\varepsilon \approx \Delta$ is not resonant) for the choice of parameters $W = 2$ eV, $V_L = 0.5$ eV, $c = 0.1$.

probable underestimate of this hump (like that in normal systems),^{28,30} it should be better described by the exact GE (7).

The expression obtained for $\hat{\Sigma}^{(sc)}$ can be in principle directly inserted in Eq. (17) in order to use the resulting $\hat{G}_k^{(SC)}$ for correction of the gap equation (11). However, at the quasiparticle energies $\xi_k \sim \varepsilon_D$ important there, renormalization effects are negligible, and thus Δ remains well approximated by the result of Appendix C.

4. NONUNIFORM EFFECTS

The SPGFs considered in the previous Section describe the uniform self-averaging characteristics of the SC state. The next important question is the behavior of fluctuations of the order parameter (both its amplitude and phase) in an inhomogeneous system, which should be closely related to the breakdown of superconductivity in the overdoped regime. A strong local suppression of d -wave order close to a single “foreign” impurity has been predicted theoretically¹⁴ and observed experimentally.¹¹ In the general case of a finite concentration of scatterers, the local d -wave order can be characterized by the operator

$$\Omega_n = \frac{V}{N} \sum_{\mathbf{k}, \mathbf{k}'} \gamma_{\mathbf{k}} e^{i(\mathbf{k}-\mathbf{k}') \cdot \mathbf{n}} c_{-\mathbf{k}, \downarrow} c_{\mathbf{k}', \uparrow}, \quad (33)$$

such that its mean value (generally complex) defines the uniform gap parameter: $N^{-1} \sum_n \langle \Omega_n \rangle = N^{-1} \sum_k \gamma_{\mathbf{k}} \Delta_{\mathbf{k}} = \Delta$ (Ref. 14).

On the other hand, it is natural to characterize local fluctuations of the order parameter by the variance of Ω_n (identified with the variance of the gap parameter):

$$\delta^2 = \frac{1}{N} \sum_n \langle (\Omega_n^2) - \langle \Omega_n \rangle^2 \rangle. \quad (34)$$

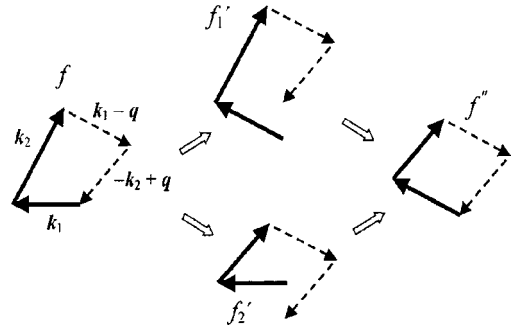


FIG. 2. Schematic of consecutive scattering processes (see Appendix E), bringing an M-nondiagonal TPGF f , through intermediate, partly M-diagonal f_1' and f_2' to fully M-diagonal f'' : the solid vectors standing for the operators of the left-hand side get fully nested with the dashed vectors for the right-hand side.

Using Eq. (33), we write

$$\begin{aligned} \delta^2 &= \frac{V^2}{N^3} \sum_{\mathbf{n}} \sum_{\mathbf{k}_1, \mathbf{k}_2, \mathbf{k}_3, \mathbf{k}_4} e^{i(\mathbf{k}_1 + \mathbf{k}_2 - \mathbf{k}_3 - \mathbf{k}_4) \cdot \mathbf{n}} \gamma_{\mathbf{k}_1} \gamma_{\mathbf{k}_2} \\ &\times [\langle c_{-\mathbf{k}_1, \downarrow} c_{\mathbf{k}_3, \uparrow} c_{-\mathbf{k}_2, \downarrow} c_{\mathbf{k}_4, \uparrow} \rangle - \langle c_{-\mathbf{k}_1, \downarrow} c_{\mathbf{k}_3, \uparrow} \rangle \\ &\times \langle c_{-\mathbf{k}_2, \downarrow} c_{\mathbf{k}_4, \uparrow} \rangle], \end{aligned} \quad (35)$$

or, summing over \mathbf{n} to close the sum of 4 momenta, and using the spectral representation (9) for $T=0$:

$$\begin{aligned} \delta^2 &= \frac{V^2}{N^2} \sum_{\mathbf{k}_1, \mathbf{k}_2, \mathbf{q}} \gamma_{\mathbf{k}_1} \gamma_{\mathbf{k}_2} \left[\int_0^\infty d\varepsilon \text{Im} \langle \langle c_{-\mathbf{k}_1, \downarrow} c_{\mathbf{k}_2, \uparrow} \rangle \rangle \right. \\ &\times |c_{-\mathbf{k}_2 + \mathbf{q}, \downarrow} c_{\mathbf{k}_1 - \mathbf{q}, \uparrow} \rangle \rangle - \int_0^\infty d\varepsilon \text{Im} \langle \langle c_{-\mathbf{k}_1, \downarrow} | \bar{n}_{\mathbf{k}_2, \uparrow} \rangle \rangle \\ &\times \left. \int_0^\infty d\varepsilon \text{Im} \langle \langle c_{-\mathbf{k}_2 + \mathbf{q}, \downarrow} | c_{\mathbf{k}_1 - \mathbf{q}, \uparrow} \rangle \rangle \right]. \end{aligned} \quad (36)$$

Here besides the previously used SPGFs, the TPGF $\langle \langle c_{-\mathbf{k}_1, \downarrow} c_{\mathbf{k}_2, \uparrow} | c_{-\mathbf{k}_2 + \mathbf{q}, \downarrow} c_{\mathbf{k}_1 - \mathbf{q}, \uparrow} \rangle \rangle$ appears. An explicit calculation of this function for the unperturbed ($V_L = 0$) SC system (see Appendix E) gives the following result

$$\begin{aligned} &\langle \langle c_{-\mathbf{k}_1, \downarrow} c_{\mathbf{k}_2, \uparrow} | c_{-\mathbf{k}_2 + \mathbf{q}, \downarrow} c_{\mathbf{k}_1 - \mathbf{q}, \uparrow} \rangle \rangle \\ &= \frac{4\varepsilon \Delta_{\mathbf{k}_1} \Delta_{\mathbf{k}_2} + \dots}{\delta_{0, \mathbf{q}} (\varepsilon^2 - E_{\mathbf{k}_1}^2 - E_{\mathbf{k}_2}^2)^2 - 4E_{\mathbf{k}_1}^2 E_{\mathbf{k}_2}^2}. \end{aligned} \quad (37)$$

Here $E_{\mathbf{k}}^2 = \xi_{\mathbf{k}}^2 + \Delta_{\mathbf{k}}^2$, and three other terms in the numerator are not mutually odd in $\gamma_{\mathbf{k}_1}$ and $\gamma_{\mathbf{k}_2}$ and thus do not contribute to δ^2 . Then it is easy to see that the resulting contribution to Eq. (36) from the M-diagonal ($\mathbf{q} = 0$) and N-nondiagonal TPGFs by Eq. (37) exactly cancels with that from the SPGFs, which confirms the uniformity of d -wave order in this case. The most important contribution to δ^2 at $V_L \neq 0$ comes from two consecutive scattering processes in the left-hand sides of an N- and M-nondiagonal ($\mathbf{q} \neq 0$) TPGF, first $c_{-\mathbf{k}_1, \downarrow} c_{\mathbf{k}_2, \uparrow} \rightarrow c_{-\mathbf{k}_1 + \mathbf{q}, \downarrow} c_{\mathbf{k}_2, \uparrow}$ and then $c_{-\mathbf{k}_1 + \mathbf{q}, \downarrow} c_{\mathbf{k}_2, \uparrow} \rightarrow c_{-\mathbf{k}_1 + \mathbf{q}, \downarrow} c_{\mathbf{k}_2 - \mathbf{q}, \uparrow}$ (or vice versa, Fig. 2), on the same scattering center \mathbf{p} . It is linear in c , while the contribution from SPGFs in this order, $-2\Delta V \int_0^\infty d\varepsilon \text{Im} \text{Tr} \hat{\tau}_1 \hat{\Sigma}$, is zero, accordingly to the N -diagonal form of $\hat{\Sigma}$ established

in the previous Section. Hence we generally estimate the variance of the gap to grow with c as $|\delta| = \Delta \sqrt{c/c_1}$, where $c_1 \sim (V/V_L)^2$ defines the upper critical concentration for SC at $T=0$.

A more detailed analysis, resolving amplitude and phase fluctuations, can be done in a similar way, but considering separately the two operators:

$$\Omega_{n,+} = \frac{\Omega_n + \Omega_n^+}{2}, \quad \text{and} \quad \Omega_{n,-} = \frac{\Omega_n - \Omega_n^+}{2i},$$

such that their mean values $\langle \Omega_{n,\pm} \rangle$ lead to real and imaginary parts of the order parameter, and constructing the corresponding variances:

$$\delta_{\pm}^2 = \frac{1}{N} \sum_{\mathbf{n}} (\langle \Omega_{\mathbf{n},\pm}^2 \rangle - \langle \Omega_{\mathbf{n},\pm} \rangle^2).$$

This approach should be particularly important upon extension of the theory to finite temperatures, in order to establish the dominant type of fluctuations due to the static disorder, responsible for breakdown of SC order at $T=T_c$, and its possible role in the persistence of a pseudogap in the density of states ρ at $T>T_c$.

5. CONCLUSIONS

The analysis presented above shows that the disordered structure of doped HTSC systems is crucial for many of their characteristic properties and for the existence of SC order itself. The interplay between doping and disorder effects can be briefly summarized as follows. Superconductivity sets in with the metallization of the system, at a critical concentration $c \sim c_0$ resulting from the competition between the kinetic energy of the charge carriers in the regular lattice and their attraction to random dopant centers. The uniform d -wave order parameter Δ increases with increasing number of charge carriers as $\Delta \sim \sqrt{c}$ (Ref. 6) and saturates at a certain optimum doping $c_{\text{opt}} \sim \varepsilon_D/W$, when the relation $\mu > \varepsilon_D$ comes to hold. With further increase in c , the increasing local fluctuations of Δ bring it to collapse at some upper critical concentration $c_1 \sim (V/V_L)^2$, resulting from the competition between the pairing and scattering potentials. This picture is quantitatively satisfied with a very natural choice of parameters $W \sim 2$ eV, $V_L \sim 0.5$ eV, $V \sim 0.22$ eV, $\varepsilon_D \sim 0.2$ eV, giving plausible estimates: $c_0 \sim 5\%$, $c_{\text{opt}} \sim 15\%$, $T_{c,\text{max}} \sim 100$ K, $c_1 \sim 20\%$. Our forthcoming work should also specify such important aspects, left beyond the scope of this paper, as the disorder effects on the cusp of density of states $\rho(\varepsilon)$ at $\varepsilon = \Delta$, the matching conditions between the self-consistent and GE descriptions of SPGF, the exact numerical coefficient for the critical value c_1 , etc. And, of course, it is of fundamental interest to extend the present self-consistent treatment to the case of finite temperatures up to T_c , in order to obtain a quantitative estimate for the bell-like $T_c(c)$ shape, and further to $T > T_c$, to study the role of doping disorder versus d -wave SC coupling in the formation and subsequent merging (at $c \sim c_{\text{opt}}$) of the pseudogap in the normal density of states.

This work was supported in parts by the Portuguese Program PRAXIS XXI under Grant 2/2.1/FIS/302/94, by the NATO Program OUTREACH under Grant CP/UN/19/C/

2000/PO, and by the Swiss National Science Foundation (SCOPES Project 7UKPJ062150.00/1). One of us (V.M.L.) expresses his gratitude for the warm hospitality he felt at visiting Centro de Física do Porto and Institute of Physics of University of Neuchatel.

APPENDIX A

For the normal phase, we consider the dispersion relation $\varepsilon_{\mathbf{k}} = 4t - 2t(\cos ak_x + \cos ak_y)$ and relate the dopant concentration c to the number (per unit cell) of occupied states below μ :

$$\begin{aligned} c &= \frac{2a^2}{(2\pi)^2} \int_{\varepsilon_{\mathbf{k}} \leq \mu} d\mathbf{k} = \arccos\left(1 - \frac{4\mu}{W}\right) \arccos \\ &\times \left(2 - \frac{4\mu}{W} - \cos ak_x\right) = \frac{2a^2}{\pi^2} \int_0^{\mu} dk_x \int_0^{\mu} dk_y \\ &= \frac{2}{\pi^2} \int_{1-4\mu/W}^1 \frac{du}{\sqrt{1-u^2}} \int_{2-4\mu/W-u}^1 \frac{dv}{\sqrt{1-v^2}} \\ &= \frac{2}{\pi^2} F\left(\frac{4\mu}{W}\right). \end{aligned} \quad (\text{A1})$$

Here the dependence of the integral

$$F(x) = \int_{1-x}^1 \frac{\arccos(2-x-u)}{\sqrt{1-u^2}} du$$

is very well approximated by a simple linear function $F(x) \approx 5x/3$ in the whole physically important range $0 \leq x = 4\mu/W \leq x_{\text{max}}$ (where $x_{\text{max}} \approx 0.6$) corresponds to $\mu_{\text{max}} \approx 0.15W$ at the maximum physical doping $c_{\text{max}} \approx 0.2$). Then we readily arrive at the estimate cited above:

$$\mu \approx \frac{3\pi^2}{40} cW \approx \frac{3cW}{4}.$$

APPENDIX B

For the uniform SC system with d -wave gap, we perform integration over the Brillouin zone with the parametrization $\mathbf{k} - \mathbf{k}_i = a^{-1}(\rho_0 \xi \mathbf{e}_i + \Delta^{-1} \eta \mathbf{e}_i \times \mathbf{e}_z)$, $\mathbf{e}_i = (\pm 1/\sqrt{2}, \pm 1/\sqrt{2}, 0)$, $\mathbf{e}_z = (0, 0, 1)$, near 4 nodal points $\mathbf{k}_i = \arccos(1 - \mu/W) \mathbf{e}_i$ of the gap function $\Delta_{\mathbf{k}} = \Delta \gamma_{\mathbf{k}}$. This integration for $G^{(0)}$ becomes

$$\begin{aligned} \hat{G}^{(0)} &= \frac{1}{N} \sum_{\mathbf{k}} \hat{G}_{\mathbf{k}}^{(0)} = \rho_0 \left[\frac{1}{2\Delta} \int_{-\Delta}^{\Delta} d\eta \int_{-\varepsilon_D}^{\varepsilon_D} d\xi \hat{g}(\varepsilon, \xi, \eta) \right. \\ &\left. + \int_{-\mu}^{-\varepsilon_D} d\xi \hat{g}(\varepsilon, \xi, 0) + \int_{\varepsilon_D}^{W-\mu} d\xi \hat{g}(\varepsilon, \xi, 0) \right], \end{aligned} \quad (\text{B1})$$

where we have defined the matrix function (cf. $\hat{G}_{\mathbf{k}}^{(0)}$ in (5))

$$\hat{g}(\varepsilon, \xi, \eta) = (\varepsilon - \xi \hat{\tau}_3 - \eta \hat{\tau}_1)^{-1} = \frac{\varepsilon + \xi \hat{\tau}_3 + \eta \hat{\tau}_1}{\varepsilon^2 - \xi^2 - \eta^2}.$$

The integration in ξ (normal to the Fermi surface) in Eq. (B1) treats the BCS shell, $[-\varepsilon_D, \varepsilon_D]$, separately from the out-of-shell segments, $[-\mu, -\varepsilon_D]$ and $[\varepsilon_D, W-\mu]$, where the gap parameter Δ becomes zero (together with $\gamma_{\mathbf{k}}$) and no integration over $\eta = \Delta \gamma_{\mathbf{k}}$ is needed. Equation (B1) permits one to define explicitly the coefficient functions g_i in the

general form $\hat{G}^{(0)} = g_0 + g_1 \hat{\tau}_1 + g_3 \hat{\tau}_3$. Let us denote $z^2 = \varepsilon^2 - \eta^2$, and then the shell contribution to g_0 results from the integral:

$$\int_{-\varepsilon_D}^{\varepsilon_D} \frac{d\xi}{z^2 - \xi^2} = \frac{2}{z} \left(\operatorname{arctanh} \frac{z}{\varepsilon_D} + i\pi \right) \approx \frac{2}{\varepsilon_D} + \frac{2i\pi}{z}, \quad (\text{B2})$$

which is followed for its last term by:

$$\int_{-\Delta}^{\Delta} \frac{d\eta}{\sqrt{\varepsilon^2 - \eta^2}} = 2 \arccos \frac{\Delta}{\varepsilon}. \quad (\text{B3})$$

The out-of-shell contributions are:

$$\int_{-\mu}^{-\varepsilon_D} \frac{d\xi}{\varepsilon^2 - \xi^2} = \frac{1}{\varepsilon} \left(\operatorname{arctanh} \frac{\varepsilon}{\mu} - \operatorname{arctanh} \frac{\varepsilon}{\varepsilon_D} \right) \approx \frac{1}{\mu} - \frac{1}{\varepsilon_D} \quad (\text{B4})$$

and

$$\int_{\varepsilon_D}^{W-\mu} \frac{d\xi}{\varepsilon^2 - \xi^2} \approx \frac{1}{W-\mu} - \frac{1}{\varepsilon_D}. \quad (\text{B5})$$

To find g_1 and g_3 , we use the obvious equations

$$\int_{-\varepsilon_D}^{\varepsilon_D} \frac{\xi d\xi}{z^2 - \xi^2} = \int_{-1}^1 \eta d\eta = 0$$

and

$$\int_{-\mu}^{-\varepsilon_D} \frac{\xi d\xi}{\varepsilon^2 - \xi^2} + \int_{\varepsilon_D}^{W-\mu} \frac{\xi d\xi}{\varepsilon^2 - \xi^2} = \frac{1}{2} \ln \frac{\mu^2 - \varepsilon^2}{(W-\mu)^2 - \varepsilon^2} \approx \ln \frac{\mu}{W-\mu}. \quad (\text{B6})$$

Summing up Eqs. (B2)–(B6) we obtain

$$g_0 = \varepsilon \rho_0 \left[\frac{W}{\mu(W-\mu)} - \frac{\pi}{\Delta} \left(\operatorname{arccosh} \frac{\Delta}{\varepsilon} - \frac{i\pi}{2} \right) \right];$$

in accordance with Eq. (15), $g_1 = 0$ and $g_3 = \rho_0 \ln[\mu/(W-\mu)]$.

APPENDIX C

The gap equation (11) for a uniform ($V_L = 0$) d -wave system at $T=0$ transforms into:

$$\frac{1}{\lambda} = \frac{16}{\pi \Delta^3} \operatorname{Im} \int_0^{\Delta} \eta^2 d\eta \int_0^{\varepsilon_D} d\xi \int_0^{\infty} \frac{d\varepsilon}{\varepsilon^2 - \xi^2 - \eta^2 - i0}, \quad (\text{C1})$$

with coupling constant $\lambda \equiv V\rho_0$. The quantity sought is the gap amplitude Δ . On the right-hand side of Eq. (C1) we perform the elementary integration over ε , using the relation $\operatorname{Im}(x-i0)^{-1} = \pi\delta(x)$:

$$\begin{aligned} \frac{16}{\pi} \operatorname{Im} \int_0^{\Delta} \eta^2 d\eta \int_0^{\varepsilon_D} d\varepsilon \int_0^{\infty} \frac{d\varepsilon}{\varepsilon^2 - \xi^2 - \eta^2 - i0} \\ = 8 \int_0^{\Delta} \eta^2 d\eta \int_0^{\varepsilon_D} \frac{d\xi}{\sqrt{\xi^2 + \eta^2}}. \end{aligned} \quad (\text{C2})$$

Then, integrating out in ξ and passing from η to $y = \hbar\varepsilon_D/\eta$, we present Eq. (C2) as

$$\begin{aligned} 8 \left(\frac{\varepsilon_D}{\Delta} \right)^3 \int_{\varepsilon_D/\Delta}^{\infty} \frac{\operatorname{arcsinh} y dy}{y^4} \\ = \frac{8}{3} \operatorname{arcsinh} \frac{\varepsilon_D}{\Delta} + 4 \frac{\varepsilon_D \sqrt{\varepsilon_D^2 + \Delta^2}}{3\Delta^2} - \frac{4}{3} \left(\frac{\varepsilon_D}{\Delta} \right)^3 \operatorname{arcsinh} \frac{\Delta}{\varepsilon_D} \\ \approx \frac{8}{3} \left(\ln \frac{2\varepsilon_D}{\Delta} + \frac{1}{3} \right). \end{aligned}$$

The equation for critical temperature T_c , corresponding to $\Delta=0$, in this case reads

$$\begin{aligned} \frac{1}{\lambda} = \frac{16}{3\pi} \operatorname{Im} \int_0^{\varepsilon_D} d\xi \tanh \left(\frac{\xi}{2k_B T_c} \right) \int_0^{\infty} \frac{d\varepsilon}{\varepsilon^2 - \xi^2 - i0} \\ \approx \frac{8}{3} \ln \left(\frac{2\gamma_E \varepsilon_D}{\pi k_B T_c} \right), \end{aligned}$$

with the Euler constant $\gamma_E \approx 1.781$. Hence for the d -wave case the effective coupling constant is $\tilde{\lambda} = 8\lambda/3$, which is 8/3 times the ‘‘Hamiltonian’’ value λ , which can serve as one more explanation for high T_c itself. Also, the ratio $r = 2\Delta/k_B T_c$ here turns out to be $\exp(1/3)$ times the common s -wave BCS value $r_{BCS} = 2\pi/\gamma_E \approx 3.52$, reaching values as high as $r_d \approx 4.92$. In turn, this means that, for other conditions (say, ρ_0 and V) equal, the s -condensate turns out more stable against thermal fluctuations and requires a higher T_c to destroy it than the d -condensate. Of course, this is directly related to the absence of a gap in the latter case, permitting quasiparticles to exist at any $T < T_c$.

APPENDIX D

Calculation of the self-consistent SPGF $\hat{G}^{(SC)} = G_0 + G_1 \hat{\tau}_1 + G_3 \hat{\tau}_3$ generalizes the scheme of Appendix B:

$$\begin{aligned} \hat{G}^{(SC)} = \frac{1}{N} \sum_{\mathbf{k}} \hat{G}_{\mathbf{k}}^{(SC)} = \rho_0 \left[\frac{1}{2\Delta} \int_{-\Delta}^{\Delta} d\eta \int_{-\varepsilon_D}^{\varepsilon_D} d\xi \hat{g}(\varepsilon) \right. \\ \left. - \Sigma_0, \xi + \Sigma_3, \eta + \Sigma_1 \right) + \int_{-\mu}^{-\varepsilon_D} d\xi \hat{g}(\varepsilon - \Sigma_0, \xi) \\ \left. + \Sigma_3, \Sigma_1 \right) + \int_{\varepsilon_D}^{W-\mu} d\xi \hat{g}(\varepsilon - \Sigma_0, \xi + \Sigma_3, \Sigma_1) \right]. \end{aligned} \quad (\text{D1})$$

Next we set $z^2 = (\varepsilon - \Sigma_0)^2 - (\eta + \Sigma_1)^2$ and $z = r + ip$, and pass from ξ to $x = \xi + \Sigma_3$, where Σ_3 can be taken real [as seen, e.g., from the final result (28)]. Then the analog to Eq. (B2) is:

$$\begin{aligned}
& \int_{-\varepsilon_D+\Sigma_3}^{\varepsilon_D+\Sigma_3} \frac{dx}{z^2-x^2} \\
&= \frac{1}{2z} \left\{ \frac{1}{2} \ln \frac{[(\varepsilon_D+\Sigma_3+r)^2+p^2][(\varepsilon_D-\Sigma_3+r)^2+p^2]}{[(\varepsilon_D-\Sigma_3-r)^2+p^2][(\varepsilon_D+\Sigma_3-r)^2+p^2]} \right. \\
&\quad - i \left[\arctan \frac{\varepsilon_D+\Sigma_3+r}{p} + \arctan \frac{\varepsilon_D+\Sigma_3-r}{p} \right. \\
&\quad \left. \left. + \arctan \frac{\varepsilon_D-\Sigma_3+r}{p} + \arctan \frac{\varepsilon_D-\Sigma_3-r}{p} \right] \right\} \\
&\approx \frac{2}{\varepsilon_D} - i \frac{\pi+2p/\varepsilon_D}{z}, \tag{D2}
\end{aligned}$$

where the small term $2p/\varepsilon_D$ can be safely dropped. The next integration, over $y = \eta + \Sigma_1$, is done only on the $i\pi/z$ term accordingly to

$$\begin{aligned}
& \int_{-\Delta+\Sigma_1}^{\Delta+\Sigma_1} \frac{dy}{\sqrt{(\varepsilon-\Sigma_0)^2-y^2}} \\
&= \arccos \frac{\Delta+\Sigma_1}{\varepsilon-\Sigma_0} + \arccos \frac{\Delta-\Sigma_1}{\varepsilon-\Sigma_0}, \tag{D3}
\end{aligned}$$

which is relevant for G_0 , supplemented with

$$\begin{aligned}
& \int_{-\Delta+\Sigma_1}^{\Delta+\Sigma_1} \frac{y dy}{\varepsilon-\Sigma_0^2-y^2} \\
&= - \frac{4\Delta\Sigma_1}{\sqrt{(\varepsilon-\Sigma_0)^2-(\Delta+\Sigma_1)^2} + \sqrt{(\varepsilon-\Sigma_0)^2-(\Delta-\Sigma_1)^2}} \tag{D4}
\end{aligned}$$

for G_1 . The out-of-shell integration of the components mentioned is much easier, giving:

$$\begin{aligned}
& \int_{\varepsilon_D-\Sigma_3}^{\mu-\Sigma_3} \frac{dx}{(\varepsilon-\Sigma_0)^2-x^2} \\
&= \frac{1}{\varepsilon-\Sigma_0} \left(\operatorname{arctanh} \frac{\varepsilon-\Sigma_0}{\mu-\Sigma_3} - \operatorname{arctanh} \frac{g-\Sigma_0}{\varepsilon_D-\Sigma_3} \right) \\
&\approx \frac{1}{\mu-\Sigma_3} - \frac{1}{\varepsilon_D-\Sigma_3}, \tag{D5}
\end{aligned}$$

and

$$\int_{\varepsilon_D-\Sigma_3}^{W-\mu-\Sigma_3} \frac{dx}{(\varepsilon-\Sigma_0)^2-x^2} \approx \frac{1}{W-\mu-\Sigma_3} - \frac{1}{\varepsilon_D-\Sigma_3}. \tag{D6}$$

Here Σ_3 can also be disregarded beside W , μ , ε_D , and then the two $-1/\varepsilon_D$ terms cancel with that from Eq. (D2). Now, combining Eqs. (D2)–(D6), we obtain

$$\begin{aligned}
G_0 = (\varepsilon-\Sigma_0)\rho_0 \left[\frac{W}{\mu(W-\mu)} - \frac{\pi}{2\Delta} \left(\operatorname{arccosh} \frac{\Delta+\Sigma_1}{\varepsilon-\Sigma_0} \right. \right. \\
\left. \left. + \operatorname{arccosh} \frac{\Delta-\Sigma_1}{\varepsilon-\Sigma_0} - i\pi \right) \right], \tag{D7}
\end{aligned}$$

and

$$G_1 = \Sigma_1 \rho_0 \left[\frac{W}{\mu(W-\mu)} - \frac{2i\pi}{\sqrt{(\varepsilon-\Sigma_0)^2-(\Delta+\Sigma_1)^2} + \sqrt{(\varepsilon-\Sigma_0)^2-(\Delta-\Sigma_1)^2}} \right].$$

At least, G_3 is obtained after

$$\begin{aligned}
& \int_{-\varepsilon_D+\Sigma_3}^{\varepsilon_D+\Sigma_3} \frac{xdx}{z^2-x^2} = \frac{1}{2} \ln \frac{(\varepsilon_D-\Sigma_3)^2-z^2}{(\varepsilon_D+\Sigma_3)^2-z^2}, \\
& \int_{\varepsilon_D+\Sigma_3}^{W-\mu+\Sigma_3} \frac{xdx}{z^2-x^2} = \frac{1}{2} \ln \frac{(\varepsilon_D+\Sigma_3)^2-z^2}{(W-\mu+\Sigma_3)^2-z^2}, \\
& \int_{-\mu+\Sigma_3}^{-\varepsilon_D+\Sigma_3} \frac{xdx}{z^2-x^2} = \frac{1}{2} \ln \frac{(\mu-\Sigma_3)^2-z^2}{(\varepsilon_D-\Sigma_3)^2-z^2}, \\
& \frac{1}{2\Delta} \int_{-\Delta+\Sigma_1}^{\Delta+\Sigma_1} y^2 dy = \frac{\Delta^2}{3} + \Sigma_1^2,
\end{aligned}$$

in the form

$$G_3 = g r_0 \left\{ \ln \frac{\mu}{W-\mu} + 2\Sigma_3 \frac{(\varepsilon-\Sigma_0)^2-\Delta^2/3-\Sigma_1^2}{\varepsilon_\Delta^3} \right\}. \tag{D8}$$

APPENDIX E

Search for solutions of Eq. (5) in the form of GE consists in consecutive iterations of its right-hand side, separating systematically the GFs already present in previous iterations.²⁷ Let us start from the M-diagonal SPGF $G_{\mathbf{k}}$, and then the iteration sequence begins with singling out the scattering term with $\hat{G}_{\mathbf{k}}$ itself from those with $G_{\mathbf{k}',\mathbf{k}}$, $\mathbf{k}' \neq \mathbf{k}$:

$$\begin{aligned}
\hat{G}_{\mathbf{k}} = \hat{G}_{\mathbf{k}}^{(0)} + \hat{G}_{\mathbf{k}}^{(0)} \frac{1}{N} \sum_{\mathbf{k}',\mathbf{p}} e^{i(\mathbf{k}-\mathbf{k}') \cdot \mathbf{p}} \hat{V} \hat{G}_{\mathbf{k}',\mathbf{k}} = \hat{G}_{\mathbf{k}}^{(0)} \\
+ c \hat{G}_{\mathbf{k}}^{(0)} \hat{V} \hat{G}_{\mathbf{k}} + \hat{G}_{\mathbf{k}}^{(0)} \hat{V} \frac{1}{N} \sum_{\mathbf{k}' \neq \mathbf{k}, \mathbf{p}} e^{i(\mathbf{k}-\mathbf{k}') \cdot \mathbf{p}} \hat{G}_{\mathbf{k}',\mathbf{k}}. \tag{E1}
\end{aligned}$$

Then for each $\hat{G}_{\mathbf{k}',\mathbf{k}}$ we again write down Eq. (5) and separate the scattering terms with $\hat{G}_{\mathbf{k}}$ and $\hat{G}_{\mathbf{k}',\mathbf{k}}$ in their right-hand sides:

$$\begin{aligned}
\hat{G}_{\mathbf{k}',\mathbf{k}} = \hat{G}_{\mathbf{k}'}^{(0)} \hat{V} \frac{1}{N} \sum_{\mathbf{k}'',\mathbf{p}'} e^{i(\mathbf{k}'-\mathbf{k}'') \cdot \mathbf{p}'} \hat{G}_{\mathbf{k}'',\mathbf{k}} \\
= c \hat{G}_{\mathbf{k}'}^{(0)} \hat{V} \hat{G}_{\mathbf{k}',\mathbf{k}} + \hat{G}_{\mathbf{k}'}^{(0)} \hat{V} \frac{1}{N} \sum_{\mathbf{k}'' \neq \mathbf{k}, \mathbf{k}'; \mathbf{p}'} e^{i(\mathbf{k}'-\mathbf{k}'') \cdot \mathbf{p}'} \hat{G}_{\mathbf{k}'',\mathbf{k}} \\
+ \hat{G}_{\mathbf{k}'}^{(0)} \hat{V} \frac{1}{N} \sum_{\mathbf{p}' \neq \mathbf{p}} e^{i(\mathbf{k}'-\mathbf{k}) \cdot \mathbf{p}'} \hat{G}_{\mathbf{k}} \\
+ \hat{G}_{\mathbf{k}'}^{(0)} \hat{V} \frac{1}{N} \sum_{\mathbf{k}'' \neq \mathbf{k}, \mathbf{k}'; \mathbf{p}'} e^{i(\mathbf{k}'-\mathbf{k}'') \cdot \mathbf{p}'} \hat{G}_{\mathbf{k}'',\mathbf{k}}. \tag{E2}
\end{aligned}$$

Note that the $\mathbf{p}' = \mathbf{p}$ term which gives the phase factor $e^{i(\mathbf{k}'-\mathbf{k}) \cdot \mathbf{p}}$ in the right-hand side of Eq. (E2), coherent to that already figured in the last sum in Eq. (E1), is explicitly sepa-

rated from incoherent ones, $e^{i(\mathbf{k}'-\mathbf{k})\cdot\mathbf{p}}$, $\mathbf{p}' \neq \mathbf{p}$ (but there will be no such separation when doing the 1st iteration of Eq. (5) for the M-nondiagonal SPGF $\hat{G}_{\mathbf{k}',\mathbf{k}}$ itself). Continuing the sequence, we shall explicitly collect the terms with the initial function $G_{\mathbf{k}}$, resulting from: (i) all multiple scatterings on the same site \mathbf{p} , and (ii) on the same pair of sites \mathbf{p} and $\mathbf{p}' \neq \mathbf{p}$. Then the summing of (i) in \mathbf{p} produces the first term of GE, and, if the pair processes are neglected, it will coincide with the well-known CPA result.³⁰ The second term of the GE, obtained by summing of (ii) in $\mathbf{p}, \mathbf{p}' \neq \mathbf{p}$, contains interaction matrices $\hat{A}_{\mathbf{p}',\mathbf{p}}$ generated by multiply scattered functions $\hat{G}_{\mathbf{k}',\mathbf{k}}$, $\mathbf{k}' \neq \mathbf{k}$ etc. (including their own renormalization). For instance, the iteration for a function $\hat{G}_{\mathbf{k}'',\mathbf{k}}$ with $\mathbf{k}'' \neq \mathbf{k}, \mathbf{k}'$ in the last term in Eq. (E2) will give:

$$\begin{aligned} \hat{G}_{\mathbf{k}'',\mathbf{k}} &= \hat{G}_{\mathbf{k}''}^{(0)} \hat{V} \frac{1}{N} \sum_{\mathbf{k}',\mathbf{p}''} e^{i(\mathbf{k}''-\mathbf{k}')\cdot\mathbf{p}''} \hat{G}_{\mathbf{k}',\mathbf{k}} \\ &= \hat{G}_{\mathbf{k}''}^{(0)} \hat{V} \frac{1}{N} e^{i(\mathbf{k}''-\mathbf{k})\cdot\mathbf{p}} \hat{G}_{\mathbf{k}} + \hat{G}_{\mathbf{k}''}^{(0)} \hat{V} \frac{1}{N} e^{i(\mathbf{k}''-\mathbf{k})\cdot\mathbf{p}'} \hat{G}_{\mathbf{k}} \\ &\quad + \text{terms with } \hat{G}_{\mathbf{k}',\mathbf{k}} \text{ and } \hat{G}_{\mathbf{k}'',\mathbf{k}} \\ &\quad + \text{terms with } \hat{G}_{\mathbf{k}'',\mathbf{k}} \text{ (}\mathbf{k}'' \neq \mathbf{k}, \mathbf{k}', \mathbf{k}''). \end{aligned} \quad (\text{E3})$$

Consequently, the GE for $\hat{G}_{\mathbf{k}}$ acquires the form given by Eq. (6).

Now turn to the TPGF

$$\langle\langle c_{-\mathbf{k}_1,\downarrow} c_{\mathbf{k}_2,\uparrow} | c_{-\mathbf{k}_2+\mathbf{q},\downarrow} c_{\mathbf{k}_1-\mathbf{q},\uparrow} \rangle\rangle,$$

beginning from the equations of motion in the absence of scattering, which develop into a 4×4 matrix form:

$$\hat{B}(\xi_1, \xi_2, \Delta_1, \Delta_2) f = \delta_{0,\mathbf{q}} d,$$

$$\hat{B}(\xi_1, \xi_2, \Delta_1, \Delta_2) = \begin{pmatrix} \varepsilon - \xi_1 - \xi_2 & \Delta_1 & \Delta_2 & 0 \\ \Delta_1 & \varepsilon + \xi_1 - \xi_2 & 0 & \Delta_2 \\ \Delta_2 & 0 & \varepsilon - \xi_1 + \xi_2 & \Delta_1 \\ 0 & \Delta_2 & \Delta_1 & \varepsilon + \xi_1 + \xi_2 \end{pmatrix} \quad (\text{E4})$$

with 4-vectors:

$$f = \begin{pmatrix} \langle\langle c_{-\mathbf{k}_1,\downarrow} c_{\mathbf{k}_2,\uparrow} | c_{-\mathbf{k}_2+\mathbf{q},\downarrow} c_{\mathbf{k}_1-\mathbf{q},\uparrow} \rangle\rangle \\ \langle\langle c_{\mathbf{k}_1,\uparrow} c_{\mathbf{k}_2,\uparrow} | c_{-\mathbf{k}_2+\mathbf{q},\downarrow} c_{\mathbf{k}_1-\mathbf{q},\uparrow} \rangle\rangle \\ \langle\langle c_{-\mathbf{k}_1,\downarrow} c_{-\mathbf{k}_2,\downarrow} | c_{-\mathbf{k}_2+\mathbf{q},\downarrow} c_{\mathbf{k}_1-\mathbf{q},\uparrow} \rangle\rangle \\ \langle\langle c_{\mathbf{k}_1,\uparrow} c_{-\mathbf{k}_2,\downarrow} | c_{-\mathbf{k}_2+\mathbf{q},\downarrow} c_{\mathbf{k}_1-\mathbf{q},\uparrow} \rangle\rangle \end{pmatrix},$$

$$d = \begin{pmatrix} 2\Delta_1\Delta_2 \\ \Delta_1 \\ \Delta_2 \\ 2 \end{pmatrix},$$

and $\xi_1 \equiv \xi_{\mathbf{k}_1}$, $\xi_2 \equiv \xi_{\mathbf{k}_2}$, $\Delta_1 \equiv \Delta_{\mathbf{k}_1}$, $\Delta_2 \equiv \Delta_{\mathbf{k}_2}$. The solution to Eq. (E4):

$$f = \delta_{0,\mathbf{q}} B^{-1}(\xi_1, \xi_2, \Delta_1, \Delta_2) d,$$

gives just the result of Eq. (37) for the 1st component of f .

In the presence of scattering, we consider only the M-nondiagonal ($\mathbf{q} \neq 0$) case, and then Eq. (E4) turns into

$$\hat{B}(\xi_1, \xi_2, \Delta_1, \Delta_2) f = -\frac{1}{N} \sum_{\mathbf{p}} (e^{-i\mathbf{q}\cdot\mathbf{p}} \hat{A}_1 f'_1 + e^{i\mathbf{q}\cdot\mathbf{p}} \hat{A}_2 f'_2), \quad (\text{E5})$$

where the vectors of “single scattered” TPGFs are

$$f'_1 = \begin{pmatrix} \langle\langle c_{-\mathbf{k}_1+\mathbf{q},\downarrow} c_{\mathbf{k}_2,\uparrow} | c_{-\mathbf{k}_2+\mathbf{q},\downarrow} c_{\mathbf{k}_1-\mathbf{q},\uparrow} \rangle\rangle \\ \langle\langle c_{\mathbf{k}_1-\mathbf{q},\uparrow} c_{\mathbf{k}_2,\uparrow} | c_{-\mathbf{k}_2+\mathbf{q},\downarrow} c_{\mathbf{k}_1-\mathbf{q},\uparrow} \rangle\rangle \\ \langle\langle c_{-\mathbf{k}_1+\mathbf{q},\downarrow} c_{-\mathbf{k}_2,\downarrow} | c_{-\mathbf{k}_2+\mathbf{q},\downarrow} c_{\mathbf{k}_1-\mathbf{q},\uparrow} \rangle\rangle \\ \langle\langle c_{\mathbf{k}_1-\mathbf{q},\uparrow} c_{-\mathbf{k}_2,\downarrow} | c_{-\mathbf{k}_2+\mathbf{q},\downarrow} c_{\mathbf{k}_1-\mathbf{q},\uparrow} \rangle\rangle \end{pmatrix},$$

$$f'_2 = \begin{pmatrix} \langle\langle c_{-\mathbf{k}_1,\downarrow} c_{\mathbf{k}_2-\mathbf{q},\uparrow} | c_{-\mathbf{k}_2+\mathbf{q},\downarrow} c_{\mathbf{k}_1-\mathbf{q},\uparrow} \rangle\rangle \\ \langle\langle c_{\mathbf{k}_1,\uparrow} c_{\mathbf{k}_2-\mathbf{q},\uparrow} | c_{-\mathbf{k}_2+\mathbf{q},\downarrow} c_{\mathbf{k}_1-\mathbf{q},\uparrow} \rangle\rangle \\ \langle\langle c_{-\mathbf{k}_1,\downarrow} c_{-\mathbf{k}_2+\mathbf{q},\downarrow} | c_{-\mathbf{k}_2+\mathbf{q},\downarrow} c_{\mathbf{k}_1-\mathbf{q},\uparrow} \rangle\rangle \\ \langle\langle c_{\mathbf{k}_1,\uparrow} c_{-\mathbf{k}_2+\mathbf{q},\downarrow} | c_{-\mathbf{k}_2+\mathbf{q},\downarrow} c_{\mathbf{k}_1-\mathbf{q},\uparrow} \rangle\rangle \end{pmatrix},$$

and the 4×4 matrices:

$$\hat{A}_1 = \begin{pmatrix} \hat{V} & 0 \\ 0 & \hat{V} \end{pmatrix}, \hat{A}_2 = \begin{pmatrix} \hat{V} \hat{\tau}_3 & 0 \\ 0 & -\hat{V} \hat{\tau}_3 \end{pmatrix}.$$

Next, the equations of motion for $f'_{1,2}$:

$$\begin{aligned} \hat{B}(\xi'_1, \xi_2, \Delta'_1, \Delta_2) f'_1 &= -\frac{1}{N} e^{-i\mathbf{q}\cdot\mathbf{p}} \hat{A}_1 f'', \\ \hat{B}(\xi_1, \xi'_2, \Delta_1, \Delta'_2) f'_2 &= -\frac{1}{N} e^{-i\mathbf{q}\cdot\mathbf{p}} \hat{A}_2 f'', \end{aligned} \quad (\text{E6})$$

with

$$\xi'_1 \equiv \xi_{\mathbf{k}_1-\mathbf{q}}, \xi'_2 \equiv \xi_{\mathbf{k}_2-\mathbf{q}}, \Delta'_1 \equiv \Delta_{\mathbf{k}_1-\mathbf{q}}, \Delta'_2 \equiv \Delta_{\mathbf{k}_2-\mathbf{q}},$$

contain the “doubly scattered” TPGF $f'' \equiv \langle\langle c_{-\mathbf{k}_1+\mathbf{q},\downarrow} c_{\mathbf{k}_2-\mathbf{q},\uparrow} | c_{-\mathbf{k}_2+\mathbf{q},\downarrow} c_{\mathbf{k}_1-\mathbf{q},\uparrow} \rangle\rangle$, which is already M-diagonal and hence can be taken just in the form of Eq. (37). Finally, the solution

$$\begin{aligned} f &= \hat{B}^{-1}(\xi_1, \xi_2, \Delta_1, \Delta_2) \\ &\quad \times \left\{ \delta_{0,\mathbf{q}} + \frac{c}{N} [\hat{A}_1 \hat{B}^{-1}(\xi'_1, \xi_2, \Delta'_1, \Delta_2) \hat{A}_1 \right. \\ &\quad \left. + \hat{A}_2 \hat{B}^{-1}(\xi_1, \xi'_2, \Delta_1, \Delta'_2) \hat{A}_2] \hat{B}^{-1}(\xi'_1, \xi'_2, \Delta'_1, \Delta'_2) \right\} d, \end{aligned} \quad (\text{E7})$$

defines the contribution $\sim c(V_L \Delta/V)^2$ to δ^2 , Eq. (36), the factor Δ^2 being due to Δ_1, Δ_2 -odd terms from $\hat{B}^{-1}(\xi'_1, \xi_2, \Delta_1, \Delta_2)$ and $1/V^2$ due to the dominating, zeroth order in Δ_1, Δ_2 , terms from $\hat{B}^{-1}(\xi'_1, \xi_2, \Delta'_1, \Delta'_2) \hat{B}^{-1}(\xi'_1, \xi'_2, \Delta'_1, \Delta'_2)$ and $\hat{B}^{-1}(\xi_1, \xi'_2, \Delta_1, \Delta'_2) \hat{B}^{-1}(\xi'_1, \xi'_2, \Delta'_1, \Delta'_2)$.

*E-mail: vloktev@bitp.kiev.ua

¹Here we don't consider the possible formation of stripe structures, where an ordered or disordered distribution of dopants cannot yet be confirmed by any reliable data.

²However, it is known that μ can differ substantially from the Fermi energy ε_F in the limit of very low doping (see, e.g., Refs. 4 and 6).

³So, we do not take into account next-neighbor hoppings.

⁴This approximation is actually justified by the fact that for $c > c_0$ the Fermi level ε_F of the metallic phase is well higher than the conduction band edge, and one can hardly suppose the existence of local pairs and the related inequality $\mu < \varepsilon_F$ at these concentrations. Therefore, in what follows we do not distinguish between μ and ε_F .

⁵Except for the special case $1/\bar{V}=0$, which corresponds to $c \approx 4c_0/3$, while the actual consideration is for $c \ll c_0$.

¹P. W. Anderson, J. Phys. Chem. Solids **11**, 26 (1959).

²A. A. Abrikosov and L. P. Gor'kov, Zh. Eksp. Teor. Fiz. **39**, 1781 (1961) [Sov. Phys. JETP **12**, 1243 (1961)].

³Z.-X. Shen and D. S. Dessau, Phys. Rep. **253**, 1 (1995).

⁴V. M. Loktev, Fiz. Nizk. Temp. **22**, 3 (1996) [Low Temp. Phys. **22**, 3 (1996)].

⁵A. V. Puchkov, D. N. Basov, and T. Timusk, J. Phys.: Condens. Matter **8**, 10049 (1996).

⁶V. M. Loktev, R. M. Quick, and S. G. Sharapov, Phys. Rep. **349**, 1 (2001).

⁷D. Bonn, S. Kamal, K. Zhang, R. Liang, D. J. Baar, E. Klein, and W. N. Hardy, Phys. Rev. B **50**, 4051 (1994).

⁸A. Maeda, T. Yabe, S. Takebayashi, M. Hase, and K. Uchinokura, Phys. Rev. B **41**, 4112 (1990).

⁹M. I. Salkola, A. V. Balatsky, and R. J. Schrieffer, Phys. Rev. B **55**, 12 648 (1997).

¹⁰Y. Fukuzumi, K. Mizuhashi, K. Takenaka, and S. Ushida, Phys. Rev. Lett. **76**, 684 (1996).

¹¹S. H. Pan, E. W. Hudson, K. M. Lang, H. Esaki, S. Ushida, and J. C. Davis, Nature (London) **403**, 746 (2000).

¹²P. A. Lee, Phys. Rev. Lett. **73**, 1887 (1993).

¹³A. V. Balatsky, A. Rozengren, and B. L. Altshuler, Phys. Rev. Lett. **73**, 720 (1994).

¹⁴Yu. G. Pogorelov, Solid State Commun. **95**, 245 (1995).

¹⁵A. M. Nersisyan, A. Tselik, and F. Wenger, Nucl. Phys. B **438**, 561 (1995).

¹⁶A. Ghosal, M. Randeria, and N. Triverdi, Preprint cond-mat/0012304 (2000); Phys. Rev. B **65**, 20505 (2001).

¹⁷A. C. Durst and P. A. Lee, Phys. Rev. B **62**, 1270 (2000).

¹⁸N. F. Mott and E. A. Davis, *Electronic Processes in Non-Crystalline Materials*, Clarendon Press, Oxford (1971).

¹⁹V. M. Loktev and Yu. G. Pogorelov, Physica C **272**, 151 (1996).

²⁰C. C. Tsuei, J. R. Kirtley, C. C. Chi, L. S. Yu-Jahnes, A. Gupta, T. Shaw, J. Z. Sun, and M. B. Ketchen, Phys. Rev. Lett. **73**, 593 (1994).

²¹D. J. Scalapino, Phys. Rep. **250**, 329 (1995).

²²D. J. Van Harlingen, Rev. Mod. Phys. **67**, 515 (1995).

²³A. A. Abrikosov, Preprint cond-mat/9912394, (1999); Phys. Rev. B **63**, 134518 (2001).

²⁴P. W. Anderson, Phys. Rev. **102**, 1492 (1958).

²⁵I. M. Lifshitz, Adv. Phys. **13**, 483 (1964).

²⁶I. M. Lifshitz, S. A. Gredeskul, and L. A. Pastur, *Introduction to the Theory of Disordered Systems*, Wiley and Sons, New York (1988).

²⁷M. A. Ivanov, Fiz. Tverd. Tela (Leningrad) **12**, 1508 (1971) [Sov. Phys. Solid State **12**, 1895 (1971)].

²⁸M. A. Ivanov, V. M. Loktev, and Yu. G. Pogorelov, Phys. Rep. **153**, 209 (1987).

²⁹Yu. Kagan and Ya. A. Iosilevskii, Sov. Phys. JETP **15**, 182 (1962).

³⁰R. J. Elliott, J. A. Krumhansl, and P. L. Leath, Rev. Mod. Phys. **46**, 465 (1974).

³¹M. A. Ivanov, V. M. Loktev, and Yu. G. Pogorelov, Sov. Phys. JETP **74**, 317 (1992).

³²L. P. Gor'kov and P. A. Kalugin, JETP Lett. **41**, 253 (1985).

³³M. Covington, M. Aprili, E. Paraoanu, L. H. Greene, F. Xu, J. Zhu, and C. A. Mirkin, Phys. Rev. Lett. **79**, 277 (1997).

This article was published in English in the original Russian journal. Reproduced here with stylistic changes by AIP.

Model for superconductivity in optimally doped electron cuprates

T. H. Geballe* and B. Y. Mozhes

Laboratory for Advanced Materials and Department of Applied Physics, Stanford University, Stanford, CA 94305-4045

(Submitted May 29, 2001)

Fiz. Nizk. Temp. **27**, 1053–1055 (September–October 2001)

The very anomalous normal state properties and superconductivity of electron-doped superconducting cuprates with the T^* structure are discussed. The high values of the electron and hole mobilities in the literature are explained by the electrons and holes existing in different layers. The annealing procedures necessary for superconductivity produce oxygen-vacancy negative- U pairing centers. The relative insensitivity of T_c to the annealing condition is attributed to stabilization of the chemical potential near the middle of the narrow oxygen band formed by oxygen vacancies, where the electronic entropy is large. © 2001 American Institute of Physics. [DOI: 10.1063/1.1401187]

INTRODUCTION

Pairing interactions which are confined only to the CuO_2 layers of optimally hole-doped high-temperature superconducting cuprates are believed to be insufficient to account for the wide range of maximum T_c values which are found in the families of superconducting cuprates which have the highest T_c (Ref. 1). In the present paper we extend our discussion to include the electron-doped superconducting cuprates.

While pairing interactions are considered to be exclusively in the CuO_2 layers in the most widely accepted models of cuprate superconductivity, there is certainly no theoretical reason why they cannot occur elsewhere. Attractive interactions across interfaces have been discussed many times in the past, starting with Ginzburg² and Bardeen.³ In their models artificial interfaces were considered.

In the cuprates nature has provided layers with well-matched interfaces, with the possibility of transferring charge (or doping) from reservoir layers which are removed from the CuO_2 layers. Ternary layered perovskites and structures with even more-complex unit cells grown either as single crystals or as films might be considered to be “self-organized” with layer sequencing that permits modulated doping. In order to account for the very high- T_c superconducting transitions of the cuprates which have Hg-, Tl-, and Bi-based charge reservoir layers, we have suggested, on the basis of well-known chemistry of these elements, that those $6S^1$ cations are negative U centers. These provide an effective attractive potential between electrons of opposite spin.¹ The negative U center forms as a result of the cation interaction with surrounding atoms (polarization, deformation, magnetic, etc.) and internal electron correlation. In the strongly ionic limit the $6S^1$ cations can disproportionate to $6S^0$ and $6S^2$ configurations. More realistically, they would form a narrow band based upon those configurations. The quasiparticles in this partially filled band can interact with the pair ordering in the CuO_2 layers and become part of the condensate. While at this stage there is no direct proof for this idea, we believe it has merit because: (i) it is well known that Hg, Bi, and Tl form negative U centers in many oxides, and (ii) there is the well-documented case discovered by

Chernik and Lykov⁴ of superconductivity resulting when small concentrations of Tl are substituted for Pb in PbTe . Two articles review the extensive research in Russia which shows convincingly that Tl (and no other dopants) forms a narrow resonant band based upon $6S^0 - 6S^2$ states inside the PbTe valence band which, when partially occupied, becomes superconducting.^{5,6} Optimum doping of about $\sim 10^{20}$ carriers per cubic centimeter results in T_c values which range up to 2 K. It is of interest that these quantities are comparable to those found in optimally oxygen-reduced SrTiO_3 .

More experiments are needed to test the idea that negative U centers enhance the superconductivity of the layered cuprates. As a first step in this direction, we refer to a model which analyzes tunneling through a barrier containing negative U impurities⁷ and predicts that an enhanced critical current should be observed due to pair resonant tunneling.

In the present paper we show that pairing due to negative U centers may be useful as a basis for understanding the perplexing chemistry and unusual normal state properties reported in the literature of the electron-doped cuprates such as $(\text{NdCe})_2\text{CuO}_4$ (NCCO) which have the T^* structure, where a separate oxygen layer exists between the rare-earth layers.

ELECTRON DOPED CUPRATES

The synthesis of electron-doped superconducting cuprates is a two step process.⁸ The first step is a straightforward substitution of a tetravalent cation (Ce or Th) for the trivalent rare earth, such as Nd. The added electron which is transferred to the CuO_2 layer remains weakly localized. The second step involves annealing in vacuum or an inert gas, which removes a small amount of oxygen (~ 1 or 2%). The second step is essential for producing superconductivity⁹ and cannot be understood in terms of simple doping or charge transfer. From chemical considerations each oxygen removed leaves two electrons in the lattice. Intuitively one might expect the increased electron doping to be the same as would be obtained by the substitution of two additional Ce^{4+} for Nd^{3+} , which results only in a small decrease in resistivity. However, a much more remarkable change occurs. The trans-

port behavior shows that mobile holes and electrons are created and that superconductivity appears below about 25 K.

The neutron diffraction data¹⁰ show no significant structural change results from the oxygen reduction (step 2). The only difference is that a barely detectable concentration of interstitial oxygen at the apical oxygen (O₃) site (which is not occupied in the ideal T^* phase) is no longer detected in the reduced (superconducting) single crystal.

The profound consequences of removing 1% or so of oxygen from the lattice are not at all clear. Studies of (Nd_{1.85}Ce_{0.15})CuO₄, the most intensively investigated system, show that the superconducting properties are only found in a narrow concentration range for compositions $0.15 \leq \text{Ce} \leq 0.18$,⁹ and only after reduced oxygen annealing. After this treatment the transport properties suggest semimetallic behavior with low carrier concentration. For some samples the Hall effect changes sign with temperature,¹¹ and the Seebeck voltage can be of either sign.¹² The positive Nernst effect is 1 to 2 orders of magnitude larger than expected for a typical Fermi liquid.¹² A large positive magnetoresistance at 60 K^{12,13} is observed, which on simple considerations suggests mobilities of the order of $100 \text{ nm}^2/(\text{V}\cdot\text{s})$. Smaller changes in the resistivity itself with doping indicate that mobility changes may be more important than doping.

SUGGESTED MODEL

There have been no satisfactory models proposed to explain the transport and superconductivity of n -type cuprates. It seems apparent to us that it will be necessary to consider interactions throughout the entire complex unit cell, much as we have argued is needed to understand the hole-doped cuprates.¹ For the electron-doped cuprates with the highest T_c , more-definitive experiments, particularly careful measurements comparing single crystals and epitaxial films before and after step 2, are needed. At present we can offer only educated guesses as to the underlying microscopic physics and chemistry.

There is no doubt that in step 1 the Ce doping transfers electrons to the CuO₂ layer. The CuO bond distance increases and the distance between the NdCe layer and the oxygen layer decreases.¹⁴

NORMAL STATE PROPERTIES

It takes 15% Ce doping to destroy the antiferromagnetic long-range order, after which the transport remains in the weak localization regime at low temperatures.

In step 2, oxygen vacancies are created and two electrons remain in the lattice for each oxygen removed. It is well known from the properties of reduced alkaline earth oxides that oxygen vacancies are never paramagnetic.¹⁵ We postulate that similar behavior occurs in the reduced cuprates. That this is not unexpected follows from a model comparing the energies of singly and doubly charged impurity centers in a dielectric continuum.¹⁶

A maximum positive magnetoresistance is expected when the electron and hole conductivities are equal. This maximum is observed approximately at the same concentration as $T_{c(\text{max})}$ (Fig. 7 of Ref. 12). The magnitude suggests

there are about 10^{20} carriers. If they were confined to single layers one would expect strong $2d$ electron-hole Coulomb scattering and low mobility.

Semimetals with high mobilities such as Sb and Bi are 3-dimensional and have very large dielectric constants; both of these factors increase the screening. We suggest that there is a different reason for the high mobility in NCCO, namely because the mobile carriers exist in different layers. The electrons are confined to the CuO₂ layers and the holes are confined to the oxygen layers, where the Madelung potential favors holes. It is significant that step 2 is only effective after the long-range antiferromagnetic order is destroyed by the Ce doping. The electrons in the CuO₂ layers are then less localized and may promote increased conductivity in the oxygen layers. This interaction in turn should promote delocalization in the CuO₂ layers.¹⁷

SUPERCONDUCTING INTERACTIONS

Without the oxygen vacancies there is no superconductivity. We propose that the oxygen-vacancy negative- U centers discussed above support superconducting pairing interactions in the oxygen layers, much as Hg, Bi, and Tl cations do in the charge reservoir layers of the hole-doped type of cuprates.¹ Experiments⁵ with Tl in PbTe wherein the hole concentration was changed by additional doping with Na, which is a lower-lying acceptor level than Tl, show that, to obtain maximum T_c , the chemical potential must be close to the middle of the narrow negative- U band, where both occupied and unoccupied negative U states are present.

This position of the chemical potential is stabilized after annealing by thermodynamics due to the highest electron density of states being near the middle of the impurity band. A somewhat related behavior has been noted in oxygen-nonstoichiometric (HgRe)Ba₂CuO_y, where a value of T_c close to $T_{c(\text{max})}$ after annealing is achieved independently of changes in Hg and Re composition.¹⁸ The procedures for obtaining T_c in step 2, which are relatively robust and independent of the exact annealing regime, i.e., whether done in a vacuum, or in an inert gas, or in oxygen at a more elevated temperature, can reasonably be attributed to a similar thermodynamic stabilization.

CONCLUSION

We have proposed a model which has the virtue of being able to explain the unusual normal state and superconducting properties of electron-doped cuprate superconductors for the first time. The model has unusual features, particularly that there are mobile electrons and holes present which exist in different layers of the unit cell. Superconducting pairing interactions are believed to arise from negative- U center oxygen vacancies which are formed upon removing oxygen by annealing. Considerably more experimental and theoretical work is required in order to prove or disprove our model.

We are grateful for the opportunity to dedicate this short note and unconventional model to the memory of L. Shubnikov and to acknowledge the enormous contributions to physics that he made during his shortened life.

The work at Stanford has been supported in part by the Air Force Office of Scientific Research.

*E-mail: geballe@stanford.edu

- ¹T. H. Geballe and B. Y. Mozyzhes, *Physica C* **341–348**, 1821 (2000).
- ²V. L. Ginzburg, *Zh. Éksp. Teor. Fiz.* **47**, 1549 (1964) [*Sov. Phys. JETP* **20**, 2318 (1964)].
- ³D. Allender, J. Bray, and J. Bardeen, *Phys. Rev. B* **7**, 1026 (1973); *Phys. Rev. B* **8**, 4443 (1973).
- ⁴I. A. Chernik and S. N. Lykov, *Pis'ma Zh. Éksp. Teor. Fiz.* **7**, 94 (1981) [*Sov. Tech. Phys. Lett.* **7**, 40 (1981)]; I. A. Chernik and S. N. Lykov, *Fiz. Tverd. Tela (Leningrad)* **23**, 1400 (1981) [*Sov. Phys. Solid State* **23**, 817 (1981)].
- ⁵V. I. Kaidanov and Yu. I. Ravich, *Sov. Phys. Usp.* **28**, 31 (1985).
- ⁶S. A. Némov and Yu. I. Ravich, *Phys. Usp.* **41**, 735 (1998).
- ⁷V. Oganessian, S. Kivelson, T. H. Geballe, and B. Y. Mozyzhes (to be published).
- ⁸Y. Tokura, H. Takagi, and S. Uchida, *Nature (London)* **337**, 345 (1989).
- ⁹Original references are given in the extensive review by J. Fontcuberta and L. Fábrega, in *Studies of High Temperature Superconductors*, Vol. 16, A. Narlicar (Ed.), Nova Science Publishers, Inc. (1996), p. 85. It is noteworthy that similar results are obtained for a variety of annealing procedures.
- ¹⁰A. J. Schultz, J. D. Jorgenson, J. L. Peng, and R. L. Greene, *Phys. Rev. B* **53**, 5157 (1996).
- ¹¹W. Jiang, S. N. Mao, X. X. Xi, X. Jiang, J. L. Peng, T. Venkatesan, C. J. Lobb, and R. L. Greene, *Phys. Rev. Lett.* **73**, 1291 (1994).
- ¹²P. Fournier, X. Jiang, W. Jiang, S. N. Mao, T. Venkatesan, C. J. Lobb, and R. L. Greene, *Phys. Rev. B* **56**, 14149 (1997).
- ¹³Nonsuperconducting samples show a negative magnetic resistance as expected for weak localization.
- ¹⁴References to original work are cited in Ref. 9.
- ¹⁵J. W. Carson, D. F. Holcomb, and H. Ru'chardt, *J. Phys. Chem. Solids* **12**, 66 (1959).
- ¹⁶B. Ya. Moizhes and S. G. Suprun, *Fiz. Tverd. Tela (Leningrad)* **24**, 209 (1982) [*Sov. Phys. Solid State* **24**, 550 (1982)].
- ¹⁷We are unaware of direct experimental evidence, but do note that a metallic overlayer produces a detectable increase in the T_c of a MoGe thin film. D. Ephron Thesis, *Correlated Electron Tunnelling and Quantum Motion of Vortices in Disordered Model Systems*, Stanford University (1996); N. Mason (private communication).
- ¹⁸A. Serquis, L. Fábrega, L. Morales, A. Basset, A. Caneiro, J. Fontcuberta, S. Short, J. P. Hodges, and J. Jorgensen, *Physica C* **341–348**, 511 (2000).

This article was published in English in the original Russian journal. Reproduced here with stylistic changes by AIP.

The influence of hydrogenation on superconducting properties of MgB_2

A. J. Zaleski,* W. Iwasieczko, D. Kaczorowski, and H. Drulis

Institute of Low Temperature and Structure Research, PAS, Wroclaw, Poland

M. Tkacz and O. J. Zogal

Institute of Physical Chemistry, PAS, Warsaw, Poland

J. Klamut

International Laboratory of High Magnetic Fields and Low Temperatures, Wroclaw, Poland

(Submitted June 5, 2001)

Fiz. Nizk. Temp. **27**, 1056–1059 (September–October 2001)

In the paper we present the results of the ac susceptibility measurements of the newly discovered superconducting diboride— MgB_2 . © 2001 American Institute of Physics.

[DOI: 10.1063/1.1401188]

1. INTRODUCTION

At the very beginning of the new millennium Akimitsu¹ proved that it is still possible to discover superconductivity with a rather high critical temperature in a compound which comes from the already well-investigated family of diborides and was commercially available. After this discovery, MgB_2 , with its critical temperature $T_c = 38$ K, was investigated with unprecedented speed. After a few months almost every characteristic of the material had been determined.

The first information about the superconducting properties of the compounds with the AlB_2 -type structure was published already in 1970 by Cooper *et al.*² They found that hexagonal NbB_2 or MoB_2 as cast are not superconducting, but increasing the amount of boron to about 2.5 or substituting with Sc, Y, Zr, Mo, Ru, Hf, or Th for Nb or additionally with Al, Ti, V, Ta, or Au for Mo resulted in a superconducting material with a critical temperature peaking at $T_c = 9.3$ K for $\text{Nb}_{1.9}\text{Y}_{0.1}\text{B}_2$ and at $T_c = 11.2$ K for $\text{Mo}_{1.69}\text{Zr}_{0.31}\text{B}_2$.

The results of another systematic search for superconductivity in diborides were published by Leyarovska *et al.*³ Investigating the magnetic susceptibility of MeB_2 (Me=Ti, Zr, Hf, V, Nb, Ta, Cr, Mo) down to 0.42 K, the authors found that only NbB_2 was superconducting, with a critical temperature of $T_c = 0.62$ K. MgB_2 was not among the materials studied.

After Akimitsu's discovery¹ it was quite natural that many research groups rechecked old or newly prepared diborides. And the results obtained by different groups were quite surprising. Kaczorowski *et al.*⁴ found a superconducting signal in old TaB_2 , with $T_c = 9.5$ K, but did not find it for TiB_2 , HfB_2 , VB_2 , NbB_2 , or ZrB_2 . In turn Gasparov *et al.*⁵ found superconductivity in ZrB_2 with $T_c = 5.5$ K, but they did not confirm its existence for TaB_2 and NbB_2 . Following the report by Felner⁶ that BeB_2 is not superconducting, there was a paper by Young *et al.*⁷ reporting superconductivity in $\text{BeB}_{2.75}$, with $T_c \approx 0.7$ K. Superconductivity was also discovered⁸ in ReB_2 (T_c in the range 4.5–6.3 K, depending on boron content) and Re_3B ($T_c = 4.7$ K).

Substituting magnesium with monovalent, divalent, or trivalent ions was studied by Medvedeva *et al.*⁹ Its influence on the superconducting properties of MgB_2 is connected with the electronic structure of the latter and is dominated by the chemical bonding of the hexagonal, graphitelike B sheets. The σ bonds between the boron atoms are unfilled and thus metallic, with more electrons in the π bonds. As a result, MgB_2 may be well characterized by the ionic form $\text{Mg}^{2+}(\text{B}_2)^{2-}$. Filling the holes in the σ band by trivalent substitution is unfavorable for superconductivity, while some monovalent substitutions may be favorable for it. These findings have been partially supported as the substitution of trivalent aluminum degraded the superconductivity in the material,¹⁰ but monovalent copper substitution only broadened the transition without changing the transition-onset value.¹¹

In our paper we describe the results of a different method of doping of MgB_2 —hydrogenation. We also mention the results of doping TaB_2 with hydrogen.

2. MATERIALS AND METHODS

In our investigations we made use of commercially available, powdered MgB_2 (Johnson Matthey GmbH Alfa—98% purity). Hydrogen absorption was performed at a constant temperature under hydrogen gas pressure of 0.5–20 bar. Our first attempts at a reacting temperature of about 250 °C resulted in decomposition of MgB_2 . So finally the reaction temperature was set at 100 °C and the pressure at 20 bars. The concentration of hydrogen was determined volumetrically by monitoring the pressure change in a calibrated, sealed volume. Under the conditions described above, the hydrogen content was not higher than about $(3 \pm 1)\%$ /f.u. In an attempt to increase the hydrogen uptake we increased the hydrogen pressure to 7 kbar, leaving the temperature equal to 100 °C. In this case the uptake of hydrogen was very similar, as measured by the mass spectrometry method, and equal to about 3 %/f.u. X-ray analysis was carried out using an STOE diffraction system. The material was characterized by ac magnetic susceptibility measurements.

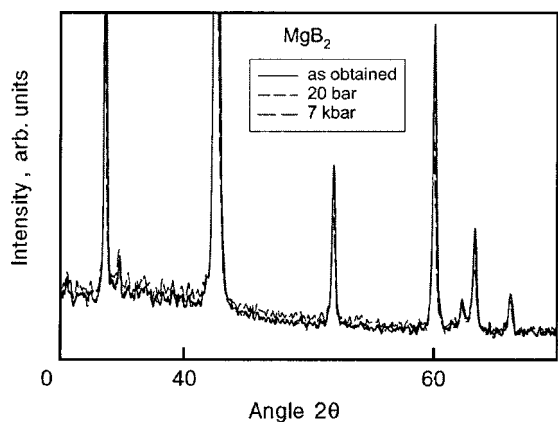


FIG. 1. X-ray diffractograms of as-obtained MgB_2 and hydrogenated under pressures of 20 bar and 7 kbar.

3. RESULTS AND DISCUSSION

X-ray diffractograms for as-obtained and hydrogenated samples are presented in Fig. 1. It is clearly seen that both the positions of the diffraction peaks and their widths are practically the same for all the measured samples. Small changes of the peak heights are to be ascribed, according to us, to the difference between the mass and thickness of the samples rather than to the different amounts of the majority phase. In principle such a result might be expected as the hydrogen uptake was rather small. Summing up—the structure and the volume of the phase with the MgB_2 -type structure remained unchanged after hydrogenation.

According to the paper by Wan *et al.*¹² the values of the lattice constants are connected with the location of the Fermi

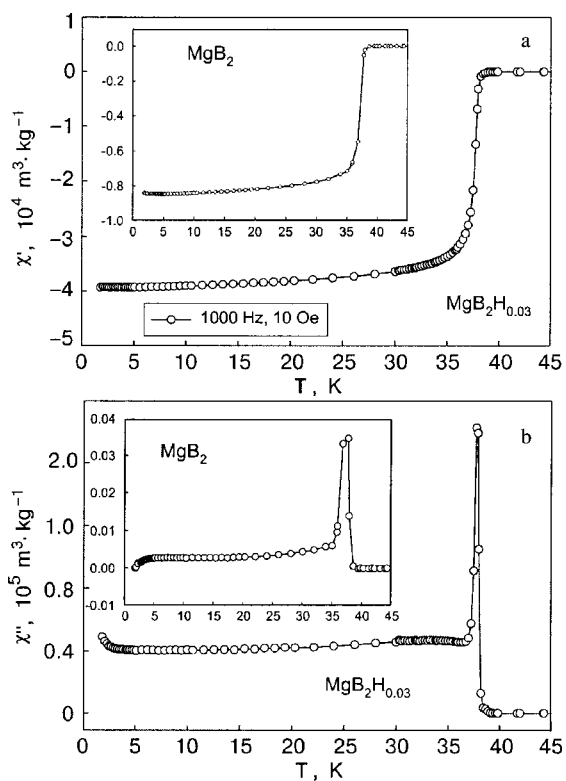


FIG. 2. Real (a) and imaginary (b) parts of the ac susceptibility of MgB_2 hydrogenated under a pressure of 20 bar. The insets show the ac susceptibility for as-obtained MgB_2 .

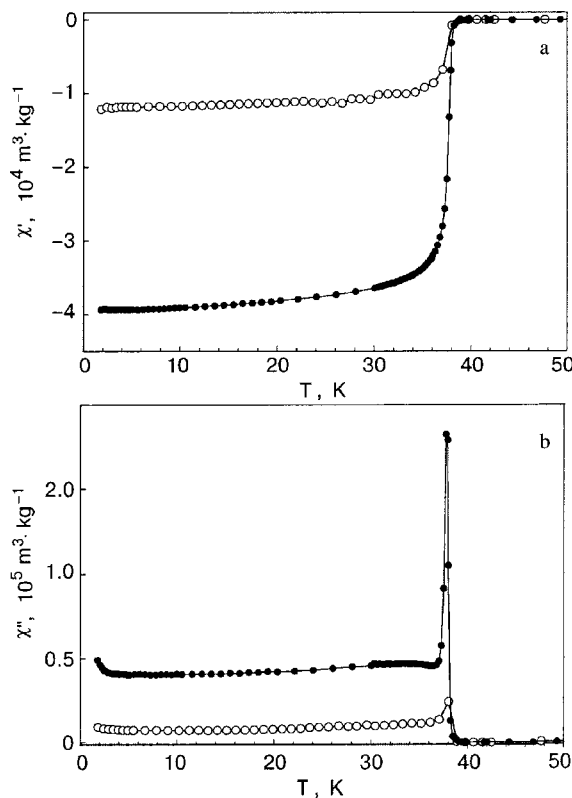


FIG. 3. Comparison of the ac susceptibility measurements results for $\text{MgB}_2\text{H}_{0.03}$ obtained under hydrogen pressures of 20 bar (●) and 7 kbar (○).

level relative to the density of states (DOS). Thus the constancy of the lattice constants probably means that the DOS is not changing meaningfully, either.

The results of ac susceptibility measurements of MgB_2 hydrogenated at 20 bar are presented in Fig. 2. For comparison, the results for the parent MgB_2 are presented in the insets. The masses of both powdered samples were very similar. So the main features of the plots are:

- the critical temperatures of both pure and hydrogenated compounds differs negligibly;
- the superconducting response (and thus the amount of superconducting phase) is two orders of magnitude lower for the hydrogenated sample;
- the superconducting transition width is narrower for the hydrated material.

Figure 3 shows a comparison between the ac susceptibilities of the MgB_2 after hydrogenation under different hydrogen pressures. As was mentioned above, the hydrogen uptake was very similar in the two cases despite the fact that the pressures during hydrogenation differ by 350 times. And, similarly to Fig. 2, one can see that the critical temperature remained unchanged and that there is an additional decrease of the amount of superconducting phase.

The two facts—unchanged critical temperature and decreasing (with hydrogenation) amount of superconducting phase—are rather surprising. The first fact implies that the density of states, electron–phonon interaction, and phonon spectrum remained unchanged after hydrogen uptake, whereas the decrease of the amount of superconducting phase may imply that the density of states was meaningfully changed.

So to account for our observations, in the picture of conventional BCS phonon-mediated superconductivity, the influence of hydrogenation on superconductivity should act in two opposing directions. We can analyze it using the modified McMillan equation:¹³

$$k_B T_c = \frac{\hbar \omega_0}{1.2} \exp\left(-\frac{1.04(1+\lambda)}{\lambda - \mu^*(1+0.62\lambda)}\right),$$

where k_B is Boltzmann's constant, ω_0 is the averaged phonon frequency, λ is the electron–phonon coupling constant, and μ^* is the Coulomb pseudopotential.

Hydrogenation can influence the phonon frequency. It was shown by Hinks *et al.*¹⁴ that the vibrations of B atoms are more strongly coupled to the electronic structure than those of Mg atoms. This may be inferred from the fact that the isotope effect for boron is much stronger than for magnesium. Both a theoretical calculation¹⁵ and experimental work support the view that the E_{2g} in-plane boron stretching mode is the main source of strong electron–phonon coupling. This mode was found to be strongly anharmonic.¹⁶ So if hydrogen is adsorbed within the boron planes (where it is easy to find the proper placement for it) it may strongly influence the stretching boron mode. But it is not easy to determine what kind of influence it might have. It might be increasing or lowering the anharmonicity or lowering or increasing the phonon frequency. This way hydrogen can also change λ or μ^* .

Absorption of hydrogen within the Mg planes also can not be excluded. Such a placement should not change the important modes of phonon frequencies,¹⁴ but it could influence the ionicity of the magnesium and boron planes.¹⁵ This in turn should change the position of Fermi level with respect to the σ boron bands and DOS. And with it also Coulomb screening and electron–phonon coupling could be changed. We believe that a change of ionicity of the layers should influence the value of the lattice constant c , perpendicular to the planes. As no such influence was observed in our study, we are inclined toward the first possibility.

We also applied hydrogenation under low pressure and temperature to the controversial compound TaB₂ studied by Kaczorowski *et al.*⁴ In this case the hydrogen uptake was equal to 36 %/f.u., much higher than for MgB₂. And in spite of such high hydrogen content, the critical temperature remained unchanged and equal to about 9.5 K, but the diamagnetic signal was an order of magnitude lower than for the undoped material.

4. SUMMARY

In conclusion, we have observed a meaningful decrease of the diamagnetic signal of hydrogenated commercial MgB₂ powder, while its critical temperature remained practically unchanged. The hydrogen uptake was very low (about 4%/f.u.) and independent on the pressure used. Such strange behavior can be explained by some opposite influence of the hydrogen on the DOS, phonon frequency, electron–phonon coupling, and Coulomb screening.

The authors would like to express their gratitude to Dr. Marek Wolczyr for x-ray measurements and to Dr. Tadeusz Kopec for valuable discussions.

*E-mail: zaleski@int.pan.wroc.pl

-
- ¹J. Akimitsu, *Symposium on Transition Metal Oxides*, Sendai, January 10, 2001.
 - ²A. S. Cooper, E. Corenzwit, L. D. Longinotti, B. T. Matthias, and W. H. Zachariasen, *Proc. Natl. Acad. Sci. U.S.A.* **67**, 313 (1970).
 - ³L. Leyarovska and E. Leyarovski, *J. Less-Common Met.* **67**, 249 (1979).
 - ⁴D. Kaczorowski, A. J. Zaleski, O. J. Zogal, and J. Klamut, *cond-mat/0103571*.
 - ⁵V. A. Gasparov, N. S. Sidorov, I. Izver'kova, and M. P. Kulakov, *cond-mat/0104323*.
 - ⁶I. Felner, *cond-mat/0102508*.
 - ⁷D. P. Young, P. W. Adams, J. Y. Chan, and F. R. Fronczek, *cond-mat/0104063*.
 - ⁸G. K. Strukova, V. F. Degtyareva, D. V. Shovkun, V. N. Zverev, V. M. Kiiko, A. M. Ionov, and A. N. Chaika, *cond-mat/0105293*.
 - ⁹N. I. Medvedeva, A. I. Ivanovskii, J. E. Medvedeva, and A. J. Freeman, *cond-mat/0103157*.
 - ¹⁰J. S. Slusky, N. Rogado, K. A. Regan, M. A. Hayward, P. Khalifah, T. He, K. Inumaru, S. M. Loureiro, M. K. Haas, H. W. Zandbergen, and R. J. Cava, *Nature (London)* **410**, 343 (2001).
 - ¹¹S. M. Kazakov, M. Angst, and J. Karpinski, *cond-mat/0103350*.
 - ¹²X. Wan, J. Dong, H. Weng, and D. Y. Xing, *cond-mat/0104216*.
 - ¹³W. L. McMillan, *Phys. Rev.* **167**, 331 (1968).
 - ¹⁴D. G. Hinks, H. Claus, and J. D. Jorgensen, *Nature (London)* **411**, 457 (2001).
 - ¹⁵J. M. An and W. E. Pickett, *cond-mat/0102391*.
 - ¹⁶A. F. Goncharov, V. V. Struzhkin, E. Gregoryanz, J. Hu, R. J. Hemley, H.-K. Mao, G. Lapertot, S. L. Bud'ko, and P. C. Canfield, *cond-mat/0104042*.

This article was published in English in the original Russian journal. Reproduced here with stylistic changes by AIP.

Quantum Hall effect in nonuniform two-dimensional electron systems

V. B. Shikin*

Institute of Solid State Physics, Russian Academy of Sciences, 142432 Chernogolovka, Moscow District, Russia

(Submitted February 26, 2001)

Fiz. Nizk. Temp. **27**, 1060-1068 (September-October 2001)

The quantum Hall effect (QHE) is inherent to uniform two-dimensional (2D) electron systems. At the same time, the basic low-dimensional conducting systems in the presence of metallic contacts are “regularly nonuniform.” Nevertheless, the QHE is well observed in them. The apparent paradox is resolved in a nontrivial manner. Regularly nonuniform 2D systems under conditions of the QHE admit the existence of integer (incompressible) channels that determine the conducting properties of the 2D system. To describe such a modification of the QHE requires a special formalism that explicitly takes into account the properties of the incompressible strips. The goal of this paper is to discuss the causes for the onset of regular nonuniformity of the 2D electron density in typical low-dimensional systems and to determine the basic characteristics of the QHE for such systems in terms pertaining to the individual incompressible strips. © 2001 American Institute of Physics. [DOI: [DOI: 10.1063/1.1401189]

It is well known that the contact of two three-dimensional (3D) metals having different work functions W_i leads to a partial transfer of electrons from one of the metals to the other so as to equalize their electrochemical potentials.¹ The corresponding disruption of the local neutrality in good metals occurs on scales of the order of the interatomic distances, while in samples with Boltzmann statistics it occurs over a length of the order of the Debye radius. It is of interest to examine the analogous problem for contacts between 2D and 3D conducting systems. This makes it clear that in 2D systems there is no characteristic length scale over which the local neutrality is disrupted, i.e., the contact-related perturbation of the electron density spans practically the entire 2D region accessible to the charge transport. Below we shall refer to such a deformation of the electron density as regularly nonuniform (in distinction to the possible random fluctuations of the density, the average value of which over the volume of the sample is usually assumed to be zero). In view of the sensitivity of many 2D problems, the QHE in particular, to the local electron density, it seems logical that the contact-related regular nonuniformity of the electron density will play an appreciable role in the effective formation of the Hall plateau. In this paper we give a consistent treatment of contact phenomena in 2D systems and discuss the details of the QHE in the presence of contact effects.

CONTACT ELECTROSTATICS

1. In setting forth the concrete results, let us start by recalling the electrostatics for a contact of two metals having different bulk characteristics, a circumstance which is effectively taken into account by the introduction of a contact potential difference ϕ_{ab} (Ref. 1),

$$e\phi_{ab} = W_a - W_b, \tag{1}$$

where W_i is the work function of the respective metal, and e is the elementary charge.

In the contact of metals A and B with open faces (see Fig. 1) an electric field with potential φ arises in the vacuum gap between the faces AO and OB (Ref. 1):

$$\varphi(\theta) = \phi_{ab} \frac{\theta}{\alpha}, \tag{2}$$

where α is the angle between faces OA and OB .

The electric field is given by

$$E_r = -\frac{1}{r} \frac{\partial \varphi}{\partial \theta} = \frac{\phi_{ab}}{\alpha r}, \quad E_r = 4\pi e \delta n(r) \tag{3}$$

and it falls off in inverse proportion to the distance r from the point O . This field is related to the surface charge density $\delta n(r)$ distributed along the free faces OA and OB .

Now let the role of ray OB be played by a 2D electron system and for simplicity take angles α and β in Fig. 1 equal to each other. Now the additional surface charge density

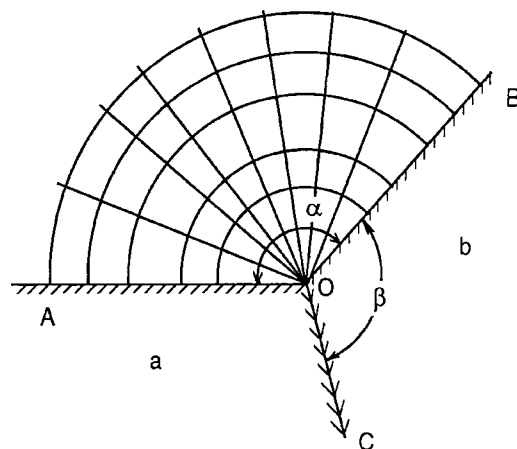


FIG. 1. Contact of two metallic samples having free boundaries.

from (3) is simultaneously an addition to the uniform electron density n_s of this system. In other words, the contact of the 2D electron gas with the conducting electrodes (2D or 3D) can at large distances noticeably disrupt the spatial uniformity of the 2D electron density if such was present in the 2D sample without the contacts.

2. The divergence of the field E (3) at small distances and the integral divergence for the total effective surface charge, which also follows from (3), are removed in the natural way. The first of these singularities vanishes when various corrections to the condition of thermodynamic equilibrium are included in the problem. For example, if one is talking about an accumulation of electrons in a 2D electron gas, then the divergence is removed at Bohr distances by allowance for the Fermi energy in the overall balance of forces (see Refs. 2–4). If we arbitrary talking about the other sign of W , corresponding to depletion of the 2D system, then the resulting equilibrium problem can contain so-called depletion layers, completely devoid of free electrons, at the ends of the 2D system. This type of equilibrium has been discussed in great detail in the literature, particularly in connection with the creation of controllable 2D systems, the geometry of which is controlled by external fields (see, e.g., Refs. 2, 3, 5–9).

Removal of the integral divergence of the charge is achieved by restricting the dimensions of the 2D system. The different versions of this problem are extremely diverse. Below we will be mainly discussing two results: a density perturbation $\delta n_0(x)$ for a quasi-1D Corbino disk, and the analogous problem for an extended Hall sample in its central part, far from the metallic contacts.

A Corbino disk is quasi-1D if $(R_1 - R_2)/(R_1 + R_2) \ll 1$, where R_1 and R_2 are the outer and inner radii of the disk. In this case the uniform part $\delta n_0(x)$ of the electron density of contact origin has been found as³

$$\delta n_0(x) = \frac{\kappa w \phi_{ab}}{\pi^2 e (w^2 - x^2)}, \quad -w \leq x \leq +w. \quad (4)$$

Here $2w = R_2 - R_1$ is the width of the 2D region between the metallic “banks,” the x axis is directed in the radial direction, the origin of coordinates is at the center of the 2D region, κ is the dielectric constant of the medium, and ϕ_{ab} is the contact potential difference. In the limit $a_B \ll w$ (a_B is the effective Bohr radius) approximation (4) works well far from the points $x = \pm w$.

For a Hall sample the contact electrostatic problem is not yet “standard,” and it therefore makes sense to give the details of its solution. The initial equation is

$$e\varphi(x, y) = \frac{2e^2}{\kappa} \int_{-L}^{+L} d\sigma \int_{-w}^{+w} ds \frac{\delta n(s, \sigma)}{[(x-s)^2 + (y-\sigma)^2]^{1/2}} = \text{const} = W, \quad (5)$$

$$-w \leq x \leq +w; \quad -L \leq y \leq +L; \quad W \equiv W_a - W_b;$$

$$\varphi(x, y, z=0) = 0, |y| > L; \quad \frac{\partial \varphi(x, y, 0)}{\partial z} = 0, |x| > w.$$

The y axis is directed along the long side of a rectangle, the electric potentials of the metallic contacts are both chosen equal to zero, and $W = e\phi_{ab}$.

The Fourier transformation of (5) with respect to the variable y gives

$$\varphi(x, q) = \text{const} = \frac{2e}{\kappa} \int_{-w}^{+w} \delta n(s, q) K_0(q|x-s|) ds, \quad (6)$$

$$2\pi/L \leq |q| \leq +\infty,$$

where $K_0(x)$ is the Bessel function of complex argument.

In the limit of small x the function $K_0(x)$ follows a logarithmic law. Consequently, if $L \gg w$, then far from the contacts the integral equation (6) takes the form

$$e\varphi(x) = \frac{2e^2}{\kappa} \int_{-w}^{+w} \delta n(s) \ln \frac{L}{x-s} ds = \text{const}. \quad (7)$$

The solution of this equation with respect to $\delta n(x)$ has the structure

$$\delta n(x) \propto \frac{\text{const}}{\sqrt{w^2 - x^2}} \quad (8)$$

with the value of the const determined by the requirement

$$W = \frac{2e^2}{\kappa} \int_{-w}^{+w} \delta n(s) \ln(L/s) ds.$$

As a result, we have

$$n(x) = n_s + \delta n \approx n_s + \frac{\kappa W}{c e^2 \sqrt{w^2 - x^2}}, \quad c = 2\pi \ln \frac{L}{w}. \quad (9)$$

The limit $q \rightarrow 0$ used in (7) applies if $w \ll L$ and the investigated x cross section of the Hall sample is far from the metallic contacts. Both assumptions are assumed to hold below.

EQUILIBRIUM CHARACTERISTICS OF THE SAMPLE IN THE QUANTUM HALL EFFECT REGIME

The formation of integer Hall strips in nonuniform 2D systems is accompanied by a redistribution of charge in the neighborhood of the integer points on the electron density profile $n(x)$. Consequently, one of the main properties of normal 2D systems—their equipotential character—is disturbed for states in the QHE regime. The corresponding predictions of the theory are checked by obvious experiments on the measurement of the local electrostatic fields (techniques utilizing the linear electrooptic effect are set forth in Refs. 10–12 and the microprobe technique is described in Refs. 13 and 14). The general conclusions that follow from Refs. 10–14 argue in favor of the existence of 2D contact phenomena and, as a consequence, integer channels in the interior of 2D systems.

The quantitative basis for the conclusions of this Section is provided by the results of Shklovskii and coworkers^{8,9} on the properties of equilibrium integer channels for 2D samples with density $n(x)$. For example, for the central channel and with a known curvature $n''(0)$ of the classical distribution of the electron density at its extremal point (the point with zero first derivative $n'(0)$), the distribution $\varphi(x)$ over the cross section of the channel with an integer filling factor $\nu_l = 1, 2, 3, \dots$ has the form

$$\varphi(x) = -\frac{\pi e n'' a^3}{3\kappa} (1 - x^2/a^2)^{3/2}, \quad (10)$$

and the width $2a$ is determined from

$$\begin{aligned} n''(0)a^2/4 &= [\nu(0) - \nu_l]n_H, \\ n''(0) &= d^2n(0)/dx^2, \end{aligned} \quad (11)$$

$$\nu(0) = n(0)/n_H, \quad n_H^{-1} = \pi l_H^2, \quad l_H^2 = \frac{c\hbar}{eH}. \quad (12)$$

Here H is the magnetic field normal to the plane of the Corbino disk.

The width of a strip is rather sensitive to the value of the magnetic field, and it varies from zero upon its nucleation to the critical dimensions

$$a_{\max}^3 = \frac{3\kappa\hbar\omega_c}{\pi e^2 |n''(0)|}, \quad (13)$$

where, as the magnetic field is increased, the maximum value of the potential (10) at the center of the channel reaches a value $\hbar\omega_c$, after which the strip splits into two (for details of this process see Ref. 9).

Substituting the expression for $n''(0)$ that follows from (4) into the definition (13), we get

$$(a_{\max}/w)^3 = \frac{3\pi\hbar\omega_c}{2e\phi_{ab}}. \quad (14)$$

For a Hall sample with $n(x)$ given by Eq. (9) we have

$$(a_{\max}/w)^3 = \frac{3c\hbar\omega_c}{\pi W}. \quad (15)$$

Formulas (10)–(15) are valid if $\hbar\omega_c \geq W$. In the opposite, altogether typical limiting case $\hbar\omega_c \ll W$ it becomes possible for a large number of incompressible strips to form, and the description of the form in (10), (11) loses meaning. An adequate formalism is needed which takes into account the large number of strips and the interactions between them. This can be done if it is taken into account that each strip has a potential difference $\hbar\omega_c$ on its “banks.” Consequently, the local value of the electrostatic potential in the problem with a large number of strips can be constructed in the form

$$e\varphi(x) \approx \hbar\omega_c \nu(x), \quad \nu(x) = \pi l_H^2 n(x), \quad (16)$$

where $\nu(x)$ is the local filling factor and l_H is the magnetic length.

According to Eq. (16), in the limit $\hbar\omega_c \ll W$ the electrostatic potential reproduces on average the local behavior of the electron density.

Formula (16), like expressions (4) and (9), loses meaning near the ends $\pm w$, where the excess electron density is divergent (or zero).

Having definitions (10)–(16) at our disposal, let us consider the experimental data for the equilibrium distribution $\varphi(x)$ in rectangular samples and Corbino disks.^{11,12} The most important result of these measurements is the qualitative difference in the behavior of the equilibrium value of $\varphi(x)$ over the cross section of the sample in the normal and “intermediate” states, when the system contains integer channels. In the first case, as expected, $\varphi(x) = \text{const}$ along the 2D system. As to the “strip” systems containing one or several integer

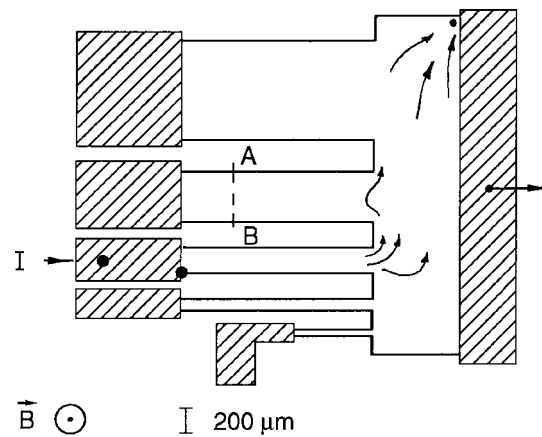


FIG. 2. Hall sample from Ref. 11; the arrows are a schematic indication of the current streamlines.

channels, here the relative value of $\varphi(x)$ falls off toward the center of the cross section. We note that the available data on the “intermediate” state do not give the absolute values of $\varphi(x)$ but only indicate that it is nonmonotonic.

Turning to a discussion of the experiments, let us begin with the results presented in Ref. 11, which attest to the nonuniformity of the distribution $\varphi(x)$ over the cross section of the Hall sample under the conditions of the QHE. Unfortunately, the data of Ref. 11 contain an uncertainty that interferes with their interpretation: in Fig. 2, taken from Ref. 11, one can clearly see an asymmetry which is apparently due to the influence of the neighboring channels; in addition, the position of the cross section, chosen by the authors from hydrodynamic considerations (decreasing the transport current through this “dead” channel as much as possible), is located at a short and poorly determined distance from the ends of this segment of complex configuration, complicating the consideration of the details of $\varphi(x)$. Nevertheless, the function $\varphi(x) \propto (1 - x^2/a^2)^{3/2}$ or, more precisely, its transform

$$\phi(x) = \frac{1}{2R} \int_{x-R}^{x+R} \varphi(s) ds, \quad (17)$$

which is shown by the solid curve in Fig. 3, gives a good approximation of the data of Ref. 11 for the central part of the sample. Here $R = 50 \mu\text{m}$ is the radius of the laser beam used in the experiments.^{11,12}

The information for the Corbino disk is more “transparent.” A comparison of the data of Ref. 12 with two versions of the distribution $\varphi(x)$ —multichannel (16) and single-channel (10)—is presented in Figs. 4 and 5. The calculated curves $\phi(x)$ were constructed using algorithm (17). The curves were “tied in” to the minimum $\phi(0)$, and the parameters R and the geometric dimensions contained in definitions (10) and (16) were varied. For example, the solid curve in Fig. 4 corresponds to the values $R = 50 \mu\text{m}$ and $\omega = 250 \mu\text{m}$. The additional lines in Fig. 4 illustrate the influence of the laser beam radius R on the behavior of $\phi(x)$. In Fig. 5 the function $\varphi(x)$ in (10) was “fit” to the same points for two different values of a ($R = 50 \mu\text{m}$).

It should be noted that the experimental points in Figs. 4 and 5 were obtained by scanning Figs. 1 and 2 from Ref. 12.

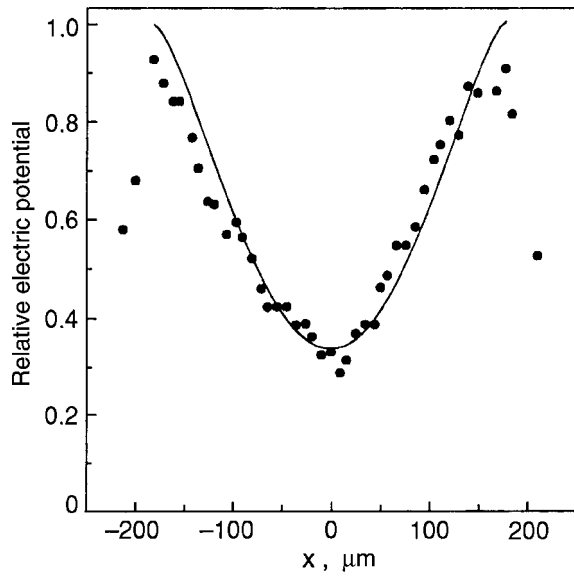


FIG. 3. Distribution of the electric potential over the cross section AB (see Fig. 2) on the so-called “dead” end (there is no transport current through the cross section). The solid line was calculated according to formulas (9), (10), and (17) with $R=50\ \mu\text{m}$, $a=160\ \mu\text{m}$.

Then, using Fig. 9 from Ref. 11, which is identical to Fig. 1 from Ref. 12, we were able to rescale the results of the scanning of Fig. 2 of Ref. 12 to the corresponding numbers for $\varphi(x)$.

Summing up, we can conclude that the Hall samples studied in Ref. 11 are well described in the single-channel approximation (10). As to the Corbino disk, the experimental data of Ref. 12 are better described by a multichannel distribution $\varphi(x)$ (16).

HALL TRANSPORT IN NONUNIFORM SAMPLES

The phenomenological theory^{8,9} of the integer Hall channels in nonuniform 2D electron systems was developed for

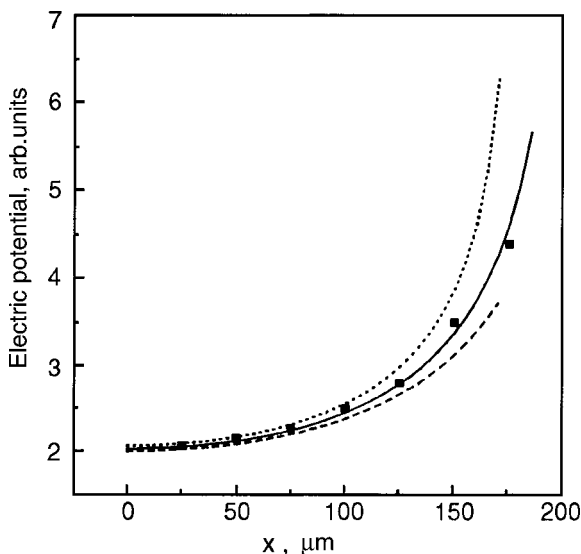


FIG. 4. Coordinate dependence of the transform (4), (16), (17) for a Corbino disk. The solid line corresponds to parameters $R=50\ \mu\text{m}$, $w=250\ \mu\text{m}$. The experimental points are from Ref. 12. The degree of sensitivity of the potential (16), (17) to variations of the radius R is illustrated by the two additional curves: $R=75\ \mu\text{m}$ (---), $R=5\ \mu\text{m}$ (.....).

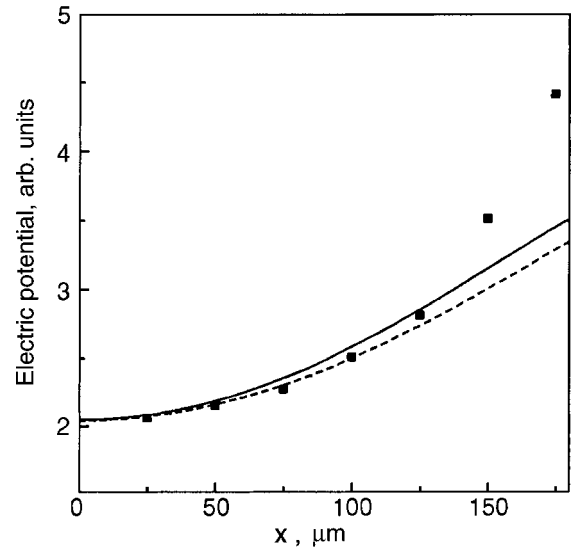


FIG. 5. The function $\psi(x)$ from (10) and (17) for a Corbino disk. $R=50\ \mu\text{m}$, $a=230\ \mu\text{m}$, (solid curve); $R=50\ \mu\text{m}$, $a=250\ \mu\text{m}$ (dashed curve).

equilibrium conditions, when the electrochemical potential μ is constant along the sample. Moreover, a large number of the experiments with nonuniform samples and, in particular, practically all the measurements of the local characteristics of various 2D systems (see Refs. 10–14) have been carried out in the transport regime, when there is a “drawing” potential difference V_H across the boundaries of the sample. The influence of $V_H \neq 0$ on the characteristics of the individual integer (incompressible) channels becomes a question. We are talking about a change in the strip width $2a$ and also a shift Δ of their position (relative to the equilibrium position) under the influence of V_H . In this Section we solve the problem for the central incompressible channel in a nonuniform 2D electron system having a one-dimensional electron density profile $n(x)$ which is symmetric about its center. Besides the one-dimensionality of the problem we shall use additional simplifications (as in Refs. 8 and 9), viz: the transverse dimensions $2w$ of the two-dimensional system are quite large (in comparison with the Bohr radius and the magnetic length), there is no screening of the electrodes, the temperature is low but finite (in order to avoid the correlation effects that lead to the fractional quantum Hall effect), and the Hall potential difference V_H is less than or comparable to the cyclotron energy, i.e., $V_H \ll \hbar \omega_c$, where ω_c is the cyclotron frequency.

General results for $\Delta(V_H)$ and $a(V_H)$ are used below in an interpretation of the observed¹⁴ details of the local characteristics of the Hall samples with a nonuniform profile $n(x)$ of contact origin.

1. Let us start with the electrochemical potential μ . Under nonequilibrium conditions this difference is no longer constant along the 2D system. Its behavior follows from the requirements

$$\nabla \cdot \text{div } \mathbf{j} = 0, \quad \nabla \times \text{rot } \mathbf{j} = 0, \tag{18}$$

$$j_i = e^{-1} \sigma_{ik} \partial \mu / \partial x_k, \tag{19}$$

where σ_{ik} is the conductivity tensor [in Ref. 9 (see Eq. (56) of that paper) and Ref. 15 Ohm's law contains the electrical potential φ instead of μ]. The combination of (18) and (19) leads to the equation

$$\nabla^2 \cdot \Delta \mu = 0 \quad (20)$$

even if $\sigma_{xx} \rightarrow 0$ (we note that the authors of Ref. 15 do not share this point of view).

Using (20) and the inequality $w \ll L$, where L is the length of the Hall sample, it is easy to see that in the presence of a Hall voltage V_H the function $\mu(x)$ for a sample far from the contacts is a linear function of the coordinate x :

$$\begin{aligned} \mu(x) &= eV_H(x + \Delta + a)/2, \quad \sigma_{xy} \gg \sigma_{xx}, \\ -a + \Delta &\leq x \leq +a + \Delta, \quad a < w \end{aligned} \quad (21)$$

(the parameter Δ is defined below).

Expression (21) and the definition of $\mu(x)$ for electrons in a magnetic field give a basis for formulating the problem of the properties of incompressible strips in the presence of transport. In a simplified version of the solution of this problem it is proposed (in analogy with Refs. 8 and 9) to start by modeling the electron density $\delta n(x)$ inside an incompressible strip so that its effective value is a constant, corresponding to an integer filling factor. Having $\delta n(x)$, we reconstruct the distribution $\varphi(x)$ with additional requirements that the tangential electric fields vanish at the boundaries of the strip. The ‘‘tie-in’’ of $\varphi(x)$ to the behavior of $\mu(x)$ occurs at these same ends. In the problem with $V_H \neq 0$ such an algorithm can be used only for the central strip. As to the ‘‘side’’ channels, in the transport version the extension of the concepts of Refs. 8 and 9 encounters difficulties that require special discussion.

Thus we assume

$$\begin{aligned} \delta n(x) &= (\nu_\Delta - l)n_H + n'_\Delta \xi + n''_\Delta \xi^2/2, \\ \xi &= x + \Delta, \quad l = 1, 2, 3, \dots \end{aligned} \quad (22)$$

$$\nu(x) = \pi l_H^2 n(x), \quad n_H = 1/(\pi l_H^2), \quad -a + \Delta \leq x \leq +a + \Delta,$$

where l_H is the magnetic length, Δ is the overall shift of the central strip relative to the coordinate origin, and $\nu_\Delta \equiv \nu(x = \Delta)$. In the limit $\Delta \rightarrow 0$ expression (22) agrees with $\delta n(x)$ from Ref. 9.

The corresponding distribution $E_x(x)$ follows from Poisson's equation written in a form which takes into account the constancy of the electrochemical potential within the limits of an integer strip:

$$e \delta n(\xi) = -\frac{\kappa}{2\pi^2} \int_{-a}^{+a} ds \frac{E_x(s)}{\xi - s}.$$

As a result

$$\begin{aligned} E_x \sqrt{(1 - \xi^2/a^2)} &= \frac{2\pi e}{\kappa} \left\{ \left[(\nu_\Delta - l)n_H T_1 \left(\frac{\xi}{a} \right) + n'_\Delta a T_2 \left(\frac{\xi}{a} \right) \right. \right. \\ &\quad \left. \left. + \frac{n''_\Delta a^2}{8} \left[T_3 \left(\frac{\xi}{a} \right) + T_1 \left(\frac{\xi}{a} \right) \right] \right] \right\} + E_H, \end{aligned} \quad (23)$$

where $T_i(s)$ are Chebyshev polynomials,¹⁶ and the constant E_H is as yet arbitrary and will be related to V_H below.

The field (23) can vanish at the ends $\xi = \pm a$ if

$$2\pi e n'_\Delta a + \kappa E_H = 0, \quad (24)$$

$$a^2 = -4[\nu_\Delta - l]n_H/(n''_\Delta), \quad l = 1, 2, 3, \dots, \quad (25)$$

where $n(x)$ is the equilibrium profile of the electron density. The difference between (25) and the definition of a^2 from Ref. 9 lies in the fact that ν_Δ and the derivative n''_Δ in our case are evaluated not at zero but at the point $x = \Delta$.

The potential $\varphi(\xi)$ is obtained from Eq. (23) by a single integration. Additionally taking into account (24) and (25), we have

$$\begin{aligned} \varphi(\xi) &= \frac{V_H}{\pi} \left(\xi \sqrt{1 - \xi^2} + \frac{\pi}{2} + \arcsin \xi \right) \\ &\quad + \frac{2\pi e n''_\Delta a^2 (1 - \xi^2)^{3/2}}{6\kappa}, \quad \xi = \xi/a, \end{aligned} \quad (26)$$

and

$$-\pi^2 e n'_\Delta a^2 / \kappa = V_H. \quad (27)$$

Requirements (27) and (24) determine the constant $E_H = 2V_H/\pi a$ in (24). Formulas (24)–(27) complete the solution of the problem of the behavior of the main channel near an extremum of the electron density with an even profile $n(x)$ in the presence of $V_H \neq 0$.

2. Recent experiments with Hall samples under conditions of the QHE with the use of a scanning potential microscope^{13,14} attest to the nonuniform but regular distribution of the equilibrium electron density in them, with a structure of the form $n(x)$ (x is the coordinate over a cross section of the sample normal to the current lines). The nonuniformity of $n(x)$ is due to contact phenomena which with a high probability are present in the experiments under discussion. In this case for Hall samples $2w2L$ ($L \gg w$) far from the contacts the distribution $n(x)$ has the form (9). Using this information, we rewrite a number of general definitions. The quantity Δ is given by

$$\Delta = -\frac{c}{\pi^2} \frac{eV_H w^3}{W a^2}. \quad (28)$$

In addition, we note that

$$\begin{aligned} \delta\varphi &= \varphi(x, V_H) - \varphi(x) \approx V_H \frac{(x + \Delta) + a}{2}, \\ -a + \Delta &\leq x \leq +a + \Delta \end{aligned} \quad (29)$$

varies in an approximately linear manner over the cross section of the central strip between the values $0, V_H$.

Turning to the experiments, we shall interpret the most complete Hall data, which are presented in Ref. 14 (see Sec. 2 of that paper) for the distribution $\delta\varphi(x)$ over a cross section in the central part of a Hall sample of width $2w = 10 \mu\text{m}$ in various magnetic fields. The experiment was done using a scanning microscope, which made it possible to work in the linear region $eV_H \leq \hbar\omega_c$. However, the tunneling technique turns out to be poorly suited for equilibrium measurements (as was the case in Refs. 11 and 12). As a result, the authors of Ref. 14 published only equilibrium data for $\delta\varphi(x)$, analogous to the difference (29). These functions are reproduced here in Fig. 6. The numbers 1–11 on the right-hand side of Fig. 6 enumerate the recordings of $\delta\varphi(x)$

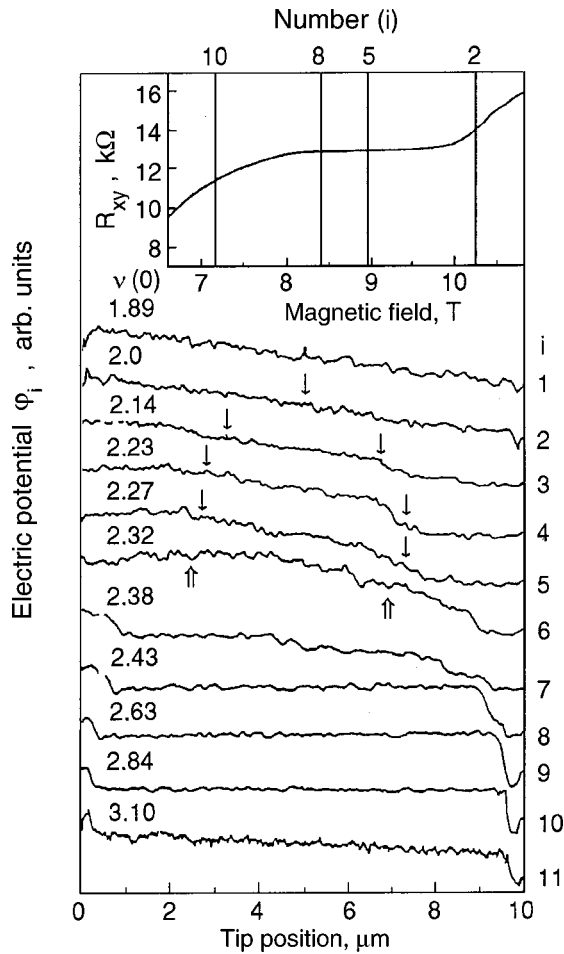


FIG. 6. Recorded traces¹⁴ of the local values of the electric potential along one of the Hall cross sections in the central region of the sample for various magnetic fields. The numbers on the right enumerate the traces, and those on the left give the local values of the filling factor $\nu(0)$ at the point of the maximum value of the electron density on the assumption that $\nu(0)=2$ on line 2 and that the Hall voltage is sufficiently small. The arrows on lines 2–5 indicate the boundaries of the central incompressible strip in the absence of transport current, as calculated using Eq. (12). The double arrows on line 6 give an idea of the scale of the asymmetry in the position of the boundaries under the influence of the transport current. Inset: Hall resistance of the sample versus the magnetic field in the neighborhood of the investigated quantum plateau.¹⁴ Also shown here is a selection of lines 1–11 of the main figure, allowing one to judge the relationship between the “quality” of the plateau and the width of the incompressible strips corresponding to these lines.

for different values of the magnetic field. These same numbers are indicated in the inset, which gives an idea of the behavior of R_{xy} of this sample in the neighborhood of the Hall plateau.

The numbers in the left-hand part of Fig. 6 give the local values of the filling factor $\nu(0)$ at each i th line. These numbers differ from those given in Ref. 14 by a linear shift and have been chosen from considerations of self-consistency of the contact scenario. In our version of events the nucleation of a quasi-symmetric incompressible strip occurs in the neighborhood of line 2 (line 1 does not show any signs of the existence of a strip, and on line 3 the strip already has a finite width). Consequently, on this line the value of $\nu(0)$ should take the value 2, and this value is taken as a basis for normalizing the values of $\nu(0)$. With increasing number i the magnetic field decreases, and the width of the central strip

grows. This behavior of $a(H)$ is possible only if the local density $n(x)$ decreases with distance from the center of the sample. In other words, the data on the behavior of $a(H)$ on lines 2–6 are evidence for a version of the contact interaction that leads to depletion of the 2D system. The positions of the boundaries $\pm a(H)$ with changing field in approximation (14) are indicated by arrows on lines 3–6. Here the free parameter $W/\hbar\omega_c$ is chosen such that under conditions corresponding to the decay of the central strip into two satellites, the value of a_{\max} (15) would be approximately equal (as is seen in Fig. 6) to one-half of ω (line 6). Hence and from Eq. (15) it follows that

$$\frac{W}{\hbar\omega_c} = \frac{3c}{\pi} \left(\frac{w}{a_{\max}} \right)^3 = \frac{24c}{\pi}. \quad (30)$$

The variation of $\delta\varphi(x)$ observed in Ref. 14 lies roughly in the region between the arrows (see Fig. 6). As follows from Eq. (29), this distribution is approximately linear between the “banks” of a strip. The small asymmetry is due to the influence of the Hall voltage on the boundaries of the central incompressible strip. As an estimate of the asymmetry we use the quantity Δ (28). With allowance for (30), the scale of the cyclotron energy on line 5 and the experimental value $eV_H \approx 0.01 \text{ eV} \leq \hbar\omega_c^{(5)}$ (see Ref. 14), we have for Δ

$$\Delta^{(5)} \leq 0.1w. \quad (31)$$

The position of the boundaries of the central strip, corrected by Δ , are indicated by the double arrows on lines 3–6 in Fig. 6.

The current asymmetry on lines 7–11 is particularly noticeable. Here the central part has undergone a transition to the “normal” state, i.e., is equipotential. The incompressible satellites are asymmetrically squeezed toward the boundaries of the Hall region. Unfortunately, the equilibrium treatment of Ref. 9 does not admit generalization to the case of the side satellites for $V_H \neq 0$. This circumstance was also mentioned above, and so we show without comment the interesting data on the splitting of the central channel (lines 7–11).

In summary, we have proposed a formalism that generalizes the results of Refs. 8 and 9 for integer (incompressible) strips in nonuniform 2D systems to the case of a finite Hall voltage $V_H \neq 0$. The results of the theory are used for interpretation of the data obtained in Refs. 11, 12, and 14 with the use of the hypothesis that the nonuniformity of the Hall sample is of contact origin. This hypothesis is very productive for discussing the equilibrium properties of nonuniform Corbino disks with integer strips (see Figs. 3 and 4). The appearance of the same channels in Hall samples is completely natural.

The picture that appears is qualitatively quite similar to the observations and explains many of the existing details. In particular, we have determined the sign of the contact energy for the samples from Ref. 14, which corresponds to depletion of the 2D region, and its scale, which is much larger than the cyclotron energy [see the definition of w in (30)]. We have given an explanation for the shift Δ of the central strip under the influence of a nonzero Hall voltage $V_H \neq 0$ [formulas (28) and (31)] and also for the shift of the extrema of $\varphi(x)$ under the influence of $V_H \neq 0$, for which a clear realization is not yet available.

This study was supported in part by the Russian Foundation for Basic Research, Grant 01 02 16467.

*E-mail: shikin@issp.ac.ru

¹L. D. Landau and E. M. Lifshitz, *Electrodynamics of Continuous Media*, 2nd ed., rev. and enl., by E. M. Lifshitz and L. P. Pitaevskii [Pergamon Press, Oxford (1984); Nauka, Moscow (1982)].

²S. Petrosyan and A. Shik, Zh. Éksp. Teor. Fiz. **96**, 2229 (1989) [Sov. Phys. JETP **69**, 261 (1989)].

³A. Shik, Fiz. Tekh. Poluprovodn. **29**, 1345 (1995) [Semiconductors **29**, 697 (1995)].

⁴V. Shikin and N. Shikina, JETP Lett. **62**, 894 (1995).

⁵S. Laux, D. Frank, and F. Stern, Surf. Sci. **196**, 101 (1988).

⁶V. Shikin, Zh. Éksp. Teor. Fiz. **96**, 1406 (1989) [Sov. Phys. JETP **69**, 797 (1989)].

⁷I. Larkin and V. Shikin, Phys. Lett. A **151**, 335 (1990).

⁸D. B. Chklovskii, B. I. Shklovskii, and L. I. Glazman, Phys. Rev. B **46**, 4026 (1992).

⁹D. B. Chklovskii, K. F. Matveev, and B. I. Shklovskii, Phys. Rev. B **47**, 12605 (1993).

¹⁰P. Fonten, P. Hedriks, F. Blom, J. Wolter, L. Giling, and C. Beenakker, Surf. Sci. **263**, 91 (1992).

¹¹R. Knott, W. Dietsche, K. von Klitzing, K. Ploog, and K. Eberl, Semicond. Sci. Technol. **10**, 117 (1995).

¹²W. Dietsche, K. von Klitzing, and K. Ploog, Surf. Sci. **361**, 289 (1996).

¹³K. McCormick, M. Woodside, M. Huang, M. Wu, P. McEuen, C. Duruoz, and J. Harris, Jr. Phys. Rev. B **59**, 4654 (1999).

¹⁴P. Weitz, E. Ahlswede, J. Weis, K. V. Klitzing, and K. Eberl, Physica E **6**, 247 (2000).

¹⁵A. H. MacDonald, T. M. Rice, and W. F. Brinkman, Phys. Rev. B **28**, 3648 (1983).

¹⁶I. S. Gradshteyn and I. M. Ryzhik, *Tables of Integrals, Series, and Products* [Academic Press, New York (1980); Nauka, Moscow (1971)].

Translated by Steve Torstveit

On the nature of the half-integer quantum features on the transport and Hall resistances of 2D electron systems in a quantizing magnetic field

E. A. Pashitskii*

Institute of Physics, National Academy of Sciences of Ukraine, pr. Nauki 46, 03028 Kiev, Ukraine

(Submitted June 18, 2001)

Fiz. Nizk. Temp. **27**, 1069–1082 (September–October 2001)

It is shown that in two-dimensional (2D) electron systems in a quantizing magnetic field, in addition to electron–hole (excitonic) pairing through the Coulomb interaction it is also possible to have Cooper pairing of the 2D electrons due to their interaction with 2D phonons and 2D plasmons localized at the interface of the crystals in semiconductor heterostructures. By summing the divergent (as $T \rightarrow 0$) ladder diagrams in the zero-sound and Cooper channels, the critical temperatures of the transition to the excitonic and Cooper phases are found. It is shown that the excitonic phase can exist only in comparatively narrow regions near half-integer values of the filling factor $\nu = (2n - 1)/2$ ($n = 1, 2, 3, \dots$), a finding which is in qualitative agreement with the experimentally observed anisotropic features in the transport resistance of 2D systems in the integer quantum Hall effect regime. By taking into account a superposition of states of bound electron pairs and unpaired 2D electrons in the Cooper phase, one can describe practically all of the experimentally observed quantum features in the fractional quantum Hall effect regime, including at values of ν that are not described by the composite fermion model. At the same time, the interelectron attraction can promote triplet Cooper pairing of composite fermions, which is accompanied by the appearance of an “exotic” quantum feature at $\nu = 5/2$.

Arguments supporting the possibility of experimental observation of the Cooper phase are presented. © 2001 American Institute of Physics. [DOI: [DOI: 10.1063/1.1414567]

1. INTRODUCTION

Experimental studies of the integer and fractional quantum Hall effects (IQHE and FQHE) in semiconductor heterostructures^{1,2} show evidence that as the quality of the samples is improved and the mobility of the two-dimensional (2D) electrons in the inversion layers is increased, ever larger numbers of new quantum features are observed on the curves of the Hall resistance $R_{xy} = R_H$ and transport resistance R_{xx} (or R_{yy}) as functions of the strength of the quantizing magnetic field H .^{3,4} In the FQHE regime one often observes fractional values of the electronic filling factor $\nu = q/k$ which cannot be described in the framework of the Laughlin theory,⁵ on the basis of the fractional statistics of anyons,^{6–8} nor with the use of the model of composite fermions,^{9,10} which leads to fractions of the form $\nu = n/(2n \pm 1)$ for $n = 2, 3, 4, \dots$

Of greatest interest recently is the quantum feature at the half-integer value $\nu = 5/2$, which was first observed in Ref. 11 for an isolated GaSb–InAs–GaSb quantum well and then in GaAs/AlGaAs heterostructures with a high electron mobility.^{12,13} Formally the value $\nu = 5/2$ belongs to the region of the IQHE, but the state corresponding to it has all the characteristic properties of a state of the FQHE and has an energy gap in the spectrum of elementary excitations.³ To interpret the “exotic” quantum state with factor $\nu = 5/2$, in Ref. 14 it was proposed to use a model of p -wave triplet Cooper pairing of composite fermions due to a weak attraction arising as a result of “overscreening” of the Coulomb repulsion.

In this connection it should be noted that the possibility

of Cooper pairing of 2D electrons in a quantizing magnetic field as a result of the electron–phonon interaction was considered previously in Ref. 15. It was shown in the self-consistent field approximation that in a high enough quantizing magnetic field under the condition $\omega_{He} > \tilde{\omega}_{ph}$ (where $\omega_{He} = eH/cm_e^*$ is the cyclotron frequency of electrons with effective mass m_e^* , and $\tilde{\omega}_{ph}$ is the maximum frequency of the phonon spectrum), when in the process of the electron–phonon interaction the electrons remain on the upper partially filled Landau level, the critical temperature of the transition to the superconducting state realized on the Landau wave functions is determined by the expression

$$T_c = \frac{N_L W_{ph}^2 \tanh[1/2 \ln(1/\nu_s - 1)]}{k_B \ln(1/\nu_s - 1)}, \quad (1)$$

where W_{ph} is the matrix element of the electron–phonon interaction, ν_s is the degree of filling of the upper Landau level s ($0 \leq \nu_s \leq 1$), $N_L = \frac{1}{2} \pi l_H^2$ is the degeneracy of the Landau level, and $l_H = \sqrt{\hbar c / eH}$ is the quantum magnetic length (Planck’s constant \hbar and Boltzmann’s constant k_B will henceforth be taken equal to unity).

It follows from Eq. (1) that T_c reaches a maximum at $\nu_s = 1/2$ and goes to zero by a logarithmic law for $\nu_s \rightarrow 0$ and $\nu_s \rightarrow 1$ (Fig. 1). As a result of the change in the number of filled Landau levels $n = s + 1$ with increasing magnetic field, T_c is an oscillatory function of H with period $\Delta H = H/s$, and with increasing H the maximum values of T_c increase by a linear law, since $N_L \sim H$.

An important feature of expression (1) is that in a sufficiently strong quantizing magnetic field the value of T_c is independent of the 2D electron density of states N_{2D}

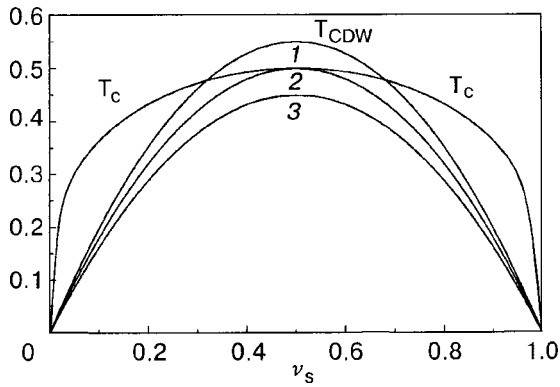


FIG. 1. Dependence on ν_s of the critical temperatures T_c and T_{CDW} normalized to $N_s W_{ph}^2$, according to formulas (1) and (5) for different relationships between the matrix elements of the electron–phonon and Coulomb interactions. Curve 1 for T_{CDW} corresponds to the condition $W_{ph}^2 < \tilde{V}_c$, curve 2 to $W_{ph}^2 = \tilde{V}_c$, and curve 3 to $W_{ph}^2 > \tilde{V}_c$.

$= m_e^*/2\pi$. This means that the Cooper pairing of electrons on the same Landau level is possible for arbitrarily small m_e^* if the interelectron attraction due to the electron–phonon interaction exceeds the Coulomb repulsion. We note that the problem of Cooper pairing of 2D electrons in a quantizing magnetic field and the related phenomenon of giant oscillations of the superconducting order parameter as a function of H were considered in Refs. 16 and 17.

In Ref. 18 it was pointed out that in semiconductor heterostructures the strongest electron–phonon interaction for 2D electrons is not with the three-dimensional (3D) bulk phonons but with surface acoustic and optical 2D phonons, which should exist at the interfaces between the different crystals. In particular, optical surface oscillations (interfacial modes) have been observed experimentally in the Raman scattering spectra of semiconductor superlattices.^{19,20} It is also possible that the superconducting transition at $T < 1$ K observed²¹ in a silicon metal–insulator–semiconductor (MIS) structure (in the absence of magnetic field) is the result of an electron–phonon interaction with surface phonons.

Another possible mechanism of attraction between 2D electrons, which was considered previously in Refs. 22 and 23, is the “dynamic overscreening” of the Coulomb interaction in layered semiconductor structures and quantum wells, an effect which arises due to the exchange of virtual quanta of the low-frequency plasma oscillations of “heavy” holes with an effective mass $m_h^* \gg m_e^*$. This electron–plasmon interaction mechanism is radically different from that proposed in Ref. 24 for explaining the experimental data²¹ on the plasmon mechanism of Cooper pairing of 2D electrons due to their interaction with intrinsic high-frequency 2D plasmons with a square-root dispersion relation $\omega_q \sim \sqrt{q}$.

In addition, in a GaAs/AlGaAs heterostructure with a high mobility of the 2D electrons in the IQHE regime at ultralow temperatures, new quantum features of the transport resistance have been observed near half-integer values of the electronic filling factor $\nu = (2n - 1)/2$, starting with $n = 3$.²⁵ Such features, in the form of alternating maxima and minima or narrow peaks of $R_{xx}(H)$ and $R_{yy}(H)$ in the region of the broad plateau on the field dependence of R_H , are characterized by strong anisotropy ($R_{yy} \neq R_{xx}$) and are apparently due

to electron–hole (excitonic) pairing and to scattering of the current carriers on quantum charge-density waves (CDWs), which were predicted in Ref. 26 and studied in more detail in Refs. 27–31. In the self-consistent-field approximation the critical temperature T_{CDW} of the transition to the spatially inhomogeneous excitonic phase is given by the expression²⁶

$$T_{CDW} = 2N_L \tilde{V}_c(q) \nu_s (1 - \nu_s), \tag{2}$$

where $\tilde{V}_c(q)$ is the matrix element of the screened Coulomb interaction in a quantizing magnetic field at a value of the momentum transfer q equal to the inverse period of the CDW. It follows that T_{CDW} , like T_c in Eq. (1), is a periodic function of magnetic field and reaches maximum values at half-filling of the upper Landau level, when $\nu_s = 1/2$.

However, the parabolic behavior of $T_{CDW}(\nu_s)$ in the interval $0 \leq \nu_s \leq 1$ (Fig. 1) does not agree with the character of the experimentally observed features of R_{xx} and R_{yy} in comparatively narrow regions in the neighborhood of the points $\nu = (2n - 1)/2$ for $n \geq 3$.²⁵ This creates some difficulties for interpreting these features as being a manifestation of excitonic pairing and the related formation of quantum CDWs.^{28–31} Moreover, it remains unclear why no features of R_{xx} and R_{yy} are observed for $\nu = 3/2$ and $1/2$.

In the present paper we make the conjecture that the features of the transport resistance of a 2D system in the IQHE regime near $\nu = 5/2, 7/2, 9/2, \dots$ and also the “exotic” quantum feature of R_{xx} and R_H at $\nu = 5/2$ and a number of other features at values of ν in the FQHE regime are consequences of an effective interelectron attraction which is due to the interaction of 2D electrons with 2D phonons and 2D plasmons localized at the heterojunction. This attraction leads to a competition between the electron–hole (excitonic) pairing due to the Coulomb interaction and the electron–electron (Cooper) pairing due to the electron–phonon and electron–plasmon interactions, because of the fact that the corresponding diagrams of the thermodynamic perturbation theory for the two-particle Green’s function at zero total energy and $T \rightarrow 0$ have divergences of the same power ($\sim 1/T$) in the zero-sound and Cooper channels.

By simultaneous summation of the divergent ladder diagrams in both channels in the local-interaction approximation the critical temperatures of the transition to the excitonic and Cooper phases are found, and the phase diagrams of the 2D system are constructed in the IQHE and FQHE regimes. It is shown that the excitonic phase with a spatially periodic quantum CDW can exist only in comparatively narrow regions around the half-integer values $\nu = (2n - 1)/2$, in qualitative agreement with the experimental data²⁵ on the observation of the features of R_{xx} and R_{yy} in the IQHE regime.

In the ultraquantum limit, by taking into account a superposition of states of the bound electron pairs and the unpaired 2D electrons on the lowest spin Landau level, one can, on the basis of the Halperin multiparticle wave function,³² describe practically all of the experimentally observed quantum features of the Hall and transport resistances, including those at values of the filling factor $\nu = 2/7, 2/9, 2/11, 3/11, \dots$, which are not described by the composite fermion model.^{9,10} At the same time, the interelectron attraction due to the electron–phonon and electron–plasmon interactions with surface phonons and plasmons can

bring about triplet Cooper pairing of composite fermions, which is accompanied by the appearance of an “exotic” quantum feature at $\nu=5/2$.^{11–14}

2. COULOMB, ELECTRON–PHONON AND ELECTRON–PLASMON INTERACTIONS IN 2D SYSTEMS IN A QUANTIZING MAGNETIC FIELD

In studying the properties of 2D electron systems in a quantizing magnetic field, one ordinarily takes into account only the Coulomb interaction between electrons^{26–31} with a characteristic energy $e^2/\varepsilon_0 l_H$ (where ε_0 is the dielectric constant of the crystal).

As was shown in Ref. 33, the Hamiltonian of the Coulomb interaction between 2D electrons found on the same Landau level in the momentum representation has a certain symmetry and is invariant with respect to a certain identity integral transformation, which enables one to eliminate all loop diagrams from the thermodynamic perturbation series with the aid of the operation of antisymmetrization of the Fourier components of the Coulomb potential.

The antisymmetrized potential for the s th Landau level has the following form:³³

$$\tilde{U}_s(q) = \frac{1}{2} [\tilde{V}_s(q) - \tilde{V}'_s(q)], \quad (3)$$

where

$$\begin{aligned} \tilde{V}_s(q) &= V_c(q) w_s^2(q); \\ \tilde{V}'_s(q) &= \frac{l_H^2}{2\pi} \int d^2 p \exp\{i\mathbf{p} \cdot \mathbf{q} l_H\} \tilde{V}_s(p); \end{aligned} \quad (4)$$

$w_s(q) = e^{-q^2 l_H^2/4} L_s(q^2 l_H^2)$, $L_s(z)$ is a Laguerre polynomial, and $V_c(q) = 2\pi e^2/q\varepsilon_0$ is the Fourier component of the unscreened Coulomb repulsion in the 2D system. In particular, for the lowest Landau level ($s=0$) in the ultraquantum limit the potential (3) with allowance for (4) is expressed as

$$\tilde{U}_0(q) = \frac{\pi e^2 l_H}{\varepsilon_0} \left[\frac{e^{-x^2/2}}{x} - \sqrt{\pi/2} I_0(x^2/4) e^{-x^2/4} \right], \quad (5)$$

where $x = ql_H$, and $I_0(z)$ is a modified Bessel function of the first kind. In the case of two filled Landau levels ($s=1$) we have, according to (3) and (4),

$$\begin{aligned} \tilde{U}_1(q) &= \frac{\pi e^2 l_H}{\varepsilon_0} \left\{ \frac{e^{-x^2/2}}{x} (1-x^2)^2 - \sqrt{\pi/2} \left[I_0 \frac{x^2}{4} e^{-x^2/4} \right. \right. \\ &\quad \left. \left. - 2\Phi\left(\frac{3}{2}, 1; -\frac{x^2}{2}\right) + 6\Phi\left(\frac{5}{2}, 1; -\frac{x^2}{2}\right) \right] \right\}, \end{aligned} \quad (6)$$

where $\Phi(\alpha, \beta; z) \equiv {}_1F_1(\alpha, \beta; z)$ is the confluent hypergeometric function.

Figure 2 shows the momentum dependence of $\tilde{U}_0(q)$ and $\tilde{U}_1(q)$. We see that $\tilde{U}_0(q) > 0$ in the region $q < q_0 \approx 0.7l_H^{-1}$, and $\tilde{U}_1(q) > 0$ in the region $q < q_1 \approx 1.4l_H^{-1}$, which corresponds to Coulomb repulsion. In the regions $q > q_0$ and $q > q_1$, however, the potentials $\tilde{U}_0(q)$ and $\tilde{U}_1(q)$ become negative, corresponding to an effective attraction between 2D electrons due to the “magnetic overscreening” of

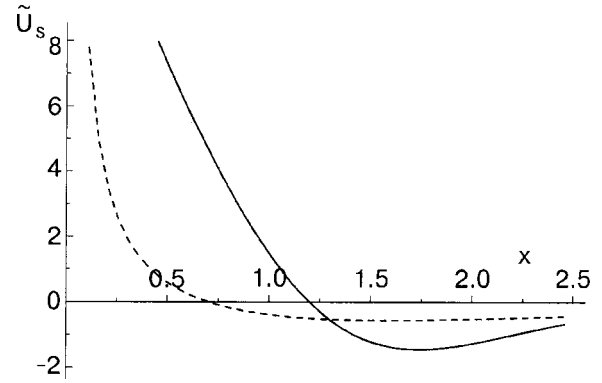


FIG. 2. Antisymmetrized matrix element of the Coulomb interaction, $\tilde{U}_s(q)$, normalized by $\pi e^2 l_H / \varepsilon_0$, as a function of the dimensionless momentum $x = ql_H$ for $s=0$ (dashed curve) and $s=1$ (solid curve).

the Coulomb interaction.³³ An analogous sign change of $\tilde{U}_s(q)$ for $q \geq l_H^{-1}$ should occur on all Landau levels.

As we have said, in real heterostructures (p – n junctions) in addition to the Coulomb interaction one must take into account the inelastic interaction of 2D electrons in the inversion layers with surface phonons localized at the interfaces of the crystals^{18–20} and also with surface plasmons, which are associated with the relatively low-frequency collective oscillations of the “heavy” holes.^{22,23} In particular, as was shown in Ref. 22, at the interface between two semiconductors, one p -type and the other n -type, with substantially different effective masses of the holes and electrons and with a high mobility of free carriers in a certain region of frequencies ω and longitudinal wave numbers q , there can exist weakly damped surface plasmons with the following dispersion relation, which is of the acoustic type at $q \rightarrow 0$:

$$\omega_{\text{pl}}(q) = \Omega_h [1 + \sqrt{1 + 1/q^2 R_e^2}]^{-1}, \quad (7)$$

where $\Omega_h = \sqrt{4\pi e^2 n_h / \varepsilon_0 m_h^*}$ is the plasma frequency of “heavy” holes with an average volume concentration n_h , and $R_e = \sqrt{E_F \varepsilon_0 / 6\pi e^2 n_e}$ is the screening radius in the case of screening by degenerate “light” electrons with a concentration n_e and Fermi energy E_F in crystals with the same dielectric constant ε_0 . Here the electric field of the surface plasma wave falls off with increasing distance z from the interface according to an exponential law $\sim \exp(-z\sqrt{q^2 + R_e^{-2}})$, and the Hamiltonian of the adiabatic (under the condition $m_h^* \gg m_e^*$) electron–plasmon interaction is analogous to the Frölich Hamiltonian for the electron–phonon interaction:

$$H_{\text{pl}}(z) = i \sum_{\mathbf{k}, \mathbf{q}, \sigma} g_{\text{pl}}(q, z) \omega_{\text{pl}}^{1/2}(q) a_{\mathbf{k}+\mathbf{q}, \sigma}^+ a_{\mathbf{k}, \sigma} + \text{h.c.}, \quad (8)$$

where

$$g_{\text{pl}}(q, z) = \left(\frac{\pi e^2}{\varepsilon_0 \sqrt{q^2 + R_e^{-2}}} \right)^{1/2} \exp(-z\sqrt{q^2 + R_e^{-2}}), \quad (9)$$

and z is the coordinate of the 2D electron layer (see below).

The corresponding effective Hamiltonian of the electron–electron interaction in second order of perturbation theory owing to the exchange of virtual 2D phonons and 2D plasmons in the Landau gauge has the form (cf. Ref. 33)

$$\begin{aligned}
 H_{ee} = & \sum_{\mathbf{k}, \mathbf{k}', q'} \sum_{s, s'} [\tilde{g}_{\text{ph}}^2(q) D_{\text{ph}}(q, \varepsilon_s - \varepsilon_{s'}) \\
 & + \tilde{g}_{\text{pl}}^2(q)^d D_{\text{pl}}(q, \varepsilon_s - \varepsilon_{s'})] \\
 & \times w_s(q) w_{s'}(q) a_{\mathbf{k}+\mathbf{q}, s}^+ a_{\mathbf{k}-\mathbf{q}, s}^+ a_{\mathbf{k}'s'} a_{\mathbf{k}s}, \quad (10)
 \end{aligned}$$

where \tilde{g}_{ph} and \tilde{g}_{pl} are the matrix elements of the electron–phonon and electron–plasmon interactions, $a_{\mathbf{k}s}^+$ and $a_{\mathbf{k}s}$ are the creation and annihilation operators for an electron with 2D momentum \mathbf{k} at the s th Landau level, and D_{ph} and D_{pl} are the phonon and plasmon Green’s functions:

$$D_{\text{ph,pl}}(q, \omega) = \frac{\omega_{\text{ph,pl}}^2(q)}{\omega^2 - \omega_{\text{ph,pl}}^2(q)}. \quad (11)$$

If the characteristic energies of the surface phonons $\omega_{\text{ph}}(q)$ and plasmons $\omega_{\text{pl}}(q)$ for $q \sim l_H^{-1}$ do not exceed a value $2\mu_B H$ (where μ_B is the Bohr magneton), then the inelastic processes due to the electron–phonon and electron–plasmon interactions do not lead to mixing of the states of different Landau levels. In that case we may neglect retardation effects in (11) for 2D electrons on the same Landau level ($s = s'$) and set $\omega = 0$, so that $D_{\text{ph}}(q, 0) = D_{\text{pl}}(q, 0) = -1$, corresponding to interelectron attraction.

The effective attraction between 2D electrons due to their interaction with surface phonons is characterized by the square of the matrix element of the electron–phonon interaction, which in the long-wavelength approximation can be written in the form

$$\tilde{g}_{\text{ph}}^2(q) = \frac{\tilde{a}^2}{2} \left[\frac{\tilde{D}_A^2}{M\tilde{s}^2} + \frac{\tilde{\gamma}_0^2}{\tilde{M}\tilde{\omega}_0^2} \right] e^{-2qd}, \quad (12)$$

where \tilde{a} is the average lattice constant at the heterojunction, d is the distance of the 2D electron layer from the interface of the crystals, \tilde{D}_A is the deformation potential of acoustic 2D phonons with phase velocity \tilde{s} along the interface, $\tilde{\gamma}_0$ is the deformation constant for optical 2D phonons with frequency $\tilde{\omega}_0$, and M and \tilde{M} are the total and reduced masses of the atoms in the unit cells of the crystals on the two sides of the interface. If the difference of the elastic constants of the crystals is sufficiently small, so that the values of \tilde{s} and $\tilde{\omega}_0$ are small (compared with the bulk values), the value of \tilde{g}_{ph}^2 can be considerably greater than the electron–phonon interaction with 3D phonons in semiconductors.³⁴

To calculate the matrix element of the electron–plasmon interaction with surface plasmons in heterostructures with size quantization of the electron spectrum in the inversion layer, we take into account that for a sufficiently thin electron layer of thickness L_e the screening radius in the case of a quadratic spectrum of degenerate 2D electrons with concentration N and Fermi momentum $k_F = \sqrt{2\pi N}$ is given by $\tilde{R}_e = \sqrt{L_e a_e^*}/2$ (where $a_e^* = \varepsilon_0/m_e^* e^2$ is the effective Bohr radius of the electron). Here the Fourier component of the screened Coulomb potential under the condition $L_e \ll a_e^*$ to good accuracy reduces to the expression (see Ref. 35)

$$\tilde{V}_c(q) \cong \frac{2\pi e^2}{q + L_e/2R_e^2} = \frac{2\pi e^2}{q + 2a_e^*}. \quad (13)$$

In this case, if the width of the localization region for “heavy” holes satisfies $L_h \gg L_e$, the frequency of the adiabatic surface plasmons is given by

$$\omega_{\text{pl}}(q) = \Omega_h / \sqrt{2(1 + 1/qa_e^*)}, \quad (14)$$

so that $\omega_s(q) \sim \sqrt{q}$ for $q \rightarrow 0$, and the electron–plasmon interaction constant has the form

$$\tilde{g}_{\text{pl}}(q) = \left(\frac{2\pi e^2}{\varepsilon_0(q + 2/a_e^*)} \right)^{1/2} \exp\left\{ -\tilde{d} \left(q + \frac{2}{a_e^*} \right) \right\}, \quad (15)$$

where \tilde{d} is the distance between the maxima of the density distributions for electrons and holes localized on opposite sides of the heterojunction ($\tilde{d} > d$).

In a magnetic field strong enough to quantize the spectrum of “light” 2D electrons but not the “heavy” holes, the spectrum of 2D plasmons acquires a finite gap at $q \rightarrow 0$:

$$\tilde{\omega}_{\text{pl}}(q) = \sqrt{\omega_{Hh}^2 + \omega_{\text{pl}}^2(q)}, \quad (16)$$

where $\omega_{Hh} = eH/m_h^* c$ is the cyclotron frequency of the holes. We note that the surface plasmon energy (16) for $m_h^* < m_0$ exceeds the value of the Zeeman splitting of the Landau levels, so that the inelastic electron–plasmon interaction can lead to mixing of the states of the nearest spin Landau levels.

Since the screening of the Coulomb interaction of the electrons is strongly suppressed in a quantizing magnetic field, the frequency of the 2D plasmons is $\omega_{\text{pl}} \approx \Omega_h/\sqrt{2}$, and the square of the matrix element of the electron–phonon interaction has the form

$$\tilde{g}_{\text{pl}}^2(q) = \frac{2\pi e^2}{q\varepsilon_0} e^{-2q\tilde{d}}. \quad (17)$$

Taking into account that the Hamiltonian (10) for $s = s'$ has the same symmetry as the Coulomb Hamiltonian,³³ by analogy with the Coulomb potential (6) we obtain the following effective antisymmetrized electron–phonon and electron–plasmon interaction potential:

$$\begin{aligned}
 \tilde{W}_s(q) & \cong \tilde{W}_s^{\text{ph}}(q) + \tilde{W}_s^{\text{pl}}(q) \\
 & = -\frac{1}{2} \left\{ [\tilde{g}_{\text{ph}}^2(q) + \tilde{g}_{\text{pl}}^2(q)] w_s^2(q) - \frac{l_H^2}{2\pi} \right. \\
 & \quad \left. \times \int d^2p \exp(i\mathbf{p} \cdot \mathbf{q} l_H^2) [\tilde{g}_{\text{ph}}^2(p) + \tilde{g}_{\text{pl}}^2(p)] w_s^2(p) \right\}. \quad (18)
 \end{aligned}$$

For calculating the matrix element $\tilde{W}_s(q)$ it is necessary to know the explicit momentum dependence of the electron–phonon and electron–plasmon interaction constants, since for a contact (point) interaction with a constant Fourier component, expression (18) is identically zero (see Ref. 33).

In the long-wavelength approximation ($qd < 1$) for the electron–phonon interaction constant for surface phonons one can to good accuracy keep only the correction linear in q [see Eq. (12)]:

$$\tilde{g}_{\text{ph}}^2(q) \cong \tilde{g}_{\text{ph}}^2(0)(1 - 2qd). \quad (19)$$

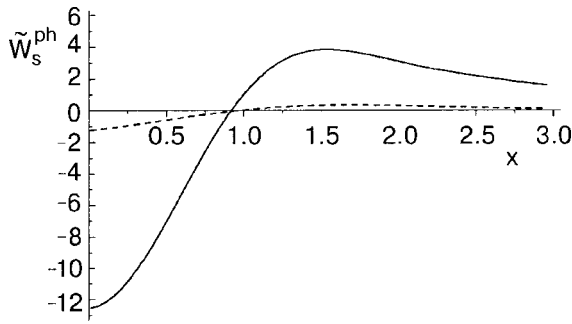


FIG. 3. Antisymmetrized matrix element of the electron–phonon interaction $\tilde{W}_s^{ph}(q)$, normalized to $\tilde{g}_{ph}^2(0)d/l_H$ and plotted versus $x=ql_H$, for $s=0$ (dashed curve) and $s=1$ (solid curve).

As a result, the phonon part of the matrix element $\tilde{W}_s(q)$ for $s=0$ becomes

$$\tilde{W}_0^{ph}(q) = \tilde{g}_{ph}^2(0) \frac{d}{l_H} \left[x e^{-x^2/2} - \sqrt{\pi/2} \Phi \left(-\frac{1}{2}, 1; \frac{x^2}{2} \right) e^{-x^2/2} \right]. \quad (20)$$

Here we have used the Kummer formula $\Phi(\alpha, \beta; z) = e^z \Phi(\beta - \alpha, \beta; -z)$. For $s=1$ the corresponding matrix element of the electron–phonon interaction is

$$\begin{aligned} \tilde{W}_1^{ph}(q) = \tilde{g}_{ph}^2(0) \frac{d}{l_H} & \left\{ x(1-x^2)^2 e^{-x^2/2} - \sqrt{2\pi} \Phi \right. \\ & \times \left(-\frac{1}{2}, 1; \frac{x^2}{2} \right) - 6\Phi \left(-\frac{3}{2}, 1; \frac{x^2}{2} \right) + 15\Phi \\ & \left. \times \left(-\frac{5}{2}, 1; \frac{x^2}{2} \right) \right\} e^{-x^2/2}. \quad (21) \end{aligned}$$

Figure 3 shows the momentum dependence of $\tilde{W}_0^{ph}(q)$ and $\tilde{W}_1^{ph}(q)$. We see that in the region $ql_H < 1$ the matrix element of the electron–phonon interaction corresponds to attraction, while repulsion is dominant for $ql_H > 1$.

Using expression (17), which in fact describes a weakening of the Coulomb repulsion by the effective interelectron attraction due to the electron–plasmon interaction, we obtain in the long-wavelength approximation

$$V_c(q) - \tilde{g}_{pl}^2(q) = V_c(q)(1 - e^{-q\tilde{d}}) \approx \frac{4\pi e^2 \tilde{d}}{\epsilon_0} (1 - q\tilde{d}). \quad (22)$$

As a result of the antisymmetrization the constant term in (22) drops out, and for the total matrix element of the Coulomb and electron–plasmon interactions, according to Eqs. (3) and (18), for $s=0$ and 1 we obtain the same momentum dependence as for the matrix elements of the electron–phonon interaction, Eqs. (20) and (21), but with the opposite sign, since the Coulomb repulsion is dominant over the attraction coming from the electron–plasmon interaction. Here the corresponding coupling constant with allowance for the electron–phonon interaction is $[\tilde{g}_{ph}^2(0) - 2\pi e^2 \tilde{d}^2 / \epsilon_0 d] d / l_H$.

Figure 4 shows the momentum dependence of the total potential of the Coulomb, electron–plasmon, and electron–phonon interactions for $s=0$ (a) and $s=1$ (b) for different values of the dimensionless parameter $\beta = \tilde{g}_{ph}^2(0)\epsilon_0 d / 2\pi e^2 \tilde{d}^2$. We see that the potential $\tilde{U}_s(q) + \tilde{W}_s(q)$ corresponds to attraction (is negative) in the region $ql_H < 1$, with a minimum at the point $q=0$, if $\beta > 1$, or in the region $ql_H > 1$ if $\beta < 1$.

If the adiabatic electron–plasmon interaction with surface plasma oscillations of “heavy” holes is suppressed for some reason, e.g., because of a large distance \tilde{d} , in which case the electron–plasmon interaction is exponentially small [see Eq. (17)], then the resulting momentum dependence of the matrix element of the Coulomb and electron–phonon interactions, according to Eqs. (5), (6), (20), and (21), has the form shown in Fig. 5 for $s=0$ (a) and $s=1$ (b) for different values of the dimensionless parameter $\tilde{\beta} = \tilde{g}_{ph}^2(0)\epsilon_0 d / \pi e^2 l_H^2$ characterizing the relative value of the electron–phonon interaction constant and the Coulomb repulsion. We see that in this case there is a certain region of momentum transfers in which attraction exists, $\tilde{U}_s(q) + \tilde{W}_s^{ph}(q) < 0$, but for $q \rightarrow 0$ the Coulomb repulsion is dominant.

3. COMPETITION BETWEEN THE COOPER AND EXCITONIC MECHANISMS OF PAIRING IN 2D SYSTEMS IN A QUANTIZING MAGNETIC FIELD

As will be shown below, the interelectron attraction due to the electron–phonon and electron–plasmon interactions,

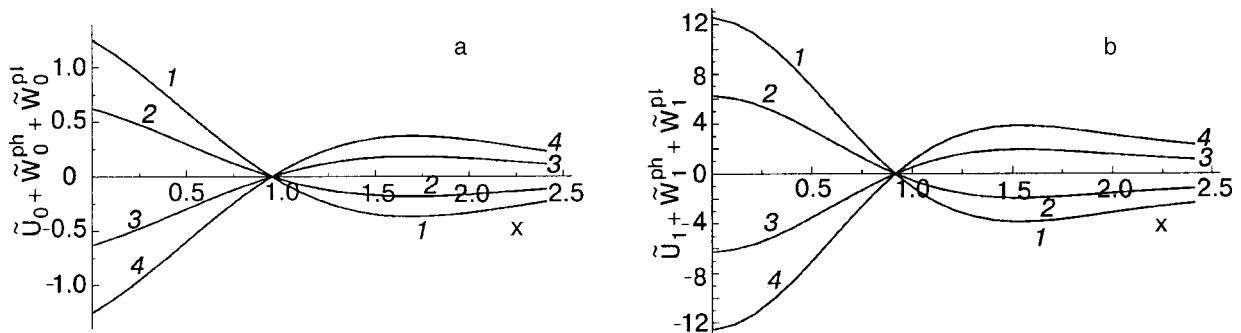


FIG. 4. Momentum dependence of the total potential of the Coulomb, electron–plasmon, and electron–phonon interactions, normalized to $\pi e^2 l_H / \epsilon_0$, for $s=0$ (a) and $s=1$ (b) and various values of the parameter $\beta = \tilde{g}_{ph}^2(0)\epsilon_0 / 2\pi e^2 d$: 0 (1), 0.5 (2), 1.5 (3), 2 (4).

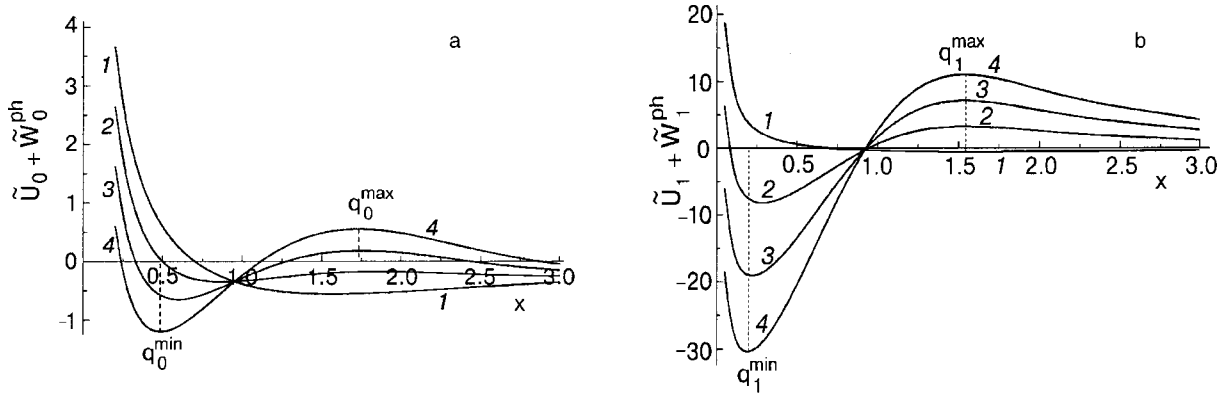


FIG. 5. Momentum dependence of the total potential of the Coulomb and electron–phonon interactions, normalized to $\pi e^2 lH/\epsilon_0$, for $s=0$ (a) and $s=1$ (b) and various values of the parameter $\tilde{\beta}=2\beta\tilde{d}^2/l_H^2$: 0 (1), 0.5 (2), 1.5 (3), 2 (4).

which was discussed in the preceding Section, promotes the Cooper pairing of 2D electrons on the same spin Landau level, and this competes with the excitonic pairing brought about by the Coulomb attraction between electrons and holes.

An analysis of the diagrams for the two-particle Green’s function of 2D electrons on the s th Landau level at $T \neq 0$ has shown³⁶ that the summation of the ladder diagrams of the form

$$T \sum_{\omega} G_s(\omega) G_s(\omega + \omega_1 - \omega_2) = -\delta_{\omega_1 \omega_2} \frac{\nu_s(1 - \nu_s)}{T} \quad (23)$$

in the zero-sound channel, which have a power-law divergence for $T \rightarrow 0$ (here $G_s(\omega)$ is the single-particle Green’s function and $\delta_{\omega_1 \omega_2}$ is the Kronecker delta with respect to the discrete Matsubara frequencies ω_1 and ω_2), gives rise to a singularity (a simple pole) at a certain finite temperature, which corresponds to the critical temperature T_{CDW} of the transition to the excitonic phase with a quantum CDW [see Eq. (2)].

At the same time, it was stated in Ref. 36 that Cooper pairing cannot occur in 2D systems, since the simplest corresponding diagram has the form

$$T \sum_{\omega} G_s(\omega) G_s(\omega_1 + \omega_2 - \omega) = \frac{2f(\epsilon) - 1}{i(\omega_1 + \omega_2) - 2\epsilon}, \quad (24)$$

where $f(\epsilon) = (e^{\epsilon/T} + 1)^{-1}$ is the Fermi distribution function of the electrons, which under the condition $T \ll \mu_B H$ is to exponential accuracy equal to the degree of filling ν_s of the upper Landau level (see Refs. 15 and 36). If $\omega_1 + \omega_2 \neq 0$, then expression (24) is nonsingular for $T \rightarrow 0$ and goes to zero at half-filling of the s th Landau level, when $f(\epsilon) = \nu_s = 1/2$.

However, for zero total energy $\omega_1 + \omega_2 = 0$ expression (24) at the point $\epsilon = 0$ has an indeterminacy of the type 0/0, which can be resolved by using the relations $f(\epsilon) = \nu_s$ and $\epsilon = T \ln(1/\nu_s - 1)$ in the region $0 < \nu_s < 1$. In that case expression (24) under the condition $\omega_1 = -\omega_2$ takes the form

$$T \sum_{\omega} G_s(\omega) G_s(-\omega) = \frac{\tanh[1/2 \ln(1/\nu_s - 1)]}{2T \ln(1/\nu_s - 1)}. \quad (25)$$

We see that, like the zero-sound diagram (23), the Cooper diagram (25) diverges in a power-law manner at $T \rightarrow 0$.

Summation of the ladder diagrams of the type (25) gives a pole in the two-particle Green’s function at a certain temperature T_c determined by the relation

$$1 + N_L [\tilde{W}_s(q) + \tilde{U}_s(q)] \frac{\tanh[1/2 \ln(1/\nu_s - 1)]}{2T_c \ln(1/\nu_s - 1)} = 0. \quad (26)$$

An analogous result was obtained in Ref. 15 in the self-consistent-field approximation [cf. Eq. (1)].

However, since diagrams of the types (23) and (25) are characterized by the same divergence $\sim 1/T$ at $T \rightarrow 0$, to calculate the critical temperature one must do a simultaneous summation of these diagrams. The situation here is analogous to the so-called “parquet” approximation for one-dimensional systems, when all of the logarithmically diverging diagrams are summed (see Refs. 37–40).

The integral equation for the vertex part (four-pole) Γ_s of the electron–electron interaction at the s th Landau level, obtained with a summation of the divergent zero-sound and Cooper diagrams, is presented in graphical form in Fig. 6. Here $\Gamma_s^{(0)}$ is the nonsingular (at $T \rightarrow 0$) part of Γ_s , and $\Gamma_s^{(1)}$ and $\Gamma_s^{(2)}$ are the irreducible parts of Γ_s corresponding to the Cooper and zero-sound channels. Adopting for simplicity the local-interaction approximation, we arrive at an expression for Γ_s containing a pole with respect to T :

$$\Gamma_s(T) = \frac{\Gamma_s^{(0)}}{1 - \lambda_s F_s(\nu_s)/T}, \quad (27)$$

where

$$\lambda_s = -2N_L [\tilde{W}_s(q_s) + \tilde{U}_s(q_s)]; \quad (28)$$

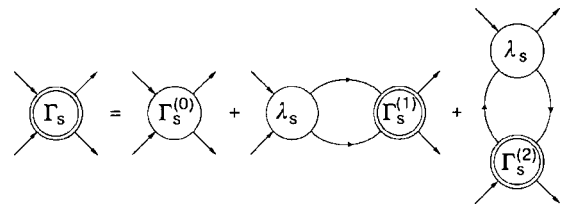


FIG. 6. Graphical form of the integral equation for the vertex part of the interelectron interaction, obtained by summation of the divergent (at $T \rightarrow 0$) ladder diagrams in the zero-sound and Cooper channels.

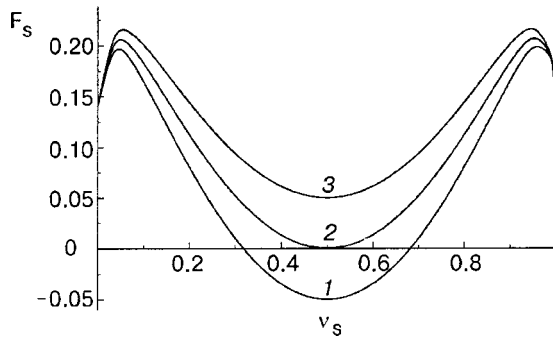


FIG. 7. The function $F_s(\nu_s)$ for different relationships between the parameters $\gamma_s^{(1)}$ and $\gamma_s^{(2)}$: $\gamma_s^{(1)} < \gamma_s^{(2)}$ (1); $\gamma_s^{(1)} = \gamma_s^{(2)}$ (2); $\gamma_s^{(1)} > \gamma_s^{(2)}$ (3).

$$F_s(\nu_s) = \gamma_s^{(1)} \frac{\tanh[1/2 \ln(1/\nu_s - 1)]}{2 \ln(1/\nu_s - 1)} - \gamma_s^{(2)} \nu_s(1 - \nu_s). \quad (29)$$

Here $\gamma_s^{(1)}$ and $\gamma_s^{(2)}$ are the relative contributions of the diagrams of the Cooper and zero-sound types, and q_s is the momentum transfer corresponding to the maximum values of the coupling constant λ_s and critical temperature:

$$T_s(\nu_s) = \lambda_s F_s(\nu_s). \quad (30)$$

Figure 7 shows curves of the function $F_s(\nu_s)$ constructed according to Eq. (29) for several different relationships between the parameters $\gamma_s^{(1)}$ and $\gamma_s^{(2)}$. We see that under the condition $\gamma_s^{(1)} \geq \gamma_s^{(2)}$ the function $F_s(\nu_s)$ is always positive and has a minimum at the point $\nu_s = 1/2$. In this case T_s is equal to the critical temperature of the transition to the Cooper phase $T_c^{(s)}$ and is nonzero only for a positive value of the coupling constant $\lambda_s > 0$, which corresponds to the maximum electron–electron attraction, i.e., a negative minimum of the potential $\tilde{W}_s(q) + \tilde{U}_s(q)$ at a momentum transfer $q = q_s^{\min}$ (see Figs. 4 and 5). Because of the interelectron attraction due to the electron–phonon and electron–plasmon interactions, in the temperature region $0 < T < T_s \equiv T_c^{(s)}$ there exists a Cooper phase with a nonzero concentration of bound electron pairs and with a finite energy (Cooper) gap in the spectrum of elementary excitations. We note that when the electron–plasmon interaction is taken into account, the maximum attraction is attained for $q = 0$ (Fig. 4), which corresponds to a spatially homogeneous Cooper phase. In this case, in spite of the fact that the surface plasmon energy $\tilde{\omega}_{pl}(q)$ can exceed the Zeeman splitting of the Landau levels [see Eq. (16)], under the condition $T_c^{(s)} \ll 2\mu_B H$ the Cooper pairing of 2D electrons is possible only for electrons on the same partially filled spin Landau level and is therefore of a triplet p -wave character.

Under the condition $\gamma_s^{(1)} < \gamma_s^{(2)}$ in the neighborhood of the point $\nu_s = 1/2$ the function $F_s(\nu_s)$ becomes negative (Fig. 7). In the region of magnetic fields where $F_s(\nu_s) < 0$ there can be nonzero values of T_s only for $\lambda_s < 0$, which corresponds to a positive maximum of the potential $\tilde{W}_s(q) + \tilde{U}_s(q)$ at the point $q = q_s^{\max}$ (see Figs. 4 and 5), i.e., electron–electron repulsion and electron–hole attraction. In this case T_s is equal to the critical temperature $T_{CDW}^{(s)}$ of the transition to a spatially homogeneous excitonic phase with a quantum CDW.

Figure 8 shows the phase diagram of a 2D electron sys-

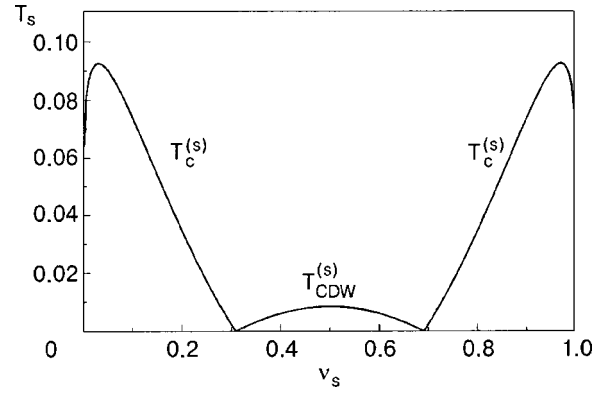


FIG. 8. Dependence on ν_s of the critical temperatures $T_c^{(s)}$ and $T_{CDW}^{(s)}$, normalized to $\lambda_s \gamma_s^{(1)}$, for $\gamma_s^{(1)} < \gamma_s^{(2)}$. The value of λ_s for the Cooper phase was chosen at the point of maximum interelectron attraction ($q = 0$) due to the electron–phonon and electron–plasmon interactions, and for the excitonic phase, at the point of maximum repulsion ($q_1^{\max} \approx 1.7l_H^{-1}$) for $s = 1$ and $\beta = 2$ (Fig. 4b).

tem in a quantizing magnetic field in the variables T and ν_s in the interval $0 \leq \nu_s \leq 1$ under the condition $\gamma_s^{(1)} < \gamma_s^{(2)}$. We see that the critical temperature of the excitonic phase $T_{CDW}^{(s)}$ is maximum at the point $\nu_s = 1/2$, so that for $T < T_{CDW}^{(s)}$ in relatively narrow intervals of magnetic field H near half-integer values of the total filling factor $\nu = (2n - 1)/2$ one may observe features in R_{xx} and R_{yy} due to the scattering of electrons on quantum CDWs,^{25,29–31} and the width of these field intervals should increase with decreasing T .

The fact that the features of R_{xx} and R_{yy} are not observed upon the filling of the two lowest Landau levels, when $\nu = 1/2, 3/2$ (Ref. 25), may be due to an insufficiently low measurement temperature or to the circumstance that $\gamma_s^{(1)} > \gamma_s^{(2)}$ in these cases. Here $T_{CDW}^{(s)} = 0$, and $T_c^{(s)} > 0$ in the entire interval $0 \leq \nu_s \leq 1$, i.e., a transition can occur only to the Cooper phase as T is lowered.

It should be noted that the coherent state of Cooper pairs in a quantizing magnetic field, analogous to the Cooper condensate in superconductors,⁴¹ can arise only in the case of rather strong overlap of their wave functions, i.e., under the condition that the average distance between pairs, $\bar{r}_p \geq (2/\pi N)^{1/2}$, is less than the localization length $2l_H$ of the electron wave functions. This corresponds to values of the total filling factor $\nu = N/N_L = 4l_H^2/\bar{r}_p^2 > 1$.

4. COOPER PAIRING OF 2D ELECTRONS AND THE PHASE DIAGRAM IN THE ULTRAQUANTUM LIMIT

A question of particular interest is that of the Cooper pairing of 2D electrons in the ultraquantum limit ($s = 0$), when the filling factor ν_0 of the lowest spin Landau level is equal to $\nu = 2\pi l_H^2 N < 1$, so that the average distance between electrons $\bar{r}_e = (\pi N)^{-1/2} > l_H \sqrt{2}$.

In this case the phase diagram of the 2D system can be presented in the variables $T-H$, since $\nu = H_0/H$, where $H_0 = N\Phi_0$ and Φ_0 is the magnetic flux quantum. Figure 9 shows the phase diagrams corresponding to the conditions $\gamma_0^{(1)} > \gamma_0^{(2)}$ (a) or $\gamma_0^{(1)} < \gamma_0^{(2)}$ (b) for the same parameter values as in Fig. 8. The temperature region below the $T_c^{(0)}(H)$ curves is the existence region of the Cooper phase, and below the curve $T_{CDW}^{(0)}(H)$ in Fig. 9b is the existence region of

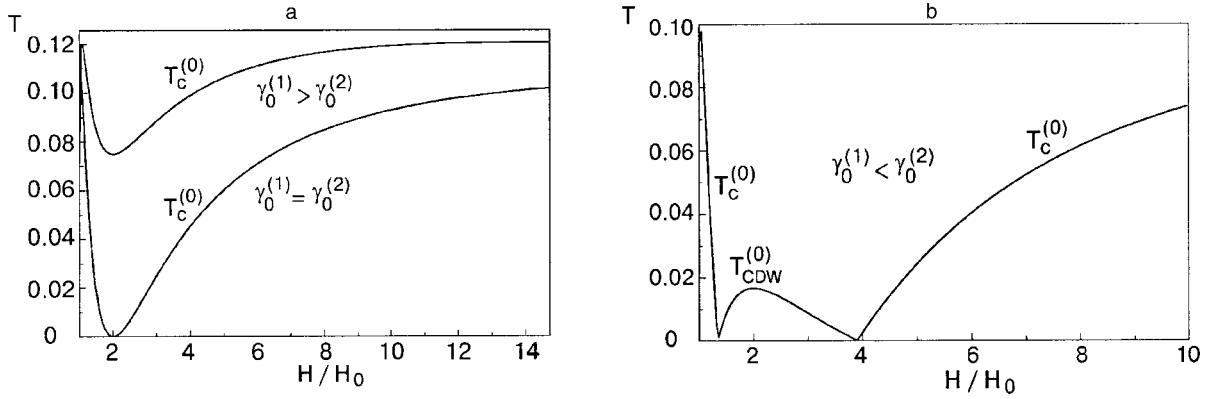


FIG. 9. Phase diagram of a 2D system in the variables T and H , normalized to $\lambda_0 \gamma_0^{(1)}$ and H_0 , respectively, in the ultraquantum limit ($s=0$) for $\gamma_0^{(1)} \geq \gamma_0^{(2)}$ and $\gamma_0^{(1)} < \gamma_0^{(2)}$ (b) for $\beta=2$ (Fig. 4a).

the excitonic phase. By analogy with superconductors⁴¹ it is natural to suppose that in the Cooper phase in the region $0 < T < T_c^{(0)}$ there is coexistence of bound electron pairs and unbound 2D electrons, whereas for $T \rightarrow 0$ all of the electrons are bound into Cooper pairs, and for $T \geq T_c^{(0)}$ all of the electrons are unpaired and form an “incompressible” Laughlin 2D liquid.⁵

The possibility of coexistence of bound pairs and unbound electrons in a 2D system in the ultraquantum limit was considered in Ref. 32 without specifying the pairing mechanism. With the use of a many-particle variational wave function of the polynomial type,^{5,27} symmetric with respect to interchanges of pairs (bosons) and antisymmetric with respect to the interchanges of free electrons (fermions), it was shown in Ref. 32 that a superposition of the states N_p of the bound pairs and N_e of the unbound 2D electrons should lead to quantum features of the Hall resistance R_H and transport resistance R_{xx} in the FQHE regime for values of the filling factor $\nu = N/N_\phi$ (where $N = N_e + 2N_p$ is the total concentration of 2D electrons, and $N_\phi = H/\Phi_0$ is the number of flux quanta Φ_0 per unit area) given by the following relation:

$$\nu = \frac{4m + p - 4r}{mp - r^2}, \quad (31)$$

where m is a positive odd number ($m \geq 3$), p is an even number ($p \geq 4$), and r is a number of arbitrary parity ($r \geq 2$). Here the relative numbers of unpaired 2D electrons and bound (Cooper) pairs are given by

$$\nu_e = \frac{N_e}{N_e + 2N_p} = \frac{p - 2r}{4m + p - 4r};$$

$$\nu_p = \frac{N_p}{N_e + 2N_p} = \frac{2m - r}{4m + p - 4r}. \quad (32)$$

Under the condition $r = 2m$ the Halperin relation (31) for any m and p (including the point $p = 2r = 4m$, at which an indeterminacy of the type 0/0 appears) gives the simple fractions $\nu = 1/m$ ($m = 3, 5, 7, \dots$). We note that the condition $r = 2m$, according to Eq. (32), corresponds to a state with zero concentration of Cooper pairs ($\nu_p = 0$, $\nu_e = 1$), i.e., a “normal” Laughlin liquid⁵ in the temperature region $T \geq T_c^{(0)}$. However, the fractions $\nu = 1/m$ can also be contained in relation (31) for any finite values $\nu_p \neq 0$, i.e., in the Cooper phase $T < T_c^{(0)}$. For example, the fraction $\nu = 1/3$ is realized,

according to (31), for $m = 7$, $p = 16$, $r = 2$ ($\nu_e = \nu_p = 1/3$), the fraction $\nu = 1/5$ for $m = 7$, $p = 22$, $r = 8$ (or $r = 12$) or for $m = 7$, $p = 28$, $r = 6$ ($\nu_e = 2\nu_p = 1/2$), and the fraction $\nu = 1/7$ for $m = 9$, $p = 46$, $r = 8$ ($\nu_e = 3/5$, $\nu_p = 1/5$).

On the other hand, for $p = 2r$ (but $r \neq 2m$) relation (31) for any m gives a sequence of fractional values $\nu = 2/r$, which for odd values of $r = (2n + 1)$ with $n \geq 1$ corresponds to the experimentally observed sequence of fractions $\nu = 2/3, 2/5, 2/7, \dots$, while for even $r = 2(2n + 1)$ it reduces to the Laughlin fractions $\nu = 1/(2n + 1)$. We note that the fractions $\nu = 2/7, 2/9, 2/11, \dots$ are not described by the composite fermion model,⁹ which gives $\nu = n/(2n \pm 1)$ for $n \geq 2$.

The condition $p = 2r$, according to Eq. (32), corresponds to a state with zero concentration of free 2D electrons ($\nu_e = 0$, $\nu_p = 1/2$), i.e., to the Cooper phase at $T = 0$, when all the electrons on the lowest spin Landau level are bound into triplet pairs with spin 1. However, fractions of the type $\nu = 2/(2n + 1)$ are contained in relation (31) for $\nu_e \neq 0$ as well. For example, the fraction $\nu = 2/5$ is realized for $m = 7$, $p = 12$, $r = 2$ ($\nu_e = \nu_p = 1/3$), the fraction $\nu = 2/7$ for $m = 3$, $p = 6$, $r = 9$ ($\nu_e = 2/3, \nu_p = 1/6$) or for $m = 7$, $p = 20$, $r = 8$ ($\nu_e = 1/4, \nu_p = 3/8$), the fraction $\nu = 2/9$ for $m = 5$, $p = 20$, $r = 2$ (or $r = 8$) or for $m = 7$, $p = 28$, $r = 4$ ($\nu_e = 2\nu_p = 1/2$), and the fraction $\nu = 2/11$ for $m = 7$, $p = 28$, $r = 8$ ($\nu_e = 2\nu_p = 1/2$).

Relation (31) also contains other experimentally observed fractional values of the filling factor which are not contained in the composite fermion model. For example, the fraction $\nu = 3/11$ follows from (31) for $m = 3$, $p = 4$, $r = 10$ ($\nu_e = \nu_p = 1/3$) or for $m = 7$, $p = 18$, $r = 4$ ($\nu_e = 2\nu_p = 1/2$), the fraction $\nu = 4/11$ for $m = 3$, $p = 20$, $r = 4$ ($\nu_e = 3/4, \nu_p = 1/8$) or $m = 3$, $p = 12$, $r = 5$ ($\nu_e = 2\nu_p = 1/2$), or for $m = 5$, $p = 12$, $r = 4$ ($\nu_e = 1/4, \nu_p = 3/8$), and the fraction $\nu = 3/13$ for $m = 7$, $p = 20$, $r = 6$ ($\nu_e = \nu_p = 1/3$). We note that as T decreases in the Cooper phase, states with a higher concentration of bound electron pairs should be realized.

In addition, under the condition $p = 2r = 4n$ ($n = 1, 2, 3, \dots$) relation (31) contains fractions with even denominators, $\nu = 1/2, 1/4, 1/6, \dots$, which, as a rule, are not observed in experiments.^{3,4} If it is assumed that the condition $\gamma_0^{(1)} = \gamma_0^{(2)}$ holds for the lowest Landau level ($s = 0$), then in accordance with (29) we obtain $T_{CDW}^{(0)} = 0$ in the entire interval $0 \leq \nu_0 \leq 1$ and $T_c^{(0)} = 0$ at the point $\nu_0 = 1/2$ (see Fig. 9a). This means that in the FQHE regime in the neighborhood of

$\nu \equiv \nu_0 = 1/2$ the quantum states with a Cooper gap are excluded and, consequently, those features of R_H and R_{xx} which are determined by relation (31) should be absent, as should the features of R_{xx} and R_{yy} due to the quantum CDW. Nevertheless, a pseudogap at $\nu = 1/2$ has been observed in tunneling experiments.⁴²

At the same time, because of the interelectron attraction due to the electron–phonon and electron–plasmon interactions with surface phonons and plasmons at sufficiently low temperatures, triplet Cooper pairing of composite fermions is, in principle, possible, and such pairing can be accompanied by the appearance of a quantum feature at $\nu = 5/2$.¹⁴

5. DISCUSSION OF THE RESULTS AND COMPARISON WITH EXPERIMENT

The mechanism proposed in this paper for the Cooper pairing of 2D electrons in a quantizing magnetic field, based on their interaction with 2D phonons and 2D plasmons localized near the interface of the crystals, enables one to describe the quantum features of the transport and Hall resistances in the IQHE and FQHE regimes in a unified approach, taking into account the power-law divergence of the Cooper and zero-sound diagrams at $T \rightarrow 0$. Summation of the divergent ladder diagrams of thermodynamic perturbation theory in the zero-sound and Cooper channels in the local approximation gives an expression for the vertex part with a pole at a certain temperature which depends on the degree of filling of the upper Landau level. This allows one to construct the phase diagram of a 2D system in a quantizing magnetic field; in the case when the contribution of electron–hole processes is dominant, this phase diagram contains both a Cooper and an excitonic phase (Fig. 8). The latter is localized near half-integer values of the filling factor $\nu = (2n - 1)/2$, in qualitative agreement with the experimental data²⁵ from observation of the anisotropic features of the transport resistance, which are due to the scattering of 2D electrons on quantum CDWs.^{29–31} The absence of such features for $n = 1$ and 2 may be due to enhancement of the contribution of electron–electron processes on the lower Landau levels, when the Cooper pairing of 2D electrons become the leading effect. Here the superposition of bound electron pairs and unpaired electrons in the Cooper phase in the ultraquantum limit gives rise to new features of the Hall and transport resistances at fractional values of ν , which are not described by the composite fermion model.

It is interesting to compare the theoretical phase diagram for a system in the FQHE regime for the Cooper phase under the conditions $\gamma_1^{(0)} = \gamma_2^{(0)}$ (Fig. 9a) with the experimental phase diagram constructed in Refs. 43 and 44 on the basis of magneto-optic measurements (Fig. 10). This empirical phase diagram was interpreted in Refs. 43 and 44 as being the result of Wigner crystallization of 2D electrons in a quantizing magnetic field as T is lowered. However, as was noted in Ref. 43, the measured temperature of the liquid–crystal transition turned out to be much lower than the classical melting temperature of the 2D Wigner crystal at the corresponding electron concentration. Furthermore, the tentative boundary of the existence region of the Wigner crystal indicated in Refs. 43 and 44 ($\nu_c = 0.26$) does not agree with the data from

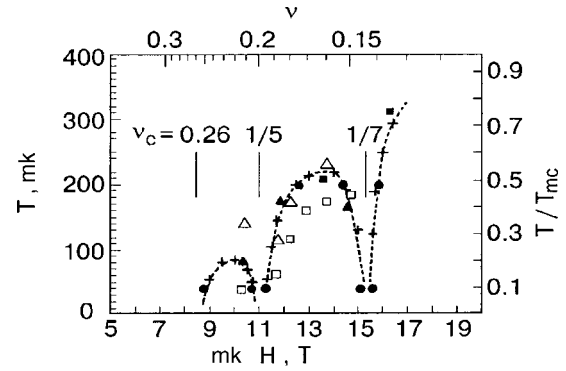


FIG. 10. Experimental phase diagram of a 2D system in the FQHE regime, obtained in Ref. 44 on the basis of the results of magneto-optic measurements on different samples: +, ●— $N = 5.3 \times 10^{10} \text{ cm}^{-2}$; ■— $N = 5.2 \times 10^{10} \text{ cm}^{-2}$; ▲— $N = 6.1 \times 10^{10} \text{ cm}^{-2}$; □—results of Ref. 45; △—results of Refs. 46 and 47.

the study of nonlinear magnetotransport phenomena ($\nu_c = 0.22$); this is most likely due to the accuracy of the corresponding experimental methods.

In the “solid” phase, which in Refs. 43 and 44 was correlated with the behavior of the a weakly damped line in the spectrum of recombination radiation, quantum features were observed in the FQHE regime (including at $\nu < \nu_c$) at values of the filling factor $\nu = 2/3, 2/5, 2/7, 2/9, 2/11$, which are characteristic for the Cooper phase (see Sec. 4) and are contained in the Halperin relation (31). In this connection one can assume that the weakly damped line in the luminescence spectrum of the 2D system may be due not to Wigner crystallization but to Cooper pairing of 2D electrons, since the Cooper phase in the FQHE regime ($\nu < 1$) may be a precursor of the superconducting coherent phase in the IQHE regime ($\nu > 1$).

An additional argument in favor of this assumption is the qualitative similarity between the theoretical dependence of $T_c^{(0)}(H)$ in Fig. 9a and the envelope of the phase boundaries in Fig. 10. As to the “fine structure” of the empirical phase diagram, which is manifested in the existence of narrow dips on the field dependence of the critical temperature near the fractional values $\nu = 1/5, 1/7$, etc., a natural explanation for this effect (as also for the case of the Wigner crystal)^{43,44} is that the energy of the ground state of the Laughlin liquid⁵ has deep minima at $\nu = 1/(2n + 1)$, which lie below the energy of the Cooper phase at the same values of ν .

Thus it is not ruled out that what was observed in the magneto-optic experiments^{43,44} was not a “solid” Wigner phase but a “liquid” Cooper phase, arising because of the interelectron attraction due to the electron–phonon and electron–plasmon interactions with surface phonons and plasmons. In the neighborhood of $\nu = 1/2$, where $T_c^{(0)} \approx 0$ for $\gamma_1^{(0)} \approx \gamma_2^{(0)}$, such attraction at low T may promote triplet Cooper pairing of composite fermions¹⁴ and the appearance of a quantum feature at $\nu = 5/2$.^{11–13}

In closing, the author thanks Yu. A. Bychkov and I. B. Levinson, V. B. Timofeev, and I. V. Kukushkin for helpful discussions.

This paper is dedicated to the centenary of the birth of the outstanding experimental physicist Lev Vasilievich Shubnikov, who was among the earliest discoverers of quan-

tum effects in high magnetic fields, of which the quantum Hall effect in 2D systems is an example.

*E-mail: pashitsk@iop.kiev.ua

- ¹K. Von Klitzing, C. Dorda, and M. Pepper, Phys. Rev. Lett. **45**, 494 (1980).
- ²D. C. Tsui, H. L. Stormer, and A. C. Gossard, Phys. Rev. Lett. **48**, 1559 (1982).
- ³Kh. Shtermer, Usp. Fiz. Nauk **170**, 304, (2000).
- ⁴D. Tsui, Usp. Fiz. Nauk **170**, 320, (2000).
- ⁵R. B. Laughlin, Phys. Rev. Lett. **50**, 1395 (1983); Science **242**, 525 (1988); Usp. Fiz. Nauk **170**, 294 (2000).
- ⁶F. D. M. Haldane, Phys. Rev. Lett. **51**, 605 (1983).
- ⁷B. I. Halperin, Phys. Rev. Lett. **52**, 1583 (1984).
- ⁸F. D. M. Haldane and E. H. Rezayi, Phys. Rev. Lett. **54**, 237 (1985).
- ⁹J. K. Jain, Phys. Rev. Lett. **63**, 199 (1989).
- ¹⁰B. I. Halperin, P. A. Lee, and N. Read, Phys. Rev. B **47**, 7312 (1993).
- ¹¹E. Mendez, L. I. Chang, C. A. Chang, L. F. Alexander, and L. Esaki, Surf. Sci. **142**, 215 (1984).
- ¹²R. Willett, J. P. Eisenstein, H. L. Stormer, D. C. Tsui, A. C. Gossard, and J. H. English, Phys. Rev. Lett. **59**, 1776 (1987).
- ¹³W. Pan, J. S. Xia, V. Shvarts, D. E. Adams, H. L. Stormer, D. C. Tsui, L. N. Pfeiffer, K. W. Baldein, and K. W. West, Phys. Rev. Lett. **83**, 3530 (1999).
- ¹⁴V. W. Scarola, K. Park, and J. K. Jain, Nature (London) **406**, 863 (2000).
- ¹⁵A. L. Kasatkin and É. A. Pashitskiĭ, Ukr. Fiz. Zh. (Russ. Ed.) **22**, 467 (1977).
- ¹⁶F. D. M. Haldeine and E. Rezayi, Phys. Rev. Lett. **60**, 956 (1988).
- ¹⁷T. Maniv, A. I. Room, I. D. Vagner, and P. Wyder *et al.*, Phys. Rev. B **46**, 8360 (1992).
- ¹⁸É. A. Pashitskiĭ, Fiz. Nizk. Temp. **25**, 920 (1999) [Low Temp. Phys. **25**, 690 (1999)].
- ¹⁹Z. V. Popovic, M. Cardona, E. Richter, D. Strauch, L. Tapfer, and K. Ploog, Phys. Rev. B **41**, 5904 (1990).
- ²⁰C. Trallero-Ginev, F. Garcia-Moliner, V. R. Velasco, and M. Cardona, Phys. Rev. B **45**, 11944 (1992).
- ²¹D. Simonyan, S. V. Kravchenko, M. P. Sarachik, and V. M. Pudalov, Phys. Rev. Lett. **79**, 2304 (1997).
- ²²É. A. Pashitskiĭ, Zh. Éksp. Teor. Fiz. **56**, 662 (1969) [Sov. Phys. JETP **29**, 362 (1969)].
- ²³A. M. Gabovich, D. P. Moiseev, É. A. Pashitskiĭ, and S. K. Uvarova, Fiz. Nizk. Temp. **1**, 984 (1975) [Sov. J. Low Temp. Phys. **1**, 473 (1975)].
- ²⁴P. Phillips, S. Knysh, and D. Davidovich, Nature (London) **395**, 253 (1998).
- ²⁵M. R. Lilly, R. B. Cooper, J. P. Eisenstein, L. N. Pfeiffer, and K. W. West, Phys. Rev. Lett. **82**, 394 (1999).
- ²⁶H. Fukuyama, P. M. Platzman, and P. W. Anderson, Phys. Rev. B **19**, 5211 (1979).
- ²⁷Yu. A. Bychkov, S. V. Iordanskiĭ, and G. M. Éliashberg, JETP Lett. **33**, 143 (1981); Poverkhnost' **10**, 33 (1982).
- ²⁸Yu. A. Bychkov and É. I. Rashba, JETP Lett. **38**, 229 (1983); Zh. Éksp. Teor. Fiz. **85**, 1826 (1983) [Sov. Phys. JETP **58**, 1062 (1983)].
- ²⁹A. A. Kulakov, M. M. Fogler, and B. I. Shklovskii, Phys. Rev. Lett. **76**, 499 (1996).
- ³⁰M. M. Fogler, A. A. Kulakov, and B. I. Shklovskii, Phys. Rev. B **54**, 1853 (1996).
- ³¹R. Moess and J. T. Chalker, Phys. Rev. B **54**, 5006 (1996).
- ³²B. I. Halperin, Helvetika Physica Acta **56**, 75 (1983).
- ³³Yu. A. Bychkov, Fiz. Tverd. Tela (Leningrad) **31**(7), 56 (1989) [Sov. Phys. Solid State **31**, 1130 (1989)].
- ³⁴V. F. Gantmakher and I. V. Levinson, Rasseyaniye nositelei toka v metal-lakh i poluprovodnikakh, Nauka, Moscow (1984).
- ³⁵L. G. Il'chenko and É. A. Pashitskiĭ, Fiz. Tverd. Tela (Leningrad) **22**, 3395 (1980) [Sov. Phys. Solid State **22**, 1987 (1980)].
- ³⁶A. V. Andreev and Yu. A. Bychkov, Phys. Rev. B **45**, 1443 (1992).
- ³⁷Yu. A. Bychkov, L. P. Gor'kov, and I. E. Dzyaloshinskiĭ, Zh. Éksp. Teor. Fiz. **50**, 738 (1966) [Sov. Phys. JETP **23**, 489 (1966)].
- ³⁸I. E. Dzyaloshinskiĭ and A. I. Larkin, Zh. Éksp. Teor. Fiz. **61**, 791 (1971) [Sov. Phys. JETP **34**, 422 (1972)].
- ³⁹L. P. Gor'kov and I. E. Dzyaloshinskiĭ, Zh. Éksp. Teor. Fiz. **67**, 397 (1974) [Sov. Phys. JETP **40**, 198 (1975)].
- ⁴⁰A. T. Zheleznyak, V. M. Yakovenko, and I. E. Dzyaloshinskiĭ, Phys. Rev. B **55**, 3200 (1997).
- ⁴¹J. R. Schrieffer, *Theory of Superconductivity* [Benjamin, New York (1964); Nauka, Moscow (1970)].
- ⁴²K. M. Brow, N. Turner, J. T. Nicholls, E. H. Linfield, M. Pepper, D. A. Ritchie, and G. A. C. Jones, Phys. Rev. B **50**, 15465 (1994).
- ⁴³I. V. Kukushkin and V. B. Timofeev, Usp. Fiz. Nauk **163**, 1 (1993).
- ⁴⁴I. V. Kukushkin and V. B. Timofeev, Adv. Phys. **45**, 147 (1996).
- ⁴⁵V. I. Goldman, M. Santos, M. Shayagan, and J. E. Cunningham, Phys. Rev. Lett. **65**, 2198 (1990).
- ⁴⁶M. A. Paalanen, R. L. Willett, P. Littlewood, R. P. Ruel, K. W. West, L. N. Pfeiffer, and D. J. Bishop, Phys. Rev. B **45**, 11342 (1992).
- ⁴⁷M. A. Paalanen, R. L. Willett, P. R. Ruel, P. Littlewood, K. W. West, and L. N. Pfeiffer, Phys. Rev. B **45**, 11784 (1992).

Translated by Steve Torstveit

Bound spin-excitons in two-dimensional electron gas

V. Fleurov*

School of Physics and Astronomy, Beverly and Raymond Sackler Faculty of Exact Sciences, Tel Aviv University, Tel Aviv 69978, Israel

K. Kikoin

Physics Faculty, Ben-Gurion University of the Negev Beer-Sheva 84105, Israel

(Submitted April 23, 2001)

Fiz. Nizk. Temp. **27**, 1083–1091 (September–October 2001)

A theory of the spin exciton capture by a magnetic impurity in a 2D electron gas is developed. We consider a resonance model for the electron scattering by a transition metal impurity and calculate the binding potential for spin excitons. This potential is spin selective and is capable of binding a spin exciton with zero angular momentum. In order to trap an exciton with a nonzero angular momentum m , the potential must exceed a certain threshold value that depends on m . © 2001 American Institute of Physics. [DOI: 10.1063/1.1414568]

1. INTRODUCTION

The Shubnikov–de Haas effect is a powerful tool for studies of a two-dimensional electron gas (2DEG) in a strong magnetic field. In particular, the oscillatory behavior of the electronic g factor in a 2DEG has been investigated with the help of this effect (see Ref. 1 and references therein). Two important parameters which predetermine the properties of the 2DEG in a strong magnetic field B are the cyclotron frequency $\omega_B = eB/mc$ and the effective Coulomb energy $E_c = e^2/\kappa l_B$ ($l_B = (\hbar c/eB)^{1/2}$) is the magnetic length. In the limit of ultrahigh magnetic fields, when $E_c \ll \hbar \omega_B$ and only the lowest Landau sublevel is filled, the low-energy branches of the excitation spectrum are represented by well-separated bands of spin waves, magnetoplasmons, etc. These excitations have been studied in detail on recent decades (see, e.g., Refs. 2–7). Various forms of spin excitations can be observed experimentally using the inelastic light scattering method as described in Ref. 8, where features are observed that are attributed to collective excitation in a 2DEG. The presence of magnetic impurities may account for additional features due to localized spin excitations.

The spin waves formed by the electrons in the down-spin and holes in up-spin $n=0$ Landau subbands make up the lowest branch of magnetic excitations. These states are separated by the Zeeman gap $\Delta_B = g\mu_B B$ from the ground state and form a band with a width of $\sim E_c$. The exciton dispersion law is quadratic at small wave numbers and saturates in the short-wave length limit, where the excitons, in fact, transform into free electron-hole pairs.²

This paper studies the interaction between spin waves and a magnetic impurity in a 2DEG. To be more specific, we consider doped heterojunctions GaAs/GaAlAs and related materials, so we refer below to a III–V semiconductor as a host material, in which some cation atoms are substituted for magnetic transition metal impurities. It is known⁹ that transition metal atoms create deep levels in the forbidden energy gap of the host semiconductor, and the main mechanism of the electron–impurity scattering is the resonance scattering by the d levels of the unfilled $3d$ shell of transition metal

ions. The intra-atomic exchange interaction leads to Hund’s rule, which governs the occupation of the deep levels. As a result, the transition atoms in a semiconductor are magnetic. We will show below that the interplay between the magnetic impurity scattering and attractive electron-hole interaction in excited 2DEG results in a bound spin exciton. The spectrum of these bound states is the subject of the present study.

2. MODEL AND APPROXIMATIONS

We start with the model of a 2DEG doped by magnetic impurities which is discussed in detail in Ref. 10. This model is described by the Hamiltonian

$$H = H_b + H_i \tag{1}$$

where

$$H_b = \sum_{nm\sigma} E_{n\sigma} a_{nm,\sigma}^+ a_{nm,\sigma} \tag{2}$$

is the Hamiltonian of a 2DEG strongly quantized by a magnetic field. It is convenient to use the symmetric cylindrical gauge for the vector potential $A = ((-B/2)y, B/2, 0)$, so that the index m in (2) describes different orbital states in a given Landau level

$$E_n = \hbar \omega_B \left(n + \frac{1}{2} \right) \equiv \frac{\hbar^2}{2m} \frac{2n+1}{l_B^2}. \tag{3}$$

Then, assuming a small impurity concentration, the impurity related part H_i of the Hamiltonian (1) can be written in the general form

$$H_i = \sum_{\Gamma} \langle i\Gamma | E_{\Gamma} | i\Gamma \rangle + \sum_{\gamma} \sum_{nm\sigma} (\langle i\gamma | V | nm \rangle d_{i\gamma\sigma}^+ a_{nm\sigma} + \text{h.c.}) + \sum_{nm\sigma} \langle nm | \Delta V | n'm' \rangle a_{nm\sigma}^+ a_{n'm'\sigma}. \tag{4}$$

Here the state of an isolated impurity ion is characterized by a configuration d^n of its unfilled d shell in a crystal field preserving the point symmetry of the bulk semiconductor

(we assume that the potential responsible for the confinement in the z direction does not perturb the crystalline environment of the impurity site). Then the electrons in the d shell are characterized by the representations $\gamma = t_2, e$ of the tetrahedral point group, and the many-electron states $|\Gamma\rangle$ of the $3d$ shell may be represented as

$$d_{\Gamma}^n = (n e_{\uparrow}^{r_1} e_{\downarrow}^{r_2} t_{2\uparrow}^{r_3} t_{2\downarrow}^{r_4})_{\sum r_i = n}$$

(\downarrow and \uparrow are two projections of the electron spin). The scattering part of H_i consists of two components:⁹ the second term in Eq. (4) describes the resonance part of the impurity scattering; the third term represents the short-range substitution potential $\Delta V = V_i(r - R_0) - V_{\text{host}}(r - R_0)$, where R_0 is the position of the substitutional impurity in the host lattice. The resonance scattering arises together with the usual “potential” scattering due to the fact that the energy level $\varepsilon_{i\gamma} = E_{\Gamma}(d^n) - E_{\Gamma}(d^{n-1})$ enters the fundamental energy gap of the host semiconductor or appears in the lowest conduction band of the topmost valence band. Here the configuration d^{n-1} is missing one electron in a state $\gamma = e$ or t_2 in comparison with the state d^n .

The impurity problem with the two scattering mechanisms can be solved in the general case.^{11,12} In our special case its solutions are essentially different for the e and t_2 channels. As is shown in Ref. 10, the t_2 component of the impurity potential results in deep levels in the forbidden energy gap or resonances in the conduction band, but only weakly perturbs the Landau levels E_n . On the other hand, e -scattering results in the appearance of bound Landau states with $m=0$ between Landau levels with nonzero orbital quantum number and in a splitting of the lowest bound state from the Landau grid. The reason for this difference is in the *short-range* nature of both components of the scattering potential. The eventual reason for this difference is the orbital dependence of the matrix element

$$\langle nm | \Delta U | \gamma \mu \rangle \sim \left(\frac{\rho}{l_B} \right)^{|m|} \ll 1 \quad (5)$$

for $m \neq 0$.⁹ Here ρ is the radial variable in the cylindrical coordinates (ρ, φ, z) . When estimating this matrix element one should choose ρ of the order of the atomic radius. As a result, only the orbitals $|e1\rangle \propto |r^2 - 3z^2\rangle \sim Y_{20}$ with $m=0$ may be strongly hybridized with the Landau states.

According to Refs. 10 and 12, the localized eigenstates of the Hamiltonian (1), (4) are given by the following equation

$$E_{i\gamma\sigma} - \varepsilon_{i\gamma\sigma} - M_{\gamma}(E_{i\gamma\sigma}) = 0, \quad (6)$$

where

$$M_{\gamma}(E_{i\gamma\sigma}) = \sum_{\beta} \frac{\langle \gamma \mu | \Delta U | \beta \rangle \langle \beta | \Delta U | \gamma \mu \rangle}{E_{i\gamma\sigma} - E_{\beta}}, \quad (7)$$

where $|\beta\rangle \equiv |bn\sigma\rangle$ stands for the eigenfunctions of the magnetically quantized electrons captured by the local potential ΔU . The latter problem was solved in Ref. 13 for an attractive potential $\Delta U < 0$. It was shown that the short-range potential also perturbs only the zero orbital states $m=0$. The general structure of the electron spectrum of a doped 2DEG is sketched in Fig. 1.

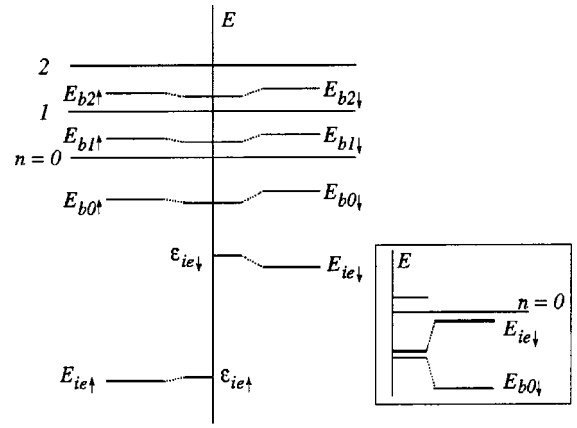


FIG. 1. A schematic representation of the interacting Landau and impurity levels. $E_{ie\sigma}$ are the impurity levels for spin-up and spin-down electrons. They result from the prime impurity levels $\varepsilon_{ie\sigma}$ shifted to new positions due to their interaction with the Landau levels with $m=0$. The Landau levels with $m=0$ are also shifted to their new positions $E_{be\sigma}$. The inset illustrates the case when an impurity prime spin-down state is nearly degenerate with the lowest Landau spin-down state.

This observation allows us to divide the states in the Landau band (2) into two groups,

$$H_b = H_{b0} + H'_b. \quad (8)$$

Here H_{b0} includes only the states with the zero angular momentum $m=0$, whereas H'_b includes all the remaining states. Only the states with $m=0$ are involved in the formation of the bound Landau states given by the solutions of Eq. (6). Similar reduction can be made in the manifold $\{i\gamma\sigma\}$ due to the “selection rule” (5): when considering the renormalization of the states $|\beta\rangle$ due to the resonance scattering, we retain only the state $|e1\rangle$ in the corresponding sector of the secular matrix. As a result, one has the following equation

$$E_{bn\sigma} - E_{bn\sigma}^{(0)} = \frac{\langle bn\sigma | \Delta U | e1\sigma \rangle \langle e1\sigma | \Delta U | bn\sigma \rangle}{E_{bn\sigma} - E_{ie\sigma}} + \delta M(E_{bn\sigma}) \quad (9)$$

for the energy shift of a given level $E_{bn\sigma}^{(0)}$ which according to Ref. 13 appears in the gap between the bare Landau levels E_{n-1} and E_n . Here we have picked up the direct mutual repulsion of the n th Landau level and the d level in the first term of the right-hand side of Eq. (9). The influence of the other bound Landau states is given by the second term,

$$\delta M(E) = \sum_{\beta' \neq \beta} \frac{\langle \beta' | \Delta U | e1\sigma \rangle \langle e1\sigma | \Delta U | \beta' \rangle (E - E_{\beta}^{(0)})}{(E - E_{ie\sigma})(E - E_{\beta'}^{(0)})}.$$

The role of these states is to keep the renormalized levels in the same energy interval $E_{n-1,\sigma} < E_{bn\sigma} < E_{n\sigma}$.

An important feature of the resonant channel of impurity scattering is its *spin selectivity*, which stems from the spin structure of the transition metal d shell. It is known⁹ that in their main features the transition metal impurities follow the “Aufbau principle” of the quantum mechanics of isolated atoms. This means that the d shell is usually filled in accordance with Hund’s rule or, in other words, the exchange interaction makes the level $E_{ie\uparrow}$ lie always below the level

$E_{ie\downarrow}$. Then the splitting $\Delta_{es} = E_{ie\downarrow} - E_{ie\uparrow}$ generates the spin splitting $\Delta_{bs}^{(n)}$ of the bound Landau states via Eq. (9). This splitting can be estimated as

$$\Delta_{bs}^{(n)} \approx \frac{\Delta_{es}}{\Delta_{\uparrow}^{(n)} \Delta_{\downarrow}^{(n)}} \left(\left| V_{er} \right|^2 + \sum_{n' \neq n} \frac{|V_{en'}|^2 \delta_n}{E_{bn}^{(0)} - E_{bn'}^{(0)}} \right). \quad (10)$$

Here $\Delta_{\sigma}^{(n)} = E_{bn} - E_{ie\sigma}$, $V_{en} = \langle e1 | \Delta U | bn \rangle$, $\delta_n = E_{bn} - E_{bn}^{(0)}$ (the spin dependence of the two last quantities is neglected). It is important for the further classification of the spin excitons that the sign of $\Delta_{bs}^{(n)}$, unlike the sign of Δ_{es} , can be both negative or positive, since the energy differences $\Delta_{\uparrow}^{(n)}$ and $\Delta_{\downarrow}^{(n)}$ can have either the same or the opposite signs depending on the type of the transition metal ion and the host matrix (see the discussion in Ref. 10). According to Eq. (10) the resonance impurity scattering results in a “transfer” of the exchange splitting Δ_{es} of the impurity d shell to the spectrum of the Landau electrons. This transfer is illustrated by the level renormalization in Fig. 1.

Now we know the general structure of the one-particle spectrum of a magnetically doped 2DEG, which should serve as a background when magnetic excitons and magnetoplasmons are formed. This spectrum consists of equidistant Landau levels with $m \neq 0$ which are unperturbed by the impurity scattering. The states with $m=0$ form their own grid: a pair of spin-split states $E_{bn\sigma}$ appears in each energy gap $E_n^{(0)} - E_{n-1}^{(0)}$, and the lowest pair of bound states $E_{bn\sigma}$ arises in the fundamental energy gap of the 2D semiconductor below the Landau level E_0 .

3. ENERGY SPECTRUM OF LOCALIZED SPIN EXCITONS

According to the general classification of the multiparticle excitations from a filled Landau level in a 2DEG,⁴ the lowest branch of the electron–hole excitations is that of the spin waves. These spin excitons arise as bound electron–hole pairs with parallel spins as a result of a spin-flip excitation from the lower filled sublevel $E_{0\uparrow}$ of the lowest Landau level to its higher empty sublevel $E_{0\downarrow}$. To calculate the spectrum of the *localized* spin excitons, one should keep only the states with $n=0$ in the bare Hamiltonian H_b (2), take into account the Zeeman splitting of the Landau states explicitly, and then add the electron-hole Coulomb interaction H_{int} ,

$$H_{\text{ex}}^0 = \sum_p (E_{0\uparrow} a_p^+ a_p + E_{0\downarrow} b_p^+ b_p) + H_{\text{int}}. \quad (11)$$

Operators $a^+(a)$ and $b^+(b)$ describe creation (annihilation) of electrons with the up or down spins σ , index $n=0$ being omitted. Here the electron wave functions are written in the asymmetric Landau gauge $A = B(y, 0, 0)$. Then the total Hamiltonian of a doped 2DEG takes the form

$$H = H_{\text{ex}}^0 + H_i. \quad (12)$$

The impurity-related term H_i was analyzed in the previous Section using the symmetric gauge. Now it should be re-derived in the Landau gauge.

Using the solution of the impurity problem found in the previous Section and taking into account that the Landau levels with $m=0$ are included in H_{ex} , contrary to the “extraction” principle formulated in Eq. (8), we can write H_i in the form (see Appendix)

$$H_i = (|A_{00}|^2 E_{b0\uparrow} - E_{0\uparrow}) a_{i0}^+ a_{i0} + (|B_{00}|^2 E_{b0\downarrow} - E_{0\downarrow}) b_{i0}^+ b_{i0} + H_{i,nd}. \quad (13)$$

Here $E_{b0\sigma}$ are the solutions of Eq. (9) for the lowest bound Landau state, and the operators a_{i0}^+ and b_{i0}^+ create the corresponding eigenfunctions in the symmetric cylindrical gauge. The coefficients A_{00}, B_{00} are defined in Eq. (A2). The off-diagonal term $H_{i,nd}$ contains the contribution from the higher Landau levels with $n > 0$, whose value is of the order of $\sim |A_{0n}|^2 / E_n \ll 1$ and will be neglected in the further calculations.

In principle, the scattering potential also contains terms corresponding to the spin-flip processes,

$$H_{\perp} = J(d_{ie\uparrow}^+ d_{ie\downarrow} b_{i0}^+ a_{i0} + d_{ie\downarrow}^+ d_{ie\uparrow} a_{i0}^+ b_{i0}). \quad (14)$$

The spin-flip terms are inessential in comparison with the leading spin-diagonal terms (13) because each spin flip costs the Hund energy $\Delta_{es} = E_{ie\downarrow} - E_{ie\uparrow}$, so that $J \sim |V_{e0}|^2 / \Delta_{es}$. The spin-flip processes, in principle, result in a multiple creation of spin excitons, but the contribution of these processes to the spin-wave spectrum is at least $\sim J^2$, and we also neglect them in the further calculations.

Then, we turn from the cylindrical gauge to the Landau gauge,

$$a_{i0}^+ = \sum_p A_p a_p^+, \quad b_{i0}^+ = \sum_p B_p b_p^+, \quad (15)$$

where

$$A_p = \langle i0\uparrow | p\uparrow \rangle, \quad B_p = \langle i0\downarrow | p\downarrow \rangle. \quad (16)$$

As a result the impurity Hamiltonian in the Landau gauge has the form

$$H_i = \sum_{pp'} [U_{\uparrow}(p, p') a_p^+ a_{p'} + U_{\downarrow}(p, p') b_p^+ b_{p'}] \quad (17)$$

where

$$U_{\uparrow}(p, p') = K_{\uparrow} J_{p\uparrow} J_{p'\uparrow}^*, \quad U_{\downarrow}(p, p') = K_{\downarrow} J_{p\downarrow} J_{p'\downarrow}^*. \quad (18)$$

Here $J_{p\sigma} = \langle \Psi_{b\sigma} | \Psi_{p,0\sigma} \rangle$, and $\Psi_{p,0\sigma}$ are the wave functions of the lowest Landau level,

$$\psi_{p,0\sigma}(x, y) = \frac{1}{(2\pi^{3/2})^{1/2}} \exp(ipx) \exp\left(-\frac{(x+p)^2}{2}\right). \quad (19)$$

Here x, y are Cartesian projections of the dimensionless vector \mathbf{r}/l_B . The coefficients K_{σ} are calculated in the Appendix.

To derive the impurity Hamiltonian in the Landau gauge, we use the identity

$$a_p^+ a_{p'} = \int \frac{dq_x}{2\pi} \exp\left[-iq_x \frac{p+p'}{2}\right] \rho_{\uparrow}(q_x, p' - p),$$

$$b_p^+ b_{p'} = \int \frac{dq_x}{2\pi} \exp\left[-iq_x \frac{p+p'}{2}\right] \rho_{\downarrow}(q_x, p' - p), \quad (20)$$

where the electron density operators are

$$\rho_{\uparrow}(\mathbf{q}) = \sum_p a_p^+ a_{p+q_y} \exp\left(iq_x \left(p + \frac{q_y}{2}\right)\right)$$

$$\rho_{\downarrow}(\mathbf{q}) = \sum_p b_p^+ b_{p+q_y} \exp\left(iq_x \left(p + \frac{q_y}{2}\right)\right) \quad (21)$$

with $\mathbf{q}=(q_x, q_y)$. Then inserting Eq. (20) into Eq. (17), we get, after straightforward calculations,

$$H_i = \sum_{\mathbf{q}, \sigma} U_\sigma(\mathbf{q}) e^{q^2/4} \rho_\sigma(\mathbf{q}), \quad (22)$$

where the matrix elements of the impurity potential are

$$U_\sigma(\mathbf{q}) = K_\sigma \int d^2r_1 d^2r_2 \psi_{b\sigma} \times \left(\frac{r_1^2}{2}\right) \psi_{b\sigma} \left(\frac{r_2^2}{2}\right) \exp\left(-\frac{|r_1 - r_2|^2}{4}\right) \times \exp\left\{\frac{1}{2}[(x_1 - x_2)q_y + (y_1 - y_2)q_x - i(y_1 + y_2)q_y + i(x_1 + x_2)q_x - i(x_1 + x_2)(y_1 - y_2)]\right\}. \quad (23)$$

Here the coefficients K_σ determined in the Appendix depend on the specific form of the scattering impurity potential acting on the electrons in the Landau subband 0σ [see Eqs. (16), (A3), (A6), (A8)]. We discuss here the limit of a strong magnetic field, when the cyclotron energy $\hbar\omega_B = \hbar^2/2ml_B$ is large compared to the Coulomb energy $e^2/\kappa l_B$. It is essential that the impurity potential is spin selective, i.e., its components acting on the electrons in the two Landau subbands can differ significantly in magnitude (see below).

We consider the case of the filling factor $\nu = 1$, when the spin-up Landau band is totally full and the spin-down Landau band is completely empty. Then the eigenfunctions of the Hamiltonian (11),

$$\Psi_{\text{ex}, \mathbf{k}}^{(0)} = \sum_p b_p^+ a_{p+k_y} \exp\left(ik_x\left(p + \frac{k_y}{2}\right)\right) |0\rangle, \quad (24)$$

correspond to the free spin-excitons with the energy spectrum $\varepsilon_{\text{ex}}(k)$,

$$H^{(0)}\Psi_{\text{ex}}^{(0)}(k) = \varepsilon_{\text{ex}}(k)\Psi_{\text{ex}, \mathbf{k}}^{(0)}. \quad (25)$$

Here $\mathbf{k} = k_x, k_y$ is the wave vector of a spin exciton. The exciton dispersion law is

$$\varepsilon_{\text{ex}}(k) = \Delta_B + \left(\frac{e^2}{\kappa l_B}\right) \left(\frac{\pi}{2}\right)^{1/2} [1 - e^{-k^2/4} I_0(k^2/4)] \equiv \Delta_B + \Omega(k^2) \quad (26)$$

(see Refs. 2–4 and 14). Here $\Delta_B = |g\mu_B B|$ is the Zeeman energy; I_0 is a modified Bessel function.

The wave function of a bound exciton is looked for in the form

$$\Psi_{\text{ex}} = \sum_{\mathbf{k}} f(\mathbf{k}) \Psi_{\text{ex}, \mathbf{k}}^{(0)}. \quad (27)$$

The function (27) must be an eigenfunction of the Hamiltonian (12). The standard procedure leads to the equation

$$[\varepsilon_{\text{ex}}(k) - \varepsilon] f(\mathbf{k}) + 2i \sum_{\mathbf{k}'} \tilde{U}_+(\mathbf{k} - \mathbf{k}') \times \sin \frac{1}{2} [\mathbf{k}' \times \mathbf{k}]_z f(\mathbf{k}') - 2 \sum_{\mathbf{k}'} \tilde{U}_-(\mathbf{k} - \mathbf{k}') \times \cos \frac{1}{2} [\mathbf{k}' \times \mathbf{k}]_z f(\mathbf{k}') = 0, \quad (28)$$

for the envelope function $f(\mathbf{k})$. Here

$$\tilde{U}_\pm(\mathbf{q}) = \frac{1}{2} (U_\uparrow(\mathbf{q}) \pm U_\downarrow(\mathbf{q})) e^{-q^2/4} \equiv U_\pm(\mathbf{q}) e^{-q^2/4}.$$

As is discussed in the Appendix, the localization radius ρ_b of the impurity wave function is substantially smaller than the magnetic length. Then the q dependence of the matrix elements (23) is insignificant, and they can be estimated as

$$U_\sigma \approx K_\sigma (2\pi^2) \left(\int_0^\infty d\xi \psi_{b\sigma}(\xi)\right)^2 \equiv K_\sigma I_b. \quad (29)$$

Taking into account the cylindrical symmetry of the problem, we seek the solutions of Eq. (28) in the form

$$f(\mathbf{k}) = f_m(k) e^{im\varphi}, \quad (30)$$

where the integer quantity m is the quantum number of the bound exciton.

Now we substitute the functions (30) in Eq. (28) and carry out the integration over the directions of the vector \mathbf{k}' . Then the term proportional to U_+ contains the integrals

$$\int_0^{2\pi} \frac{d\varphi}{2\pi} \exp\left(\frac{kk'}{2} \cos \varphi\right) \sin\left(\frac{kk'}{2} \sin \varphi\right) \sin m\varphi = \frac{(kk')^{|m|}}{2^{|m|+1}|m|} \text{sign}(m) \quad (31)$$

in which the sign function is defined as

$$\text{sign}(m) = \begin{cases} 1, & m > 0 \\ 0, & m = 0, \\ -1, & m < 0. \end{cases} \quad (32)$$

The term proportional to U_- contains the integrals

$$\int_0^{2\pi} \frac{d\varphi}{2\pi} \exp\left(\frac{kk'}{2} \cos \varphi\right) \sin\left(\frac{kk'}{2} \sin \varphi\right) \cos m\varphi = \frac{(kk')^{|m|}}{2^{|m|+1}|m|} \quad (33)$$

for all values of the quantum number m .

The equations defining the radial parts $f_m(k)$ of the envelope functions (30) are

$$f_m(k) = W_n k^{|m|} e^{-k^2/4} \frac{1}{\varepsilon - \varepsilon_{\text{ex}}(k)} F_m, \quad (34)$$

where

$$W_m = \frac{1}{2^{|m|+1}|m|!} \{U_\downarrow[1 + \text{sign}(m)] - U_\uparrow[1 - \text{sign}(m)]\}$$

and

$$F_m = \sum_{\mathbf{k}} e^{-k^2/4} k^{|m|} f_m(k).$$

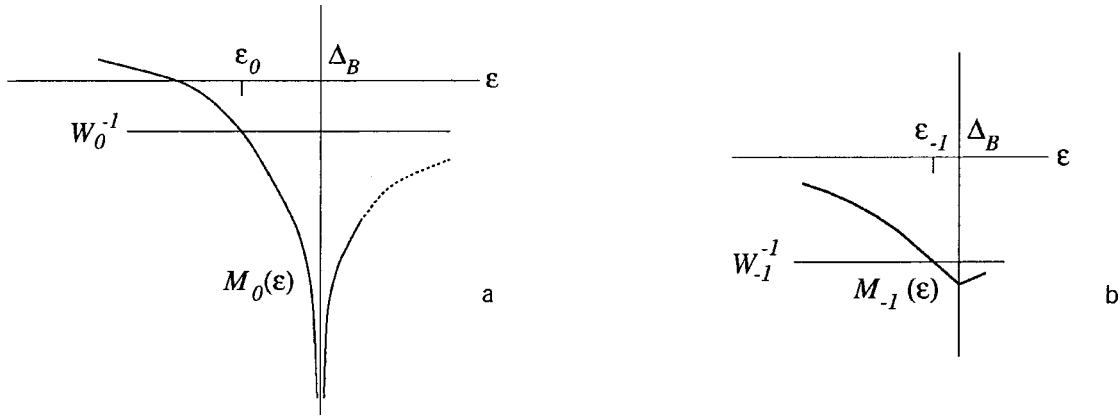


FIG. 2. A graphical solution of Eq. (35) for $m=0$. Due to the logarithmic divergence of the function $M_0(\epsilon)$ at $\epsilon=\Delta_B$, a spin exciton can be always bound with an energy ϵ_0 below the bottom of the spin-exciton band (a). A graphical solution of Eq. (35) for $m=-1$. The function $M_{-1}(\epsilon)$ is now nondivergent. Hence, a spin exciton can be bound with an energy ϵ_{-1} below the bottom of the spin-exciton band if the parameter W_{-1} is larger than the threshold value $\bar{W}_{-1}=1/M_{-1}(\Delta_B)$ (b).

The energy ϵ_m of the bound exciton with the quantum number m can be found as a solution of the equation

$$1 = W_m M_m(\epsilon_m), \quad (35)$$

where

$$M_m(\epsilon) = \sum_{\mathbf{k}} \frac{k^{2|m|} e^{-k^2/2}}{\epsilon - \epsilon_{\text{ex}}(k)}. \quad (36)$$

We introduce now the new variable $\omega = k^2$ and convert the summation in Eq. (36) to integration. Then the fact that at small ω the dispersion law $\Omega(\omega) \propto \omega$ allows us to find the behavior of the quantity $M_m(\epsilon)$ at $\epsilon \rightarrow \Delta_B$.

$$M_m(\epsilon) = \pi \int_0^D d\omega \frac{\omega^m e^{-\omega/2}}{\epsilon - \Delta_B - \Omega(\omega)} \approx \begin{cases} -2\pi m_{\text{ex}}^* \ln m_{\text{ex}}^* |\Delta_B - \epsilon|, & m=0 \\ M_m(\Delta_B) - M'_m(\Delta_B) |\epsilon - \Delta_B|, & \epsilon \rightarrow \Delta_B - 0, m \neq 0 \end{cases} \quad (37)$$

Here $m_{\text{ex}}^* = 2\kappa\hbar^2/e^2(2eB/\pi\hbar c)^{1/2}$ is the effective mass of the free exciton at small momenta,² $M_m(\Delta_B) < 0$, $M'(\Delta_B) = (dM(\epsilon)/d\epsilon)|_{\epsilon \rightarrow \Delta_B - 0} > 0$.

Now using the normalization condition

$$\sum_{\mathbf{k}} |f_m(k)|^2 = 1,$$

one finds that

$$F_m = |W_m| [M'(\epsilon_m)]^{-1/2}. \quad (38)$$

This equation closes the procedure. Now the spectrum of spin excitations in 2DEG pinned by the resonance impurity with its own localized spin is determined by Eqs. (35)–(37). The coupling constants are determined in Eqs. (29), (A7), (A8), and the wave function of the bound spin exciton is given by Eqs. (27), (34), and (38).

Starting the analysis of the bound exciton solutions with the $m=0$ case, we see that in the weak-scattering limit the magnitudes of both coupling constants (29) are determined by the coefficient (A7). Then the potential in Eq. (35) is given by the following equation

$$W_0 = -U_- = -V_{eb} I_b (\beta_{\uparrow} - \beta_{\downarrow}) = V_{eb}^2 \frac{\Delta_{es}}{\Delta_{\uparrow} \Delta_{\downarrow}} > 0. \quad (39)$$

The scattering potential (39) is repulsive and Eq. (35) for $m=0$ has no bound solutions below the exciton band.

Such a solution appears when the resonance scattering for the spin-down electrons is strong (see inset in Fig. 1). This is a realistic condition for transition metal impurities.⁸ In that case we use Eq. (A7) for the potential acting on the spin-up electrons, and Eq. (A8) for the potential acting on the spin-down electrons. The coupling constant is

$$W_0 = -U_- \approx -\frac{1}{2} (V_{eb} - w_0) I_b. \quad (40)$$

Due to the logarithmic divergence of the function $M_0(\epsilon)$ near the bottom of the excitonic band (see Eq. (37)), a discrete solution of Eq. (35) appears, provided the resonance component of impurity scattering is stronger than the potential component, $V_{eb} > w_0$, i.e., $W_0 < 0$ (see Fig. 2).

The selectivity with respect to the orbital quantum number m of the bound spin exciton is intrinsically connected with the spin selectivity of the impurity potential. The orbital momentum is the sum of the electron and hole momenta, $m = m_e + m_h$. As is shown in Refs. 10 and 13, only the electrons or holes with $m_{e,h} = 0$ can be captured by the short-range impurity potential, which is U_{\downarrow} for electrons and $-U_{\uparrow}$ for holes. Therefore, in a bound exciton with $m \neq 0$ one of the carriers (electron or hole) must have zero momentum. Then the momentum of the whole exciton is, in fact, the momentum of the second carrier. This second carrier is bound by the combined action of the Coulomb attraction of the first carrier and the diamagnetic contribution of the Lorenz force. The sign of the orbital momentum and the charge of the carrier predetermines the sign, attractive or repulsive, of the Lorenz force contribution to the total potential. As a result, only the electrons with $m_e > 0$ and the holes with $m_h < 0$ can be captured in the limit of a strong magnetic field. Hence, the sign of the exciton orbital momentum provides information on which carrier is bound by the short-range

potential. It is the hole, bound by the potential $-U_{\downarrow}$, in the case $m < 0$ and the electron, bound by the potential $-U_{\uparrow}$, in the case $m < 0$.

In the case $m = 0$ both carriers are captured by their corresponding short-range potentials, and then their total coupling strength, $U_{\downarrow} - U_{\uparrow}$, determines the binding energy of the exciton.

4. CONCLUSIONS

To conclude, we have found that a magnetic impurity can bind a spin exciton in a 2DEG. It turned out that the mechanism of the exciton capture is the *spin-selective resonance scattering* by the deep impurity levels. This spin selectivity stems from Hund's rule in the particular case of transition-metal impurities. The interaction in the second order in scattering potential can be described in terms of an indirect spin exchange J [see Eq. (14)], and only the longitudinal component of this exchange is essential for the formation of a bound spin exciton. The transverse components of this exchange give a contribution to the binding energy only in fourth order in the scattering potential.

It is found that the spin-selective impurity potential is always capable of binding the exciton in a state with the moment $m = 0$ due to the edge van Hove singularity of the density of states in a 2DEG. Excitons with $m \neq 0$ can be also trapped, but then the conditions for the capture are more restrictive.

The analysis of the electronic structure of 3d transition metal impurities in GaAs-related systems shows that the strongest binding potential is created by the light elements (V, Cr).

This work was supported by the German-Israeli Foundation for Research and Development, Grant No. 0456-220.07195. K. K. thanks Israeli Science Foundation for support (grant "Nonlinear Current Response of Multilevel Quantum Systems"). The authors are indebted to Yu. Bychkov, S. Dickmann, T. Maniv, and I. Vagner for valuable discussions.

APPENDIX

In order to derive the impurity Hamiltonian for 2D electrons in the Landau gauge, we use the fact that the resonance scattering involves only the Landau states with $m = 0$. These states are included in the Hamiltonian (11), so one should subtract them from H_i , which then acquires the form

$$H_i = E_{b0\uparrow} + a_{i0}^+ a_{i0} + E_{b0\downarrow} b_{i0}^+ b_{i0} - E_{0\uparrow} a_0^+ a_0 - E_{b0\downarrow} b_0^+ b_0. \quad (\text{A1})$$

Then the bound Landau states with $m = 0$ can be re-expanded in free Landau states,

$$a_{i0} = \sum_n A_{0n} a_{n0}, \quad b_{i0} = \sum_n B_{0n} b_{n0} \quad (\text{A2})$$

(Ref. 13). As a result we come to Eq. (13).

In order to calculate the expansion coefficients A_p, B_p in Eq. (15), one needs the wave functions of the bound electron in the lowest Landau level. The wave functions of the lowest localized Landau states correspond to the solutions $E_{b0\sigma}$ of Eq. (9). If these states are deep enough below the unper-

turbed Landau spectrum, one can neglect the contribution $\delta M(E)$ of the higher Landau levels, and the eigenfunctions $\psi_{i0\sigma}$ has the form¹⁰

$$\psi_{i0\sigma} = -\sin \theta_{\sigma} \psi_{ie\sigma} + \cos \theta_{\sigma} \psi_{b\sigma} \quad (\text{A3})$$

with the mixing coefficient given by $\tan 2\theta_{\sigma} = 2V_{eb}/\Delta_{\sigma}$, and $V_{eb} = \langle e1 | \Delta U | b0 \rangle$. The wave functions $\psi_{b\sigma}$ describe the Landau state bound in a short range attractive potential,¹³

$$\psi_{b\sigma}(\xi) = \frac{\Gamma(\xi)}{l_B [2\pi\psi'(\xi)]^{1/2}} \frac{W_{\alpha,0}(\xi)}{\xi^{1/2}}, \quad (\text{A4})$$

where $2\xi = (\rho/l_B)^2$, Γ , ψ' , and $W_{\alpha,m}$ are the gamma function, trigamma function, and Whittaker function, respectively. The index α is determined by the corresponding eigenstate, $\alpha = 2^{-1}(1 - \varepsilon_{b0\sigma} l_B^2)$ with $\varepsilon = 2m^* E/\hbar^2$. When the level $\varepsilon_{b0\sigma}$ is deep enough or the magnetic field is weak enough, i.e., $|\varepsilon_{b0\sigma}| l_B^2 \gg 1$, the wave function $\psi_{b\sigma}$ (A4) has the standard asymptotic form

$$\psi_{b\sigma} \sim \frac{e^{-\varphi}}{\sqrt{\varphi}}. \quad (\text{A5})$$

Here $|\alpha| \approx l_B^2/2\rho_b^2$, $\mathcal{P} = \rho/\rho_b$, and $\rho_b^{-1} = \varepsilon_b$. Thus the localization radii of the d electron (ρ_d), bound Landau electron (ρ_b), and free Landau electron (l_B) obey the hierarchy $\rho_d \ll \rho_b \ll l_B$. As a result one can safely neglect the contribution of the d component $\psi_{ie\sigma}$ (A3) into the overlap integral (16). Then in the case of weak scattering one has $\beta_{\sigma} = V_{eb}/\Delta_{\sigma} \ll 1$ ($\theta \ll 1$), and the overlap integrals (16) can be approximated by the following equations

$$A_p = (1 - \beta_{\uparrow}^2) J_{p\uparrow}, \quad B_p = (1 - \beta_{\downarrow}^2) J_{p\downarrow}. \quad (\text{A6})$$

Thus the spin dependence of the matrix elements (A6) is determined by the energy differences Δ_{σ} in front of the integral and by the index α of the Whittaker function. Having in mind the difference in localization degrees of the wave functions (A4) and (19), we can estimate the magnitude of the overlap integrals $J_{p\sigma}$ as $J_{p\sigma} \sim (\rho_{b\sigma}/l_B)$, i.e., these integrals are sensitive both to the spin splitting and to the magnetic field. The energy differences in the Hamiltonian (13) are determined by the short-range component of the impurity potential, which in our theory enters as a phenomenological parameter ω_0 . In the weak-scattering limit one has $E_{b0\sigma} - E_0 = -\omega_0 + \beta_{\sigma} V_{eb}$ (if the short-range potential is attractive).¹⁰ As a result, the latter factor is dominant in this limit, so that

$$K_{\sigma} = -(\omega_0 - \beta_{\sigma} V_{eb}). \quad (\text{A7})$$

In accordance with Hund's rule for 3d impurities $\Delta_{\uparrow} > \Delta_{\downarrow}$, and so $K_{\uparrow} > K_{\downarrow}$.

Next we consider the situation where one of the resonance d levels, namely $\varepsilon_{ie\downarrow}$, is above the lowest Landau level, and the scattering is strong for the spin-down electrons, $\theta_{\downarrow} \sim -\pi/4$. The inequality $\theta_{\uparrow} \ll 1$ still holds, since the estimates (A6) and (A7) for spin-up states are still valid. As for the spin-down states, the coefficient $\sin \theta_{\downarrow}$ is $\sim 1/2$ and

$$K_{\downarrow} = -\frac{1}{2}(\omega_0 + V_{eb}). \quad (\text{A8})$$

The magnitudes of the scattering potentials U_{\uparrow} and U_{\downarrow} differ noticeably in this case.

*E-mail: fleurov@post.tau.ac.il

- ¹R. J. Nicolas, R. J. Haug, K. von Klitzing, and G. Weimann, *Phys. Rev. B* **37**, 1294 (1988).
- ²I. V. Lerner and Yu. E. Lozovik, *Zh. Éksp. Teor. Fiz.* **78**, 1167 (1980) [*Sov. Phys. JETP* **51**, 588 (1980)].
- ³Yu. A. Bychkov, S. V. Iordanskii, and G. M. Eliashberg, *JETP Lett.* **33**, 143 (1981).
- ⁴C. Kallin and B. I. Halperin, *Phys. Rev. B* **30**, 5655 (1984).
- ⁵C. Kallin and B. I. Halperin, *Phys. Rev. B* **31**, 3635 (1985).
- ⁶D. Antoniou and A. H. MacDonald, *Phys. Rev. B* **43**, 11686 (1991).
- ⁷J. P. Longo and C. Kallin, *Phys. Rev. B* **47**, 4429 (1993).
- ⁸A. Pinczuk, D. Heiman, S. Schmitt-Rink, C. Kallin, B. S. Dennis, L. N. Pfeiffer, and K. W. West, in *Light Scattering in Semiconductor Structures and Superlattices*, edited by D. J. Lockwood and J. F. Young, Plenum, New York (1991).
- ⁹K. A. Kikoin and V. N. Fleurov, *Transition Metal Impurities in Semiconductors*, World Scientific, Singapore (1994), Chapt. 8.
- ¹⁰P. Dahan, V. Fleurov, K. Kikoin, and I. Vagner, cond-mat/0106339 (submitted to *Phys. Rev. B*).
- ¹¹G. Picoli, A. Chomette, and M. Lannoo, *Phys. Rev. B* **30**, 7138 (1984).
- ¹²V. N. Fleurov and K. A. Kikoin, *J. Phys. C* **19**, 887 (1986).
- ¹³Y. Avishai, M. Ya. Azbel, and S. A. Gredeskul, *Phys. Rev. B* **48**, 17280 (1993).
- ¹⁴Yu. A. Bychkov, T. Maniv, I. D. Vagner, and P. Wyder, *Phys. Rev. Lett.* **73**, 2911 (1994).

This article was published in English in the original Russian journal. Reproduced here with stylistic changes by AIP.

Shell effects in alkali metal nanowires

A. I. Yanson* and J. M. van Ruitenbeek

Kamerlingh Onnes Laboratorium, Leiden University, PO Box 9504, NL-2300 RA Leiden, The Netherlands

I. K. Yanson

*Kamerlingh Onnes Laboratorium, Leiden University, PO Box 9504, NL-2300 RA Leiden, The Netherlands,
B. Verkin Institute for Low Temperature Physics and Engineering of the National Academy of Sciences,
47 Lenin ave., 61103, Kharkov, Ukraine*

(Submitted July 3, 2001)

Fiz. Nizk. Temp. **27**, 1092–1109 (September–October 2001)

After making a cold weld by pressing two clean metal surfaces together and then gradually separating the two pieces, a metallic nanowire is formed, which progressively thins down to a single atom before the contact is lost. We show evidence that the radii of such nanowires are influenced by electronic shell filling effects, in analogy to electronic shell structure in metal clusters. A modulation of the shell effect, known as supershell structure, is clearly observed. For sodium and potassium at larger diameters there is a crossover to crystalline facets with shell-closings corresponding to the completion of an additional atomic layer. We conclude that a complete analogy exists between shell structure in metallic clusters and nanowires. © 2001 American Institute of Physics. [DOI: 10.1063/1.1414569]

1. INTRODUCTION

The understanding of processes that occur on an atomic scale when two materials are brought into contact is of fundamental importance to problems such as adhesion, hardness, plastic and elastic response to external strength, fracture, friction, and wear.¹ For conducting materials a new phenomenon appears due to quantization of conduction channels.^{2–4} Novel techniques enable one to create and study the properties of nanowires down to a chain of single atoms.^{5,6} For these experiments, as well as for the above-mentioned problems, the processes connected with stability and cohesive energy of nanoscopic contacts are of primary importance.

The stability of microscopic and nanoscopic objects is tightly connected with the so-called shell effects. In three dimensions, shell effects are concerned with the numbers of microscopic particles (baryons in nuclei, electrons in an atom, atoms in a cluster) for which an enhanced stability of the system is found. These are called “magic numbers.” For the periodic table of elements the noble gases, with fully occupied electronic shells, acquire the highest stability, since they possess the largest ionization potential and are chemically inert. For the clusters emitted by a vapor jet in a mass spectrometer, the abundance of “magic masses” is enhanced, since these clusters possess higher stability as compared to the others.^{7–9}

In metallic clusters, one distinguishes two different shell effects: one is connected with conduction electrons, for which the cluster behaves like a giant atom,^{7–9} and the other relates to the configuration of atoms in the cluster.^{9,10} Both are due to minima in the cluster free energy, but the first requires conduction electrons, while the second also applies to nonconducting materials.

In this paper we describe in detail the shell effects discovered by us in an open system: a metallic nanowire.^{11–13} In

these objects electrons are not confined along the wire axis. In spite of this, shell effects manifest themselves as peaks in a histogram for the electrical conductance of the wire recorded for wires while the wire diameters are changed, showing the most stable configurations. Since the conductance depends on the wire cross-sectional area, the latter quantity gives, on the one hand, the number of conduction electron modes in the two lateral dimensions, and, on the other hand, the number of atoms. Both of these effects, electronic and atomic, are distinctly seen in the conductance histograms, which exhibit their coexistence and crossover. Thus, there appears to be a complete analogy between the shell effects in metallic clusters and nanowires.

2. EXPERIMENTAL TECHNIQUE

For our study of nanowires we use (Fig. 1a) the mechanically controllable break-junction (MCB) technique developed in Ref. 14. The metallic sample was fixed by Stycast epoxy on a flexible substrate made from phosphor bronze (bending beam) and supported by three points: two are on the upper side of the bending beam (counter supports), and the third is at the opposite side supported by a movable piezo driver. A metallic sample, prepared as a thick wire, is electrically isolated from the bronze substrate. The wire was circularly notched in the middle in order to concentrate the pulling strength at the center while the substrate was bent by mechanical (not shown) and piezo drivers. By fixing the sample as close as possible near the notch, a large reduction (100–1000) is achieved in the ratio between movement of the electrodes with respect to each other and the expansion of the piezo driver, in the perpendicular direction.

In order to study alkali metals, two important modifications are made. First, due to the extraordinary reactivity of alkaline elements, contact with the ambient environment must be avoided. This is achieved by making all the prepa-

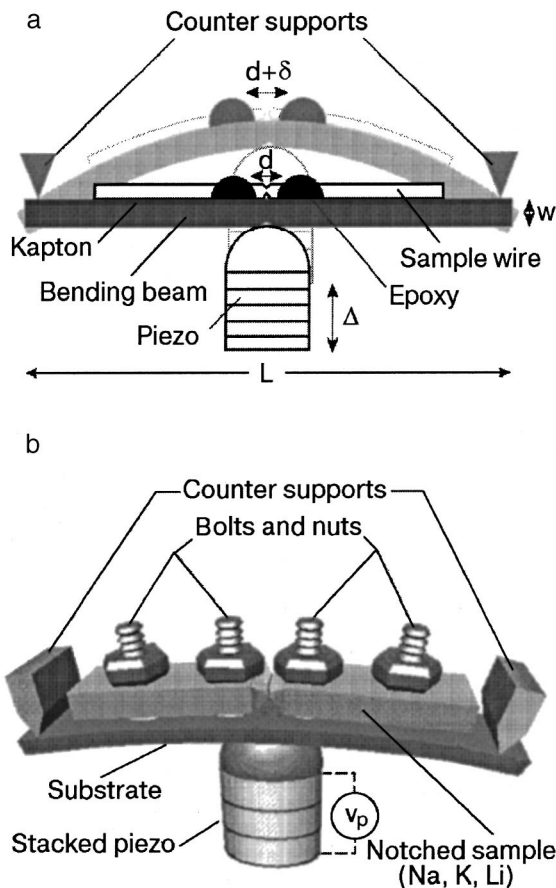


FIG. 1. a—Schematic drawing of a substrate with a sample mounted in a three-point bending configuration. The bending of the substrate due to the movement (or expansion) of the piezo over a distance Δ , shown in gray, causes the epoxy droplets to move apart by δ , leading to the breaking of the junction. The amount of bending is exaggerated for clarity. b—A model of an alkali break junction. The principle is the same here as in part (a) but the two epoxy drops are replaced by four M1 bolts with nuts fixing the sample to the substrate. The length of the substrate remains 22 mm.

rations in paraffin oil. The sample is cut into the shape of a rectangular bar, at the center of which we cut a notch. Since the bar with the notch is also covered by the oil, it cannot be glued and must be fixed mechanically. For this purpose we use four tiny bolts and nuts that are electrically isolated from the substrate (Fig. 1b).⁴ After mounting, the whole setup is rapidly placed in an evacuated metallic can and put into a cryostat with an environmental temperature of 4.2 K. The walls of the can that are being kept at helium temperature serve as a cryogenic pump ensuring a very high vacuum around the sample. The bar is then broken at the notch by mechanical bending of the substrate. The cyclic electrical movement of the piezo drive rod periodically sweeps the electrical conductance between the electrodes from a desired value (of the order of tens to hundreds of conductance quanta¹) down to complete separation (conductance much less than one quantum unit). The important advantage of the MCB device is that the cryopumping action of the low-temperature environment ensures that the freshly exposed fracture surfaces are not polluted by adsorbates.

The conductance is measured in a four-terminal dc constant voltage mode. A fixed bias voltage is applied, in the range 1–100 mV, so that the current through the contact is proportional to its conductance. Since the high bias heats the

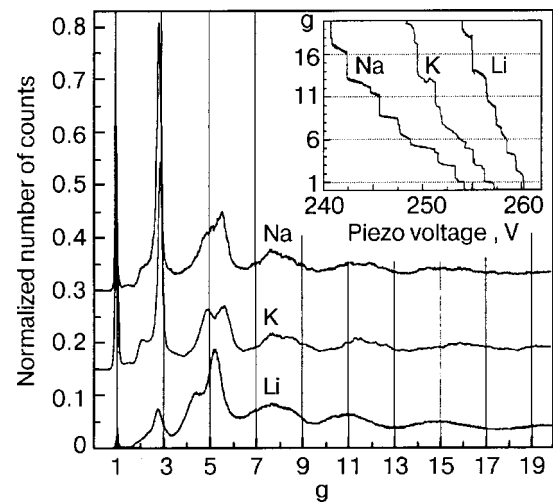


FIG. 2. Normalized conductance histograms of >1000 individual conductance traces of Na, K, and Li measured at 4.2 K under cryogenic vacuum at a constant voltage bias of 10 mV. The curves for K and Na are shifted for clarity by 0.15 and 0.3, respectively. Typical individual conductance traces (scans) are shown in the inset. $g = G/G_0$, where $G_0 = 2e^2/h$, is the reduced conductance.

wire at large conductances, we prefer to use the smallest possible biases. Our experience leads to the conclusion that up to a bias of ~ 10 mV the heating can be neglected. The drift and calibration of the current-to-voltage converter is verified against standard conductors of 1, 10, and $100G_0$, ensuring an overall accuracy in the conductance better than 1% for $G > 10G_0$. Scans are taken continuously by ramping the displacement $\delta \equiv l$ of the electrodes with respect to each other, using the piezo driver. Each individual curve of the conductance versus the displacement, $G(l)$, is recorded in ~ 0.1 seconds from the highest conductance into the tunneling regime. The curves are digitized with 16-bit resolution and a data acquisition rate of $\sim 10^5$ point/s. The conductance scale is divided into 1500 bins and data points from up to $\sim 10^5$ individual scans are accumulated automatically, creating a conductance histogram at the given experimental conditions (temperature, voltage bias, indentation depth). For most cases we have found that about 10^3 scans are enough to achieve convergence in the shape of the histograms. The speed of scanning is limited from above by the data acquisition rate of the electronics, and from below by a reasonable time required for the experiment (normally, several hours). To compare different histograms, we normalized them by their area over a fixed conductance range.

3. RESULTS

3.1. Experiment

Low-temperature histograms and scans. In Fig. 2 we show histograms for Na, K, and Li taken at $T = 4.2$ K, along with typical scans (see inset). All histograms display the characteristic series of peaks in succession at 1, 3, 5, 6, in units of reduced conductance² which has been shown in theoretical and experimental works^{4,15,16} to be the hallmark of quantum mode degeneracy for electronic wave functions in a waveguide with circular cross section. This degeneracy arises from the azimuthal quantum number, which takes two

values (– and +). When this happens (at $g = 1, 3, 6$, and so on) the conductance increases by 2 quanta for increasing nanowire diameter.

First we discuss the positions of these peaks. They are more or less shifted to the left compared to the integer values. The least shift occurs for the $g = 1$ peak and it increases noticeably for higher g . Phenomenologically, this increase can be described by a series resistance of the order of $\sim 100\Omega$, originating from the backscattering of electron wave functions by defects and surface irregularities,^{4,17,18} and inelastic scattering by phonons. The latter may be the cause for a noticeably larger shift for Li, for which it is known that the electron–phonon interaction parameter is several times larger than for Na and K.¹⁹

The intensities of the first few peaks for Na and K, on the one hand, and Li on the other hand, are also quite different. The height of the peaks at $g = 1$ and 3 in Li is much lower than for Na and K. On the contrary, the peaks at $g = 5, 6$ in Li is noticeably higher than those for Na and K. This may be explained qualitatively by a much higher mobility of Li atoms even at helium temperature, which may be due to tunneling because of the light Li mass and the decrease in the potential barriers at the surface, making a contact of just a few atoms unstable.

Next, we draw attention to the broad maxima at $g \approx 8, 11, 15$, which are slightly more intense in Li, presumably again because of the enhanced mobility of Li surface atoms. We shall see below that these broad peaks are precursors of the electronic shell effect for alkali metal nanowires. Together with the peak at $g = 5$ they give the most favorable diameters, corresponding to the local minima in the electronic part of the thermodynamic potential. As to the peak at $g = 5$, this point of view is supported by the fact that, according to the theoretical calculation of the sodium histogram,²⁰ the intensity of the $g = 5$ peak should be noticeably smaller than the peak at $g = 6$. In fact, in the experimental histograms (see Fig. 2) they are approximately of the same intensity. Another confirmation that the $g = 5$ peak is not connected with the fully open conducting channel comes from Ref. 18, where its behavior is radically different from that of the peaks at $g = 1, 3, 6$. Thus, we propose that the enhanced intensity of the $g = 5$ peak is due to the broad maximum of the favorable diameters dictated by the electronic shell effect.

Scans taken at helium temperature and shown in the inset in Fig. 2 exhibit smooth variations (plateaus) interrupted by sharp decreases (steps), evidencing that the elastic elongations are followed by atomic rearrangements. This points at the crystalline structure of the neck. Only for the low-lying conductances do the plateaus coincide with quantum units ($\approx 1, 3, 5, 6$), which can be even seen statistically on the average scan plotted by integrating the histogram. For higher conductance, $g \geq 7$, though the steps in the scans look as sharp as for lower g , no peaks on the low-temperature histogram appear. This means that the plateaus occur with nearly equal probabilities for any conductances in different scans, leading on average to the smooth background in the histograms. According to Ref. 21, from the smooth part of the scans one can find the approximate shape of the neck. We shall turn to this issue below when discussing the atomic

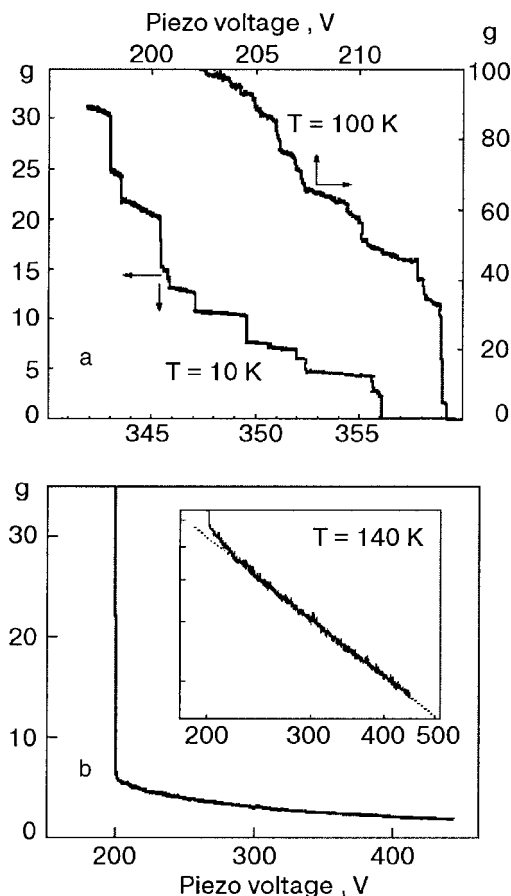


FIG. 3. a—Typical individual scans for Li break-junctions at two different temperatures. 1 piezo volt corresponds approximately to 0.5 Å. b—Long plateau at 140 K, shown on a logarithmic scale in the inset.

shell structure of the nanowires. At low temperatures, the piezo voltage versus elongation of the neck can be calibrated using the Fowler-Nordheim formula or the Gundlach oscillations²² for the tunnel regime at biases of the order of a few volts.

By storing several intermediate histograms during the accumulation of the final histograms, for the full number of scans for a given contact, one can obtain an impression of their evolution with increasing numbers of scans. One can observe both the purification of the metal under the contact, which leads to more distinct shell-effect structure with increasing number of indentations, as well as to the opposite behavior, which we ascribe to the adsorbed impurities.²³

Temperature dependence of the scans. Let us describe the temperature dependence of the scans, taking Li as example (Fig. 3). Figure 3a shows two scans for low and elevated temperatures, typical for all the alkali metals studied. As the temperature increases, the low-lying conductance plateaus become unstable. Moreover, the piezo voltage is no longer the only parameter controlling the evolution of the neck, as a result of the strongly enhanced diffusion of the surface atoms. The atoms in the wire experience tension not only from the external force but also from the Laplace pressure. This means that upon putting the external force to zero the conductivity of the neck still evolves with time until the contact disappears.

We mentioned above that Li atoms revealed increased diffusion when we considered the low intensity of the $g = 1$

peak in the Li histograms at helium temperatures. The enhanced mobility of the atoms also leads to the anomalous behavior of the conductance trace $G(V_{\text{piezo}})$ at high temperatures shown in Fig. 3b, where it steeply drops to zero from a fairly high conductance. For Li at $T = 140$ K all steps on the $G(V_{\text{piezo}})$ scans disappear and all structure in the histograms disappears except at $g \approx 5$. This peak in the histogram becomes very high, corresponding to anomalously long plateaus in the scans. The length of the plateaus reaches several tens of Å, while typical plateaus correspond to less than 1 Å. The same qualitative behavior was observed for Na, although for this metal it was more difficult to register scans at such elevated temperature. We interpret this phenomenon in the following way.

At $T \approx 140$ K the Li nanowire “melts,” although the temperature of the bulk melting point is much higher. By this we mean that the diffusion of atoms over the length of the nanowire becomes much faster than our data acquisition rate. According to Refs. 24 and 25, a strong depression of the melting point is expected for small systems due to the Laplace tension. The change of the melting temperature T_m compared to the bulk value T_0 is approximately given by $(T_m - T_0)/T_0 = 2(\sigma_1 - \sigma_2)/QR$, where $\sigma_{1,2}$ is the surface tension in the liquid and solid phases, respectively, Q is the heat of fusion, and R is the wire radius.²⁶ Thus we suggest that at the starting point of the long plateau a liquidlike metallic neck appears, which connects the solid banks. Further elongation of the neck proceeds continuously, decreasing its diameter as the wire is stretched, approximately as a power law $g \propto (V_{\text{piezo}})^n$, with $n \approx -1.3$.

Temperature dependence of the histograms. The temperature dependences of Na and Li histograms are shown in Fig. 4. One recognizes the low-temperature curves similar to those shown in Fig. 2. While raising the temperature, the low-conductance peaks gradually disappear due to increasing thermal instabilities. On the other hand, for thicker wires a new succession of strong peaks grows, owing to the increased mobility of atoms at elevated temperatures. We shall consider these series of peaks in detail in the next Sections. Here we only point out that the positions of these peaks on the conductance axis does not correspond to those that might arise due to individual quantum modes, which would increment either by one or two conductance quanta. Instead, these peaks are broader and reveal a separation that grows with conductance. The intensities of these peaks depend, among other parameters, on the depth of indentation, which can approximately be characterized by the highest value of the conductance scale in the histogram. A second parameter is the voltage bias at which the scans are recorded. Unfortunately, there are additional parameters that we can hardly control with the technique used. These include possible surface contaminations and the orientation of the crystallites on the two electrodes. We stress that these drawbacks mainly concern the intensity of the peaks and much less their positions on the conductance axis, while the period of the peak series remains almost unaltered. Since, as will be shown below, there are two mechanisms leading to different series of peaks with different periods (namely, electronic and atomic shell series), the positions of the peaks depend upon the relative intensity of these mechanisms. Fortunately, the true frequencies of the

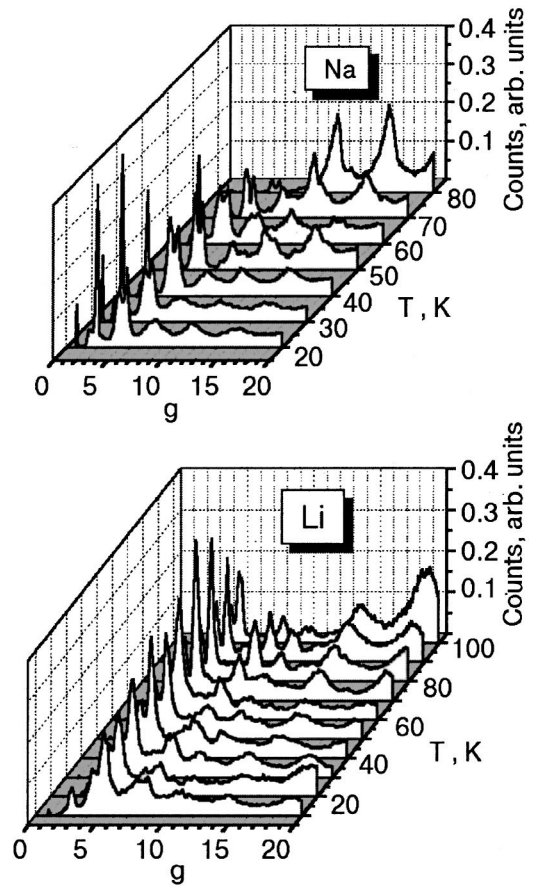


FIG. 4. Temperature evolution of conductance histograms for Na and Li. The histograms have been normalized to the total area under the curves.

oscillations can be obtained from the Fourier transform of the experimental histograms.

3.2. Electronic shell and supershell effects

In this Section we describe the observation of electronic shell-effect oscillations^{11,12} in alkali metal nanowires. The experimental results depend on several factors discussed above. We emphasize once again that all shell-effect structures are observed at elevated temperature, at which atoms have enough mobility to occupy the most favorable positions in the lattice structure. This structure corresponds to the local minima of the total free energy of the nanowire.

Histograms and peak positions. A typical histogram for sodium is shown in Fig. 5a. The positions of the main peaks, labeled by sequential numbers, are regularly spaced as a function of $g^{1/2}$. That means that they periodically appear as a function of the radius of the wire, since for a circular nanowire the radius of the smallest cross section R , obtained from the Weyl semiclassical²⁷ expression for a ballistic regime, reads:

$$g_w \approx \left(\frac{k_F R}{2} \right)^2 \left(1 - \frac{2}{k_F R} \right) \approx \left(\frac{k_F R}{2} \right)^2, \quad (1)$$

where k_F is the Fermi wave vector and $(k_F R/2)^2 = g_S$ is the Sharvin conductance. We prefer to plot $g^{1/2}$ along the abscissa, since it is the experimentally measured quantity, while the inferred radius depends somewhat on the shape of nanowire. For example, for a contact in the form of an orifice

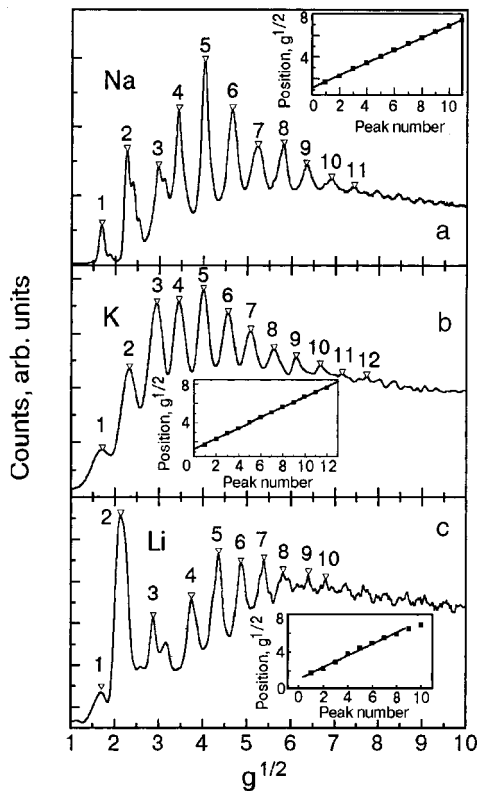


FIG. 5. Conductance histogram for sodium, constructed from ≈ 14000 individual traces recorded at $T=90$ K and at 100 mV voltage bias (a); conductance histogram for potassium, constructed from ~ 5000 individual traces recorded at $T=100$ K and 8 mV voltage bias (b); conductance histogram for lithium, constructed from ~ 8000 individual traces recorded at $T=100$ K and 10 mV voltage bias (c). We count the split peak #3 as a single peak, as for Na (see (a)). The peaks are numbered as shown, and a plot of peak positions vs their index number is fit by a straight line in the insets. The slopes are 0.581 ± 0.005 , 0.54 ± 0.005 , and 0.62 ± 0.02 for Na, K, and Li, respectively. Note that the horizontal axis is given as the square root of g .

one has $g_W \approx g_S [1 - 1/(k_F R)]$, which makes the correction to the Sharvin conductance smaller.¹⁶ The inset in Fig. 5a demonstrates that the peak positions are periodic, with a period of ~ 0.58 . We see that at elevated temperatures the $g=1$ peak is absent and the highest intensity is reached at $g \approx 16$. The shape of the background is determined by the global variation of the conductance with elongation, which in turn depends on the effective length of nanowire that deforms during elongation^{21,28} (see below). This length is located near the narrowest cross section of the nanowire and can be qualitatively described with the model considered in Ref. 21. The latter is valid when diffusion of the atoms from the neck to the electrodes can be neglected.³⁾ Superimposed in the main periodic structure we note an oscillating behavior of the envelope of the maxima in the histogram of Fig. 5a. This modulation is the signature of the supershell effect and will be considered in more detail in the section on the Fourier transformation. Finally, we draw attention to the low-intensity oscillations at $g^{1/2} \geq 7.5$. They have a much smaller period and are due to the crossover from the electronic to the atomic shell effect (see below).

Similar periodic structure is seen for potassium (Fig. 5b) and lithium (Fig. 5c). The periods shown in the insets are 0.54 and 0.62 for K and Li, respectively. Maximal amplitudes are observed at $g^{1/2} \approx 4-5$, and the peak at $g=1$ is

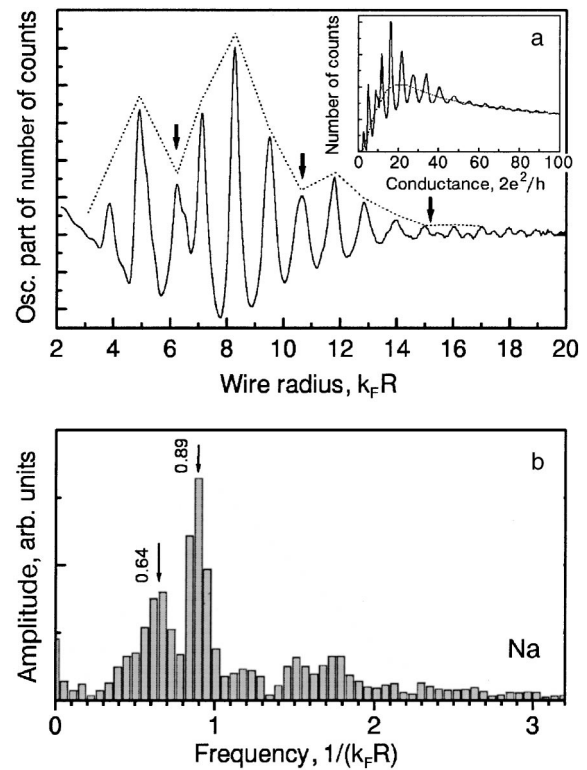



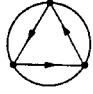
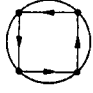
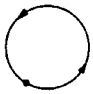



FIG. 6. a—Conductance histogram for sodium from Fig. 5a with a smooth background subtracted (the original curve and the background are shown in the inset). The arrows point at the positions of the minima in the oscillation amplitudes. b—Fourier spectrum of the curve in part (a).

missing, just as for Na. The periods are close to what is observed in Na, although a small change in the slope is often observed for different samples. The modulation of the peak heights also varies from contact to contact. While a modulation is clearly seen in the Li histogram (Fig. 5c), for the given K contact (Fig. 5b) only a nonmonotonic behavior around the peaks with indices 3–5 is found. In the next Section we present a different K histogram, which exhibits much more modulation by the superposition of different shell effects (Fig. 7).

Fourier transformations. Determination of the average period from the slope of the peak positions in terms of $g^{1/2}$ versus their indices (see insets in Fig. 5) gives limited information about the probabilities for observing specific conductance values. For example, in this way, one cannot account for the nonmonotonic behavior of the peak heights. The problem arises, whether to count the peaks with smaller amplitude.

Fortunately, we can make use of a direct Fourier analysis of the histograms, which exposes a superposition of several periodic components. A typical example for sodium is shown in Fig. 6. In order to avoid a huge low-frequency tail in the Fourier spectra, we subtract a smooth background shown by the dashed curve in the inset of Fig. 6a. The resulting curve is displayed on the main panel of Fig. 6a. It reveals a clear low-frequency modulation with a period of ~ 4.0 . Here, we use the variable $k_F R$ instead of $g^{1/2}$ for the abscissa, by use of the Weyl expression (1), which will prove convenient for comparison with the theoretical results in the discussion section below. The Fourier spectrum for this histogram is shown in Fig. 6b. It contains two prominent frequencies, 0.64 and

TABLE I. First few shortest classical periodic orbits and their frequencies in circular geometry. The circle ($t=1, p=\infty$) marks the end of the first band ($t=1$); the second one contains trajectories which make two revolutions around the center ($t=2$), the third—three, etc.

Shape	t	p	Perimeter L	Frequency $f = 1/\Delta(k_F R)$
	1	2	$4R$	$2/\pi \approx 0.64$
	1	3	$3\sqrt{3}R$	$3\sqrt{3}/2\pi \approx 0.83$
	1	4	$4\sqrt{2}R$	$2\sqrt{2}/\pi \approx 0.90$
...
	1	∞	$2\pi R$	1
	2	4	$8R$	$4/\pi \approx 1.27$
	2	5	$10R \sin\left(\frac{2\pi}{5}\right)$	$5 \sin\left(\frac{2\pi}{5}\right) \approx 1.51$
	2	6	$6\sqrt{3}R$	$3\sqrt{3}/\pi \approx 1.65$

0.89, where the first has a lower intensity than the second. The latter of the two frequencies is very close to the (average) one obtained for the magic numbers in spherical clusters.¹¹ As will be discussed below, for clusters the intensity of the first principal frequency is negligibly small, and the observed frequency equals the average of triangular and square orbits: $(0.83+0.90)/2=0.86$ (see Table I). The presence of the lower-frequency component for the nanowires explains why the frequency of the second prominent peak is a little bit higher than what would be obtained from the averaged period $\Delta(g^{1/2})\approx 0.58$ given by the slope in the inset of Fig. 5a.⁴⁾ In Fig. 6b the low-intensity peaks at frequencies above 1 are presumably due to the harmonics and combinations of the two principal frequencies.

Considering the histogram for potassium (Fig. 7a), which is different from the one in Fig. 5b, we see that there are again two prominent peaks in the Fourier transform, at 0.63 and 0.84, close to those observed for sodium. In addition, there is an appreciable maximum around 2.2, which is difficult to explain in terms of overtones but stems from the atomic shell effect, as we will see below. For the given K histogram one obtains an average period of $\Delta(k_F R)\approx 1.15$ from the slope of the peak positions, giving an average frequency of $1/\Delta(k_F R)=0.87$. This nearly coincides with the upper principal frequency because of the small intensity of the first principal frequency.

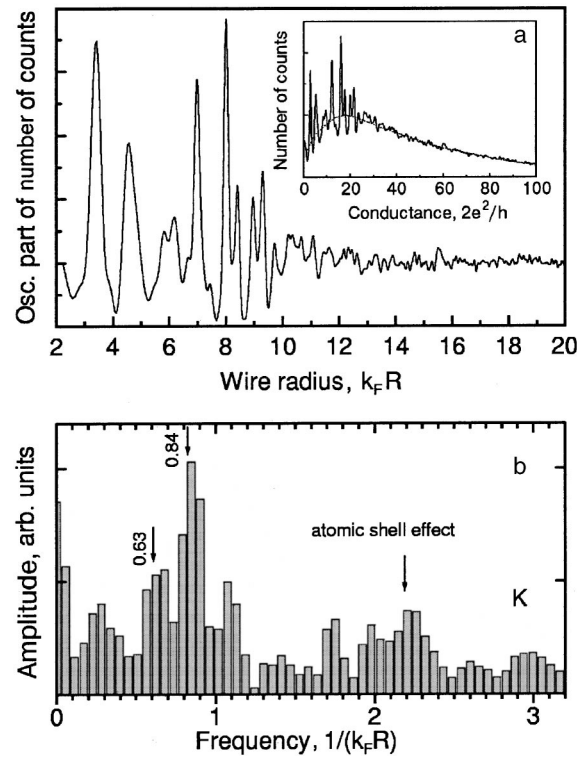


FIG. 7. a—Conductance histogram for potassium at $T=50$ K, constructed from 1000 individual scans recorded at 125 mV voltage bias, after subtracting a smooth background (the original curve and the background are shown in the inset). b—Fourier spectrum of the curve in part (a).

Finally, let us consider the Fourier transform of the Li histogram from Fig. 5c. Figure 8b shows three peaks of

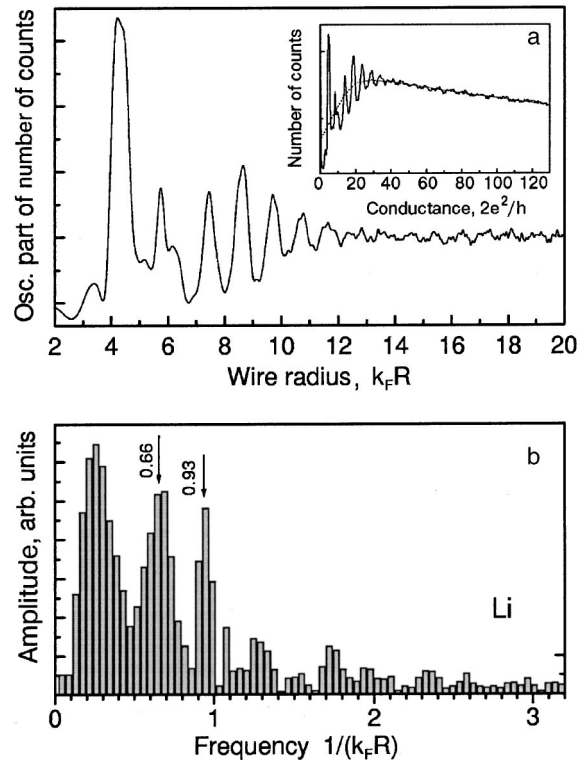


FIG. 8. a—Conductance histogram for lithium from Fig. 5c with a smooth background subtracted (the original curve and the background are shown in the inset). b—Fourier spectrum of the curve in part (a).

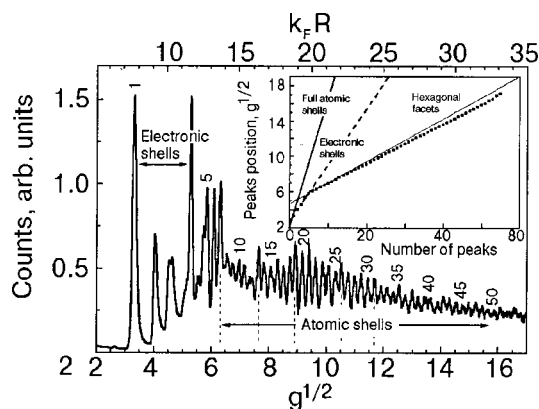


FIG. 9. Potassium histogram constructed from 1000 individual conductance traces recorded at 1 mV voltage bias and at $T=100$ K. The peaks are numbered sequentially and their position is plotted as a function of this number in the inset. Straight solid lines show the slopes 1.447 and 0.241 for full atomic shells and single hexagonal facets, respectively. A linear fit for the electronic-shell points gives 0.61 (dashed straight line). A linear fit to the experimental data starting with number 6 gives a slope of 0.224. Along with $g^{1/2}$ values on the horizontal axis the corresponding $k_F R$ values are given on top, according to formula (1).

about the same intensity. Those at frequencies 0.66 and 0.93 are of the same origin as the principal frequencies in Na and K. As to the lowest frequency at 0.25, it may be due to an anomalously strong interference of the principal frequencies, giving rise to a difference frequency with a period of 4.2. This may be due to the fact that the intensity of the first principal peak (at 0.66) is as strong as the second one. It is interesting to note that both principal Fourier frequencies in Li are higher than in Na and K. However, the average frequency of $(0.66+0.93)/2=0.78$ is lower than in Na, corresponding to a larger average period $\Delta(g^{1/2})=0.64$ (or $\Delta(k_F R)\approx 1.27$). Indeed, since in Li the intensities of the two principal peaks are approximately the same, we can simply average their frequencies, while this would not be correct for Na and K.

3.3. Atomic shell effect¹³

Searching for the shell oscillations at still higher conductance, we have found a new series that appears to be due to a purely-classical effect, similar to that found in clusters. As in clusters, we named it an “atomic shell effect” and discuss its origin in the next Section. We start by presenting the main experimental facts concerning this effect.

Crossover from electronic to atomic shell effect. The most spectacular results are achieved for potassium. The corresponding histogram is shown in Fig. 9. It shows two types of oscillations with a relatively sharp crossover at $g^{1/2}\approx 6$. In the inset, the reduced conductances, corresponding to the peaks in the histogram, are plotted against their sequentially numbered indices. The index number of the peaks is also shown in the histogram, where they are labeled at increments of five. The first few points in the inset, corresponding to the strong peaks in the histogram, have an approximate slope of 0.61, which agrees reasonably well with the slope determined for the electronic shells. Beyond the first few points, up to 48 points obey a linear relation with a slope of 0.225 ± 0.001 . Structure in the histograms with this particular period has been reproducibly observed for many contacts. One

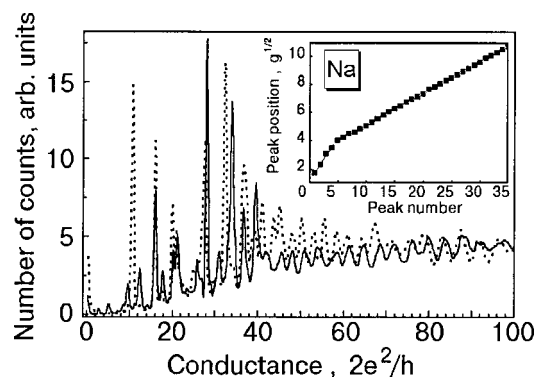


FIG. 10. Sodium histogram constructed from 10424 individual conductance scans recorded at 100 mV voltage bias and at $T=100$ K. The peaks are numbered sequentially and their position vs number is plotted in the inset. A straight-line fits give slopes of 0.62 and 0.224 for the electronic and atomic series, respectively. One of the typical histograms for potassium is shown for comparison (dotted curve).

can see that the transition between these two sets of oscillations (electronic and atomic) is quite sharp, although the shorter period pattern extends a little with reduced amplitude into the lower conductance range, where it overlaps with the electronic shell oscillations.

For sodium, the crossover is found at larger diameters than for potassium (Fig. 10) with periods equal to $(0.62\pm 0.05)g^{1/2}$ and $(0.224\pm 0.001)g^{1/2}$ for the electronic and atomic shells, respectively. For comparison in Fig. 10 we plot the histogram for the potassium nanowires as a thinner curve. Some discrepancies between the Na and K histograms are seen in the low conductance range, which are mostly influenced by the different voltage bias. However, the behavior remains basically the same.

Superposition of electronic and atomic-shell structure at low conductances. Atomic-shell oscillations can be observed at conductances starting as low as $g\approx 6-7$. In Fig. 11 we show some of the histograms recorded in a single series under seemingly the same experimental conditions. In the first recording no distinct oscillations were observed (not shown). Each trial, which consisted of many scans, was performed by making a contact with a resistance of about $1\ \Omega$ ($\sim 10^4 g$) and then mechanically receding the electrodes to bring the conductance down to the tunneling regime. The next several trials are displayed in Fig. 11 (curves 1–5). It is seen that for this particular sample the histograms change drastically from those resembling the atomic-shell oscillations (curves 1, 2, and 3) to ones having the electronic shell periodicity (curves 4 and 5). Presumably, this is due to the increase in the mobility of the surface atoms. Namely, for the last trials the mobility of atoms at the surface is increased so much that no crystalline facets (see below) could be created during the acquisition time for the scans. Other causes may be the random crystal orientation of the neck, creating a favorable condition for one of the two shell effects, and altering of the shape of the nanowire during many indentations. Interestingly, the extreme shape of histograms presented in Fig. 11 (curves 4 and 5) reproduces quite satisfactorily the electronic-shell histograms presented above. The same is true for the atomic-shell histograms at low conductances (curves 2 and 3). As an illustration, in Fig. 12a we show by a thick

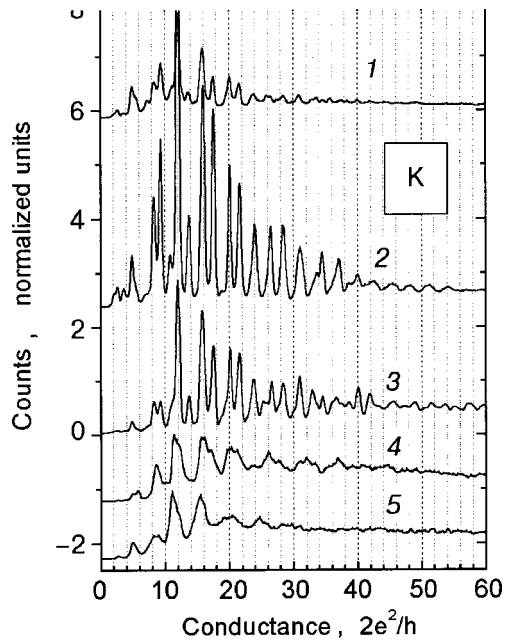


FIG. 11. Evolution of shell-oscillations obtained in successive runs in the same experiment for a potassium nanowire at $T=80$ K, $V_{\text{bias}}=10$ mV. In curves 2 and 3 the atomic-like period is clearly seen, while for curves 4 and 5 the period is due to the electronic shell effect. Each histogram consists of from several thousands up to several tens of thousands of scans.

line the histogram for another sample (recorded in an experiment approximately a year later) and superimposed on curve 2 from Fig. 11 (note the change in the x coordinate). The

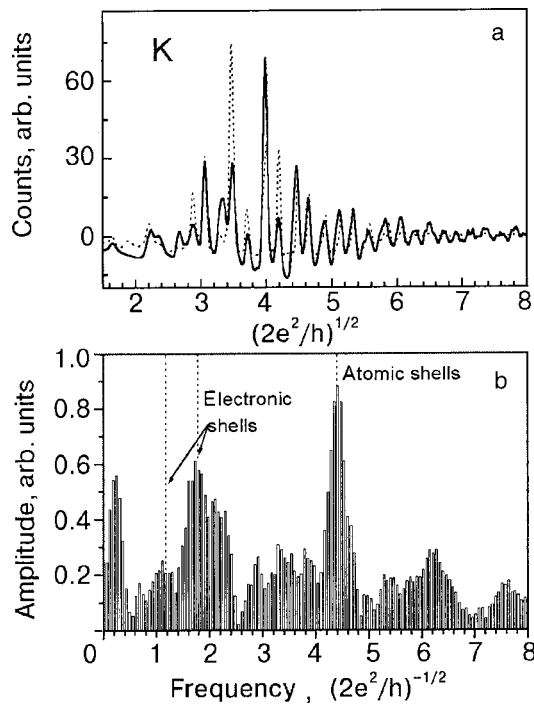


FIG. 12. a—Two conductance histograms for potassium showing mainly atomic-shell oscillations. The dotted curve is curve 2 from Fig. 11, while the full curve was taken almost a year later. Good reproducibility is seen for the measurements. b—Fourier spectrum of the full curve in part (a). Superposition of two shell effects is seen from the peaks in the Fourier spectrum at 1.2 and 1.8, and 4.4 for electronic and atomic principal frequencies, respectively. $T=80$ K, $V_{\text{bias}}=10$ and 20 mV for the dotted and solid curves, respectively.

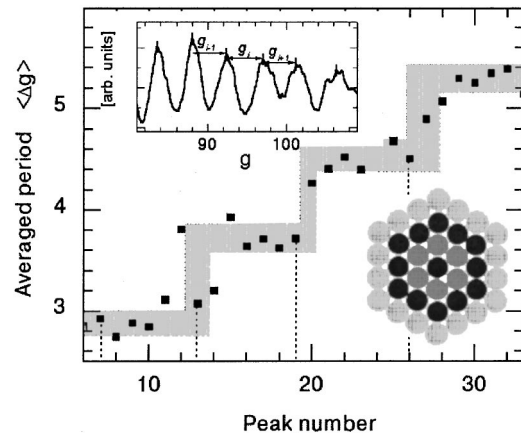


FIG. 13. The averaged period of the oscillations in Fig. 9 plotted vs peak index. The vertical dotted lines mark the positions of peaks with maximal amplitude (numbers 7, 13, 19, 26). The gray staircase is a guide to the eye to identify the step structure. A fragment of a conductance histogram is shown in the inset to explain the averaging procedure $\langle \Delta g_i \rangle = 1/2[(g_i - g_{i-1}) + (g_{i+1} - g_i)]$. An artist's impression of the atomic positions in the normal cross section of the wire is sketched in the lower right corner. For simplicity, we have drawn a two-dimensional structure. The six facets symbolize the six data points at each plateau, while the height of the step corresponds to successive layers for a close-packed structure.

reproducibility of the peak positions is quite good, despite important variations in the amplitudes. One should not think that the electronic-shell structure is negligibly small for these curves. The Fourier transformation shown in Fig. 12b for the solid curve in Fig. 12a clearly shows the characteristic frequencies for both shell effects: electronic peaks at 1.2 and 1.8 and the atomic peak at 4.4. Other features with lower intensity may be explained as harmonics and sub-harmonics of the principal frequencies.

Additional structure of atomic-shell oscillations. Occasionally, the atomic-shell oscillations reveal additional structure in their amplitude and periodicity. The peaks can be grouped by sixes, based on the amplitudes, as seen for example in Fig. 9. Here, the thin vertical lines at $g^{1/2} \approx 6.3, 7.6, 8.9,$ and 10.5 indicate higher amplitudes and correspond to the index numbers 7, 13, 19, and 26. For other contacts, there may be other envelope patterns. The period of these higher-amplitude peaks equals $1.36 \approx 0.224 \times 6$, which is very close to a single close-packed monatomic layer covering the nanowire (see below). Moreover, the period between adjacent peaks as a function of the reduced conductance g appears not to scatter randomly around a linear dependence as one might expect. A linear dependence follows when the period is constant as a function of $g^{1/2}$. Instead, when the distance between the adjacent peaks is averaged over 3 points (as shown in the inset of Fig. 13) in order to smoothen fluctuations, they can again be grouped by approximately six peaks (Fig. 13). For this particular contact, the averaged period exhibits a smooth staircase in which the vertical steps closely coincide with the higher-amplitude peak indices (numbers 7, 13, 19, and 26). The difference in height of the plateaus is approximately one G_0 . This behavior will be explained in the next Section.

4. DISCUSSION

4.1. Electronic shells

Exact quantum mechanical result. To understand semi-quantitatively the electronic shell effect in the formation of metallic nanowires, we use the simple model of a metallic circular cylinder^{15,29,30,33} connecting two metallic reservoirs (electrodes). A more realistic shape for the wires²¹ will be considered later. When the wire diameter d is comparable with the de Broglie wave length of conduction electrons at the Fermi energy, quantum size effects in the lateral dimensions lead to a finite number of conductance channels, each corresponding to an electron wave propagating along the wire axis z . In order to obtain the energy spectrum $\varepsilon(k_z)$ of these modes, one solves the Schrödinger equation to obtain

$$\varepsilon(k_z) = \varepsilon_{mn} + \frac{\hbar^2 k_z^2}{2m_e}, \quad (2)$$

where

$$\varepsilon_{mn} = \frac{\hbar^2}{2m_e R^2} \gamma_{mn}^2,$$

m_e is the electron mass, γ_{mn} is the n th zero of the m th Bessel function of the first kind, R is the radius of the nanowire, $d = 2R$, and k_z is the z component of the electron wave number. In any single one-dimensional subband the total number of states per unit length of the wire (including spin degeneracy) is

$$N_{mn}(\varepsilon) = 2 \frac{2|k_z(\varepsilon)|}{2\pi} = 2 \left(\frac{2m_e}{\pi^2 \hbar^2} \right)^{1/2} \sqrt{\varepsilon - \varepsilon_{mn}}, \quad (3)$$

and the density of states is

$$D_{mn}(\varepsilon - \varepsilon_{mn}) \equiv \frac{dN_{mn}(\varepsilon)}{d\varepsilon} \left(\frac{2m_e}{\pi^2 \hbar^2} \right)^{1/2} \frac{1}{\sqrt{\varepsilon - \varepsilon_{mn}}}. \quad (4)$$

Let us now consider a cylinder of finite length L , radius R , and volume V , which is elongated at the ends so that its volume $V = \pi R^2 L$ remains constant. To use expressions (2)–(4) we should impose the condition $L \gg R$, which allows us to consider the cylinder as quasi-infinite in the z direction. The total number of occupied states in such a cylinder filled up to the bulk Fermi energy ε_F is⁵⁾

$$\begin{aligned} N(\varepsilon_F) &= \sum_{m,n} N_{mn}(\varepsilon_F) = \sum_{m,n} \int_{\varepsilon_{mn}}^{\varepsilon_F} L D_{mn}(\varepsilon - \varepsilon_{mn}) d\varepsilon \\ &= \sum_{m,n} 2L \left(\frac{2m_e}{\pi^2 \hbar^2} \right)^{1/2} \sqrt{\varepsilon_F - \varepsilon_{mn}}. \end{aligned}$$

The total energy of the electron system is

$$\begin{aligned} E &= \sum_{m,n} \int_{\varepsilon_{mn}}^{\varepsilon_F} L \varepsilon D(\varepsilon - \varepsilon_{mn}) d\varepsilon \\ &= \sum_{m,n} \left[\frac{2}{3} L \left(\frac{2m_e}{\pi^2 \hbar^2} \right)^{1/2} (\varepsilon_F - \varepsilon_{mn})^{3/2} + \varepsilon_{mn} N_{mn}(\varepsilon_F) \right]. \end{aligned}$$

Assuming $\mu = \varepsilon_F$ at low temperatures, we can write the thermodynamic potential

$$\Omega = E - \mu N = -\frac{4}{3} L \left(\frac{2m_e}{\pi^2 \hbar^2} \right)^{1/2} \sum_{m,n} (\varepsilon_F - \varepsilon_{mn})^{3/2},$$

whose derivative with respect to the length gives us the force

$$\begin{aligned} F &= -\frac{d\Omega}{dL} = \left(\frac{2m_e}{\pi^2 \hbar^2} \right)^{1/2} \\ &\quad \times \sum_{m,n} \left(\frac{4}{3} (\varepsilon_F - \varepsilon_{mn})^{3/2} - 2\varepsilon_{mn} (\varepsilon_F - \varepsilon_{mn})^{1/2} \right). \end{aligned}$$

The density of states, the thermodynamic potential, and the force are calculated as functions of the wire radius for a given Fermi energy using the formulas

$$\begin{aligned} D(k_F R) &= \frac{1}{\pi \varepsilon_F} \sum_{m,n} \left[1 - \left(\frac{\gamma_{mn}}{k_F R} \right)^2 \right]^{-1/2}, \\ \Omega(k_F R) &= \frac{2\hbar^2 k_F^5 V}{3\pi^2 m_e (k_F R)^2} \sum_{m,n} \left[1 - \left(\frac{\gamma_{mn}}{k_F R} \right)^2 \right]^{3/2}, \\ F(k_F R) &= \frac{\hbar^2 k_F^3}{\pi m_e} \times \sum_{m,n} \left[\frac{2}{3} \left(1 - \left(\frac{\gamma_{mn}}{k_F R} \right)^2 \right)^{3/2} \right. \\ &\quad \left. - \frac{\gamma_{mn}^2}{(k_F R)^2} \left(1 - \left(\frac{\gamma_{mn}}{k_F R} \right)^2 \right)^{1/2} \right]. \end{aligned} \quad (5)$$

The results for a sodium nanowire with a constant volume of 10 nm^3 and the bulk Fermi energy are plotted in Fig. 14. Whenever the bottom of another subband falls below the Fermi energy, the density of states and the force exhibit singularities. The force, being the derivative of the thermodynamic potential with respect to the length of the cylinder, describes the response of the system to elongation. When its value is nonzero the wire tends to shorten (negative force) or stretch (positive force) spontaneously in order to reduce its free energy; only when the force is zero is a true state of stability achieved. We should also take into account that in the classical limit of large diameters we should recover a constant destabilizing force resulting from the surface tension. Therefore we do not have truly stable nanowires but rather ones with enhanced stability at the radii where the force is minimal. Those minima in the absolute value of the force give the diameters at which the wires are particularly stable. At the lowest conductances these minima occur synchronously with the conductance jumps, coinciding with the maxima in the density of states. But when multiple singularities of the spectrum are very close to each other, forming a bunch (like those at $k_F R \approx 8.5, 10.5, 12$ etc.) the force shows one global extremum. This bunching and the corresponding pronounced force extrema mark the fundamental differences between the conductance quantization and shell effects: the former stems from individual spectral singularities, while the latter is due to the inhomogeneous distribution of the features in the spectrum (caused by geometrical symmetries), which results in their periodic grouping, or bunching. At this point we cannot say anything about the periodicities of the bunching as a function of radius. While it is easy to calculate them numerically for not too large $k_F R$, an exact analytical approach using the double Poisson summation formula³² is complicated, and a much more transparent derivation based on the semiclassical Bohr-Sommerfeld quantization condi-

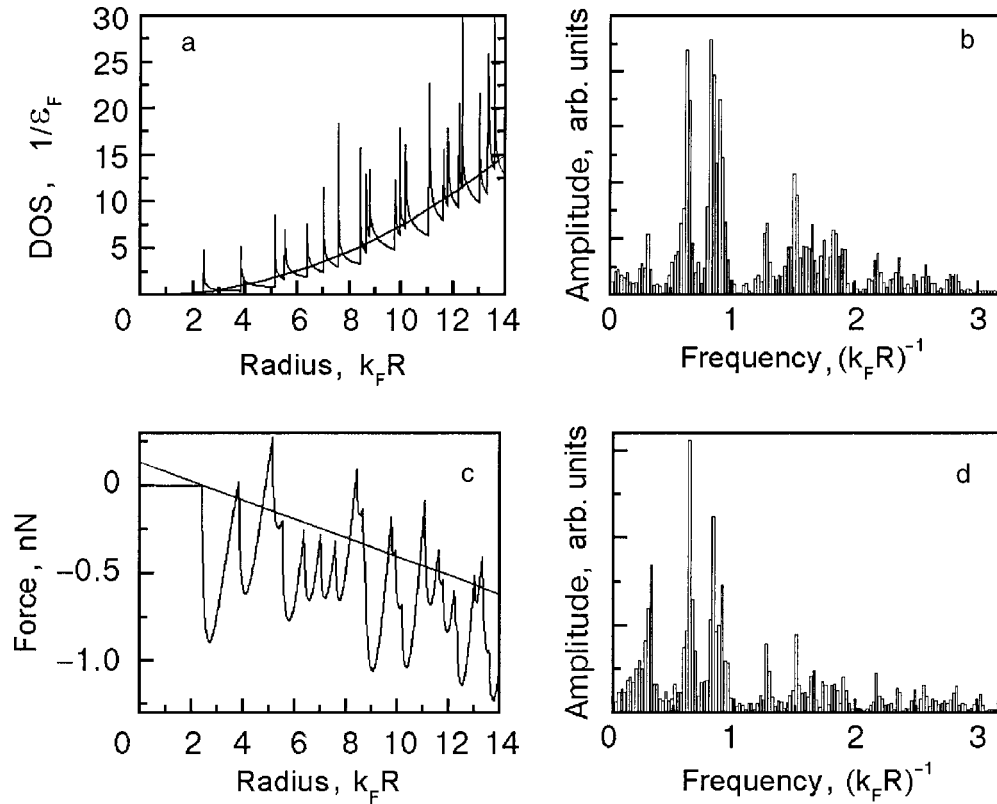


FIG. 14. Density of states (DOS) (a) and force (c) in the nanowire calculated using Eq. (5). Smooth backgrounds, subtracted before performing the Fourier transforms, are also shown. Parts (b) and (d) show Fourier transforms of the oscillating parts of DOS and the force, respectively.

tion is used instead. Even if we plot the density of states (or any other quantity dependent on it) numerically on a large scale, the periodicities are not yet seen with the naked eye (Fig. 14a). So naturally we would like to take a Fourier transform of exactly calculated thermodynamic quantities (5) to see whether the periodicities are indeed there, and we follow the same procedure as we used above for experimental data processing. Thus we simply subtract the smoothed background by hand (see the smooth curves in Figs. 14a and 14c) and perform the Fourier transformation. Both frequency spectra (Figs. 14b and 14d) give us three prominent peaks⁶⁾ at 0.63, 0.83, and 0.90. The latter two are very close to each other, and, taking into account the reduced amplitude of the third peak and its proximity to the second one, we can say that the oscillating part of the density of states as well as the force is mainly composed of two major frequencies, 0.62 and 0.87. These correspond to the two peaks in the experimental Fourier spectra at 0.64 and 0.89 (Fig. 6). This is a very important result, which shows that quantum oscillations in each of the quantities of Eq. (5) possess the principal periodicities of the energy spectrum, and that this seemingly irregular spectrum of electron energies in a cylindrical nanowire can be decomposed into a few basic harmonics.

Semiclassical approximation. Much more information about the bunching of energy levels, leading to periodicities in the spectrum, can be obtained from the semiclassical approach.^{30,34–36} In this approach we consider an electron as a wave packet constructed from many quantum mechanical eigenstates. The wave packet has wave vectors k concentrated in the range satisfying the uncertainty principle in the space region where we would like to localize our particle.

For a circular cross section of the nanowire, the condition for validity of the semiclassical approximation reads $kR \gg 1$. Instead of finding the discrete quantum mechanical eigenvalues, one uses the approximate Bohr-Sommerfeld semiclassical quantization condition:

$$\frac{1}{2\pi\hbar} \oint p dx = \nu + \frac{1}{2},$$

where ν is a positive integer, p is the momentum, and the integration is performed over one period of classical motion of the particle in the plane perpendicular to the wire axis.

For an axially symmetric circular cylinder, this condition transforms into a one-dimensional quantization condition along the radius variable, of the form:³⁷

$$\int_{m/k}^R \sqrt{k^2 - m^2/r^2} dr = \pi(n + \varepsilon/4), \quad (6)$$

where $k = \sqrt{2m_e E}/\hbar$, E is the kinetic energy, $m = \dots, -1, 0, 1, 2, \dots$ is the azimuthal quantum number, n is a positive integer, $\varepsilon/4 < 1$, and r is the wire radius, which has two turning points: m/k and R , respectively. Integrating Eq. (6), we obtain the quantization condition for k :

$$kR(\sin \varphi - \varphi \cos \varphi) = (n + \varepsilon/4)\pi, \quad (7)$$

$$\cos \varphi = m/(kR).$$

This is an implicit dependence of k on n and m from which the semiclassical spectrum can be derived.

In the case of a complicated geometry, this approach is preferred to solving the Schrödinger equation exactly, but in our simple symmetric case we can obtain the spectrum ex-

actly (see above) and therefore we shall rather use this relation to analyze the behavior of k . Following Balian and Bloch,³⁸ we shall look for bunching of the eigenvalues—those intervals of k where the energy levels are very close to each other. In order to find them, we should consider the variations δm and δn and find the conditions at which the corresponding $\delta(kR) \ll 1$ for some fixed R . As we are looking at the semiclassical approximation, we should consider only the part of the spectrum for large k and n where we can ignore ε . Combining both equations in (7) and varying m and n , we obtain:

$$\delta(kR) \sin \varphi = \pi \delta n + \varphi \delta m; \quad \delta n, \delta m \in Z. \quad (8)$$

In order to have $\delta(kR) = 0$ for nonzero δm and δn , the value of φ should be a rational fraction of π : $\varphi/\pi = t/p$. Of course φ has to satisfy Eqs. (7), which have solutions of the form³⁸ $\varphi = (t/p)\pi + O(1/kR)$, where p and t are two integers, satisfying the condition $p \geq 2t$. Since they enter only in the form of a fraction t/p , we can assume that they are co-prime.

We can now fix the values of $t, p \neq 0$ and look for the corresponding periodicity in kR . Substituting $\varphi = t\pi/p$ into the same variation (8), we obtain

$$\Delta(kR) \sin \varphi = \frac{\pi}{\rho} (p \Delta n + t \Delta m).$$

In order to determine the period of this dependence, we have to find the smallest possible value of $\Delta(kR) \neq 0$. It follows from Bezout's theorem that for integers p and t prime to each other there exist integers Δn and Δm such that $p \Delta n + t \Delta m = 1$. Thus we obtain the periodicity of the bunches: $\Delta k = 2\pi/(2pR \sin \varphi)$. On the other hand, it is easy to see that $L(p, t) = 2pR \sin \varphi$, $\varphi = t\pi/p$ is just the perimeter of a polygon inscribed into a circle of a radius R having p vertices and making t revolutions around the center. Therefore we see that our spectrum will contain multiple sets of periodic bunches of levels determined by the choice of p and t (or, alternatively, Δn and Δm), and each set can be described as a closed semiclassical trajectory inside a circular cross section of a cylinder. Some of them are shown in Table I. This is a very general result: it allows one to take a full set of eigenfunctions of the system determined by varying two quantum numbers m and n , and using the above-mentioned relations to “create” particles in the form of wave packets moving along certain trajectories (polygons inscribed in a circle).

Now let us compare the frequencies which we obtain in the exact quantum mechanical treatment (Fig. 14b, d) with the ones determined by semiclassical trajectories. As the number of vertices of a polygon with winding number $t=1$ inscribed in a circle grows, its perimeter approaches the circle itself. Thus, the minimum period $\Delta(kR) = 2\pi R/L(p, t) = 1$ would be for a trajectory which is the circle itself, setting the maximum frequency in the spectrum. The positions of the first few periods are calculated, and the corresponding trajectories are shown in Table I.

It is important to note that the values that we obtain for the frequencies of the first few orbits coincide perfectly with the positions of the peaks on the Fourier spectrum of the calculated electronic density of states (or force) in a perfect cylinder (Fig. 14b, d). We can therefore draw the important

conclusion that the peaks in the Fourier spectrum of the oscillating part of the force in the nanowire, located at the frequencies of Table I, each correspond to a single semiclassical trajectory. Every trajectory is characterized by two parameters (t, p) and is composed of all eigenstates with quantum numbers (m, n) chosen such that $\Delta m = p$, $\Delta n = t$. In other words, by grouping together the wave functions Ψ_{mn} based on this principle ($\Delta m = p$, $\Delta n = t$, where p and t are fixed), one can construct a wave packet or a “particle” traveling along a classical trajectory of a polygon with p vertices inscribed in a circle and making t turns around the center.

There is an important difference between cluster physics and that of nanowires. In spherical clusters the spectral weight of the diametric orbit $(t, p) = (1, 2)$ is much smaller than that of the triangular and square orbits.⁷⁾ Then, in order to observe the beating between the latter two, one has to register a large number of oscillations, since the first minimum occurs at about 11–12 maxima due to the closeness of the frequencies. This is not a simple task because of the strongly decaying amplitudes, but one can make use of an additional feature: the nearly identical intensities of the triangular and square orbits give rise to the missing of one half of the oscillation period at the minimum.³⁹ In the nanowire, in contrast, because of the less symmetric configuration, the intensity of the diametric orbit is approximately similar to that of the triangular and square orbits (see Fig. 14). Thus the beating between them is observed at a much higher frequency, as can easily be seen in the experimental histograms. The missing half-period is not observed in the nanowire, because of the small number of oscillations between the nodes in the beating pattern.

The intensities of the spectral contributions of each trajectory are determined by their weight in the semiclassical expansion. From Figs. 14b, d one can see that for all $p > 4$ and $t > 1$ the contributions become negligibly small. This can be explained if one recalls that $p = \Delta m$, $t = \Delta n$, so the smaller these are, the more individual energy levels (or wave eigenfunctions) for a given limiting Fermi energy ε_F will be present in the spectrum and contribute to a particular trajectory, increasing its weight in the spectrum. An exact derivation of this fact can be found in Ref. 38.

4.2. Atomic shells

Structure of alkali nanowires: 6-fold symmetry. Recently several papers have appeared that consider unconventional structures for nanowires.^{40–42} In Ref. 40 a 5-fold cluster-like structure was observed for a sodium nanowire through computer simulation. For gold, Kondo and Takayanagi claimed to observe spiral-like shell structures with an incremental number of 7 atoms in cross section.⁴² Molecular dynamic simulations for the s - p metals Al and Pb were reported in Ref. 41, where a “weird” spiral-like structure was predicted for nanowires with conductances smaller than $10G_0$. Some of these weird wires resemble the structures observed in Ref. 42. Note that for thicker nanowires the calculations predict a close-packed hexagonal structure.

When searching for an explanation for the structure that we have called “atomic” in our experiment, we are again led by the research on metal clusters. For alkali-metal clusters produced in vacuum a clear transition has been observed

between the series of magic numbers given by the closing of electronic shells and the other series of magic numbers determined by the closing of geometric shells of atoms.^{8–10} The latter series result from the fact that the clusters have a highly symmetric crystalline shape, and the surface energy of a cluster attains a minimum when a new layer of atoms completely covers the surface. Let us assume that nanowires have a similar tendency toward crystalline order, and form facets. Such faceting has indeed been observed recently in transmission electron microscope images of gold nanobridges under thinning of the bridges by the electron beam current.⁴³ If many hundreds of wires are drawn, the facets should be expressed due to a well-defined minimum in the surface energy. Since the periodic pattern extends to large wire diameters, we first start with the assumption that the lattice structure in the wire is that of the bulk metal. The bulk lattice structure of potassium is bcc and the lowest energy surfaces are the [110] surfaces. A wire with only [110] facets can be formed with the wire axis along [100] and [111]. The cross section of the former would be square while that of the latter is a hexagon. The hexagonal wire clearly has a smaller surface area and would be preferred.

In order to calculate the slope of $g^{1/2}$ versus the peak index i , we approximate the relation between the conductance and wire cross section A by the lowest-order term, $g \approx k_F^2 A / 4\pi$, which is appropriate for $k_F R \gg 1$. The distance between the [110] atomic layers is $h = a_0 / \sqrt{2}$, where a_0 is the size of the cubic unit cell. We thus obtain

$$\frac{\partial \sqrt{g}}{\partial i} = \frac{3^{1/4}}{2\sqrt{\pi}} k_F a_0.$$

For a bcc lattice $k_F a_0 = (6\pi^2)^{1/3}$, and for the slope we obtain a value $\alpha = 1.447$, which is shown in the inset in Fig. 9 as a line labeled “full atomic shell.” This is clearly a much higher slope than the one we observe, and even higher than the slope for the electronic shell structure.

Sodium has a low-temperature martensitic phase transition toward a close-packed atomic structure and it is possible that the surface tension favors close packing in nanowires. It turns out that one can construct a similar shape of a nanowire, as proposed above for the bcc structure having close packing. Such a wire would have an fcc lattice, with the wire axis along [011], and six facets that are perpendicular to [100], [1 $\bar{1}$ 1], [$\bar{1}$ 1 $\bar{1}$], [$\bar{1}$ 00], [$\bar{1}$ 1 $\bar{1}$], and [11 $\bar{1}$]. For this arrangement we obtain $\alpha = 3^{5/6} \pi^{1/6} / 2^{13/12} = 1.427$, which is very close to the value for the bcc structure.

When we assume that a stable configuration is obtained each time when a single *facet* of the nanowire is completed, in analogy to what is observed for some metal clusters (e.g., for aluminum),^{10,44} then the slope becomes a factor of 6 lower, equal to 0.241, in close agreement with the experimental data. Further support for this interpretation comes from considering the conductance values for closing of a full shell. We can write

$$g^{1/2} = \alpha(j + j_0), \quad (9)$$

where j is the index of a full shell of atoms, with all facets covered, and $j_0 = 0.5$ is an offset value, which depends somewhat on the boundary conditions for the electrons. From this expression, and using the experimental value $\alpha = 6 \times 0.224$

$= 1.34$, we find that the beginning of the atomic-shell structure in Fig. 9 is described by the shell numbers $j = 4, 5$, and 6 , which are closed at $g^{1/2} = 6.02, 7.36$, and 8.70 , respectively. Apart from the small shift, which may be absorbed in a new choice of the offset $j_0 = 0.66$, these values correspond to the higher-intensity peaks with indices $7, 13$, and 19 , and five smaller peaks between them. By analogy to the observation on Ca clusters,¹⁰ this suggests an enhanced stability for nanowires with all six facets covered. Alternatively, one can check the self-consistency of the linear relation (9) by assuming that the first fully covered layer with 6-fold symmetry should contain at least 6 alkali atoms in the cross section, taking into account that 1 monovalent atom approximately corresponds to a single conductance channel and, correspondingly, to a reduced conductance $g \approx 6$. Thus, following formula (9), for the slope α we obtain $\sqrt{6}/(1 + 0.66) = 1.47$, very close to the theoretical value 1.447 and the experimental slope 1.34.

Furthermore, proceeding this way, we obtain the explanation for the step structure shown in Fig. 13. When we successively remove 6 hexagonal facets with the same number (on average) of atoms (see the inset in Fig. 13), they should give 6 successive stability peaks, which increase the conductance g by the same average increment, depending on the size of the hexagon. While receding the electrodes, the next full atomic shell should give us the next 6 stability facets with an increment decreasing approximately by one atom, i.e., by one conductance quantum, etc. This is just what is observed in Fig. 13, where the edges of the “plateaus” coincide with the maximal peaks with indices $7, 13, 19$, and the increment between successive “plateaus” amounts to about 1 quantum unit.

One-atomic-layer slab model for stretching nanowire.

In this paragraph we show that the hexagonal close-packed structure of a nanowire is compatible with the often-discussed model of plastic flow of a metallic nanowire during pulling off of the electrodes.

Molecular dynamics simulations performed by Landman *et al.*¹ suggest that plastic flow of a nanometer-sized contact involves a series of successive structural transformations of a small number of atomic layers adjacent to the narrowest part of the constriction. In each transformation the neck shrinks as one atomic layer is added. Let us consider for simplicity the circular symmetric model described in Refs. 20 and 21. The narrowest part of a wire is responsible for its electrical conductance. Untiedt *et al.* propose that a part of the cylindrical constriction of the junction, which they call the transformation length λ , depends on the minimal cross section area A as $\lambda = \alpha_0 A^n$, where α_0 is a constant and n is an exponent.⁸⁾ Depending on the indentation procedure and other parameters of the experiment (temperature, elongation rate, presence of adsorbates, etc.), α_0 and n may have various values.

According to Ref. 21, the process of pulling the nanowire can be represented schematically as shown in the inset of Fig. 15. Starting with a relatively thick bridge of cross section A_0 [see (a)], the length λ_0 first transforms elastically, which is schematically shown in (b). The elastic elongation corresponds to a plateau in the conductance versus elongation curve. Next, it goes through a yielding stage, which

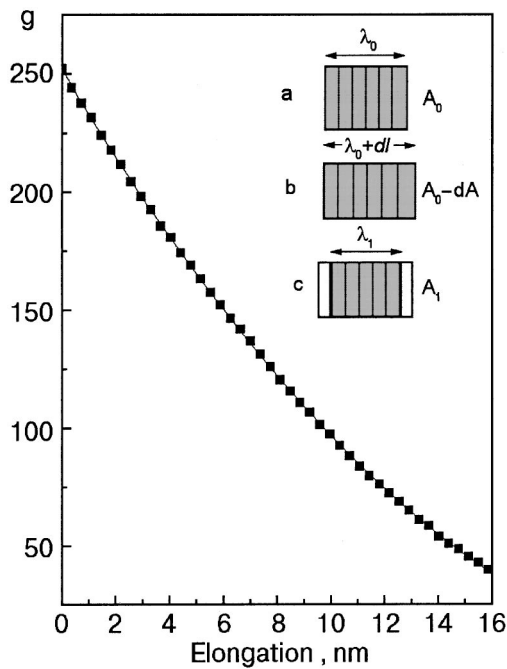


FIG. 15. Dependence of the conductance versus elongation for an averaged scan obtained by plotting positions of the atomic shell peaks in the range $30 < g < 250$ versus the elongation, which is calculated as $i \times h$, where i is a successive integer and h is the interlayer distance. The fit (curve) of the experimental data points (squares) by Eq. (11) gives an exponent $n=0.51$ and a transformation length at $g=250$ of $\lambda_0=13.3$ nm.

corresponds to a jumplike shrinking of the diameter. Following Refs. 1, 20, and 28, we assume that the wire relaxes by creating one more atomic layer (see Figs. 15b and 15c of the inset). We take into account the discreteness of the atomic structure, which consists of close-packed atomic layers with thickness h . Then, due to volume conservation, the atoms from a fraction x of the surface layer with a transformation length λ and a wire radius R , $2\pi R x \lambda(A)h$, should be transferred to the new atomic layer along the wire axis $\pi R^2 h$ (see Fig. 15). Equating these two quantities we obtain

$$2\pi R x \lambda(A)h = \pi R^2 h, \text{ or } \lambda(A) = R/2x. \quad (10)$$

In this model a proportionality between λ and R exists regardless of the presence of the atomic shell effect, as was shown in Ref. 21. Taking into account that at elevated temperatures the proportionality between piezo voltage and elongation may be violated, we use instead a model to extract a scale for the elongation. We assume that the distance between the conductance peaks of the atomic-shell structure corresponds to an elongation $h = \sqrt{8/3}r_0$, equal to the distance between the close-packed layers of atoms (r_0 is the atomic radius). In this way we obtain the conductance-versus-elongation curve shown in Fig. 15. Fitting this curve to the model dependence²¹

$$g(l) = g_{\max} \left(1 - \frac{nl}{\lambda_0} \right)^{1/n}, \quad (11)$$

where l is the elongation, $g_{\max} = g(l=0)$ and $\lambda_0 = \lambda(l=0)$, we obtain $\lambda/R \approx 3.1$. Here we start the elongation at the conductance $g_{\max} = 250$, which corresponds to $R_{\max} = 4.26$ nm and $\lambda_0 = 13.3$ nm. From $\lambda \approx 3R$ it follows that $x = 1/6$, which perfectly correlates with hexagonal symmetry of close-

packed atoms in the nanowire. This is important, because as the nanowire is stretched the crystal facets do not evaporate like in mass spectroscopy but should be built into the thinning wire, if we neglect their escape to the electrodes.

5. SUMMARY

We have presented evidence for two sets of magic numbers in metallic nanowires: electronic and atomic, in complete analogy with cluster physics. These two sets of oscillations in the conductance histogram compete with each other, as in cluster physics, where the transition from the electronic shell structure to the atomic shell structure is also observed for larger diameters.⁹ One shell-closing effect is related to the energy of the total volume of electrons, for which the amplitude of the oscillations in the thermodynamic potential decreases as $1/R$. The other is due to the surface energy, for which the amplitude of the oscillations is roughly constant as a function of R . The transition between them depends on the parameters of experiment. The atomic-shell oscillations are observed at larger diameters (conductances) than the electronic ones, but they may overlap substantially. For Li, and in many cases for Na, the electronic-shell structure oscillations completely dominate the spectrum.

The periodic peak structure in the histograms is only observed at temperatures well above helium temperature. Thermal energy is required in order to have sufficient mobility of the atoms allowing the structure to accommodate to the lowest free energy. Potassium has the lowest melting temperature among three alkali metals (Li, Na, K) studied by us. This means that at a given temperature its atoms have the highest mobility, and for this metal we obtain the largest number of oscillations in the conductance histogram. From our data we cannot exclude other atomic wire arrangements, since they depend strongly on the material studied.^{41,42} However, in the latter studies, beyond a critical radius of the order of three atomic distances the bulk lattice structure is recovered. Therefore, it is likely that the nanowires with diameters in the range of the atomic-shell structure oscillations observed here have a regular atomic stacking structure. On the other hand, the alkali metals Li and Na have low-temperature martensitic phase transitions toward a close-packed atomic structure, and it is likely that the surface tension favors close packing in the nanowires.

Since we have studied conductance histogram for alkali metals up to high conductances, we can claim that almost all the structure observed originates from favorable atomic configurations and not from conductance quantization, unlike the initial few peaks (1, 3, 6) at low temperatures, where transmission measurements convincingly show degenerate quantized conductance modes.¹⁸ However, the favorable atomic configurations are influenced by the quantization of the electronic levels, and only the atomic shell structure is a purely classical effect, but still on the atomic scale.

I. K. Y. is grateful to the Kamerlingh Onnes Laboratory of Leiden University for its hospitality and for the opportunity to participate in the work presented in this paper. Special thanks to Prof. L. J. de Jongh for his interest and continuous support.

*Present address: Dept. of Physics, 510 Clark Hall, Cornell University, Ithaca, NY 14853

¹One conductance quantum equals $G_0 \equiv 2e^2/h = (12907 \Omega)^{-1}$.

²From now on we shall use the reduced conductance as $g = G/G_0$, where $G_0 = 2e^2/h$.

³We shall discuss the transformation length²¹ in the paragraph concerning the atomic shell structure.

⁴The latter corresponds to the frequency 0.866.

⁵The assumption that the Fermi energy of the wire is always equal to that of the bulk is, generally speaking, invalid.³¹ This correction, however, does not change the results qualitatively and, since we are only interested in the periodicities of the thermodynamic quantities, it can be ignored for the sake of simplicity.

⁶The features at about 1.3, 1.6, and higher are the higher-order harmonics of the main frequencies; their presence will be explained later. The minor peak at 0.3 is probably a subharmonic due to the size of the interval of transformation. This “extra” feature is an artifact of our crude method—it is absent if one treats the problem exactly.³⁵

⁷Any polygon inscribed in a diametric cross section of a sphere has an additional degree of freedom, that of rotation around an axis lying in the plane of the polygon. Only the diametric orbit does not have this feature, and hence its contribution to the spectrum is reduced.

⁸This form is a generalization of the expression $\lambda = \text{const}$ which was adopted in Ref. 28 and corresponds to $n=0$.

¹U. Landman, W. D. Luedtke, N. A. Burnham, and R. J. Colton, *Science* **248**, 454 (1990).

²B. J. van Wees, H. van Houten, C. W. J. Beenakker, J. G. Williamson, L. P. Kouwenhoven, D. van der Marel, and C. T. Foxon, *Phys. Rev. Lett.* **60**, 848 (1988).

³D. A. Wharam, T. J. Thornton, R. Newbury, M. Pepper, H. Ahmed, J. E. F. Frost, D. G. Hasko, D. C. Peacock, D. A. Ritchie, and G. A. C. Jones, *J. Phys. C* **21**, L209 (1988).

⁴J. M. Krans, J. M. van Ruitenbeek, V. V. Fisun, I. K. Yanson, and L. J. de Jongh, *Nature (London)* **375**, 767 (1995).

⁵A. I. Yanson, G. Rubio Bollinger, H. E. van den Brom, N. Agrait, and J. M. van Ruitenbeek, *Nature (London)* **395**, 783 (1998).

⁶H. Ohnishi, Y. Kondo, and K. Takayanagi, *Nature (London)* **395**, 780 (1998).

⁷W. D. Knight, K. Clemenger, W. A. de Heer, W. A. Saunders, M. Y. Chou, and M. L. Cohen, *Phys. Rev. Lett.* **52**, 2141 (1984).

⁸W. A. de Heer, *Rev. Mod. Phys.* **65**, 611 (1993).

⁹M. Brack, *Rev. Mod. Phys.* **65**, 677 (1993).

¹⁰T. P. Martin, *Phys. Rep.* **273**, 199 (1996).

¹¹A. I. Yanson, I. K. Yanson, and J. M. Ruitenbeek, *Nature (London)* **400**, 1440 (1999).

¹²A. I. Yanson, I. K. Yanson, and J. M. Ruitenbeek, *Phys. Rev. Lett.* **84**, 5832 (2000).

¹³A. I. Yanson, I. K. Yanson, and J. M. Ruitenbeek (to be published).

¹⁴C. J. Muller, J. M. van Ruitenbeek, and L. J. de Jongh, *Physica C* **191**, 485 (1992).

¹⁵E. N. Bogachev, A. N. Zagoskin, and I. O. Kulik, *Sov. J. Low Temp. Phys.* **16**, 796 (1990).

¹⁶J. A. Torres, J. I. Pascual, and J. J. Saenz, *Phys. Rev. B* **49**, 16581 (1994).

¹⁷B. Ludoph and J. M. van Ruitenbeek, *Phys. Rev. Lett.* **82**, 1530 (1999).

¹⁸B. Ludoph and J. M. van Ruitenbeek, *Phys. Rev. B* **61**, 2273 (2000).

¹⁹I. K. Yanson and A. V. Khotkevich, *Atlas of Point-Contact Spectra of Electron-Phonon Interaction in Metals*, Naukova Dumka, Kiev (1986).

²⁰J. A. Torres and J. J. Saenz, *Phys. Rev. Lett.* **77**, 2245 (1996).

²¹C. Untiedt, G. Rubio, S. Vieira, and N. Agrait, *Phys. Rev. B* **56**, 2154 (1997).

²²O. Yu. Kolesnychenko, O. I. Shklyarevskii, and H. van Kempen, *Rev. Sci. Instrum.* **70**, 1442 (1999).

²³C. Z. Li, H. Sha, and N. J. Tao, *Phys. Rev. B* **58**, 6775 (1998).

²⁴Yu. F. Komnik, *Fiz. Tverd. Tela (Leningrad)* **10**, 312 (1968) [*Sov. Phys. Solid State* **10**, 248 (1968)].

²⁵L. J. Lewis, P. Jensen, and J. L. Barrat, *Phys. Rev. B* **56**, 2248 (1997).

²⁶*Tables of Physical Quantities (A Handbook)*, edited by I. K. Kikoin, Atomizdat, Moscow (1976).

²⁷C. Höppler and W. Zwerger, *Phys. Rev. Lett.* **80**, 1792 (1998).

²⁸A. Stalder and U. Dürig, *J. Vac. Sci. Technol. B* **14**, 1259 (1996).

²⁹S. Blom, H. Olin, J. L. Costa-Krämer, N. Garsia, M. Jonson, P. A. Serena, and R. I. Shekhter, *Phys. Rev. B* **57**, 8830 (1998).

³⁰C. Höppler and W. Zwerger, *Phys. Rev. B* **59**, R7849 (1999).

³¹J. M. van Ruitenbeek, M. H. Devoret, D. Esteve, and C. Urbina, *Phys. Rev. B* **56**, 12566 (1997).

³²E. N. Bogachev and G. A. Gogadze, *Zh. Éksp. Teor. Fiz.* **63**, 1839 (1972) [*Sov. Phys. JETP* **36**, 973 (1973)].

³³C. A. Stafford, D. Baeriswyl, and J. Bürki, *Phys. Rev. Lett.* **79**, 2863 (1997).

³⁴C. Yannouleas and U. Landman, *J. Phys. Chem. B* **101**, 5780 (1997).

³⁵C. Yannouleas, E. N. Bogachev, and U. Landman, *Phys. Rev. B* **57**, 4872 (1998).

³⁶J. Lermé, Ch. Bordas, M. Pellarin, B. Baguenard, J. L. Vialle, and M. Broyer, *Phys. Rev. B* **48**, 12110 (1993).

³⁷L. D. Landau and E. M. Lifshitz, *Course of Theoretical Physics*, Vol. 3, Pergamon Press (1976).

³⁸R. Balian and C. Bloch, *Ann. Phys.* **69**, 76 (1972).

³⁹J. Pedersen, S. Björnholm, J. Borggreen, C. Bréchnignac, K. Hansen, T. P. Martin, and H. D. Rasmussen, *Nature (London)* **353**, 733 (1991).

⁴⁰R. N. Barnett and U. Landman, *Nature (London)* **387**, 788 (1997).

⁴¹O. Gülseren, F. Ercolessi, and E. Tossati, *Phys. Rev. Lett.* **80**, 3775 (1998).

⁴²Y. Kondo and K. Takayanagi, *Science* **289**, 606 (2000).

⁴³Y. Kondo and K. Takayanagi, *Phys. Rev. Lett.* **79**, 3455 (1997).

⁴⁴T. P. Martin, U. Näher, and H. Schaber, *Chem. Phys. Lett.* **199**, 470 (1992).

This article was published in English in the original Russian journal. Reproduced here with stylistic changes by AIP.

Thermoelectric effects in a Luttinger liquid

I. V. Krive*

B. Verkin Institute for Low Temperature Physics and Engineering of the National Academy of Science of Ukraine, 47 Lenin Ave., Kharkov 61103, Ukraine

I. A. Romanovsky

V. N. Karasin Kharkov National University, 4 Svobody Sq., Kharkov 61077, Ukraine

E. N. Bogachek, A. G. Scherbakov, and Uzi Landman

School of Physics, Georgia Institute of Technology, Atlanta, GA 30332-0430, USA

(Submitted March 19, 2001)

Fiz. Nizk. Temp. **27**, 1110–1122 (September–October 2001)

Thermoelectric effects in a Luttinger liquid (LL) wire adiabatically connected to the leads of noninteracting electrons are considered. For a multichannel LL a staircase-like behavior of the thermal conductance as a function of chemical potential is found. The thermopower for a LL wire with an impurity is evaluated for two cases: (i) LL constriction, and (ii) infinite LL wire. We show that the thermopower is described a Mott-like formula renormalized by an interaction-dependent factor. For an infinite LL the renormalization factor decreases with increase of the interaction. However, for a realistic situation, when a LL wire is connected to the leads of noninteracting electrons (LL constriction), the repulsive electron-electron interaction enhances the thermopower. A nonlinear Peltier effect in a LL is briefly discussed.

© 2001 American Institute of Physics. [DOI: 10.1063/1.1414571]

1. INTRODUCTION

Charge and heat transport through a narrow wire whose width is comparable to the electron Fermi wavelength occur via a finite number of transport channels associated with quantization of the electron's transverse momentum in the wire. Furthermore, at low temperatures the phase-breaking length, $\lambda_\rho(T)$, can exceed the length of the wire, $\lambda_\rho(T) > L$, and the electron transport becomes phase coherent. In the Landauer approach¹ to such quantum mechanical transport problems the complexity of calculating the relevant transport coefficients is reduced to a single-particle scattering problem, with the transport properties of the electrons described in terms of the probability for transmission of the electrons through the effective scattering potential represented by the wire. Indeed, this approach, whose implementation is often simpler than the use of the Kubo treatment of such problems, has proved to be most useful for the description of the transport properties of noninteracting electrons through wires (constrictions) of reduced dimensions (see reviews in Ref. 2).

It is well known that for strictly one-dimensional (1D) interacting electron systems the Fermi liquid (FL) description of the low-energy excitations does not hold. Instead, for such systems with interactions which leave the electronic spectrum gapless, the corresponding “long-wavelength” theory is that of the Luttinger liquid (LL).³ Unlike the Fermi liquid description, where charged excitations are represented by quasiparticles (electrons and holes), electrons do not propagate in an (infinite) LL. Rather, the excitation spectrum of the LL consists of gapless bosonic excitations (charge and spin density waves); harmonic oscillations of boson fields

are neutral, whereas their topological excitations carry charge and spin.

Since the LL and the FL have qualitatively different excitation spectra, the transport properties of LLs have been the subject of theoretical interest, and it was shown rather early⁴ that the electric conductance G of an impurity-free infinite LL depends on the interelectron interaction, i.e., $G = gG_0$, where $G_0 = e^2/h$ is the quantum of conductance and g is the dimensionless electron–electron interaction parameter of the LL. Subsequent intensive investigations pertaining to transport properties of LLs were triggered by the studies of Kane and Fisher⁵ and of Glazman *et al.*,⁶ who considered the transport of charge through a local impurity in the LL, finding that for repulsive electron–electron interactions the conductance scales with temperature (at low temperatures) as a power law $G(T) \sim T^{2/g-2}$; such behavior has been reported in recent experiments.^{7,8}

Heat transport in a LL was first considered in Ref. 9, where it was shown that in an infinite homogeneous LL the thermal conductance $K(T)$ is not renormalized by the interactions, i.e., $K(T) = K_0(T) = (\pi^2/3)k_B^2 T/h$, while in the presence of an impurity $K(T) \sim T^3$. This result, together with the one for the electrical conductance, predicts violation of the Wiedemann-Franz law in a LL.

The above results, which were derived for effectively infinite LLs, cannot be tested directly in quantum wires connected to source and drain leads. To address this issue, the transport properties of the LL were considered for a finite 1D wire adiabatically connected to FL leads modeled by 1D reservoirs of noninteracting electrons. The results obtained for such a finite and impurity-free LL wire were found to be qualitatively different from those derived for the infinite LL.

In particular, it was shown that for finite LL wires with adiabatic contacts to the reservoirs the electric conductance is not renormalized by the interelectron interaction¹⁰ and that the thermal conductance is significantly suppressed (for spinless electrons) for a strong repulsive interparticle interaction.^{11,12} These predictions have a rather simple physical explanation. Since the electrons in the reservoirs are taken as noninteracting particles, one could use the Landauer approach for calculation of the electric and thermal conductances. For an adiabatic LL constriction the electrons are not backscattered by the confining potential of the wire, and consequently charge is transmitted through the wire with unit probability. Therefore, the electric conductance of a LL constriction coincides with the conductance of a single-channel quantum point contact. In contrast, heat is transported in the LL by plasmons (charge-entropy separation)¹¹ which, for strong interactions, are significantly backscattered at the “transition” region between the LL wire and the FL reservoirs, and consequently heat transport is suppressed.

The aforementioned studies dealt with spinless electrons and a single-channel LL. However, in many real situations the quantum wires may support several 1D (transport) channels, and currently thermoelectric effects in LLs remain largely unexplored. In this context, we remark that it has been noted¹³ that the thermopower of a Hubbard chain, in the vicinity of a Mott-Hubbard phase transition to a dielectric phase, can be calculated using the Mott formula (see, e.g., Ref. 14) for noninteracting fermions. This observation has been exploited¹⁵ in a derivation of the thermopower of a homogeneous infinite Hubbard chain in the limits when the Hubbard model can be mapped onto a model of spinless Dirac fermions.

In light of the above, we report here on studies of heat transport through a multichannel LL constriction connected to Fermi liquid leads, as well as investigations of the thermopower (Seebeck) and Peltier effect in a LL wire (Fig. 1).

First, we study heat transport through a multichannel LL constriction. In this case the thermal conductance as a function of the chemical potential μ demonstrates a staircase-like behavior. We show that at low temperatures $T \ll T_0 \approx \hbar v_0/L$ (v_0 is the characteristic velocity, which is determined by the strength of the confining potential, and L is the length of the LL wire) the steps in the conductance $K(\mu)$ are practically unaffected by electron-electron interactions. On the other hand, strong interactions suppress the heat conduction at temperatures $T \sim T_0$; however, the steps are pronounced even in this high-temperature region. Subsequently, we evaluate the thermopower for a finite LL wire connected to FL leads. In this case a simple physical approach to the prob-

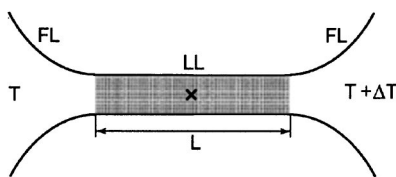


FIG. 1. Schematic of a Luttinger liquid (LL) nanowire of length L , connected to Fermi liquid (FL) reservoirs that are kept at different temperatures. The impurity (scattering potential, denoted by X) is placed in the middle of the LL wire.

lem was used. The finite LL wire is modeled by an effective transmission coefficient which in the Landauer-Buttiker approach determines the charge and heat transport between the leads. We predict that the thermopower of a LL with an impurity is described by a Mott-like formula—it depends linearly on the temperature and is proportional to the logarithmic derivative of the bare (unrenormalized by the electron-electron interactions) electric conductance. At low temperatures $k_B T \ll \Delta_L \approx \hbar s/L$ (L is the length of the LL wire, and s is the plasmon velocity) the thermopower is not renormalized by the electron-electron interactions, and it is described by the well-known formula for the thermopower S_0 for a system of noninteracting electrons (see, e.g., Ref. 14). At temperatures $k_B T \gg \Delta_L$ the interaction renormalizes the thermopower, and consequently for a strong interaction $S_{LL} \sim S_0/g^2 \gg S_0$. The renormalization factor is different for spinless and spin-1/2 electrons, and the enhancement of the thermopower is more pronounced for spinless particles.

Next, we calculate the thermopower for an infinite LL. Although the situation when the effects of the leads are excluded appears somewhat artificial from the experimental point of view, it is useful to elaborate this problem by a powerful LL calculation technique. In particular, we note that the transport properties of 1D interacting electrons have been studied mostly for an infinite LL, and thus the evaluation of the thermopower for this case represents an interesting and important theoretical problem. We show that for an infinite LL wire with an impurity the thermopower is described by the Mott formula, S_0 , multiplicatively renormalized by the electron-electron interaction.

For an infinite LL the renormalization factor decreases with increase of the interaction, $S(g \ll 1) \sim g S_0$. This result does not contradict our previous claim, since the two problems under study (infinite LL wire and LL wire adiabatically connected to metallic leads) are not identical. In particular, the driving voltage which enters the definition of the thermopower is different for the two cases in question. For an infinite LL it is the voltage drop V across the impurity. In the case of the LL constriction the bias voltage U is defined as the difference of the chemical potentials of the leads, $U = \Delta\mu/e$. It has been shown¹⁶ that for a strong impurity (weak tunneling) $V = g^2 U$. Thus the thermopower of a LL wire, when expressed in terms of U , is enhanced by interaction. This derivation supports our finding that the strong interelectron interaction strongly enhances the thermopower of a LL with an impurity.

It is well known (see, e.g., Ref. 14) that in the linear-response regime the Peltier effect is determined by the same thermoelectric coefficient as the Seebeck effect. However, in the nonlinear regime the Onsager symmetry relations between the transport coefficients cease to be valid, and the Peltier coefficient for $eV \gg k_B T$ (V is the bias voltage) describes an independent thermoelectric phenomenon. We evaluate the nonlinear Peltier coefficient for an impurity-containing LL wire connected to leads. The phenomenological approach, when the finite LL wire is modeled by an effective transmission coefficient, does not predict the renormalization of the nonlinear differential Peltier coefficient by the interaction.

The paper is organized as follows. In Sec. 2 the thermal

conductance of a multichannel LL is studied. In Sec. 3 the thermopower of a LL constriction with an impurity is evaluated in a phenomenological approach. In Sec. 4 bosonization technique in conjunction with a tunneling Hamiltonian method is used for a calculation of the thermopower of an infinite LL. In Sec. 5 we investigate the Peltier effect in a Luttinger liquid. The main results are summarized in Sec. 6.

2. INTERACTION-ENHANCED STAIRCASE BEHAVIOR OF THE THERMAL CONDUCTANCE

To calculate the thermal conductance of a multichannel LL wire adiabatically connected to 2D reservoirs of noninteracting electrons we will use the multimode LL model developed in Ref. 16. The Hamiltonian of the model in the boson representation takes the form

$$H = \sum_{j=1}^N \int dx \left[\frac{p_j^2(x)}{2mn_j} + \frac{mn_j}{2} v_j^2 (u'_j)^2 \right] + \frac{U_0}{2} \sum_{i,j=1}^N n_i n_j \int dx f_L(x) u'_i(x) u'_j(x), \quad (1)$$

where $u_j(x)$ is the displacement operator of the j th mode; $u'_j \equiv \partial u_j / \partial x$; p_j is the conjugate momentum, with $[u_i(x), p_j(y)] = i\hbar \delta_{ij} \delta(x-y)$; n_j is the number density of the electrons in the j th mode and $v_j = \pi\hbar n_j / m$ is the corresponding Fermi velocity, and U_0 determines the strength of the electron-electron interaction, which is assumed to be local: $U(x-y) = U_0 \delta(x-y)$. We introduced into the Hamiltonian in Eq. (1) a smooth function $f_L(x)$ that restricts the electron-electron interaction to a finite region of length L . The electron reservoirs are modeled as 1D N -channel Fermi gases and they are represented, in the boson form, by the noninteracting part of the Hamiltonian.

The Hamiltonian in Eq. (1) is quadratic and can be easily diagonalized. In diagonal form it describes N noninteracting “bosonic” modes with velocities s_n ($n = 1, \dots, N$) which are adiabatically transformed into N modes with velocities v_n ($n = 1, \dots, N$). The latter modes correspond to the N noninteracting electron channels in the leads. The plasmon velocities s_n are determined by the equation¹⁷

$$\sum_{n=1}^N \frac{v_n}{s^2 - v_n^2} = \frac{\pi\hbar}{U_0}. \quad (2)$$

For a two-channel ($N=2$) case the above equation can be easily solved, yielding

$$s_{1(2)} = \sqrt{\frac{1}{2} (u_1^2 + u_2^2) \pm \frac{1}{2} \sqrt{(u_1^2 - u_2^2)^2 + (2U_0/\pi\hbar)^2 v_1 v_2}}, \quad (3)$$

where

$$u_{1(2)} = v_{1(2)} \sqrt{1 + U_0 / (\pi\hbar v_{1(2)})}. \quad (4)$$

In the limit of strong interelectron repulsion, i.e., $U_0 \gg \pi\hbar v_{1(2)}$, the interaction parameters of the two-channel LL, defined as $g_n = v_n / s_n$, take the form ($v_1 \gg v_2$)

$$g_1 \equiv \frac{v_1}{s_1} \approx \left(\frac{\pi\hbar v_1}{U_0} \frac{v_1}{v_1^2 + v_2^2} \right)^{1/2} \ll 1; \quad g_2 \equiv \frac{v_2}{s_2} \approx \sqrt{v_2 / v_1} \ll 1. \quad (5)$$

Note that for spin-1/2 interacting electrons the Hamiltonian of a single channel LL is given by Eq. (1) with $N=2$ and $v_1 = v_2 = v$. In this case the velocity of the “spin” mode $s_2 = v$ is not renormalized by the interaction, i.e., $g_s = 1$. In the following we will see that “spin” channels offer “easy pathways” for heat transport through a LL constriction.

In the absence of electron backscattering (see discussion below) the plasmon modes are noninteracting. Consequently, the Landauer approach¹ can be used for calculation of the thermal conductance. The corresponding expression reads^{11,12}

$$K(T) = \frac{1}{Th} \sum_{n=1}^N \int_0^\infty d\varepsilon \varepsilon^2 \left(-\frac{\partial f_B}{\partial \varepsilon} \right) t_n(\varepsilon), \quad (6)$$

where $f_B \equiv [\exp(\varepsilon/k_B T) - 1]^{-1}$ is the Bose-Einstein distribution function of the plasmons, and $t_n(\varepsilon)$ is the probability of plasmon transmission through the n th mode of the LL. As we have said, we assume here that the contacts of the LL to the Fermi liquid reservoirs are adiabatic, which means that there is no backscattering of charged excitations in the LL. Formally Eq. (6) represents the thermal conductance of a purely bosonic noninteracting system.¹⁸ As was shown in Refs. 11 and 12, this formula also applies to an adiabatic (no electron backscattering) LL wire, where the heat is transported by bosonic excitations (plasmons), whose dynamics, in the absence of local scatterers, is described by a quadratic Hamiltonian. These considerations lead one to conclude that Eq. (6) yields the exact thermal conductance of a LL wire in the absence of impurities. However, the plasmons could be backscattered by the “transition region” between the LL and the FL reservoirs. Since the width d of the transition regions obeys $\lambda_F \ll d \ll L$, we can model them as zero-width boundaries located at $x=0$ and $x=L$. Consequently, the mismatch of the plasmon velocities at the boundaries will cause strong backscattering of the plasmons. Thus the transmission coefficient $t_n(\varepsilon)$ in Eq. (6) can be obtained by taking the function $f_L(x)$ in Eq. (1) to be of the form $f_L(x) = \theta(x)\theta(L-x)$ [where $\theta(x)$ is the Heaviside step function] and matching the wave functions of the plasmons at the boundaries. Since there is no channel mixing, $t_n(\varepsilon)$ takes a form analogous to that calculated in Ref. 12:

$$t_n(\varepsilon) = \left[\cos^2 \left(\frac{\varepsilon}{\Delta_n} \right) + \frac{1}{4} \left(g_n + \frac{1}{g_n} \right)^2 \sin^2 \left(\frac{\varepsilon}{\Delta_n} \right) \right]^{-1}, \quad (7)$$

where $\Delta_n \equiv \hbar s_n / L$ is the characteristic energy scale for the finite LL wire, and the plasmon velocities s_n ($n = 1, \dots, N$) are determined by Eq. (2). Note that for spin-1/2 electrons the “spin” mode is not renormalized by interaction, and the corresponding correlation parameters $g_n^{(s)} = 1$ ($n = 1, \dots, N/2$); i.e., for the “spin channels” one has $t_n^{(s)} = 1$, and the heat transport associated with spin density wave excitations is not affected by the electron-electron interaction.

The expressions given in Eqs. (2), (5), and (7) generalize the problem of heat transport through a single-mode spinless LL^{11,12} to a multichannel LL. Now the Fermi velocities v_n depend both on the chemical potential μ and the “transverse” quantum number n which characterizes the quantization of the transverse electron momentum. For a parabolic confining potential $U_c(y) = m\Omega^2 y^2/2$ the corresponding transverse energy takes the values $E_n^\perp = \hbar\Omega(n-1/2)$ ($n = 1, \dots, N$), and the Fermi velocity of the n th mode is given by

$$v_n = v_0 \theta \left(\frac{\mu}{\hbar\Omega} + \frac{1}{2} - n \right) \left(\frac{\mu}{\hbar\Omega} + \frac{1}{2} - n \right)^{1/2}, \quad (8)$$

where $v_0 = \sqrt{2\hbar\Omega/m}$. The appearance of the step function in the definition of the Fermi velocities of the multimode LL results in a staircase behavior of the electric $G(\mu)$ and thermal $K(\mu)$ conductances as functions of the chemical potential μ .

An important comment concerning Eqs. (6)–(8) is warranted here. Note that Eq. (7) is an exact result for noninteracting plasmon excitations—that is, when the electrons are not backscattered by the confining potential in the LL constriction. Such a condition is fulfilled at low temperatures and for chemical potentials satisfying $\mu \neq \hbar\Omega(n-1/2)$. In the vicinity of $\mu = \hbar\Omega(n-1/2)$ an additional electron mode is converted from an evanescent to a propagating mode. This implies that upon reaching the threshold μ for entrance into the contact, the character of the corresponding mode changes, and in doing so the mode is strongly influenced by the confining potential. Consequently, at such threshold values of the chemical potential the assumption of adiabaticity of the LL constriction fails, and in calculating the thermal conductance the contribution due to electron transport needs to be considered. However, it is well known that the transport of charge through a local (of the order of λ_F) potential in a LL is strongly suppressed due to plasmon renormalization of the bare scattering potential,⁹ implying that for sufficiently long wires and for strong electron-electron repulsion the contribution of electron transport to the thermal conductance $K(T)$ is small and can be neglected. Therefore, we conclude that under such circumstances Eq. (6) is valid for practically all values of the chemical potential except at the very beginning of the steps. We note that at low temperatures, $T \ll \hbar v_0/L$, the staircase-like behavior of the thermal conductance is practically unaffected by electron-electron interaction (Fig. 2a). At high temperatures $T \gg \hbar v_0/L$ the thermal conductance, although being suppressed in the case of strong interaction,^{11,12} still demonstrates a clear staircase behavior as a function of chemical potential (Fig. 2b).

3. IMPURITY-INDUCED THERMOPOWER IN A LUTTINGER-LIQUID CONSTRICTION

The thermopower is a measure of the capability of a system of charged particles to generate an electromotive force when a temperature gradient is applied across the system. In the linear-response regime it can be represented as a ratio of transport coefficients,

$$S(T, \mu) = - \frac{L(T, \mu)}{G(T, \mu)}, \quad (9)$$

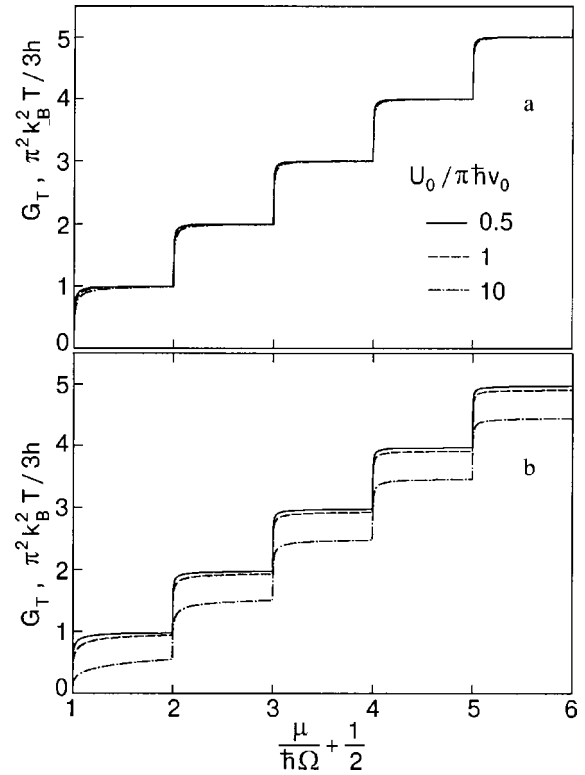


FIG. 2. The thermal conductance, in units of $\pi^2 k_B^2 T/3h$, plotted as a function of the dimensionless chemical potential $\mu/(\hbar\Omega) + 1/2$ for several values of the strength of the electron-electron interaction $U_0/(\pi\hbar v_F)$. In (a) the temperature was taken to be $\tilde{T} = k_B T L/(\hbar v_0) = 0.1$, and in (b) $\tilde{T} = 10$.

where G is the electric conductance and L is the cross-transport coefficient which connects the electric current to the temperature difference for noninteracting particles. These coefficients can be calculated using a formalism developed in Ref. 19 and adapted in Ref. 18 to the Landauer scheme.¹ In this approach the transport coefficients are expressed in terms of the transmission probability $t_j(\varepsilon)$ for an electron to arrive at the drain electrode in the j th channel as

$$G(T, \mu) = G_0 \sum_{j=1}^N \int_0^\infty d\varepsilon \left(- \frac{\partial f_F}{\partial \varepsilon} \right) t_j(\varepsilon), \quad (10)$$

and

$$L(T, \mu) = G_0 \frac{k_B}{h} \sum_{j=1}^N \int_0^\infty d\varepsilon \left(- \frac{\partial f_F}{\partial \varepsilon} \right) \frac{\varepsilon - \mu}{k_B T} t_j(\varepsilon). \quad (11)$$

Here G_0 is the conductance quantum and $f_F(\varepsilon - \mu)$ is the Fermi-Dirac distribution function of the electrons in the leads.

Equations (10) and (11) cannot be applied to an infinite LL, where electrons are not propagating particles and the conventional scattering problem is “ill-posed.” A general approach for calculating transport coefficients in a system of strongly interacting particles is the Kubo formalism, and a recent publication where it was used for calculation of the thermopower for a Hubbard chain can be found in Ref. 15. As may be seen from that study, with the Kubo approach it is difficult to calculate the thermopower in the whole range of external parameters (temperature, interaction strength, density of particles, etc.), and indeed the final analytical expressions for the desired quantities were derived^{13,15} only in the

limits when the Hubbard model can be mapped to a model of noninteracting fermions, for which a Mott-type expression for the thermopower could be used.

To obtain thermopower results pertaining specifically to the transport properties of systems of strongly interacting electrons, and to consider quantum-wires thermoelectric effects which could be tested in experiments, we choose to invoke at first certain simplified (yet physically reliable) models of strongly interacting electron systems. Such physical models of charge transport in LLs of strongly, as well as weakly, interacting electrons were proposed in Refs. 6 and 20 and were shown to yield the same results as those obtained from more conventional (and rigorous) treatments of LL effects,^{5,21} through the use of Landauer-like expressions for estimating the dependence of the conductance on the temperature and on the bias voltage. In this Section and in Sec. 5 we use such a phenomenological approach (see also Ref. 22) for studying the Seebeck and Peltier effects in multichannel LLs.

When a LL is connected to FL reservoirs with given temperatures and chemical potentials one could make use of Eqs. (10) and (11), with $t_j(\varepsilon)$ now regarded as the probability of transmission of the electrons (in the j th channel) through the effective potential barrier formed by the LL piece of the wire. For a wire which is adiabatically connected to the leads the transmission coefficient is unity as long as we neglect the backscattering of electrons by the confining potential. For a perfect wire the backscattering effect is exponentially small for practically all values of the chemical potential, except at the narrow regions in the vicinity of conductance jumps (steps) where an additional mode is converted from an evanescent to a strongly propagating mode. Such a physical picture results in a staircase-like behavior of the conductance as a function of the chemical potential and is often modeled by abrupt jumps of the electron transmission coefficient from zero (reflected mode) to one (transmitted mode). This model is too simplified for real quantum point contacts, where the specific features of the confining potential could be important for a correct description of the transition region between the conduction plateaus. However, for strongly interacting electrons this simple model, which does not depend on the details of the bare scattering potential, could be a correct approximation. Indeed, the transmission of electrons through a long but finite LL is determined by an effective scattering potential that includes the effects of electron-electron interactions. This potential for sufficiently long wires and for temperatures $k_B T \ll E_F$ quenches all modes whose bare transmission coefficients t_0 are not very close to unity (see the corresponding discussion in Ref. 22). Since according to Eqs. (9)–(11) the thermopower $S(T, \mu) \propto \partial G / \partial \mu$ we observe that for a multimode LL constriction the thermopower vanishes on the conductance plateaus and it peaks at the conduction steps (that is, at the transition regions from one conductance plateau to the next). The qualitative distinction of the thermopower in a LL from that evaluated for noninteracting electrons^{23,24} lies in the shape of the thermopower peaks. For strongly interacting electrons a simple approximation in which the (now effective) transmission coefficient is modeled by a Heaviside step function could be a quite reliable procedure. Then the temperature behavior of

the peaks will be universal (it will not depend on the concrete shape of the confining potential). To make more-definite predictions we need to evaluate the thermopower for a quantum wire with a single impurity.

Since it is known that in the presence of an impurity the conductance of a LL is strongly suppressed, one may naively expect that the thermopower $S \propto \partial G / \partial \mu$ will also be strongly suppressed in such a wire. However, as we show below, that is not the case. Instead, we find that for strong (repulsive) electron-electron interactions the impurity-induced thermopower of a LL is significantly enhanced in comparison with the thermopower of a system of noninteracting particles.

To calculate the thermopower of a finite-length LL in the presence of a local impurity (which we place for simplicity at the middle of the constriction) we will model the effective transmission coefficient as

$$t^{\text{eff}}(\varepsilon) = t_0(\varepsilon) \left(\frac{\Delta_L}{\Lambda} \right)^\alpha \quad \text{for } |\varepsilon - E_F| \ll \Delta_L, \quad (12)$$

and

$$t^{\text{eff}}(\varepsilon) = t_0(\varepsilon) \left| \frac{\varepsilon - E_F}{\Lambda} \right|^\alpha \quad \text{for } |\varepsilon - E_F| \gg \Delta_L. \quad (13)$$

Here $t_0(\varepsilon) \ll 1$ is the bare transmission coefficient determined by the unrenormalized scattering potential (we restrict ourselves to a single-mode LL); $\Delta_L = \hbar s / L$ is the characteristic low-energy scale (s is the plasmon velocity), and Λ is the cutoff energy, which for a purely 1D LL is of the order of the Fermi energy E_F . The exponent α depends on the electron-electron interaction strength and is different for spinless and spin-1/2 electrons:¹⁷

$$\alpha = 2 \left(\frac{1}{g} - 1 \right); \quad g = \left(1 + \frac{U_0}{\pi \hbar v_F} \right)^{-1/2} \quad \text{for } s = 0, \quad (14)$$

and

$$\alpha = \frac{2}{g_s} - 1; \quad g_s = 2 \left(1 + \frac{2U_0}{\pi \hbar v_F} \right)^{-1/2} \quad \text{for } s = 1/2. \quad (15)$$

The transmission probability t^{eff} in Eq. (12) results in an expression for the linear conductance which coincides (up to an irrelevant numerical constant) with that obtained in Ref. 25 via a renormalization group calculation. In fact, the same expression has been used⁶ for estimation of the temperature dependence of the LL conductance in the limit of strong interaction ($g \ll 1$); this is also the limit of interest to us, since for weak interactions LL effects would be much weaker.

The bare transmission is commonly assumed to be a smooth function of the energy around E_F , i.e.,

$$t_0(\varepsilon) \approx t_0(E_F) + (\varepsilon - E_F) \left(\frac{\partial t_0}{\partial \varepsilon} \right)_{\varepsilon = E_F}. \quad (16)$$

With this form, Eqs. (10) and (11) yield

$$G_{LL}(T) = G_0 t_0(E_F) \times \begin{cases} \left(\frac{\Delta_L}{\Lambda}\right)^\alpha, & k_B T \ll \Delta_L, \\ 2(1-2^{1-\alpha})\Gamma(1+\alpha)\zeta(\alpha)\left(\frac{k_B T}{\Lambda}\right)^\alpha, & \Delta_L \leq k_B T \leq \Lambda, \end{cases} \quad (17)$$

and

$$L_{LL}(T) = G_0 \left(\frac{\pi^2 k_B^2 T}{3e}\right) t'_0(E_F) \times \begin{cases} \left(\frac{\Delta_L}{\Lambda}\right)^\alpha, & k_B T \ll \Delta_L, \\ \frac{6}{\pi^2}(1-2^{-1-\alpha})\Gamma(3+\alpha)\zeta(2+\alpha)\left(\frac{k_B T}{\Lambda}\right)^\alpha, & k_B T \geq \Delta_L, \end{cases} \quad (18)$$

where $\Gamma(x)$ and $\zeta(x)$ are the gamma function and the Riemann zeta function, respectively.

From Eqs. (9), (17), and (18) we conclude that at low temperatures $k_B T \ll \Delta_L$ the thermopower of a LL constriction with an impurity is not renormalized by the interelectron interactions. Instead it is described by a Mott-type formula for noninteracting electrons,²⁴

$$S_0(T) = -\frac{\pi^2 k_B^2}{3e} \left(\frac{\partial \ln G^0(\varepsilon)}{\partial \varepsilon} \right)_{\varepsilon=E_F}, \quad (19)$$

where $G^0(\varepsilon)$ is the corresponding (bare) conductance of the noninteracting electrons. This finding is not surprising, since at $k_B T \ll \Delta_L$ the electrons in the leads determine the transport properties of the LL constriction. However, at temperatures $k_B T \gg \Delta_L$ the thermopower, being still a linear function of temperature, undergoes a strong multiplicative renormalization:

$$S_{LL}(T \geq \Delta_L/k_B) = C_s(g) S_0(T), \quad (20)$$

$$C_s(g) = \frac{3}{\pi^2} \frac{1-2^{-1-\alpha}}{1-2^{1-\alpha}} \frac{\zeta(\alpha+2)}{\zeta(\alpha)} (\alpha+1)(\alpha+2).$$

Note that unlike the electric conductance $G_{LL}(T)$ and the cross-coefficient $L_{LL}(T)$, the thermopower $S_{LL}(T)$ does not depend on the cutoff parameter, and therefore the interaction- and spin-dependent factor $C_s(g)$ cannot be absorbed into a definition of Λ .

For noninteracting electrons $C_s(g=1) = 1$, and the Mott-type formula (Eq. (19)) holds (as it should) for all temperatures ($k_B T \ll E_F$). In the limit of strong interaction $U_0 \gg \pi \hbar v_F$

$$C_0(g \ll 1) = 12 \frac{U_0}{\pi^3 \hbar v_F}, \quad (21)$$

$$C_{1/2}(g \ll 1) = 6 \frac{U_0}{\pi^3 \hbar v_F}. \quad (22)$$

From Eqs. (20)–(22) we observe that the LL effects on the thermopower are most significant for strong interactions, $U_0 \gg \pi \hbar v_F$, and that they are more pronounced for spinless particles than for spin-1/2 electrons (Fig. 3).

Since for the thermopower the interaction dependence factorizes. Equation (20) could be readily generalized for the case of wires with dilute impurities, where the average spacing between the impurities is large enough so that the impurities act incoherently. In this case the thermopower will still be described by Eq. (20) at temperatures $k_B T > \hbar s \bar{n}$, where \bar{n} is the mean concentration of the impurities. An interesting example is a LL junction made of a perfect LL wire of length L connected to leads through a potential barrier at the contacts. The thermopower of such a LL junction for temperatures $k_B T \geq \Delta_L$ is described by Eqs. (19) and (20) with the total (bare) conductance $G^0 = G_1^0 G_2^0 / (G_1^0 + G_2^0)$, where G_1^0 and G_2^0 are the (bare) conductances of the contacts.

The thermopower, being the ratio of transport coefficients, is less affected by interaction than the transport coefficients themselves (Eqs. (17), (18)). It is the prefactors in the power-law dependences of $G(T)$ and $L(T)$ on the temperature that determine the dependence of the thermopower on the interaction strength. In the phenomenological approach developed above, the quantitative correctness of these coefficients cannot be proved. Therefore, we conclude that the electron-electron interaction enhances the thermopower of a LL wire, and we will attempt to find a more rigorous treatment of the problem. In the next Section we evaluate the thermopower of an infinite LL with an impurity by making use of the bosonization technique when calculating the current in the wire induced by the bias voltage and by the temperature difference.

4. THERMOPOWER OF AN INFINITE LUTTINGER LIQUID

Let us consider an infinite LL wire with a single impurity placed (for definiteness) at $x=0$ (i.e., the middle of the wire; see Fig. 1). It is known that for a LL with repulsive electron-electron interaction the charge transport through an impurity

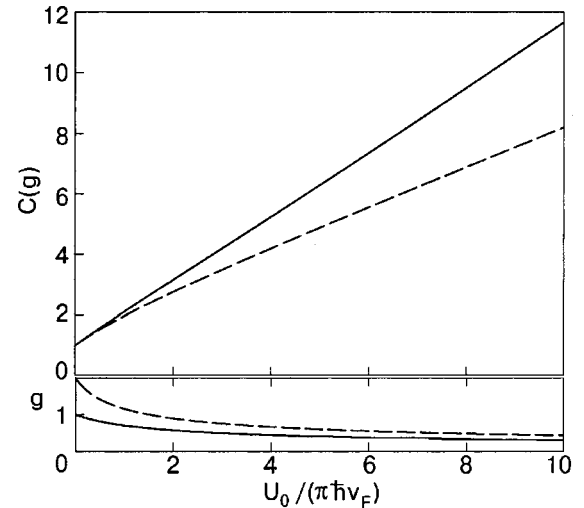


FIG. 3. The renormalization parameter $C(g)$ and the dimensionless electron interaction parameter g plotted versus the dimensionless strength of the electron-electron interaction $U_0 / (\pi \hbar v_F)$ for spinless (solid line) and spin-1/2 (dashed line) electrons.

is sharply suppressed at low temperatures. Therefore, the LL is “split” by the impurity into two disconnected semi-infinite segments, and the charge current through the impurity can be evaluated with the use of the tunneling Hamiltonian method.

We start with the Hamiltonian

$$H = \sum_{m=1,2} H_{0,m} + H_t,$$

where $H_{0,m}$ describes two ($m=1,2$) identical semi-infinite parts of the LL wire. In the bosonic form it reads

$$H_{0,m} = \frac{s\hbar}{8\pi} \int dx [g(\partial_x \Theta_m)^2 + g^{-1}(\partial_x \Phi_m)^2]. \quad (23)$$

Here s is the plasmon velocity, $g = v_F/s$ is the LL correlation parameter, $\Phi_m(x)$ is the displacement field, and $\Theta_m(x)$ is the field complementary to $\Phi_m(x)$, obeying the commutation relation (see, e.g., Ref. 25) $[\Theta_m(x), \Phi_m(x')] = 2\pi i \delta_{mm'} \text{sgn}(x-x')$. The tunneling Hamiltonian is

$$H_t = \int_{-\infty}^0 dx_1 \int_0^{+\infty} dx_2 [\langle x_2 | \hat{T} | x_1 \rangle \psi_2^+(x_2) \psi_1(x_1) + \langle x_1 | \hat{T} | x_2 \rangle \psi_1^+(x_1) \psi_2(x_2)], \quad (24)$$

where $\psi_m(\psi_m^\dagger)$ is the electron annihilation (creation) operator, the index m labels two identical semi-infinite segments of the LL wire, and $\langle x_2 | \hat{T} | x_1 \rangle$ is the tunneling matrix element in the coordinate representation, i.e., the amplitude for the process of electron tunneling from the point x_1 to the point x_2 .

Let us introduce the “slow” annihilation and creation operators of two types—for right- and left-moving electrons: $\psi_m(x) = e^{ip_F x} \Psi_{m,R}(x) + e^{-ip_F x} \Psi_{m,L}(x)$. At first we suggest that our contact is pointlike. Then one can simplify the tunneling Hamiltonian and write it in the form

$$H_t = \sum_{r_1, r_2} (\lambda_0 \Psi_{2,r_2}^+(0) \Psi_{1,r_1}(0) + \text{h.c.}), \quad (25)$$

where $\Psi_{m,r_m}(\Psi_{m,r_m}^\dagger)$ is the operator of annihilation (creation) of an electron from the m th half of the wire (for right-moving (R) electrons $r_m = +1$, for left-moving (L) electrons $r_m = -1$).

We assume that the bare tunneling amplitude λ_0 is small. Then the tunneling rate of electrons through the barrier can be obtained to leading order from Fermi’s “golden rule.” The total rate of electrons from the left (“1”) LL to the right (“2”) LL is of the form (see, e.g., Ref. 27)

$$\Gamma_{12} = \frac{2\pi}{\hbar} \sum_{E_1, E_2, E_1', E_2'} |\langle E_1 E_2 | H_t | E_1' E_2' \rangle|^2 \times P_{12} \delta\left(E_1' + E_2' - E_1 - E_2 - \frac{eV}{2}\right), \quad (26)$$

where P_{12} is the probability of finding the system in the state $|E_1 E_2\rangle$, and V is the bias voltage. The standard evaluation (see below) of the tunnel current $J(V, T) = e[\Gamma_{12}(V, T) - \Gamma_{21}(V, T)]$ results in the well-known expression for the conductance $G(T)$ of an LL with an impurity.⁵

Let us assume now that the temperatures of the left (T_1) and right (T_2) parts of the wire are different. In this case one

can expect the contribution (J_T) to the charge current induced by the temperature gradient. The Hamiltonian given by Eq. (25) with a constant bare tunneling amplitude does not allow one to evaluate this contribution. To obtain the temperature-induced current we have to take into account the finite size of the barrier. We can do it by modifying the tunneling Hamiltonian. The modified Hamiltonian includes extra terms containing the derivatives of the field operators:

$$H_t = \sum_{r_1, r_2} (\lambda_0 \Psi_{2,r_2}^+(0) \Psi_{1,r_1}(0) + \text{h.c.}) + \sum_{r_1, r_2} \{-i\hbar\lambda_1 [r_1 \Psi_{2,r_2}^+(0) \partial_x \Psi_{1,r_1}(0) - r_2 \partial_x \Psi_{2,r_2}^+(0) \Psi_{1,r_1}(0)] + \text{h.c.}\}. \quad (27)$$

Here $|\lambda_1|$ is a small additional parameter ($|\lambda_1|/p_F \sim |\lambda_0|$). Notice that this form of the Hamiltonian corresponds to a tunneling amplitude which depends upon the momentum of the tunneling electron $\langle p_2 | T | p_1 \rangle = \lambda_0 + \lambda_1 r_1 q_1 + \lambda_1 r_2 q_2$, where $q_m = p_m - r_m p_F$ is the momentum of the electron toward the Fermi level.

Now the total electron current through the barrier can be written in the form

$$J = 2ie|\lambda_0|^2 \sum_{r_1, r_2} \int_{-\infty}^{+\infty} dt \sin(eVt) \langle \Psi_{2,r_2}(t) \Psi_{2,r_2}^+ \rangle \times \langle \Psi_{1,r_1}^+(t) \Psi_{1,r_1} \rangle + 2ie\hbar(\lambda_0 \lambda_1^* + \lambda_0^* \lambda_1) \sum_{r_1, r_2} \int_{-\infty}^{+\infty} dt \cos(eVt) \times (r_1 \partial_x \langle \Psi_{1,r_1}^+(t, x) \Psi_{1,r_1} \rangle) \langle \Psi_{2,r_2}(t) \Psi_{2,r_2}^+ \rangle \Big|_{x \rightarrow 0} - 2ie\hbar(\lambda_0 \lambda_1^* + \lambda_0^* \lambda_1) \sum_{r_1, r_2} \int_{-\infty}^{+\infty} dt \cos(eVt) \times (r_2 \partial_x \langle \Psi_{2,r_2}(t, x) \Psi_{2,r_2}^+ \rangle) \langle \Psi_{1,r_1}^+(t) \Psi_{1,r_1} \rangle \Big|_{x \rightarrow 0}, \quad (28)$$

where $\langle \dots \rangle$ denotes the thermal average, and $\Psi_{m,r_m}(t)$ are the field operators in the Heisenberg representation, $\Psi_{m,r_m} \equiv \Psi_{m,r_m}(0)$. The correlation functions in Eq. (28) can be calculated by making use of the bosonization formula

$$\Psi_{m,r_m}(x, t) = \frac{1}{\sqrt{2\pi a}} U_{m,r_m}^+ e^{-i[r_m \Phi_m(x, t) + \Theta_m(x, t)]/2}. \quad (29)$$

Here a is the cutoff parameter ($a \sim \hbar v_F / E_F$), and U_{m,r_m}^+ is the unitary raising operator, which increases the number of electrons on the branch r_m by one particle but does not affect the bosonic excitations. We will not specify its form, since this operator enters the formulas we are studying only in the combination $U U^\dagger = 1$. Now the bosonic fields $\Phi_m(x, t)$ and $\Theta_m(x, t)$ are in the Heisenberg representation.

In our case we have to impose a boundary condition on the displacement field $\Phi_m(x)$ at $x=0$ to account for the semi-infiniteness of each segment of the LL wire, i.e.,

$$\Phi_1(0) = \Phi_2(0) = 0. \quad (30)$$

Besides this, the boson fields $\Theta_m(x)$ in Eqs. (23), (29) satisfy the boundary condition

$$j(x=0) = \frac{1}{2\pi} \partial_x \Theta_m(0) = 0. \quad (31)$$

The boson fields obeying the boundary conditions Eqs. (30), (31) in the momentum representation take the form

$$\begin{aligned} \Theta_m(x) &= i \int_{-\infty}^{+\infty} dp \left(\frac{2s}{g_p} \right)^{1/2} (b_p - b_p^+) \cos\left(\frac{p}{s}x\right), \\ \Phi_m(x) &= \int_{-\infty}^{+\infty} dp \left(\frac{2sg}{p} \right)^{1/2} (b_p + b_p^+) \sin\left(\frac{p}{s}x\right), \end{aligned} \quad (32)$$

where b_p and b_p^+ are the standard bosonic annihilation and creation operators ($[b_p, b_{p'}^+] = \delta_{p,p'}$); $\frac{0}{p} = s|p|$ is the energy of bosonic excitation with momentum p .

With the help of Eqs. (29) and (32) it is straightforward to evaluate the correlation functions. In the vicinity of the contact ($x \sim 0$) one gets the desired correlator

$$\begin{aligned} \langle \Psi_{m,r_m}^+(x,t) \Psi_{m,r_m} \rangle &\approx \frac{1}{2\pi a} \\ &\times \left[\frac{1}{1 + i v_F \chi / a} \frac{\pi T_m \chi}{\sinh(\pi T_m \chi)} \right]^{1/2(1/g+r_m)} \\ &\times \left[\frac{1}{1 + i v_F \eta / a} \frac{\pi T_m \eta}{\sinh(\pi T_m \eta)} \right]^{1/2(1/g-r_m)}, \end{aligned} \quad (33)$$

where $\chi = t - x/s$ and $\eta = t + x/s$. By substituting Eq. (33) into Eq. (28) we find the total electron current. In the linear-response approximation $V \rightarrow 0$, $T_1 - T_2 = \Delta T \rightarrow 0$, the voltage-induced (J_V) and temperature-induced (J_T) currents take the form

$$J_V = 8i \frac{|\lambda_0|^2 e^2}{(2\pi a)^2} V \int_{-\infty}^{\infty} dt \frac{t}{(1 + i v_F t / a)^{2/g}} \left[\frac{\tilde{T}t}{\sinh(\tilde{T}t)} \right]^{2/g}, \quad (34)$$

$$\begin{aligned} J_T &= \frac{16i\pi e}{(2\pi a)^2} (\lambda_0 \lambda_1^* + \lambda_0^* \lambda_1) \frac{k_B \Delta T}{v_F} \int_{-\infty}^{\infty} \frac{dt}{\tilde{T}} \\ &\times \left(1 + i \frac{v_F t}{a} \right)^{-2/g} \left[\frac{\tilde{T}t}{\sinh(\tilde{T}t)} \right]^{2/g} [\tilde{T}t \cosh(\tilde{T}t) - 1] \\ &\times \left[\tilde{T}t \cosh(\tilde{T}t) - \left(1 + i \frac{v_F t}{a} \right)^{-1} \right]. \end{aligned} \quad (35)$$

Here $\tilde{T} \equiv \pi k_B T / \hbar$, where $T = (T_1 + T_2) / 2$ is the mean temperature.

The integrals in Eqs. (34) and (35) look very complicated. Fortunately we are interested only in the limit $a \rightarrow 0$. In this case the asymptotics of the above integrals can be easily found. Both currents $J_{V,T}$ are power-law functions of the small dimensionless parameter $Y \equiv \pi k_B T a / \hbar v_F \ll 1$. The leading terms in the asymptotics $Y \rightarrow 0$ are

$$J_V = V G(T), \quad (36)$$

$$G(T) \approx \frac{|\lambda_0|^2 e^2}{4\pi \hbar^3 v_F^2} B\left(\frac{1}{2}, g^{-1}\right) \left(\frac{\pi k_B T a}{\hbar v_F} \right)^{2/g-2},$$

$$J_T = k_B \Delta T L(T), \quad (37)$$

$$\begin{aligned} L(T) &\approx \frac{\pi e}{2\hbar^3 v_F^3} (\lambda_0 \lambda_1^* + \lambda_0^* \lambda_1) k_B T B\left(\frac{3}{2}, g^{-1}\right) \\ &\times \left(\frac{\pi k_B T a}{\hbar v_F} \right)^{2/g-2}. \end{aligned}$$

Here $B(x,y) = \Gamma(x)\Gamma(y)/\Gamma(x+y)$ is the beta function. Equation (36) coincides with the one found in Ref. 28. It predicts the power-law dependence of conductance on temperature. Equation (37) is a new result. From Eqs. (36) and (37) one easily gets the thermopower

$$S(g) = - \frac{k_B^2 \pi^2}{e} \frac{B(3/2, g^{-1})}{B(1/2, g^{-1})} \frac{T}{|\lambda_0|^2} \frac{2}{v_F} (\lambda_0 \lambda_1^* + \lambda_0^* \lambda_1). \quad (38)$$

For noninteracting electrons ($g=1$) Eq. (38) has to transform into the Mott formula, Eq. (19). This allows us to relate the parameters λ_0, λ_1 of the tunneling Hamiltonian to the conductance and its derivative at the Fermi energy

$$\frac{2}{v_F |\lambda_0|^2} (\lambda_0 \lambda_1^* + \lambda_0^* \lambda_1) = \frac{1}{G^0} \left. \frac{\partial G^0}{\partial \varepsilon} \right|_{\varepsilon = E_F}, \quad (39)$$

where G^0 is the bare (unrenormalized by interaction) conductance. Thus, the thermopower of an infinite LL takes the form

$$S(g) = - \frac{\pi^2 g}{2+g} \frac{k_B^2 T}{e} \left. \frac{\partial \ln G^0(\varepsilon)}{\partial \varepsilon} \right|_{\varepsilon = E_F} = \frac{3g}{2+g} S_0. \quad (40)$$

We showed that the electron-electron interaction in 1D systems modeled by a Luttinger liquid multiplicatively renormalizes the thermopower S_0 of the Fermi liquid. For an infinite Luttinger liquid the renormalization factor decreases with increasing interaction. At first glance this result, Eq. (40), contradicts the conclusion derived in the previous Section. Notice, however, that the two problems in question are not equivalent. It is well known, for instance, that the dependence of the conductance on the interaction strength is different for an infinite LL and for a finite LL wire connected to reservoirs of noninteracting electrons (see, e.g., Ref. 10). To relate the two problems under study we will follow the considerations presented in Ref. 16. In that paper it was shown that for a LL wire adiabatically connected to electron reservoirs the voltage drop V across the strong impurity (no electron tunneling) is connected to the voltage drop U measured on the leads by the simple relation $V = g^2 U$. This formula is the manifestation of the Coulomb blockade phenomenon. Physically it is evident that in the limit of strong interaction $g^2 \sim \hbar v_F / e^2 \ll 1$ the shift of the chemical potentials in the leads ($\Delta \mu_L = eU$) cannot change significantly the charge densities in the LL wire “split” into two parts by a strong impurity potential. So, to relate (at least qualitatively) the thermopower $S(g)$ evaluated for infinite LL to the thermopower $S_{LL}(g)$ of a LL smoothly connected to the leads of noninteracting electrons we first of all have to replace the voltage V in Eqs. (26), (28), (34), and (36) by $g^2 U$. Then

$S_{LL}(g) \sim S(g)/g^2 \xrightarrow{g \ll 1} S_0/g$. This means that for a real situation, when the voltage drop U is measured between the leads, the interaction enhances the thermopower. This supports our claim based on the calculations done in the phenomenological approach. Notice that there is still a discrepancy (by a factor $g^{-1} \gg 1$) between the above estimates and Eq. (40) in the limit of strong interaction. This inconsistency could be attributed to the qualitative nature of our estimations based on the phenomenological model (Sec. 3).

5. NONLINEAR Peltier EFFECT IN A LUTTINGER LIQUID

According to the Thompson relation for the cross-coefficients of the 2×2 matrix of transport coefficients in the linear response theory, the Peltier coefficient $\Pi(T, V)$ (defined as the ratio of heat current to the electric current in the absence of a temperature gradient across the system).

$$\Pi(T, V) = \left(\frac{J_Q}{J_e} \right)_{\Delta T=0}, \quad (41)$$

obeys the relation $\Pi = -k_B T S$, where S is the thermopower. It is rather easy to verify that this relation also holds for a LL if $eV \ll k_B T$, and thus the linear Peltier coefficient in the LL can be described using Eqs. (17)–(22). In the nonlinear regime, $eV \ll k_B T$, the Onsager symmetry relations between the transport coefficients cease to be valid. For noninteracting electrons the nonlinear Peltier effect has been studied in Ref. 29, and here we remark on its behavior for a LL with an impurity.

In the Landauer-Buttiker approach the electric and heat currents between reservoirs of noninteracting electrons at fixed temperatures and chemical potentials $\mu_{1(2)}$ are given by^{18,19}

$$J_e(T, V) = \frac{G_0}{e} \int_0^\infty d\varepsilon t^{\text{eff}}(\varepsilon) [f_1(\varepsilon) - f_2(\varepsilon)], \quad (42)$$

$$J_Q(T, V) = \frac{1}{h} \int_0^\infty d\varepsilon t^{\text{eff}}(\varepsilon) (\varepsilon - \mu) [f_1(\varepsilon) - f_2(\varepsilon)], \quad (43)$$

where

$$f_{1(2)}(\varepsilon) = \left[\exp\left(\frac{\varepsilon - \mu_{1(2)}}{k_B T}\right) + 1 \right]^{-1}$$

are the distribution functions of the electrons in the reservoirs, $\mu_{1(2)} = \mu \pm eV/2$ for a symmetric LL wire, and V is the voltage drop across the wire. In the following we will use Eq. (12) (as in Sec. 3) to model the transmission probability $t^{\text{eff}}(E)$ for a finite LL with an impurity placed in the middle of the wire.

Prior to proceeding with our analysis we note that the $J-V$ characteristics of a finite LL connected to FL reservoirs were studied in Refs. 30 and 22 using different approaches. In Ref. 22 the current–voltage dependence was calculated using a qualitative physical approach, similar to that employed by us in the present study, while a more rigorous treatment of charge transport through a finite LL with an impurity, based on renormalization group analysis, was elaborated in Ref. 30. Unlike the linear-response transport regime, where the above two approaches arrived at similar results, in the nonlinear regime they yield different behaviors

for the current as a function of voltage at low temperatures ($T \rightarrow 0$). Since the backscattering of the electrons by a local impurity in an infinite LL leads to a power-law dependence of the electric current on the voltage,⁵ it may be expected, and is indeed found in our model, that for a finite LL this behavior would cross over to ordinary Ohmic $J-V$ behavior for $eV \ll \Delta_L$. However, the analysis given in Ref. 30 revealed the occurrence of additional oscillations of the current as a function of the bias voltage, which do not appear in our model. Underlying these oscillations is the multiple scattering of the plasmon by the impurity potential and at the boundaries of the LL, and the phase of these oscillations is sensitive to the position of the impurity. While our approximation scheme does not reveal these mesoscopic oscillations, one may expect that such fine structure in the $J-V$ characteristics would be obliterated upon averaging over the position of the impurity.

With the above assumptions, and using Eq. (12) in Eq. (42), we obtain for the differential electric conductance at $k_B T \ll eV$,

$$\frac{\partial J_e}{\partial V} = G_0 t_0(E_F) \left(\frac{\Delta_L}{\Lambda} \right)^\alpha \quad \text{for } eV \ll \Delta_L, \quad (44)$$

and

$$\frac{\partial J_e}{\partial V} = G_0 t_0(E_F) \left(\frac{\Delta_L}{2\Lambda} \right)^\alpha \quad \text{for } eV \gg \Delta_L. \quad (45)$$

In a similar fashion we obtain for the heat current at $k_B T \ll eV$

$$\frac{\partial J_Q}{\partial V} \approx \frac{e}{h} t_0'(E_F) \left(\frac{eV}{2} \right)^2 \left(\frac{\Delta_L}{\Lambda} \right)^\alpha \quad \text{for } eV \ll \Delta_L, \quad (46)$$

and

$$\frac{\partial J_Q}{\partial V} \approx \frac{e}{h} t_0'(E_F) \left(\frac{eV}{2} \right)^2 \left(\frac{eV}{2\Lambda} \right)^\alpha \quad \text{for } eV \gg \Delta_L. \quad (47)$$

From Eqs. (44)–(47) it is readily seen that within the framework of our calculations the nonlinear Peltier coefficient for a symmetric LL constriction with an impurity placed at the middle of the LL wire does not depend on the interelectron interactions, and the differential Peltier coefficient is given by (at $k_B T \ll eV$)

$$\Pi(V) \equiv \frac{\partial J_Q / \partial V}{\partial J_e / \partial V} \approx \frac{1}{e} \left(\frac{eV}{2} \right)^2 \left(\frac{\partial \ln t_0(\varepsilon)}{\partial \varepsilon} \right)_{\varepsilon=E_F}. \quad (48)$$

We remark, however, that an influence of the interelectron interactions on the Peltier coefficient may occur for asymmetric LL wires or when the aforementioned mesoscopic oscillations are included.

6. CONCLUSIONS

In this paper we have used physically motivated models to investigate the heat transport through a multichannel LL wire and also the thermopower and Peltier effect in a single-channel LL with an impurity.

(i) For a multichannel LL wire, we predict that electron-electron interactions would stabilize the staircase-like behavior of the thermal conductance $K(T, \mu)$ as a function of the chemical potential (which can be controlled through the use

of a gate voltage). For strongly interacting particles the jumps in the thermal conductance at each value $\mu = \mu_n$ at which a new propagating channel is allowed to enter the constriction remain sharp even at comparatively “high” temperatures.

(ii) For a perfect (impurity-free) LL wire the thermopower (Seebeck coefficient) vanishes on the conductance plateaus and it peaks sharply at the conductance jumps. We also considered the thermopower effect for a single-channel LL constriction with an impurity placed at the middle of the constriction. For this system the Mott expression for the thermopower holds at low temperatures $k_B T \ll \Delta_L = \hbar s/L$, where s is the plasmon velocity and L is the length of the LL wire. However, at $k_B T > \Delta_L$ the thermopower is multiplicatively renormalized by the electron-electron interactions. The effect of this renormalization is predicted to be more pronounced for spinless particles than for spin-1/2 electrons. This conclusion is supported by an evaluation of the thermopower for an infinite LL with an impurity by the tunnel Hamiltonian method. The Peltier coefficient $\Pi(T, V)$ of a LL wire, in the *linear*-response regime, is determined by the thermopower, $\Pi(T) = -k_B T S_{LL}(T)$. Unlike the thermopower (Seebeck coefficient) the nonlinear Peltier coefficient is found in our model to be unaffected by the interelectron interactions, and thus it is determined by the energy dependence of the bare probability of transmission through the wire.

We gratefully acknowledge support of this work from the National Research Council through the Twinning Program 1999–2000. I. V. K. thanks the School of Physics at the Georgia Institute of Technology for its hospitality. The research of E. N. B., A. G. S., and U. L. was also supported by the U.S. Department of Energy, Grant No. FG05-86ER45234.

*E-mail: krive@ilt.kharkov.ua

¹R. Landauer, IBM J. Res. Dev. **1**, 223 (1957); Philos. Mag. **21**, 863 (1970).

²M. Buttiker, Semicond. Semimet. **1**, 223 (1957); **35**, 191 (1992); Y. Imry, *Introduction to Mesoscopic Physics*, Oxford University Press, New York (1997).

³F. D. M. Haldane, J. Phys. C **14**, 2585 (1981); Phys. Rev. Lett. **48**, 1840 (1981).

⁴W. Apel and T. M. Rice, Phys. Rev. B **26**, 7063 (1982).

⁵C. L. Kane and M. P. A. Fisher, Phys. Rev. Lett. **68**, 1220 (1992).

⁶L. I. Glazman, I. M. Ruzin, and B. Z. Shklovskii, Phys. Rev. B **45**, 8454 (1992).

⁷F. P. Milliken, C. P. Umbach, and R. A. Webb, Solid State Commun. **97**, 309 (1996); A. M. Chang, L. N. Pfeiffer, and K. W. West, Phys. Rev. Lett. **77**, 2538 (1996).

⁸M. Bockrath, D. H. Cobden, J. Lu, A. G. Rinzler, R. E. Smalley, L. Balents, and P. L. McEuen, Nature (London) **397**, 598 (1999).

⁹C. L. Kane and M. P. A. Fisher, Phys. Rev. Lett. **76**, 3192 (1996).

¹⁰D. L. Maslov and M. Stone, Phys. Rev. B **52**, R5539 (1995); V. V. Ponomarenko, Phys. Rev. B **52**, R8666 (1995); I. Safi and H. J. Schulz, Phys. Rev. B **52**, R17040 (1995).

¹¹R. Fazio, F. W. J. Hekking, and D. E. Khmel'nitskii, Phys. Rev. Lett. **80**, 5611 (1998).

¹²I. V. Krive, Fiz. Nizk. Temp. **24**, 498 (1998) [Low Temp. Phys. **24**, 377 (1998)]; Phys. Rev. B **59**, 12338 (1999).

¹³H. J. Schulz, Int. J. Mod. Phys. B **5**, 57 (1991).

¹⁴J. M. Ziman, *Principles of the Theory of Solids*, Cambridge University Press, Cambridge (1986).

¹⁵C. A. Stafford, Phys. Rev. B **48**, 8430 (1993).

¹⁶R. Egger and H. Grabert, Phys. Rev. B **58**, 10761 (1998).

¹⁷K. A. Matveev and L. I. Glazman, Physica B **189**, 266 (1993).

¹⁸U. Sivan and Y. Imry, Phys. Rev. B **33**, 551 (1986).

¹⁹E. N. Bogachek, I. O. Kulik, A. G. Shkorbatov, Fiz. Nizk. Temp. **11**, 1189 (1985) [Sov. J. Low Temp. Phys. **11**, 656 (1985)].

²⁰D. Yue, L. I. Glazman, and K. A. Matveev, Phys. Rev. B **49**, 1966 (1994).

²¹A. Furusaki and N. Nagaosa, Phys. Rev. B **47**, 4631 (1993).

²²M. Jonson, P. Sandstrom, R. I. Shekhter, and I. V. Krive, Superlattices Microstruct. **23**, 957 (1998).

²³H. van Houten, L. W. Molenkamp, C. W. J. Beenakker, and C. T. Foxon, Semicond. Sci. Technol. **7**, B215 (1992).

²⁴E. N. Bogachek, A. G. Scherbakov, and U. Landman, Phys. Rev. B **54**, R11094 (1996).

²⁵A. Furusaki and N. Nagaosa, Phys. Rev. B **54**, R5239 (1996).

²⁶A. O. Gogolin, A. A. Nersisyan, and A. M. Tsvetlik, *Bosonization and Strongly Correlated Systems*, Cambridge University Press (1998).

²⁷G. L. Ingold and Yu. V. Nazarov, in *Single Charge Tunneling*, edited by H. Grabert and M. H. Devoret, NATO ASI series B, V. 294, Plenum Press, p. 21.

²⁸C. L. Kane and M. P. A. Fisher, Phys. Rev. B **46**, 15233 (1992).

²⁹E. N. Bogachek, A. G. Scherbakov, and U. Landman, Solid State Commun. **108**, 851 (1998); Phys. Rev. B **60**, 11678 (1999).

³⁰V. V. Ponomarenko and N. Nagaosa, Phys. Rev. B **56**, R12756 (1997).

This article was published in English in the original Russian journal. Reproduced here with stylistic changes by AIP.

Magnetic susceptibility of $\text{La}_{0.875}\text{Sr}_{0.125}\text{MnO}_3$ under hydrostatic pressure to 1 GPa

A. E. Petrova,* E. S. Itskevich, V. A. Ventcel', V. F. Kraidenov, and A. V. Rudnev

L. V. Vereshchagin Institute of High Pressure Physics, Russian Academy of Sciences, 142190 Troitsk, Moscow District, Russia

(Submitted March 6, 2001)

Fiz. Nizk. Temp. **27**, 1123–1127 (September–October 2001)

The magnetic susceptibility of single-crystal $\text{La}_{0.875}\text{Sr}_{0.125}\text{MnO}_3$ is measured under hydrostatic pressure up to 1 GPa. The Curie temperature T_C and the temperatures T_M and T_{OO} of quantum phase transitions are determined. The pressure dependence of these transition temperatures is determined: $dT_C/dP=18$ K/GPa, $dT_M/dP=16$ K/GPa, and $dT_{OO}/dP=22$ K/GPa. The phase diagram obtained demonstrates that an applied pressure can have the same effect on the phase transitions as a change in the degree of doping x . © 2001 American Institute of Physics. [DOI: 10.1063/1.1414572]

A great interest in perovskite manganates has arisen in connection with the discovery of colossal magnetoresistance in these materials. The “double exchange” theory proposed in Refs. 1 and 2 was later supplemented to include the electron–phonon interaction and the resulting Jahn–Teller deformations of the lattice.³ These disruptions of the lattice are often accompanied by structural transitions and the formation of small polarons. Manganates have complex phase diagrams involving structural, orbital, spin, and charge orderings.^{4,5} Several orderings can occur simultaneously, and they can have a static or a dynamic character. Experimentally obtained phase diagrams in the temperature and external pressure remain extremely rare for manganates.⁶

The effect of pressure on the thermopower and resistivity of a $\text{La}_{1-x}\text{Sr}_x\text{MnO}_3$ sample with $x=0.125$ was investigated previously.⁷ There have been many studies of samples with this special composition.^{5,7–16} For an ordered distribution of the Sr impurity over the volume of the crystal, a doubling of the lattice period should occur, and that could lead to the formation of a crystalline superstructure and, as a consequence, to the appearance of interesting new effects. The P – T phase diagram has its greatest complexity near that concentration.¹⁷

At higher concentrations ($x > x_C = 0.18$) the samples are found in a ferromagnetic metallic state in which no magnetic transitions below the Curie temperature T_C have yet been observed. Indeed, a study¹⁸ of the temperature dependence of the magnetic susceptibility χ on samples of $\text{La}_{1-x}\text{Sr}_x\text{MnO}_3$ with $x=0.2$ and 0.3 under hydrostatic pressure up to 1.8 GPa did not reveal any features in the behavior of $\chi(T)$. However, a clear understanding of the nature of magnetic transitions upon changing temperature has not yet been achieved. We have therefore measured the temperature dependence of the magnetic susceptibility under hydrostatic pressures of up to 1 GPa on the same $\text{La}_{0.875}\text{Sr}_{0.125}\text{MnO}_3$ samples that were used for the thermopower and resistivity measurements in Ref. 7.

MEASUREMENT TECHNIQUES

The magnetic susceptibility of single-crystal samples of $\text{La}_{0.875}\text{Sr}_{0.125}\text{MnO}_3$ was measured by a modulation method

with the signal recorded at the fundamental modulation frequency, equal to 19 Hz.¹⁹ The amplitude of the modulating signal was 800 A/m. The pressure was created in a fixed-pressure chamber.²⁰ The pressure-transmitting medium used was a 1:1 kerosene–oil mixture. The modulating coil was placed on the housing of the chamber, and the measuring coil was placed inside the chamber with the sample. As the chamber was cooled, the pressure was measured by a manganese resistance manometer, and the temperature by a copper–(copper+iron) thermocouple placed inside the high-pressure chamber. The rate of cooling did not exceed 1 K/min.

As the temperature was lowered, the pressure in the chamber decreased.²¹ The critical points on the P – T phase diagram are shown with allowance for the drop in pressure. In Fig. 1, which illustrates the temperature dependence $\chi(T)$, the pressure corresponds to room temperature. The pressure dependence of the emf of the thermocouple is small. For example, at 1 GPa for a (Au+Fe)–Cu thermocouple at liquid-helium temperatures the change is less than 2% (Ref. 22).

The $\text{La}_{0.875}\text{Sr}_{0.125}\text{MnO}_3$ were furnished by the laboratory of A. M. Balbashov. The quality of the samples was established by a detailed x-ray structural analysis.²³

RESULTS

Figure 1 shows the results of the measurements of the temperature dependence of the magnetic susceptibility χ for two single-crystal samples at different pressures. The measurements were made under identical conditions except for the difference in pressure. The change of the amplitude of the signal may be due to mechanical stresses or to annealing during the pressure cycling. For constructing the phase diagram the important thing is the position of the characteristic points and not the amplitude of the signal. On cooling below 200 K a rapid growth of the susceptibility begins, and then one observes two anomalous peaks, after which the susceptibility $\chi(T)$ follows the usual trend for a ferromagnet. As in Ref. 15, we attribute the sharp rise in $\chi(T)$ to a transition from the paramagnetic to the ferromagnetic state. The Curie temperature T_C was determined from the inflection point on the $\chi(T)$ curve. At standard pressure one has $T_C=187$ K,

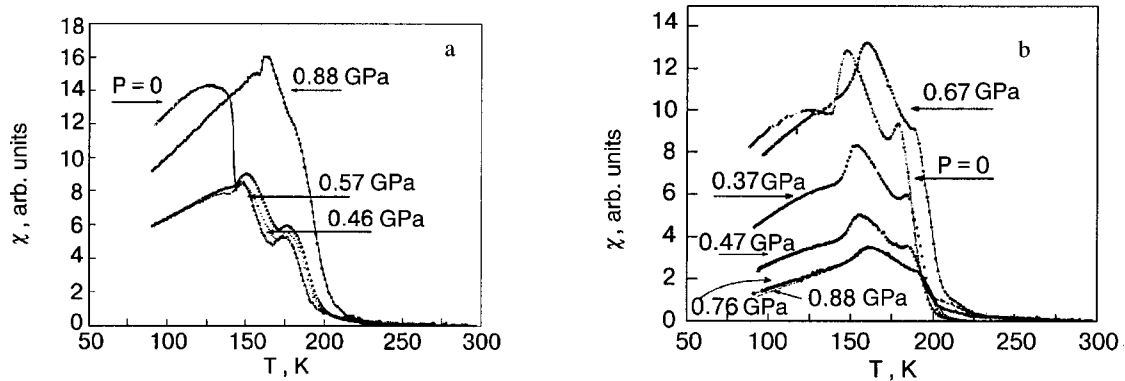


FIG. 1. Magnetic susceptibility χ versus temperature T for two single-crystal samples of $\text{La}_{0.875}\text{Sr}_{0.125}\text{MnO}_3$ (a and b) of arbitrary orientation at different pressures. The pressure values are given for room temperature.

which agrees with the data of Refs. 5,7,14, and 16. With increasing pressure T_C increases at a rate of $dT_C/dP=18$ K/GPa.

The maximum on the $\chi(T)$ curve at $T \approx 150$ K is apparently due to a second-order phase transition from a conducting ferromagnetic phase to a ferromagnetic insulator.^{6,15} It is customary in the literature to denote this temperature as T_{OO} . With increasing pressure T_{OO} increases at a rate of $dT_{OO}/dP=22$ K/GPa.

The origin of the maximum at 180 K at standard pressure will be discussed in detail below. We denote the temperature at which this maximum is observed by T_M . With increasing pressure $dT_M/dP=16$ K/GPa.

The pressure dependence of the temperatures T_C , T_{OO} , and T_M are presented on the P - T diagram (see Fig. 2).

DISCUSSION OF THE RESULTS

The presence of features on the $\chi(T)$ curve (see Fig. 1) near 150 and 180 K suggests that two quantum magnetic transitions occur in addition to the transition from the paramagnetic to the ferromagnetic state ($T_C=187$ K). Similar behavior of $\chi(T)$, with peaks at $T_{OO}=149$ K and $T_M=175$ K at atmospheric pressure, was observed on a $\text{La}_{0.875}\text{Sr}_{0.125}\text{MnO}_3$ sample in Ref. 15.

Figure 3 shows the temperature dependence of χ and of the thermopower α ,⁷ which has a minimum at $T \approx 175$ K. With increasing pressure the temperature at which the mini-

mum of $\alpha(T)$ is observed increases at practically the same rate as the temperature T_M of the maximum of $\chi(T)$: 16 and 17 K/GPa, respectively. This suggests that the features on the $\chi(T)$ and $\alpha(T)$ curves may be due to the same transition.

The nature of the transition at $T_M=175$ –180 K is not completely clear. It may be due to phase separation into a conducting and a nonconducting phase. The conducting phase is usually identified with ferromagnetic (FM) polarons, which are nucleated already in the paramagnetic (PM) phase at $T > T_C$ (Ref. 24) and whose existence in the PM and antiferromagnetic (AFM) matrices has been detected over a wide temperature range, 4.2–300 K.^{25–27} Apparently the growth of the thermopower below T_M as the resistivity continues to decrease⁷ is also indicative of phase separation of the sample. Optical measurements in Ref. 16 revealed a bifurcation of the peak of the phonon mode at a frequency of 350 cm^{-1} , due to the bending of the MnO_6 octahedra, starting at a temperature of $T=180$ K. This bifurcation increased as the temperature was lowered. The authors of Ref. 16 attributed this effect to phase separation.

Ferromagnetic ordering makes the Jahn–Teller distortions of the lattice energetically unfavorable. When the temperature is lowered below the Curie point, the Jahn–Teller distortions begin to decrease strongly.^{25,28} The decrease continues below the temperature T_M , until a structural transition $O'-O^*$ occurs at $T_{OO}=150$ K^{7,14,15} (in Ref. 5 a value $T_{OO}=160$ K was found). The O^* phase is very close to the high-temperature orthorhombic phase O but with somewhat larger Jahn–Teller lattice distortions, the value of which re-

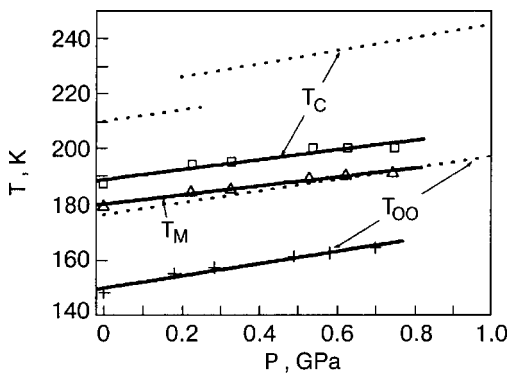


FIG. 2. Temperatures of the magnetic transitions versus applied pressure. The solid lines show our measurements ($x=0.125$), and the dotted lines the data of Ref. 6 ($x=0.14$).

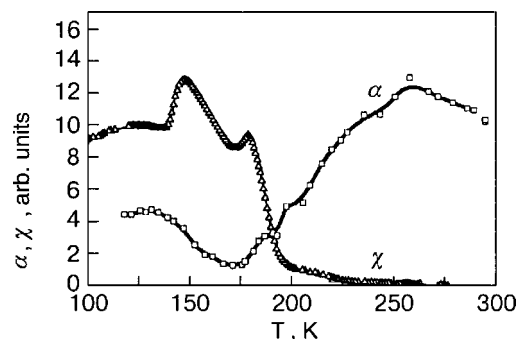


FIG. 3. Temperature dependence of the susceptibility χ and thermopower α (Ref. 7) at standard pressure.

mains practically unchanged as the temperature is lowered further. This structural transition is accompanied by a strong rearrangement of the electronic structure: the ferromagnetic metal (FMM) is transformed into a ferromagnetic insulator (FMI).

In addition to the peak on the temperature dependence of the magnetic susceptibility, which we also observed in Refs. 9 and 15, the presence of a magnetic transition at $T_{OO} = 150$ K is also evidenced by anomalies in the behavior of the magnetic moment \mathbf{M} , which were observed in Refs. 5, 12, and 14. The start of the localization of the carriers at $T = 150$ K is confirmed by the temperature dependence of the resistivity, which increases rapidly as the temperature is lowered below 150 K.^{7,10,12,14}

On the basis of neutron measurements made in Ref. 8, it was concluded that the metal–insulator transition at $T = T_{OO}$ in samples with $x = 0.125$ is due to the formation of a commensurate polaron-ordered phase. In such a phase, Mn–O layers containing only Mn^{3+} ions and having Jahn–Teller distortions like those in the O' phase alternate with undistorted layers in which polarons (Mn^{4+} ions with holes localized on them) form a regular charge-ordered square lattice. Resonance x-ray scattering on such samples at 150 K has revealed the appearance of a static antiferromagnetic orbital ordering of hybridized e_g orbitals.¹¹ As the temperature is lowered, the AFM type of orbital ordering gives way to a FM type, while the spin ordering remains of the FM type. The AFM type of orbital ordering lowers the electron kinetic energy E_{kin} and greatly weakens the double exchange. The ferromagnetism of the spins is then due entirely to superexchange, which is favored by the orbital ordering.¹² The absence of double exchange promotes localization of the carriers and a FMM–FMI transition.

The question of the influence of charge ordering on the dielectric properties of doped manganates was discussed in Ref. 13. A calculation by the Hartree–Fock model gave two stable solutions for a $\text{La}_{0.875}\text{Sr}_{0.125}\text{MnO}_3$ sample, with possible orbital and charge orderings. Even in this case, however, the FM state is realized only in the presence of a finite lattice deformation, which persists at $T \leq T_{OO}$ (Ref. 28). It is this deformation that can give rise to a superstructure (e.g., a doubling of the lattice period) and to the opening of a gap in the carrier spectrum.

In $\text{La}_{1-x}\text{Sr}_x\text{MnO}_3$ compounds, because of the different equilibrium lengths of the La–O and Mn–O bonds, the cubic lattice is distorted and is transformed to rhombohedral or orthorhombic. The Mn–O–Mn line is bent at an angle φ . Hydrostatic pressure decreases the Mn–O distance, the lattice asymmetry, and the angle φ . This leads to an increase in the exchange integral of neighboring Mn ions and in the hopping matrix element. Pressure also decreases the angle between the t_{2g} spins of the neighboring Mn ions, so that in the temperature region near T_C the double exchange and the number of ferromagnetic clusters increase, and that is accompanied by a decrease in resistivity. The growth of the ferromagnetic phase is accompanied by a decrease in the Jahn–Teller lattice distortions.²⁹ With decreasing temperature this leads to an earlier structural transition $O'–O^*$ and to the appearance of orbital ordering. Because of the spin–orbit interaction, orbital ordering leads to FM ordering of the

spins and to their localization, i.e., to a ferromagnetic insulator phase. The dependence of the bending angle of the Mn–O–Mn line on the degree of doping x in the compounds $\text{La}_{1-x}\text{Sr}_x\text{MnO}_3$ in the orthorhombic structure was studied in Ref. 9.

In the presence of Jahn–Teller distortions the influence of pressure on T_C is enhanced significantly because of the optical vibrations of the oxygen ions.³⁰ This leads to a broadening of the effective band W_{eff} and to an increase in T_C . The system undergoes a transition from strong ($J \gg W_{\text{eff}}$) to weak ($J \ll W_{\text{eff}}$) coupling, where J is the exchange energy. Increasing the Sr concentration in $\text{La}_{1-x}\text{Sr}_x\text{MnO}_3$ increases the average ionic radius, an effect analogous to an external pressure, i.e., an increase in the covalency of the bonds, W_{eff} , and T_C .

A calculation using our data and previously published data shows that for matching of the characteristic values of T_{OO} , T_M , and T_C for samples with $x = 0.125$, 0.14, and 0.15, a change $\Delta x = +0.01$ corresponds to a pressure increase $\Delta P \sim 0.7$ GPa.

Our results on the pressure dependence of T_C agree and with the data of Ref. 7 to within the error limits ($dT_C/dP = 18$ and 16 K/GPa, respectively). As the degree of doping x increases, the pressure derivative initially remains unchanged (16 K/GPa for $x = 0.15$) and then drops sharply in the FM phase for $x > x_C$ (2 K/GPa for $x = 0.4–0.5$).¹⁸ Our results on the temperatures T_{OO} and T_C are very close to the data of Ref. 6, obtained on a sample with $x = 0.14$. Both of these temperatures increase substantially with increasing applied pressure, showing that pressure, like doping (for $x \leq 0.15$), tends to stabilize the ferromagnetic polarons.

CONCLUSIONS

1. The temperature dependence of the magnetic susceptibility of $\text{La}_{1-x}\text{Sr}_x\text{MnO}_3$ single crystals with $x = 0.125$ has peaks at two temperatures. The first peak, at $T = T_{OO} = 150$ K, is attributed by the authors to a FMM–FMI transition. The second peak, at $T = T_M = 180$ K, is attributed to magnetic ordering in the FM matrix.
2. Under hydrostatic pressure to 1 GPa the temperatures of the magnetic transitions T_{OO} , T_M , and T_C increase at rates of 22, 16, and 18 K/GPa, respectively. This means that pressure stabilizes the ferromagnetic phase.
3. The $P–T$ phase diagrams obtained here and in Ref. 6 demonstrate that a change in the degree of doping x and an applied pressure P can have an identical effect on the quantum phase transitions.

The authors thank É. L. Nagaev and L. I. Koroleva for a helpful discussion of the results, and M. I. Baneeva for analysis of the phase composition of the samples.

This study was supported by Grant No. 00-02-16019 from the Russian Foundation for Basic Research, as part of the Russian Federation Program on High-Temperature Superconductivity.

*E-mail: apetrova@ns.hppi.troitsk.ru

- ¹C. Zener, *Phys. Rev.* **82**, 403 (1951).
²P.-G. de Gennes, *Phys. Rev.* **118**, 141 (1960).
³A. J. Millis, P. B. Littlewood, and B. J. Shraiman, *Phys. Rev. Lett.* **74**, 5144 (1995); A. J. Millis, B. J. Shraiman, and R. Mueller, *Phys. Rev. Lett.* **77**, 175 (1996).
⁴A. Urushibara, Y. Moritomo, T. Arima, A. Asamitsu, G. Kido, and Y. Tokura, *Phys. Rev. B* **51**, 14103 (1995).
⁵H. Kawano, R. Kajimoto, M. Kubota, and H. Yoshizawa, *Phys. Rev. B* **53**, 2202 (1996); **53**, R14709 (1996).
⁶J.-S. Zhou and J. B. Goodenough, *Phys. Rev. B* **62**, 3834 (2000).
⁷E. S. Itskevich and V. F. Kraidenov, *Fiz. Tverd. Tela (St. Petersburg)* **43**, 1220 (2001) [*Phys. Solid State* **43**, 1267 (2001)].
⁸Y. Yamada, O. Hino, S. Nohdo, R. Kanao, T. Inami, and S. Katano, *Phys. Rev. Lett.* **77**, 904 (1996).
⁹D. N. Argyriou, J. F. Mitchell, C. D. Potter, D. G. Hinks, J. D. Jorgensen, and S. D. Bader, *Phys. Rev. Lett.* **76**, 3826 (1996); J. F. Mitchell, D. N. Argyriou, C. D. Potter, D. G. Hinks, J. D. Jorgensen, and S. D. Bader, *Phys. Rev. B* **54**, 6172 (1996).
¹⁰L. Pinsard, J. Rodríguez-Carvajal, A. H. Moudden, A. Anane, A. Revcolevschi, and C. Dupas, *Physica B* **234–236**, 856 (1997).
¹¹Y. Endoh, K. Hirota, S. Ishihara, S. Okamoto, Y. Murakami, A. Nishizawa, T. Fukuda, H. Kimura, H. Nojiri, K. Kaneko, and S. Maekawa, *Phys. Rev. Lett.* **82**, 4328 (1999).
¹²H. Nojiri, K. Kaneko, M. Motokawa, K. Hirota, Y. Endoh, and K. Takahashi, *Phys. Rev. B* **60**, 4142 (1999).
¹³T. Mizokawa, D. J. Khomskii, and G. A. Sawatzky, *Phys. Rev. B* **61**, R3776 (2000).
¹⁴S. Uhlenbruck, R. Teipen, R. Klingeler, B. Buchner, O. Friedt, M. Hucker, H. Kierspel, T. Niemoller, L. Pinsard, A. Revcolevschi, and R. Gross, *Phys. Rev. Lett.* **82**, 185 (1999).
¹⁵V. Skumryev, J. Noguez, J. S. Muñoz, B. Martínez, R. Senis, J. Fortcuberta, L. Pinsard, A. Revcolevschi, and Y. M. Mukovskii, *Phys. Rev. B* **62**, 3879 (2000).
¹⁶J. H. Jung, K. H. Kim, H. J. Lee, J. S. Ahn, N. J. Hur, T. W. Noh, M. S. Kim, and J.-G. Park, *Phys. Rev. B* **59**, 3793 (1999).
¹⁷J.-S. Zhou, J. B. Goodenough, A. Asamitsu, and Y. Tokura, *Phys. Rev. Lett.* **79**, 3234 (1997).
¹⁸Y. Moritomo, A. Asamitsu, and Y. Tokura, *Phys. Rev. B* **51**, 16491 (1995).
¹⁹A. G. Budarin, V. A. Ventcel', O. A. Voronov, and A. V. Rudnev, *Izmeritel'naya Tekhnika*, No. 4, 66 (1982).
²⁰E. S. Itskevich, *Prib. Tekh. Ékper.*, No. 4, 148 (1963).
²¹V. A. Ventcel', E. S. Itskevich, A. E. Petrova, and A. V. Rudnev, *Fiz. Tverd. Tela (St. Petersburg)* **37**, 351 (1995) [*Phys. Solid State* **37**, 191 (1995)].
²²E. S. Itskevich and V. F. Kraidenov, *Prib. Tekh. Ékper.*, No. 6, 164 (1978).
²³A. M. Balbashov and S. K. Egorov, *J. Cryst. Growth* **52**, 498 (1981).
²⁴J. M. De Teresa, M. R. Ibarra, P. A. Algarabel, C. Ritter, C. Marquina, J. Blassco, J. García, A. del Moral, and Z. Arnold, *Nature (London)* **386**, 256 (1997).
²⁵D. Louca, T. Egami, E. L. Brosha, H. Ruder, and A. R. Bishop, *Phys. Rev. B* **56**, R8475 (1997).
²⁶M. Hennion, F. Moussa, G. Biotteau, J. Rodríguez-Carvajal, L. Pinsard, and A. Revcolevschi, *Phys. Rev. Lett.* **81**, 1957 (1998).
²⁷G. Allodi, R. De Renzi, and G. Guidi, *Phys. Rev. B* **57**, 1024 (1998).
²⁸E. L. Nagaev, *Phys. Status Solidi B* **186**, 9 (1994).
²⁹X. Xiong, B. Dabrowsky, O. Chmaisén, Z. Bukowski, S. Kolesnik, R. Dybzinski, and C. W. Kimball, *Phys. Rev. B* **60**, 10186 (1999).
³⁰V. Laukhin, J. Foutcuberta, J. I. García-Muñoz, and X. Obradors, *Phys. Rev. B* **56**, R10009 (1997).

Translated by Steve Torstveit

Relaxation processes in amorphous films of monoatomic metals

V. M. Kuz'menko* and B. G. Lazarev†

Kharkov Physicotechnical Institute National Research Center, ul. Akademicheskaya 1, 61108 Kharkov, Ukraine

(Submitted July 23, 2001)

Fiz. Nizk. Temp. **27**, 1128–1137 (September–October 2001)

The relaxation of the electrical resistance in amorphous films of Bi, Yb, Be, and Mn is investigated at low temperatures. It is shown that this process during an isothermal hold is ordinarily a simple exponential process with a single characteristic relaxation time. In amorphous metal–hydrogen films a subbarrier tunneling of hydrogen atoms apparently occurs. It is conjectured that this is the cause of the delay in the onset of superconductivity at $T=4.2$ K after completion of the condensation of amorphous Be–H films. © 2001 American Institute of Physics. [DOI: 10.1063/1.1414573]

1. INTRODUCTION

Amorphous metallic alloys, obtained by the rapid quenching of a melt or deposition of a vapor on a cold substrate, are configurationally frozen far from internal equilibrium. If they have sufficient atomic mobility, they can lower their free energy through some change in the parameters of the amorphous structure. Such structural relaxation can substantially alter many properties. The main types of experiments on the study of relaxation processes in amorphous materials deal with relaxation of stress, volume, enthalpy, viscosity, electrical properties, and superconducting properties.^{1–5} The links between the various changes in properties remain little studied. There have been a few studies in which the kinetics of different processes (e.g., relaxation of the enthalpy and volume² or relaxation of the electrical resistance and elastic constants⁶) have been investigated on the same material and in the same temperature interval, and these have shown a significant similarity in the relaxation behavior of the quantities measured, attesting to the existence of a unified mechanism for their change. In metallic amorphous alloys, in addition to the irreversible relaxation usually due to a change in topological structure, a reversible relaxation, due to a change in local chemical order, has also been observed.³

The atomic basis of structural relaxation is most easily understood in amorphous monoatomic metals, in which there is no influence from atoms of another species. In particular, it has been shown calorimetrically that reversible relaxation is not observed in glasses consisting of only a metal or a metalloid.³

Systematic studies of relaxation processes in amorphous films of monoatomic metals at temperatures close to liquid helium temperature have been extremely rare. Nevertheless, a few experimental papers on this topic are known.^{7–11}

The present paper is devoted to a preliminary study of the relaxational change in the resistance of amorphous films of Bi, Ga, Be, V, Yb, and Mn both during their heating to temperatures slightly below the crystallization temperature T_{cr} and during an isothermal hold at lower temperatures. The value of T_{cr} depends on the purity and thickness of the amorphous layer of metal^{12,13} and for the amorphous films (except

for Mn) investigated in this study ranges from 13 to 70 K. The relaxation behavior of the resistance of amorphous films was studied in the temperature interval $4.2-T_{cr}$. Naturally, at such low temperatures the relaxational changes in the resistance are small. However, first, the high accuracy of the measurements makes it possible to reveal the main behavioral regularities of this change, and, second, as will be shown below, the tiny relaxational changes of the resistance are sometimes accompanied by large changes in the superconducting and kinetic parameters of the films.

2. METHODOLOGICAL NOTES

It is known that the only way of obtaining amorphous films of pure monoatomic metals is condensation of their vapors in an ultrahigh vacuum on a substrate cooled by liquid helium. The details of the technique used in this experiment have been described by us previously.^{12,14} The technique ensures a residual pressure of $\approx 10^{-10}$ Pa in the film-condensation vessel prior to the start of condensation. Although the pressure was not varied during condensation, the parameters of the films obtained (the resistance, T_{cr} , critical thickness,¹² superconducting transition temperature T_c , etc.) demonstrate that our films are every bit as pure as those obtained in a controlled vacuum with a residual gas pressure of 1.33×10^{-8} – 1.33×10^{-9} Pa.¹⁵

In addition to studying the processes of resistance relaxation in pure amorphous films of the metals listed above, we also investigated the influence of hydrogen (up to 50 at.%) on these processes in Be, Bi, and Yb films. The hydrogen was introduced into the amorphous films of these metals by condensing them at a partial pressure of pure hydrogen $\approx 4.67 \times 10^{-5}$ Pa (and partial pressures of the components of the residual air of less than 10^{-10} Pa). The technique of obtaining the metal–hydrogen films is described in detail in Ref. 14.

The resistance of the samples obtained was measured using a potentiometer in a four-probe scheme. The temperature of the samples was determined by a platinum resistance thermometer. The accuracy of the temperature measurements in the interval 4.2–20.4 K was 0.05–0.1 K; at higher temperatures it was 0.5 K or better. The average temperature of

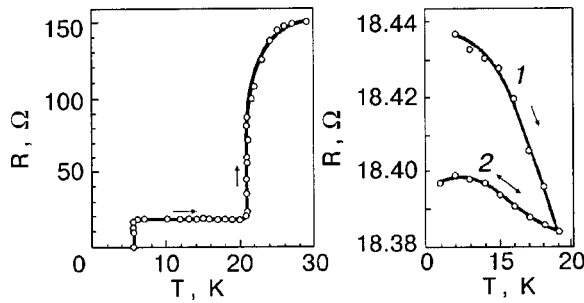


FIG. 1. The temperature dependence of the electric resistance of a bismuth film, including the crystallization process (a); the relaxational change in the resistance of this same film in the amorphous state (b) (see explanation in text).

the Yb, Bi, Ga, Be, Mn, and V films at the time of their condensation was measured in auxiliary experiments with the aid of a film thermometer deposited directly on the substrate prior to condensation of the metal to be investigated; it did not exceed 5, 5.5, 6, 10, 15, and 18 K, respectively.¹⁶ The superconductivity of the pure amorphous films of Bi, Ga, and Be during their condensation confirms that their average temperature did not exceed their respective values of T_c . The heating of the samples to the crystallization temperature was done at a rate of 0.5–1 K/min. To fix the relaxation processes more completely, the approach to the temperature of the isothermal hold was made at a much higher rate. Film thicknesses greater than 60 nm were determined from the optical density of the films, and the thickness of the thinner films was measured by an interferometric method.

3. EXPERIMENTAL RESULTS

The existence of relaxation processes in amorphous films of pure metals is clearly manifested even during their heating, starting at the very lowest temperatures. Figure 1a shows the temperature dependence of the resistance R on heating of an amorphous film of bismuth ≈ 10 nm thick. The sharp increase of the resistance at a temperature ≈ 21 K ($= T_{cr}$) is due to crystallization of the sample. The part of the curve at $T < T_{cr}$ characterizes the amorphous state of the film. Figure 1b shows on an enlarged scale the irreversible change of the resistance of this sample on heating to $T = 19$ K (curve 1) and the reversible path of $R(T)$ in the interval 11–19 K (curve 2). Curve 2 characterizes the temperature dependence of the resistance of the relaxed film. Curve 1 reflects both the negative temperature coefficient of resistance of this particular sample and the lowering of R with increasing temperature owing to structural relaxation.

The relaxational decrease of the resistance of an amorphous film can be characterized by the parameter $\delta = \Delta R/R_0$, where R_0 is the resistance of an as-condensed film at a temperature above the superconducting transition (for Bi and Be) or at $T = 4.2$ K (for V, Yb, and Mn);¹⁾ $\Delta R = R_0 - R_T$, where R_T is the resistance of the film at the same temperature after it has been heated to a certain temperature $T_h < T_{cr}$ or after an isothermal hold at $T_i < T_{cr}$.

The relaxational decrease of the resistance is manifested particularly clearly during heating of the thinnest films (< 5 nm) (see Ref. 9, for example). This behavior may be due, in particular, to the fact that the rate of heat removal

TABLE I. Percent relaxational decrease of the resistance (δ) of amorphous films condensed on a liquid-helium cooled substrate, as a result of their heating to $T_h < T_{cr}$.

Metal	d , nm	T_h , K	T_{cr} , K	δ , %
Bi	10	20	21	0.2
V	16	34	40	0.55
Yb	6	12.5	19	0.39
Yb	26	9	13	0.09
Be–H	30	55	60	0.79
Be–H	71	58	65	0.29

from the film during condensation is inversely proportional to its thickness.¹⁷ The heat removal from the surface of thick films is slower, and so there is a greater possibility for relaxational processes to take place during condensation. For the metals investigated in the present study the values of δ are small, usually only a few tenths of a percent (see Table I) as a consequence of the small difference between the temperature of the film during its condensation and the crystallization temperature, which sets a ceiling on the temperature at which relaxation processes can be studied in the homogeneous amorphous state. Amorphous Mn films condensed at $T < 15$ K are an exception; for them $T_{cr} \approx 380$ K.¹⁸

Figure 2a shows the relaxational decrease of the resistance of an amorphous Mn film ≈ 100 nm thick at $T = 4.2$ K as a function of the heating temperature. For the maximally relaxed film the value of δ is $\approx 10\%$. The relaxational decrease of the resistance on heating of amorphous Mn films is accompanied by an appreciable change in the Hall constant R_H . This is shown in Fig. 2b, where the values of R_H of the film at $T = 4.2$ are plotted as a function of the heating temperature.

Relaxation processes in amorphous films of pure metals are clearly manifested even during an isothermal hold at T_i

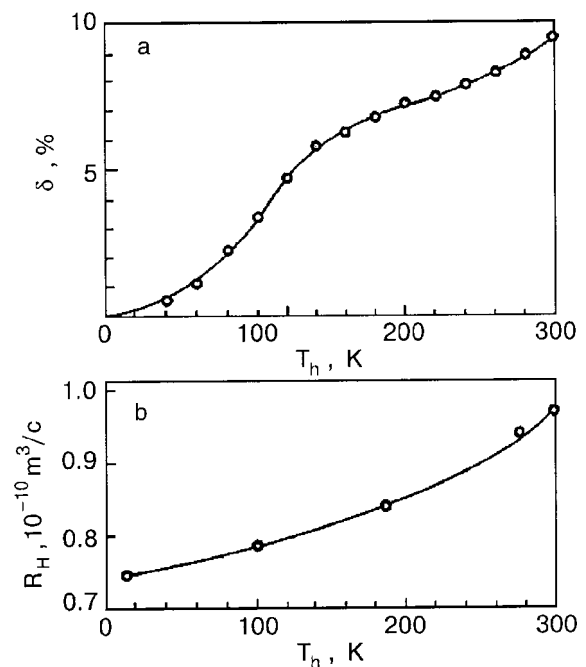


FIG. 2. Relaxational change in the resistance (a) and Hall constant (b) of an amorphous manganese film at $T = 4.2$ K as functions of the heating temperature T_h .

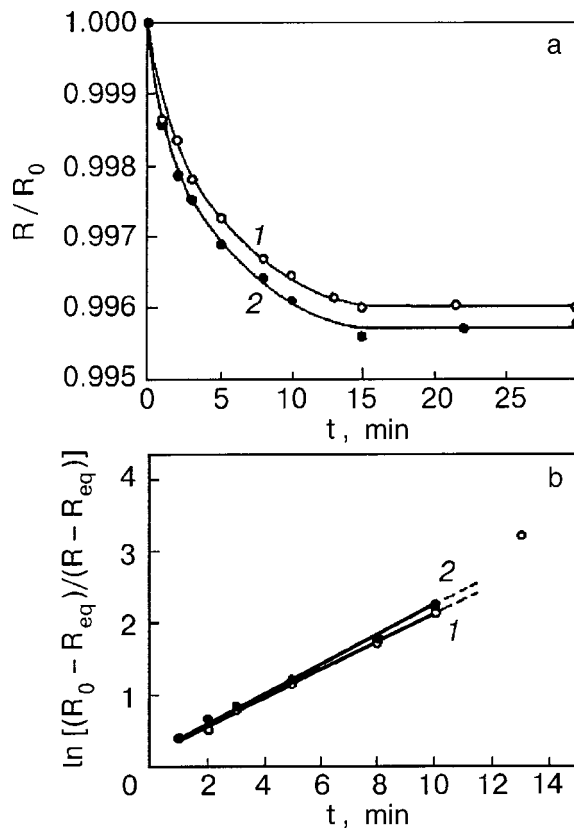


FIG. 3. Reduced electrical resistance of amorphous vanadium films of thickness 12 nm (curve 1) and 20 nm (curve 2) as functions of the time of a hold at $T_i=4.2$ K (a) and a plot of $\ln[(R_0 - R_{eq})/(R - R_{eq})]$ versus t for these same films (b).

$=4.2$ K, i.e., at a temperature even lower than the average temperature of the film during its condensation. As is known from studies of the structural relaxation of amorphous metallic alloys, at each temperature of an isothermal hold an investigated property changes rapidly at first and then progressively slows in time, although in many cases there is no discernable tendency for the property to stabilize at some final value.³ This type of relaxation ordinarily takes place for annealing below the glass temperature T_g . A glass relaxes in the direction of the greatest equilibrium but, as a rule, does not reach it.

Amorphous films of monoatomic metals behave in an analogous way during an isothermal hold at $T_i < T_{cr}$, but in their case equilibrium is often attained. As an example, Fig. 3a shows the relative change of the resistance of amorphous vanadium films at a temperature of 4.2 K as a function of the hold time after condensation was stopped.

As we see from Fig. 3a, the resistance R of the V films decreases rapidly during the first 15 min of the hold, after which R reaches a certain final value (at which $\delta \approx 0.4\%$).

In many cases the relaxational change in the properties of amorphous solids is described satisfactorily by the expression²

$$R - R_{eq} = (R_0 - R_{eq}) \exp\left(-\frac{t}{\tau}\right)^n, \quad (1)$$

where R is the instantaneous value of the property (in our case the resistance) at time t , R_0 and R_{eq} are the initial ($t=0$) and equilibrium ($\tau \rightarrow \infty$) values of R ;² τ is the charac-

teristic relaxation time (for a given hold temperature), and n is an exponent (≤ 1) that depends on the temperature of the isothermal hold.²⁾ The relaxational change in the resistance of amorphous films of vanadium at $T_i=4.2$ K, shown in Fig. 3a, is satisfactorily described by Eq. (1) with $n=1$ (Fig. 3b). A deviation from Eq. (1) is observed only in the initial stage of the relaxation process, $t \rightarrow 0$, and in the stage where the system is approaching equilibrium. Ytterbium films behave in a qualitatively similar way during a hold at 4.2 K. However, the parameter δ characterizing the relaxational decrease in the resistance is much smaller for Yb than for V. The value of δ varies from 0.13% for a Yb film of thickness ≈ 3 nm to 0.002–0.004% for films thicker than 15 nm. It is clear that in Yb films the relaxation processes are able to take place at the time of condensation. However, even such a small relaxational change of the resistance can lead to a catastrophic effect in ytterbium films of subcritical thickness—to the spontaneous onset, at $T_i=4.2$ K, of avalanche (explosive) crystallization of the entire sample. We attribute this to the formation, in a localized region of the film, of a “hot center”¹⁶ having a coordination structure close to that of Yb in the stable fcc phase, which initiates a self-sustaining process of avalanche crystallization.

Pure amorphous films of Bi and Be are superconductors even during condensation, once they reach a certain thickness (~ 5 nm). Heating the samples from 4.2 K to T_c in our technique is done in approximately half an hour. By this time a substantial part of the relaxation process will already have occurred. For this reason, in studying relaxation processes it is important to take into account the relation between the time of the relaxation process and the time necessary for measurement of the relaxing property.

However, in our experiments it is methodologically simple to heat the films from 4.2 K to liquid hydrogen temperature (≈ 20.4 K) over a time of the order of 1–2 min. This makes it possible to study at $T=20.4$ K the relaxational change of the resistance of amorphous films obtained at temperatures close to that of liquid helium. Of course, this is possible only for thin films for which $T_{cr} > 20.4$ K. Figure 4a shows the relaxational decrease of the resistance of an amorphous Bi film ≈ 8 nm thick, obtained by condensation of a liquid-helium cooled substrate and rapidly heated to liquid hydrogen temperature. The time dependence of the resistance of this film during an isothermal hold at $T_i=20.4$ K is described satisfactorily by Eq. (1) with $n=1/2$ (see Fig. 4b). In this case, as we see in Fig. 4a, $\delta \approx 0.74\%$. We note that the relaxational change of the resistance of a Bi film of approximately the same thickness, condensed at a substrate temperature of ≈ 20.4 K, is only 0.08% during a 150-min hold at this same temperature. In the latter case, apparently, the relaxation was practically completed during condensation.

The same situation is observed for gallium. The resistance of an amorphous Ga film ≈ 10 nm thick, condensed on a liquid-hydrogen cooled substrate and held at $T_i=20.4$ K for 25 min after the evaporator was turned off, decreased by only 0.03%. During a further hold (up to 50 min) the resistance of this film remained unchanged.

For amorphous manganese films an isothermal hold at $T_i=4.2$ K for several hours did not lead to a noticeable change in resistance. However, after heating of the film to

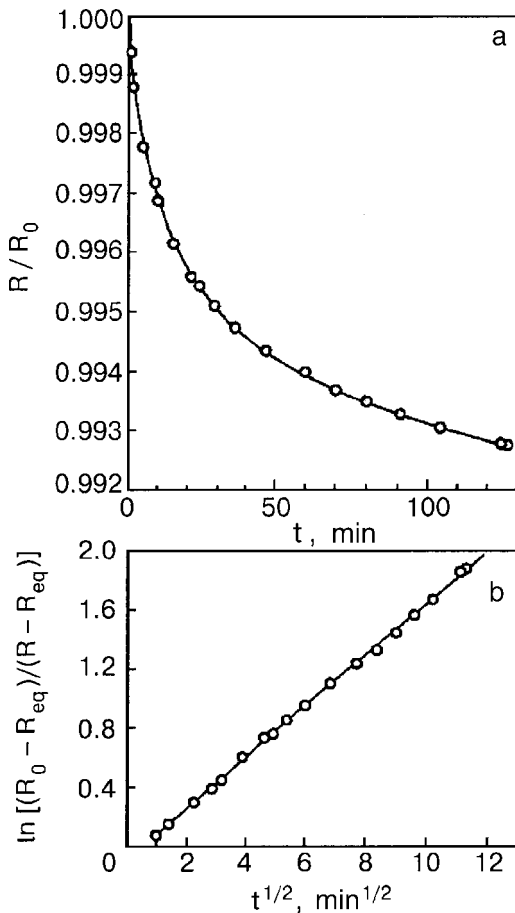


FIG. 4. Relaxational decrease of the resistance of an amorphous Bi film during a hold at $T_i = 20.4$ K (a); a plot of $\ln[(R_0 - R_{eq})/(R - R_{eq})]$ versus $t^{1/2}$ for this same film (b).

room temperature, which is a process accompanied by an irreversible decrease in resistance (see Figs. 2 and 5), an isothermal hold at $T_i \approx 295$ K leads to a further drop in resistance. Figure 5 shows portions of the heating curves for two identical amorphous Mn films. Curve 1 corresponds to a continuous heating at an average rate of ≈ 3 K/min, and curve 2 corresponds to heating with an isothermal hold at room temperature for 22 days.

The interpolation of curve 2 between points A and C shows the presumed (by analogy with curve 1) path of

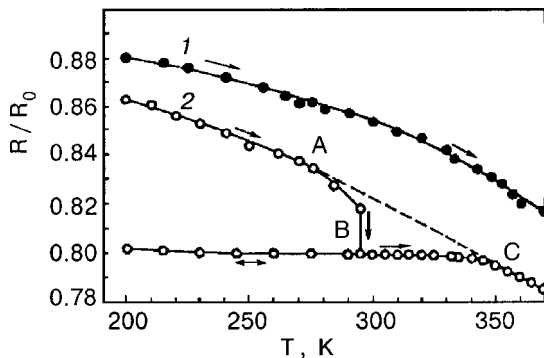


FIG. 5. Temperature dependence of the resistance during the heating of amorphous Mn films condensed on a liquid-helium cooled substrate: 1—continuous heating at a rate of ≈ 3 K/min; 2—heating with an isothermal hold at $T_i = 295$ K for 22 days.

$R/R_0(T)$ in the case of a continuous heating of this film. The path of curve 2 shows that the relaxational decrease of the resistance of an amorphous Mn film during a 22-day hold at room temperature is equivalent to a continuous heating of that film at a rate of ≈ 3 K/min up to $T \approx 350$ K. In the case of Mn the change of R with time during the isothermal hold cannot be described using a single characteristic relaxation time τ , i.e., by a relation of the form (1).

Relaxation phenomena are sometimes manifested most interestingly in the superconducting properties. It has been noted^{7,8,11} that in certain cases amorphous Bi and Ga films have a finite resistance immediately after condensation is stopped, and it decreases smoothly with hold time at 4.2 K until a transition occurs to the superconducting state. When the experimental conditions are changed so as to reduce to a minimum the introduction of impurities into the condensed layer of metal, this effect is eliminated,¹¹ i.e., the superconductivity arises right during the process of condensation.

We studied the behavior of the resistance of amorphous Bi films containing up to ≈ 50 at.% hydrogen, during and after their condensation. Without exception, in all experiments the superconductivity of the films arose during condensation, when the thickness of the film reached 5–6 nm.³ Apparently the aforementioned anomalous behavior of the resistance of amorphous Bi films^{7,8,11} during a hold at 4.2 K was due to some other impurities.

In amorphous beryllium films stabilized by a hydrogen impurity we routinely observed a phenomenon similar to that described in Ref. 11. Pure beryllium films, upon reaching a thickness of ~ 5 nm, become superconducting during condensation.¹⁶ At a smaller thickness or if the film has been heated above T_c , the superconductivity sets in immediately after the evaporator is shut off (curve 1 in Fig. 6, where the arrow indicates the time at which the condensation was stopped).

The parts of the curves to the left of the arrow show the change in resistance of the films during condensation before the evaporator was shut off. Curves 2 and 3 in Fig. 6 (to the right of the arrow) describe the behavior of Be–H films after the evaporator was shut off. It is seen that the superconductivity of the Be–H films at 4.2 K arises during the first minute or so of the hold at this temperature. After the film is heated to $T \approx 13$ K over a time of about half an hour, their T_c was already about 10 K with a transition width of ≈ 0.3 K. Thus in the time interval $1 \text{ min} < t < 30 \text{ min}$ the value of T_c of the Be–H films increases from below 4.2 to ≈ 10 K. Here the normal resistance of these films decreases by approximately 2% in comparison with the resistance at the time the condensation was stopped. Thus the relatively small relaxational decrease of the resistance of Be–H films is accompanied by a significant change in the superconducting transition temperature. It should be noted that curves 2 and 3 in Fig. 6 describe the behavior of two Be–H films of the same thickness and containing approximately the same amount of hydrogen. One can discern a tendency toward increasing delay of the onset of superconductivity in the as-condensed films of Be–H with increasing hydrogen concentration. Unfortunately, we cannot determine the hydrogen concentration in these films to sufficient accuracy, and anyway it decreases rapidly as the samples are heated to room temperature. Very

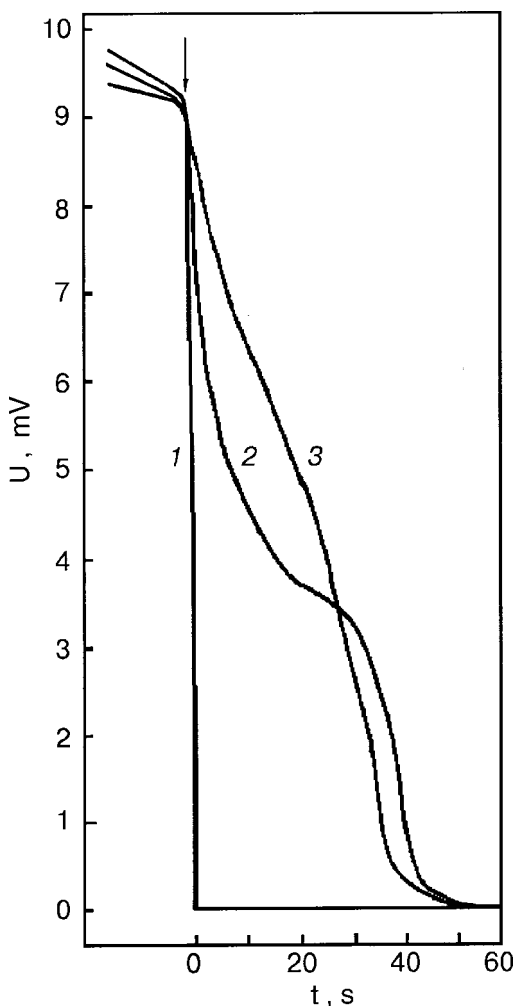


FIG. 6. Change in voltage with time at $T_i=4.2$ K for amorphous Be–H films of thickness ≈ 27 nm, after condensation was stopped (measurement current $\approx 30 \mu\text{A}$).

rough estimates according to formula (16) from Ref. 19 give values of the initial hydrogen concentration of 1–3 at.% in the Be–H films.

The superconductivity temperature of the amorphous Bi, Ga, and Be–H films established after heating to $T_h > T_c$ no longer varies on further heating to very high (but less than T_{cr}) temperatures, in contrast to the behavior of certain amorphous metallic alloys, where, as a result of relaxation processes on heating to $T_h < T_{cr}$, a lowering of T_c by 0.15–0.35 K has been observed.^{4,5,20} We observed approximately the same decrease in T_c (by 0.15–0.20 K) for Be–H films (50–70 nm thick) heated to the temperature at which crystallization begins (≈ 66 –68 K), when, according to our estimates, 1.5–2.5% of the sample had already formed the hcp phase of Be. The cause of the decrease in T_c in that case is the proximity effect.

4. DISCUSSION OF THE RESULTS

Let us start by noting some of the most general trends discerned in the study of the irreversible structural relaxation of amorphous metallic alloys.^{1–3} Diffraction studies show that upon structural relaxation the height of the interference peaks increases and the dips become more individual, i.e., the degree of regularity of the short-range structural order

becomes higher (but long-range three-dimensional order does not arise). The distances over which the atoms move during relaxation is around 0.1 of the average interatomic distance, but the positions of almost all the atoms change.¹ For example, the relaxational change of the resistance in an amorphous $\text{Mg}_{70}\text{Zn}_{30}$ alloy is accompanied by a displacement of the atoms by 0.01–0.03 nm.²¹

The most complete electron diffraction studies (using the method of constructing the radial distribution functions of the atomic density) of the structure of low-temperature condensates of Bi, Ga, Yb, and Be have been done by Komnik and co-workers.^{9,10} In particular, it was shown that irreversible changes in the electrical properties of amorphous Bi films of small thickness (< 5 nm) with increasing temperature (analogous to those seen in Fig. 1b) are due mainly to changes in the coordination structure. Structural transformations in amorphous Bi films of thickness 40–50 nm have also been observed to occur during a hold at $T_i \approx 4.2$ K after condensation was stopped. On heating to $T_h < T_{cr}$ the coordination structure of the Bi films of all the thicknesses studied became approximately the same (“typical”). As the thickness of the amorphous ytterbium films was increased (from 2 to 20 nm) a decrease in the coordination number from 9 to 7 was observed. For Yb films of small thickness the coordination number decreased from 9 to 7 as the temperature was raised.¹⁰

Qualitative results of electron diffraction studies of low-temperature condensates of Be have shown that with increasing temperature the changes of the radial distribution function manifest the same tendencies as in the case of ytterbium and bismuth.¹⁰

Thus we can assume that the relaxational changes of the resistance and Hall effect described above and shown in Figs. 1–6 are due to the structural changes observed in films of this sort in Refs. 9 and 10. Ultimately these structural changes amount to a displacement of the metal atoms into positions with lower free energy. It might seem that these displacements are negligibly small, since even the crystallization of monoatomic amorphous metals is realized via a diffusionless mechanism involving single “hops” of atoms across the crystallization front, and the length of such “hops” is a small fraction of the interatomic distance.¹⁶

It should be emphasized that, in contrast to the decrease in resistance as a result of relaxation of amorphous Bi films, the process of crystallization of these films is accompanied by a sharp increase in resistance (see Fig. 1a). In the case of amorphous Mn films the relaxation process on heating is characterized by an increase of the Hall constant at $T = 4.2$ K (Fig. 2b), whereas the crystallization of these films is accompanied by a decrease of R_H (at this same temperature) to such a degree that it changes sign.¹⁸ Furthermore, unlike the relaxation process (see Figs. 3 and 4) the initial period of isothermal crystallization of amorphous metals is characterized by acceleration of the change in resistance with hold time.¹⁶ These facts are evidence that the relaxation processes in the cases discussed above are in fact occurring in the amorphous phase of the metals and are not due to an initial stage of crystallization.

The main relaxation process of monoatomic amorphous metals (V, Yb, Bi) is a simple exponential process with a

single relaxation time, since it is satisfactorily described by Eq. (1). Although the time is raised to a power different from unity in that equation, its differentiation with respect to time gives a linear differential equation of the first degree:²

$$\frac{d}{dt}(R - R_{\text{eq}}) = (-n\tau^{-n}t^{n-1})(R - R_{\text{eq}}). \quad (2)$$

The characteristic relaxation time τ is determined by the slope of the linear plot of $\ln[(R_0 - R_{\text{eq}})/(R - R_{\text{eq}})]$ versus t or $t^{1/2}$ shown in Figs. 3b and 4b and has a value, according to these plots, of ≈ 5 min for the vanadium films and ≈ 33 min for the bismuth. The physical meaning of the relaxation time is not always clear; there is apparently no simple relation between τ and the characteristics of the material.² It can be assumed¹ that τ is the time required for the atoms of the metal to form a new configuration when they have occupied positions close to equilibrium.

As can be seen from Table I and Figs. 3–5, the relaxational changes of the resistance of the investigated amorphous films during an isothermal hold at a temperature T_i and during continuous slow heating to a higher temperature T_h ($T_i < T_h < T_{\text{cr}}$) are quantities of the same order. Apparently, during the relaxation of amorphous metals a certain equivalence of parameters (temperature and time) is manifested which is characteristic of temperature–time superposition.² This circumstance is in agreement with the aforementioned linearity of the main relaxation process in the films under study.

In amorphous manganese films there is apparently a covalent component of the bonding between atoms in addition to the metallic. That would account for the very high values of the resistivity ($\rho \approx (420 \pm 40) \times 10^{-6} \Omega \cdot \text{cm}$) and crystallization temperature on heating ($T_{\text{cr}} \approx 380 \text{ K}$).¹⁸ As we have said, the relaxational decrease of the resistance in amorphous Mn is not described by a single relaxation time. It seems that in this case for describing the stabilization of the amorphous state it is necessary to take into account a spectrum of possible relaxation times.² The presence of such a spectrum can reflect the objective participation of various molecular processes. To explain these processes it will be necessary, in particular, to perfect techniques that will permit a rapid approach to the temperature of the isothermal hold in order to obtain more-precise data on the time dependence of the change in resistance at different temperatures.

The state of atomic configurations in as-condensed amorphous films of pure metals is apparently close to the labile state predicted by Palatnikov and co-workers.²² Therefore the amorphous films of the metals studied (except for Mn), which were condensed at $T > 4.2 \text{ K}$, relax noticeably even at a lower temperature, transforming into a metastable amorphous state with a lower free energy. The mechanism of local rearrangement of the atomic configurations by means of structural relaxation are not yet sufficiently clear. The most widely used description of the atomic transport and structural relaxation is based on the free-volume theory.²³ It appears that in our experiments an important condition facilitating the atomic rearrangement is the presence in the amorphous films of a “frozen” free volume v_f , which is defined by Turnbull and Cohen²³ as

$$v_f = \bar{v} - v_0' \approx \bar{v} - 1.17v_0, \quad (3)$$

where \bar{v} , v_0 , and v_0' are, respectively, the average volumes per atom in the amorphous film, in the ideal close-packed crystal, and in the close-packed disordered structure (Bernal glass²⁴), which models an amorphous solid with internal equilibrium. The regions of free volume in amorphous alloys have been detected experimentally.²⁵ Positron annihilation experiments have shown that the amorphous structure contains vacancylike defects with a size of $(0.2-0.7)d_0$ (d_0 is the size of an atom of the metal), the concentration of which reaches 3%.²⁶ These defects also contribute to the free volume of amorphous films. The atomic rearrangement in an amorphous film is accompanied by a redistribution and escape of the free volume. Proof of this is given by the increase in the density of the amorphous alloys on annealing, which is due to the escape of the free volume, the time dependence being of a logarithmic character.²⁷

It appears that the change of the topological structure of amorphous films of Bi, Ga, Yb, and Be^{9,10} and the accompanying change of the electronic properties, which is described in the present paper, are also directly due to the redistribution of the free volume both during a hold of the films at a fixed temperature and during their heating to $T_h < T_{\text{cr}}$. This view is supported, in particular, by experiments on the structural relaxation of ytterbium films deposited at a nonzero angle α between the direction of the molecule beam and the normal to the substrate. It would seem that the relaxational change in the resistance of such films should be larger than in the case of films deposited normally, since the latter have a higher density.^{28,29} In other words, the films deposited at an angle have a larger free volume. Indeed, we found that a hold at $T_i = 4.2 \text{ K}$ of amorphous Yb films condensed at an angle $\alpha \approx 50^\circ$ leads to an increase of the parameter δ by an order of magnitude in comparison with films deposited normally (under otherwise similar conditions).

It is known that the insertion of hydrogen atoms into the lattices of metals usually causes an increase in volume and a distortion of the lattice. Nevertheless, the presence of up to 50 at.% hydrogen in amorphous Yb and Bi films^{14,30} has little effect on their electronic characteristics, stability, and kinetic parameters of crystallization. Apparently, because of the large size of the Yb and Bi atoms the micropores in their amorphous structures are larger in size than the hydrogen atoms, and the presence of the latter does not have much effect on the parameters of the short-range order. It can be assumed that the low-temperature mobility of hydrogen atoms in the amorphous phases of Yb and Bi are high, possibly because of the appearance of quantum effects (subbarrier tunneling). For this reason the relaxation processes in amorphous Bi–H and Yb–H films occur just as fast as in the pure films.

In beryllium, whose atomic radius is 38–41% smaller than the atomic radii of Bi and Yb, hydrogen stabilizes the amorphous phase substantially.³¹ Nevertheless, even in amorphous Be–H films the diffusive mobility of the hydrogen atoms is evidently quite high. The activationless regrouping of hydrogen atoms in the as-condensed films of Be–H is, we believe, responsible for the delay in the onset of superconductivity in them, since in pure Be films such a delay is not observed (see curve 1 in Fig. 6). Finally, the

behavior of curves 2 and 3 in Fig. 6 is not the result of a simple cooling of the film after condensation is stopped. A study of the thermal regime during avalanche crystallization of amorphous Yb films³² has shown that under identical experimental conditions the cooling of the avalanche crystallization front from a temperature ≈ 150 K^{16,17} to 5.6 K occurs in ≈ 10 ms, i.e., the rate of cooling of the superheated film under these conditions reaches ~ 15000 K/s.

Since amorphous beryllium is a superconductor with weak coupling, one can use the BCS formula for T_c :

$$T_c \approx 1.14\Theta_D \exp\left(-\frac{1}{N(E_F)V^*}\right), \quad (4)$$

where Θ_D is the Debye temperature, $N(E_F)$ is the density of states of the electrons at the Fermi level, and V^* describes the interaction between two electrons through the exchange of phonons with allowance for the screened Coulomb interaction.

As we have said, the relaxation of the as-condensed Be–H films, leading to an increase of T_c from 4.2 to ≈ 10 K, is accompanied by a decrease of the electrical resistance (in the normal state) by $\approx 2\%$. The accompanying change in the Debye temperature is hardly noticeable. For example, the complete structural relaxation of some amorphous alloys (e.g., $Zr_{54}Cu_{46}$)⁵ leads to a decrease of Θ_D by only 2–3%. Elementary estimates using the formulas of free-electron theory show that the observed $\approx 2\%$ decrease in the resistance of amorphous Be–H films corresponds to an increase in the density of states by $\approx 1\%$. (Here we have made the assumption that the mean free path of the electrons for these films, which is approximately equal to the interatomic distance,¹⁶ does not change in the course of the relaxation.)

According to formula (4), a change of the value of T_c from 4.2 to 10 K corresponds to an increase in $N(E_F)V^*$ by $\approx 18.5\%$. Apparently, the sharp increase in T_c as a result of relaxation of the as-condensed Be–H films is due mainly to growth of the electron–phonon interaction parameter V^* . The same conclusion was reached by the authors of Ref. 4, who showed that the relaxational change in T_c on heating of amorphous Cu–Zr films is due specifically to a change of the parameter V^* and not of $N(E_F)$, since, according to their magnetic susceptibility measurements, the change in $N(E_F)$ is small. Unfortunately, we cannot propose a more rigorous explanation for the observed changes of T_c with time in amorphous Be–H films, since an estimate of T_c requires detailed knowledge of the electronic and phonon spectra, and hydrogen is known³³ to have a strong influence on both.

CONCLUSIONS

1. In amorphous films of monoatomic metals there is appreciable relaxation of the electrical resistance even at a temperature of 4.2 K, due to a structural rearrangement.

2. The structural relaxation of amorphous metals is not an incipient crystallization process but is a process of stabilization of the amorphous structure.

3. This relaxation, as a rule, is a simple exponential process with a single characteristic relaxation time.

4. An apparent exception is the case of amorphous metals with a substantial covalent contribution to the bonding

(e.g., Mn), for which a description of the stabilization requires taking into account a spectrum of possible relaxation times.

5. It appears that the process of structural relaxation of monoatomic amorphous metals is due to a redistribution of the free volume in the samples.

6. In amorphous metal–hydrogen films the redistribution of the free volume is apparently combined with an activationless regrouping (subbarrier tunneling) of hydrogen atoms.

7. Comparatively small relaxational changes in the resistance in amorphous Be–H films (at $T_i=4.2$ K) are accompanied by a substantial change in the superconducting properties, a fact which we attribute to enhancement of the electron–phonon interaction in the process of structural relaxation of these films.

*E-mail: marbor@rocket.kharkov.ua

†Deceased.

¹For amorphous V films the value of $T_c \leq 3$ K.¹⁶

²If the equilibrium value of the resistance was not reached during the isothermal hold, then R_{eq} was determined by extrapolating the R versus t^{-1} plot to $t \rightarrow \infty$.

³It is known that the value of T_c for amorphous metallic films decreases strongly with decreasing thickness below 10 nm.^{13,16}

¹K. Suzuki, H. Fujimori, and K. Hasimoto, *Amorphous Metals* [Russian translation], Metallurgiya, Moscow (1987).

²D. R. Ullman and R. W. Hopper, in *Metallic Glasses* J. J. Gilman and H. J. Leamy (Eds.), ASM International, Metals Park, Ohio (1979); *Metallurgiya*, Moscow (1984).

³A. L. Greer, *J. Non-Cryst. Solids* **61–62**, 787 (1984).

⁴Z. Altounian, Tu Guo-hua, and J. O. Strom-Olsen, *Solid State Commun.* **40**, 221 (1981).

⁵P. Garoche, Y. Calvayrac, W. Cheng, and J. J. Veyssic, *J. Phys. F: Metal Phys.* **12**, 2783 (1982).

⁶J. Hillairet, E. Balanzat, N.-E. Derradji, and A. Chamberod, *J. Non-Cryst. Solids* **61–62**, 781 (1984).

⁷B. G. Lazarev, E. E. Semenenko, and A. I. Sudovtsov, *Fiz. Met. Metalloved.* **28**, 954 (1969).

⁸V. V. Postnikov, Author's Abstract of Candidate's Dissertation [in Russian], Voronezh (1971).

⁹Yu. F. Komnik, B. I. Belevtsev, and L. A. Yatsuk, *Zh. Éksp. Teor. Fiz.* **63**, 2226 (1972) [*Sov. Phys. JETP* **36**, 1177 (1973)].

¹⁰Yu. F. Komnik and L. A. Yatsuk, in *Whisker Crystals and Thin Films* [in Russian], Part 2, Voronezh (1975), p. 85.

¹¹E. E. Semenenko, B. G. Lazarev, and V. I. Tutov, *Abstracts of the 21st All-Union Conference on Low Temperature Physics* [in Russian], Part 1, Kharkov (1980), p. 104.

¹²V. M. Kuz'menko, B. G. Lazarev, V. I. Mel'nikov, and A. I. Sudovtsov, *Ukr. Fiz. Zh. (Russ. Ed.)* **21**, 883 (1976).

¹³Yu. F. Komnik, *Physics of Metallic Films* [in Russian], Atomizdat, Moscow (1979).

¹⁴V. M. Kuz'menko and A. N. Vladychkin, *Fiz. Tverd. Tela (St. Petersburg)* **41**, 177 (1999) [*Phys. Solid State* **41**, 155 (1999)].

¹⁵J. C. Suits, *Phys. Rev.* **131**, 588 (1963).

¹⁶V. M. Kuz'menko, Doctoral Dissertation [in Russian], B. Verkin Institute for Low Temperature Physics and Engineering, National Academy of Sciences of Ukraine, Kharkov (1992).

¹⁷V. A. Shklovskii and V. M. Kuz'menko, *Usp. Fiz. Nauk* **157**, 311 (1989).

¹⁸V. M. Kuz'menko and V. I. Mel'nikov, *Fiz. Met. Metalloved.* **50**, 984 (1980).

¹⁹H. L. Caswell, in *Physics of Thin Films*, edited by G. Hass, Vol. 1 [Academic Press, New York (1963); Mir, Moscow (1967)].

²⁰P. Esquinazi, M. E. De la Cruz, and F. De la Cruz, *Physica B & C* **108**, 1215 (1981).

²¹T. Mizoguchi, H. Narumi, N. Akutsu, N. Watanabe, N. Shiotati, and M. Ito, *J. Non-Cryst. Solids* **61–62**, 285 (1984).

- ²²L. S. Palatnik, Yu. A. Bykovskii, P. A. Panchekha, A. G. Dudoladov, V. I. Verchenko, and S. V. Marun'ko, Dokl. Akad. Nauk SSSR **254**, 632 (1980) [Sov. Phys. Dokl. **25**, 770 (1980)].
- ²³D. Turnbull and M. H. Cohen, J. Chem. Phys. **52**, 3038 (1970).
- ²⁴J. D. Bernal, Proc. R. Soc. London, Ser. A **280**, 299 (1964).
- ²⁵T. Egami, in *Glassy Metals*, H. J. Güntherodt and H. Beck (Eds.) [Springer-Verlag, Berlin (1981); Mir, Moscow (1983)], p. 45.
- ²⁶Yu. V. Barmin and I. V. Zolotukhin, in *Physics and Physical Chemistry of Amorphous (Glassy) Metallic Materials* [in Russian], Nauka, Moscow (1987), p. 80.
- ²⁷T. N. Mikhailova, V. V. Molokanov, and G. A. Kuvshinov, in *Physical Chemistry of Amorphous (Glassy) Metallic Materials* [in Russian], Nauka, Moscow (1987), p. 127.
- ²⁸L. S. Palatnik and A. I. Fedorenko, Fiz. Tverd. Tela (Leningrad) **7**, 3163 (1965) [Sov. Phys. Solid State **7**, 2561 (1965)].
- ²⁹N. G. Nakhodkin and A. I. Shaldervan, Thin Solid Films **10**, 109 (1972).
- ³⁰B. I. Belevtsev, Yu. F. Komnik, V. I. Odnokozov, and A. V. Fomin, Fiz. Nizk. Temp. **8**, 549 (1982) [Sov. J. Low Temp. Phys. **8**, 272 (1982)].
- ³¹V. M. Kuz'menko, V. I. Mel'nikov, T. P. Chernyaeva, and V. V. Bryk, Fiz. Met. Metalloved. **8**, 41 (1990).
- ³²V. M. Kuz'menko and V. I. Mel'nikov, Fiz. Nizk. Temp. **14**, 972 (1988) [Sov. J. Low Temp. Phys. **14**, 533 (1988)].
- ³³R. A. Andrievskii, *Materials Science of Hydrides* [in Russian], Metallurgiya, Moscow (1986).

Translated by Steve Torstveit

Isotope effects and the manifestation of 2D phase transitions in the kinetics of low-temperature (down to 5 K) hydrogen adsorption

V. D. Osovskii, Yu. G. Ptushinskiĭ,* V. G. Sukretnyi, and B. A. Chuĭkov

Institute of Physics of the National Academy of Sciences of Ukraine, pr. Nauki 46, 03650 Kiev, Ukraine

(Submitted April 2, 2001)

Fiz. Nizk. Temp. **27**, 1138–1147 (September–October 2001)

The adsorption–desorption characteristics of hydrogen isotopes on the (110) surfaces of W and Mo are investigated at a temperature $T_s \sim 5$ K. It is found that the characteristics for hydrogen and deuterium are very different. Isothermal desorption from W(110) at $T_s \sim 5$ K is observed in the case of H_2 , while that of D_2 is practically absent. The desorption of H_2 is suppressed as the flux of molecules to the surface increases; this, in the opinion of the authors, is a consequence of phase transition from a 2D gas to a 2D condensate. The initial sticking probability of H_2 on W(110) depends strongly on the flux, while that of D_2 is nearly independent of flux; in the H_2 case this is explained by the formation of nuclei of the 2D condensed phase during the lifetime of the molecule in the precursor state. In the case of H_2 adsorption on Mo(110) a sharp and deep minimum is observed in the dependence of the sticking probability on the coverage, which is absent in the case of D_2 . These isotope effects are explained by the deeper position of the levels of the zero-point vibrations of the heavier molecule D_2 . © 2001 American Institute of Physics. [DOI: 10.1063/1.1414574]

1. INTRODUCTION

The study of the adsorption interaction of hydrogen with the surface of metals is of interest from at least two standpoints. First, hydrogen is a participant in such important catalytic reactions as the synthesis of ammonia and is also a prospective environmentally clean fuel. In the latter application it is necessary to dissolve and store the hydrogen in a solid-state carrier. In both catalysis and dissolution the key stage of the processes is the dissociative adsorption of hydrogen. Second, in the case of hydrogen adsorption one can expect significant isotope effects, especially at low temperatures. This is one of the reasons that have prompted us to do an experimental study of the kinetics of H_2 and D_2 adsorption at a substrate temperature $T_s \sim 5$ K.

The second reason was the desire to investigate the weakly bound states of molecular adsorption of hydrogen in connection with their possible participation in the mechanism of dissociative adsorption in the capacity of precursor states (prestates). The idea of the participation of prestates in the adsorption process has become widely disseminated. Two types of prestates are distinguished: intrinsic and extrinsic. The first is realized above an unoccupied site and influences the initial sticking probability S_0 (at a coverage $\theta \rightarrow 0$), and the second is above an occupied adsorption site with the possibility of migration to an unoccupied site. The very small binding energy and, hence, the short lifetime of a molecule on the surface at ordinary temperatures are characteristic properties of prestates. Therefore, in order to stabilize and study the prestates it is necessary to cool the sample to liquid-helium temperature. Although the study of hydrogen adsorption on metals at ordinary temperatures has been the subject of an enormous number of published works (see, e.g., the reviews^{1–4}), the number of experimental studies on low-temperature adsorption of hydrogen is extremely limited. References to the papers we know of can be found in Ref. 5.

In view of what we have said, we undertook an experimental investigation of the low-temperature adsorption of the hydrogen isotopes H_2 and D_2 on the (110) surfaces of single crystals of tungsten and molybdenum. Adsorption systems based on tungsten and molybdenum have become widespread in surface physics as model systems with a comparatively easily obtained atomically clean surface.

2. TECHNIQUES

These studies were carried out in an ultrahigh-vacuum apparatus of the “black chamber” type, the general features of which are described in Refs. 6 and 7. The apparatus has provisions for the formation of a molecular beam of the effusion type, the straight-line registration of desorbed particles, and cooling of the sample to a temperature $T_s \sim 5$ K. Here we give only a block diagram of the layout of the main elements of the apparatus (Fig. 1). The vacuum conditions in the apparatus are extremely perfect: with the sample manipulator flooded with liquid helium and the hydrogen molecular beam open, the residual gas pressure is less than 10^{-11} Torr, and the flux of molecules from the molecular beam source to the sample is 4 orders of magnitude greater than the background flux.

Tungsten or molybdenum samples in the form of disks 12 mm in diameter and 0.8 mm thick were welded on as the bottom of a tubular rocking manipulator. The samples were subjected to heat treatment in vacuum by the standard technology for ensuring an atomically clean surface. The heating of the samples to temperatures $T < 1000$ K was done by means of the thermal radiation from an incandescent tungsten coil, and to temperatures $T > 1000$ K by electron bombardment of the back side of the sample. The temperature was monitored by means of a tungsten–rhenium thermocouple. Three types of experiments were done:

1. On a substrate cooled to $T_s \sim 5$ K a layer of hydrogen (deuterium) was adsorbed until saturation, i.e., until a dy-

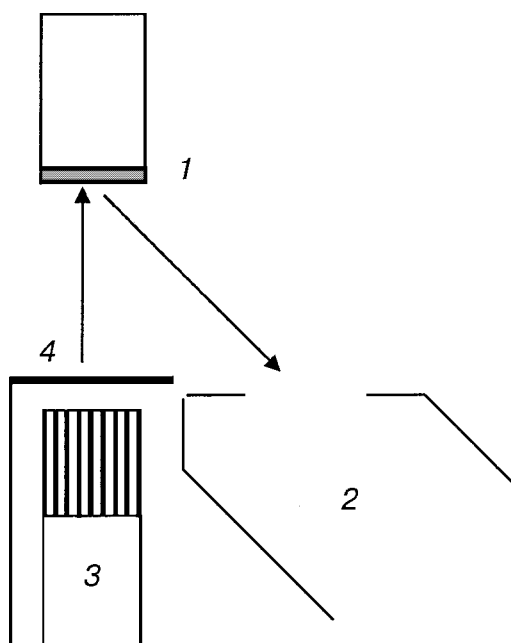


FIG. 1. Diagram of the arrangement of the basic elements of the apparatus: 1—sample, 2—mass-spectrometric detector, 3—molecular beam source, 4—shield.

dynamic equilibrium was established between the incident and desorbing fluxes. During the formation of the adsorbed layer (adlayer) the intensity of the beam of desorbing (and reflected) molecules was continuously measured. These measurements made it possible to determine the sticking probability S and the surface density n from the following expressions:

$$S(t) = 1 - I(t)/I_m, \quad (1)$$

$$n(t) = F \int_0^t S(t) dt, \quad (2)$$

where $I(t)$ and I_m are the ion currents of the detector at the time t and after the formation of a saturated adlayer, respectively, and F is the flux of molecules to the surface of the sample. The coverage $\theta(t) = n(t)/n_a$, where n_a is the density of surface atoms of the substrate ($\sim 1.4 \times 10^{15} \text{ cm}^{-2}$) for the investigated faces of W and Mo). The intensity of the molecular beam was calibrated by a method described in Ref. 8.

2. After the formation of a saturated adlayer the molecular beam was shut off and the isothermal desorption of molecules at $T_s \sim 5 \text{ K}$ was observed.

3. The saturated adlayer was desorbed as the temperature of the sample was gradually raised, and the thermodesorption spectrum, which characterizes the set of adsorption states, was measured.

The isotope effects are most clearly manifested in experiments of types 1 and 2, and the discussion below will be mainly devoted to a description of them. We will turn to the thermodesorption spectra in connection with the interpretation of the results.

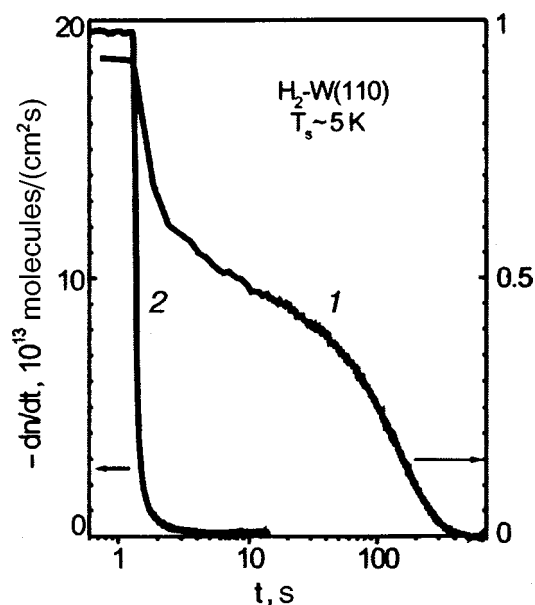


FIG. 2. Isothermal desorption of H_2 molecules: low flux during formation of the adlayer (1), high flux (2).

3. RESULTS AND DISCUSSION

3.1. Isothermal desorption of hydrogen from the W(110) surface and the influence of the molecular flux

The isothermal desorption of hydrogen after the molecular beam was shut off was investigated for several different values of the flux to the surface during formation of the adlayer.⁹ Figure 2 shows the time dependence of the rate of isothermal desorption of hydrogen molecules from adlayers formed at fluxes of $\sim 1 \times 10^{13}$ and $\sim 2 \times 10^{14}$ molecules/($\text{cm}^2 \text{ s}$). Since the duration of the desorption process is considerably different for the different fluxes, in Fig. 2 the time is plotted on a logarithmic scale. It is seen that increasing the flux causes a sharp suppression of the isothermal desorption. The number of molecules desorbed in the case of the high flux was smaller by a factor of 50 than for the low flux.

Let us begin with a discussion of the data for the case of a low flux during formation of the adlayer. The desorption process is conveniently divided into a rapid and a slow stage. The rapid stage is completed in several seconds, and during this stage less than 1% of the total number of molecules is desorbed. We think that the rapid stage represents the desorption of a small number of molecules that had been in dynamic equilibrium when the flux was on, residing in a state of the polylayer condensation type. The slow stage continues for hundreds of seconds and, in our opinion, represents the desorption from a state of physical adsorption (physisorption).

For analysis of the slow stage of isothermal desorption we use the Polanyi–Wigner equation in logarithmic form:

$$\log(-dn/dt) = \log \nu_d + a \log n - 0.43 E_d / k T_s, \quad (3)$$

where n is the surface density of adsorbed molecules, ν_d is the frequency factor, a is the order of the desorption reaction, and E_d is the activation energy for desorption. As we see from Eq. (3), the dependence of $\log(-dn/dt)$ on $\log n$ is linear, and its slope can be used to determine the value of a .

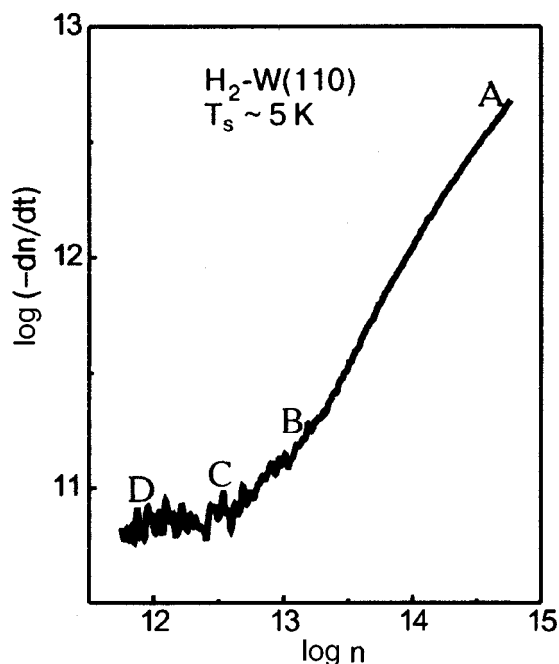


FIG. 3. Dependence of the rate of isothermal desorption of H₂ on the surface density.

Figure 3 shows the experimentally measured dependence. It can be approximated by two linear segments AB and CD. For segment AB the value of a is close to unity, and for segment CD it is close to zero. These results indicate that the isothermal desorption of physisorbed molecules occurs from two different states. We assume that segment AB represents desorption from a two-dimensional (2D) gas state, and segment CD represents desorption with the participation of islands of a 2D condensed phase. Under conditions such that the 2D gas phase is exhausted and the rate of desorption becomes very low, a substantial role is played by the mechanism wherein the gas phase is replenished through 2D evaporation of the islands of the 2D condensate. After a certain time this stabilizes the surface density in the 2D gas phase (although the total number of adsorbed molecules is continuously decreasing), and the order of the desorption reaction approaches zero. It is expected that the activation energy for desorption from the 2D condensate into vacuum should be greater than from the 2D gas because of the attraction between molecules in the condensate.

That the physisorbed H₂ layer has a two-phase structure is also indicated by the thermodesorption spectrum measured some time after the start of the slow stage of isothermal desorption (Fig. 4). Although the whole spectrum is shown, including the chemisorbed atomic phase (410 and 550 K), we are now interested only in the low-temperature part. It is reasonable to assume that the peak at 6 K corresponds to thermodesorption from the 2D gas state, and the peak at 10 K to that from the 2D condensate. We shall refer to the adsorption states by the temperature of the desorption peak.

Assuming that at the temperature of the desorption peak, the lifetime τ of a molecule in the corresponding adsorption state is close to 1 s, we can estimate the activation energy for desorption E_d from the Frenkel equation:

$$\tau = \tau_0 \exp(E_d/kT_s), \quad (4)$$

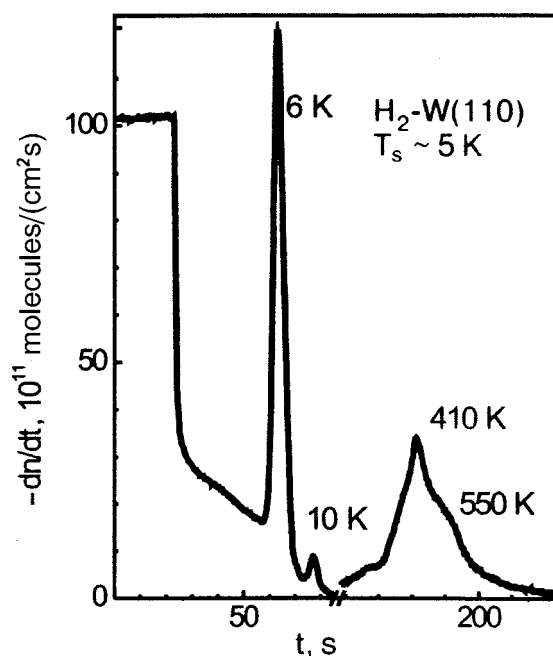


FIG. 4. Thermodesorption spectrum in the case of a low flux of H₂ molecules. The rate of increase of the sample temperature was ~ 0.3 K/s in the temperature interval 5–100 K, and ~ 7 K/s in the interval 200–700 K.

where $\tau_0 = h/kT_s$ is the vibrational period of the molecules. An estimate gives $E_d \approx 15$ meV for the 6 K state and $E_d \approx 25$ meV for the 10 K state. On the basis of the results discussed above, we propose the hypothetical model of a hydrogen adlayer at $T_s \sim 5$ K which is illustrated in Fig. 5.

Let us now turn to a discussion of the data on the isothermal desorption in the case of a high flux of hydrogen molecules during formation of the adlayer. If our assumption as to the influence of the islands of 2D condensate on the isothermal desorption is correct, we would expect that with increasing flux the probability of island formation would increase and, accordingly, so would the fraction of the surface covered with the 2D condensed phase. It is known that the critical size of the nuclei of the condensed phase should decrease with increasing supersaturation, i.e., with increasing flux of molecules. Then it becomes more probable for a gas–condensate phase transition to occur during the time of the experiment. As we see in Fig. 2, increasing the flux did indeed lead to strong suppression of the isothermal desorption. We assume that the suppression of the isothermal desorption at $T_s \sim 5$ K in the case of a high flux is due to the fact that a large fraction of the H₂ molecules is adsorbed in the form of a 2D condensed phase, whereas for the low flux only a small fraction of the adsorbed molecules is contained in the islands. The substantial increase in the 10 K peak in the ther-

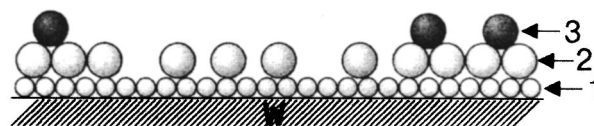


FIG. 5. Hypothetical model of an H₂ adlayer at a sample temperature $T_s \sim 5$ K: 1—chemisorbed monolayer of atoms; 2—physisorbed monolayer of molecules in the 2D gas and 2D condensate states; 3—molecules in a state of the polylayer condensation type.

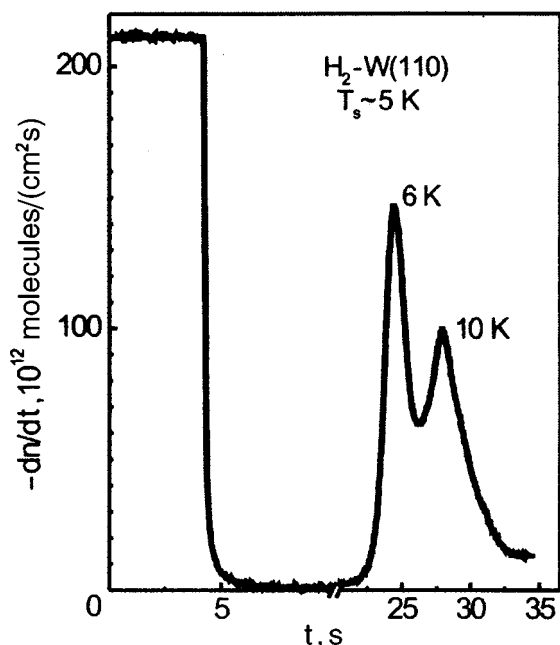


FIG. 6. Thermodesorption spectrum in the case of a high flux of H_2 molecules. The rate of increase of the temperature was ~ 1 K/s.

modesorption spectrum in the case of a high flux (Fig. 6) argues in favor of the proposed interpretation.

If a change of state of the adsorbed molecules does not occur upon the change in flux, then the dynamic-equilibrium coverage θ_s should follow the Langmuir isotherm. In our experiments we determined θ_s from the number of isothermally desorbed H_2 molecules; the experimental results are shown by the small squares in Fig. 7, and the continuous curve is the Langmuir isotherm.¹⁰

$$\theta_s = F / [n_a v_d \exp(-E_d/kT_s) + F]. \quad (5)$$

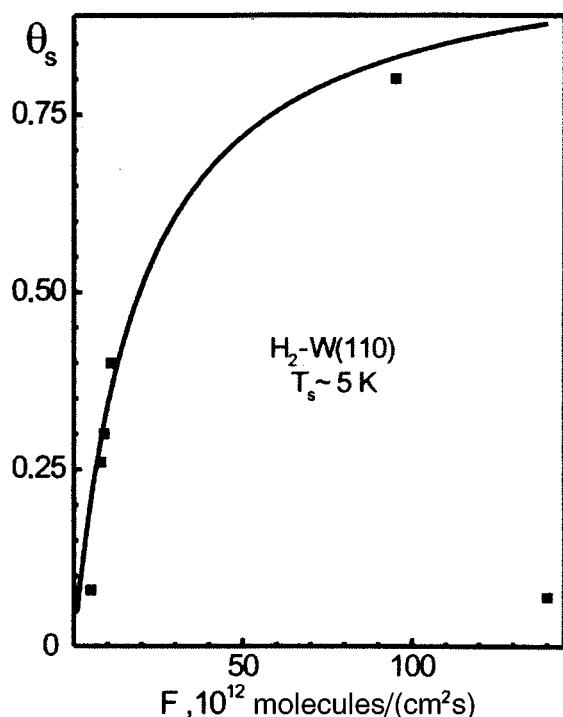


FIG. 7. Langmuir isotherm; ■—experimental points.

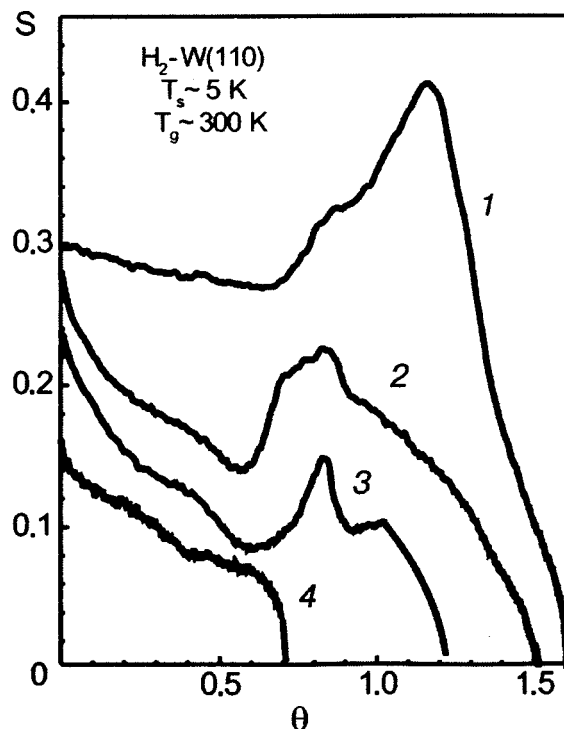


FIG. 8. Dependence of the sticking probability of H_2 on the coverage for $F = 2 \times 10^{14}$ (1), 4×10^{13} (2), 9×10^{12} (3), and 5×10^{12} (4) molecules/($cm^2 s$); T_g is the gas temperature.

In Eq. (5) the pressure has been replaced by the flux. We see that at moderate values of the molecular flux the experimental data are satisfactorily described by the Langmuir isotherm, but for $F > 10^{14}$ molecules/($cm^2 s$) a sharp deviation is observed, the result, we believe, of a phase transition from the 2D gas to the 2D condensate.

In experiments with deuterium, shutting off the molecular beam after the formation of a saturated adlayer at $T_s \sim 5$ K led to a sharp drop in the ion current of the detector, i.e., the isothermal desorption of deuterium under these conditions is practically absent. The reason for this difference in behavior of the adsorbed D_2 molecules from that of H_2 molecules may be found in the difference of the quantum properties of these molecules. The level of the zero-point vibrations of the two-times heavier D_2 molecule lies considerably deeper in the physisorption potential well than does that of the H_2 molecule. Therefore, the activation energy for desorption of the D_2 molecule is greater, and at $T_s \sim 5$ K no appreciable isothermal desorption of deuterium is observed.

3.2. Kinetics of hydrogen adsorption and the influence of the molecular flux

In view of the results of the previous subsection, we expect, starting from the principle of detailed balance, that a change in the flux of molecules to the surface will also lead to a change in the adsorption kinetics. We measured the dependence of the sticking probability of the hydrogen molecules on the W(110) surface as a function of coverage, $S(\theta)$, for fluxes in the range 10^{12} – 10^{14} molecules/($cm^2 s$) (see Fig. 8).¹¹ As we see from Fig. 8, increasing the flux leads to significant growth of the initial sticking probability

S_0 (at $\theta \rightarrow 0$) and of the maximum (saturation) coverage θ_s , and also leads to the appearance and growth of a peak on the $S(\theta)$ curves.

Let us discuss the possible mechanisms by which the molecular flux can influence $S(\theta)$. An increase of S_0 can arise if there is an interaction of molecules being adsorbed in an intrinsic prestate. Although we are talking about the initial sticking probability, which, strictly speaking, pertains to the clean surface, in the real experiment its measured value corresponds to some finite coverage of the surface. The time constant of our apparatus is 0.1 s, and during that time, at a flux of 5×10^{12} molecules/(cm²s), some 5×10^{11} molecules/cm² strike the surface, or, with a sticking probability ~ 0.1 , a coating of 5×10^{10} molecules/cm² is formed. The average distance between molecules in this case is $\sim 5 \times 10^{-6}$ cm.

In order to assess whether molecules found in the prestate, by moving along the surface, encounter and interact with each other, we can compare the distance between molecules with the diffusion path length L at $T_s \sim 5$ K. We have not found any published data on the diffusion coefficient of H₂ molecules along the W(110) surface, but in Ref. 12 there is information about the activation energy for the diffusion of molecular hydrogen. Using those data, we can obtain a rough estimate of the diffusion coefficient from the expression

$$D = D_0 \exp(-E_m/kT_s), \quad (6)$$

where E_m is the activation energy for surface diffusion, and the pre-exponential factor D_0 was assumed equal to $b^2 kT_s/h$ (b is the lattice constant of the substrate).¹³ The estimate gave a value $D \approx 10^{-7}$ cm²/s and $L = \sqrt{Dt} = 10^{-4}$ cm. Thus L is much larger than the average distance between molecules even at the minimal flux, and it is quite probable that the molecules encounter each other and interact in a time of 0.1 s.

Let us now discuss what specific mechanisms could lead to an increase in the initial sticking probability. If the elastically reflected molecules, are not taken into account, the sticking probability can be expressed as follows:^{14,15}

$$S_0 = \left[1 + \frac{\nu_d}{\nu_a} \exp\left(\frac{E_a - E_d}{kT_s}\right) \right]^{-1}, \quad (7)$$

where ν_a and ν_d are frequency factors, and E_a and E_d are the activation energies for the transition from an intrinsic prestate to a state of chemisorption and desorption, respectively. What we have said is illustrated in Fig. 9 by a one-dimensional potential diagram. It is seen from Eq. (7) that an increase in the activation energy for desorption leads to an increase of S_0 , and if the interaction of molecules in the prestate increases E_d , then this should be accompanied by an increase in S_0 . It seems to us that the results considered in Sec. 3.1 are evidence that the increase in the initial sticking probability of hydrogen molecules with increasing flux is indeed caused by an increase in E_d . We see that increasing the flux suppresses the isothermal desorption of the hydrogen molecules, i.e., increases E_d . As to the specific mechanism for the increase in E_d , we propose that it is due to the formation of nuclei of the 2D condensed phase.

The dependence of the maximum coverage on the flux of molecules (Fig. 8) is typical for an adsorption phase that is not maintained steady at the given temperature but for which

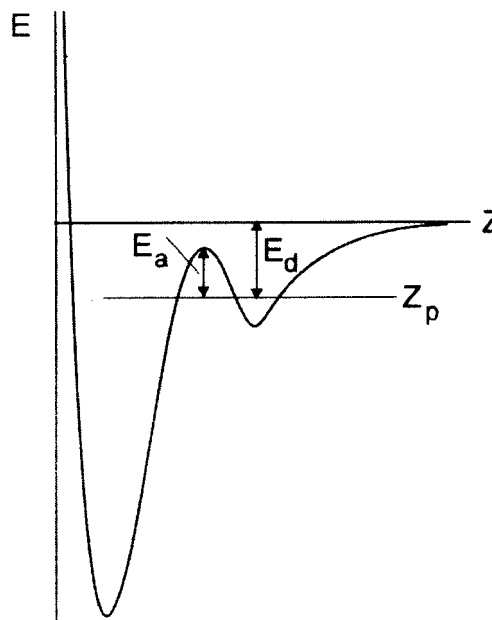


FIG. 9. One-dimensional potential diagram: E_a and E_d are the activation energies of the transition to the states of chemisorption and desorption, respectively; Z_p is the level of the zero-point vibrations.

a dynamic equilibrium density is established, with equal rates of adsorption and desorption. As to the cause of the increase of the sticking probability with increasing coverage upon the formation of a molecular adsorption phase, we hold to the view expressed in one of our previous papers.¹⁶ We suppose that the main cause of the growth of S is an increase in the efficiency of a loss of kinetic energy (accommodation) by the incident molecules in collisions with weakly bound molecules adsorbed previously.

Figure 10 shows the $S(\theta)$ curves for the adsorption of

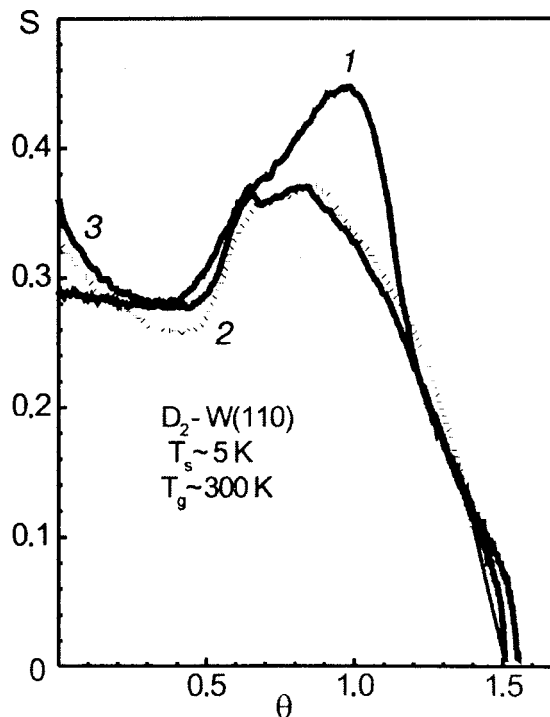


FIG. 10. Dependence of the sticking probability of D₂ on the coverage for $F = 2 \times 10^{14}$ (1), 4×10^{13} (2), and 8×10^{12} (3) molecules/(cm²s).

deuterium. We see that these curves are qualitatively different from those for hydrogen. The maximum coverage and the initial sticking probability respond weakly to an increase in the flux of molecules during formation of the adlayer (S_0 even decreases somewhat). The maximum on the $S(\theta)$ curves is observed even at the lowest value of the flux, while it is absent in the corresponding case for H_2 .

We assume that the differences in the adsorption kinetics of H_2 and D_2 and the influence of the flux on the adsorption kinetics are also determined by the difference in the positions of the levels of zero-point vibrations in the physisorption potential well. Since the level of zero-point vibrations of D_2 is deeper, the activation energy for the desorption of D_2 is substantially higher. Therefore, at $T_s \sim 5$ K, where the physisorbed H_2 layer is unstable, the physisorbed layer of D_2 is stable and responds weakly to a change in flux. The reason for the absence of growth of S_0 upon an increase in the flux of D_2 molecules, we believe, is also the deeper position of the level of zero-point vibrations. The process of nucleation of the 2D condensed phase, which we think is responsible for the growth of the initial sticking probability for H_2 , does not take place in the case of D_2 because of the deeper potential relief and, accordingly, the lower mobility of the molecules. Support for this view can be found in Ref. 12, where the activation energy for surface diffusion of D_2 is estimated as 6.6 meV, while for H_2 it is 2.7 meV.

3.3. Adsorption of H_2 and D_2 on the Mo(110) surface

It is of interest to compare the adsorption characteristics for hydrogen isotopes on the W(110) surface with those for Mo(110), which hardly differs in its atomic structure. In the case of Mo(110) we measured $S(\theta)$ at a single value of the flux of molecules onto the surface, but we varied the gas temperature T_g in the molecular beam source and thus varied the kinetic energy of the incident molecules. The influence of a change in T_g on the adsorption characteristics of hydrogen on W(110) was investigated by us previously.¹⁷

Figure 11 shows the dependence of the initial sticking probability for H_2 and D_2 on Mo(110) as a function of T_g . In both cases a monotonic decrease of S_0 with increasing T_g is observed. This behavior of S_0 argues in favor of an adsorption mechanism involving an intrinsic prestate and the absence of an appreciable activation barrier for transition to a state of chemisorption. In this respect the Mo(110) surface is different from W(110), for which a two-channel mechanism of H_2 adsorption is observed: adsorption via a prestate, and activation adsorption.¹⁷ The sticking probability of D_2 is considerably larger than that of H_2 , a circumstance which is indicative of a phonon mechanism for the loss of kinetic energy of the molecules incident on the surface. On the other hand, the larger value of S_0 for deuterium may also be due to the deeper-lying level of zero-point vibrations and, accordingly, to a larger value of E_d in Eq. (7).

Figure 12 shows the $S(\theta)$ curves for the adsorption of H_2 and D_2 on the Mo(110) surface for $T_g \sim 100$ K. In the case of H_2 the curve is extremely complex: after a slight increase of S there is a steep decrease to a sharp minimum at $\theta \sim 0.5$, and then it passes through a maximum and finally falls gradually to zero. The behavior of S in the interval $0 < \theta < 0.5$ is evidence for adsorption through an extrinsic pre-

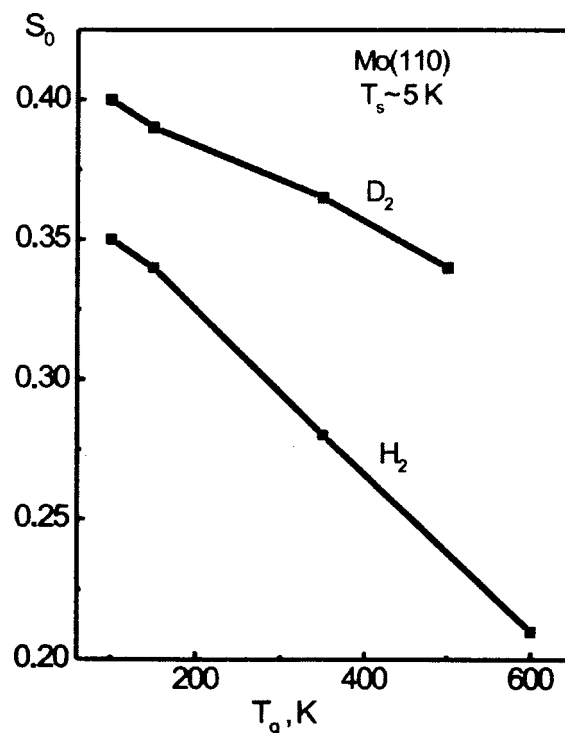


FIG. 11. Initial sticking probability of H_2 and D_2 on Mo(110) versus the gas temperature.

estate. We note that a coverage $\theta = 0.5$ (in molecules) corresponds to a monolayer of chemisorbed atoms. Thus S decreases to an extremely small value when the atomic phase of adsorption is saturated. The initially unfilled chemical bonds of the surface atoms of Mo are saturated at the end of the first stage and can no longer effect the capture and sub-

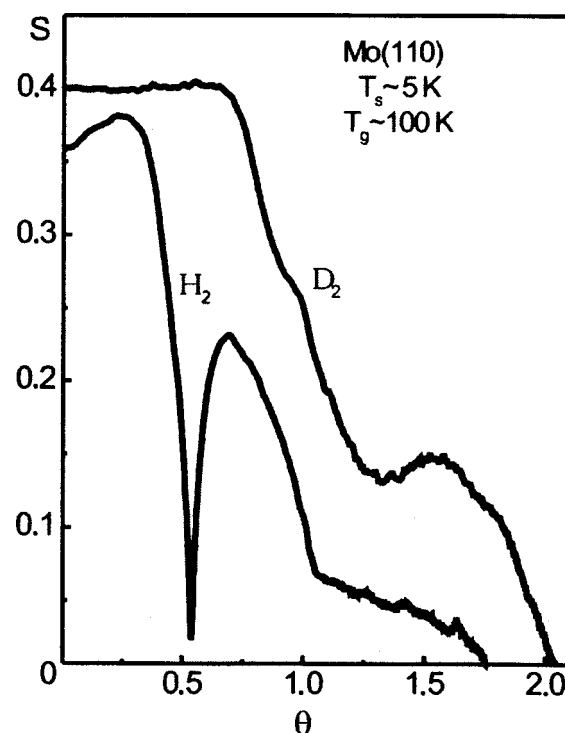


FIG. 12. Sticking probability of H_2 and D_2 on Mo(110) versus the coverage.

sequent dissociation of H₂ molecules, and the mass difference of the complex Mo/H and the H₂ molecule is too large for efficient accommodation.

In the interval $0.5 < \theta < 1$ the value of S increases sharply owing to the formation of a weakly bound molecular phase, which facilitates the loss of kinetic energy of the incident molecules. Granted, one cannot rule out the influence of a “softening” of the surface phonons, as was conjectured in Refs. 18 and 19. However, the increase in S is too sharp for it to be due to a simple accumulation of physisorbed H₂ molecules. It is probable that a change of state of the physisorbed molecules occurs. We assume that the formation of nuclei of a 2D condensed phase occurs, which, as we have said, suppresses the thermodesorption, further increasing S . The cresting and subsequent decline of S in the second stage is probably due to the limited number of adsorption sites in the physisorbed layer.

Fig. 12 also shows the $S(\theta)$ curve for the adsorption of D₂. This curve is qualitatively different from that for H₂ in that there is no minimum near $\theta=0.5$. To explain this difference we again turn to a consideration of the quantum properties of the H₂ and D₂ molecules. Because of the deeper position of the level of zero-point vibrations of the D₂ molecule, its mobility in the extrinsic prestate should be substantially lower than for H₂. This circumstance favors the formation of a molecular physisorbed phase of D₂ even before the formation of the atomic phase is completed. The presence of a weakly bound molecular phase leads to an increase in the sticking probability, compensating its decrease due to the saturation of the atomic phase. Because of their high mobility the H₂ molecules easily “skip” to unoccupied sites, and until those are all filled, the formation of a molecular phase of adsorption does not occur. It seems to us that one should not rule out the possibility that quantum diffusion is partly responsible for the high mobility of the H₂ molecules on the Mo(110) surface.

As we showed in the previous subsection, in the case of H₂ adsorption on W(110) there is no sharp feature on the $S(\theta)$ curve near $\theta=0.5$ like that considered above for H₂/Mo(110). This indicates that the potential relief along the surface is substantially deeper for H₂/W(110) than for H₂/Mo(110). This is also confirmed by the data of Ref. 12 on the relative values of the activation energies for surface diffusion of H₂ on W(110) and Mo(110).

4. CONCLUSION

We have observed the following isotope effects in the kinetics of low-temperature adsorption and desorption of hydrogen.

1. Isothermal desorption of H₂ molecules from the W(110) surface at $T_s \sim 5$ K is observed. Increasing the flux of molecules onto the surface during the formation of a saturated adsorbed layer at $T_s \sim 5$ K sharply suppresses the subsequent isothermal desorption of H₂. The suppression of the desorption is explained by the occurrence of a phase transition from the 2D gas to the 2D condensate.

Under the same conditions, isothermal desorption of D₂ molecules was not observed. The reason for this difference in the behavior of the H₂ and D₂ molecules, we believe, is the difference in their quantum properties—the deeper position

of the level of zero-point vibrations of the heavier D₂ molecules in the physisorption potential well.

2. At $T_s \sim 5$ K one observes in the case of hydrogen, but not for deuterium, an increase in the initial sticking probability S_0 and in the maximum coverage of the W(110) surface when the flux of molecules to the surface is increased. We attribute this increase of S_0 to an increased probability of formation of nuclei of the 2D condensed phase during the lifetime of the H₂ molecules in the intrinsic precursor state. The absence of such an effect in the case of D₂ adsorption is explained by the deeper position of the level of zero-point vibrations in the physisorption potential well.

3. The curve of the sticking probability of the H₂ molecule as a function of coverage for the Mo(110) surface has a very sharp and deep minimum near $\theta=0.5$. This feature is absent on the $S(\theta)$ curve for the adsorption of D₂. We attribute this difference in the adsorption kinetics of H₂ and D₂ to the difference in the mobilities of these molecules along the Mo(110) surface, which, in turn, is due to the deeper position of the level of zero-point vibrations of the D₂ molecule. The very high mobility of the H₂ molecules makes it possible to complete the formation of the atomic phase of adsorption before the formation of the molecular phase begins; this makes the surface inert in this stage of the process. We do not rule out the possibility of a contribution from quantum diffusion of the H₂ molecules in creating this high mobility. The deeper potential relief for the D₂ molecule and its larger mass apparently make for a low probability of tunneling diffusion for deuterium.

This study was supported by the Foundation for Basic Research of Ukraine, project No. 2.4/104.

*E-mail: ptush@iop.kiev.ua

- ¹K. Christman, Surf. Sci. Rep. **9**, 1 (1988).
- ²K. D. Rendulic, Surf. Sci. **272**, 34 (1992).
- ³A. Gross, Surf. Sci. Rep. **32**, 291 (1998).
- ⁴G.-J. Kroes, Prog. Surf. Sci. **60**, 1 (1999).
- ⁵B. A. Chuikov, V. D. Osovskii, Yu. G. Ptushinskii, and V. G. Sukretnyi, Surf. Sci. **448**, L201 (2000).
- ⁶B. A. Chuikov, V. D. Osovskii, Yu. G. Ptushinskii, and V. G. Sukretnyi, Surf. Sci. **213**, 359 (1989).
- ⁷Yu. G. Ptushinskii, B. A. Chuikov, V. D. Osovskii, and V. G. Sukretnyi, Fiz. Nizk. Temp. **19**, 570 (1993) [Low Temp. Phys. **19**, 406 (1993)].
- ⁸Yu. G. Ptushinskii, B. A. Chuikov, V. D. Osovskii, and V. G. Sukretnyi, Ukr. Fiz. Zh. (Russ. Ed.) **44**, 165 (1999).
- ⁹V. D. Osovskii, Yu. G. Ptushinskii, V. G. Sukretnyi, and B. A. Chuikov, JETP Lett. **67**, 959 (1998).
- ¹⁰E. A. Melvin-Hughes, *Physical Chemistry*, Izd. Inostr. Lit., Moscow (1962), p. 833.
- ¹¹B. A. Chuikov, V. D. Osovskii, Yu. G. Ptushinskii, and V. G. Sukretnyi, Surf. Sci. **473**, 143 (2001).
- ¹²P. P. Lutsishin, O. A. Panchenko, and V. F. Shpagin, Surf. Sci. **278**, 218 (1992).
- ¹³R. Gomer, Rep. Prog. Phys. **57**, 917 (1990).
- ¹⁴C. T. Rettner, H. Stein, and E. K. Schweizer, J. Chem. Phys. **89**, 3337 (1988).
- ¹⁵Yu. G. Ptushinskii and B. A. Chuikov, Poverkhnost' **9**, 5 (1992).
- ¹⁶V. D. Osovskii, Yu. G. Ptushinskii, V. G. Sukretnyi, and B. A. Chuikov, Fiz. Nizk. Temp. **23**, 779 (1997) [Low Temp. Phys. **23**, 587 (1997)].
- ¹⁷V. D. Osovskii, Yu. G. Ptushinskii, V. G. Sukretnyi, and B. A. Chuikov, JETP Lett. **60**, 586 (1994).
- ¹⁸E. Hulpke and J. Ludechke, Phys. Rev. Lett. **68**, 2846 (1992).
- ¹⁹M. Okada, A. P. Baddorf, and D. M. Zehner, Surf. Sci. **373**, 145 (1997).

Translated by Steve Torstveit

A vitrifying structure transition in the Dy/Mo(112) adsorption system

A. Fedorus,* V. Koval,[†] and A. Naumovets

Institute of Physics, National Academy of Sciences of Ukraine, 46 Nauki Ave., Kiev, 03028, Ukraine

H. Pfnür**

Institut für Festkörperphysik, Universität Hannover, Appelstrasse 2, D-30167 Hannover, Germany

(Submitted April 25, 2001)

Fiz. Nizk. Temp. **27**, 1148–1152 (September–October 2001)

Annealing-driven irreversible structural transitions are studied by low-energy electron diffraction in submonolayer Dy films adsorbed on the Mo(112) surface. In a wide coverage range $\theta > 0.07$, Dy overlayers deposited at low temperatures ($T \approx 100$ K) are ordered and keep their structure upon annealing up to 350–600 K. Near $\theta = 0.68$, the overlayers are stable to high-temperature annealing ($T_a = 1000$ K) as well, whereas the denser films are metastable and transform to more stable ordered structures. An unusual annealing effect is found for $\theta < 0.58$: the initially ordered metastable phases are replaced by phases having no extended order, which are assumed to be two-dimensional glasses. © 2001 American Institute of Physics. [DOI: 10.1063/1.1414575]

INTRODUCTION

The glassy state of matter has been attracting a great and abiding interest from both the basic and practical standpoints (see, e.g., Ref. 1). There are a lot of methods of producing various kinds of glasses. Among them, special attention is paid at present to the preparation and study of thin glassy and amorphous films, which combine a number of useful properties provided by the disordered structure and low dimensionality. In this communication, we report on a new method allowing one to obtain ultrathin (submonolayer) films which, in contrast to the usual amorphous films, are stable against annealing and retain their disordered structure in a broad temperature range.

Our results have been obtained with Dy submonolayers on the Mo(112) surface. The adsorbed Dy atoms possess an appreciable positive electrical charge, and their interaction with one another is of complex nature, including both dipole-dipole and substrate-mediated interactions. The energy of such interactions can reach 10^{-2} – 10^{-1} eV for nearest neighbors, so the adsorbed films are usually ordered below $T = 100$ – 1000 K.^{2,3} Owing to the considerable dipole moment associated with the adsorption bond (above 1 D at low Dy coverage), the adsorbate strongly reduces the work function of the surface. The work function and structure of Dy/Mo overlayers have been studied earlier,⁴ but the annealing-driven structural transitions and work function changes were not revealed. Specifically, the $c(2 \times 2)$ lattice was reported to exist up to $\theta = 0.5$, which is followed by uniaxially compressed lattices at $\theta > 0.5$ in the submonolayer coverage range. The coverage is defined as the ratio of adsorbate to substrate surface atom concentrations. We have investigated the structure of Dy adlayers both as-deposited at a low temperature ($T = 100$ K) and successively annealed in the range $100 \text{ K} < T_a < 1200 \text{ K}$, with recording of the resulting structures at the low temperature. The rate of temperature decrease after each annealing step did not exceed -5 K/s. In such experiments, we have found a strong effect of annealing on the character of the order.

RESULTS AND DISCUSSION

To carry out this study, we have used the ultrahigh-vacuum system and the experimental setup described earlier.^{5–7} Briefly, a SPECTALEED instrument equipped with a charge-coupled device (CCD) camera was used to study the surface structure. The stored video records of the low energy electron diffraction (LEED) patterns were utilized to measure the peak intensities for the particular spots. The contact potential difference method was applied for monitoring the work function changes. The same molybdenum specimen as in our previous work^{6,7} was used for the substrate. Its surface consists of (112) terraces as broad as $350 \text{ \AA} \times 550 \text{ \AA}$ along the $[\bar{1}\bar{1}1]$ and $[1\bar{1}0]$ axes, respectively. The atomic beam of Dy was obtained from a piece of dysprosium metal spot-welded to a tantalum ribbon serving as a heater. Auger electron spectroscopy was used to check the cleanliness of the substrate and the adsorbate. The coverage θ was determined from the deposition time and work function measurements, which were calibrated by means of LEED in the coverage range $\theta = 0.68$ – 0.75 . This range is specific for the existence of a single-phase incommensurate structure undergoing uniaxial compression and therefore is not likely to contain other phases which might be overlooked by LEED.

At annealing temperatures below $T_a = 350$ – 600 K, a set of ordered overlayer structures is found with increasing coverage from $\theta = 0.07$, until the formation of a close-packed physical monolayer at $\theta = 0.77$. These structures in their majority are different from those reported in Ref. 4. As we intend to discuss in detail the phase transitions for the Dy/Mo(112) system in a separate paper, we will not present here the whole series of ordered film structures observed in this work but will focus on the annealing-driven irreversible order-disorder transition.

In general, the periodicity of an ordered film structure differs from that of a substrate. Therefore LEED usually reveals an order in the adsorbed overlayer via extra (fractional-

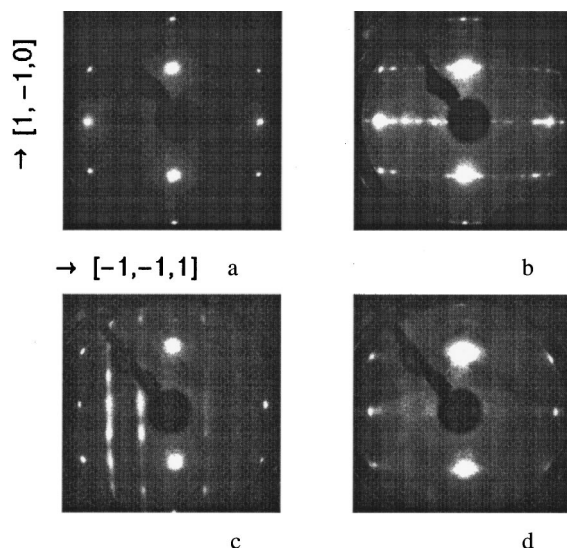


FIG. 1. Low-energy electron diffraction patterns from Dy/Mo(112) overlayers. The pattern from the clean substrate (a) is presented for a reference, with the principal axes indicated. Coverage (monolayers): 0 (a); 0.25 (b); 0.68 (c); 0.45 (d). Annealing temperature, K: 200 (b); 800 (c, d). Electron energy, eV: 67 (a,b); 55 (c,d).

order) diffraction beams which are absent in the cases of a clean substrate or a disordered adsorbed layer. For example, Fig. 1b shows a LEED pattern from an ordered (6×1) Dy overlayer which is observed in the coverage range $\theta = 0.07–0.3$. The pattern differs from that of the clean substrate (Fig. 1a) by the presence of five extra beams between the integer-order beams along the $[\bar{1}\bar{1}1]$ direction. Figure 2 shows a possible model of the (6×1) structure which is consistent with the LEED pattern and the coverage value. It should be mentioned that the (6×1) structure is one of those transforming into a glassy phase in the progress of annealing. Patterns with fractional-order LEED spots are indeed observed in the whole submonolayer coverage range at the low annealing temperatures mentioned above. A full list of the ordered structures found will be given in the diagram of annealed states presented below.

An increase of the annealing temperature exerts a different effect on the order in Dy adfilms depending on their

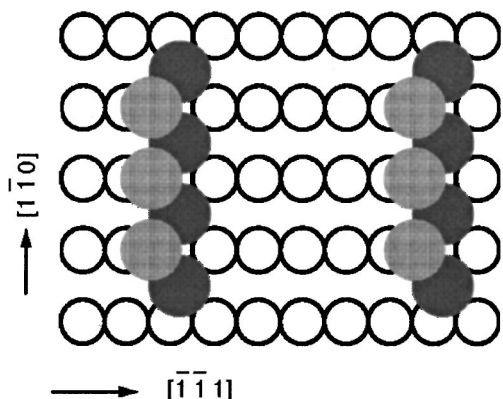


FIG. 2. A hypothetical hard-sphere model for an ordered dysprosium overlayer (6×1) corresponding to $\theta=0.3$. The unfilled circles show the topmost substrate layer, and the gray disks show the adsorbate layer, with heavier darkness corresponding to greater vertical depth. The principal axes are indicated.

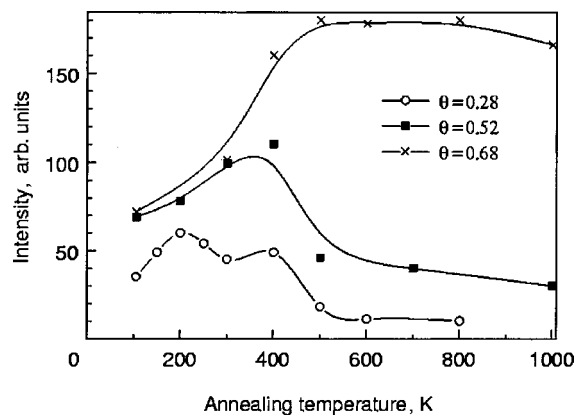


FIG. 3. Annealing-driven changes in intensity of fractional-order LEED beams specific to the structures observed at different Dy coverages. The beam intensity after annealing is always measured at $T=100$ K.

coverage. As a measure of the degree of order we use the peak intensity of LEED. Above $\theta>0.6$, the annealing results in a usual effect of improvement of the order. This is illustrated in Fig. 3 for $\theta=0.68$: the fractional-order beam intensity gradually increases and then levels off. The relevant LEED pattern from the eventually annealed overlayer is shown in Fig. 1c. The steady growth of the order, starting from the lowest annealing temperature, is indicative of considerable mobility of adatoms already at 100 K. Designating as T_{mob} a certain minimum temperature at which adatoms can move over neighboring adsorption sites during the time of an experiment, we conclude that T_{mob} is <100 K. According to this designation, T_{mob} can be expressed in terms of the parameters of surface diffusion as $T_{mob} \approx E_d/30k_B$, where E_d is the activation energy and k_B is Boltzmann’s constant.^{2,8} Besides promoting adatom mobility, an increase of temperature can also cause an order–disorder transition if the temperature reaches some critical value T_c specified by the interaction energy of adatoms E_i as $T_c \approx E_i/k_B$ (see Ref. 8). Ordering is realized within the time of an experiment ($10–10^2$ s) if

$$T_{mob} < T_c, \text{ or } E_d < 30 E_i; \tag{1}$$

otherwise, upon the cooling that follows each annealing step, a frozen disorder is observed instead of order. The overlayer under consideration ($\theta=0.68$) is apparently what results when inequality (1) is fulfilled. It should be noted that the lattice retains its original symmetry under annealing only in a narrow coverage range close to $\theta=0.68$. The denser films (from $\theta=0.68$ up to the close-packed monolayer at $\theta = 0.77$) are metastable and undergo irreversible transitions to the more stable ordered structures. In this case, LEED records the replacing of one pattern of superstructure spots by another.

For the coverages $0.07 < \theta < 0.58$ the annealing results in an unusual effect: first only a limited improvement of the order occurs, which is followed by decay of the previous order without transition to any other ordered phase. This peculiarity is illustrated qualitatively by an irreversible disappearance of the fractional-order LEED features in pattern (d) of Fig. 1 and quantitatively by intensity curves with local maxima followed by virtual fading of intensity (see Fig. 3). At low temperatures ($T_a < 200–400$ K), inequality (1) seems

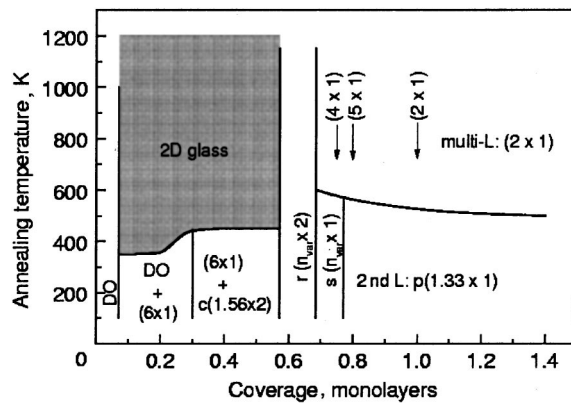


FIG. 4. Diagram of annealing-driven changes in structure of Dy overlayer on Mo(112). DO: disordered phase; 2D glass: two-dimensional glass (shaded area); $r(n_{\text{var}} \times 2)$ and $s(n_{\text{var}} \times 1)$: rectangular (diatomic) and skew-angle (primitive) structures, respectively, having lattice spacing varying with θ ; 2nd L: second layer; multi-L: multilayer structure. The other notations of ordered structures are conventional. The arrows show the coverages at which the specified structures form.

to be valid. However, at a later stage, annealing evidently causes an irreversible change in the overlayer properties (such as the diffusion parameters and adatom interaction energy), so that inequality (1) reverses its sign:

$$T_{\text{mob}} > T_c. \quad (2)$$

The irreversible transitions are summarized in Fig. 4, which shows a wide area (shaded and designated as 2D glass) of annealing temperature in the submonolayer coverage range at which the overlayer loses an extended order. The notations of the all ordered structures found are also listed in Fig. 4. Though Fig. 4 resembles a phase diagram, that is not the case: here the overlayer state is presented at a standard temperature of 100 K, contrary to a phase diagram, which shows the state at a current temperature.

To prove that the effect of high-temperature annealing on LEED patterns at low coverage is not a trivial result of the removal of Dy adatoms from the surface, the work function changes caused by annealing were monitored. The coverage dependences of these changes taken after low- ($T_a < 350\text{--}600$ K) and higher-temperature annealing are presented in Fig. 5. It is seen that at no value of the coverage does high-temperature annealing return the work function to its value specific for the clean surface.

One of possible interpretations of the described annealing irregularity might be a transition to another more stable phase which is characterized by too low a disordering temperature, unavailable in our experiment, so that $T_{\text{mob}} < T_c < 100$ K. However, the quite small variation of the work function (and thereby of the adatom dipole moment) due to high-temperature annealing indicates that no essential weakening of at least dipole-dipole adatom interactions happens. Therefore, taking into account the rather wide coverage range in which the order is lost, we consider that even this interaction only can provide a sufficiently high T_c at medium coverages where the inter-adatom distances become very short.

Though some decrease of T_c should not be ruled out, especially at low coverages, another possibility seems to be more realistic: a poor order can be explained by an

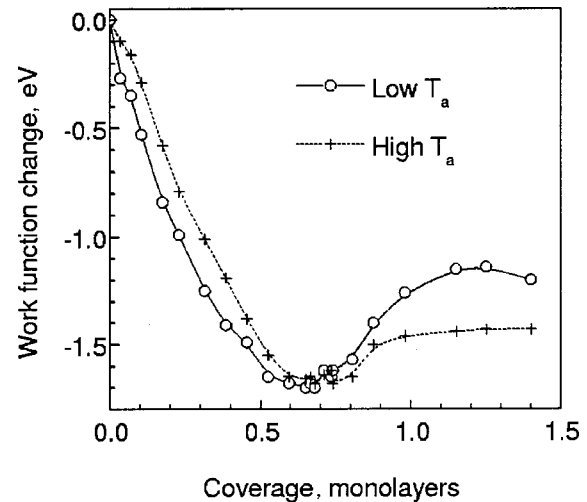


FIG. 5. Coverage dependence of the work function changes obtained after low- ($T_a < 350\text{--}600$ K) and higher-temperature annealing.

annealing-driven change of adatom mobility, which becomes insufficient to ensure equilibration. Direct experimental investigations of surface diffusion show evidence that the mobility of Dy atoms adsorbed on Mo(112) in the given coverage range and subjected to high-temperature annealing is indeed low.⁹ The diffusivity equals $10^{-9}\text{--}10^{-8}$ nm²/s at $T = 700\text{--}800$ K. It is lower by two order of magnitude than that, e.g., for strontium films adsorbed on the same substrate at comparable coverages.¹⁰ An estimate of the time necessary for diffusion over the path of an inter-adatom distance, which is obtained by extrapolation of the diffusivity data to the temperature range optimal for the ordering of metastable phases, $T_a = 200\text{--}300$ K, gives $10^5\text{--}10^3$ s. This value is apparently distinct from the much shorter diffusion time providing rapid equilibration of metastable phases at low temperatures. Hence this fact corroborates our suggestion about the dramatic drop of adatom mobility in the range $\theta = 0.07\text{--}0.58$ upon high-temperature annealing. The low-temperature ordering of Dy phases such as (6×1) described above is not the only significant fact. Precovering of the Mo(112) surface with a dilute Dy film ($\theta \approx 0.1$), with its subsequent high-temperature annealing, strongly suppresses the Sr and Li overlayer ordering, whereas without high-temperature annealing, the same Dy dope to the Sr or Li overlayer even improves the ordering process, indicating a high adatom mobility.

We suggest that the origin of the hindering of the adatom mobility by high-temperature annealing may consist in adsorption-induced surface reconstruction. The Mo(112) surface is close-packed in the direction along the channels (see Fig. 2). However, adsorption followed by high-temperature annealing can induce a reconstruction of its topmost layer into some loose-packed structure, and the ordering is known to advance very slowly on the rough surfaces.² The roughness of the reconstructed surface means that adatoms are mixed with surface substrate atoms, and one actually obtains a kind of two-dimensional alloy. For example, such a carbon-induced reconstruction to a rough “checkerboard” structure is detected for Mo(112) both by LEED and STM techniques.¹¹ Contrary to this, the mobility of Dy adatoms on the original (non-reconstructed) surface Mo(112) seems to be

high enough to provide some ordering for all coverages even at temperatures as low as 100 K. Some suggestion concerning the mechanism of formation of a rough surface can be deduced from data on the work function changes (Fig. 5). Up to at least 0.5 monolayer, the curves corresponding to low-temperature and high-temperature anneals are seen to run almost in parallel, as if 5 to 10% of the adsorbate monolayer is no longer contributing to the work function change after the high-temperature anneal. It seems that approximately this amount of dysprosium must have “reacted” with the surface during high-temperature annealing (as a random process), so that this fraction is leveled down from the position of an adatom, protruding into the vacuum, to a position within the two-dimensional alloy incorporated in the surface substrate layer. The result is that it makes little contribution to the surface potential barrier. This reaction obviously happens already with the first few percent of the monolayer, and after completion of the surface reaction (limited presumably by buildup of surface stress due to incorporation of Dy into the Mo layer), nothing more happens. Since the surface now has a random and rougher corrugation, Dy adsorbed on top of this two-dimensional alloy cannot order at low coverage. However, at high coverages ($\theta > 0.58$) the situation seems to differ due to domination of direct lateral interactions of adatoms, which are strong at short inter-adatom distances and switch on a more intense driving force of ordering.

Thus, the high-temperature annealing of low-coverage Dy submonolayers ($0.07 < \theta < 0.58$) results in their transition to a disordered state. At $T > 600$ K, Dy adatoms possess a high mobility in this state,⁹ so this is actually a melted phase. However, while as the temperature is lowered, the mobility seems to decrease dramatically before the overlayer is able to order. This is just what is typical for a vitrifying transition.

A peculiarity of the submonolayer vitrification is a strong influence of the substrate potential corrugation on the behavior of an overlayer. At an arbitrary coverage, a disordered film generally has an incommensurate structure. A lack of overlayer mobility implies the pinning of adatoms to the wells of the Peierls relief (the substrate potential corrugation modified by adatom lateral interaction).⁸ For incommensurate structures, the pinning means transformation into a phase termed chaotic.¹² In this phase, the potential wells have no standard depth due to a random distribution of the adatoms over the adsorption sites, and consequently, to a

random value of the interaction energy between neighboring adatoms. Besides poor mobility, this is a fundamental property of an amorphous state.

It is worth noting that a low-coverage glassy overlayer of Dy and other similar adatoms which possess an appreciable magnetic moment may exhibit properties of ultrathin (actually two-dimensional) amorphous magnetic materials.

CONCLUSION

To conclude, we have found a set of metastable ordered states in two-dimensional Dy overlayers deposited onto Mo(112) at low temperatures. Upon high-temperature annealing, they are irreversibly replaced by stable ordered structures at high coverages and by a glassy state at low and medium coverages.

Support of this work by the Basic Research Foundation of the Ministry of Ukraine for Education and Science and by the Volkswagen-Stiftung is gratefully acknowledged. We thank I. Yakovkin for a critical reading of the paper.

*E-mail: fedorus@iop.kiev.ua

†Deceased

**E-mail: pfnuer@fkp.uni-hannover.de

-
- ¹J. M. Ziman, *Models of Disorder*, Cambridge Univ. Press, London (1979).
 - ²A. G. Naumovets, *Sov. Sci. Rev., Sect. A* **5**, 443 (1984).
 - ³O. M. Braun and V. K. Medvedev, *Usp. Fiz. Nauk* **157**, 631 (1989) [*Sov. Phys. Usp.* **32**, 328 (1989)].
 - ⁴F. M. Gonchar, V. K. Medvedev, T. P. Smereka, and G. V. Babkin, *Fiz. Tverd. Tela* **32**, 1872 (1990) [*Sov. Phys. Solid State* **32**, 1092 (1990)].
 - ⁵D. Jürgens, G. Held, and H. Pfnür, *Surf. Sci.* **303**, 77 (1994).
 - ⁶A. Fedorus, D. Kolthoff, V. Koval, I. Lyuksyutov, A. G. Naumovets, and H. Pfnür, *Phys. Rev. B* **62**, 2852 (2000).
 - ⁷A. Fedorus, G. Godzik, V. Koval, A. Naumovets, and H. Pfnür, *Surf. Sci.* **460**, 229 (2000).
 - ⁸I. Lyuksyutov, A. G. Naumovets, and V. Pokrovsky, *Two-Dimensional Crystals*, Academic Press, New York (1992).
 - ⁹A. T. Loburets, A. G., Naumovets, and Yu. S. Vedula, *Surf. Sci.* **399**, 297 (1998).
 - ¹⁰A. T. Loburets, N. B. Senenko, A. G. Naumovets, and Yu. S. Vedula, *Phys. Low-Dimens. Semicond. Struct.* **10/11**, 49 (1995).
 - ¹¹T. McAvoy, C. Waldfried, J. Zhang, P. A. Dowben, O. Zeybek, T. Bertrams, and S. D. Barrett, *Eur. Phys. J. B* **14**, 747 (2000).
 - ¹²P. Bak, *Rep. Prog. Phys.* **45**, 587 (1982).

This article was published in English in the original Russian journal. Reproduced here with stylistic changes by AIP.

Muonium diffusion in solid CO₂

D. G. Eshchenko*

Institute for Nuclear Research, Moscow 117312, Russia

V. G. Storchak

Russian Research Centre “Kurchatov Institute,” 46 Kurchatov Sq., Moscow 123182, Russia

J. H. Brewer

Canadian Institute for Advanced Research and Department of Physics and Astronomy, University of British Columbia, Vancouver, B.C., Canada V6T 1Z1

S. P. Cottrell and S. F. J. Cox**

Rutherford Appleton Laboratory, Chilton, Oxfordshire OX11 0QX, United Kingdom

E. Karlsson and R. Waeppling

Department of Physics, Uppsala University, Box 530, 751 21 Uppsala, Sweden

(Submitted April 25, 2001)

Fiz. Nizk. Temp. **27**, 1153–1158 (September–October 2001)

The quantum diffusion of interstitial muonium atoms in solid CO₂ is studied in the temperature range from 5 to 200 K using the technique of muonium spin rotation and relaxation.

Muonium exhibits coherent bandlike dynamics between 140 and 160 K. At low temperature Mu undergoes strong localization. © 2001 American Institute of Physics. [DOI: 10.1063/1.1414576]

When positive muons are implanted into insulators they often form muonium (μ^+e^- or Mu) atoms, analogous to hydrogen atoms but nearly an order of magnitude lighter.¹ The dynamics of such light atoms, being intrinsically quantum mechanical in nature, is of special interest because it provides critical tests of quantum diffusion theories.^{2–4} The basic issue in nonclassical transport is whether a wavelike or particlelike description is appropriate, i.e., whether the tunneling is coherent or incoherent. This depends on whether the interaction with the environment is such as to lead to spatial localization of the wave function or to bandlike (Bloch wave) motion. One of the possible channels for localization of a particle is through its interaction with lattice excitations (phonons, librations, magnons, etc.). In a dissipative environment^{5,6} the lattice excitations can be represented as a bath of harmonic oscillators; interaction with this environment causes a crossover from coherent quantum tunneling to incoherent hopping dynamics when the particle “dressed” with the lattice excitations can be effectively thought of as a polaron.

At low temperatures, the environmental excitations are frozen out. In this case, conventional understanding suggests that the only possible channel for particle localization is the introduction of crystal disorder, which thus may dramatically change the transport properties of a solid. A well-known example is the spatial localization of electron states near the Fermi level in a disordered metallic system, which leads to a transition into a dielectric state (the Anderson transition):⁷ coherent tunneling of a particle is possible only between levels with the same energy (e.g., between equivalent sites in a crystalline lattice); in the case of strong randomness, states with the same energy may be too spatially separated for tunneling to be effective.

Although the concept of localization by disorder has been introduced primarily in order to describe the electronic transport properties of solids, it may also be applied to the quantum dynamics of heavier particles, whether charged or neutral.^{4,8,9} Recent experimental results for positive muons (μ^+) in dilute metallic alloys,¹⁰ as well as for muonium atoms ($\text{Mu} = \mu^+ + e^-$) in “dirty” insulators,^{11,12} have clearly indicated that crystal disorder introduced by impurities dramatically changes the nature of quantum diffusion for particles ~ 200 times heavier than the electron. In these experiments the environmental coupling could be varied or switched on and off by changing the temperature—for interstitial muons in aluminum metal,¹⁰ the low-energy couplings to conduction electrons are suppressed below the superconducting transition, as a BCS energy gap opens at the Fermi surface, while for muonium in insulators^{11,12} the inelastic interactions with phonons are frozen out at low temperatures. Similar arguments apply for the well-known system of a dilute solution of heavy ³He atoms in a ⁴He crystal.^{13,14}

A common and crucial feature of all the above-mentioned experiments is that the particle tunneling bandwidth Δ is small compared with all other relevant energy parameters, especially U , the characteristic shift in the particle’s energy level (relative to its value in the perfect lattice) due to crystalline disorder. For elastic strains, U is expected to vary as $U_0(a/r)^{-3}$ with the distance r from a point defect, where U_0 is the maximum shift corresponding to a site one lattice constant a away from the defect center. (Of course, U actually has discrete values near the center; this continuous formulation is only meaningful when $r \gg a$.) For example, typical values of $U_0 \sim 10^3$ K exceed muon bandwidths in metals by 6–7 orders of magnitude; in insulators the difference is not so extreme, but still $U_0 \gg \Delta$.^{4,15} Under these cir-

cumstances, the influence of crystalline defects extends over distances $R \sim a[U_0/\Delta]^{1/3} \gg a$. The quantum diffusion of the interstitial particle is therefore dominated in these case by strong, long-range crystal disorder.

An essential characteristic of particle transport under conditions of long-range crystal disorder is its inhomogeneity at low temperatures,^{4,16,17} where the particle dynamics cannot be described in terms of a single correlation time τ_c . The particle hop rate is in this case predicted⁴ to follow

$$\tau_c^{-1}(R) \propto \tilde{\Delta}_0^2 \frac{\Omega(T)}{\xi^2(R) + \Omega^2(T)}, \quad (1)$$

where $\tilde{\Delta}_0$ is the renormalized tunneling amplitude, $\Omega(T)$ is the particle's energy level broadening due to coupling with lattice excitations, and $\xi(R) = a[dU/dr]_{r=R}$ is the difference between energy levels at two adjacent tunneling sites due to disorder. (We ignore the possibility of degenerate adjacent sites at the same R .) At low temperatures the phonon width is reduced and

$$\tau_c^{-1}(R) \propto \tilde{\Delta}_0^2 \frac{\Omega(T)}{\xi^2(R)}. \quad (2)$$

Equation (2) describes the dynamics of particles in the vicinity of defects, where the inhomogeneity of the crystal results in a spatial distribution of hop rates, $\tau_c^{-1}(R)$. Another fraction of particles, initially located so far from impurities or defects that $\tilde{\Delta}_0$ exceeds $\xi(R)$ [as well as $\Omega(T)$], undergoes bandlike propagation. In the limiting case of very low temperatures (or below a superconducting transition), inelastic scattering by phonons (or conduction electrons) is strongly suppressed. The two fractions cannot then exchange particles—they are manifest in the appearance of two distinct components in the muon polarization function $P(t)$;^{10–12} this may be taken as a signature of spatial inhomogeneity of the particle dynamics when the disorder is described by a long-range potential.

The foregoing discussion, like all previous theoretical treatments of quantum diffusion (see, e.g., Refs. 4, 8, and 9) implicitly assumed that the diffusing particle has access to only one site per unit cell.

In the harmonic approximation, the transport properties of a neutral particle in a simple crystalline insulator (e.g., a monoatomic or ionic crystal) depend only on the phonon modes of the lattice. For crystals composed of molecules, two additional contributions enter from the internal vibrational and rotational degrees of freedom of the molecules. Internal vibrations of molecules scarcely change the particle dynamics because of their extremely high frequencies. Molecular rotation, however, is a different matter. Two extremes are possible: the molecules may rotate almost freely in the crystal, or the rotational motion may be severely restricted and hence transformed into torsional excitations (librons). Since the typical rotational frequencies of molecules in crystals are still much higher than the particle bandwidth, in the first extreme the energy levels for a particle moving in different unit cells are degenerate, and therefore its dynamics remain unperturbed. In the second extreme the anisotropic interaction between molecules (which causes orientational ordering in the first place) changes the crystalline potential so that this degeneracy is lifted. As far as the particle dynam-

ics are concerned, this splitting of adjacent energy levels acts as an effective disorder, creating the bias ξ in Eq. (1). Here we report our study of muonium dynamics in solid CO₂, in which the anisotropic part of intermolecular interaction is so strong that the lattice keeps its orientational order in the entire solid phase.

Solid carbon dioxide was one of the first few solids (also quartz and ice) in which muonium atom formation was observed, about 30 years ago.¹⁸ However, there was no explanation for the mysterious muonium relaxation in CO₂. The muonium relaxation rate was measured in a transverse magnetic field of 7.2 Oe to be about $0.6 \times 10^6 \text{ s}^{-1}$. This relaxation rate, although not high, is, however, noticeable and cannot be associated with nonuniformity of the magnetic field, inasmuch as in the same experiment a few-times-lower relaxation rate has also been measured. Nor can the muonium relaxation in CO₂ be explained by its interaction with nuclear magnetic moments, as all of them are equal to zero in carbon dioxide.

The source of muonium relaxation in solid CO₂ can be understood if muonium is anisotropic. The reason for the muonium anisotropy is that in the environment of surrounding atoms of the medium, muonium's electron function is not necessarily the spherically symmetric $1S$ state. The effective spin Hamiltonian for static Mu in solid CO₂ in an external field \mathbf{H} , assuming an anisotropic muon-electron hyperfine interaction, has the form¹⁹

$$H = hA \mathbf{S}_e \cdot \mathbf{S}_\mu - g_e \mu_B \mathbf{S}_e \cdot \mathbf{H} - g_\mu \mu_\mu \mathbf{S}_\mu \cdot \mathbf{H}, \quad (3)$$

where A is the muonium hyperfine tensor, and \mathbf{S} , g , and μ are the spins, g factors, and magnetic moments of the respective particles. For example, in a variety of cubic semiconductors muonium centers are observed with a hyperfine interaction that is axially symmetric about any of the [111] crystal axes. For a state of this type (which is the simplest case of anisotropic muonium), A is diagonal with elements A_{\parallel} and A_{\perp} . The essential feature of anisotropic muonium is that at zero magnetic field the muon spin will oscillate at a frequency which is equal to one-half of the anisotropic part of the hyperfine interaction ($A_{\parallel} - A_{\perp}$) divided by Planck's constant. In the general case (when A is a matrix of high order) several frequencies are observed.²⁰ The amplitudes of oscillations at these frequencies are functions of the angles between the principal axes of A (which are determined by the configuration of muonium sites in the crystalline cell) and the initial muon polarization. In the case of muonium diffusion this will result in apparent muonium relaxation.²¹ The hopping sites are equivalent, but have principal axes making different angles with the muon polarization direction; thus when a Mu atom hops to a new site its spin begins to oscillate with different amplitudes for all the frequency components, resulting in an effective relaxation mechanism on the time scale of a mean oscillation quarter-period. To date the theory of the time evolution of the anomalous muonium polarization function in the hopping regime is undeveloped. In quartz,²¹ anomalous muonium diffusion was described using a Kobayashi zero-field stochastic relaxation function with hopping,²² using a constant empirical "static width" of 4 times the highest oscillation frequency. In the current paper we present a way of estimating anomalous muonium hop

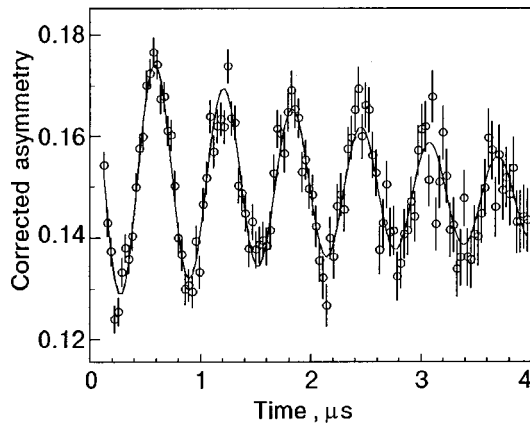


FIG. 1. Experimental μ SR spectrum in pure CO_2 in zero magnetic field at 40 K.

rates in a host with zero nuclear moments regardless of the exact notions about the muonium hyperfine tensor and depolarization function.

The experiments were performed on the EMu beamline of the ISIS Pulsed Muon Facility at the Rutherford Appleton Laboratory. Ultrahigh-purity CO_2 (less than 10^{-5} impurity content) was condensed from the gas phase into a liquid and then frozen into a disc-shaped cell (24 mm in diameter and 5 mm deep). Solid samples were carefully grown from the liquid phase at typical speeds of about 5 mm/h by applying a vertical temperature gradient of about 5 K across the cell. Positive muons of 28 MeV/ c momentum and 100% spin polarization were stopped in the samples, and μ^+ spin rotation (SR) time spectra were recorded at various different temperatures and applied magnetic fields. Positrons from the muon decay are emitted preferentially along the direction of the muon polarization, so that the time-differential μ^+ SR technique, details of which can be found elsewhere,¹ produces direct measurements of the time dependence of the muon decay asymmetry $A(t)$, which is proportional to the muon polarization function $P(t)$.

The formation of anisotropic muonium in solid CO_2 was detected by observing the oscillation signal in zero magnetic field. A typical experimental spectrum in zero magnetic field at low temperature is represented in Fig. 1. Then a set of μ^+ SR spectra was measured in a weak transverse magnetic field $H=2G$. Transverse magnetic field spectra show a nice anisotropic muonium precession signal. In all the temperature interval the envelope of this precession is approximated by a simple exponential function $P(t) \sim \exp(-\lambda t)$. Usually the technique of muonium transverse relaxation is used to extract hopping rates of isotropic muonium in a host with nonzero nuclear moments. In this case the effective spin Hamiltonian of muonium in a crystal in an external magnetic field consists of electron, muon, and nuclear Zeeman interactions, the muonium hyperfine (HF), and the nuclear hyperfine (NHF) interactions (see, e.g., Ref. 15). Qualitatively, modulation of the NHF interactions results in relaxation of the muonium electron spin, which in turn leads to the observed muon depolarization via the muonium HF interaction. As the muonium HF constant A is usually several orders of magnitude higher than the NHF interaction (which for simplicity we characterize by a single parameter δ), it is the

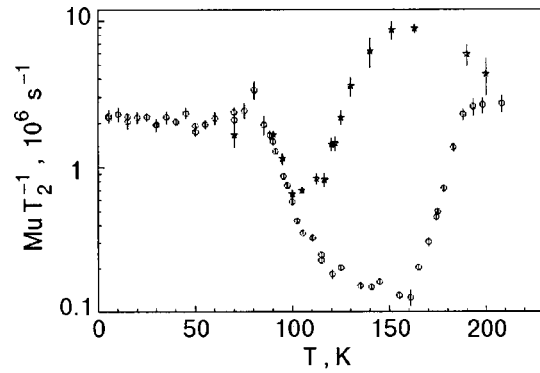


FIG. 2. Temperature dependence of muonium relaxation rate in solid CO_2 in weak transverse field $H=2G$ (circles: pure CO_2 ; stars: $\text{CO}_2+0.1\% \text{N}_2\text{O}$).

latter which sets the time scale for isotropic muonium spin relaxation. In the case of anisotropic muonium, the hyperfine interaction changes from site to site or the HF interaction is modulated “by itself,” and the value of the muonium hyperfine interaction anisotropy about $2(A_{\parallel}-A_{\perp})/h$ will set the time scale for the anisotropic muonium spin relaxation. To make a connection with the standard theory of muonium diffusion this modulation can be presented by “effective” δ or $\tilde{\delta}$. In the standard theory the envelope of the muonium precession signal can be approximated by a simple exponential,

$$P(t) \sim \exp(-t/T_2), \quad (4)$$

where T_2 is the transverse relaxation time of the muonium spin. The muonium relaxation rate T_2^{-1} has a simple form in two limits: if muonium “hops” from site to site at a rate $\tau_c^{-1} \gg \tilde{\delta}$ (fast hopping limit), then the transverse relaxation rate is given by $T_2^{-1} \approx \tilde{\delta}^2 \tau_c$. For very slow diffusion ($\tau_c^{-1} \lesssim \tilde{\delta}$) the muonium spin relaxation takes place on a time scale shorter than τ_c , and $T_2^{-1} \approx \tilde{\delta}$. [In this case $P(t)$ is better approximated by a Gaussian relaxation function].

Figure 2 presents the temperature dependences of the muonium transverse relaxation rate T_2^{-1} in solid CO_2 and CO_2 plus 0.1% of N_2O impurities, extracted from the spectra by fitting single-exponential relaxation functions (4).

In pure CO_2 at high temperatures above 160 K, T_2^{-1} decreases with decreasing temperature, or the hop rate increases with decreasing temperature. This is an unambiguous manifestation of quantum diffusion which has also been recognized for muonium in KCl (Ref. 23) and solid nitrogen (Ref. 24). Such strong temperature dependences of the muonium relaxation at high temperatures in solid CO_2 cannot be due solely to the $\Omega(T)$ dependence in Eq. (1) in the regime of dynamical destruction of the band ($\Omega \gg \xi$), but must rather be caused by exponential renormalization of the tunneling amplitude, due to strong one-phonon scattering.

The muonium relaxation levels off at lower temperatures below about 160 K. This plateau must represent the onset of muonium band motion,^{4,15} which occurs if the coherence is preserved, $\Omega \ll \tilde{\Delta}_0$ (but still $T > \tilde{\Delta}_0$), and the disorder is weak, $\xi \ll \tilde{\Delta}_0$.

The band motion does not extend to the lowest temperatures, however: T_2^{-1} begins to increase with decreasing temperature below about 140 K. These data indicate that inter-

stitial muonium atoms undergo gradual localization in CO₂ at low temperatures where $\Omega \ll \xi$ and that the particle dynamics follow Eq. (2).

Experiments with doped CO₂ were performed to estimate the muonium hopping rate from the trapping regime of muonium diffusion. Transverse relaxation data in solid CO₂ with 0.1% N₂O impurities are represented in Fig. 2 by stars. When the Mu atom hops rapidly in CO₂ (causing low values of T_2^{-1} due to dynamical “narrowing”), it finds a N₂O impurity in the CO₂ crystal and reacts chemically (probably to form the MuNNO* radical),²⁵ which explains the fact that the maximum T_2^{-1} value for Mu in CO₂+N₂O significantly exceeds that for slowly hopping Mu in pure CO₂ at low temperatures, where it is determined by the anisotropy of Mu hyperfine tensor. This chemical reaction results in an exponential relaxation of the Mu polarization, the rate of which is determined by the time required for Mu to approach the N₂O impurity within a distance a of about one lattice constant, after which the reaction occurs immediately. Then the rate of trapping is²⁶

$$\lambda = 4\pi a D c, \quad (5)$$

where $D = a^2/4\tau_c$ is the muonium diffusion coefficient, and c is the concentration of impurities. From the maximum relaxation rate $T_{2\max}^{-1} \sim 10^7 \text{ s}^{-1}$ we can estimate $\tau_{c\max} \sim \pi c/T_{2\max}^{-1} \sim 3 \times 10^9 \text{ s}^{-1}$. For the bandlike regime the “hop rate” is given by $\tau_c^{-1} = 2\sqrt{2}\tilde{\Delta}_0$ (Ref. 27). By substituting $\tau_{c\max}$ we can estimate the muonium bandwidth in CO₂ to be about 10^{-2} K . This value may be compared with muonium bandwidths in KCl and solid nitrogen (0.16 and 10^{-2} K , respectively).¹⁵

At high temperatures the clear maximum in T_2^{-1} for Mu in CO₂+N₂O marks the crossover from fast to slow Mu diffusion near N₂O impurities. In this temperature range the strong coupling to phonons allows Mu to overcome the defect potential and move to react with N₂O. However, the energy shift ξ which the particle has to overcome is much larger close to the defect than far from it, making the Mu hop rate strongly dependent on the distance from the defect.

At low temperatures the suppression of inelastic interactions with the lattice changes Mu diffusion drastically—Mu atoms are stuck (or “frozen”) at some distance far from N₂O impurities, causing a strong reduction of the reaction rate (Mu relaxation rate). At very low temperature Mu atoms simply cannot approach N₂O impurities due to suppression of the inelastic interactions, and T_2^{-1} becomes the same in pure and doped crystals (Fig. 2).

In conclusion, we have presented evidence for the bandlike motion of light interstitial muonium atoms in CO₂ crystals.

This work was supported by the Canadian Institute for Advanced Research, the Natural Sciences and Engineering Research Council of Canada, the National Research Council

of Canada, the Engineering and Physical Sciences Research Council of the United Kingdom and the Russian Research Center “Kurchatov Institute.” Two of us (V.G.S. and D.G.E.) were also supported by the INTAS Foundation (through grant 97-30063) and NATO (through Grant PST.CLG.977687).

*E-mail: eschenko@a120.inr.troitsk.ru

**And Department of Physics and Astronomy, University College London, Gower Street, London WC1E 6BT, UK

- ¹A. Schenck, *Muon Spin Rotation: Principles and Applications in Solid State Physics*, Adam Hilger, Bristol (1986); S. F. J. Cox, *J. Phys. C* **20**, 3187 (1987); J. H. Brewer, *Muon Spin Rotation/Relaxation/Resonance*, in *Encyclopedia of Applied Physics*, edited by G. L. Trigg, VCH, New York (1995).
- ²A. F. Andreev and I. M. Lifshitz, *Zh. Éksp. Teor. Fiz.* **56**, 2057 (1969) [*Sov. Phys. JETP* **29**, 1107 (1969)].
- ³C. P. Flynn and A. M. Stoneham, *Phys. Rev. B* **1**, 3966 (1970).
- ⁴Yu. M. Kagan and N. V. Prokof'ev, *Quantum Tunneling Diffusion on Solids*, in *Quantum Tunneling in Condensed Media*, edited by A. J. Leggett and Yu. M. Kagan, North-Holland (1992), p. 37.
- ⁵A. O. Caldeira and A. J. Leggett, *Phys. Rev. Lett.* **46**, 211 (1981); *Ann. Phys. (N.Y.)* **149**, 374 (1983).
- ⁶U. Weiss and H. Grabert, *Phys. Lett. A* **108**, 63 (1985); H. Grabert and U. Weiss, *Phys. Rev. Lett.* **54**, 1065 (1985).
- ⁷P. W. Anderson, *Phys. Rev.* **109**, 1492 (1958).
- ⁸U. Weiss, *Quantum Dissipative Systems*, in *Series in Modern Condensed Matter Physics*, Vol. 2, World Scientific, Singapore (1993).
- ⁹T. Regelman, L. Schimmele, and A. Seeger, *Philos. Mag. B* **72**, 209 (1995).
- ¹⁰E. Karlsson et al., *Phys. Rev. B* **52**, 6417 (1995).
- ¹¹R. Kadono, R. F. Kiefl, W. A. MacFarlane, and S. R. Dunsiger, *Phys. Rev. B* **53**, 3177 (1996).
- ¹²V. Storchak, J. H. Brewer, and G. D. Morris, *Phys. Rev. B* **53**, 11300 (1996).
- ¹³M. J. Richards, J. Pope, and R. Widom, *Phys. Rev. Lett.* **29**, 708 (1972); A. R. Allen, M. G. Richards, and J. Schratte, *J. Low Temp. Phys.* **47**, 289 (1982).
- ¹⁴V. N. Grigor'ev, B. N. Esel'son, V. A. Mikheev, and Yu. E. Shul'man, *JETP Lett.* **17**, 25 (1973).
- ¹⁵V. G. Storchak and N. V. Prokof'ev, *Rev. Mod. Phys.* **70**, 929 (1998).
- ¹⁶Yu. M. Kagan and N. V. Prokof'ev, *Phys. Lett. A* **159**, 289 (1991).
- ¹⁷N. V. Prokof'ev, *Hyperfine Interact.* **85**, 31 (1994).
- ¹⁸G. G. Myasishcheva et al., *Zh. Éksp. Teor. Fiz.* **53**, 451 (1968) [*Sov. Phys. JETP* **26**, 298 (1968)].
- ¹⁹B. D. Patterson, *Rev. Mod. Phys.* **60**, 69 (1988).
- ²⁰J. H. Brewer, D. P. Spencer, D. G. Fleming, and J. A. R. Coope, *Hyperfine Interact.* **8**, 405 (1981).
- ²¹J. H. Brewer, *Hyperfine Interact.* **8**, 375 (1981).
- ²²R. H. Hayano, Y. J. Uemura, J. Imazato, N. Nishida, T. Yamazaki, and R. Kubo, *Phys. Rev. B* **20**, 850 (1979).
- ²³R. F. Kieff, R. Kadono, J. H. Brewer, G. M. Luke, H. K. Yen, M. Celio, and E. I. Ansaldo, *Phys. Rev. Lett.* **62**, 792 (1989).
- ²⁴V. Storchak, J. H. Brewer, W. N. Hardy, S. R. Kreitman, and G. D. Morris, *Phys. Rev. Lett.* **72**, 3056 (1994).
- ²⁵J. J. Pan, D. J. Arseneau, M. Senba, M. Shelly, and D. G. Fleming, *J. Phys. Chem. A* **101**, 8471 (1997).
- ²⁶T. R. Waite, *Phys. Rev.* **107**, 463 (1957).
- ²⁷K. G. Petzinger, *Phys. Rev. B* **26**, 6530 (1982).

This article was published in English in the original Russian journal. Reproduced here with stylistic changes by AIP.

Search for the minimum thermal conductivity in mixed cryocrystals $(\text{CH}_4)_{1-\xi}\text{Kr}_\xi$

V. A. Konstantinov,* V. G. Manzhelii, and V. P. Revyakin

B. Verkin Institute for Low Temperature Physics and Engineering of the National Academy of Sciences of Ukraine, 47 Lenin ave., Kharkov, 63103, Ukraine

R. O. Pohl

Laboratory of Atomic and Solid State Physics, Cornell University, Ithaca, New York, USA

(Submitted March 21, 2001)

Fiz. Nizk. Temp. **27**, 1159-1169 (September-October 2001)

The isochoric thermal conductivity of $(\text{CH}_4)_{1-\xi}\text{Kr}_\xi$ solid solutions is studied between 40 K and ~ 150 K over a wide range of concentrations ($\xi=0.013, 0.032, 0.07, 0.115, 0.34, 0.71, 0.855, 0.937, \text{ and } 0.97$). A gradual transition from the thermal conductivity of a highly perfect crystal to the minimum thermal conductivity is observed as the crystal becomes increasingly more disordered. A qualitative description is given in the framework of Debye model of thermal conductivity, which takes into consideration the fact that phonon mean free path cannot decrease indefinitely. © 2001 American Institute of Physics. [DOI: 10.1063/1.1414577]

INTRODUCTION

The question of what occurs when the mean free path of a phonon becomes comparable to the lattice parameter or to its own wavelength is one of the most intriguing problems in the thermal conductivity of solids.¹⁻⁶ Some progress in the description of the heat transport in strongly disordered materials has come about through the concept⁴⁻⁶ of the minimum thermal conductivity Λ_{\min} which is based on the picture where the lower limit of the conductivity is reached when the heat is being transported through a random walk of the thermal energy between the neighboring atoms or molecules vibrating with random phases. In this case Λ_{\min} can be written as the following sum of three Debye integrals:^{5,6}

$$\Lambda_{\min} = \left(\frac{\pi}{6}\right)^{1/3} k_B n^{2/3} \sum_i v_i \left[\left(\frac{T}{\Theta_i}\right)^2 \int_0^{\Theta_i/T} \frac{x^3 e^x}{(e^x - 1)^2} dx \right]. \quad (1)$$

The summation is taken over three (two transverse and one longitudinal) sound modes with the sound speeds v_i , Θ_i is the Debye cutoff frequency for each polarization expressed in degrees Kelvin, $\Theta_i = v_i (\hbar/k_B) (6\pi^2 n)^{1/3}$, and n is the number density of atoms or molecules. Although no theoretical justification exists as yet for this picture of the heat transport, evidence for its validity has been obtained on a number of amorphous solids in which the high-temperature thermal conductivity has been found to agree with the value predicted by this model.⁵ Indirect evidence has also been obtained in measurements of the thermal conductivity of highly disordered crystalline solids, in which no thermal conductivity smaller than that predicted by this model seems to have ever been observed.⁶ What has been missing so far, however, has been a systematic study of the gradual transition from the thermal conductivity of a highly perfect crystal to the minimum thermal conductivity as the crystal becomes increasingly disordered. Such measurements will be presented here.

The objects of this study were $(\text{CH}_4)_{1-\xi}\text{Kr}_\xi$ solid solutions ($0 \leq \xi \leq 1$). This choice was based on the following considerations:

i) The phase diagram of $(\text{CH}_4)_{1-\xi}\text{Kr}_\xi$ has been studied quite well. It was found⁷ that the components form a homogeneous solid solution with fcc structure above 30 K at all ξ .

ii) Kr and CH_4 have similar molecule/atom radii and parameters of the pair potential.⁸ The Debye temperatures Θ_D of Kr and CH_4 are 72 and 143 K, respectively.^{7,8} At the same time the masses of the Kr atom and the CH_4 molecule are very different, 83.8 and 16 atomic units, respectively. The fractional mass difference $\Delta M/M$ is 0.81 for the CH_4 impurity in Kr and 4.23 for the Kr impurity in methane. One can thus expect strong impurity scattering, especially in the latter case.

iii) The peculiarities of the heat transfer in pure Kr and CH_4 have been studied in detail (Refs. 9-12 and 13-15, respectively). There have been separate studies of the low-temperature thermal conductivity at $T < 20$ K in the mixed cryocrystals, which indicate strong point-defect scattering.^{12,15} The thermal conductivity Λ_{meas}^P of solid CH_4 and Kr measured at the saturated vapor pressure is shown in

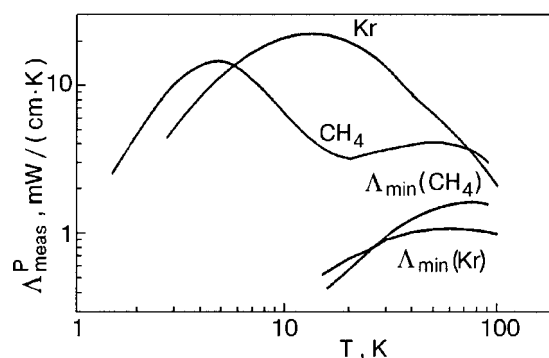


FIG. 1. The thermal conductivities Λ_{meas}^P of solid Kr and CH_4 measured at saturated vapor pressures according to data of Refs. 9-15. Λ_{\min} of solid Kr and CH_4 calculated by Eq. (1) are shown at the bottom.

Fig. 1 together with Λ_{\min} calculated by Eq. (1) for equilibrium conditions. The corresponding values of the density and sound velocities at different temperatures needed for the calculation were taken from Refs. 8 and 16. As can be seen from Fig. 1, the thermal conductivity of Kr goes through a maximum at 12 K and then decreases, approaching its lower limit Λ_{\min} at premelting temperatures. The thermal conductivity of CH_4 goes through a maximum at 4.5 K in the orientationally ordered α phase and decreases subsequently to the α - β transition temperature $T_{\alpha-\beta} = 20.4$ K. In the orientationally disordered (OD) β phase the thermal conductivity begins to increase again, goes through another maximum at 50 K, and then decreases as far as the melting-point temperature $T_m = 89.8$ K. The ratio $\Lambda_{\text{meas}}^P / \Lambda_{\min}$ is shown in Fig. 2. It is seen that Λ_{meas}^P exceeds the lower limit Λ_{\min} by a factor of two to four in the entire region of the OD phase.

For these reasons, the $(\text{CH}_4)_{1-\xi}\text{Kr}_\xi$ mixed cryocrystals enable us to study the influence of atomic-size defects upon the thermal conductivity near its lower limit and to test the validity of the concept of the minimum thermal conductivity in the form it was reported in Refs. 5 and 6.

EXPERIMENTAL TECHNIQUE

To compare correctly experimental results on thermal conductivity with theory at $T \geq \Theta_D$ it is necessary to perform experiments at constant density to exclude the effect of thermal expansion. The simplest molecular crystals and solidified inert gases are best suited, since their thermal expansion coefficients are much larger than those of the materials commonly used in high-pressure cells. If a high-pressure cell is filled with a solid sample of quite high density, on subsequent cooling the volume of the sample will remain practically constant while the pressure of the sample decreases. The small deviations from constant volume caused by thermal and elastic deformation of the measuring cell can easily be taken into account.

The V - T diagram of solid Kr plotted according to data of Ref. 16 is shown in Fig. 3. As an example, two isochores are shown, which correspond to the volumes 28.5 and 29.0 nm^3/mole . T_0 is the temperature at which the $V = \text{const}$ condition comes into play in the experiment. Below T_0 the isochoric data convert to the data measured at saturated vapor pressure, and on further cooling the sample can pull away from the cell walls. The temperature T_m and pressure P_m

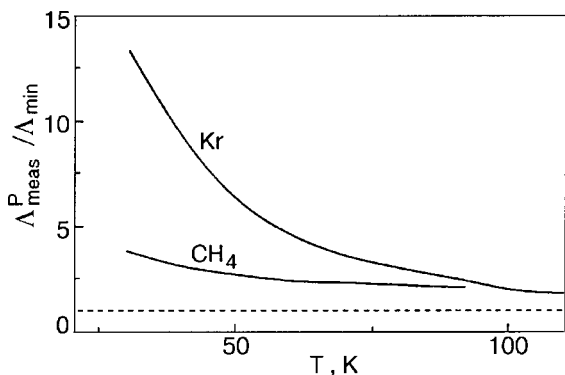


FIG. 2. The ratio $\Lambda_{\text{meas}}^P / \Lambda_{\min}$ for solid Kr and CH_4 . The dashed line corresponds to $\Lambda_{\text{meas}}^P / \Lambda_{\min} = 1$.

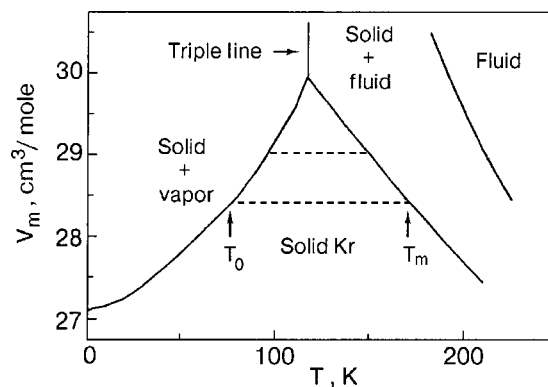


FIG. 3. The V - T diagram for solid Kr according to Ref. 16. The two isochores shown correspond to the volumes 28.5 and 29.0 nm^3/mole .

correspond to the onset of sample melting. T_0 and T_m shift towards lower and higher temperature as the density of the sample increases.

The molar volume of $(\text{CH}_4)_{1-\xi}\text{Kr}_\xi$ solid solution varies appreciably (about 10% at the saturated vapor pressure) as a function of the component concentrations.⁷ In this context it is convenient to compare the experimental results taken at different concentrations for those samples which reach the $V = \text{const}$ condition at the same temperature T_0 . There are certain experimental difficulties to prepare the samples with the same temperature T_0 . However, if the thermal conductivity is studied on several isochores at the same concentration of the components, it can be recalculated to any T_0 , using the volume dependence of thermal conductivity in the form: $g = -(\partial \ln \Lambda / \partial \ln V)_T$, where g is the Bridgman coefficient. Since the pressure at temperature T_0 is zero, $\Lambda(T_0)$ corresponds to the isobaric thermal conductivity $\Lambda_P(P=0)$ as well.

This study was carried out on a coaxial-geometry setup, using the steady-state method. The measuring beryllium bronze cell (160 mm long, 17.6 mm inner diameter) was engineered for a maximum pressure of 800 MPa. The inner measuring cylinder was 10.2 mm in diameter. The sample was between the outer and inner cylinders. The temperature was measured with platinum resistance thermometers, mounted in special channels of the inner and outer cylinders and unaffected by high pressure. During the sample growth, a temperature gradient ~ 1 K/cm was maintained along the measuring cell. The pressure in the inlet capillary and the cell was produced by a special thermocompressor and was varied from 50 to 250 MPa for obtaining samples of various densities. Under identical growing conditions (a capillary pressure ≈ 200 MPa and a temperature gradient along the cell ≈ 1 K/cm) we were able to prepare denser samples of solid solutions with CH_4 prevailing ($\xi < 0.3$) than with Kr prevailing. This may be due to the higher compressibility of CH_4 as compared to that of Kr. When the sample growth was completed, the inlet capillary was blocked at liquid hydrogen temperature and the samples were annealed at premelting temperatures for 5–6 h to remove density gradients. After completion of the experiment the samples were evaporated into a thin-wall vessel and their masses were determined by weighing. The molar volumes of the samples were estimated from the known volume of the measuring cell and from the

TABLE I. Smoothed values of the isobaric Λ_P and isochoric Λ_V coefficients of thermal conductivity of the $(\text{CH}_4)_{1-\xi}\text{Kr}_\xi$ solid solution ($\xi > 0.7$) in mW/(cm·K). Molar volumes of the samples are given in nm³/mole.

T, K	$\xi = 0.97$			$\xi = 0.937$			$\xi = 0.855$		$\xi = 0.71$					
	Λ_P	Λ_V at V_m			Λ_P	Λ_V at V_m			Λ_P	Λ_V at V_m				
		28.5	28.9	29.5		28.82	29.31	29.72		29.25	29.85	Λ_P	29.75	30.30
40	3.60				2.75									
50	3.00				2.50									
60	2.93				2.30									
70	2.60				2.12									
80	2.30	2.43			1.85	1.88			1.5	1.5		1.05	1.08	
90	2.00	2.32	2.08		1.65	1.84			1.4	1.49		1.03	1.12	1.03
100	1.72	2.20	1.95	1.72	1.46	1.80	1.61		1.26	1.48	1.34	1.02	1.15	1.05
110	1.45	2.10	1.85	1.60	1.28	1.75	1.58	1.41	1.18	1.47	1.32	1.00	1.19	1.08
120		1.98	1.74	1.50		1.70	1.52	1.38		1.46	1.31		1.22	1.12
130		1.90	1.62	1.38		1.67	1.50	1.36		1.45	1.30		1.25	
140		1.82	1.52	1.25		1.65	1.48			1.45			1.28	
150		1.73	1.40			1.63	1.46							
160		1.68				1.60								

sample mass. The total systematic error was dominant, but did not exceed 4% for the thermal conductivity and 0.2% for molar volume. The purity of the Kr and CH₄ gases used was better than 99.98%. The experimental details are described more comprehensively in Ref. 17.

RESULTS

The smoothed coefficients of isobaric Λ_P and isochoric Λ_V thermal conductivities are presented in Tables I and II.

The molar volumes V_m of the samples, the temperatures T_0 at which the $V = \text{const}$ condition comes into play in the experiment, and the temperatures T_m of the beginning of sample melting are given in Table III along with the Bridgman coefficients $g = -(\partial \ln \Lambda / \partial \ln V)_T$ calculated from the measured results. The isochoric thermal conductivity of pure Kr (Ref. 11) and solid solution $(\text{CH}_4)_{1-\xi}\text{Kr}_\xi$ with Kr prevailing ($\xi > 0.7$) rescaled to $T_0 = 75$ K is shown in Fig. 4 together with low-temperature data.¹² Figure 5 shows the iso-

TABLE II. Smoothed values of the isobaric Λ_P and isochoric Λ_V coefficients of thermal conductivity of the $(\text{CH}_4)_{1-\xi}\text{Kr}_\xi$ solid solution ($\xi < 0.4$) in mW/(cm·K). Molar volumes of the samples are given in cm³/mole.

T, K	$\xi = 0.011$			$\xi = 0.032$			$\xi = 0.07$			$\xi = 0.115$		$\xi = 0.34$					
	Λ_P	Λ_V at V_m			Λ_P	Λ_V at V_m			Λ_P	Λ_V at V_m		Λ_P	Λ_V at V_m				
		31.03	31.60	32.05		31.00	31.62	Λ_P		30.85	31.42		31.80	Λ_P	30.70	31.22	30.50
40	2.20				2.05				1.83	1.85			1.30	1.32			
50	2.40	2.55			2.18	2.30			1.95	2.14			1.45	1.55		1.2	1.2
60	2.50	2.75			2.25	2.50			2.05	2.37	2.11		1.53	1.70	1.56	1.2	1.3
70	2.52	2.90	2.70		2.28	2.65	2.38		2.12	2.55	2.30		1.55	1.80	1.65	1.2	1.35
80	2.52	3.02	2.80	2.55	2.29	2.74	2.48		2.15	2.65	2.40	2.20	1.56	1.85	1.72	1.22	1.40
90	2.50	3.05	2.87	2.60	2.29	2.78	2.53	2.17	2.17	2.70	2.45	2.26	1.56	1.88	1.75	1.22	1.45
100		3.07	2.87	2.60		2.80	2.55			2.72	2.48	2.28		1.90	1.76		1.48
110		3.05	2.85			2.80	2.55			2.72	2.48			1.90	1.75		1.50
120		3.02				2.80	2.55			2.70				1.88			1.51
130										2.68				1.88			

TABLE III. Molar volumes V_m of the samples, the temperatures T_0 at which the experiment reaches the condition $V=\text{const}$, the temperatures T_m of the onset of sample melting, and the Bridgman coefficients $g = -(\partial \ln \Lambda / \partial \ln V)_T$.

ξ	Number of the sample	$V_m, \text{Åm}^3/\text{mole}$	T_0, K	T_m, K	g
0.013	1	31.03	45	125	4.8
	2	31.60	63	114	
	3	32.05	79	103	
0.032	1	31.0	44	126	4.2
	2	31.62	65	111	
0.07	1	30.85	37	130	4.2
	2	31.42	60	115	
	3	31.80	72	108	
0.115	1	30.70	35	130	3.9
	2	31.22	55	118	
0.34	1	30.50	49	135	3.8
0.71	1	29.75	70	144	4.2
	2	30.30	86	125	
0.855	1	29.25	75	148	5.2
	2	29.85	95	130	
0.937	1	28.82	77	158	7.7
	2	29.31	92	145	
	3	29.72	102	133	
0.97	1	28.5	72	168	8.5
	2	28.95	86	154	
	3	29.5	100	140	

choric thermal conductivity of pure CH₄ (Ref. 13) and of the solid solution with CH₄ prevailing ($\xi < 0.35$), rescaled to $T_0 = 40 \text{ K}$, together with low-temperature data.¹⁵ Although there is a temperature gap between the two sets of data, one can conclude that they agree quite well. The lower limits of the isochoric thermal conductivity Λ_{min} of pure Kr and CH₄ are shown in Figs. 4 and 5 as broken lines. The molar volumes and sound velocities needed for the calculation were taken to correspond to the temperature T_0 from Refs. 8 and 16 and were assumed to be independent of temperature. For the crystals with Kr prevailing ($\xi \geq 0.97$), the isochoric thermal conductivity increases steeply as the temperature decreases. As ξ decreases, the thermal conductivity decreases

as a whole and increases less steeply with decreasing temperature. At $0.3 \geq \xi \geq 0.7$ the thermal conductivity becomes practically temperature independent, as expected for the lower limit of the thermal conductivity Λ_{min} at $T \geq \Theta_D$. The measured data lie between the predicted Λ_{min} for pure Kr and CH₄, calculated according to Eq. (1). As ξ decreases further (CH₄-rich crystal), the thermal conductivity increases again, and it approaches that of pure CH₄ as the concentration of Kr decreases to zero. The concentration dependence of the thermal conductivity of the (CH₄)_{1- ξ} Kr ξ solid solution at $T = 75 \text{ K}$ and $P = 0$ is shown in Fig. 6. The Λ_{min} of pure Kr and CH₄ are shown as broken lines. It is seen that

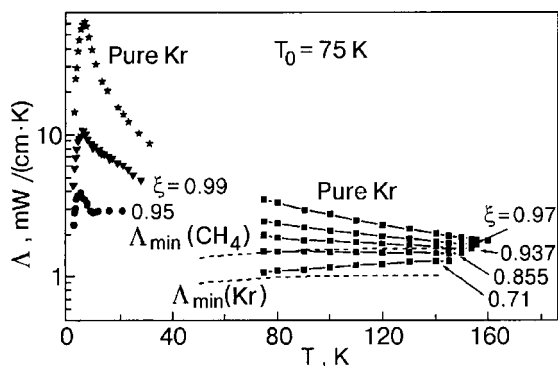


FIG. 4. Smoothed values of the isochoric thermal conductivity of pure Kr (Ref. 11) and Kr with a CH₄ admixture, rescaled to $T_0 = 75 \text{ K}$ (■), together with low-temperature data.¹² The broken lines are the isochoric Λ_{min} of pure Kr and CH₄.

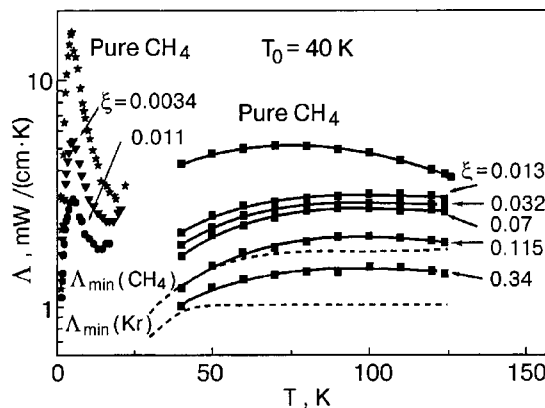


FIG. 5. Smoothed values of the isochoric thermal conductivity of pure CH₄ (Ref. 13) and CH₄ with a Kr admixture, rescaled to $T_0 = 40 \text{ K}$ (■), together with low-temperature data.¹⁵ The broken lines are the isochoric Λ_{min} of pure Kr and CH₄.

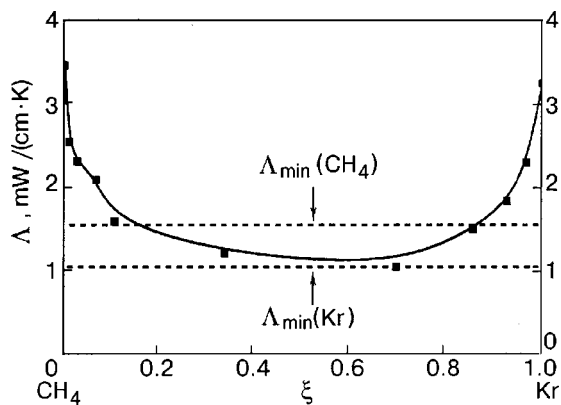


FIG. 6. The concentration dependence of the thermal conductivity of $(CH_4)_{1-\xi}Kr_\xi$ solid solutions at $T=75$ K and $P=0$. The horizontal lines are Λ_{\min} of pure Kr and CH_4 under the same conditions.

thermal conductivity changes rapidly at $\xi < 0.2$ and $\xi > 0.8$ and is practically concentration independent at $0.2 < \xi < 0.8$.

DISCUSSION

In the solidified inert gases Ar, Kr, and Xe the phonon-phonon interaction is the main mechanism determining the value and the temperature dependence of the thermal conductivity $\Lambda(T)$ at the Debye temperature and higher (He and Ne melt at temperatures much below Θ_D (Ref. 16, Chapter 11)). If the scattering is not too strong and the model of elastic waves is appropriate, the theory predicts^{1–4,18} that the isochoric thermal conductivity should vary as $\Lambda_V \propto 1/T$ at $T \gg \Theta_D$. However, experiments at constant volume revealed appreciable deviations from this dependence at the highest temperatures, with the conductivity varying slower than $1/T$.^{11,16,19} Such behavior implies^{3,19} an approach of the thermal conductivity toward its lower limit Λ_{\min} . The proximity of the thermal conductivity of solidified inert gases to Λ_{\min} at premelting temperatures was first pointed out by Slack.⁴

A characteristic peculiarity of molecular crystals is the presence of both translational and rotational motions of molecules in their lattice sites. For normal (orientationally ordered) molecular solids the intermolecular modes generally have a mixed translational-librational character and cannot be considered as independent. It is assumed, however, that separation can be made in orientationally ordered phases at low temperatures, and then collective translational vibrations (phonons) and rotational vibrations (librons) can be treated separately.²⁰ The contribution of librons to the heat transfer is assumed to be relatively small because the bands associated with the angular motion of the molecules are narrow. At the same time, the role of librons in scattering processes is important.²⁰ In orientationally disordered phases, however, the absence of orientational long-range order means that well-defined, librational modes cannot propagate through the crystal: they are always rapidly damped out.²¹ The additional phonon scattering (beyond the phonon-phonon) may originate in the OD phases of molecular crystals due to the short-range fluctuations of the orientational order in the vicinity of the phase transition. For example, in solid CH_4 this additional scattering above the α - β transition temperature $T_{\alpha-\beta} = 20.4$ K is of the same magnitude as the phonon-phonon

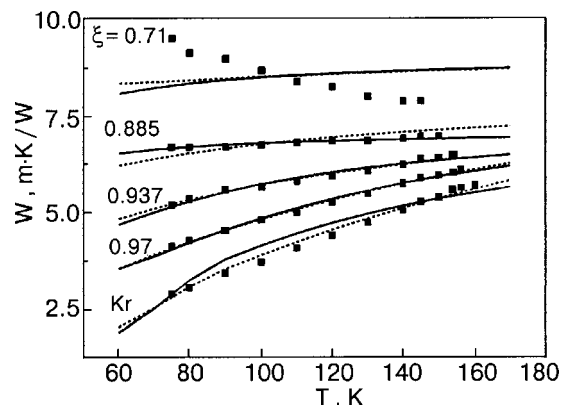


FIG. 7. The isochoric thermal resistivity of pure Kr and Kr with a CH_4 admixture, rescaled to $T_0=75$ K. The solid and dashed lines correspond to the best fit within the Debye model of the thermal conductivity according to i) and ii), respectively.

scattering.^{13,14} However, it decreases rapidly when the temperature increases and it practically disappears above 90 K, whereas the phonon-phonon scattering continues to increase. The competition of these two (phonon-phonon and phonon-rotational) mechanisms of scattering in the OD phase of solid CH_4 results in another high-temperature maximum of the thermal conductivity, in addition to the low-temperature one at 4.5 K. The models describing the phonon scattering on fluctuations of the orientational short-range order in solid methane were suggested in Refs. 14 and 22. It has already been mentioned above that Λ_{meas} exceeds Λ_{\min} by a factor of two to four in the OD phase of methane. The additional scattering mechanism due to Kr impurity (which is supposed to be very strong because of the big mass difference) decreases the thermal conductivity with increasing ξ to values which are between the predicted Λ_{\min} for pure Kr and CH_4 , calculated according to Eq. (1).

Defects of atomic dimensions weaken the temperature dependence of the lattice thermal conductivity caused by U -processes.^{3,23} The theoretical consideration of point defect scattering in the framework of the Debye model at $T \gg \Theta_D$ is made with the assumption that the perturbation theory is valid at all frequencies and temperatures.^{18,23,24} Point defects at small concentrations ($\xi < 0.05$) have to lead to an additional contribution to the thermal resistivity $W = 1/\Lambda$ of the crystal, which is independent of temperature.²⁴ The slowest variation in the limit of very strong point-defect scattering is $\Lambda \propto 1/T^{1/2}$ (Ref. 25). It has been already noted above that the thermal conductivity of Kr appears to approach its lower limit Λ_{\min} at premelting temperatures (see Fig. 1). If Λ_{\min} actually is the lower limit to the thermal conductivity of a lattice, the point-defect scattering should be different from that discussed above. Intuitively, one would expect that the contribution of small concentrations of point defects to the thermal resistivity should decrease with increasing temperature. In the case of very strong point-defect scattering Λ may coincide with Λ_{\min} in a wide temperature range. To check this assumption the thermal resistivity of pure Kr and $(CH_4)_{1-\xi}Kr_\xi$ solid solutions with Kr prevailing is shown in Fig. 7 ($T_0 \approx 75$ K). It is seen clearly that the additional contribution of CH_4 impurities to the total thermal resistivity decreases with increasing temperature at all $\xi > 0.7$. At 0.85

$\geq \xi \geq 0.7$ the thermal conductivity lies between the predicted Λ_{\min} for pure Kr and CH_4 , calculated according to Eq. (1) (see Fig. 4).

A quantitative description of the thermal conductivity of $(\text{CH}_4)_{1-\xi}\text{Kr}_\xi$ solid solutions with Kr prevailing ($\xi > 0.7$) is made by taking into consideration only U -processes and Rayleigh scattering. Phonon scattering on excitations of the rotational motion of the methane molecules, which play an important role at low temperature,¹² is expected to be weak at high temperatures. It was shown earlier that molecules undergo a almost free rotation in pure CH_4 at $T \sim 90$ K and higher,¹³ and that this kind of rotation does not lead to additional phonon scattering. For matrix-isolated molecules in solidified inert gases the onset of almost free rotation takes place at lower temperatures.⁸

The thermal conductivity can be described using the Debye model as

$$\Lambda(T) = 3nk_B v \left(\frac{T}{\Theta_D} \right)^3 \int_0^{\Theta_D/T} l(x) \frac{x^4 e^x}{(e^x - 1)^2} dx, \quad (2)$$

where $\Theta_D = v(\hbar/k_B)(6\pi^2 n)^{1/3}$ is the Debye temperature, v is the polarization-averaged sound velocity, and $l(x)$ is the phonon mean free path. At $T \geq \Theta_D$ the boundary scattering is negligible and the phonon mean free path is determined by the U -processes and Rayleigh scattering.¹⁸

$$l(x) = (l_{\text{Rayl}}^{-1} + l_{\text{Umkl}}^{-1})^{-1}, \quad (3)$$

where $x = v\hbar/k_B T \lambda$, and λ is the phonon wavelength.

Frequently used expressions for the phonon mean free path resulting from the individual scattering mechanisms are

$$l_{\text{Umkl}}^{-1} = \frac{CT}{\lambda^2}, \quad (4)$$

where

$$C = \frac{12\pi^3}{\sqrt{2}n^{1/3}} \frac{\gamma^2 k_B}{m v^2} \quad (5)$$

and

$$l_{\text{Rayl}}^{-1} = \frac{4\pi^3 \Omega_0 T}{\lambda^4}, \quad (6)$$

where

$$\Gamma = \xi(1 - \xi) \left[\frac{\Delta M}{M} + 2\gamma \frac{\Delta \Omega_0}{\Omega_0} \right]^2. \quad (7)$$

Here γ is the Grüneisen parameter, taken as 2.5 for Kr and CH_4 (Refs. 8 and 16), m is the atomic/molecular mass, and M and Ω_0 are the average atomic/molecular weight and volume, respectively, of the mixed crystals (for pure CH_4 $\Omega_0 = 5.18 \times 10^{-23} \text{ nm}^3$, $M = 16$, and for pure Kr $\Omega_0 = 4.73 \times 10^{-23} \text{ nm}^3$, $M = 83.8$), and ΔM and $\Delta \Omega_0$ are the atom/molecule weight and volume difference from their average values, respectively.

Expression (3) cannot apply when $l(x)$ becomes less than the interatomic spacing or shorter than the phonon wavelength. In that case a lower limit of the mean free path is reached. This problem has been discussed previously for

the case of U -processes only.³ Let us extend this consideration to the case of combined U -processes and Rayleigh scattering.

i) Let us assume that the lower limit of the phonon mean free path is of the order of one-half of the phonon wavelength. In this case $l(x)$ is given by Eq. (3) when $l(x) \geq \alpha\lambda/2$ or otherwise by

$$l(x) = \alpha\lambda/2, \quad (8)$$

where α is some numerical coefficient of the order of unity which is assumed to be independent of T and λ . The crossover from behavior described by Eq. (3) to Eq. (8) occurs at the phonon wavelength λ_* , which is determined from

$$\left(\frac{CT}{\lambda_*^2} + \frac{B}{\lambda_*^4} \right)^{-1} = \alpha \frac{\lambda_*}{2}. \quad (9)$$

This corresponds to the effective crossover temperature $\Theta_* = \hbar v/k_B \lambda_*$. (It is supposed that $\Theta_* < \Theta_D$; otherwise $\Theta_* = \Theta_D$.) The thermal conductivity integral is broken into two parts:

$$\Lambda(T) = 3nk_B v \left(\frac{T}{\Theta_D} \right)^3 \left[\int_0^{\Theta_*/T} l(x) \frac{x^4 e^x}{(e^x - 1)^2} dx + \int_{\Theta_*/T}^{\Theta_D/T} \alpha \frac{\lambda}{2} \frac{x^4 e^x}{(e^x - 1)^2} dx \right]. \quad (10)$$

In the high-temperature limit $T \geq \Theta_D$, when only the U -processes are in effect, $\Lambda(T) = A_1/T^2 + \Lambda'_{\min}$ (Refs. 3 and 27), where A_1 is some temperature-independent numerical coefficient, and Λ'_{\min} is

$$\Lambda'_{\min} = 3\alpha \left(\frac{\pi}{6} \right)^{1/3} n^{2/3} k_B v \left(\frac{T}{\Theta_D} \right)^2 \int_0^{\Theta_D/T} \frac{x^3 e^x}{(e^x - 1)^2} dx. \quad (11)$$

This expression for Λ'_{\min} is identical to that predicted by Eq. (1) if the polarization-averaged speed of sound is used and it is assumed that $\alpha = 1$. In the case of strong phonon scattering caused by point defects (when $\Theta_* \ll \Theta_D$), the lower limit on the thermal conductivity is accurately found from Eq. (11).

ii) Let us assume that the lower limit of the phonon mean free path is of the order of the interatomic distance. In this case the phonon mean free path $l(x)$ is given by Eq. (3) when $l(x) \geq \alpha n^{-1/3}$ or otherwise by

$$l(x) = \alpha n^{-1/3}. \quad (12)$$

The crossover from behavior described by Eq. (3) to Eq. (12) occurs at the phonon wavelength λ_* , which is determined from

$$\left(\frac{CT}{\lambda_*^2} + \frac{B}{\lambda_*^4} \right)^{-1} = \alpha n^{-1/3}. \quad (13)$$

The effective crossing temperature is $\Theta_* = \hbar v/k_B \lambda_*$. (It is supposed, just as in the previous case, that $\Theta_* < \Theta_D$; otherwise $\Theta_* = \Theta_D$.) The thermal conductivity is again a sum of two integrals:

$$\Lambda(T) = 3nk_B v \left(\frac{T}{\Theta_D} \right)^3 \left[\int_0^{\Theta_*/T} l(x) \frac{x^4 e^x}{(e^x - 1)^2} dx + \alpha n^{-1/3} \int_{\Theta_*/T}^{\Theta_D/T} \frac{x^4 e^x}{(e^x - 1)^2} dx \right]. \quad (14)$$

TABLE IV. Parameters of the Debye model fits for $(\text{CH}_4)_{1-\xi}\text{Kr}_\xi$ solid solutions for cases i) and ii),

ξ	$n \times 10^{-22}, \text{cm}^{-3}$	$v, \text{km/s}$	Γ_{calc}	i)		ii)	
				$C, \text{cm/K}$	α	$C, \text{cm/K}$	α
1	2.11	0.86	0	1.07×10^{-9}	1.29	0.95×10^{-9}	1.16
0.97	2.10	0.88	0.055	1.17×10^{-9}	1.22	1.07×10^{-9}	1.24
0.937	2.09	0.92	0.12	2.03×10^{-9}	1.41	1.63×10^{-9}	1.26
0.855	2.06	0.97	0.26	3.5×10^{-9}	1.3	3.8×10^{-9}	1.20
0.71	2.04	1.07	0.54	6.2×10^{-9}	1.05	4.5×10^{-9}	0.97

In the high-temperature limit $T \geq \Theta_D$, when only the U -processes are in effect, $\Lambda(T) = A_2/T^{3/2} + \Lambda''_{\text{min}}$ (Refs. 3 and 27), where A_2 is some numerical coefficient, and Λ''_{min} is

$$\Lambda''_{\text{min}} = 3\alpha n^{2/3} k_B v \left(\frac{T}{\Theta_D} \right)^3 \int_0^{\Theta_D/T} \frac{x^4 e^x}{(e^x - 1)^2} dx. \quad (15)$$

In the case of strong phonon scattering by point defects (when $\Theta_* \ll \Theta_D$), the lower limit on the thermal conductivity is accurately found from Eq. (15). It can be shown easily that the ratio $\Lambda''_{\text{min}}/\Lambda'_{\text{min}} = 0.83$ at $T \geq \Theta_D$, for the same α .

iii) We also consider the case when a term $\alpha\lambda/2$ or $\alpha n^{-1/3}$ has simply been included in Eq. (3) for the phonon mean free path to eliminate the nonphysical case when $l(x)$ becomes smaller than one-half the wavelength or than the interatomic distance:

$$l(x) = (l_{\text{Umkl}}^{-1} + l_{\text{Rayl}}^{-1})^{-1} + \alpha\lambda/2, \quad (16)$$

$$l(x) = (l_{\text{Umkl}}^{-1} + l_{\text{Rayl}}^{-1})^{-1} + \alpha n^{-1/3}, \quad (17)$$

and then Eq. (2) is used to calculate the thermal conductivity.²⁶ In the high-temperature limit $T \geq \Theta_D$, this assumption leads to the expressions: $\Lambda = A_3/T + \Lambda'_{\text{min}}$ and $\Lambda = A_4/T + \Lambda''_{\text{min}}$ (Ref. 27), where A_3 and A_4 are some numerical coefficients.

The computer fit using Eqs. (10), (14), (16), and (17) was performed for the isochoric thermal conductivity of pure Kr and $(\text{CH}_4)_{1-\xi}\text{Kr}_\xi$ solid solutions ($\xi = 0.97, 0.937, 0.855, 0.71$) for the isochores with $T_0 = 75$ K. The density was estimated by interpolation of experimental data. The sound velocity was calculated assuming that it changes linearly with the concentration from Kr (Ref. 16) to CH_4 (Ref. 8). To

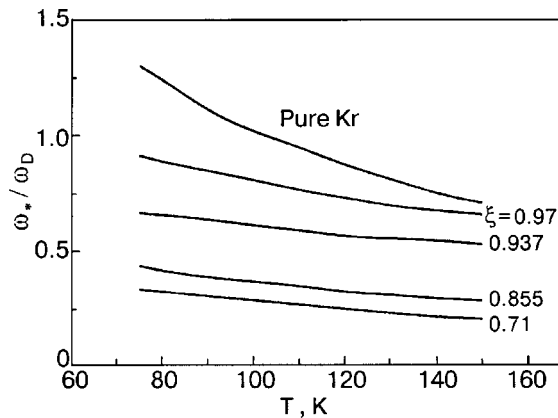


FIG. 8. The temperature dependence ω_*/ω_D , where $\omega_* = 2\pi\nu/\lambda_*$ is the frequency at which the crossover from the wave picture to the picture of localized excitations occurs.

reduce the number of variable parameters, the coefficient B describing the Rayleigh scattering was calculated in accordance with Eqs. (6) and (7). The Debye model parameters used for fitting (n, v, Γ) and the C and α values obtained by fit for variants i) and ii) are shown in Table IV. When Eqs. (16) and (17) are used for the phonon mean free path, we obtain $\alpha \approx 0.3-0.4$, while elementary considerations lead to $\alpha \geq 1$. The coefficient C determining the intensity of the U -processes is in good agreement with low-temperature data,¹² where it was evaluated as 1.5×10^{-9} cm/K.

The fitting results are shown in Fig. 7. It is seen that both the variants describe well the behavior of the isochoric thermal conductivity of the solid solution, except for the concentration $\xi = 0.71$. In the case of pure Kr variant ii) ensures a somewhat better fit, as was discussed earlier for the isochore with $T_0 = 0$ K.²⁷ Roufousse and Klemens³ preferred assumption ii) to i) for the following reason. Assumption i) means that the vibrational excitations can be described as waves. However, when the wave picture is questioned, the alternative description assumes localized excitations that hop from site to site. The mean free path for those excitations is given by the interatomic distance.

This point of view may hold for amorphous materials as well, in which the heat transfer by low-frequency phonons is negligible at quite high (above 50 K) temperatures.²⁸ We should remember that in our case the model assumes a gradual change from pure extended-phonon thermal conductivity (a perfect crystal and low temperatures) to a heat transfer by localized excitations (a solid solution in the middle of the composition range and at high temperatures). We believe it is more reasonable to consider the vibrations localized in the $\lambda/2$ regions as the limiting case of the phonon picture (see Refs. 5 and 6).

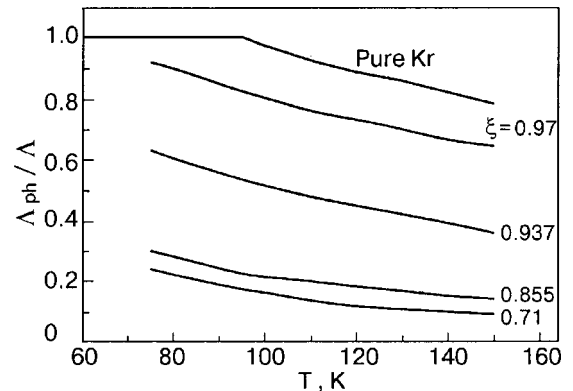


FIG. 9. The relative extended-phonon contribution to the thermal conductivity of pure Kr and the $(\text{CH}_4)_{1-\xi}\text{Kr}_\xi$ solid solution.

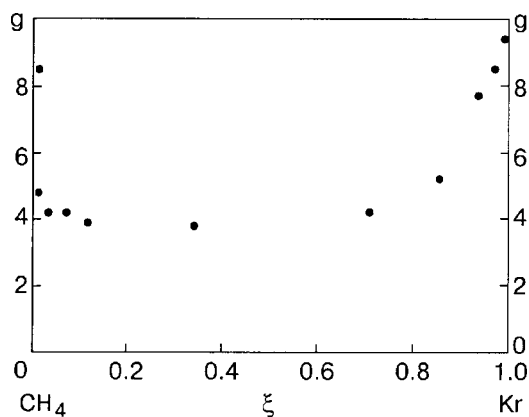


FIG. 10. The concentration dependence of the Bridgman coefficient $g = -(\partial \ln \Lambda / \partial \ln V)_T$ of the solid solution $(\text{CH}_4)_{1-\xi}\text{Kr}_\xi$ at $T = 90$ K.

Figure 8 shows the temperature dependence of ω_*/ω_D , where $\omega_* = 2\pi\nu/\lambda_*$ is the frequency at which the crossover from the wave picture to the picture of localized excitations occurs. Equation (10) actually describes the sum of contributions to the thermal conductivity resulting from extended phonons and localized excitations. Figure 9 presents the relative extended-phonon contribution to the thermal conductivity of pure Kr and the $(\text{CH}_4)_{1-\xi}\text{Kr}_\xi$ solid solution. It is seen that in Kr the thermal conductivity is of pure extended-phonon character up to about 90 K. As the CH_4 concentration grows, progressively more heat is transferred by the localized excitations, but even at the highest concentration (29%) and the highest temperatures (150 K) an appreciable part of the heat (about 10%) is transferred by the low-frequency extended phonons. The values of α vary from 1 to 1.4. This supports the interpretation of the vibrations being localized in $\lambda/2$ regions as the limiting case of the phonon picture and the validity of Eq. (1) for prediction of the lower limit to the thermal conductivity of the crystalline lattice.

The concentration dependence of the Bridgman coefficient $g = -(\partial \ln \Lambda / \partial \ln V)_T$ is shown in Fig. 10. It is seen that the value of g is highest for pure components and decreases strongly for solid solutions. The same behavior was also observed for mixed alkali-halide crystals,²⁹ though the decrease in g was not as large. Small Bridgman coefficients ($g \approx 3-4$) are typical for amorphous materials and strongly disordered crystals.³⁰

CONCLUSION

A gradual transition from the thermal conductivity of a highly perfect crystal to the minimum thermal conductivity Λ_{\min} is observed at $T \geq \Theta_D$ in the $(\text{CH}_4)_{1-\xi}\text{Kr}_\xi$ solid solutions as the crystal becomes increasingly disordered. A qualitative description is given in the framework of Debye model of thermal conductivity, which takes into consideration the fact that phonon mean free path cannot decrease indefinitely. The concept of the minimum thermal conductivity^{3,4} gives a

proper description of the isochoric thermal conductivity of the $(\text{CH}_4)_{1-\xi}\text{Kr}_\xi$ solid solution in the middle of composition range $0.2 < \xi < 0.8$.

The authors would like to acknowledge B. Ya. Gorodilov and A. I. Krivchikov for helpful discussions. This work was supported by National Research Council of USA under Twinning Program 1999–2000.

*E-mail: konstantinov@ilt.kharkov.ua

- ¹ P. B. Allen and J. L. Feldman, *Phys. Rev. B* **48**, 12581 (1993).
- ² P. Sheng, M. Zhou, and Z. Zhang, *Phys. Rev. Lett.* **72**, 234 (1994).
- ³ M. C. Roufosse and P. G. Klemens, *J. Geophys. Res.* **79**, 703 (1974).
- ⁴ G. A. Slack, in *Solid State Physics*, Vol. 34, edited by F. Seitz and D. Turnbull, Academic Press, New York (1979).
- ⁵ D. G. Cahill and R. O. Pohl, *Solid State Commun.* **70**, 927 (1989).
- ⁶ D. G. Cahill, S. K. Watson, and R. O. Pohl, *Phys. Rev. B* **46**, 6131 (1992).
- ⁷ V. G. Manzhelii, A. I. Prokhvatilov, I. Ya. Minchina, and L. D. Yantsevich, *Handbook of Binary Solutions of Cryocrystals*, Begell House Inc., N. Y., Wallingford, UK (1996).
- ⁸ V. G. Manzhelii, A. I. Prokhvatilov, V. G. Gavrilko, and A. P. Isakina, *Structure and Thermodynamic Properties of Cryocrystals*, Begell House Inc., N. Y., Wallingford, UK (1999).
- ⁹ I. N. Krupskii and V. G. Manzhelii, *Sov. Phys. JETP* **55**, 2075 (1968).
- ¹⁰ P. Korpiun, J. Moser, F. J. Piezinger, and E. Lusher, in *Phonon Scattering in Solids*, edited by L. J. Challis, V. W. Rampton, and A. F. G. Wyatt, Plenum Press, New York, and London (1975), p. 377.
- ¹¹ A. I. Bondarenko, V. G. Manzhelii, V. A. Popov, M. A. Strzhemechnyi, and V. G. Gavrilko, *Fiz. Nizk. Temp.* **86**, 1215 (1982) [*Sov. J. Low Temp. Phys.* **8**, 617 (1982)].
- ¹² V. V. Dudkin, B. Ya. Gorodilov, A. I. Krivchikov, and V. G. Manzhelii, *Fiz. Nizk. Temp.* **26**, 1023 (2000) [*Low Temp. Phys.* **26**, 762 (2000)].
- ¹³ V. A. Konstantinov, V. G. Manzhelii, V. P. Revyakin, and S. A. Smirnov, *Physica B* **262**, 421 (1999).
- ¹⁴ V. G. Manzhelii and I. N. Krupskii, *Fiz. Tverd. Tela (Leningrad)* **10**, 284 (1968) [*Sov. Phys. Solid State* **10**, 221 (1968)].
- ¹⁵ B. Ya. Gorodilov, V. V. Sumarokov, P. Stachowiak, and A. Jezowski, *Phys. Rev. B* **58**, 3089 (1998).
- ¹⁶ *Rare Gas Solids, V. II*, edited by M. L. Klein and J. A. Venables (Eds.), Academic Press, London-New York (1977).
- ¹⁷ V. A. Konstantinov, S. A. Smirnov, and V. P. Revyakin, *Prib. Tekh. Exp.* **42**, 145 (1999) [*Instrum. Exp. Tech.* **42**, 133 (1999)].
- ¹⁸ R. Berman, *Thermal Conduction in Solids*, Oxford, Clarendon Press (1976).
- ¹⁹ V. A. Konstantinov, V. G. Manzhelii, M. A. Strzhemechnyi, and S. A. Smirnov, *Fiz. Nizk. Temp.* **14**, 90 (1988) [*Sov. J. Low Temp. Phys.* **14**, 48 (1988)].
- ²⁰ V. G. Manzhelii, V. B. Kokshenev, L. A. Koloskova, and I. N. Krupskii, *Fiz. Nizk. Temp.* **1**, 1302 (1975) [*Sov. J. Low Temp. Phys.* **1**, 624 (1975)].
- ²¹ B. M. Powell and G. Dolling, *Can. J. Chem.* **66**, 897 (1998).
- ²² H. Yasuda, *J. Low Temp. Phys.* **31**, 223 (1978).
- ²³ P. G. Klemens, *Phys. Rev.* **119**, 507 (1960).
- ²⁴ V. S. Oscotskii and L. A. Smirnov, *Defects in Crystals and Heat Conduction* [in Russian], Nauka, Leningrad (1972).
- ²⁵ L. A. Turk and P. G. Klemens, *Phys. Rev. B* **9**, 4422 (1974).
- ²⁶ J. R. Olson, R. O. Pohl, J. W. Vandersande, A. Zoltan, T. R. Anthony, and W. F. Banholzer, *Phys. Rev. B* **47**, 14850 (1993).
- ²⁷ V. A. Konstantinov, *J. Low Temp. Phys.* **122**, 459 (2001).
- ²⁸ M. S. Love and A. S. Anderson, *Phys. Rev. B* **42**, 1845 (1990).
- ²⁹ D. Gerlich, *J. Phys. C* **20**, 5479 (1987).
- ³⁰ R. G. Ross, P. A. Andersson, B. Sundqvist, and G. Backstrom, *Rep. Prog. Phys.* **47**, 1347 (1984).

This article was published in English in the original Russian journal. Reproduced here with stylistic changes by AIP.

Vibrational dynamics of solid molecular nitrogen to megabar pressures

A. F. Goncharov,* E. Gregoryanz, H.-K. Mao, and R. J. Hemley

Geophysical Laboratory and Center for High Pressure Research, Carnegie Institution of Washington, 5251 Broad Branch Road, N. W., Washington, D. C. 20015

(Submitted July 2, 2001)

Fiz. Nizk. Temp. **27**, 1170–1174 (September–October 2001)

We report the results of Raman and synchrotron infrared absorption measurements of several molecular phases of solid nitrogen to pressures above 100 GPa (300 K). Low-temperature vibrational spectra to 45 GPa are also presented. The changes in Raman and infrared spectra at 60 GPa and 300 K are interpreted as arising from the $\epsilon \rightarrow \zeta$ transition reported at low temperature. The character of splitting of the Raman vibron ν_2 observed at 25 GPa and low temperatures differs from that previously reported, a difference that we ascribe to different experimental procedures employed and metastability of the low-temperature phase. © 2001 American Institute of Physics. [DOI: 10.1063/1.1414578]

1. INTRODUCTION

With the recent progress in diamond-anvil cell techniques (see Ref. 1), a growing number of examples of orientational ordering and subsequent transformations to framework structures in pressurized molecular solids have been documented.^{2–6} For transformation to framework structure, information about the type and character of the ordering is important, since it affects the energy barriers associated with the transition. Solid nitrogen is an important system for such studies because of stability and simple electronic structure of the isolated molecule. Moreover, solid nitrogen has been well studied theoretically, and accurate experimental data provide an important test of condensed matter theory.^{7–12}

Solid nitrogen has a complex phase diagram with a wealth of molecular phases that differ in the types of orientational ordering and crystal structures formed.^{5,13–33} The ordering of the low-pressure, low-temperature α and γ phases is controlled by quadrupole–quadrupole interactions, whereas at higher pressures a class of molecular structures (δ , δ_{loc} , ϵ , ζ) stabilized by additional anisotropic intermolecular interactions is found.³⁴ The δ phase is proposed to have a disordered cubic structure (space group $Pm\bar{3}n$)²⁰ with two different types of molecules exhibiting spherelike and disklike disorder and giving rise to two classes of vibron bands ν_1 and ν_2 . With increasing pressure and/or decreasing temperature, nitrogen molecules exhibit orientational order through a sequence of phase transformations (to δ_{loc} and then ϵ) as determined by vibrational spectroscopy and x-ray diffraction.^{27–31} The structure of the ϵ phase is rhombohedral (space group $R\bar{3}c$), which can be viewed as a distortion of cubic.²³

Theoretical calculations have been contradictory in their predictions of stable molecular ordered phases.^{10–12} In particular, Monte Carlo (MC)¹⁰ and molecular dynamics (MD)¹¹ simulations based on a proposed intermolecular potential favor tetragonal structures, while *ab initio* calculations¹² predict the stability of the $R\bar{3}c$ phase, in agreement with experiment. Recent MC calculations^{35,36} have pointed out the importance of using accurate atom–atom potentials (espe-

cially anisotropic terms) to obtain adequate results.

At 20–25 GPa and 10 K a transformation has been found by Raman spectroscopy²¹ and confirmed by later Raman and IR measurements.³³ No x-ray data are currently available for this phase (called ζ). According to vibrational spectroscopy data, its structure has a strong similarity to phases ϵ and δ . It has been inferred to have $R3c$ symmetry,²¹ but more recent observations do not support this interpretation.³³ The ϵ – ζ phase boundary has been extended recently to 180 K and 40 GPa.³³ At low temperatures, a significant region of metastability is reported,³³ making it difficult to clarify the mechanism of the transformation.

At room temperature, the vibrational spectroscopy data are still contradictory concerning the number and nature of the transformations above 20 GPa. A sequence of new phases has been reported on the basis of several branchings of the Raman vibron modes,²² including one just above 20 GPa.²⁷ In contrast, x-ray studies indicate the stability of ϵ phase to 50 GPa.^{26,30} A change of x-ray diffraction pattern was observed above 60 GPa,²⁵ but interpretation requires additional measurements. The most-recent Raman and IR measurements to 42 GPa show a clear correspondence between the number of observed lattice and vibron modes and group-theoretical predictions for the ϵ phase.³³ Here we report the results of a combined Raman and synchrotron IR high-pressure study of N_2 to 40 GPa at low temperatures and beyond 100 GPa at room temperature.

2. EXPERIMENTAL

Samples of nitrogen were loaded in diamond anvil cells at 0.2 GPa using a standard gas-loading technique. The low-temperature experiment was performed at the NSLS (beamline U2A). The description of our experimental setup has been published elsewhere.³⁷ The typical spectral resolution was about 4 nm^{-1} in both IR, and Raman measurements. A diamond cell containing the sample at 8 GPa was cooled to 15 K in a continuous-flow He cryostat. The cryostat is equipped with windows that are interchangeable at low temperature, which allows *in situ* IR and Raman/ruby fluorescence measurements without changing the P – T conditions

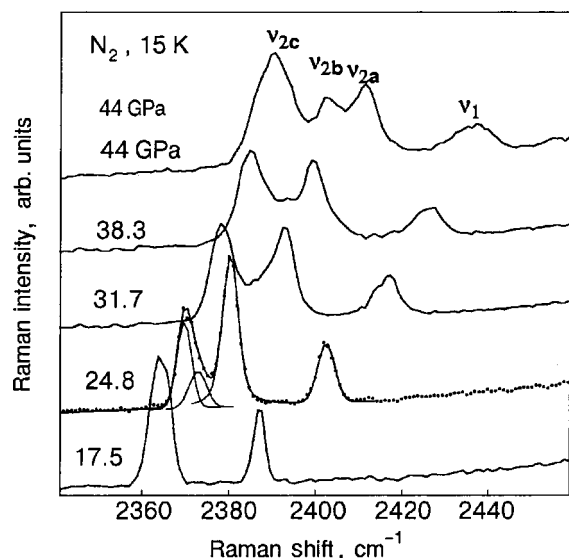


FIG. 1. Raman spectra of nitrogen through the low-temperature transition to the ζ phase. The spectra are shifted in vertically for clarity. The spectrum at 24.8 GPa (points) is shown along with the fitting to multiple components (Voigt profiles).

on the sample.³⁸ Pressure can be controlled from the outside by a mechanical change in the load on the diamond cell lever arm through vacuum feedthroughs. In the room-temperature experiments we used diamond anvil cells with external heating capabilities. This allows us to release the internal stresses that build up during a loading of the cell by heating the sample to 200–400 °C.

3. RESULTS

The sequence of Raman spectra measured as a function of pressure at low temperatures is shown in Fig. 1. At 17.5 GPa we observe two Raman peaks in the vibron region—slightly broadened ν_2 (lower frequency) and ν_1 . This is in excellent accord with the experiments for the ϵ phase (see also Refs. 21 and 33). Low-frequency lattice modes (not shown) are also in agreement with previous studies^{21,33} for ϵ -N₂. Increasing pressure splits the ν_2 peak, so three components can be seen. This splitting becomes obvious at the highest pressure (44 GPa), while at 24–38 GPa a peak-fitting is required to reveal the two components (e.g., the spectrum at 24.8 GPa in Fig. 1). Only a slight broadening of the ν_1 peak is observed as the pressure is increased. Lattice modes also change dramatically at 18–25 GPa, which is beyond the scope of the present paper.

The infrared spectra at 17.5 GPa (Fig. 2) show a very weak absorption in the spectral range of the ν_2 vibron. The absorbance increases substantially at 18–25 GPa, so a doublet of IR vibrons is clearly visible at higher pressure. As in the case of the Raman bands, a moderate broadening of the IR peaks is observed as the pressure is increased.

The pressure dependence of the observed Raman frequencies is shown in Fig. 3. Corresponding data from Ref. 33 are also shown for comparison. Earlier results²¹ for the ν_2 multiplet are very close to those reported in Ref. 33 and are not shown for clarity. For the ν_1 band, our low-temperature data are very close to those measured at room temperature (see also Ref. 32). The substantial difference in the pressure

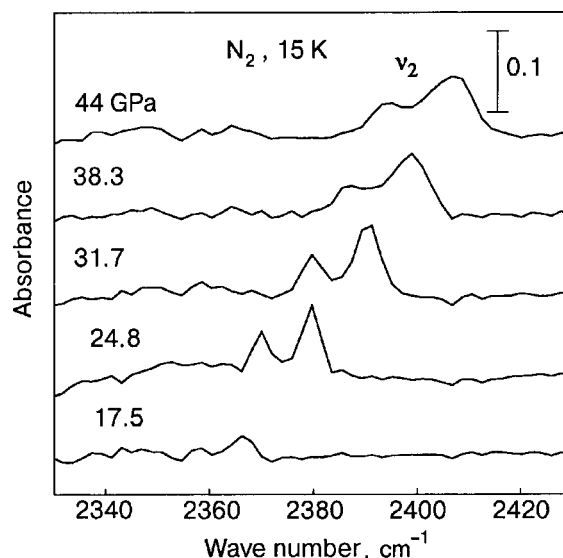


FIG. 2. Infrared absorption spectra of nitrogen at 15 K as a function of pressure. The spectra are shifted in vertically for clarity.

dependence of the frequency of the Raman ν_2 multiplet will be discussed later. The pressure dependences of the Raman and infrared frequencies are compared in the inset of Fig. 3. We find that Raman and infrared frequencies do not coincide (cf. Ref. 33). Unlike the Raman data, our infrared frequencies are in good agreement with those reported in Ref. 33 in the pressure range overlapped by the two studies (to 25.2 GPa).

Raman spectra measured close to room temperature are presented in Fig. 4. At 60 GPa Raman spectra already contain more vibron bands (four) than is allowed by group theory for the $R\bar{3}c$ symmetry of ϵ -N₂ (three).²¹ Surprisingly, at this pressure we did not observe the low-frequency shoulder of the most intense ν_{2c} Raman band, as reported in Ref. 32. Increasing the pressure through the 60 GPa range gives

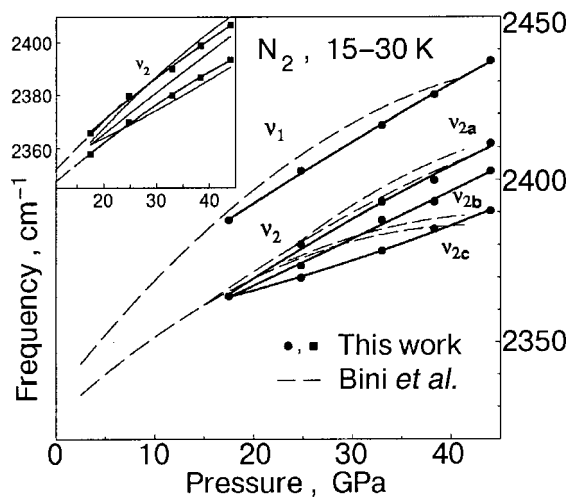


FIG. 3. Raman vibrational frequencies as a function of pressure at 15 K. Filled circles are the Raman data from this work. The solid thick solid lines are the guides to the eye. The dashed lines are the Raman data from Ref. 33. The inset shows the comparison between Raman and infrared frequencies. Filled squares are the infrared data from this work. The solid thick solid lines are the guides to the eye. Thin solid lines are the Raman data from this work. The dashed lines are the infrared data from Ref. 33.

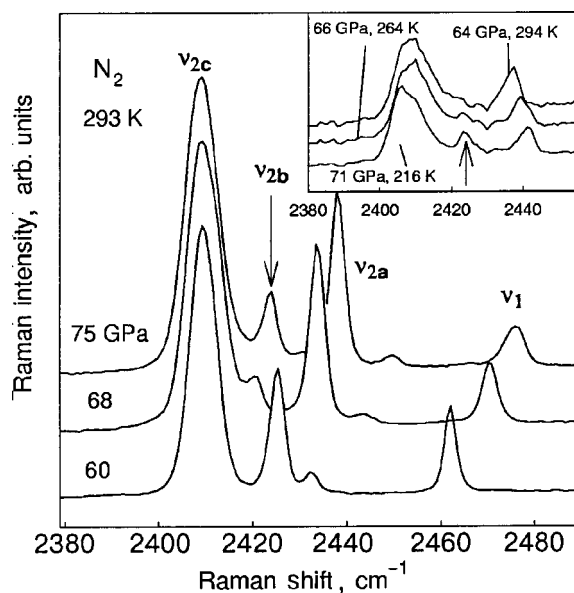


FIG. 4. Raman spectra of the nitrogen vibrons through the transition to the ζ phase at room temperature. The inset shows the variation of spectra with temperature. The arrow designates a new peak, that appears at the transition. The spectra are shifted vertically for clarity.

rise to a new Raman peak (ν_{2b}), indicated by an arrow in Fig. 4 (see also Ref. 32). A similar observation was made when cooling down from approximately the same starting point (inset in Fig. 4). At this pressure (and room temperature) we also observed an increase in intensity of the infrared vibron.³ Raman spectra in the lattice mode range show splittings of the characteristic bands of the low-pressure phase and appearance of new low-frequency bands. The splitting of the lattice modes increases with pressure, with the multiplets evolving into distinct bands. Representative Raman spectra in the lattice-mode region are presented in Fig. 5. The complexity of the spectra suggests a large number of molecules and low symmetry of the unit cell. The spectra at 95 GPa agree well with those presented in Ref. 32 in terms of the number and positions of the bands, with the exception of a very weak additional vibron band near 2473 cm^{-1} . With further pressure increase, the intensity of the lower-frequency vibron increases and all other vibron peaks gradually vanish.^{3,22} Similarly, in the lattice-mode region the intensity of the 500 nm^{-1} band increases prior to the transition to the

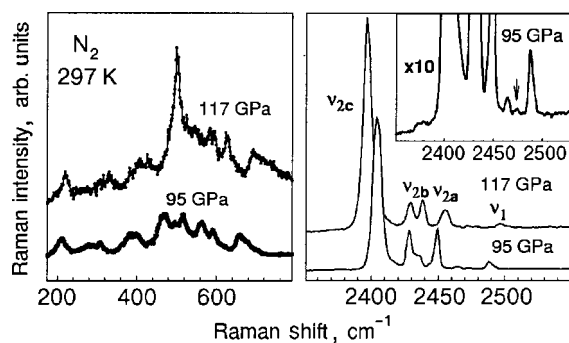


FIG. 5. Raman spectra of nitrogen at 95 and 117 GPa. The inset shows a weak vibron peak (indicated by arrow) that develops under high pressure. The spectra are shifted in vertically for clarity.

nonmolecular phase. This behavior will be examined in detail elsewhere.

4. DISCUSSION

The splitting of the vibron bands and change in the lattice-mode spectrum observed at low temperature indicate a phase transformation related to orientational ordering of the nitrogen molecules. The phase diagram of Ref. 33 suggests that these changes correspond to the $\varepsilon \rightarrow \zeta$ transition. Qualitatively, our data and those presented in Refs. 21 and 33 show similar trends, but detailed comparison shows different Raman spectra for the high-pressure phase (Fig. 3). We believe that the disagreement arises from the use of different experimental procedures and the nature of the high-pressure phase (or phases). In contrast to the experiments reported in Refs. 21 and 33, we changed pressure at low temperature. It is useful to note that when infrared spectra were measured in a manner similar to ours,³³ the results from the two studies agree very well (inset to Fig. 3). The evidence that the properties of the high-pressure phase depend on the thermodynamic path suggests that this phase is not thermodynamically stable (i.e., is metastable at the indicated P – T conditions). This is supported by observations of a large hysteresis of the transition at low temperatures.³³ An alternative (but related) explanation is that the different properties of the high-pressure phase arise from relatively large pressure inhomogeneities in our experiment (since we changed pressure at low temperature). This is indicated by broadening of Raman and infrared bands at higher pressures (Figs. 1 and 2).

The changes in the Raman and infrared spectra above 60 GPa at room temperature are very similar to those observed at low temperatures. Moreover, the reported transition boundary³³ extrapolated to high pressure and temperature matches this room-temperature point. According to the observed Raman and infrared spectra, the vibrational properties of the high-pressure phase are very similar at room and low temperature. Thus, we will consider it to be the same phase (ζ).

In view of the absence of sufficient x-ray data for the ζ phase, we can only speculate on its crystal structure. The number of vibron modes (in either our experiment or those reported in Ref. 32) exceeds that predicted for $R3c$ structure based on the space group theory proposed in Ref. 21. According to Ref. 32, the increase of number of vibron modes is due to the increase in the number of different site symmetries occupied by N_2 molecules. Following this idea, up to 5 different site symmetry positions should be invoked to explain the observed number of Raman vibron peaks above 60 GPa, which does not seem plausible. A critical examination of the spectra of Ref. 32 shows that this number can probably be reduced to 3 according to the number of observed distinct peaks in the Raman excitations of the guest molecules. Thus it seems natural to propose that the branching of vibron modes is related to sequential lifting of the degeneracy of the ν_2 term of the cubic δ phase. In the first stage (δ to ε transition), the ν_2 band splits into A_{1g} and E_g components by the crystal field. In the second one (ε to ζ transition), the symmetry is further reduced (to orthorhombic or monoclinic), with doubly degenerate level splitting into two singlets. Additional splitting (vibrational or Davydov-type)

of these major components could be caused by intermolecular interactions. This is related to a possible increase in the number of molecules in the unit cell as well as associated symmetry lowering. High-quality diffraction data are required in order to examine these hypotheses.

5. CONCLUSIONS

We find that the properties of the high-pressure, low-temperature phase of nitrogen obtained by “cold” compression are different from those for the phase quenched from high temperature. This suggests that the ζ phase is metastable and/or transitions to it are sensitive to nonhydrostatic effects. Raman and infrared spectra of ε -N₂ above 40 GPa and ζ -N₂ are not compatible with the $R\bar{3}c$ and $R3c$ symmetries proposed in Ref. 21 because the number of vibron bands is larger than predicted for the standard structures based on these space groups. This increase in the number of bands is probably related to additional lowering of the symmetry and multiplication of the size of the unit cell.

The present vibrational spectroscopy data provide additional constraints on the structure and properties of the high-pressure phases. They also suggest that known phases are not necessarily thermodynamically stable in the P – T region in which they can be observed. As for other molecular crystals, sluggish kinetics can complicate the determination of the true thermodynamic phase diagram (see, e.g., Ref. 39). Further theoretical and experimental effort is necessary to obtain a better understanding of the phase diagram of nitrogen at these high-pressure conditions.

This work was supported by the NSF. The NSLS is supported by DOE.

*E-mail: goncharov@gl.ciw.edu

- ¹R. J. Hemley and H.-K. Mao, in *Encyclopedia of Applied Physics*, edited by G. L. Trigg, New York, VCH Publishers, Vol. 18 (1997), p. 555.
- ²V. Iota, C. S. Yoo, and H. Cynn, *Science* **283**, 1510 (1999).
- ³A. F. Goncharov, E. Gregoryanz, H.-K. Mao, Z. Liu, and R. J. Hemley, *Phys. Rev. Lett.* **85**, 1262 (2000).
- ⁴M. I. Eremets, R. J. Hemley, H. K. Mao, and E. Gregoryanz, *Nature* (London) **411**, 170 (2001).
- ⁵E. Gregoryanz, A. F. Goncharov, R. J. Hemley, and H.-K. Mao, *Phys. Rev. B* **64**, 52103 (2001).
- ⁶E. Katoh, H. Yamawaki, H. Fujihisa, M. Sakashita, and K. Aoki, *Phys. Rev. B* **61**, 119 (2000).
- ⁷A. K. McMahan and R. LeSar, *Phys. Rev. Lett.* **54**, 1929 (1985).

- ⁸R. M. Martin and R. J. Needs, *Phys. Rev. B* **34**, 5082 (1986).
- ⁹C. Mailhot, L. H. Yang, and A. K. McMahan, *Phys. Rev. B* **46**, 14419 (1992).
- ¹⁰J. Belak, R. LeSar, and R. D. Eters, *J. Chem. Phys.* **92**, 5430 (1990).
- ¹¹S. Nosé and M. L. Klein, *Phys. Rev. Lett.* **50**, 1207 (1983).
- ¹²R. D. Eters, V. Chandrasekharan, E. Uzan, and K. Kobashi, *Phys. Rev. B* **33**, 8615 (1986).
- ¹³C. A. Swenson, *J. Chem. Phys.* **23**, 1963 (1955).
- ¹⁴R. L. Mills and A. F. Schuch, *Phys. Rev. Lett.* **23**, 1154 (1969).
- ¹⁵F. Schuch and R. L. Mills, *J. Chem. Phys.* **52**, 6000 (1970).
- ¹⁶J. R. Brookeman and T. A. Scott, *J. Low Temp. Phys.* **12**, 491 (1973).
- ¹⁷W. E. Streib, T. H. Jordan, and W. N. Lipscomb, *J. Chem. Phys.* **37**, 2962 (1962).
- ¹⁸R. LeSar, S. A. Ekberg, L. H. Jones, R. L. Mills, L. A. Schwalbe, and D. Schiferl, *Solid State Commun.* **32**, 131 (1979).
- ¹⁹S. Buchsbaum, R. L. Mills, and D. Schiferl, *J. Phys. Chem.* **88**, 2522 (1984).
- ²⁰D. T. Cromer, R. L. Mills, D. Schiferl, and L. A. Schwalbe, *Acta Crystallogr., Sect. B: Struct. Crystallogr. Cryst. Chem.* **37**, 8 (1981).
- ²¹D. Schiferl, S. Buchsbaum, and R. L. Mills, *J. Phys. Chem.* **89**, 2324 (1985).
- ²²R. Reichlin, D. Schiferl, S. Martin, C. Vanderborgh, and R. L. Mills, *Phys. Rev. Lett.* **55**, 1464 (1985).
- ²³R. L. Mills, B. Olinger, and D. T. Cromer, *J. Chem. Phys.* **84**, 2837 (1986).
- ²⁴S. Zinn, D. Schiferl, and M. F. Nicol, *J. Chem. Phys.* **87**, 1267 (1987).
- ²⁵A. P. Jephcoat, R. J. Hemley, H.-K. Mao, and D. E. Cox, *Bull. Am. Phys. Soc.* **33**, 522 (1988).
- ²⁶H. Olijnyk, *J. Chem. Phys.* **93**, 8968 (1990).
- ²⁷H. Schneider, W. Haefner, A. Wokaun, and H. Olijnyk, *J. Chem. Phys.* **96**, 8046 (1992).
- ²⁸M. I. M. Scheerboom and J. A. Schouten, *Phys. Rev. Lett.* **71**, 2252 (1993).
- ²⁹M. I. M. Scheerboom and J. A. Schouten, *J. Chem. Phys.* **105**, 2553 (1996).
- ³⁰M. Hanfland, M. Lorenzen, C. Wassilew-Reul, and F. Zontone, in *Abstracts of the International Conference on High Pressure Science and Technology*, Kyoto, Japan, 1997, p. 130.
- ³¹R. Bini, M. Jordan, L. Ulivi, and H. J. Jodl, *J. Chem. Phys.* **108**, 6869 (1998).
- ³²H. Olijnyk and A. P. Jephcoat, *Phys. Rev. Lett.* **83**, 332 (1999).
- ³³R. Bini, L. Ulivi, J. Kreutz, and H. J. Jodl, *J. Chem. Phys.* **112**, 8522 (2000).
- ³⁴V. G. Manzhelii and Y. A. Freiman, *Physics of Cryocrystals*, American Institute of Physics, College Park, MD (1997).
- ³⁵A. Mulder, J. P. J. Michels, and J. A. Schouten, *J. Chem. Phys.* **105**, 3235 (1996).
- ³⁶A. Mulder, J. P. J. Michels, and J. A. Schouten, *Phys. Rev. B* **57**, 7571 (1998).
- ³⁷A. F. Goncharov, V. V. Struzhkin, R. J. Hemley, H.-K. Mao, and Z. Liu, in *Science and Technology of High Pressure*, M. H. Manghnani, W. J. Nellis, and M. F. Nicol (Eds.), Universities Press, Hyderabad, India; Honolulu, Hawaii (1999), Vol. 1, p. 90.
- ³⁸Z. Liu, A. F. Goncharov, H. Mao, and R. Hemley, *Eos Trans. AGU* **81** (48), Fall Meet. Suppl., Abstract T71B-22 (2000).
- ³⁹R. Jeanloz, *J. Geophys. Res.* **92**, 10352 (1987).

This article was published in English in the original Russian journal. Reproduced here with stylistic changes by AIP.

Lattice modes of solid nitrogen to 104 GPa

H. Olijnyk* and A. P. Jephcoat

Department of Earth Sciences, University of Oxford, Oxford OX1 3PR, United Kingdom

(Submitted May 4, 2001)

Fiz. Nizk. Temp. **27**, 1175–1178 (September–October 2001)

Lattice modes of solid nitrogen are studied by Raman spectroscopy at room temperature to 104 GPa using the diamond-anvil technique. Changes in the lattice mode spectral features correlate with those observed in the vibronic spectra suggesting symmetry changes of the crystal lattice. The changes in the spectral features mainly appear as branchings of existing modes, supporting the view of a close structural relationship among these high-pressure phases. © 2001 American Institute of Physics. [DOI: 10.1063/1.1414579]

1. INTRODUCTION

Solid nitrogen exhibits a complicated P - T phase diagram with a variety of different phases, which appears to be well established in the pressure range up to ≈ 20 GPa.^{1–22} Above ≈ 20 GPa solid nitrogen is less well understood, both from an experimental and theoretical point of view. Room temperature x-ray diffraction patterns between 16 and ≈ 60 GPa are compatible with the $R\bar{3}c$ structure (ϵ -phase).^{14,16,21} Raman studies at low temperatures and higher pressures^{10,11,18,22–25} suggest several structural modifications above ≈ 25 GPa. Theoretical investigations²⁶ have predicted a tetragonal lattice as the stable structure above 20 GPa, in disagreement with the experimental results,^{14,16,21} and above 12 GPa the calculated pressure–volume relations²⁷ significantly depart from the accurate equations of state.¹⁶ Since the existence and properties of all these phases are determined by the nature of the intermolecular interactions, these results demonstrate that improvements of the interaction potentials are necessary to correctly describe the properties of solid nitrogen above 20 GPa. In this context, the importance of the anisotropic part of the interaction potential for high-pressure structures of solid nitrogen has been pointed out recently.^{28,29} It was shown that the anisotropic term may be important in stabilizing the ϵ -phase and also influences the orientational behavior of the molecules.^{28,29} A stringent test of the intermolecular interaction potentials is provided by the lattice modes and their pressure dependences. In this paper we report Raman measurements of the external modes for pressures up to 104 GPa at room temperature.

2. EXPERIMENTAL

The sample, $^{14}\text{N}_2$ enriched with 3% $^{15}\text{N}_2$ and 1.4% $^{14}\text{N}^{15}\text{N}$, was the same for which Raman studies of the internal modes were recently reported.²³ The isotopic mixture was loaded into a high-pressure diamond-anvil cell at 0.2 GPa using a gas-loading technique.³⁰ Raman spectra were excited by the 647 nm Kr^+ laser line. Scattered light, collected through a spatial filtering aperture, was analyzed at an angle of 135° with respect to the incoming laser beam using a 0.6-m triple spectrograph and a liquid-nitrogen-cooled CCD multichannel detector. Pressure was determined with the hydrostatic ruby fluorescence scale.^{31,32} The peak positions were determined by fitting Voigt profiles to the Ra-

man spectra. This procedure also allows the determination of the frequencies of such modes, which manifest themselves as asymmetries or shoulders in the spectra.

3. RESULTS

Typical Raman spectra of the lattice-mode region at various pressures are shown in Fig. 1. One can note that the Raman spectra become increasingly more complex due to the appearance of additional modes as pressure is increased. The mode frequencies and their pressure shifts are shown in Fig. 2. The previous room temperature results of Schneider *et al.*¹⁸ and Goncharov *et al.*²⁵ are also plotted. There is good agreement with the data of Ref. 18 in the common pressure range to 54 GPa, which indicates that any effects on the lattice modes due to the presence of the dilute isotopic species can be neglected in the present study. In the pressure

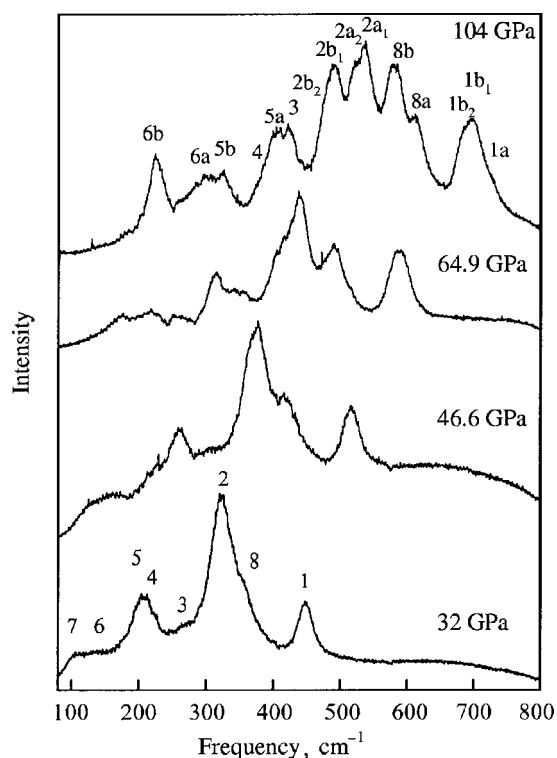


FIG. 1. Lattice mode Raman spectra of solid nitrogen at various pressures.

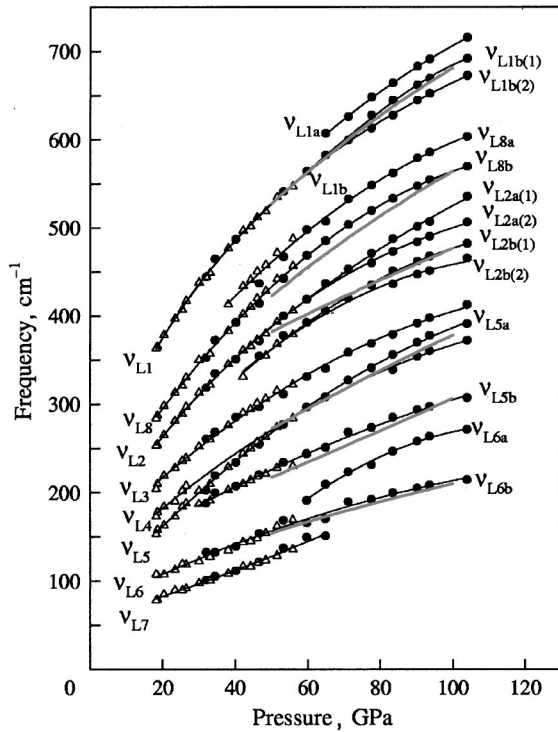


FIG. 2. Pressure shift of lattice mode frequencies of solid nitrogen. Solid circles: present study; open triangles: Ref. 18. The thick gray lines represent the lattice mode data from Ref. 25, which were recorded to ≈ 150 GPa.

range between 50 and 100 GPa, Goncharov *et al.*²⁵ have reported six external Raman modes, whereas in the present study more than these six modes could be resolved in this pressure range, as can be noticed in Figs. 1 and 2. All modes show a positive frequency shift as pressure is increased. In comparison to the earlier high-pressure Raman studies the following additional observations have been made in the present investigation. New modes, ν_{L6a} and ν_{L1a} , appeared around 60 GPa, and further splittings, $\nu_{L2a} \rightarrow \nu_{L2a(1)}, \nu_{L2a(2)}$ and $\nu_{L1b} \rightarrow \nu_{L1b(1)}, \nu_{L1b(2)}$ can be observed around 80 GPa. With the exception of ν_{L7} , which becomes difficult to observe above 60 GPa, all modes already present in the ϵ -phase above 16 GPa are still existent at the maximum pressure. Above 80 GPa the mode ν_{L4} , which merges into mode ν_{L5a} around 25 GPa, reappeared a few wave numbers below mode ν_{L5a} , indicating crossing of modes ν_{L5a} and ν_{L4} around 55 GPa. The frequency–pressure data are well represented by the expression

$$\nu(P)/\nu_0 = [1 - (\delta'_0/\delta_0)P]^{-\delta_0^2/\delta_0'}, \quad (1)$$

where ν_0 is the mode frequency at $P=0$ GPa, $\delta_0 = (d \ln \nu/dP)_{P=0}$ is the logarithmic pressure coefficient, and δ'_0 is the pressure derivative of δ for $P=0$. The pressure coefficients for the lattice modes are collected in Table 1.

We have determined the mode Grüneisen parameters $\gamma_i = -d \ln \nu_i / d \ln V$ for the lattice modes. The $V(P)$ values were obtained from the P – V data of Refs. 14 and 16 using a Birch-Murnaghan equation of state with bulk modulus $B_0 = 2.55$ GPa, its pressure derivative $B'_0 = 3.97$, and $V_0 = 50.99 \text{ \AA}^3/\text{molecule}$. The average values of the γ_i 's thus obtained for the pressure range 16–65 GPa are also given in Table 1.

TABLE I. Pressure coefficients and mode Grüneisen parameters of lattice modes of solid nitrogen for the pressure range from 16 to 104 GPa.

Mode	ν_0, cm^{-1}	$\delta_0, \text{GPa}^{-1}$	$\delta'_0, \text{GPa}^{-2}$	γ
ν_{L1a}	249.9	0.05457	−0.00781	—
$\nu_{L1b(1)}$	141.2	0.2201	−0.124	1.51
$\nu_{L1b(2)}$	130.5	0.3191	−0.2780	1.51
ν_{L8a}	157.3	0.109	−0.02956	1.59
ν_{L8}, ν_{L8b}	90.87	0.3242	−0.2481	1.71
$\nu_{L2a(1)}$	97.40	0.1777	−0.06896	1.72
$\nu_{L2a(2)}$	79.98	0.3564	−0.3062	1.72
$\nu_{L2b(1)}$	126.0	0.09057	−0.01887	1.83
$\nu_{L2b(2)}$	119.2	0.1479	−0.0599	1.83
ν_{L3}	91.25	0.1409	−0.04678	1.59
ν_{L4}	69.23	0.1606	−0.05489	1.79
ν_{L5}, ν_{L5a}	37.87	0.3404	−0.2039	2.23
ν_{L5b}	98.62	0.04155	−0.00338	1.54
ν_{L6a}	46.20	0.08627	−0.01102	—
ν_{L6}, ν_{L6b}	59.10	0.05706	−0.00626	1.62
ν_{L7}	55.52	0.02308	−0.0003884	2.04

4. DISCUSSION

The available x-ray diffraction data^{14,16,21} are compatible with the $R\bar{3}c$ lattice above 16.3 GPa and indicate a phase transition at around 60 GPa by clear changes in the x-ray diffraction pattern.¹⁴ The $R\bar{3}c$ lattice of the ϵ -phase is a slight distortion of the cubic δ -phase and has two inequivalent sites, which correspond to the disklike and spherelike site of the δ -phase, respectively.¹² In the lattice-mode region eight Raman-active modes are allowed for $R\bar{3}c$, two of which are librations and originate from the former spherelike site, whereas the remaining six modes are of translational character and are associated with the disklike site.¹⁰

The observed branchings or appearance of new lattice modes around 30, 40, 65, and 80 GPa correlate well with the branchings observed for the internal modes of the host^{11,18,23} as well as of the dilute isotopic species,²³ as can be noted from the summary of Table II.

The branchings in the internal modes occur only in the ν_2 branch, which is related to the molecules on the disklike site. The splittings observed in the dilute isotopic species are thought to result from inequivalent sites, since factor-group interactions, an alternative explanation for the splitting, are switched off at these small concentrations.²³

Above 30 GPa, with nine lattice modes present, the Raman spectra of the external modes are no longer compatible with $R\bar{3}c$, as are the vibronic spectra, which contrasts with the lack of change observed in the x-ray diffraction patterns

TABLE II. Summary of branchings of lattice and vibronic modes in solid N_2 . The number of inequivalent sites is determined from the splittings of the isotopic guest vibrons.²³

Branching pressure	Lattice modes: Ref. 18, present study	Host vibrons (Ref. 23)	Dilute guest vibrons (Ref. 23)	Number of inequivalent sites
≈ 30 GPa	ν_{L5b}	ν_{2a}	ν_{2a}, ν_{2b}	3
≈ 40 GPa	ν_{L2b}, ν_{L8a}	$\nu_{2c(2c)}$	ν_{2c2}	≥ 4
≈ 65 GPa	ν_{L6a}, ν_{L1a}	$\nu_{2c(2b)}$	ν_{2c1}	≥ 5
≈ 80 GPa	$\nu_{L1b(1,2)}, \nu_{L2a(1,2)}, \nu_{L2b(1,2)}$	$\nu_{2c(1a)}$	splitting of ν_{2c2}	≥ 6

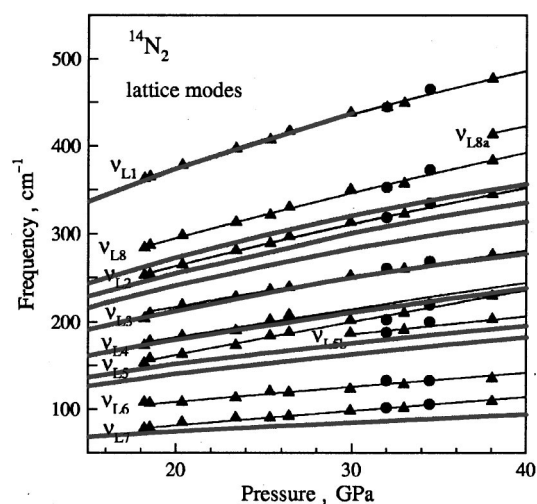


FIG. 3. Thick gray solid lines are the calculated Raman-active lattice-mode frequencies for the $R\bar{3}c$ phase from Ref. 27. The solid triangles (Ref. 18) and solid circles (present study) are the experimentally observed frequencies.

in this pressure range. These changes in the spectral features might be due to slight modifications in the lattice symmetry, possibly due to subtle changes in the orientation of molecules at the disklike site, which may lead to two sites with slightly different symmetry. Similar arguments may also be valid for the 40 GPa branching. Another possibility might be that these branchings indicate the onset of the phase transition, which has been observed by clear changes in the x-ray diffraction pattern¹⁴ around 60 GPa and which would then occur gradually over a large pressure range. In this connection it is interesting to note that the boundary between the ϵ -phase and the higher-pressure ζ -phase,²⁴ extrapolated to room temperature, implies an $\epsilon \rightarrow \zeta$ transition at 50–60 GPa. The 80 GPa branching has also been interpreted as an indication of a further phase transition, which is supported by the observed splitting of the ν_{2c2} mode of the $^{15}\text{N}_2$ isotopic species. One characteristic feature common to both the external and internal modes is the persistence of the lower-pressure modes at the highest pressures, which implies a close structural relationship among the various high-pressure phases.

The observed lattice-mode frequencies are compared with calculated frequencies of the $R\bar{3}c$ lattice²⁷ to 40 GPa in Fig. 3. The calculated frequencies of modes ν_{L1} , ν_{L3} , and ν_{L4} are in very good agreement with experiment, whereas for the other modes the good agreement found at lower pressures²⁷ gets lost at higher pressures. Possible reasons for this increasing discrepancy might involve the inadequacy, at higher pressures, of the interaction potential used in these calculations, a different crystal structure above 30 GPa, and finite temperature effects.

5. CONCLUSION

The Raman spectra of the lattice modes of solid N_2 are compatible with the $R\bar{3}c$ structure between 16.3 GPa and ≈ 30 GPa. At higher pressures (30, 40, 65, and 80 GPa) changes in the spectral features of the lattice modes correlate with changes in the spectral features of the internal modes, probably related to changes in the lattice symmetry.

The persistence of the low-pressure modes to the highest pressures, also observed for the internal modes, supports the argument of a close structural relationship among these high-pressure phases. The present data on lattice modes provide additional constraints, which have to be considered in future theoretical attempts at a quantitative interpretation of highly compressed solid nitrogen.

*E-mail: olijnykHGH@aol.com

- ¹W. E. Streib, T. H. Jordan, and W. N. Lipscomb, *J. Chem. Phys.* **37**, 2962 (1962).
- ²R. L. Mills and A. F. Schuch, *Phys. Rev. Lett.* **23**, 1154 (1969).
- ³F. Schuch and R. L. Mills, *J. Chem. Phys.* **52**, 6000 (1970).
- ⁴J. A. Venables and C. A. English, *Acta Crystallogr., Sect. B: Struct. Crystallogr. Cryst. Chem.* **30**, 929 (1974).
- ⁵R. LeSar, S. A. Ekberg, L. H. Jones, R. L. Mills, L. A. Schwalbe, and D. Schiferl, *Solid State Commun.* **32**, 131 (1979).
- ⁶D. T. Cromer, R. L. Mills, D. Schiferl, and L. A. Schwalbe, *Acta Crystallogr., Sect. B: Struct. Crystallogr. Cryst. Chem.* **37**, 8 (1981).
- ⁷D. Schiferl, D. T. Cromer, R. R. Ryan, A. C. Larson, R. LeSar, and R. L. Mills, *Acta Crystallogr., Sect. C: Cryst. Struct. Commun.* **39**, 1151 (1983).
- ⁸B. M. Powell, G. Dolling, and H. F. Nieman, *J. Chem. Phys.* **79**, 982 (1983).
- ⁹S. Buchsbaum, R. L. Mills, and D. Schiferl, *J. Phys. Chem.* **88**, 2522 (1984).
- ¹⁰D. Schiferl, S. Buchsbaum, and R. L. Mills, *J. Phys. Chem.* **89**, 2324 (1985).
- ¹¹R. Reichlin, D. Schiferl, S. Martin, C. Vanderborgh, and R. L. Mills, *Phys. Rev. Lett.* **55**, 1464 (1985).
- ¹²R. L. Mills, B. Olinger, and D. T. Cromer, *J. Chem. Phys.* **84**, 2837 (1986).
- ¹³S. Zinn, D. Schiferl, and M. F. Nicol, *J. Chem. Phys.* **87**, 1267 (1987).
- ¹⁴A. P. Jephcoat, R. J. Hemley, H.-K. Mao, and D. E. Cox, *Bull. Am. Phys. Soc.* **33**, 522 (1988).
- ¹⁵D. Schiferl, R. LeSar, and D. S. Moore, in *Simple Molecular Systems at Very High Density*, edited by A. Polian, P. Loubeyre, and N. Boccara, Plenum Press, New York (1989), p. 303 and references therein.
- ¹⁶H. Olijnyk, *J. Chem. Phys.* **93**, 8968 (1990).
- ¹⁷B. J. Baer and M. Nicol, *High Press. Res.* **4**, 511 (1990).
- ¹⁸H. Schneider, W. Haefner, A. Wokaun, and H. Olijnyk, *J. Chem. Phys.* **96**, 8046 (1992).
- ¹⁹M. I. M. Scheerboom and J. A. Schouten, *Phys. Rev. Lett.* **71**, 2252 (1993).
- ²⁰M. I. M. Scheerboom and J. A. Schouten, *J. Chem. Phys.* **105**, 2553 (1996).
- ²¹M. Hanfland, M. Lorenzen, C. Wassilew-Reul, and F. Zontone, in *Abstracts of the International Conference on High Pressure Science and Technology*, Kyoto, Japan, 1997, p. 130.
- ²²R. Bini, M. Jordan, L. Ulivi, and H. J. Jodl, *J. Chem. Phys.* **108**, 6869 (1998).
- ²³H. Olijnyk and A. P. Jephcoat, *Phys. Rev. Lett.* **83**, 332 (1999).
- ²⁴R. Bini, L. Ulivi, J. Kreutz, and H. J. Jodl, *J. Chem. Phys.* **112**, 8522 (2000).
- ²⁵A. F. Goncharov, E. Gregoryanz, H.-K. Mao, Z. Liu, and R. J. Hemley, *Phys. Rev. Lett.* **85**, 1262 (2000).
- ²⁶J. Belak, R. LeSar, and R. D. Eters, *J. Chem. Phys.* **92**, 5430 (1990).
- ²⁷R. D. Eters, V. Chandrasekharan, E. Uzan, and K. Kobashi, *Phys. Rev. B* **33**, 8615 (1986).
- ²⁸A. Mulder, J. P. J. Michels, and J. A. Schouten, *J. Chem. Phys.* **105**, 3235 (1996).
- ²⁹A. Mulder, J. P. J. Michels, and J. A. Schouten, *Phys. Rev. B* **57**, 7571 (1998).
- ³⁰A. P. Jephcoat, H.-K. Mao, and P. M. Bell, in *Hydrothermal Experimental Techniques*, edited by G. C. Ulmer and H. L. Barnes, Wiley Interscience, New York (1987), p. 469.
- ³¹R. A. Forman, G. J. Piermarini, J. D. Barnett, and S. Block, *Science* **176**, 284 (1972).
- ³²H.-K. Mao, J. Xu, and P. M. Bell, *J. Geophys. Res.* **91**, 4673 (1986).

Real-space condensation in a dilute Bose gas at low temperature

I. O. Kulik*

Department of Physics, Bilkent University, Bilkent, Ankara 06533, Turkey
(Submitted May 16, 2001)

Fiz. Nizk. Temp. **27**, 1179–1182 (September–October 2001)

We show with a direct numerical analysis that a dilute Bose gas in an external potential—which is chosen for simplicity as a radial parabolic well—undergoes at a certain temperature T_c a phase transition to a state supporting a macroscopic fraction of particles at the origin of the phase space ($\mathbf{r}=0, \mathbf{p}=0$). Quantization of particle motion in a well wipes out the sharp transition but supports a distribution of a radial particle density $\rho(r)$ peaked at $r=0$ (a real-space condensate) as well as a phase-space Wigner distribution density $W(\mathbf{r}, \mathbf{p})$ peaked at $\mathbf{r}=0$ and $\mathbf{p}=0$ below a crossover temperature T_c^* of order of T_c . A fixed-particle-number canonical ensemble, which is a combination of the fixed- N condensate part and the fixed- μ excitation part, is suggested to resolve the difficulty of large fluctuation of the particle number ($\delta N \sim N$) in the Bose-Einstein condensation problem treated within the orthodox grand canonical ensemble formalism. © 2001 American Institute of Physics. [DOI: 10.1063/1.1414580]

The phenomenon of Bose-Einstein (BE) condensation (see textbooks, e.g., Refs. 1–3) manifests itself in the formation of macroscopic fraction of zero-momentum particles uniformly distributed in a coordinate space. Such transition was recently observed in laser-trapped, evaporation-cooled atomic vapors^{4–6} in magnetic traps (see recent reviews^{7–9}). We will show by a direct numerical analysis, partly similar to and sometimes overlapping with the previous theoretical works on the subject,^{10–13} that a Bose gas in an external confining potential condenses at low temperature to a position of minimum potential energy; the particles of that “condensate” also have zero kinetic energy. Quantization of particle states in a well makes the real-space condensation a continuous transition rather than a phase transition but still supports a macroscopic fraction of particles near the origin of the coordinate space below a crossover temperature T_c^* which is of the order of Bose-condensation temperature T_c .

Experimental realization of BE condensation implies confinement of a dilute gas within some region of space in a “trap” cooled by its interaction with an “optical molasses” created by laser irradiation¹⁴ and finally cooled to microwave-range temperature by evaporative cooling.¹¹ Bose gas in a trap may be considered to be interacting with two thermal reservoirs, the first one representing the thermal environment (walls, blackbody radiation at temperature T_1) and the second one the optical molasses at temperature $T_2 \ll T_1$. The equilibrium distribution of particles $f(\mathbf{p}, \mathbf{r}, t)$ can be obtained by solving the Boltzmann kinetic equation

$$\frac{df}{dt} = \hat{I}_1\{f\} + \hat{I}_2\{f\}, \tag{1}$$

where \hat{I}_1 is the interaction term (Stoss integral) corresponding to coupling with a media 1, and \hat{I}_2 , respectively, with media 2. If we choose for simplicity the relaxation time approximation for $\hat{I}_{1,2}$,

$$\hat{I}_i = -\frac{f - f_i}{\tau_i}, \tag{2}$$

then the solution for the equilibrium state will be

$$f = \frac{\tau_1^{-1} f_1^0 + \tau_2^{-1} f_2^0}{\tau_1^{-1} + \tau_2^{-1}}. \tag{3}$$

The relaxation rate τ_2^{-1} is proportional to the laser intensity P . At large intensity, assuming $\tau_2^{-1} \gg \tau_1^{-1}$, Eq. (3) gives $f \approx f_2^0$.

In a semiclassical approximation, the particle energy is

$$\varepsilon = \frac{\mathbf{p}^2}{2m} + \frac{1}{2} m \Omega^2 \mathbf{r}^2, \tag{4}$$

where the thermodynamic potential $\Omega = -T \ln Z$, Z is the grand partition function (assuming zero spin of particles)

$$Z = \int \frac{d\mathbf{p}d\mathbf{r}}{(2\pi\hbar)^3} \ln(1 - e^{(\mu - \varepsilon)/T}), \tag{5}$$

where \hbar is Planck’s constant. The chemical potential μ is determined from (5) to satisfy an equation

$$N = \int \frac{d\mathbf{p}d\mathbf{r}}{(2\pi\hbar)^3} \frac{1}{e^{(\varepsilon - \mu)/T} - 1}, \tag{6}$$

where N is the number of particles. After integration over the directions of \mathbf{r} and \mathbf{p} we obtain

$$N = \frac{(4\pi)^2}{(2\pi\hbar)^3} (2mT)^{3/2} \left(\frac{2T}{m\Omega^2}\right)^{3/2} \times \int_0^\infty x^2 dx \int_0^\infty y^2 dy \frac{1}{e^{x^2 + y^2 - \zeta} - 1}, \tag{7}$$

where $\zeta < 0$ is the chemical potential in appropriate dimensionless units.

At low temperature, no nonzero value of ζ can satisfy Eq. (7). It therefore vanishes at a temperature $T = T_{c0}$ determined from the condition $\zeta = 0$, thus giving

$$T_{c0} = \hbar \Omega (N/\zeta(3))^{1/3} = 0.94 \hbar \Omega N^{1/3}, \tag{8}$$

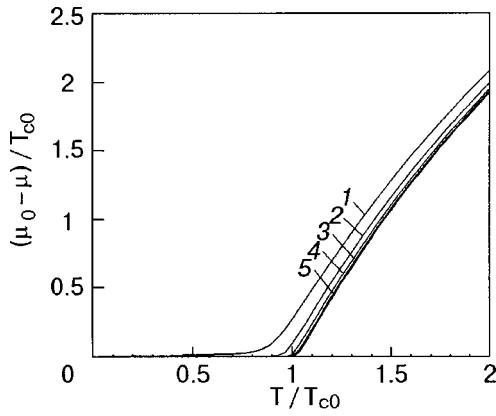


FIG. 1. Chemical potential versus temperature for various values of N : 10^2 (1), 10^3 (2), 10^4 (3), 10^5 (4), 10^6 (5).

where $\zeta(z)$ is the Riemann zeta function. Below T_{c0} , ζ remains equal to zero with the total number of particles N_0 having both $\mathbf{r}=0$ and $\mathbf{p}=0$ values, determined from

$$N_0 = \left(1 - \frac{T^3}{T_{c0}^3}\right) N. \tag{9}$$

Of course, the $\mathbf{r}=0, \mathbf{p}=0$ state is not allowed quantum-mechanically, and the derivation leading to Eqs. (6), (7) needs modification. The energy of a particle in a parabolic well, Eq. (4), is

$$\varepsilon = \hbar\Omega(n_1 + n_2 + n_3 + 3/2), \quad n_i = 0, 1, \dots$$

Then the normalization condition, Eq. (6), reduces to

$$N = \sum_{n=0}^{\infty} \frac{S_n}{\eta e^{nx} - 1} \tag{10}$$

with

$$S_n = \sum_{n_1, n_2, n_3=0}^n \delta_{n_1+n_2+n_3, n} = \frac{1}{2}(n+1)(n+2)$$

and $\eta = \exp((\mu_0 - \mu)/T)$, $x = \hbar\Omega/T$; μ_0 is the value of the chemical potential at $T=0$ ($\mu_0 = 3/2\hbar\Omega$).

The solution of Eq. (10) shows the dependence $\mu(T)$ (Fig. 1) with a crossover between almost linear dependence above the crossover temperature T_c^* and a practically zero value below that temperature. The value of T_c^* is very near to T_{c0} at large number of particles, $N \gg 1$.

The particle density distribution is expressed through the sum of Hermite polynomials.¹⁵ Employing the identity for these polynomials

$$\sum_{n_1+n_2+\dots+n_r=n} \prod_{k=1}^r \frac{H_{n_k}^2(x_k)}{2^{n_k} n_k!} = \sum_{m=0}^n r_{n-m} \frac{1}{2^m m!} H_m^2\left(\left(\sum_{k=1}^r x_k^2\right)^{1/2}\right), \tag{11}$$

where $r_m = 1$ for m even and $r_m = 0$ for m odd, we receive by putting $r=3$

$$n(\mathbf{r}) = \frac{e^{-r^2}}{\pi^{3/2}} \sum_{m=0}^{\infty} \frac{H_m^2(r)}{2^m m!} \sum_{k=0}^{\infty} \frac{1}{\eta e^{(m+2k)x} - 1}. \tag{12}$$

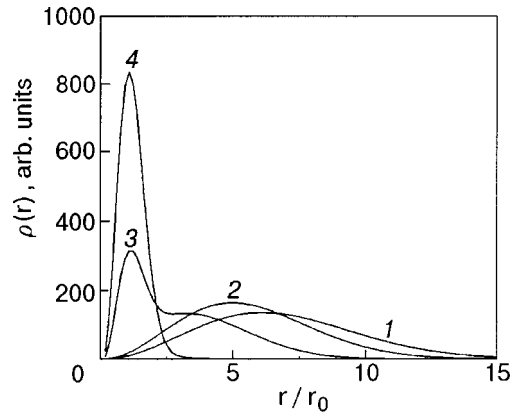


FIG. 2. Radial density distribution $\rho(r) = 4\pi r^2 n(r)$ for $N = 1000$ and various temperatures: $T/T_{c0} = 0.2$ (1), 0.8 (2), 1.4 (3), 2.0 (4).

Figure 2 shows the radial density distribution $\rho(r) = 4\pi r^2 n(r)$ at various temperatures. Below T_c^* , $\rho(r)$ displays a second maximum at small r , which grows in amplitude as the temperature decreases: the real-space condensate. The formation of such a condensate is even more explicit in the evolution of the z -projected density distribution, Fig. 3, as the temperature is decreased from above to below T_{c0} .

At zero temperature, all excited particles above the condensate vanish. The joint momentum–coordinate distribution function (the Wigner distribution function¹⁶) takes a value

$$W(\mathbf{p}, \mathbf{r}) = \frac{N_0}{\pi r_0} e^{-p^2 r_0^2} e^{-r^2/r_0^2}, \tag{13}$$

where $r_0 = (\hbar/m\Omega)^{1/2}$ is the zero-point oscillation amplitude in a parabolic well.

The question remains, how to reconcile the above results with the free-space Bose-Einstein condensation. The BE condensation temperature equals¹

$$T_0 = 3.31 \frac{\hbar^2}{m} n^{2/3}. \tag{14}$$

The average density of particles in a well above the condensation temperature is

$$\bar{n} \sim N/T^3, \quad \text{where } \bar{r} = \left(\frac{T}{m\Omega}\right)^{1/2} \sim r_0 N^{1/6} (T/T_0)^{1/2}, \tag{15}$$

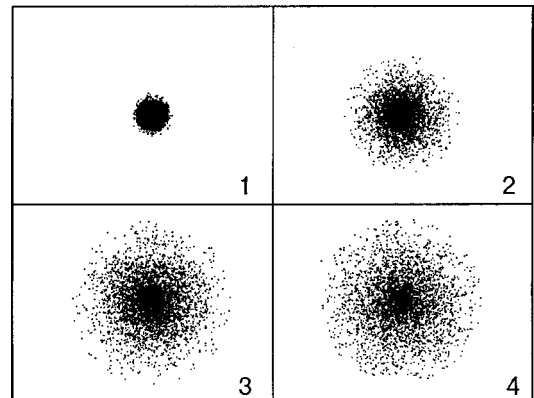


FIG. 3. Side view of particle distribution: 1— $T = 0.2T_{c0}$, 2— $T = 0.8T_{c0}$, 3— $T = 1.4T_{c0}$, 4— $T = 2.0T_{c0}$.

where \bar{r} is a confinement radius (mean radius of the gaseous cloud). It is related to the minimal quantum radius r_0 as $\bar{r} \sim r_0 N^{1/6} (T/T_c)^{1/2}$. By putting $T \sim T_c^*$ as defined above, we obtain T of the order of the BE condensation temperature (14). Therefore, the phenomenon we discussed is just the BE condensation mechanism,¹ except that in a trap the condensation occurs in both the momentum and coordinate spaces or, if we choose to explore the behavior of a dilute low-temperature Bose gas in real space, it will condense there, making up a high-density globular fraction coexisting with the spatially dispersed “excitations” in a region of size comparable to the thermal confinement radius \bar{r} .

In the grand canonical ensemble which we so far have been considering, the number of particles is not fixed. The mean square fluctuation of particle number in a state α is $\langle \delta n_\alpha^2 \rangle = n_\alpha (n_\alpha + 1)$. In a condensate, by putting $\langle n_{\alpha=0} \rangle = N_0$ we get $\mu \approx \varepsilon_0 - T/N_0$ and $\langle \delta n_0^2 \rangle^{1/2} \approx N_0$. This means a huge fluctuation of particle number $\delta N \sim N$ at $T \ll T_0$, an unrealistic property of the model.¹⁷

In a canonical ensemble, which better fits to experiments with dilute gases in traps, the average value of the condensate population is given by

$$\langle n_0 \rangle = \frac{\sum_{n_0=0}^N n_0 \sum_{\{n_\alpha\}'} e^{-\beta \sum_{\alpha>0} (\varepsilon_\alpha - \varepsilon_0) n_\alpha} \delta_{\sum_{\alpha>0} n_\alpha, N-n_0}}{\sum_{n_0=0}^N \sum_{\{n_\alpha\}'} e^{-\beta \sum_{\alpha>0} (\varepsilon_\alpha - \varepsilon_0) n_\alpha} \delta_{\sum_{\alpha>0} n_\alpha, N-n_0}}, \quad (16)$$

where $\{n_\alpha\}'$ stands for a collection of all state numbers except n_0 , and $\beta = 1/T$. The average over such states does not fluctuate strongly and therefore can be replaced by its grand canonical value corresponding to an appropriate choice of chemical potential $\mu = \mu_{N-n_0}$. We thus get

$$\langle n_0 \rangle \cong \frac{\sum_{n_0=0}^N n_0 Z_{N-n_0}}{\sum_{n_0=0}^N Z_{N-n_0}}, \quad (17)$$

where $Z_n = e^{-\beta \Omega_n}$, and Ω_n is the thermodynamic potential of the grand canonical ensemble.¹

The quantity $Z_n = e^{-\beta N}$ is not exponentially small for a number of particles n smaller than the Bose-condensate fraction, $n < N_0$. Therefore, we can change expression (17) to

$$\langle n_0 \rangle \cong \frac{\sum_{n_0=N_0}^N n_0 e^{-\beta \Omega_{N-n_0}}}{\sum_{n_0=N_0}^N e^{-\beta \Omega_{N-n_0}}}. \quad (18)$$

The quantity Ω_n is strongly peaked at $n = N_0$, thus giving $\langle n_0 \rangle \approx N_0$ and, similarly, $\langle \delta n_0^2 \rangle^{1/2} \sim \sqrt{N_0}$ rather than $\langle \delta n_0^2 \rangle^{1/2} \sim N_0$ as in the orthodox grand canonical ensemble. Indeed, at $N \ll N_0$ (corresponding to $T \gg T_0$) we obtain for the thermodynamic potential Ω_N a value $\Omega_N \approx -NT$, and Z_N

$\approx e^N$. This agrees with the conclusion, reached in a different way in Ref. 12, that the thermodynamic properties of a Bose condensate in a trap with fixed total number of particles are very similar to those in the orthodox grand canonical ensemble with a fixed average number of particles. The above results are consistent with a known statement that the Bose-Einstein condensation temperature T_0 is the same in the canonical and in the grand canonical ensembles.²

In conclusion, I hope I have met the goal of elucidating in a direct way the properties of the low-temperature state of an ideal Bose gas of finite-size, finite-particle-number systems. I express my deep gratitude to Prof. B. Tanatar for stimulating discussions and help.

*Also at: B. Verkin Institute for Low Temperature Physics and Engineering of the National Academy of Sciences of Ukraine, 47 Lenin. Ave., Kharkov 61103, Ukraine.
E-mail: kulik@fen.bilkent.edu.tr

¹L. D. Landau and E. M. Lifshitz, *Statistical Physics*, Vol. 1, Pergamon, New York (1987).

²K. Huang, *Statistical Mechanics*, Wiley, New York (1987).

³A. H. Carter, *Classical and Statistical Thermodynamics*, Prentice Hall, New Jersey (2001).

⁴M. H. Anderson, J. R. Ensher, M. R. Matthews, C. E. Wieman, and E. A. Cornell, *Science* **269**, 198 (1995).

⁵K. B. Davis, M. O. Mewes, M. A. Joffe, M. R. Andrews, and W. Ketterle, *Phys. Rev. Lett.* **74**, 5202 (1995).

⁶W. Petrich, M. H. Anderson, J. R. Ensher, and E. A. Cornell, *Phys. Rev. Lett.* **74**, 3352 (1995).

⁷F. Dalfovo, S. Giorgini, L. P. Pitaevskii, and S. Stringati, *Rev. Mod. Phys.* **71**, 463 (1999).

⁸W. Ketterle, D. S. Dufree, and D. M. Stamper-Kurn, *Making, Probing and Understanding Bose-Einstein Condensates*, Preprint xxx.lanl.gov/abs/cond-mat/9904034 (1999).

⁹E. A. Cornell, J. R. Ensher, and C. E. Wieman, *Experiments in Dilute Atomic Bose-Einstein Condensation*, Preprint xxx.lanl.gov/abs/cond-mat/9903109 (1999).

¹⁰N. L. Balazs and T. Bergeman, *Phys. Rev. A* **58**, 2359 (1998).

¹¹W. Ketterle and N. J. van Druten, *Phys. Rev. A* **54**, 656 (1996).

¹²P. Navez, D. Bitouk, M. Gajda, Z. Idziaszek, and K. Rzazewski, *Phys. Rev. Lett.* **79**, 1789 (1997).

¹³F. Brosens, J. T. Devreese, and L. F. Lemmens, *Phys. Rev. E* **55**, 6795 (1997).

¹⁴Y. Castin, J. Dalibard, and C. Cohen-Tannoudji, *Laser Cooling and Trapping of Neutral Atoms*, in *Atoms in Electromagnetic Fields*, edited by C. Cohen-Tannoudji, World Scientific, Singapore (1994).

¹⁵I. S. Grdsteyn and I. M. Ryzhik, *Tables of Integrals, Sums and Products*, edited by A. Jeffrey, Acad. Press, New York (1994).

¹⁶E. P. Wigner, *Phys. Rev.* **40**, 749 (1932).

¹⁷M. Fierz, *Helv. Phys. Acta* **29**, 47 (1955).

This article was published in English in the original Russian journal. Reproduced here with stylistic changes by AIP.

Linear and nonlinear waves on the charged surface of liquid hydrogen

M. Yu. Brazhnikov, G. V. Kolmakov, A. A. Levchenko,* and L. P. Mezhev-Deglin

Institute of Solid State Physics, 142432 Chernogolovka, Moscow District, Russia

(Submitted June 22, 2001)

Fiz. Nizk. Temp. **27**, 1183–1191 (September–October 2001)

The results of research on the properties of linear and nonlinear waves on the charged surface of liquid hydrogen in a cylindrical cell are reported. It is found that the spectrum of oscillations of linear waves softens with increasing applied electric field. Weak turbulence in a system of capillary waves on the charged surface of liquid hydrogen is investigated. The formation of a Kolmogorov cascade is observed in the inertial interval from 100 Hz to 10 kHz. It is found that the correlation function of the deviation of the surface from its flat equilibrium state can be described by a power-law function of the frequency, with an exponent $m = -3.7 \pm 0.3$ when the surface is excited at a single resonance frequency, and $m = -3.0 \pm 0.3$ in the case of two-frequency excitation. The results of these studies are in qualitative agreement with the theoretical predictions. © 2001 American Institute of Physics. [DOI: 10.1063/1.1414581]

INTRODUCTION

Research on the dynamics of waves and turbulence on the surface and in the bulk of a liquid is of great interest both for basic nonlinear physics and from the standpoint of practical applications. One approach to the description of the turbulent state has been proposed in the theory of weak turbulence (see Ref. 1 and the references cited therein), which in the case of capillary and gravity waves on the free surface of a liquid predicts a power-law dependence of the distribution of the energy of the waves over their frequency—an isotropic Kolmogorov spectrum. The predictions of the theory of weak turbulence are in good agreement with the results of a numerical simulation. Meanwhile, despite an appreciable number of studies on the nonlinear dynamics of surface waves, at the present time there are only a few published reports of experimental observations of isotropic spectra on the surface of a liquid. For example, in Refs. 2 and 3 the transition to a regime of weak capillary turbulence on increasing amplitude of the surface waves was observed at frequencies up to 1 kHz.

In this paper we report a study of linear and nonlinear capillary waves on the charged surface of liquid hydrogen. The spectrum of small oscillations of the surface of the liquid and its evolution with increasing surface charge density are investigated up to the critical value at which the flat surface loses stability. The formation of a Kolmogorov cascade in the system of capillary waves on the surface of liquid hydrogen was observed at frequencies up to 10 kHz when the surface was excited at one or two frequencies.

We describe a technique of excitation of waves on the charged surface of liquid hydrogen and of measuring the frequency dependence of the correlation function of the deviations of the surface from equilibrium.

The advantages of liquid hydrogen in experiments on nonlinear dynamics include the relatively low kinematic viscosity and the large coefficient of nonlinearity of capillary waves, making it possible to broaden significantly the frequency band in which a turbulent cascade is formed. In addition, because of the low density, oscillations can be excited

on the surface of liquid hydrogen by an external force which is many times smaller than in the case of an ordinary liquid such as water. This circumstance is decisive for the use of a technique in which the waves on the surface are excited by electrical forces. Previous experiments have shown that the surface of liquid hydrogen can be charged by injecting charges into the bulk of the liquid, that the charges can be held near the surface for a long time, and that surface waves can be excited by an alternating electric field.^{4,5} An advantage of this technique is that the external force can act directly on the surface of the liquid, almost completely excluding the bulk, and also the high degree of isotropy of the exciting force, which makes it possible to study turbulence under well-controlled experimental conditions.

2. THEORETICAL MODEL

2.1. Spectrum of small oscillations of the charged surface of a liquid

The spectrum of linear oscillations of the charged surface of a liquid found in a gravity field between horizontal plates of a flat capacitor is described by the known expression⁶

$$\omega_k^2 = k \tanh(kh) \left[g + \frac{\sigma k^2}{\rho} - \frac{2kP}{\rho} \coth(kd) \right], \quad (1)$$

where ω_k is the frequency of a wave with wave vector k , h is the thickness of the liquid layer, σ is the coefficient of surface tension, d is the distance from the surface of the liquid to the upper plate of the capacitor, $P = (U/d)^2/8\pi$ is the pressure exerted by the electrical forces on the flat, undisturbed surface, U is the potential difference across the capacitor plates, g is the acceleration of free fall, and ρ is the density of the liquid. It is assumed in this formula that the electric field is completely screened by surface charges. In the limiting case when the distance from the surface of the liquid to the control plate of the capacitor is small, so that $kd \ll 1$, and the depth is large, $kh \gg 1$, the spectrum of the charged surface of a liquid can be written in the form

$$\omega_k^2 = k \left(G + \frac{\sigma k^2}{\rho} \right), \quad (2)$$

where the quantity $G = g - 2P/\rho d$ plays the role of an effective acceleration of free fall. At voltages near the critical value at which the surface loses stability for the case of a thin film, $U_{c1} = (4\pi\rho g d^3)^{1/2}$ (Ref. 6), the effective acceleration G goes to zero, and ω_k becomes a monotonic power-law function of the wave vector with exponent 3/2, starting with small k :

$$\omega_k \cong (\sigma/\rho)^{1/2} k^{3/2}. \quad (3)$$

This circumstance is important for choosing the lowest pump frequency in studying turbulence. In our experiments in the low-frequency region the conditions $kd < 1$, $kh < 1$ hold, and the minimum wave vector above which relation (3) is valid must be estimated experimentally.

For a deep liquid $kh \gg 1$ and a large distance to the control electrode $kd \gg 1$, as the voltage U is increased, relation (1) develops a local minimum at a value of the wave vector of the order of the inverse capillary length $1/\lambda$. At a critical value $U_c = (2\pi\sigma\lambda^{-1/2})^{1/2}d$ the frequency ω_k goes to zero. This means that the flat charged surface loses stability at the critical voltage.⁷

2.2. Weak turbulence in a system of capillary waves

Turbulence is the name given to a highly excited state of a system with many degrees of freedom, the system being far from its thermodynamic equilibrium.¹ The turbulent regime is characterized by a strong nonlinear interaction of the degrees of freedom and by significant energy dissipation. Turbulence can be observed in systems where the excitation (pump) frequencies and the frequency at which strong energy dissipation occurs are widely separated on the frequency scale. The nonlinear interaction leads to an efficient redistribution of energy among the degrees of freedom (modes).

The main question in the study of turbulence is to find the energy distribution law over the frequency scale, E_ω —the stationary spectrum of the turbulence.

An ensemble of interacting waves can be described in the framework of a kinetic equation analogous to the Boltzmann equation of gas dynamics. The dispersion relation for capillary waves, $\omega = (\sigma/\rho)^{1/2}k^{3/2}$ is of the decay type, and, consequently, the main contribution to the interaction of waves is from three-wave processes—the decay of a wave into two with conservation of the total wave vector and total frequency, and also the inverse of this process, the confluence of two waves into one. In the system of capillary waves there exists a frequency interval (inertial interval) bounded below by the pump frequency ω_p and at high frequencies by the viscous damping, in which a power-law dependence of the energy distribution over the frequency of the waves is observed. The theory of uniform capillary turbulence⁸ predicts an energy distribution law (Kolmogorov spectrum) of the form

$$E_\omega = c p^{1/2} \omega^{-17/6}, \quad (4)$$

where p is the energy flux in k space, and c is a constant. The distribution (4) is characterized by a constant energy

flux in the direction of higher frequencies and, consequently, is realized at frequencies above the pump frequency (direct cascade).

The stationary distribution of the energy of surface waves in the inertial interval can be described by a pair correlation function in the Fourier representation, $I_\omega = \langle |\eta_\omega|^2 \rangle$, for the deviations $\eta(r, t)$ of the surface from the flat state:

$$I_\omega = \text{const} \cdot \omega^{-17/6}. \quad (5)$$

The energy distribution is related to the pair correlation function by the relation

$$E_\omega = \rho g I_\omega.$$

The theoretical prediction is confirmed by the results of numerical calculations of the nonlinear evolution of capillary waves directly from first principles on the basis of the equations of hydrodynamics.⁹

In the case of spectrally narrow pumping a numerical calculation¹⁰ shows that a system of equidistant peaks at multiples of the pump frequency arises on the I_ω curve. The frequency dependence of the height of the peaks is described by a power-law function with an exponent of $-21/6$. This value differs by 2/3 from the exponent in Eq. (5), which was obtained for the case of pumping in a wide frequency interval.

We note that the power-law dependence on frequency for the correlation function of the deviations of the surface from equilibrium has been observed at frequencies up to 1 kHz in experiments on water,^{2,3} from measurements of the power spectrum of radiation transmitted through a layer of liquid whose surface was excited at a low frequency by means of a vibrating platform. It was shown that for observation of a power-law distribution of energy over frequency it is necessary that the amplitude of the wave at the pump frequency be higher than a certain critical value (around 1 mm). In the experiments of Ref. 2 the exponent in the correlation function was equal to $-3/2$, and in Ref. 3 the exponent was close to the theoretical value $-17/6$.

Our preliminary results for the charged surface of liquid hydrogen were published in Ref. 11, where we showed that in the frequency interval 100–5000 Hz the function I_ω can be described by a power-law function with an exponent of -3 ± 0.5 .

3. METHODS OF MEASUREMENT AND PROCESSING OF RESULTS

The scheme of the measurements of the spectrum of surface oscillations is shown in Fig. 1. The experiments were done in an optical cell placed in a helium cryostat. Inside the cell was a horizontal flat capacitor. A radioactive plate was

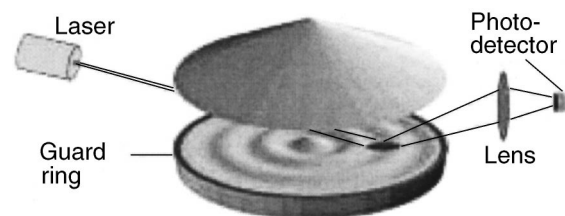


FIG. 1. Scheme of the measurements of the spectrum of surface oscillations.

placed on the lower capacitor plate, which was made in the form of a disk 25 mm in diameter. Hydrogen was condensed into a cup formed by the lower plate and a guard ring 25 mm in diameter and 2.7 mm in height. The upper plate of the capacitor, situated above structure surface of the liquid, was made in the form of a cone with a flat base 25 mm in diameter. The distance from the liquid to the upper plate was 2.5 mm in the experiments on measurement of the dispersion $\omega(k)$ and 4 mm for the study of turbulence. The temperature of the liquid in the experiments was around 16 K.

The free surface of the liquid was charged by means of a radioactive plate emitting β electrons. The electrons ionized a thin layer of the liquid near the plate. A dc voltage was applied across the capacitor plates. The sign of the charges forming a quasi-two-dimensional layer beneath the surface of the liquid was determined by the polarity of the voltage. In the experiments reported here the oscillations of a positively charged surface were investigated. A metal guard ring mounted around the radioactive plate prevented the charges from escaping beneath the surface to the walls of the container, and it can therefore be assumed that the density of charges in the layer is proportional to the applied voltage and that the electric field in the bulk of the liquid is close to zero.

The oscillations of the surface of liquid hydrogen were excited by an ac voltage applied to the guard ring in addition to the dc voltage. The amplitude of the ac voltage was much less than the dc voltage. The oscillations of the surface of the liquid were registered with the aid of a laser beam reflected from the surface.

We used two schemes for registering the oscillations of the liquid surface. In the experiments on measurement of the dispersion relation $\omega(k)$ the frequency of the ac voltage applied to the guard ring was varied smoothly from 1.5 to 150 Hz. At certain frequencies a resonant standing wave was established on the liquid hydrogen surface. The amplitude of the oscillations of the laser beam reflected from the surface increased sharply and became larger than the dimensions of the photodetector (the collecting lens shown in Fig. 1 was removed in this scheme), and so the average value of the light intensity registered by the photodetector decreased significantly. To improve the accuracy of the measurements the signal from the photodetector was averaged in time. Thus the minima on the curve describing the frequency dependence of the voltage registered on the photodetector (Fig. 2) corre-

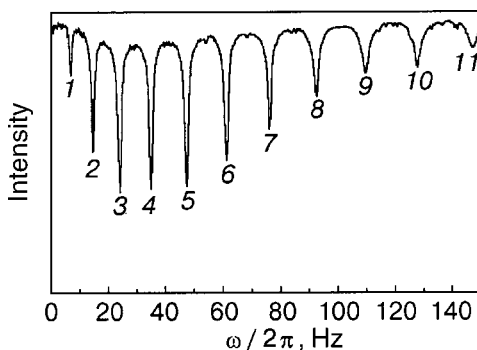


FIG. 2. Experimental trace of the average intensity of light as a function of the frequency of the ac voltage applied to the guard ring. The numbers of the standing-wave resonances on the hydrogen surface are indicated near the minima. The dc voltage was $U=954$ V.

spond to the situation when the excitation frequency coincides with one of the resonance frequencies of the surface oscillations. This makes it possible to determine the discrete spectrum of eigenfrequencies of the oscillations of the surface of the liquid in the experimental cell, $\omega_n=f(n)$, where n is the number of the resonance.

Under conditions of a cylindrical geometry a standing wave on the surface of the liquid is described by the equation

$$\zeta(r,t)=A_n J_0(k_n R) \cos(\omega_n t), \quad (6)$$

where J_0 is the Bessel function of order zero, R is the inner radius of the guard ring, and A_n is the amplitude of the wave. The relation between the number of the resonance and the wave vector of the resonant standing wave $k_n=s(n)$ is found from the equation

$$J_1(k_n R)=0.$$

This is equivalent to the condition that there are $2n$ nodes of the standing wave along the diameter $2R$ of the cell.

Thus, knowledge of the functions $\omega_n=f(n)$ and $k_n=s(n)$ enables one to uniquely determine the dispersion relation $\omega_n=\omega(k_n)$ of the surface waves.

In the experiments on turbulence the beam reflected from the oscillating surface of the liquid was focused on the photodetector by the lens. Thus in that experiment the total power of the beam was measured. The angle between the beam and the undisturbed flat surface of the liquid (the grazing angle) was $\alpha=0.2$ rad. The laser beam lay in a vertical plane passing through a diameter of the cell. In the experiments we used a narrow and a wide laser beam. The light spot on the surface of the liquid was an ellipse with axes $a_1=0.5$ mm and $b_1=0.1$ mm in the case of the narrow beam, or $a_2=2.5$ mm and $b_2=0.5$ mm for the wide beam. The output signal of the photodetector, which was directly proportional to the total power $P(t)$ of the beam, was stored in a computer with the aid of a 12-bit analog-to digital converter for several seconds at a frequency of 25 KHz.

We analyzed the frequency spectrum P_ω of the total power of the reflected laser beam, obtained by Fourier transforming the $P(t)$ data with respect to time.

The total power of the laser beam depends on the grazing angle and on the relationship between the wavelength λ on the surface of the liquid and the linear dimensions of the light spot. In our experiments the amplitude of the oscillations of the surface at the pump frequency was small, so that the angle of deviation of the oscillating surface from the flat state, $\varphi \leq 10^{-2}$ rad, was much less than the grazing angle α .

For small-amplitude waves with wavelengths much greater than the size of the light spot, $\lambda \gg a$, the power of the reflected beam is a linear function of the angle φ .¹² The angle φ can be estimated as the ratio of the amplitude of the wave to its wavelength. Then in the frequency representation the correlation function of the deviations of the surface from equilibrium (the “low-frequency limit”) is written as

$$I_\omega = \langle |\eta_\omega|^2 \rangle \sim (\omega^{-2/3} \varphi_\omega)^2 \sim P_\omega^2 \omega^{-4/3}. \quad (7)$$

In the opposite case, $\lambda < a$, when several wavelengths lay within the dimensions of the spot, the registered power of the reflected beam is determined by the value of the angle of inclination of the surface averaged over the area of the light

spot. A calculation shows that the change in power of the reflected beam on the whole is proportional to the product of the amplitude of the variation of the angle φ and the wavelength λ , i.e., $P_\omega \sim \lambda \varphi_w$. This leads to the relation (the “high-frequency limit”)

$$I_\omega \sim P_\omega^2. \tag{8}$$

The frequency of a wave on the surface of liquid hydrogen with a wavelength $\lambda \approx a$, near which one expects a crossover from the “low-frequency” regime of registering the oscillations to the “high-frequency” regime, is equal to $\omega_l/2\pi \approx 500$ Hz for the narrow beam and $\omega_l/2\pi \approx 50$ Hz for the wide beam.

4. EXPERIMENTAL RESULTS

4.1. Linear waves

Figure 2 shows a typical experimental trace of the averaged light intensity registered by the photodetector as a function of the frequency $\omega/2\pi$ of the ac voltage applied to the guard ring. The deep minima on the curve correspond to the formation of standing waves on the surface. The number of the resonance is given near the minima. The Q factor of the experimental cell in the investigated frequency interval was 30–50, permitting reliable measurement of the resonance frequency ω_n . From the experimental traces of the intensity like that shown in Fig. 2, we found the relation between the number of the resonance and the frequency of the ac voltage, $\omega_n = f(n)$. From this function and the wave vectors calculated from the function $k_n = s(n)$, we recovered the spectrum of oscillations of the surface, $\omega_n(k_n)$. The results of a processing of the experimental data obtained at three different voltages between the capacitor plates, $U = 283, 954,$ and 1080 V, are shown by the data points in Fig. 3 on a log–log scale. The temperature of the measurements was $T = 16.0$ K. The measured critical voltage, at which reconstruction of the flat charged surface of the liquid occurs, was $U_{c1} = 1140$ V, i.e., measurements were made both at voltages much less than the critical value U_{c1} and also at voltages close to U_{c1} .

The solid lines in Fig. 3 were calculated according to relation (1) for voltages of 283 and 1080 V and the specified values of the liquid layer thickness $h = 2.7$ mm and the dis-

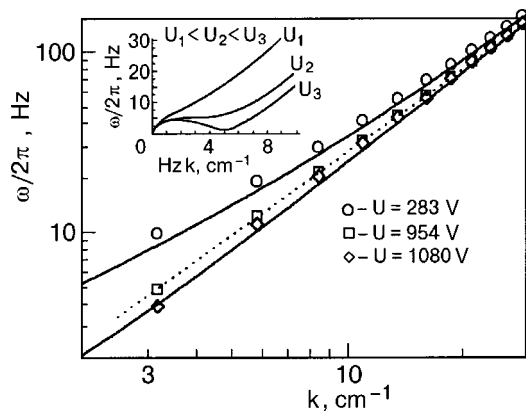


FIG. 3. Dispersion curves for waves on the charged surface of a liquid hydrogen layer 2.7 mm thick. The inset shows the evolution of the dispersion curve $\omega(k)$ on the charged surface of a deep liquid.

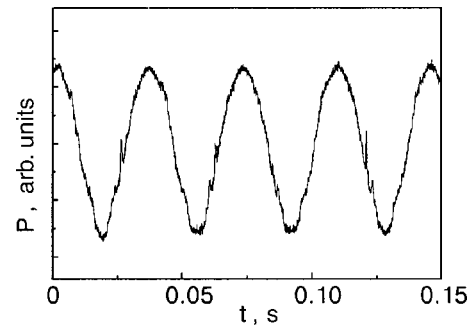


FIG. 4. Total power P of the narrow laser beam reflected from the charged hydrogen surface as a function of time t . The pumping frequency was 27.5 Hz.

tance from the surface to the upper plate $d = 2.5$, which were of the order of the capillary length. Relation (1) gives a good description of the experimental data in the entire interval of voltages. With increasing voltage the spectrum of the surface waves softens—the frequency of the oscillations with a given wave vector k_n decreases. The dotted line corresponds to the power-law function $\omega \sim k^{3/2}$, which describes the dispersion of capillary waves on the surface of a deep liquid. We see that at voltages above $0.8 U_{c1}$ the dispersion relation $\omega_n(k_n)$ of the surface waves under the conditions $h \approx d \approx k_c^{-1}$ is well approximated by this function.

The inset shows the spectrum of oscillations of the charged surface of liquid hydrogen calculated according to formula (1) for conditions when the depth of the liquid and the distance from the charged surface to the control electrode are much greater than the wavelengths ($kh \gg 1, kd \gg 1$, i.e., $\tanh(kh) = 1, \coth(kd) = 1$) for three different voltages U less than the critical value (unlike the case of the experimental plots, here a linear scale is used). We see that as the voltage U is increased, a local minimum develops on the $\omega(k)$ curve in the region of wave vectors of the order of the inverse capillary length $k_c = (\rho g / \sigma)^{1/2} \approx 5 \text{ cm}^{-1}$. A similar spectrum with a minimum was observed previously in experiments with helium in Ref. 7.

Notice the qualitative difference of the spectra in the two limiting cases: the spectrum of oscillations of the surface of a thin layer does not exhibit the local minimum at $k_c \approx 1/\lambda$ that is observed for the deep liquid.

4.2. Nonlinear waves

We investigated the frequency distribution of the amplitude of the deviations $\eta(r, t)$ of the surface of the liquid hydrogen from equilibrium for excitation of the surface by a harmonic force at frequencies from 25 to 300 Hz (at resonances with numbers 3 and higher) for different levels of pumping.

Figure 4 shows an experimental trace of the time dependence $P(t)$ of the total power of a narrow laser beam reflected from the surface. The surface was excited at a frequency $\omega_p/2\pi = 27.5$ Hz. The maximum angle of deviation of the surface from equilibrium at the pump frequency was 0.03 rad, and the maximum amplitude of the wave was of the order of 0.1 mm. The frequency spectrum P_ω of the total power was obtained by Fourier transforming the measured dependence $P(t)$. Figure 5 shows the square of the Fourier

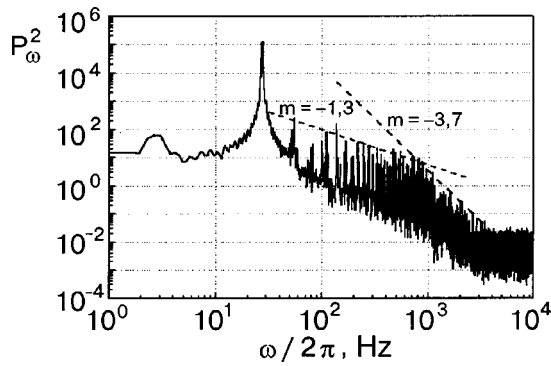


FIG. 5. Distribution of the square of the Fourier harmonics of the total power of a narrow laser beam reflected from the liquid hydrogen surface. The pumping frequency was 27.5 Hz.

amplitude P_ω^2 as a function of frequency $\omega/2\pi$. The P_ω^2 curve has a main peak at the pump frequency ω_p and peaks at multiples of that frequency. These peaks correspond to capillary waves which are generated on the surface of the liquid due to nonlinearity. At frequencies up to 800 Hz the frequency dependence of the height of the peaks can be described by a power-law function of the type $P_\omega^2 \sim \omega^{-1.3}$. At high frequencies $\omega/2\pi > 800$ Hz the frequency dependence of the height of the peaks is described by a stronger power-law function with an exponent close to -3.7 . At frequencies above 4 kHz the peak disappears into the instrument noise.

The change of the exponent of the power-law function describing the frequency dependence of the peak height observed near 800 Hz can be attributed to a transition from the regime of registration of long-wavelength oscillations with $\omega < \omega_l$ to the regime of registration of short-wavelength oscillations ($\omega > \omega_l$). The observed value of the crossover frequency $\omega_l/2\pi = 800$ Hz is close to the value of the crossover frequency estimated in Sec. 3 (~ 500 Hz).

Using formulas (7) and (8), we find that the correlation function of the deviations of the surface at frequencies below 800 Hz is proportional to $\omega^{-2.6}$, while at high frequencies $I_\omega \sim \omega^{-3.7}$.

Thus the experimental data demonstrate a power-law frequency dependence of the correlation function of the deviations of the surface (scaling) in the frequency interval 100–4000 Hz, but with different values of the exponent at low and high frequencies.

Figure 6 shows the frequency dependence of P_ω^2 ob-

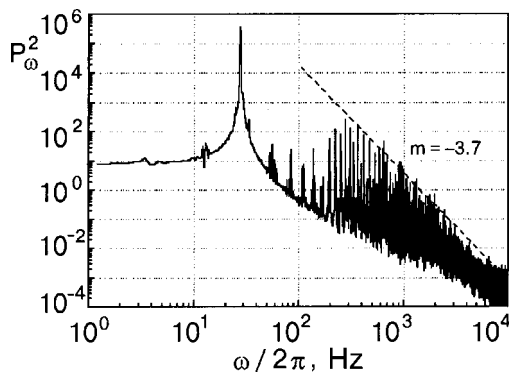


FIG. 6. Distribution of the square of the Fourier harmonics of the total power of a wide laser beam. The pumping frequency was 27.5 Hz.

tained in the experiment with the wide beam. The measurements were made under the same conditions as in the experiment with the narrow beam: pump frequency 27.5 Hz, dc voltage $U = 1170$ V, amplitude of the wave at the pump frequency around 0.1 mm. We recall that an estimate of the frequency of the crossover from the regime of registration of long-wavelength oscillations to the regime of registration of short-wavelength oscillations gave a value of 50 Hz. Thus, according to Eq. (8), over almost all of the frequency range the correlation function is directly proportional to the square of the amplitude of the Fourier harmonic of the measured total power of the reflected laser beam. We see that the variation of the height of the peaks with frequency on the graph of P_ω^2 can be described by a power law $\omega^{-3.7}$, starting at 300 Hz and on up to 7 kHz. The difference of the exponent from $-17/6$ agrees qualitatively with the conclusion¹⁰ that in the case of a spectrally narrow pump the exponent increases in absolute value in comparison with the value of the exponent in the case of pumping in a wide frequency interval.

In addition, in our experiments the spectrum of surface oscillations $\omega(k_n)$ is discrete, and the width of the resonances is much less than the distance between them. This may be an additional circumstance leading to the difference in the values of the observed exponents of the power laws from the value predicted by the theory,^{8,10} since the calculations were done for systems with a quasicontinuous spectrum of oscillations.

One notices the strong difference of the frequency dependence of P_ω^2 at low frequencies for the cases of the narrow (Fig. 5) and wide (Fig. 6) laser beams. In Fig. 6 the height of the peaks of P_ω^2 in the frequency interval from 27.5 to 300 Hz is not described by the power-law function of frequency of the form ω^m .

The differences in the spectra shown in Figs. 5 and 6 are due solely to a change in the diameter of the laser beam and, consequently, relate only to the condition for the onset of the crossover regime. The nonmonotonicity of P_ω^2 can be attributed to a feature of the optical method used to detect the surface oscillations.¹³ One of the reasons for this, as our observations show, may be that in the spectrum P_ω of the registered signal the amplitudes of the Fourier harmonics at low frequencies depend on the position of the laser spot on the surface of the liquid. At the same time, the high-frequency part of the spectrum does not depend on the position of the laser beam, since the size of the spot is much greater than the wavelengths.

It should be noted that increasing the amplitude and frequency of the pump leads to a broadening of the frequency interval in which power-law frequency dependence of the correlation function is observed. Figure 7 shows plots of P_ω^2 obtained for excitation of the surface at 135 Hz for two different pumping levels, corresponding to standing-wave amplitudes of 0.004 and 0.03 mm at the excitation frequency. The sharp drop in the height of the peaks on P_ω^2 at frequencies from 2 to 3.5 kHz in Fig. 7a may be due to viscous damping of the oscillations at the edge of the inertial interval. As expected,¹ when the amplitude of the exciting force is increased, the high-frequency edge of the inertial interval shifts to higher frequencies. We can conclude from Fig. 7b that the frequency of this edge exceeds 10 kHz.

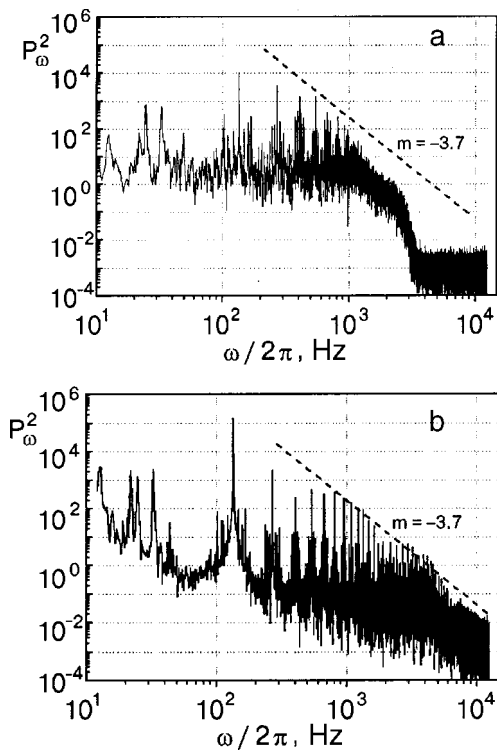


FIG. 7. Evolution of the distribution of the square of the Fourier harmonics of the total power of a wide laser beam with increasing pumping level. The amplitude of the standing wave at the pumping frequency, 135 Hz, is 0.004 mm (a) and 0.03 mm (b).

Thus one can assert that for excitation of the surface of liquid hydrogen in a cylindrical cell by a periodic external force, when a standing wave with an amplitude of the order of 0.1 mm arises on the surface, there exists a wide frequency interval in which the correlation function of the deviations of the surface from equilibrium are proportional to a power-law function of the frequency, with an exponent close to -3.7 ± 0.3 , i.e., $I_\omega \sim \omega^{-3.7 \pm 0.3}$.

4.3. Combination frequencies

In order to elucidate the influence of the conditions of excitation of the surface and to mitigate the effect of the choice of the position of the laser spot on the surface of the liquid on the form of the low-frequency part of the registered spectrum P_ω^2 , we did a series of experiments in which the surface was excited simultaneously at two resonance frequency of the cell. Figure 8 shows a plot of P_ω^2 in the case of pumping at the frequencies $\omega_1/2\pi = 27.5$ Hz and $\omega_2/2\pi = 81$ Hz (the third and seventh resonances). The pumping was done by two independent generators, so that the phase relation between the standing waves was arbitrary. The two main peaks at the frequencies ω_1 and ω_2 are clearly visible in the figure, and one can also see combination peaks corresponding to frequencies $\omega_2 - \omega_1$ and $\omega_2 + \omega_1$. For each peak at a frequency ω one can find a combination frequency $\omega = p\omega_2 \pm q\omega_1$, where p and q are integers. With this change in the conditions of excitation, the dip in the frequency interval 27.5–200 Hz that is clearly seen in Fig. 6 has practically vanished.

At frequencies above 100 Hz the frequency dependence of the height of the peaks of the spectrum P_ω^2 is close to

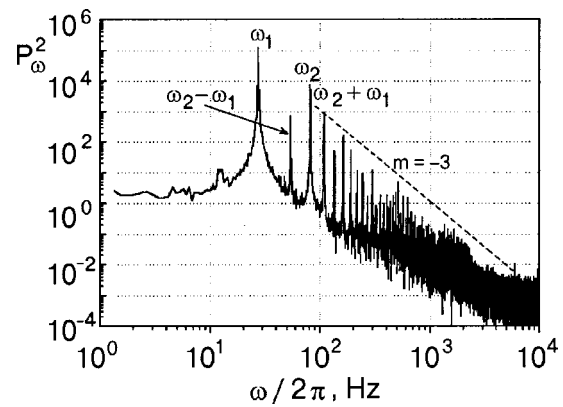


FIG. 8. Distribution of the square of the Fourier harmonics of the total power of a wide laser beam for pumping at frequencies of 27.5 and 81 Hz.

$\omega^{-3 \pm 0.3}$. This differs from the dependence $\omega^{-3.7 \pm 0.3}$ observed in the experiments with the excitation of the surface at a single frequency. The decrease of the absolute value of the exponent from 3.7 to 3 may be due to the change of the conditions of excitation of the waves on the surface. We note that the value $m = -3$ is close to the theoretical estimate $m = -17/6$ obtained for the case of pumping in a wide frequency interval.⁸

Figure 9 shows another spectrum of excitation of oscillations at two frequencies, $\omega_1/2\pi = 27.5$ Hz (the third resonance) and $\omega_2/2\pi = 45$ Hz. Since the frequency ω_2 does not coincide with a resonance frequency of the cell, for observation of the combination frequencies it was necessary to increase the amplitude of the ac voltage at the frequency ω_2 as much as possible and to decrease the amplitude at the frequency ω_1 , so that the amplitude of the waves would be comparable to each other. In the figure we see peaks corresponding to oscillations of the surface at the combination frequencies $\omega_2 - \omega_1$ and $\omega_2 + \omega_1$. The excitation frequency $\omega_2 - \omega_1$ would coincide with the second resonance of the cell, 17.5 Hz, and the combination frequency $\omega_2 + \omega_1$ would be found between the fifth and sixth resonances. As a result, the amplitude of the peak at the frequency $\omega_2 - \omega_1$ is almost 10 times greater than the amplitude of the peak at the frequency $\omega_2 + \omega_1$. Consequently, the discrete character of the spec-

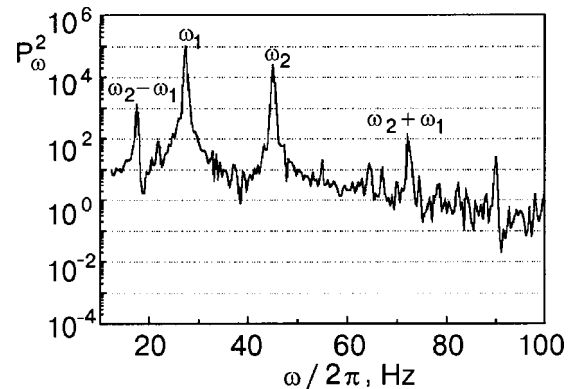


FIG. 9. Frequency dependence of the square of the Fourier harmonics of the total power of the wide laser beam for pumping at frequencies of 27.5 and 45 Hz.

trum of eigenfrequencies of the oscillations of the liquid surface turns out to have a substantial influence on the dependence of P_ω^2 at low frequencies.

5. CONCLUSIONS

The experimentally measured spectrum of linear oscillations of the charged surface of liquid hydrogen in an external electric field is in good agreement with the predictions of the theoretical calculations⁶ of the dispersion relation (1) of surface waves on an equipotential charged surface of a liquid layer located between the plates of a flat capacitor. With increasing value of the external stretching field the spectrum of oscillations of the charged surface of liquid hydrogen softens and approaches the dependence $\omega \sim k^{3/2}$ characteristic for capillary waves on the surface of a deep liquid.

In the experiments investigating nonlinear waves excited by a periodic external force, a powerlike dependence on frequency (scaling) was observed for the correlation function of the deviations of the surface of the liquid hydrogen from equilibrium at frequencies up to ≈ 10 kHz. For excitation of the surface by a harmonic force at a fixed frequency, corresponding to one of the resonance frequencies of the cell, the correlation function $I_\omega \sim \omega^{-3.7 \pm 0.3}$.

For excitation of the surface simultaneously at two frequencies, the correlation function depends on frequency as $I_\omega \sim \omega^{-3 \pm 0.3}$.

Combination frequencies of the surface oscillations were observed and studied. It was shown that the discrete character of the eigenfrequencies of the oscillations of the surface in a cell of finite size has a substantial influence on the frequency distribution of the amplitudes of the oscillations at low frequencies.

The authors thank V. E. Zakharov and E. A. Kuznetsov for helpful discussions, E. Henry, P. Alstrom, and M. Levinsen for providing the text of Ref. 3 prior to its publication, and V. N. Khlopinskii for assistance in preparing the experiments. This study was supported in part by the Ministry of Industry, Science and Technology of the Russian Federation (project “Kristall-6”) and by the grant INTAS-NETWORK 97-1643.

*E-mail: levch@issp.ac.ru

¹V. Zakharov, V. L'vov, and G. Fal'kovich, *Kolmogorov Spectra of Turbulence*, Vol. 1, *Wave Turbulence*, Springer-Verlag, Berlin (1992).

²W. Wright, R. Hiller, and S. Putterman, *J. Acoust. Soc. Am.* **92**, 2360 (1992).

³E. Henry, P. Alstrom, and M. T. Levinsen, *Europhys. Lett.* **52**, 27 (2000).

⁴A. A. Levchenko and L. P. Mezhov-Deglin, *Fiz. Nizk. Temp.* **22**, 210 (1996) [*Low Temp. Phys.* **22**, 162 (1996)].

⁵A. A. Levchenko, G. V. Kolmakov, L. P. Mezhov-Deglin, M. G. Mikhailov, and A. B. Trusov, *J. Low Temp. Phys.* **119**, 343 (2000).

⁶D. M. Chernikova, *Fiz. Nizk. Temp.* **2**, 1374 (1976) [*Sov. J. Low Temp. Phys.* **2**, 669 (1976)].

⁷P. Leiderer, *Phys. Rev. B* **20**, 4511 (1979).

⁸V. E. Zakharov and N. N. Filonenko, *Zh. Prikl. Mekh. Tekh. Fiz.* **5**, 62 (1967).

⁹A. N. Pushkarev and V. E. Zakharov, *Phys. Rev. Lett.* **76**, 3320 (1996).

¹⁰G. E. Fal'kovich and A. B. Shafarenko, *Zh. Éksp. Teor. Fiz.* **94**, 172 (1988) [*Sov. Phys. JETP* **67**, 1393 (1988)].

¹¹M. Yu. Brazhnikov, A. A. Levchenko, G. V. Kolmakov, and L. P. Mezhov-Deglin, *JETP Lett.* **73**, 398 (2001).

¹²L. D. Landau and E. M. Lifshitz, *Electrodynamics of Continuous Media*, 2nd ed., rev. and enl., by E. M. Lifshitz and L. P. Pitaevskii, Pergamon Press, Oxford (1984), Nauka, Moscow (1982), p. 405.

¹³M. Yu. Brazhnikov and A. A. Levchenko, *Prib. Tekh. Éksper.* (in press).

Translated by Steve Torstveit

Excitonic luminescence in the drift of excess electrons through liquid and solid rare gases

E. B. Gordon*

*Branch of the Institute of Energy Problems of Chemical Physics, Russian Academy of Sciences,
142432 Chernogolovka, Moscow District, Russia*

A. F. Shestakov**

*Institute of Problems of Chemical Physics, Russian Academy of Sciences, 142432 Chernogolovka, Moscow
District, Russia*

(Submitted June 25, 2001)

Fiz. Nizk. Temp. **27**, 1192–1201 (September–October 2001)

It is shown that the excitation of electronic states is the main channel of energy loss of excess electrons drifting in moderate ($\geq 10^3$ V/cm) electric fields through condensed heavy rare gases (Rg). These losses, together with scattering on resonances of metastable negative ions $(\text{Rg}^*)^-$, determine the dependence of the average energy of the electrons and their drift velocity v_d on the electric field E both in condensed Rg and in dense gases. In particular, explanations are given for the constancy of v_d at large E and for the transformation of the electroluminescence spectrum upon changes in the density of heavy particles and their temperature. Thus it is predicted that localized excitons can be efficiently excited in the bulk of crystalline and liquid Xe, Kr, and Ar, with a yield of around 10^2 excitons (and UV photons) per electron. © 2001 American Institute of Physics. [DOI: [10.1063/1.1414582]]

The elucidation of the properties of collective electronic excitations—excitons—in insulator and semiconductor crystals is one of the universally recognized outstanding achievements of the Kharkov scientific school co-founded by L. V. Shubnikov.¹ Particular attention was devoted to the study of rare-gas crystals, which served Frenkel as a first model for creating a theory of excitons.² Three types of collective excitations have been observed in rare gases (Rg): coherent excitons, and one-center (quasi-atomic) and two-center (quasi-molecular) localized states. The last of these are mainly responsible for the luminescence of crystals of heavy rare gases (Xe, Kr, and Ar) excited by vacuum ultraviolet (VUV) radiation or by an electron beam. A distinguishing feature of heavy rare-gas crystals is the extraordinarily high efficiency of conversion of the energy of photons or fast electrons into excitonic luminescence occurring in the VUV region: $\lambda = 172$ nm for Xe, $\lambda = 148$ nm for Kr, and $\lambda = 127$ nm for Ar.

At that same time work was ongoing at the P. N. Lebedev Physics Institute (FIAN) to study the features of the electronic excitation and the resulting luminescence in dense rare gases. Those studies led to the discovery of a new object in molecular physics—excimer molecules or exciplexes, chemical compounds which are quite stable but exist only in an electronically excited state. The absence of a bound ground state automatically ensures a population inversion of the levels of the corresponding phototransition and a wide luminescence spectrum; this, together with another feature of excimer molecules—a huge increase in the probability of an optical transition in comparison with the analogous transition in a united atom, immediately aroused interest in excimer molecules as a possible active medium for high-power UV lasers.

Those hopes, as we know, were completely justified, and, although the most widely used excimer lasers utilize rare-gas halides, the first report of light amplification on excimer molecules was in a paper devoted to the excitation of liquid xenon by an electron beam.³

Since the characteristics of an exciton are largely determined by the properties of the electronically excited particle generating it, in respect to its general features (position of the spectral bands, transition probability) a quasi-atomic exciton bears a surprising resemblance to an excited rare gas atom Rg, and the molecular exciton, which we are mainly interested in, resembles the excimer molecule Rg_2^* (Ref. 1). The specifics of a solid are manifested in the dynamics of transformation of an “atomic” excitation into a “molecular” excitation and in the features of the structure of the spectral bands. Naturally, investigators had a keen desire to create an excitonic laser using condensed inert gases, primarily xenon, but efforts to do so did not meet with much success,⁴ and for what we think is not a fundamental reason: the impossibility of arranging a high-power pump. Indeed, pumping by the radiation from another UV laser⁵ was not of practical interest, the use of a VUV lamp was inefficient, and fast electron beams, which are used to pump the dense-gas Xe_2 excimer laser,⁶ do not penetrate deeply enough into the volume of a crystal or liquid.

At the same time, it happens by a chance coincidence that in heavy rare gases, the same substances in which diatomic excimer molecules are characteristically formed in the gas phase (in He and Ne this is impossible for a number of fundamental reasons),⁷ the mobility of excess electrons in the solid and liquid is quite high, almost the same as for conduction electrons in metals (for He and Ne it is low because of the formation of so-called “bubbles”).⁸ In principle,

the reasons for such a high mobility are clear: first, rare gases condense as close-packed atoms; second, the high values of the mass ratio of the Rg atom to the electron; third, the absence of electron affinity among Rg atoms.

The drift of excess electrons in an electric field through liquid and solid rare gases has been studied by many authors,⁹ and a number of hypotheses have been put forth to explain the observed effects, viz.: 1) the existence of a plateau in the dependence of the electron drift velocity v_d on the applied field E at large E , and the essential lack of dependence of v_d on the phase state of the rare gas; 2) a sharp (by more than 3 order of magnitude in Xe) increase of the electron mobility in low fields upon the transition of the gas to the condensed state and the nonmonotonic character of the temperature dependence of the mobility in the condensed state, in combination with the absence of any features at the solid–liquid phase transition. Another important question that has been discussed is whether “hot” electrons can exist in the drift of electrons through condensed rare gases; some authors have assumed that the velocity of the electrons inside a solid cannot exceed the speed of sound,¹⁰ while others have assumed that electrons are heated to energies of several electron-volts.¹¹

Finally, in 1994, one of the present authors (E.B.G.) proposed¹² a model in which it was assumed that not only can the excess electrons acquire high energy from the electric field, all the way up to the first excitation potential of the Rg atom, but this excitation is even the main channel of energy loss for an excess electron and determines its average energy and drift velocity. The electronically excited Rg atom formed on electron impact (a one-center exciton) rapidly (especially in the case of Xe) reacts with the neighboring atoms and transforms into a two-atom excimer molecule (two-center exciton) which upon its decay emits a VUV photon. This means, in particular, that simple means (an electric field in an electrolytic cell) can be used to form excitonic excitations in the bulk of a crystal or liquid, and one primary electron can generate a large number of excited centers. Furthermore, in a cell with a photocathode, on account of the appearance of secondary electrons upon their photoemission under the action of the excimeric VUV radiation, it is possible for interesting critical phenomena to arise, in particular, electron and, hence, photon avalanches.

The practical aspects of the problem are also important: if the model proposed in Ref. 12 is valid, it would mean that it is possible in principle to create an efficient direct converter of electrical energy into VUV radiation, including coherent.¹³

Generally speaking, UV emission upon the application of an electric field in liquid rare gases has been observed experimentally, primarily in Xe; it was ascribed to a so-called “glow discharge” and was not given a reliable explanation. Only the recent direct experiments of Wyder’s group¹⁴ have confirmed the conclusions of our papers;^{12,13} in particular, they recorded the intensity of VUV emission in the emission band of Xe₂^{*} in the drift of electrons emitted by a cold cathode in liquid xenon in moderate electric fields, and they found that the influence of the emission depended linearly on the applied voltage.

In the present paper we analyze the advantages and fea-

tures of the method of forming electronic excitations inside rare-gas crystals on the basis of the drift of excess electrons through them. For analysis we use a simple two-parameter model that is surely valid for a dense gas and which is often used for describing the drift of excess electrons in condensed rare gases (the aforementioned nonspecificity of the behavior of the drift velocity with respect to the phase state serves as a justification for this).

We consider the drift of an electron as a process of its random walk in the force field eE .¹⁵ We introduce the following parameters: λ_m —the mean free path with respect to total loss of momentum direction, so that after a “collision” the average velocity of the electron is equal to zero; λ_w —the mean free path with respect to loss of energy; now $\varepsilon \equiv \lambda_m/\lambda_w$ is the fraction of the energy lost after one “collision” accompanied by loss of momentum ($\varepsilon \ll 1$).

Neglecting the time of collision in comparison with the mean free time, we can assume that the electron acquires energy from the electric field during the time of its free motion between collisions. Then its energy after the i th collision with loss of momentum is equal to

$$\frac{m\mathbf{v}_{i+1}^2}{2} = (1-\varepsilon) \frac{m(\mathbf{v}_i + \mathbf{a}t_i)^2}{2} = (1-\varepsilon) \left[\frac{m\mathbf{v}_i^2}{2} + \frac{ma^2t_i^2}{2} \right],$$

where m is the mass of the electron, $a = eE/m$ is its acceleration in the field E , and t_i is the time between the i th and $(i+1)$ th collisions. Thus if we neglect the change in the total velocity over the time between two successive collisions and the difference of the trajectory from rectilinear, i.e., $t_i = \lambda_m/v_i$, the recursion relation for the kinetic energy of an electron has the form

$$\frac{W_{i+1}^2}{2} = (1-\varepsilon) \left[W_i + \frac{w_0}{4W_i} \right], \quad (1)$$

where w_0 is the energy acquired by the electron from the field over its mean free path:

$$\omega_0 = eE\lambda_m, \quad (2)$$

or, in differential form, for $\varepsilon \ll 1$,

$$2 \frac{d(W^2)}{di} = \omega_0^2 - 4\varepsilon W^2. \quad (3)$$

In low electric fields the electrons are in thermal equilibrium with the substance. Isothermal drift is characterized by a constant mobility, since $v_d = at_0/2$, and t_0 , the mean free time of the electron in its steady drift, is constant and equal to λ_m/v_T , where v_T is the thermal speed of the electron. Thus $v_d \sim E$ and is given by the equation

$$v_d = \frac{eE\lambda_m}{2mv_T} = \frac{w_0}{2^{3/2}\sqrt{mkT}}. \quad (4)$$

Expression (4), up to a numerical coefficient of 1.5, agrees with the formula obtained by Bardeen and Shockley¹⁰ for the electron mobility in nonpolar crystals on the basis of the Boltzmann equation.

For moderately high fields, when the electron energy $W \gg kT$, and under the condition of stationarity of Eq. (3) is equal to

$$W = \frac{w_0}{2\sqrt{\varepsilon}}, \tag{5}$$

the gas approximation is even more realistic: even for the motion of an electron in the conduction band in a xenon crystal, the mass of a conduction electron is close to m , as a calculation shows.¹ Condition (5) can be rewritten in the form

$$v = \frac{1}{\sqrt{\varepsilon}} \left(\frac{eE}{m} \right) \left(\frac{\lambda_m}{v} \right) = \frac{at_0}{2^{3/2}\sqrt{\varepsilon}}. \tag{6}$$

The drift velocity of an electron under these conditions is, as before, equal to $v_d = at_0/2$. Hence

$$\frac{v_d}{v} = \frac{\sqrt{\varepsilon}}{2}; \quad v_d \sim \sqrt{E}. \tag{7}$$

The physical meaning of expression (7) is obvious—in the random walk of a particle its displacement is always determined by the square root of the number of steps (in this case, to the loss of energy). For free atoms (a gas, the hard-spheres approximation) $\bar{\varepsilon} = 2m/M$, and expression (7) becomes

$$\frac{v_d}{v} = \sqrt{m/2M}, \tag{8}$$

which is practically the same as the result $v_d/v \cong \sqrt{m/M}$ which is known from calculations and experiments on the drift of electrons in a gas (M is the mass of the Rg atom).¹⁶ Thus in the drift of an electron in an electric field (with accuracy up to the dependence of the electron scattering cross section on its energy on account of the Ramsauer effect, which is rather smooth and reduces to a parametric dependence $\varepsilon(E)$) the linear dependence of the drift velocity on the applied field, which is characteristic for thermal electrons, gives way at higher fields (when the electron temperature “detaches” from the temperature of the heavy particles) to a square-root dependence on E .

It is hard to expect that the hard-spheres approximation and, hence, formula (8) will be valid for a liquid and solid, particularly in view of the fact that at the densities characteristic for the condensed state the effective electron scattering cross section of Rg atoms is an order of magnitude smaller than in a dense gas.^{17,18} However, the results of experiments¹⁷ and calculations¹⁹ show that the energy loss per electron scattering event, ε , remains close to $2m/M$. Moreover, the dependence $v_d(E)$ in condensed rare gases follow the indicated law $\sim E \rightarrow \sim \sqrt{E}$ even more strictly, because there is practically no dependence $\lambda_m(W)$ (see Fig. 1).

The kinetic energy of the excess electron in steady drift increases in proportion to E , and the logical question arises: how high can it go? The statement first made in Ref. 12 is essentially that this energy cannot appreciably exceed the first excitation potential I_0 of the Rg atom (for Xe, $I_0 = 8.3$ eV). As we see from Eq. (5), this should occur in fields E that are very high, so that

$$\frac{w_0}{2I_0\sqrt{\varepsilon}} \equiv \alpha^{-1} \geq 1. \tag{9}$$

In this case the excitation cross section increases so rapidly from the threshold that, upon exciting an atom, the elec-

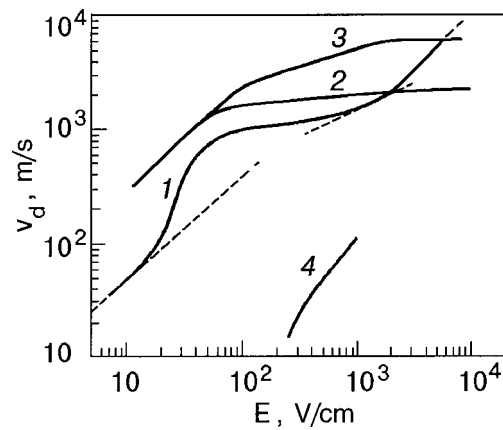


FIG. 1. Electron drift velocity in Xe versus the electric field according to the data of Ref. 17: 1—gas, $n = 6 \times 10^{19}$, $T = 172$ K; 2—liquid, $T = 165$ K; 3—solid, $T = 155$ K. The dashed lines have slopes of 1 and 1/2. For comparison the electroluminescent yield of Xe at $P = 0.35$ bar and $T = 300$ K from Ref. 20 is also shown (4).

tron immediately loses all of its energy. Therefore, under condition (9) the kinetic energy of the drifting electron, having increased to I_0 , then falls sharply back practically to zero, and these cycles repeat during the whole course of the drift, so that the average energy W and average velocity v of the electron remain constant. The question arises, how will the drift velocity v_d of an excess electron behave as a function of the applied electric field E ?

The approximate solution of equation (1) for the energy of an excess electron W_i after the i th step of a random walk has the form

$$W_i^2 = \frac{w_0^2}{4\varepsilon} (1 - e^{-2i\varepsilon}), \tag{10}$$

and its average drift velocity is given by

$$v_d^{i_m} = \frac{\sum_{i=0}^{i_m} i^s}{\sum_{i=0}^{i_m} t_i} = \frac{\sum_{i=0}^{i_m} \frac{at_i^2}{2}}{\sum_{i=0}^{i_m} t_i} = \frac{w_0}{2m} \frac{\sum_{i=0}^{i_m} v_i^{-2}}{\sum_{i=0}^{i_m} v_i^{-1}}. \tag{11}$$

The step number i_m at which the energy of the electron reaches the energy of electronic excitation is determined from the equation $W_{i_m} = I_0$ and is equal to

$$i_m = -\frac{1}{2\varepsilon} \ln(1 - \alpha^2). \tag{12}$$

Already the threshold determined by condition (9) the condition $\alpha^2 \ll 1$ holds. This (as is seen from Eq. (3)), is equivalent to neglecting the energy lost by an electron in collisions in comparison with the energy it acquires from the field, when

$$W_i = \frac{w_0}{\sqrt{2}} i^{1/2} \tag{13}$$

and

$$i_m \cong \frac{2I_0^2}{w_0^2}; \quad i_m \sim E^{-2}. \tag{14}$$

Using relation (13) and changing the sums in (11) to integrals, we obtain

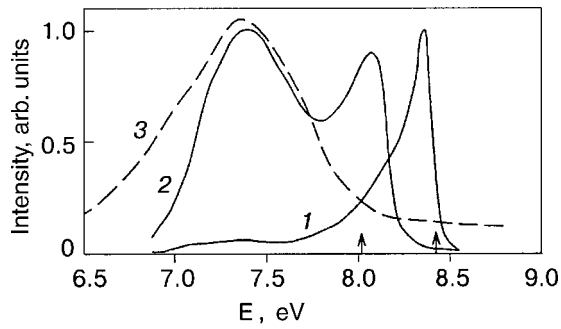


FIG. 2. Electroluminescence spectra of gaseous Xe at pressures of 100 (1), 500 (2) and 760 torr (3).²³ The arrows indicate the positions of the transition energies of the xenon atoms $\text{Xe}(^3P_1 \rightarrow ^1S_0)$, 8.44 eV, and of the negative ions $\text{Xe}^-(^2P_{3/2}) \rightarrow \text{Xe}(^1S_0) + e$, 8.02 eV.

$$v_d \approx \frac{3}{2^{5/2}} \frac{w_0}{\sqrt{mI_0}}; \quad v_d \sim E. \quad (15)$$

In other words, contrary to crass intuition, when an upper limit is placed on the random motion of the electron its drift velocity does not remain constant but increases in proportion to the applied field, i.e., faster than for stationary drift. The yield of excimer molecules (two-center excitons) and, accordingly, the number of VUV photons per drifting electron, starting from their appearance threshold (9), should also grow in proportion to the field:

$$\eta = \frac{eEl}{I_0}, \quad (16)$$

where l is the thickness of the sample.

Let us compare the predictions of our simple proposed model with the results of experiments. As we see in Fig. 1, where as an example we present the experimental curves of $v_d(E)$ for gaseous, liquid, and solid xenon, the linear growth segment (corresponding to isothermal drift) does indeed give way to a square-root dependence on E . Moreover, in gaseous xenon at a comparatively low pressure, when the drift velocity reaches a value approximately equal to that found from Eq. (8) for $W = I_0$, i.e., $v_d = \sqrt{I_0/M} \approx 5 \times 10^5$ cm/s, the function $v_d(E)$ actually does again become linear, and it is in this range of electric field E that the VUV radiation in the 170 nm region (the luminescence of Xe_2^*) appears in a threshold manner, its yield depending linearly on the applied voltage; and, in agreement with the above model, this dependence is the same when the gas pressure is increased at least to 1.4 bar.²⁰ Furthermore, at low pressures one observes a spectral band in the 150 nm region, i.e., in the region where the atomic transition $\text{Xe}(5p^6 - 5p^5(^2P_{3/2})6s)$ is found, shaded to the red side²⁰ (see Fig. 2).

However, in gaseous xenon at high pressure, as in condensed xenon, the $v_d(E)$ curve goes over not to a linear trend as implied by the proposed model but rather to a constant value. This behavior is even more strange in that it contradicts simple physical ideas—an increase of the energy loss, by decreasing the effective number of random walks, should always lead to an increase in the drift velocity. This is also confirmed by the results of experiments—the introduction of a molecular impurity in rare gases always leads to an increase in v_d (Ref. 21).

One of the first explanations for the existence of a limiting drift velocity of the electron in solid and liquid rare gases¹⁹ assumed the existence of structural traps that kept the electron trapped for a long time. This explanation, however, did not hold up to a critical scrutiny, since only impurities could serve as such traps; at the same time, as we have said, the presence of impurities only increases the drift velocity. Furthermore, that assumption does not account for the limitation of the drift velocity in gases.

The model proposed in Ref. 12 and developed in the present paper in principle can explain the existence of rather deep traps in pure rare gases. Unlike the atoms in the ground state, the electronically excited Rg atoms have a appreciable electron affinity and, since immediately after excitation of an atom the electron has practically no kinetic energy, it can be assumed that, at least in condensed rare gases, the electron can be trapped by the centers they themselves create. As an upper estimate of the lifetime of such a formation one can take the radiation lifetime τ_R of the negative ion $(\text{Rg}_2^*)^-$. If it is assumed that this time is close to that for the two-center exciton ($\tau_R \approx (2-3) \times 10^{-8}$ s for Xe_2^*), then we find that, starting at an electric field $E = 10^3$ V/cm, the lifetime of a trapped electron in liquid and solid Xe become comparable to the time it takes for a drifting electron to acquire an energy equal to the energy of electronic excitation of the xenon atom.

It is not hard to obtain an expression for the drift velocity of electrons with allowance for this effect:

$$\frac{1}{v_d} = \frac{\sum_{i=0}^m t_i + \tau_R}{\sum_{i=0}^m s_i} = \frac{1}{v_d^0} + \frac{\tau_R}{\sum_{i=0}^m s_i} \approx \frac{1}{v_d^0} + \frac{eE}{I_0}. \quad (17)$$

We see from Eq. (17) that taking into account the effect of electron trapping by the excited xenon (first by the atom, and then by the Xe_2^* molecule) gives a term that causes a decrease in the limiting drift velocity ($v_d \sim E^{-1}$ at large E). Without assuming a substantial dependence of the radiation lifetime of $(\text{Xe}_2^*)^-$ on E (which is unlikely for an allowed optical transition) it is hard to explain the observed constancy of the drift velocity at high electric fields (for Xe, in the range $1 \times 10^3 - 6 \times 10^4$ V/cm²) by a competition of the contributions proportional to E and E^{-1} . For gaseous Xe the formation of long-lived negative ions is unlikely altogether.

This leaves us to consider the problem of the interaction of Rg atoms with an electron in more detail. The metastable states of the corresponding negative ions are well known, and the lowest in energy of them are the resonance $^2P_{3/2}$ states with the configuration $np^5(n+1)s^2$ (an additional electron is found on the same orbit as an outer electron of the lowest 3P_2 state of the excited Rg atom) lie an amount $\Delta = 0.4$ eV lower in energy than the excited 3P_2 Rydberg state of the atom (see Table I). They have a rather long lifetime²³ and decay as a result of the weak Coulomb interaction of the electrons in a process involving the removal of one of the electrons and a transition of the other to the ground state. In two-particle collisions these resonances are manifested as rather sharp (with a width of about 0.01 eV) and therefore intense peaks in the elastic and inelastic electron scattering cross sections. These scattering cross sections, $\sigma_R = 10^{-15}$ cm², are much larger than the cross sections typical for the region after the Ramsauer minimum.¹⁷ Neverthe-

less, in gaseous Xe at densities up to 10^{20} cm^{-3} , on account of the energy acquired by the electron from the field over the mean free path in fields of the order of 1 kV/cm, i.e., $W \cong E/\sigma_R n = 10^{-2} \text{ eV}$, there is a high probability of “slipping past” these so-called core excited resonances. Accordingly, in this case the model presented above is valid, and the experimental $v_d(E)$ curves have a regular form (see Fig. 1), the transition to a linear dependence of v_d on E occurring precisely in the region where the VUV emission due to the electronic excitation of xenon appears.

In a denser gas and in the condensed state, the motion of an excess electron in the energy region corresponding to the resonant scattering peak in the configuration of the negative ion can be regarded as a sharp transition to its drift with a markedly smaller step of the random walk. As we see from Eq. (3) for the electron energy, the first term on the right-hand side of the part corresponding to the acquisition of energy from the field decreases as σ_R^{-2} , while the second term, describing the loss of energy, decreases more weakly than σ_R^{-1} . (The electron energy loss in the region of the resonances due to states of the negative ion is small—for the decay of a negative ion the momentum conservation law gives, as before, $\varepsilon \sim m/M$.) This means that during drift in the resonance region the electron energy tends to decrease, thereby removing it from the resonance region. As a result of this negative feedback, the electron energy W remains constant, $W = I_0 - \Delta$, over a rather long time, regardless of the value of the electric field. Accordingly, the average drift velocity v_d of the electron after this time reaches its steady value given by formula (7) with a certain effective value of the parameter ε . Thus, taking into account the scattering on structure resonances of the negative ion indeed leads to constancy of v_d at large E , and only when the field is increased by a factor $\beta = \sigma_R/\sigma_0$ (σ_0 and σ_R are the cross sections for ordinary and resonance scattering, respectively) does the drift velocity of the electron begin to grow as \sqrt{E} .

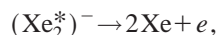
During drift motion in a dense gas, with a kinetic energy remaining constant at $W = I_0 - \Delta$ for a long time, an electron can either: 1) skip the resonance peak because of fluctuations of its energy, and having acquired insufficient energy to excite a rare-gas atom (and this, as we have said, subsequently leads to emission at a transition of the atom or excimer molecule); 2) having been incorporated into a metastable negative ion, undergo a transition to a free state in the process of its decay, with the emission of a VUV photon; 3) with a constant velocity of around 10^{-30} cm/s enter into a trimolecular reaction forming an excimer molecule:



(since the energy of Xe_2^* at 0.7 eV (see Table I) is lower than the energy of atomic excitation, the final energy of the electron is 0.3 eV, which is quite sufficient for delocalization of the latter).

The published data available²⁴ on the transformation of the VUV emission spectrum generated by electrons drifting in gaseous xenon as the Xe density is increased agree surprisingly well with the arguments presented above. Indeed, as can be seen in Fig. 2, at low densities the electroluminescence is dominated by a narrow band with $\lambda = 150 \text{ nm}$, corresponding to the transition of the excited atom. When the density is increased on account of a weakening of this band (the total radiation yield is independent of the density) there arise: 1) a wide band, close in shape and position ($\lambda = 170 \text{ nm}$) to the emission spectrum of the excimer molecule Xe_2^* , and 2) a narrower peak centered at $\lambda = 160 \text{ nm}$, which corresponds precisely to the energy of a state of the negative ion $(\text{Xe}^*)^-$. Finally, at high densities there remains only the band corresponding to the emission of the excimer molecule.

In the condensed state, as in the dense gas, the main channels of electron energy loss are the formation and subsequent decay of a one-center negative ion $(\text{Xe}^*)^-$ and a two-center exciton. This is confirmed by the spectrum of quasi-molecular emission observed when solid Xe is irradiated by fast electrons.¹ With allowance for the matrix shift, the L_x band corresponds well to the position of the transition in $(\text{Xe}^*)^-$ (see Fig. 3). However, in the liquid and solid the electron can with a certain probability be localized near a binuclear center. As we have said, the excited state $(\text{Xe}_2^*)^-$ rapidly decays:



leading to a radiationless energy loss of around 0.4 eV and thereby reducing the yield of excitons per electron.

In dense gases and in the condensed state there is apparently one more important cause of the decrease in the efficiency η of energy conversion of electric field into VUV radiation as the electric field E is increased. In the steady drift of an electron near $W = I_0 - \Delta$ the distance traveled by it in the direction of the field does not, of course, lead to a change of the electron energy. Therefore, in high fields the value of η is determined by the ratio of the distance traveled

TABLE I. Characteristics of the excited states of atoms of the rare gases Rg in eV¹.

Rg	Energy of lowest excited states of the atom Rg^* (3P_2)	Energy of dissociation of the exciplex Rg_2^*, D_0	Energy of phototransition in the exciplex	Electron affinity of Rg^* (Ref. 22)
Ar	11.624	1.2	9.76	0.44
Kr	10.032	0.9	8.38	0.40
Xe	8.440	0.7	7.2	0.455

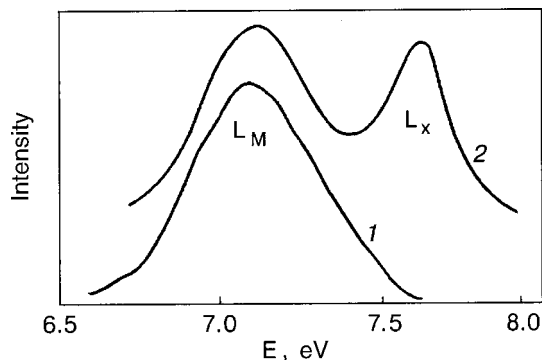


FIG. 3. Quasi-molecular emission of crystalline Xe at 10 K (1) and 76 K (2).¹ The “hot” band L_x can be interpreted as emission at a transition of the negative ion $(\text{Xe}^*)^-$.

by the electron in the period of its intense absorption of energy from the field, to the total distance, the main contribution to which is from the aforementioned steady drift stage:

$$\eta = \frac{\sum_{i=0}^m s_i}{\sum_{i=0}^m s_i + v_d^0 \tau} = \frac{1}{1 + (v_d^0 \tau e E) / I_0}, \quad (18)$$

where τ is the time prior to trapping of the electron. Accordingly, the number of photons, m , generated by one electron drifting through a sample of thickness l tends, in high fields, toward a constant value

$$m = \frac{l}{v_d^0 \tau}. \quad (19)$$

It is easily estimated that $m \approx 100$, which in principle would permit obtaining an electron avalanche in a cell with a photocathode, as was proposed in Ref. 12.

The analysis in this paper does not leave any doubt that in gaseous xenon at densities $n \leq 10^{20} \text{ cm}^{-3}$ the characteristics of the drift of an excess electron in a high electric field is determined by the electronic excitation of the gas, which is thus an efficient converter of energy from a static electric field directly into VUV radiation. The conclusion that a similar mechanism is realized in liquid and solid xenon is also quite convincing, particularly since it can explain a whole set of existing experimental results. Among the most important of these is the recently published direct observation of VUV emission in the two-center excitonic band in liquid xenon during the drift in it of electrons emitted by a cold cathode.¹⁴ At the present time it is not possible to estimate the field corresponding to the threshold observed in Ref. 14 for the appearance of VUV electroluminescence, since a more detailed acquaintance with the experimental technique²⁵ used by the authors of Ref. 14 indicates the possibility of considerable nonuniformity of the electric field, although the threshold cannot be very high, since the voltage used was only 70 V.

Nevertheless, the final answer to the question will require doing experiments with solid or liquid Xe in a uniform field with a determination of the absolute value of the VUV emission yield. We are currently doing such experiments in conjunction with the Kamerlingh Onnes Leiden University.

Let us conclude by noting an interesting feature of the VUV electroluminescence in Xe, which follows from the above analysis. By combining formulas (4) and (9), one can obtain the following expression for the threshold value of the field at which this emission appears:

$$E_{\text{th}} = \frac{v_T}{2kT} \frac{I_0 \sqrt{\varepsilon}}{\mu}, \quad (20)$$

where $\mu \equiv v_d / E$ is the electron mobility measured in a low field. Figure 4 shows a plot of $E_{\text{th}}(n)$ according to Eq. (20) with the use of the experimental values of $\mu(n)$ from Ref. 17, where n is the density of Xe. We see that whereas at low densities (10^{19} cm^{-3}) the threshold is around 1 kV/cm and

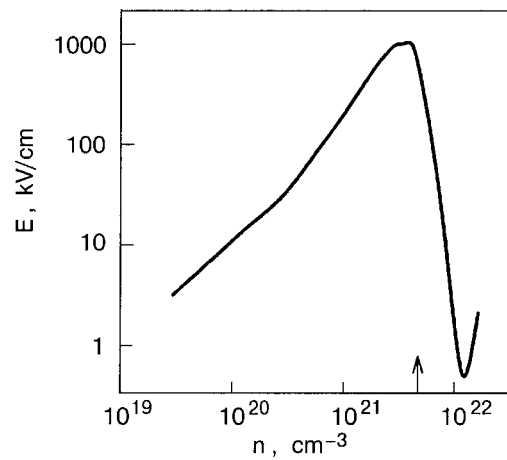


FIG. 4. Dependence of the threshold electric field for the appearance of VUV emission as a function of the density n of Xe at $T=290$ K. The arrow indicates the position of the critical density n_c .

increases in proportion to the density in accordance with Refs. 20 and 26, at densities of $5 \times 10^{21} \text{ cm}^{-3}$ it has already become 3 orders of magnitude higher, reaching values of 1000 kV/cm, which would be hard to achieve experimentally. However, once the liquid has formed, the threshold returns to a value of around 1 kV/cm (in agreement with Ref. 14). In other words, in compressed rare gases the drift of electrons is unaccompanied by luminescence all the way up until condensation. The calculations whose results are presented in Fig. 4 were done for a temperature close to the critical temperature $T_c = 290$ K. The analysis of the behavior of $E_{\text{th}}(n)$ in the condensed state should be done at temperatures $T = 160\text{--}200$ K, close to those used in the experiments on the measurement of the mobility.¹¹ It turns out that, although in the liquid and solid states the value of E_{th} depends nonmonotonically on n , it remains low—around 1 kV/cm.

We have based the above analysis on experimental data obtained for the drift of electrons in xenon, the most studied of the heavy rare gases. However, the basic conclusions are also valid for Kr and Ar, which are potential sources of even harder UV radiation.

If this line of research is successful, experimenters will acquire a new way of studying electronic excitations in liquid and solid rare gases, the features of which include comparative simplicity of the experiment and high intensity of emission on the one hand, and a specific means of excitation, including the physical presence of an electron at the site of localization of the exciton, on the other. The high efficiency of excitonic luminescence not only facilitates the recording of its characteristics but holds promise for a number of practical applications, such as the creation of excitonic VUV lasers and lamps and the refinement of luminescent detectors of high-energy particles.

The authors thank P. Wyder (Grenoble High Magnetic Field Laboratory) for providing the dissertation of A. S. Schussler, which contains the details of their work. This study was supported in part by the Russian Foundation for Basic Research, grants Nos. 01-03-32247 and 00-15-97400.

*E-mail: gordon@binep.ac.ru

**E-mail: as@icp.ac.ru

- ¹E. V. Savchenko, I. Ya. Fugol', in *Cryocrystals* edited by B. I. Verkin and A. F. Prikhod'ko [in Russian], Naukova Dumka, Kiev (1983), Part 4.
- ²Ya. Frenkel, *Phys. Rev.* **37**, 1279 (1931).
- ³N. B. Basov, V. A. Danilychev, Yu. M. Popov, and D. D. Khodkevich, *JETP Lett.* **12**, 329 (1970).
- ⁴H. Nahme and N. Schwentner, *Appl. Phys. B: Photophys. Laser Chem.* **51**, 177 (1990).
- ⁵N. Schwentner and V. A. Apkarian, *Chem. Phys. Lett.* **154**, 413 (1989).
- ⁶A. V. Elets'kii and B. M. Smirnov, *Physical Processes in Gas Lasers* [in Russian], Énergoatomizdat, Moscow (1985), p. 124.
- ⁷C. K. Rhodes (Ed.), *Excimer Lasers*, Springer-Verlag, Berlin (1979).
- ⁸J. P. Hernandez, *Rev. Mod. Phys.* **63**, 675 (1991).
- ⁹G. Ascarelli, *J. Phys. Chem.* **84**, 1193 (1980).
- ¹⁰J. Bardeen and W. Shockley, *Phys. Rev.* **80**, 72 (1950).
- ¹¹E. M. Gushchin, A. A. Kruglov, and I. M. Obodovskii, *Zh. Éksp. Teor. Fiz.*, 82, 1114 (1982) [*Sov. Phys. JETP* **55**, 650 (1982)].
- ¹²E. B. Gordon, V. V. Khmelenko, and O. S. Rzhevsky, *Chem. Phys. Lett.* **217**, 605 (1994).
- ¹³E. B. Gordon, O. S. Rzhevsky, and V. V. Khmelenko, *Kvantovaya Élektron. (Moscow)*, **21**, 227 (1994).
- ¹⁴A. S. Schussler, J. Burghorn, P. Wyder, B. I. Lembrikov, and R. Baptist, *Appl. Phys. Lett.* **77**, 2786 (2000).
- ¹⁵Yu. P. Raizer, *Physics of the Gas Discharge* [in Russian], Nauka, Moscow (1992).
- ¹⁶B. M. Smirnov, *Physics of Weakly Ionized Gases* [Mir, Moscow (1981); Nauka, Moscow (1978)].
- ¹⁷S. S.-S. Huang and G. R. Freeman, *J. Chem. Phys.* **68**, 1355 (1978).
- ¹⁸S. S.-S. Huang and G. R. Freeman, *Phys. Rev. A* **24**, 714 (1981).
- ¹⁹J. Lekner, *Phys. Rev.* **158**, 130 (1967).
- ²⁰F. Favata, A. Smith, M. Bavadaz, and T. Z. Kowalski, *Nucl. Instrum. Methods* **294**, 595 (1990).
- ²¹D. W. Swan, *Proc. Phys. Soc. (London)* **83**, 659 (1964).
- ²²H. S. W. Massey, *Negative Ions*, Cambridge University Press, Cambridge (1976), Mir, Moscow (1979).
- ²³E. B. Gordon and O. S. Rzhevsky, *Molecular Physics* (2001).
- ²⁴B. A. Monich, *Prib. Tekh. Éksp.* **5**, 7 (1980).
- ²⁵A. S. Schussler, *Thesis*, Hartung-Gorre Verlag, Konstanz (1998).
- ²⁶A. El-Habachi and K. H. Schoenbach, *Appl. Phys. Lett.* **73**, 885 (1998).

Translated by Steve Torstveit

Ionization and hydrolysis of dinitrogen pentoxide in low-temperature solids

J. Agreiter, M. Frankowski,* and V. E. Bondybey**

Institute for Physical and Theoretical Chemistry, Technical University of Munich, Lichtenbergstrasse 4, 85747 Garching, Germany

(Submitted June 21, 2001)

Fiz. Nizk. Temp. **27**, 1202-1207 (September-October 2001)

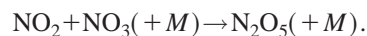
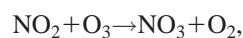
Solid layers of interest for the chemistry of polar stratospheric clouds are investigated. Mixtures of covalent N_2O_5 and water in various molar ratios are deposited from the vapor phase on a cold 12 K substrate. By repeatedly recording Fourier transform infrared spectra of the samples during gradual warmup to 200 K over a period of several hours the hydrolysis process can be followed. At each concentration the process is found to proceed in several distinct steps with sharp temperature thresholds. In samples containing only small amounts of water the covalent N_2O_5 is first, at around 110 K, converted to an ionic nitronium nitrate, and only in a subsequent step does $NO_2^+NO_3^-$ react to form nitric acid. © 2001 American Institute of Physics. [DOI: 10.1063/1.1414583]

INTRODUCTION

The structures, optical spectra, and other properties of molecules in condensed phases often differ quite substantially from those in the gas phase. Strongly polar compounds like HCl or HI, which occur as covalent compounds in the gas phase, ionize spontaneously when dissolved in water. Even though the autoionizing reaction of water itself, $2H_2O \rightarrow H_3O^+ + OH^-$ requires an energy $H = 933$ kJ/mol, every liter of pure room-temperature water contains in thermal equilibrium some $10^{17} H_3O^+$ cations and a corresponding number of OH^- anions, which greatly affect its properties. Some substances, which in the gas phase are present in a covalent form tend to ionize completely in a solid or liquid, where the substance itself acts as its own "solvent." While in the gas phase a covalent form AB is usually lower in energy, in a condensed phase where an A^+ ion can interact with a number of nearby B^- anions, the lattice energy may more than compensate for this deficit, and the ionic A^+B^- alternative becomes energetically preferable. A well-known example of this type is dinitrogen pentoxide, N_2O_5 , which occurs in the gas phase in the form of covalent $O_2N-O-NO_2$ molecules, but in the solid usually in the ionic form $NO_2^+NO_3^-$, nitronium nitrate.^{1,2}

NITROGEN OXIDE IN THE STRATOSPHERE

Nitrogen oxides and their condensation are of considerable importance in the chemistry of the stratosphere and contribute in several ways to the balance of stratospheric ozone.³⁻⁸ The major path of N_2O_5 formation is due to reaction of nitric oxide with ozone:^{9,10}

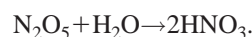


Since during the daytime NO_3 is efficiently photolyzed by sunlight, the N_2O_5 concentration reaches its maximum at night. The dinitrogen pentoxide is ultimately also photolyzed back to $NO_2 + NO_3$, but it acts as a relatively unreactive "reservoir" reducing, albeit temporarily, the concentration of

the so-called NO_x or "odd nitrogen" species. These, and in particular NO_2 , in turn have importance in reacting with ClO to form the relatively unreactive chlorine nitrate, $ClONO_2$, thus removing reactive chlorine from a catalytic, ozone destroying cycle.

Perhaps somewhat paradoxically for the rarefied stratosphere, the properties of N_2O_5 and other nitrogen oxide in the solid phase or on solid surfaces may be even more important for stratospheric chemistry than their gas-phase reactions.³⁻⁸ When in the course of the polar winter the temperature of the stratosphere drops below about 190 K, the formation of so-called polar stratospheric clouds (PSCs) takes place. These consist of micron-size particles, whose main components are water and the oxides of nitrogen. Heterogeneous processes on their surfaces are then believed to be responsible for converting relatively unreactive, so-called "reservoir" chlorine containing compounds, mainly chlorine nitrate and hydrogen chloride, into more active species, such as Cl_2 or $NOCl$. During polar spring, when the temperature rises again and the PSCs evaporate, chlorine in this more reactive form is returned into the gas phase, with photolysis yielding atomic chlorine. Cl atoms then very efficiently catalyze O_3 destruction and are ultimately responsible for the seasonal ozone depletion and catalytic destruction, referred to popularly as the "ozone hole."

Also the relatively nonvolatile dinitrogen pentoxide condenses on the surface of PSCs and contributes in a variety of ways to the ozone and its balance. Important is the hydrolysis of N_2O_5 to form nitric acid, presumably by the reaction catalyzed on a PSC surface:¹¹⁻¹³



This reaction is in fact believed to be the major pathway of "denitrification" of the stratosphere, that is, for the loss of NO_x species, and thus to contribute indirectly to an increase in the concentrations of active chlorine radicals and to ozone destruction. The nitric acid concentration also affects the PSC formation itself: the so-called type-II PSCs, containing nitric oxides and, in particular, nitric acid trihydrate (NAT),

can form at a higher temperature than “pure water,” type-I PSCs. While the above hydrolytic reaction forming nitric acid could in principle also occur during gas phase collisions, this is believed to be far too inefficient to explain the observed chemistry.

This added practical importance of N_2O_5 and of its condensation and hydrolysis has motivated a number of recent experimental and theoretical studies. Thin layers consisting of nitrogen oxides, nitric acid and water were studied by spectroscopy, and their reactions were also extensively investigated at a variety of temperatures. Also theoretical, *ab initio* or density functional theory (DFT) studies of N_2O_5 and its hydrolysis have appeared.¹⁴ In spite of this extensive attention, numerous open or controversial problems remain. A considerable discussion centers on the question of whether the reactants occur and the reaction products are formed in an ionized or in a molecular form. Based on an infrared study it was concluded that N_2O_5 itself does not play a major role in the heterogeneous chemistry directly but rather through its hydrolysis products. The structure and reactivity of nitrogen oxides is known to be a sensitive function of their temperature and of the dynamics of their formation. To gain additional insights, we reinvestigate here the N_2O_5 hydrolysis using Fourier transform infrared (FTIR) spectroscopy.

Even though in solid the ionic $NO_2^+NO_3^-$ form is lower in energy, if gaseous dinitrogen pentoxide is condensed on a very cold surface, a solid consisting of discrete, covalent N_2O_5 molecules is formed, whose infrared or Raman spectra are very similar to the gas-phase spectrum. When the energy needed to overcome the activation barrier is supplied, either by optical irradiation or by heating the sample, it is converted into the ionic form. As is well known, annealing such samples above about 120 K results in an abrupt and complete change in the structure of the solid, and naturally also in its infrared or Raman spectrum. In the present work we take advantage of the ability of a modern FTIR instrument to rapidly acquire and store digitally infrared spectra. We prepare solid mixtures of water and covalent N_2O_5 at about 12 K by deposition from the gas phase. Then we slowly allow the samples to warm up over several hours, and we repetitively take infrared spectra every few minutes. The spectra then provide information about structural changes, phase transitions, or chemical reactions taking place in the solid. The interpretation of the results is naturally greatly assisted by the availability of numerous previous studies of the spectroscopy of nitrogen oxides, nitric acid, and of its hydrates.

EXPERIMENTAL

The N_2O_5 , prepared in a standard way by the reaction of commercial nitric oxide (or N_2O_4) with ozone, was purified by vacuum distillation and by several pump–freeze–thaw cycles. The oxide stored in Pyrex containers at liquid nitrogen temperature was then deposited via a corrosion-resistant needle valve onto a metal substrate cooled to ~ 12 K by a closed-cycle refrigerator. Simultaneously with the N_2O_5 , water was deposited from a separate inlet, to yield a solid mixture in a desired molar ratio of $H_2O:N_2O_5$. Infrared spectra were recorded on a Bruker IFS 120 HR Fourier transform spectrometer. The 100–300 spectra acquired during over 4–6 h during the slow sample warmup could then be used

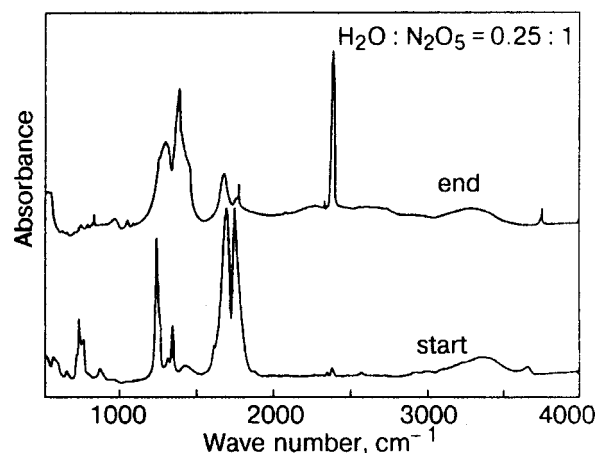


FIG. 1. Experiment with $H_2O:N_2O_5$ ratio of about 0.25:1. The initial 10 K infrared spectrum of covalent N_2O_5 in the bottom trace is in the top trace after gradual annealing over 4 h to 160 K converted to ionic $N_2O_5^+NO_3^-$, with small amounts of nitric acid, HNO_3 .

and displayed in a variety of ways. Initial spectra, final spectra, or intermediate spectra at any time during the warmup could be plotted. Alternatively, by plotting the absorption at a selected wavelength, the decay of a reacting compound or the appearance a product as a function of time and temperature could be displayed. Finally one could produce a “three-dimensional” diagram with the abscissa indicating the wave number, the ordinate the time (or the temperature, which was rising approximately linearly with time) and the “color” or shade of gray the band intensity. In the samples studied here there was little change in the spectrum up to about 100 K. To shorten the duration of the experiments, the sample temperature was first “rapidly,” over about ten minutes, raised to 80 K. After that it was allowed to rise further, over the course of about 4–6 h, to about 160–200 K, at which point the experiment was terminated and the sample allowed to evaporate.

RESULTS AND DISCUSSION

Figure 1 exemplifies the results of such an experiment obtained with a sample containing N_2O_5 with a relatively low water concentration ($H_2O:N_2O_5$ molar ratio 0.25:1) deposited at a temperature of ~ 12 K. The initial spectrum in the bottom trace of Fig. 1 shows the known bands of the covalent N_2O_5 , e.g., near 1740, 1240, and 756 cm^{-1} , most of which are only slightly shifted with respect to the gas phase. The presence of water is evidenced by the broad band centered near 3350 cm^{-1} .

As the sample is warmed up, the spectrum initially remains unchanged until a temperature of about 110 K is reached. Here over a temperature range of less than 10 K the covalent N_2O_5 bands almost completely disappear and are replaced by absorptions of the ionic solid, the most characteristic being the asymmetric stretch of the nitronium cation NO_2^+ at 2386 cm^{-1} and the ν_2 vibration of the nitrate anion near 820 cm^{-1} . A simple program was written which displays the information obtained from the repetitive spectral scans during the sample warmup in the form of a colored two dimensional diagram, in which the spectral changes occurring in the sample can be very nicely seen. As an example we present in Fig. 2 a black and white version of one of these

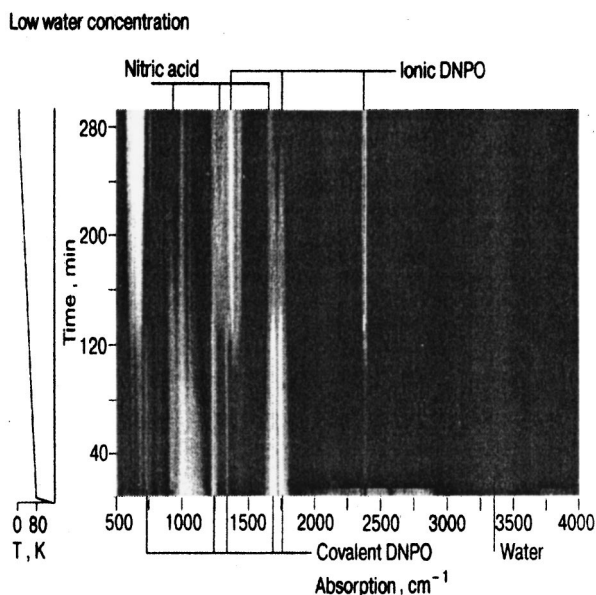


FIG. 2. “3D” diagram, from the same experiment showing the changes of spectrum during the controlled warm-up. The initial bands of covalent N_2O_5 disappear after ~ 120 min (at 110 K), with concurrent appearance of the ionic nitronium nitrate. After about 220 min (~ 140 K) nitric acid bands appear.

diagrams. Even though in the shades of gray version the changes are much less apparent, one can still follow the disappearance of the covalent solid and growth of the ionic solid as a function of time.

With some time delay after the conversion to ionic N_2O_5 is complete, a second, less prominent change occurs in the spectrum near 140 K, when bands of nitric acid begin to grow in. While some of these are partially overlapping, the HNO_3 absorptions are easily identified near 775 and 945 cm^{-1} . Another strong HNO_3 band, nearly coincident with an N_2O_5 absorption, occurs around 1680 cm^{-1} . The final spectrum resulting from annealing of the sample to 160 K can be seen in the top trace of Fig. 1, where the nitric acid bands can be easily identified. These observations provide clear evidence that under the conditions of our experiments, the neutral dinitrogen pentoxide does not react with the water present in the sample. The formation of nitric acid only takes place with a considerable delay, after a complete conversion of the nitrogen pentoxide solid into an ionic form.

A different presentation of these data and of the conversion of the covalent dinitrogen pentoxide into the ionic nitronium nitrate is shown in Fig. 3. Here one can see the simultaneous and abrupt appearance of the ionic solid absorptions at 820, 1400, and 2386 cm^{-1} after about 115 min during controlled sample heating. The spectral change occurs within a narrow range around 110 K, and concurrently one can observe a decrease in the absorptions due to the covalent pentoxide. Note that the thin solid line gives the changes in the sample temperature, as indicated by the right-hand scale.

The formation of nitric acid hydrates which are particularly important in the formation and chemistry of polar stratospheric clouds, and apparently in the ozone balance, can be studied by increasing the proportion of water in the deposited $H_2O:N_2O_5$ samples.^{15–18} Interesting are the intermediate-concentration samples with an $H_2O:N_2O_5$ ratio

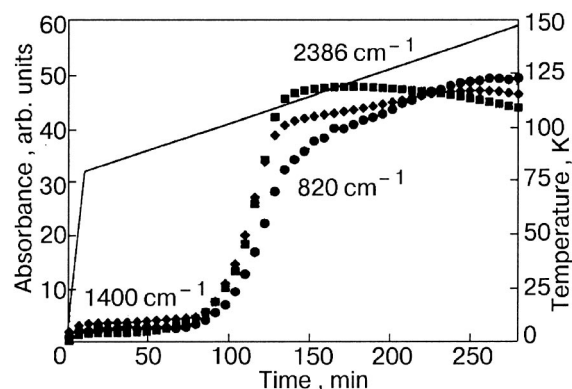


FIG. 3. Intensity profiles showing the simultaneous growth of the $N_2O^+NO_3^-$ bands within a relatively narrow, ~ 5 K temperature range.

of about 3:1, stoichiometry which should lead to nitric acid monohydrate (NAM):



Such a sample when deposited at 12 K shows again a superposition of the spectrum of covalent N_2O_5 , with in this case a much more prominent water band near 3360 cm^{-1} , as shown in Fig. 4. Interestingly, a minor amount of the ionic form seems to be present, perhaps small “clusters” whose conversion during deposition is “catalyzed” by the water-rich surface. During the warmup little happens until about 130 K is reached, when major changes in the spectrum begin to take place. In the first step the bands of the covalent N_2O_5 start to disappear, with simultaneous appearance of the absorptions of nitric acid. The concentration of HNO_3 , which can be followed by monitoring its absorptions near 775 and 945 cm^{-1} , reaches a maximum near 145 K and then starts to disappear again. Before the final temperature of 180 K is reached, the nitric acid is completely replaced by NAM. This is best identified by the H_3O^+ absorptions near 1670, 2250, and 2650 cm^{-1} and the nitrate anion bands near 735, 812, and 1260 cm^{-1} . The absorptions of NAM then remain until the sample is lost.

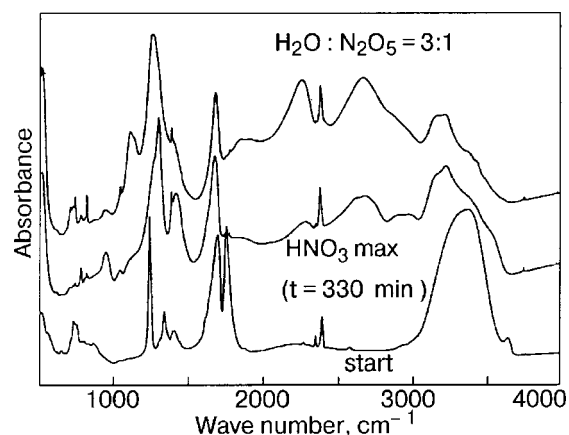


FIG. 4. Experiment with $H_2O:N_2O_5$ ratio of 3:1, corresponding to nitric acid monohydrate (NAM). The initial, bottom spectrum shows mainly covalent N_2O_5 , and a very strong, broad water band near 3360 cm^{-1} . The middle spectrum after 330 min exhibits maximum HNO_3 concentration. The top spectrum after 400 min is mainly that of the NAM.

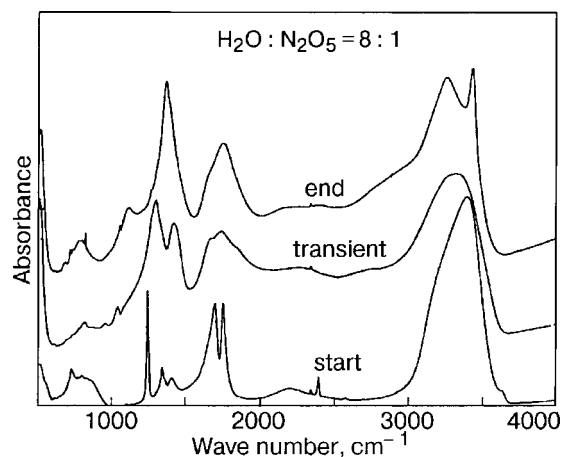
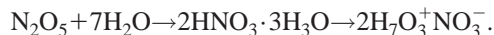


FIG. 5. $\text{H}_2\text{O}:\text{N}_2\text{O}_5$ ratio of about 8, with enough water to form nitric acid trihydrate, NAT. The initial, bottom spectrum contains covalent N_2O_5 , and a strong water band. In the middle spectrum after about 300 min (~ 140 K) the dinitrogen pentoxide has disappeared, and the observed absorptions agree with the known spectrum of NAD. After 320 min (~ 145 K) another sharp change takes place and the top spectrum identified as NAT results as final product.

A considerably different behavior can be found in samples containing still larger relative concentrations of water, where one can naturally observe a higher degree of nitric acid hydration. As in the less concentrated samples, the reaction again proceeds in several distinct steps. Such an experiment is presented in Fig. 5, where the molar ratio of H_2O to N_2O_5 was about 8:1, allowing the formation of nitric acid trihydrate:



In this case conversion of N_2O_5 from covalent to ionic form is hardly observed at all, with the covalent form persisting up to about 150 K. Apparently under these conditions one effectively has discrete N_2O_5 monomers “isolated” in water glass. As the temperature is gradually raised, the changes start only above 140 K, but unlike in the more concentrated N_2O_5 case, neither nitric acid nor nitric acid monohydrate is detected. The new bands, which grow in, can on the basis of previous spectroscopic work^{15–19} be easily identified as nitric acid dihydrate (NAD). The most characteristic feature is the presence of two strong bands near 1290 and 1420 cm^{-1} , interpreted previously in terms of the asymmetric nitrate stretching mode split by the asymmetric environment. However, the NAD bands do not persist long but are, at 155 K, abruptly replaced by the spectrum of the final product, nitric acid trihydrate. In NAT the two nitrate stretching bands collapse to a single strong absorption at 1390 cm^{-1} , and two bands appear in the OH stretching region, a sharper one at 3424 cm^{-1} and a much broader band near 3205 cm^{-1} . The apparently quite stable trihydrate, NAT, which is believed to be one of the major components of the polar stratospheric clouds, then remains unchanged until the sample is lost.

Similarly to Fig. 3, Fig. 6 shows the time dependent change in the product infrared absorption intensities for the 8:1 sample of Fig. 5. As demonstrated by the 1030 cm^{-1}

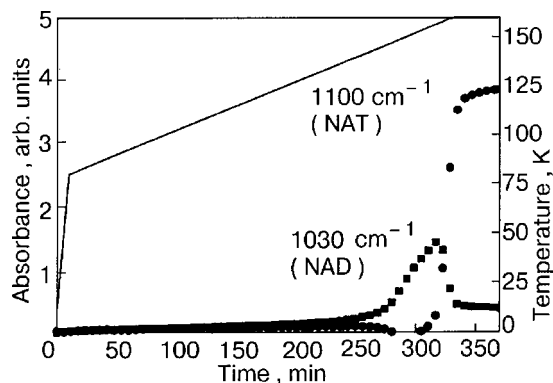


FIG. 6. Time resolved intensity profiles showing the NAD absorptions growing in after ~ 280 min, reaching a maximum after ~ 305 min (~ 145 K) and then abruptly disappear with concurrent appearance of the NAT.

band, at a temperature near 145 K the NAD appears but only transiently, only to be replaced by the strong 1100 cm^{-1} band of the final product, NAT.

SUMMARY

In summary, in this study we have investigated the structural changes in solid layers with relevance to the chemistry of PSCs. We condensed the samples at low temperatures and then repeatedly recorded their infrared spectra as a function of time as the sample temperature was slowly raised, to gain insight into processes and structural changes that take place. We found that the hydrolysis of N_2O_5 proceeds in each case in several well-defined sequential steps. Specifically, in samples of dinitrogen pentoxide there is a distinct transition to an ionic $\text{NO}_2^+\text{NO}_3^-$ form around 120 K. When only small amounts of water ($\sim 0.2:1$) are present, a further reaction to form nitric acid occurs only with delay, after a complete conversion into the ionic form. When enough water is present ($>3:1$) the nitric acid produced in the first step after some delay reacts further with water to form NAM. In samples containing a large excess of water ($>7:1$) almost no conversion of the pentoxide into an ionic form takes place. The covalent form persists up to about 150 K, where it reacts directly with H_2O first to yield nitric acid dihydrate and, in a second reaction step, finally to trihydrate.

*Permanent address: Institute of Fluid-Flow Machinery, Polish Academy of Sciences, J. Fiszerza 14, 80-231 Gdańsk, Poland

*E-mail: bondybey@uci.edu

¹R. Teranishi and J. C. Decius, *J. Chem. Phys.* **22**, 896 (1954).

²E. Grison, K. Eriks, and J. L. de Vries, *Acta Crystallogr.* **3**, 290 (1950).

³S. Solomon, R. R. Garcia, F. S. Rowland, and D. J. Wuebbles, *Nature (London)* **321**, 755 (1986).

⁴M. Molina, T. L. Tsao, L. T. Molina, and F. C. Y. Wang, *Science* **238**, 1253 (1987).

⁵S. Solomon, *Nature (London)* **347**, 347 (1990).

⁶M. A. Tolbert, *Science* **264**, 527 (1994).

⁷A. G. Russell, G. J. McRae, and G. R. Cass, *Atmos. Environ.* **19**, 893 (1985).

⁸T. F. Mentel, D. Bleilebens, and A. Wahner, *Atmos. Environ.* **30**, 4007 (1996).

⁹C. R. Webster, R. D. May, R. Toumi, and R. Pyle, *J. Geophys. Res.* **95**, 13851 (1990).

¹⁰F. J. Dentener and P. J. Crutzen, *J. Geophys. Res.* **98**, 7949 (1993).

¹¹M. T. Leu, *Geophys. Res. Lett.* **15**, 851 (1988).

- ¹²D. R. Hanson and A. R. Ravishankara, *J. Geophys. Res.* **96**, 5081 (1991).
- ¹³M. A. Quinlan, C. M. Reihls, D. M. Golden, and M. A. Tolbert, *J. Phys. Chem.* **94**, 3255 (1990).
- ¹⁴J. P. McNamara and I. H. Hillier, *J. Phys. Chem.* **104**, 5307 (2000).
- ¹⁵G. Ritzhaupt and J. P. Devlin, *J. Phys. Chem.* **95**, 90 (1991).
- ¹⁶B. G. Koehler, A. M. Middlebrook, and M. A. Tolbert, *J. Geophys. Res.* **97**, 8065 (1992).
- ¹⁷N. Barton, B. Rowland, and J. P. Devlin, *J. Phys. Chem.* **97**, 5848 (1993).
- ¹⁸R. H. Smith, M. T. Leu, and L. F. Keyser, *J. Phys. Chem.* **95**, 5924 (1991).
- ¹⁹A. B. Horn, T. Koch, M. A. Chesters, M. R. S. McCoustra, and J. R. Sodeau, *J. Phys. Chem.* **98**, 946 (1994).

This article was published in English in the original Russian journal. Reproduced here with stylistic changes by AIP.

Weak ferromagnetism in the antiferromagnetic magnetoelectric crystal LiCoPO_4

N. F. Kharchenko and Yu. N. Kharchenko*

B. Verkin Institute for Low Temperature Physics and Engineering, National Academy of Sciences of Ukraine, pr. Lenina 47, 61103 Kharkov, Ukraine

R. Szymczak and M. Baran

Institute of Physics, Polish Academy of Sciences, Al. Lotnikow 32/46, PL-02-668 Warsaw, Poland

H. Schmid

University of Geneva, Department of Inorganic, Analytical and Applied Chemistry, CJ-1211 Geneva 4, Switzerland

(Submitted August 3, 2001)

Fiz. Nizk. Temp. **27**, 1208–1213 (September–October 2001)

A study of the magnetization of the antiferromagnetic magnetoelectric crystal LiCoPO_4 as a function of temperature and the strength of a magnetic field oriented along the antiferromagnetic vector reveals features due to the presence of a weak ferromagnetic moment. The value of the magnetic moment along the **b** axis at 15 K is approximately 0.12 G. The existence of a ferromagnetic moment can account for the anomalous behavior of the magnetoelectric effect observed previously in this crystal. © 2001 American Institute of Physics.
[DOI: 10.1063/1.1414584]

Cobalt lithium orthophosphate is a well-known magnetoelectric crystal of the family of orthorhombic antiferromagnets with the olivine structure and having the general formula LiMPO_4 (where $M = \text{Fe}^{2+}, \text{Mn}^{2+}, \text{Co}^{2+}, \text{Ni}^{2+}$). It has been attracting attention because it has large values of the constants α_{xy} and α_{yx} of the linear magnetoelectric effect^{1,2} and unusual and as yet unexplained behavior of the magnetoelectric effect in a magnetic field.^{2–4} The magnetoelectric effect in this crystal is the largest among the compounds of 3d elements. The crystal structure of LiCoPO_4 , like that of the other lithium phosphates of transition elements of the olivine family, has a symmetry described by the space group $Pnma$ (D_{2h}^{16}) (Refs. 5,6). In this structure the unit cell ($a = 10.20 \text{ \AA}$, $b = 5.92 \text{ \AA}$, $c = 4.70 \text{ \AA}$) contains four formula units, and the magnetic ions are crystallographically equivalent and occupy four *c* positions. According to the results of neutron-diffraction studies⁷ carried out on polycrystalline samples of LiCoPO_4 , upon antiferromagnetic ordering ($T_N = 21.9 \text{ K}$)² the number of formula units in the unit cell remains unchanged ($z = 4$), and the magnetic moments of the Co^{2+} ions are collinear and directed along the **b** axis, completely compensating each other. The magnetic structure of the crystal is described in a collinear four-sublattice model with the Shubnikov symmetry group Sh_{62}^{445} ($Pnma'$) (Ref. 7).

In studying the magnetoelectric effect in LiCoPO_4 , it was found^{2,3} that for preparation of a homogeneous (single-domain) antiferromagnetic state of the crystal, as must be done in order to measure the magnetoelectric effect, it is sufficient to decrease the temperature of the sample from $T > T_N$ to $T < T_N$ in a magnetic field **H** oriented along the **B** axis, or to apply a sufficiently strong magnetic field along the **b** axis at temperatures $T < T_N$. This is atypical for all of the compensated antiferromagnetic magnetoelectric crystals that

have been studied, for which it is necessary to apply magnetic and electric fields simultaneously in order to prepare a single-domain state. The behavior of the magnetoelectric effect observed by the authors of Refs. 1–3 could be due to the existence of a weak ferromagnetic moment in the crystal. However, previous studies of the magnetic properties of both polycrystalline^{7,8} and single-crystal⁹ LiCoPO_4 have not detected weak ferromagnetism.

The creation of a homogeneous magnetic state in a compensated antiferromagnet in the presence of only a magnetic field may also be caused by quadratic (in the field) magnetization effect.¹⁰ In this case the magnetic field induces in the crystal a magnetic moment that is even with respect to the field strength. In antiferromagnetic (AFM) states with oppositely directed sublattice moments, oppositely directed magnetic moments will be induced. Therefore, when a magnetic field is applied in a certain direction, the energy of the collinear antiferromagnetic domains will be different. When the difference of the energies of the antiferromagnetic domains, which varies in proportion to H^3 , reaches a threshold value determined by the coercivity of the antiferromagnetic domain wall, the crystal will go to a single-domain state or a magnetization reversal of its antiferromagnetic state will occur.¹¹ A quadratic magnetization effect is allowed by symmetry only in AFM crystals which are not symmetric with respect to the operation of anti-inversion (or complete inversion): $\bar{1}' = \bar{1} \cdot 1'$. However, the group mmm' that has been established for LiCoPO_4 , although it does not contain the operation of spatial inversion, does have a center of anti-inversion. Consequently, the quadratic magnetization and weak ferromagnetic moment (WFM) should be forbidden in LiCoPO_4 .

Magneto-optic studies¹² of LiCoPO_4 have revealed new features of the behavior of this antiferromagnetic crystal in a

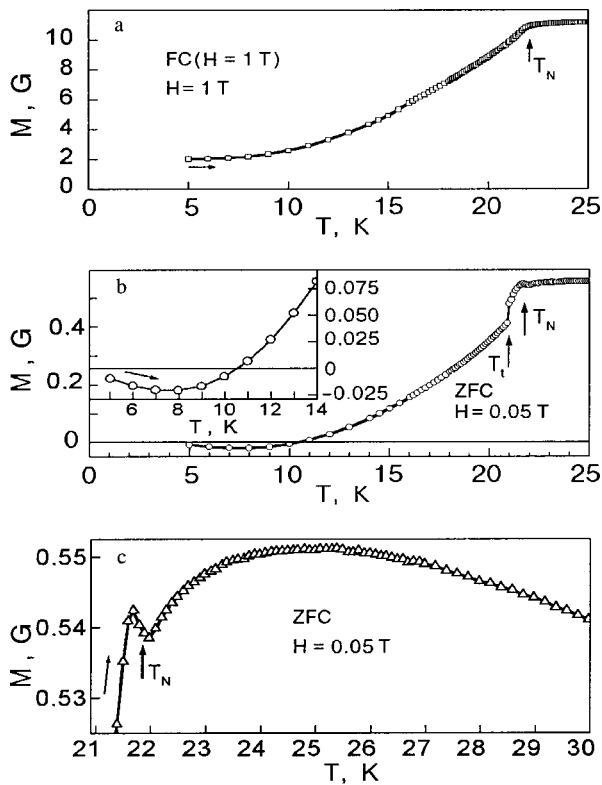


FIG. 1. Temperature dependence of the magnetization of the LiCoPO₄ crystal in an external magnetic field $\mathbf{H}\parallel\mathbf{b}$ with a field strength of 1 T (a) and 0.05 T (b); the $M(T)$ curves near the Néel temperature at $H=0.05$ T (c). FC ($H=1$ T) — the value of the magnetic field in which the sample was cooled.

magnetic fields. It was found that the birefringence of linearly polarized light induced by a magnetic field $\mathbf{H}\parallel\mathbf{b}$ is comparable to the spontaneous magnetic linear birefringence at a value of the external field much smaller than the value of the effective exchange field. This property suggests the presence of transverse projections of the magnetic moments in the crystal and, hence, a noncollinear magnetic structure in it.

Given this situation, it is advisable to make highly sensitive measurements of the magnetization of the LiCoPO₄ crystal. In this paper we report the results of measurements of the magnetization M as a function of temperature and magnetic field strength. All of the measurements were made with a SQUID magnetometer (Quantum Design MPMS-5). The sample studied had a mass of 7.46 mg and was in the form a parallelepiped with dimensions of $0.96\times 1.22\times 1.76$ mm.

The experimental results are presented in Figs. 1–3. Figure 1 shows the curves of the temperature dependence of the magnetization obtained in magnetic fields H of 1.0 and 0.05 T. The behavior of the magnetization in the 1.0 T field is similar to that which was observed previously in Ref. 9 at $H=1.2$ T. The temperature dependence of M is similar to the typical behavior for 2D antiferromagnets in which the interaction between magnetic ions in the plane is dominant over the interaction between ions belonging to neighboring planes.¹³ For $M(T)$ there is a broad hump, the top of which lies above T_N (at $T\sim 25$ K).

In the 0.05 T field the $M(T)$ curves is qualitatively different from that discussed above. It clearly displays the following features.

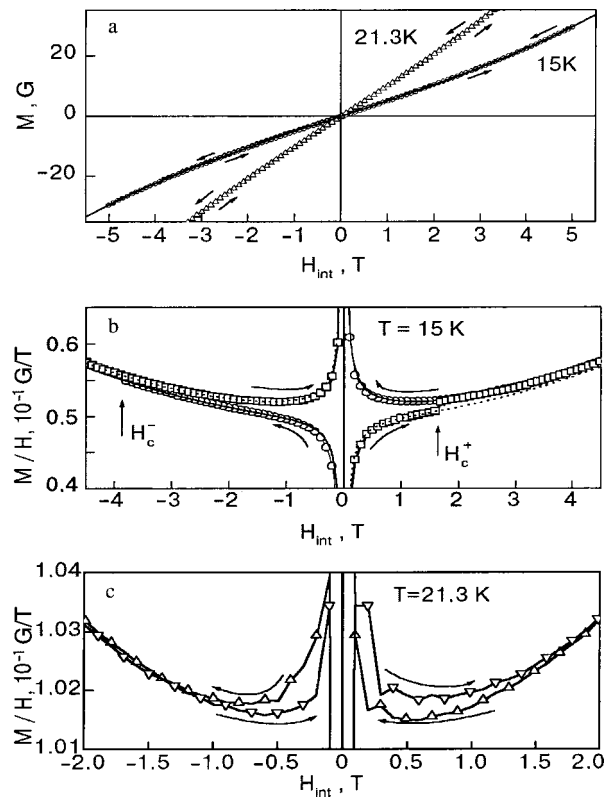


FIG. 2. Magnetization of the LiCoPO₄ crystal as a function of the internal magnetic field H_{int} in an external magnetic field $\mathbf{H}\parallel\mathbf{b}$ (a); the $M(H)/H$ curves at crystal temperatures of 15 K (b) and 21.3 K (c).

a) In the temperature interval 5–10.5 K the projection of the magnetic moment of the sample on the magnetic field direction is negative. With increasing temperature its absolute value initially increases and then, at $T>8$ K, decreases to zero, changes sign, and increases monotonically with temperature out to the neighborhood of T_t (see Fig. 1b and 1c).

b) At a temperature $T_t=20.9$ K there is a jump in the magnetization (occurring in a single interval between experimental points, which in this part of the curve is 0.1 K).

c) Near the Néel temperature at 21.6 K (see Fig. 1c) a weak but clearly registered peak is observed. The increase of the magnetization with further increase in temperature only at $T>T_N$.

All of these anomalies can be explained by assuming that the sample in the initial state had a ferromagnetic moment directed oppositely to the direction of the applied magnetic field. Thus the sample was initially cooled in “zero” field (ZFC) and then a field $H=0.05$ T, in which the measurements were made, was applied. The residual field of the superconducting solenoid can be as high as 0.002 T. The direction of that field could accidentally be directed opposite to the direction of the applied magnetic field in the $M(T)$ measurement. It follows from the trend of the $M(T)$ curve that the orientation of the spontaneous moment, directed opposite to the field, persists to a temperature T_t , at which the “switching” of the antiferromagnetic state of the sample occurred. In a narrow temperature interval 21–21.9 K the spontaneous moment is directed along the field. When the temperature approaches T_N the spontaneous moment rapidly decreases to zero, and a peak appears on the $M(T)$ curve (see Fig. 1d).

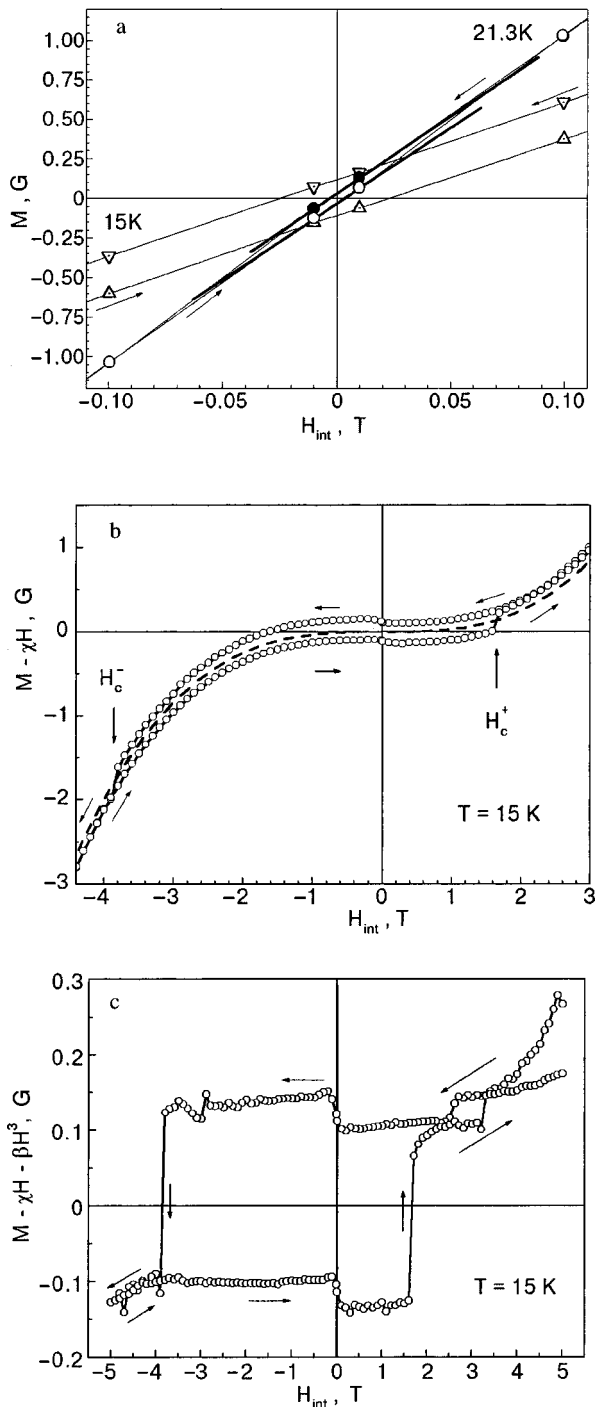


FIG. 3. Hysteresis of the magnetization in the LiCoPO₄ crystal: the $M(H)$ curve in the neighborhood of zero field at temperatures of 15 and 21.3 K (a); the $M(H)$ curve after subtraction of the linear contribution χH ; the dashed curve shows a dependence of the type βH^3 (b); the $M(H)$ curve after subtraction of the linear and cubic contributions: $M(H) - (\chi H + \beta H^3)$ (c).

Further confirmation of the presence of a weak ferromagnet moment in the LiCoPO₄ crystal was obtained in a study of the field dependence of the magnetization at different temperatures. Figure 2 shows the $M(T)$ curves obtained at 15 and 21.3 K. The temperature 21.3 K was chosen so as to lie in the narrow temperature interval between the jump and the peak on the $M(T)$ curve for $H = 0.05$ T (see Fig. 1c).

Figure 2a shows the field curves of the magnetization, obtained for a completely cycle of variation of the field from

+5 to -5 T and back to +5 T. The $M(H)$ curves are well approximated by the function $M(H) = M_s \chi + H + \beta H^3$. This function is shown by the solid curve in Fig. 2a for $T = 15$ K. The presence of a nonzero spontaneous moment M_s is demonstrated by the $M(H)/H$ curves in Figs. 2b, 2c. The position of the experimental points obtained at $T = 15$ K are well described by the function $\chi + \beta H^2 + M_s/H$, where $M_s = \pm 0.12$ G, $\chi = 5.06$ G/T, and $\beta = 3.2 \times 10^{-2}$ G/T³. They are shown by the solid and dotted curves in Fig. 2.

Because of the nonzero value of M_s , as H goes to zero the quantity $M(H)/H = \chi + \beta H^2 + M_s/H$ increases by a hyperbolic law, M_s/H changes sign when the direction of the field is switched, and then it decreases by the same law. One can see that when the field reaches certain threshold values ($H_c^+ = +1.7$ T and $H_c^- = -3.8$ T) a jumplike transition of the experimental points from one branch of the $M(H)/H$ curve to the other occurs. The $M(H)/H$ curve obtained at 21.3 K differs from that described above in that the sign of $M(H)/H$ in the field interval from 5 to 0.1 T is always positive. Only in the field interval from -0.1 to 0.1 T is the behavior of $M(H)/H$ at 21.3 K sign-varying and similar to that observed at 15 K in a wider field interval. This means that at that temperature the spontaneous moment M_s can be directed counter to the field only in a narrow field interval.

The hysteresis of the magnetization of the sample is more clearly demonstrated in Fig. 3. In Fig. 3a the part of the curve shown in Fig. 2a is shown in an enlarged scale in the field interval from -0.1 to +0.1 T. It is seen that a linear extrapolation of $M(H)$ to $H = 0$ near zero gives a nonzero spontaneous magnetization for both temperatures. The field dependence of that part of the magnetic moment of the sample which is not due to a simple field-independent susceptibility, i.e., $M(H) - \chi(H)$, is shown in Fig. 3b. The hysteresis loop is seen against the background of a cubic dependence. It is even more clearly seen after subtraction of the cubic contribution βH^3 (Fig. 3c). The revealed hysteresis of the magnetization convincingly attests to the presence of a weak spontaneous magnetic moment in the sample. Its value, determined as $M_s = (M_s^+ - M_s^-)/2$, is 0.12 G at 15 K and around 0.015 G at 21.3 K.

Other features can also be seen in Fig. 3c. The most intriguing of them is the change in magnetization in the field interval from -0.1 T to +0.1 T, which has a diamagnetic character. Such behavior of the sample is unusual. It brings to mind “superdiamagnetism,”^{14,15} which is allowed by symmetry in this antiferromagnetic magnetoelectric crystal, where the symmetry of the leading magnetic ordering admits the existence of a toroidal moment.⁴ In the presence of a density gradient of the toroidal moment (e.g., near defects of the crystal) it is possible to have a diamagnetic response of the system to a magnetic field.¹⁵ However, before drawing any conclusions about the causes of the observed feature it is necessary to carry out special experiments and to eliminate possible artifacts.

As to the causes of the weak ferromagnetism (or, more precisely, weak ferrimagnetism), there are several possible mechanisms for its appearance in the LiCoPO₄ crystal. Using the well-known methods of constructing invariants of the thermodynamic potential,¹⁶ one can see that although the usual second-order weak-ferromagnetic invariants of the type

$M_i L_{2y}$ are forbidden in LiCoPO_4 , the $Pnma$ symmetry of the crystal allows fourth-order invariants containing the product $M_y L_{2y}$.

These invariants are the following: $M_y L_{2y} L_{1y} L_{3y}$, $M_y L_{2y} L_{1x} L_{3x}$, $M_y L_{2y} L_{1z} L_{3z}$, $M_y L_{2y} L_{1x} L_{2z}$, $M_y L_{2y} L_{1z} L_{2x}$, $M_y M_z L_{2y} L_{2z}$, $M_y M_z L_{2y} L_{3x}$, $M_y M_x L_{2y} L_{2x}$, and $M_y M_z L_{2y} L_{3z}$. In addition, “gradient” invariants are allowed, which can lead to the formation of a modulated magnetic structure. Among them we mention the second-order invariant $(M_y dL_{2y}/dx - L_{2y} dM_y/dx)$.⁴ Since the projection of the antiferromagnetic vector L_{2y} transforms in the same way as the projection of the toroidal moment T_z (Ref. 4), the corresponding homogeneous and inhomogeneous invariants with a toroidal moment are also possible. At the present time it is not possible to answer the question of which mechanism gives rise to the weak ferromagnetism in LiCoPO_4 . We can only say that the nonmonotonic behavior of the spontaneous magnetic moment on heating of the sample, which is attested to by the behavior of the magnetization of the crystal in a field of 0.05 T, indicates the presence of competing mechanisms. A similar dependence of the weak-ferromagnetic moment has been observed in crystals of antiferromagnetic vanadates, in particular, yttrium vanadate.¹⁷ It must also be noted that the features of the behavior of the magnetic linear birefringence in a cyclically varying magnetic field¹² implies that LiCoPO_4 must have an incommensurate modulated structure, if not spontaneous then magnetic-field induced. Depending on the mechanism giving rise to the weak ferromagnetism, the magnetic point group of the crystal may be one of the following noncentrosymmetric groups: $m(\perp y)$ (this group admits a “longitudinal” weak-ferromagnetic structure $M_y L_{2y} L_{1y} L_{3y}$); $2'(\parallel x)$ (which admits the structures $M_y L_{2y} L_{1x} L_{2z}$, $M_y L_{2y} L_{1x} L_{3x}$, $M_y M_z L_{2y} L_{2z}$, and $M_y M_z L_{2y} L_{3x}$), $m'(\perp z)$ (which admits the structures $M_y L_{2y} L_{1z} L_{3z}$, $M_y L_{2y} L_{1z} L_{2x}$, $M_y M_x L_{2y} L_{2x}$, and $M_y M_z L_{2y} L_{3z}$).

The presence of a quadratic magnetization effect in the LiCoPO_4 crystal for $\mathbf{H} \parallel \mathbf{b}$ remains open question. Although

an approximation of the $M(H)$ curves by third-order polynomials does give corrections quadratic in H which have different signs for the two antiferromagnetic states, they are too small. Their small value and substantial difference leaves uncertainty as to whether they correspond to a physical effect or are the result of a small systematic error and scattering in the experimental data.

The authors thank V. I. Fomin and V. I. Kut'ko for a helpful discussion of the results.

*E-mail: kharchenko@ilt.kharkov.ua

-
- ¹M. Marcier, J. Gareyte, and E. F. Bertaut, C. R. Acad. Sci. Paris B **264**, 979 (1967).
²J.-P. Rivera, Ferroelectrics **161**, 147 (1994).
³H. Wiegmann, *Magnetolectric Effects in Strong Magnetic Fields*, PhD Thesis, University of Konstanz, Konstanz Dissertationen, Vol. 461, Hartung-Gorre, Konstanz (1995).
⁴I. Kornev, M. Bichurin, J.-P. Rivera, S. Gentil, H. Schmid, A. G. Jansen, and P. Wyder, Phys. Rev. B **62**, 12247 (2000).
⁵R. E. Newham and M. J. Redman, J. Am. Ceram. Soc. **48**, 547 (1965).
⁶F. Kubel, Z. Kristallogr. **209**, 755 (1994).
⁷R. P. Santoro, D. J. Segal, and R. E. Newham, J. Phys. Chem. Solids **27**, 1192 (1966).
⁸A. Goni, L. Lezama, G. E. Barberis, J. L. Pizzarro, M. I. Arriortua, and T. Rojo, J. Magn. Magn. Mater. **164**, 251 (1996).
⁹J.-P. Rivera and J. Korean, Phys. Soc. **32**, S1855 (1998).
¹⁰G. Gorodetsky and D. Treves, Phys. Rev. A **135**, 97 (1964); G. Gorodetsky, B. Sharon, and S. Shtrikman, Solid State Commun. **5**, 739 (1967).
¹¹A. V. Bibik, N. F. Kharchenko, and S. V. Petrov, Fiz. Nizk. Temp. **15**, 1280 (1989) [Sov. Phys. JETP **15**, 707 (1989)]; N. F. Kharchenko, R. Szymczak, and M. Baran, J. Magn. Magn. Mater. **140**, 161 (1995).
¹²M. F. Kharchenko, O. V. Miloslavskaya, Yu. M. Kharchenko, H. Schmid, and J.-P. Rivera, Ukr. J. Phys. Opt. **1**, 16 (2000).
¹³M. F. Sykes and M. E. Fisher, Physica **28**, 919 (1962).
¹⁴V. L. Ginzburg, A. A. Gorbatevich, Yu. V. Kopayev, and B. A. Volkov, Solid State Commun. **50**, 339 (1984).
¹⁵A. A. Gorbatevich and Yu. V. Kopayev, Ferroelectrics **161**, 321 (1994).
¹⁶E. A. Turov, *Physical Properties of Magnetically Ordered Crystals* [in Russian], Izd. Akad. Nauk SSSR, Moscow (1963).
¹⁷Y. Ren, T. T. M. Palstra, D. I. Khomskii, and G. A. Sawatsky, Phys. Rev. B **62**, 6577 (2000).

Translated by Steve Torstveit

Orthogonal-to-unitary ensemble crossover in the electronic specific heat of metal nanoclusters

S. I. Mukhin* and O. V. Kurapova

Theoretical Physics Department, Moscow Institute for Steel and Alloys, Moscow, Russia

I. I. Moiseev and M. N. Vargaftik

N. S. Kurnakov Institute of General and Inorganic Chemistry, Russian Academy of Sciences, Moscow, Russia

Y. E. Volokitin, F. L. Mettes, and L. J. de Jongh

*Kamerlingh Onnes Laboratory, Leiden University, Leiden, The Netherlands***

(Submitted August 27, 2001)

Fiz. Nizk. Temp. **27**, 1214–1220 (September–October 2001)

We present a theoretical and experimental study on the influence of a magnetic field on the energy-level statistics in metal nanoparticles. Based on the random-matrix theory, a gradual field-induced crossover behavior is predicted from the orthogonal to the unitary ensemble. Experimental data of the electronic specific heat of metal nanoparticles for different field in the quantum size temperature regime compare favorably with these theoretical (analytical) predictions. © 2001 American Institute of Physics. [DOI: 10.1063/1.1415943]

1. INTRODUCTION

A large number of papers have been devoted to the experimental and theoretical investigation of the thermodynamic properties of small metal particles (nanoclusters). In order to test the predictions based on the random-matrix theory of the energy-level statistics (for reviews see Refs. 1–4). The discrete character of the energy spectrum of a nanocluster can be regarded as a direct manifestation of the quantum size effect. The Wigner–Dyson^{5,6} random ensemble description relies upon the functional $\mathcal{A}(\mathcal{H})$:

$$\mathcal{A}(\mathcal{H}) \propto \exp[-v \text{Tr}v(\mathcal{H})]. \tag{1}$$

This functional is chosen to describe the probability distribution for the random ensemble of $N \times N$ Hamiltonian matrices of the electrons in the nanoclusters. An ensemble is called Gaussian if $v(\mathcal{H}) \propto \mathcal{H}^2$. This distribution is successfully used in the absence of strong electron-electron correlations.^{1,2} In the Gaussian distribution the argument of the exponential becomes a simple sum over all the matrix elements: $\text{Tr} \mathcal{H}^2 = \sum_{ij} |H_{ij}|^2 = \sum_i E_i^2$, so that it does not contribute to the correlations between the levels $\{E_i\}$, because the probabilities for the different E_j 's factorize:

$$\mathcal{A}(\mathcal{H}) \propto \exp[-v \text{Tr} \mathcal{H}^2] \propto \prod_i \exp[-v E_i^2] = P(\{E_n\}). \tag{2}$$

Therefore, the spectral correlations in the Gaussian ensemble are of a purely geometrical nature,¹ since they follow solely from the Jacobian $J(\{E_n\})$:³

$$J(\{E_n\}) = \prod_{i < j} |E_i - E_j|^v. \tag{3}$$

The term “geometrical” used above is based on the fact that the Jacobian relates volumes in the two equivalent abstract spaces of the random variables, thus reflecting their geometrical structure:

$$\mathcal{A}(\mathcal{H}) d\mu(\mathcal{H}) = d\mu(U) \left(P(\{E_n\}) J(\{E_n\}) \prod_i dE_i \right). \tag{4}$$

Here the volume element $d\mu(\mathcal{H})$ is the “natural” volume measured in the space of the Hermitian matrix elements \mathcal{H}_{ij} , which factorizes into the product $d\mu(U) \prod_i dE_i$ of the volume elements $d\mu(U)$ and $\prod_i dE_i$ in the subspaces of the eigenvectors and eigenvalues of the matrix \mathcal{H} . As is apparent from Eq. (3) and (4), the character of the statistical distribution of the level-spacings depends only on the index v ,⁷ which counts the number of degrees of freedom in the matrix elements \mathcal{H}_{ij} . This number reflects the symmetry of the system in question and can only take the values 1, 2 or 4 for the real, complex or real quaternion matrix elements, respectively. The matrix elements may be chosen real when time-reversal symmetry exists, while they become imaginary when this symmetry is broken, e.g., by an external magnetic field or magnetic impurities. In time-reversal symmetric systems with broken spin-rotation symmetry, e.g., as a consequence of spin-orbit interaction, the matrix elements are real quaternions. The details of the interactions inside the system do not change these general symmetries, and hence, the spectral correlations possess universality. The corresponding Gaussian ensembles of random matrices, depending on their symmetry, are called orthogonal ($v=1$), unitary ($v=2$) or symplectic ($v=4$) ensembles respectively, or in the abbreviated form: GOE, GUE or GSE. Thus, the symmetry of the Hamiltonian matrices of the clusters changes either from GOE to GUE, or from GSE to GUE upon application of an external magnetic field. We remark that the consequences of random perturbations on the energy level spectra of an as-

sembly of small metal particles and the ensuing thermodynamic properties were first investigated by Kubo,⁸ using the Poisson distribution for the energy level statistics. Shortly afterwards, Gor'kov and Eliashberg⁹ pointed out the relevance of the Wigner–Dyson formalism for small metal particles and demonstrated the profound influence of the level repulsion on the low-temperature thermodynamics of the small metal particles in the two limiting cases of GOE and GUE. A more detailed consideration of the metal-cluster thermodynamics in these two limits was later made in.¹⁰ Theoretical justification of the Wigner–Dyson statistics was provided in¹¹ for the case of diffusive (nonballistic chaotic) electron motion inside the cluster. The most recent theoretical achievements, which include justification of the Wigner–Dyson statistics for the nonintegrable chaotic systems, “ballistic billiards,” with random scattering at the boundaries, and summarized in.¹

In this note we present a preliminary report on detailed theoretical predictions,¹² together with a comparison to recently obtained experimental data,^{13–15} for the specific heat behavior of metal nanoclusters in the crossover regime induced by an external magnetic field. The crossover manifests itself as a gradual transition from the orthogonal to unitary Gaussian distribution of the electronic energy levels (GOE-to-GUE transition) of the nanoclusters. We remark that these measurements represent the first experimental observation of the presence of the quantum-size effect in the electronic specific heat and susceptibility of metal nanoparticles.

Mathematically, the basic change resulting from the GOE-to-GUE crossover lies in the appearance of the (random) imaginary part of the electron Hamiltonian matrix due to the breaking of the time-reversal symmetry by the external magnetic field. This phenomenon was modeled by Pandey and Mehta¹⁶ by the addition of a random antisymmetric real matrix A with imaginary weight $i\alpha$ to the real symmetric Hamiltonian matrix \mathcal{H}_0 :

$$\mathcal{H} = \mathcal{H}_0 + i\alpha A. \quad (5)$$

The parameter α is proportional to the magnetic flux Φ through the system, i.e., through the nanoparticle, so that the relation between α and Φ depends on the geometry of the particle and on the ratio of its size (radius R) to the electron mean free path l . For a ballistic sphere ($R \ll l$) with diffuse boundary scattering of electrons this relation is²

$$N\alpha^2 = \left(\frac{e\Phi}{h}\right)^2 \frac{\hbar v_F}{R\delta} \frac{8\pi}{45}, \quad (6)$$

where v_F is the Fermi velocity, δ is the mean level spacing at the Fermi energy of the nanoparticle, and N is the matrix dimension indicating the total number of the single-electron states taken into account in the model of the nanoparticle. The addition of an independently randomly distributed matrix A to the (random) real symmetric matrix \mathcal{H}_0 , effectively doubles the number of degrees of freedom in the elements of the Hamiltonian matrix \mathcal{H} , so that the Gaussian distribution of \mathcal{H} takes the form

$$\mathcal{P}(\mathcal{H}) \propto \exp\left(-\sum_{i,j} \frac{\mathcal{H}_{0ij}^2}{4v^2} + \frac{A_{ij}^2}{4v^2}\right). \quad (7)$$

Here the variance v^2 determines the mean level spacing $\delta = \pi v / \sqrt{N}$ in the vicinity of the Fermi energy of the cluster in the limit $N \gg 1$ and $\alpha \ll 1$. As was explained above, the doubling of the dimensionality of the phase-space of the off-diagonal matrix elements leads¹⁶ in turn to the doubling of the exponent v in the eigenvalue (level) distribution function $P(\{E_n\})$, from $v = 1$ in GOE to $v = 2$ in GUE:

$$\begin{aligned} P_{\text{GOE}}(\{E_n\}) J_{\text{GOE}}(\{E_n\}) &\propto \prod_{i < j} |E_i - E_j| \prod_k \\ &\times \exp[E_k^2] \rightarrow \prod_{i < j} |E_i - E_j|^2 \prod_k \\ &\times \exp[-2E_k^2] \propto P_{\text{GUE}}(\{E_n\}) J_{\text{GUE}}(\{E_n\}). \end{aligned} \quad (8)$$

The subtle feature of this crossover is that the doubling of v is actually energy-dependent.² The GOE-to-GUE transition is completed on the energy scale E if $|\delta E_i| \geq E$, where δE_i is the energy shift due to the “perturbation” $i\alpha A$ in the Hamiltonian (5):

$$\delta E_i = \alpha^2 \sum_{i \neq j} \frac{A_{ij}^2}{E_i - E_j}. \quad (9)$$

Simultaneously, the “high-energy” part of the spectrum on the scale $E \gg \delta E_i$ remains distributed according to the upper line of Eq. (8) with $v = 1$, as it would be in the case of an orthogonal ensemble. Therefore, measuring the thermodynamic properties of the nanoparticles in the external magnetic field may give an experimental verification of the relation (8) and of the gradual nature of the GOE-to-GUE transition, provided that these properties depend on the different energy scales at the different temperatures.

On basis of the above discussion we expect the specific heat of the nanoclusters to be a relevant thermodynamic characteristic for the observation of the GOE-to-GUE crossover in magnetic field. In order to investigate this problem quantitatively, we consider an ensemble of metal particles with half of the clusters having an even number of electrons and the other half having an odd number. Our calculation was done¹² in the low temperature limit, $T \ll \delta$, so that only a few electronic levels need to be explicitly considered. Taking into account all the different possibilities of the formation of the lowest excited energy states, one finds the following expressions for the low-temperature partition functions of the even and odd clusters, Z_{even} and Z_{odd} respectively:

$$Z_{\text{even}} = (1 + 2e^{-\beta\delta} \cosh(h\beta))(1 + 2e^{-\beta\delta}) + O(e^{-2\beta\delta}), \quad (10)$$

$$Z_{\text{odd}} = 2 \cosh(h\beta/2)(1 + 2e^{-\beta\delta}) + O(e^{-2\beta\delta}), \quad (11)$$

where $\beta = 1/T$ is the inverse temperature in energy units, i.e., taking $k_B = 1$. Also $h = g\mu_B H$, where μ_B is the Bohr magneton, $g = 2$ is the Landé factor, and H is the external magnetic field.

Using Eqs. (10) and (11) we have for the free energy F

$$F = -\frac{1}{2} T (\ln Z_{\text{even}} + \ln Z_{\text{odd}}), \quad (12)$$

where the coefficient 1/2 represents the fifty/fifty probability to find an even/odd cluster in the macroscopically large assembly of otherwise identical metal particles.

The specific heat C_V , magnetization M , and magnetic susceptibility χ can be derived from the well-known relations

$$C_V = -T \frac{\partial^2 F}{\partial T^2}, \quad M = -\frac{\partial F}{\partial H}, \quad \chi = -\frac{\partial^2 F}{\partial H^2}. \quad (13)$$

In the simplest equidistant model for a metal nanoparticle, due to Fröhlich,¹⁷ in which all the levels are at a constant interlevel spacing δ , these thermodynamic functions are given by the formulas:

$$C_V = \frac{1}{8} (h\beta)^2 \frac{1}{\cosh^2(h\beta/2)} + 2(\delta\beta)^2 \frac{e^{-\delta\beta}}{(1+2e^{-\delta\beta})^2} + \frac{1}{2} \beta^2 \frac{4h^2 e^{-2\delta\beta} + (h-\delta)^2 e^{\beta(h-\delta)} + (h+\delta)^2 e^{-\beta(h+\delta)}}{(1+2e^{-\delta\beta} \cosh(h\beta))^2}, \quad (14)$$

$$M = g\mu_B \left[\frac{1}{4} \tanh(h\beta/2) + \frac{\sinh(h\beta)}{e^{\delta\beta} + 2 \cosh(h\beta)} \right], \quad (15)$$

$$\chi = \beta(g\mu_B)^2 \left[\frac{1}{8 \cosh^2(h\beta/2)} + \frac{2 + e^{\delta\beta} \cosh(h\beta)}{(e^{\delta\beta} + 2 \cosh(h\beta))^2} \right]. \quad (16)$$

It is obvious from the above expressions that in the equidistant model there is effectively a gap in the density of states at the Fermi-level, leading to an exponentially vanishing specific heat at low enough temperatures, i.e., $T \ll \delta$. The opposite extreme to the current model is the Poisson level distribution $P_0(E_i - E_j) \propto \exp[-|E_i - E_j|/\delta]$, corresponding to no gap at all, which was used by Kubo.⁸ Unlike in the distributions (8), the Poisson's distribution entails a finite probability for the two levels to “stick together,” thus neglecting the level repulsion. Hence, the pseudo-gap in the density of states at the Fermi-energy, caused by the off-diagonal random matrix elements between different electronic states in the cluster, disappears in the Poisson model.

2. AVERAGING OVER THE LEVEL DISTRIBUTION IN THE CROSSOVER REGION

Our aim here is to obtain more realistic expressions for the thermodynamic functions of the metal nanoclusters than those given in Eqs. (14), (15), and (16), which were derived for an equidistant model of the energy levels. Actually, for small particles one usually assumes that minor perturbations such as surface irregularities (even of an atomic scale) will be sufficient to make the level distribution random. Here, we will suppose the random distribution to obey the Wigner–Dyson Gaussian ensemble statistics. Indeed, the published experimental data¹⁴ for the temperature dependences of the specific heat of the metal nanoparticles clearly showed the inapplicability of the equal level spacing model, in which case the specific heat becomes exponentially small at the temperatures $T \ll \delta$. Comparison of the experimental curves in¹⁴ with the theory leads to the conclusion that the experimental behavior has to be described by a model based on a

non-vanishing probability of even the smallest level spacings. When these spacings are much less than the average distance between the levels (δ), they will make essential contributions to the specific heat at the lowest temperatures, $T \ll \delta$, so that the energy gap due to the quantum size effect becomes a pseudo-gap. Then, the explicit averaging over the appropriate level distribution is essential to describe the data.

It proved to be possible to perform such an averaging analytically¹² for the case of the low enough temperatures, where only the lowest excited states of the clusters should be important. The approximation used here consists in the averaging of the low-temperature thermodynamic functions $A(\delta, T, H)$, found for the equidistant model, with the two-level correlation function R_2 . For this purpose we substitute an equidistant level spacing δ by a random variable ε and then perform an integration over this variable:

$$\bar{A}(T, H, \delta) = \int_0^\infty R_2\left(\frac{\varepsilon}{\delta}\right) A(\varepsilon, T, H) d\left(\frac{\varepsilon}{\delta}\right). \quad (17)$$

Let the level distribution function $p_n(x)$ define the probability to find a spacing x between two energy levels, while there are n other energy levels being located between those two. Here we normalize the random level spacing ε by the average interlevel spacing δ near the Fermi-level of a cluster: $x = \varepsilon/\delta$. Then, the two-level correlation function is defined as follows:

$$R_2(x) = \sum_0^\infty p_n(x). \quad (18)$$

At small enough $x \ll 1$, we have $R_2(x) \rightarrow p_0(x)$, and in the limit $x \gg 1$, $R_2(x) \rightarrow 1$. From the work of Pandey and Mehta,¹⁶ using also relation Eq. (6) (see Ref. 2), we have an analytical expression for R_2 for an arbitrary external magnetic field H :

$$R_2(x) = 1 - \left(\frac{\sin(\pi x)^2}{\pi x} \right) + \frac{1}{\pi^2} \int_0^\pi k \sin(kx) \times e^{2k^2 \rho^2} dk \int_\pi^\infty \frac{\sin(zx)}{z} e^{-2z^2 \rho^2} dz, \quad (19)$$

where $\rho = 1.15 \mu_B H / \delta$ for a spherical particle and where ballistic electron motion inside the particle is supposed.¹² Then, without magnetic field, $\rho = 0$, $R_2(x \ll 1) \sim x$, while in the strong field limit, $\rho \gg 1/\pi$, $R_2(x \ll 1) \sim x^2$. The probability to find two levels close together, $x \ll 1$, decreases with the field from $\sim x$ to $\sim x^2$. This effect is called the “interlevel repulsion” in a magnetic field and causes a change of the low-temperature dependence of the field-independent contribution to the electronic specific heat (second term on the right hand side (rhs) of Eq. (14)) from $C_{el}^{GOE} \propto T^2$ for GOE ($H = 0$) to $C_{el}^{GUE} \propto T^3$ for GUE ($\mu_B H \gg \delta$).^{9,10} Incidentally, in case of metal nanoparticles with strong spin-orbit coupling (GSE level-statistics), this contribution to specific heat is expected to behave as $C_{el}^{GSE} \propto T^5$ at low enough temperatures.¹⁰ On the other hand, the spin-flip contribution to C_{el} [incorporated in the third term on the rhs of Eq. (14)], after averaging with the function $R_2(x)$, brings T -linear contribution to the electronic specific heat (C_{el}), which masks the crossover in the temperature dependence described above. This later fact,

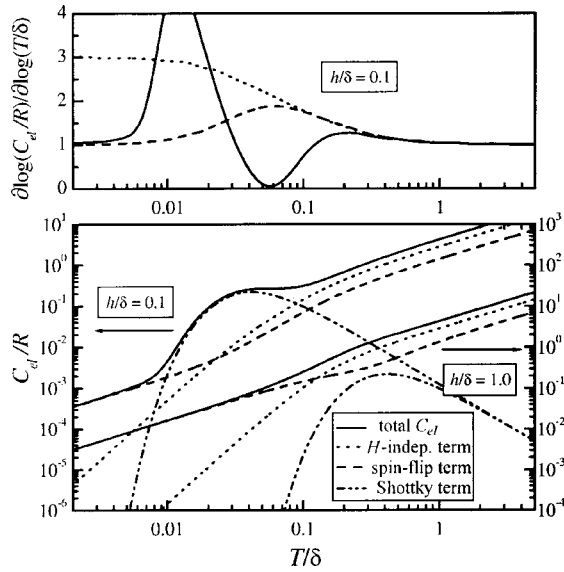


FIG. 1. Calculated temperature dependences of the electronic specific heat C_{el} and its different constituents (lower panel), and of their logarithmic derivatives (upper panel, for $h/\delta=0.1$ only) for a random Gaussian ensemble of metal clusters at two different values of the external magnetic field H (in units $g\mu_B H/\delta$). The temperature is expressed in units T/δ (putting $k_B=1$).

as far as we know, was not considered in the previous works, see.^{9,10} Below we present the calculated dependences of C_V on the temperature and the external magnetic field H and compare them with the recently obtained experimental results.

3. DISCUSSION

As a main result to be concluded from the calculated dependences shown in Fig. 1, we point out that the GOE-to-GUE transition in magnetic field has a gradual crossover character. The underlying reason is that the distribution of the level spacings on the “small energy scale,” $\varepsilon/h \ll 1$, obeys GUE statistics already at small fields $h/\delta \ll 1$, while the level spacings for large energy, $\varepsilon/h \gg 1$ remain distributed according to GOE until the field becomes strong enough, i.e., $h/\delta \gg 1$. Thus, in small fields, $h/\delta \ll 1$, the temperature dependence of the specific heat may be separated into three different regions. In the lowest temperature region, $T \ll h \ll \delta$, the electronic specific heat C_{el} contains the unitary ensemble part: $C_{el}^{GUE}(T) \propto T^\alpha$, with $\alpha=3$, together with the spin-flip contribution: $C_{el}^{sf}(T) \propto TR_2(h/\delta)$. In the intermediate temperature interval, $h \ll T \ll \delta$, the temperature dependence remains the same as in the orthogonal ensemble, i.e., with $\alpha=2$: $C_{el}(T) \propto T^2$, because the spin-flip contribution in this case merely changes the numerical prefactor in front of T^2 . Finally, in the “high temperature” region, $T \gg \delta$, the temperature dependence of the electronic specific heat follows the usual Fermi-liquid bulk behavior: $C_{el}(T) \propto T$. Different characteristic regions are clearly seen in Fig. 1, where the contributions to specific heat are plotted separately for the two different magnetic field values as functions of the temperature in units of the average level spacing δ . As can be seen in Fig. 1, in the weakest field, $h=0.1\delta$, the Schottky contribution due to the odd clusters masks the $C_{el}^{GUE}(T) \propto T^3$ term within a substantial part of the low temperature

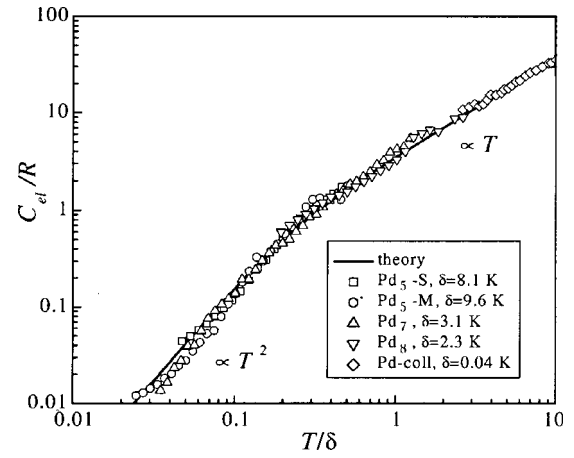


FIG. 2. Electronic specific heat (in zero field) of the metal nanoclusters discussed in the text. Data were scaled on the theoretical prediction (solid curve) with the average energy level spacing δ as the adjustable parameters. The transition from bulk-like behavior ($\propto T$) to quantum-size behavior ($\propto T^2$) can be clearly seen.

interval, while the crossover from $\alpha=3$ via $\alpha=2$ to $\alpha=1$ in the higher temperature region is quite pronounced in the upper panel of Fig. 1. In the higher magnetic field $h=1\delta$ the Schottky peak had moved to higher temperatures where it is superimposed on the much larger even cluster contribution to the specific heat and so it does not mask substantially the T^3 term in the total C_{el} as in the weakest field case. Nevertheless, the spin-flip contribution, which is $\propto TR_2(h/\delta)$, still masks the T^3 GUE term in the low temperature interval: $T \ll \{h, \delta\}$. In the even stronger magnetic field $h=1.62\delta$ (not shown in Fig. 1) practically the whole low temperature interval $T \ll \delta$ is occupied by the unitary ensemble contribution to the specific heat $C_{el}^{GUE}(T) \propto T^3$. The spin-flip term $C_{el}^{sf} \propto T$ is again the strongest one here, as $R_2(h/\delta)$ saturates at $h/\delta \gg 1$: $R_2 \rightarrow 1$. Hence, the spin-flip term mimics the “bulk” behavior at low temperatures $T \leq \delta < h$. Then, at $T \geq \delta$, $C_{el}(T)$, smoothly crosses-over into the “actual” bulk behavior, $C_{el}(T) \propto T$. The two regions are separated by the Schottky contribution, which in this case could be visible only in the $\partial \ln C_{el}/\partial \ln T$ vs. $\ln T$ dependence, but is hardly noticeable in the $C_{el}(T)$ curve (not shown). Furthermore, based on the above discussion, we would expect a direct crossover from the GOE, $C_{el}(T) \propto T^2$ to the bulk $C_{el}(T) \propto T$ behavior of specific heat in zero magnetic field, where the spin-flip contribution is absent. Indeed, this behavior was measured in a series of Pd metal clusters of different sizes ranging from 2 nm to 15 nm in diameter,^{13–15} and is shown in Fig. 2. In this figure the electronic contributions to the specific heat are shown, which were obtained at very low temperatures ($T < 1$ K), by subtracting the phonon (lattice) contributions from the measured data. The special feature of these metal clusters is that they appear as part of chemically synthesized, molecular compounds, each compound containing metal clusters of a given uniform size embedded in a stabilizing ligand shell.^{18–21} The metal cluster compounds mentioned here were made by two different groups, namely that of Profs. Moiseev and Vargafik in Moscow, and the group of Prof. G. Schmid at the University of Essen. The compounds indicated by Pd₅, Pd₇, and Pd₈ contain respectively 561, 1415, and 2057 Pd atoms per cluster. There are

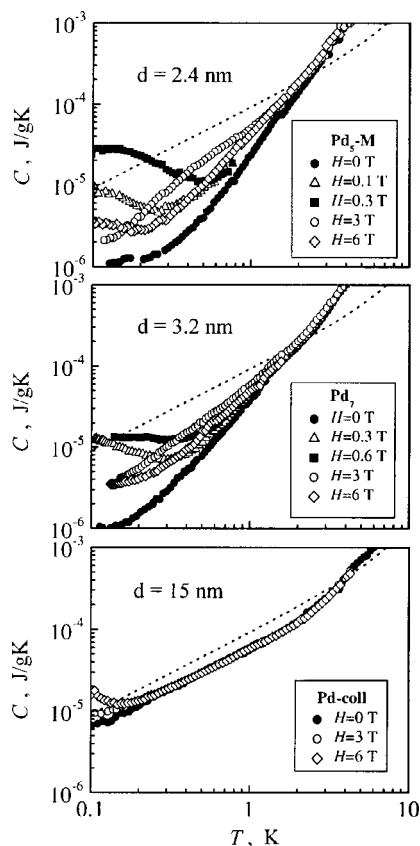


FIG. 3. Temperature dependence of the measured specific heat (including phonon contributions) for Pd₅, Pd₇, and Pd-coll. The dotted curves give the behavior found for bulk Pd.

two Pd₅ compounds, namely with chemical formula Pd₅₆₁Phen₆₀(Dac)₁₈₀ synthesized by Moiseev and Vargaftik (Pd₅-M), and Pd₅₆₁Phen₃₆O₂₀₀ synthesized by Schmid (Pd₅-S). The chemical formulas of Pd₇ and Pd₈ are Pd₁₄₁₅Phen^(bu)₁₁₄O₁₆₅₀ and Pd₂₀₅₇Cinch₅₆, respectively. Here, Cinch stands for cinchonidine, Phen for phenanthroline and Phen^(bu) is a phenanthroline derivative. The sample denoted by Pd-coll is a Pd colloid with average particle size of 1.25×10^5 atoms/particle and a small size distribution of 5–10%. The Pd₇ and Pd₈ metal clusters compounds and the Pd-coll were also synthesized by Schmid and coworkers.

It is worth pointing out that the only adjustable parameter needed to scale the experimental C_{el} vs. T data upon the theoretical curve in Fig. 2 is the average energy level spacing δ . The values used are given in the figure and indeed vary roughly with the inverse volume of the particles, as expected from theory (the particle diameters are approximately 2.4, 3.2, 3.7, and 15 nm for Pd₅, Pd₇, Pd₈, and Pd-coll, respectively). Accordingly, the crossover from quasi-bulk behavior ($C_{el} \propto T$) to the quantum-size regime ($C_{el} \propto T^2$) near $T/\delta = 0.2$ actually occurs at lower temperature, the larger is the particle. This same trend can also be seen in the experimental field dependence of the specific heat, as shown in Fig. 3. It should be pointed out here that the mere presence of a field dependence is in itself a quantum size effect, since the bulk metal will not show such behavior. Comparing the data of Pd₅, Pd₇, and Pd-coll, one observes that the onset temperature of the field-dependence is indeed lower, the larger the particle. We note that the data in Fig. 3 show the raw mea-

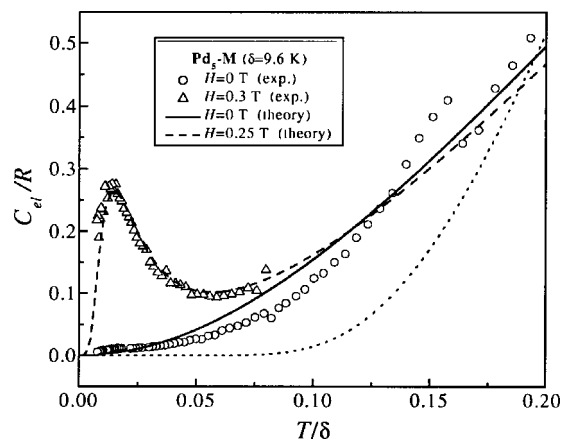


FIG. 4. Temperature dependence of the electronic specific heat of Pd₅ obtained after subtraction of the lattice contribution. Dotted curve: equal level spacing model. The other curves follow from the calculations discussed in the text (compare Fig. 1).

surements, i.e., with the lattice contributions not yet subtracted. The latter give a T^3 term, which becomes rapidly negligible below 1 K, as can be seen most clearly from the Pd-coll data. The specific heat behavior of the bulk Pd has been included in Fig. 3 as the dotted curves. Comparing this with Pd-coll, one observes that for the latter the linear term is still 20–30% lower than for the bulk, which can be understood in terms of a lower average density of states at the Fermi-energy in the nanoparticles due to surface effects.²²

Finally, Fig. 4 shows the field-dependence measured for Pd₅ on linear temperature scale, with the phonon contribution subtracted. The zero-field data clearly display the T^2 dependence predicted for the GOE model, in contrast with the exponential dependence following from the equal level spacing model (dotted curve). The Schottky anomaly found in low field is ascribed to the odd-electron clusters and is in good agreement with the theoretical prediction (also shown in Fig. 1 for $h/\delta = 0.1$).

In conclusion, we have presented theoretical and experimental results describing the quantum-size effects in the thermodynamic properties of nanosize metal clusters with random distribution of the electronic energy levels in different external magnetic field in the few-Kelvin temperature range. The experimental data show a good qualitative agreement with theoretical predictions based on the Wigner–Dyson/Mehta–Pandey random-matrix theory.

We like to thank Prof. G. Schmid for providing the samples quoted in this study. This work is part of the research program of the Stichting voor Fundamenteel Onderzoek der Materie (FOM), which is sponsored by the Nederlandse Organisatie voor Wetenschappelijk Onderzoek (NWO).

DEDICATION

It is our great pleasure to dedicate this paper to the memory of Prof. Lev Shubnikov, who was a prominent visitor of the Kamerlingh Onnes Laboratory in the last century, where, together with Prof. W. J. de Haas. He discovered the famous effect that bears their names. As witnessed by this paper, also recently there have been intensive relations between scientists at the Kamerlingh Onnes Laboratory and the

former Soviet Union. It is our hope that these fruitful collaborations, from which we have had so much profit and pleasure, will be an inspiration for future workers to continue and intensify scientific exchange worldwide.

*E-mail: sergeimoscow@online.ru and sergei@lorentz.leidenuniv.nl

**E-mail: sergei@lorentz.leidenuniv.nl

¹T. Guhr, A. Müller-Groeling, and H. A. Weidenmuller, *Phys. Rep.* **299**, 189 (1998).

²C. W. J. Beenakker, *Rev. Mod. Phys.* **69**, 731 (1997).

³W. P. Halperin, *Rev. Mod. Phys.* **58**, 533 (1986).

⁴J. A. A. J. Perenboom, P. Wyder, and F. Meier, *Phys. Rep.* **78**, 175 (1981).

⁵E. P. Wigner, *Proc. Cambridge Philos. Soc.* **47**, 790 (1951); E. P. Wigner, in *Statistical Theories of Spectral: Fluctuations*, edited by C. E. Porter, Academic Press, New York (1965).

⁶F. J. Dyson, *J. Math. Phys.* **3**, 1199 (1962); F. J. Dyson and M. L. Mehta, *ibid.* **4**, 701 (1963).

⁷See C. E. Porter (Ed.), *Statistical Theories of Spectra: Fluctuations*, Academic Press, New York (1965).

⁸R. Kubo, *J. Phys. Soc. Jpn.* **17**, 975 (1962).

⁹L. P. Gor'kov and G. M. Eliashberg, *Zh. Eksp. Teor. Fiz.*, (1965) [*Sov. Phys. JETP* **21**, 940 (1965)].

¹⁰R. Denton, B. Muhlshlegel, and D. J. Scalapino, *Phys. Rev. B* **7**, 3589 (1973).

¹¹K. B. Efetov, *Adv. Phys.* **32**, 53 (1983).

¹²S. I. Mukhin and O. V. Kurapova, manuscript in preparation.

¹³Y. E. Volokitin, Ph.D. Thesis Leiden University (March, 1997).

¹⁴Y. E. Volokitin, J. Sinzig, L. J. de Jongh, G. Schmid, M. N. Vargaftik, and I. I. Moiseev, *Nature (London)* **384**, 621 (1996).

¹⁵F. L. Mettes, Ph.D. Thesis Leiden University (in preparation).

¹⁶A. Pandey and M. L. Mehta, *Commun. Math. Phys.* **87**, 449 (1983).

¹⁷H. Frolich, *Physica* **4**, 406 (1937).

¹⁸M. N. Vargaftik, V. P. Zagorodnikov, I. P. Stolyarov, I. I. Moiseev, V. A. Likholobov, D. I. Kochubey, A. L. Chuvilin, V. I. Zaikovskiy, K. Zama-raev, and G. I. Timofeeva, *J. Chem. Soc. Chem. Commun.* **937**, 1985 (1985).

¹⁹G. Schmid, *Chem. Rev.* **92**, 1709 (1992); G. Schmid, *Struct. Bonding (Berlin)* **62**, 5285 (1985).

²⁰*Clusters and Colloids: From Theory to Applications*, G. Schmid (Ed.), VCH, Weinheim (1994).

²¹*Physics and Chemistry of Metal Cluster Compounds*, L. J. de Jongh (Ed.), Kluwer Academic, Dordrecht (1994).

²²D. A. van Leeuwen, J. M. van Ruitenbeek, and L. J. de Jongh, *Phys. Lett. A* **170**, 325 (1992).

This article was published in English in the original Russian journal. Reproduced here with stylistic changes by AIP.